Let's do the Twist

Chiral Information Transfer in Self-Assembled Supramolecular Functionalised Coiled-Coils

Danielle Aria Liebnitz

Submitted in fulfilment of the requirements for the Degree of Doctor of Philosophy

School of Chemistry
College of Science and Engineering
University of Glasgow
April 2025

Author's Declaration

I declare that, except where explicit reference is made to the contribution of others, that the substance of this thesis is the result of my own work and has not been submitted for any other degree at the University of Glasgow or any other institution.

_____

Danielle Aria Liebnitz

Acknowledgements

I've met a lot of people throughout my time as a PhD student who have told me in no uncertain terms that at some point, yes, you will want to quit and that you will question whether or not you even are good enough to be here. As nice as it is to know you aren't alone and that imposter syndrome does in fact come to us all, as a glance into your mental state for the next three and a half years of your life, it's absolutely terrifying! At some point during that time, my mindset was flipped, and I realised that if something is important to you, and you want to do it, even if it frightens the life out of you, just do it while scared.

The first person I must acknowledge is my supervisor, Dr Drew Thomson, because without him I wouldn't even be writing this. Drew has been incredibly helpful in developing my confidence and honestly just believing that I know what I'm talking about. When I started my PhD, I was painfully shy and very unlikely to speak up if I disagreed with someone's science, not to mention a little bit rusty in the lab (thanks Covid). Through Drew's (sometimes lengthy) discussions of science and constant optimism that my project would in fact work out, I now back myself and my ideas a lot more and most importantly, I think I am a much better scientist now, thanks to him. This is a good point to also thank my second supervisor Prof. Ross Forgan for his invaluable help with inorganic chemistry and support throughout my studies. In addition to this all of the technical staff in the School of Chemistry were astronomically helpful throughout my time so a thanks must also be extended to them.

There's no easy way to thank your family for putting up with your constant complaining that you are tired, broke and that your experiments aren't ever working, but I'm about to try so bear with me. Everyone in my family has always supported my academic interests, from encouraging me by asking for a 'fun fact of the day' when I was in school, to listening to me run through all my presentations during my undergrad, to now, where they still listen to me ramble on about 'whatever a coiled-coil even is'. They might not have a clue what I'm talking about anymore but without a doubt they always try and understand, and most importantly, have given me their unwavering support and without that I would've given up a long time ago.

Coming into this experience I never expected to meet as many people that I can now call my best friends, and yet here we are. Working in this shared office where I am sitting writing right now, I can look all around me and see people who I spend Friday nights at the pub with, people I can have a joke with, people who will go on unreasonably long coffee breaks with me and people who would not judge me for sneaking away to have a cry in the bathroom

when the work gets a little too overwhelming. I think the shared experience of all doing a PhD can bring people together, and maybe that's because we have all bonded over mutual stress, or our shared love of science, either way I don't care, because thanks to them, the days in this office have always been bearable.

Last but certainly not least I need to acknowledge the three people who mean the most to me in the world and have been there for me during the most stressful times during this PhD. First my partner, Matthew. Since we met, he has been an absolute star, providing constant reassurance that I'm not a terrible scientist I am in fact just tired and/or hungry, and especially for coming to visit me every time I had to spend an afternoon in the dingy basement where they keep the CD. I will be thanking him for the rest of my life because he gives me the confidence that I need to be good at what I do. Secondly, my cats, Captain and Skipper. A day in the lab can be long and hard sometimes and coming home and still being meowed at by a cat that wants nothing else except his dinner is incredibly humbling. They don't particularly care that I've been in the lab all day as long as I'm there for breakfast and dinner, they do really help my work life balance. All jokes aside, seeing those little guys everyday keeps me going, I owe many smiles to them.

Finally, thanks for sticking with me there, I want to thank you, for reading this work, making it to the end of my soppy acknowledgements, and hopefully, deciding to give me my PhD.

For my childhood self, who used to dream of being able to call herself Dr Liebnitz.

Table of Contents

List of Abbreviations

8-HQ	8-Hydroxyquinoline
AA	Amino Acid
AFM	Atomic Force Microscopy
Ala/A	Alanine
Arg/R	Arginine
Asn/N	Asparagine
Asp/D	Aspartic Acid
Boc	Tert-Butyloxycarbonyl
Bpy	Bipyridine
CC	Coiled Coil
CD	Circular Dichroism
CuAAC	Copper(I) Azide Alkyne Cycloaddition
Cys/C	Cysteine
DCM	Dichloromethane
DIC	*N,N*′-Diisopropylcarbodiimide
DIPEA	*N,N*-Diisopropylethyl Amine
DMF	*N,N*-Dimethylformide
DNA	Deoxyribonucleic acid
EDC	1-Ethyl-3-(-3-dimethylaminopropyl)carbodiimide
EtOAc	Ethyl Acetate
Et_2O	Diethyl Ether
Fmoc	Fluorenylmethoxycarbonyl
Glu/E	Glutamic Acid
Gln/Q	Glutamine

Gly/G	Glycine
His/H	Histidine
HPLC	High Performance Liquid Chromatography
HR-MS	High Resolution Mass Spectrometry
Ile/I	Isoleucine
LC-MS	Liquid Chromatography Mass Spectrometry
Leu/L	Leucine
Lys/K	Lysine
MD	Molecular Dynamics
Met/M	Methionine
MIM	Mechanically Interlocked Molecule
MOPS	(3-(*N*-Morpholino)propanesulfonic Acid
MRE	Mean Residue Ellipticity
MS	Mass Spectrometry
NMR	Nuclear Magnetic Resonance
PEG	Polyethylene Glycol
Phe/F	Phenylalanine
Phen	Phenanthroline
Pro/P	Proline
PyBOP	Benzotriazole-1-yloxytripyrrolidinophosphonium Hexafluorophosphate
Pytri	Pyridine-Triazole
rt	Room Temperature
RT	Retention Time
Ser/S	Serine
SPPS	Solid Phase Peptide Synthesis

TEM	Transmission Electron Microscopy
TCEP	(Tris(2-carboxylethyl)phosphine)
TFA	Trifluoroacetic Acid
TIPS	Triisopropylsilane
Trp/W	Tryptophan
Tyr/Y	Tyrosine
UV-Vis	Ultraviolet-Visible
Val/V	Valine

Abstract

Chirality is an inherent feature of life and can be found across many natural systems, from DNA to snail shells. This concept spans from the molecular level, up to visible phenomena at the macroscale, with each step in this increasing scale influencing the next as a result of chiral information transfer. Despite the prevalence of chirality across the scientific field, the exact mechanisms and controls of chiral information transfer are poorly understood.

To aid in the understanding of these mechanisms, a model system taking advantage of the innate chiral information transfer in the self-assembly of peptide sequences, known as coiled coils, has been developed and investigated in this work. By modifying these sequences to feature an aromatic chelating unit at the N-terminus, this work demonstrates a cooperative relationship in which the aromatic chelating units (2,2′-bipyridine and 8-hydroxyquinoline) enhance the α-helical character of the peptide assembly, while the chiral information from the peptide is simultaneously transmitted to the complex, resulting in a chiral bias for one-handedness of the resulting complex.

After discussion of the relevant literature in Chapter 1, Chapter 2 of this work introduces the chiral information transfer exhibited by the coiled coils onto the coordination complex. This chapter focuses on the stabilisation of a homotrimeric coiled coil peptide sequence by the introduction of an aromatic chelating unit (bipyridine/phenanthroline) to the N-terminus of the peptide sequence. It was found that the sequences resulted in the preferential formation of the Δ-[tris-bpy]-peptide and Δ-[tris-phen]-peptide complexes in response to coordination with first row transition metals, Co^{2+}, Ni^{2+}, Cu^{2+} and Zn^{2+}. Furthermore, a cooperative relationship between the degree of coiled coil helicity and the degree of chiral bias in the resulting complex has been uncovered, with sequences with more helical character exhibiting more chiral preference as a result. Through comparison to non-helical sequences, it was shown that the chirality of the complex occurs as a result of the helicity of the peptide and not the inherent chirality of the amino acid subunits.

In Chapter 3, the structural tolerances of this cooperative relationship have been investigated. By variation of sequence length, helical content, register position and the distance of the 2,2′-bipyridine from a chiral centre on the peptide, 17 coiled coil forming peptides were synthesised and investigated. By altering these aspects of the structure, it was found that preference for the Δ- and Λ-isomers of the complex can be controlled by altering the register position of the chelating unit, with the *d*-position being found to favour the Δ-isomer and the

e-position favouring the Λ-isomer. Furthermore, the strength of this preference can be controlled by altering the proximity of the chelate to a chiral centre. The identity of the achiral spacers, however, have been found to be an important factor, their ability to H-bond in an *i*-*i*+4 pattern being crucial for continuation of the α-helical turns.

In Chapter 4 an alternate chelating unit, 8-hydroxyquinoline, is investigated. The coordination of this ligand to transition metal ion Co^{2+}, and p-block metal ions Ga^{3+} and Al^{3+} has been investigated and analysed by circular dichroism and UV-absorbance spectroscopy. The preferential formation of Δ-tris-(8HQ-peptide) and Λ-tris-(8HQ-peptide) complexes were found to be controlled by alteration of the 8-HQ register position, with 8-HQ in the *d*-position favouring the Λ-isomer and 8-HQ in the *e*-position favouring the Δ-isomer. The behaviour of these systems in response to pH was also investigated in this chapter and aims to show that the differences between the 2,2′-bipyridine and the 8-HQ chiral preferences are as a result of H-bonding interactions between the 8-HQ chelating units and the peptides.

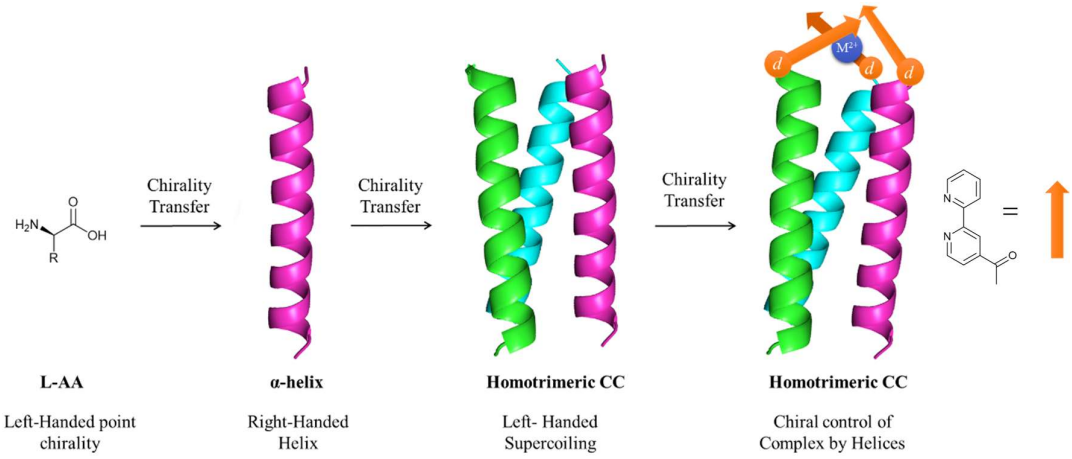

Graphical Abstract – Cartoon representation of the transfer of chiral information in the systems investigated in this thesis. The information is transferred from the point chirality in the amino acid structures (L-AAs), to helical chirality in the secondary structure (*P*-Helices), to folding of the super-secondary structure into the opposite handedness helical chirality (M-Supercoiling) and finally, controlling the directionality of an 6-coordinate complex at the N-terminus of the sequence (Λ/Δ).

1. Introduction

1.1 Scope

The concept of chirality or asymmetry is found all across nature and can be observed from the molecular level, in the point chirality of D-nucleic acids and L-amino acids, to the macroscopic, in the helicity of plant tendrils and snail shells or the asymmetrical distribution of organs in the body.[1-3] Chiral information from the molecular level is transmitted up length scales, influencing what can be seen at the macroscale, but the mechanisms in which this information is communicated are poorly understood.[4-7] Pioneering studies by Pasteur in the mid-19th century discovered this concept of chiral communication across length scales. By observation of the optical rotation enantiomers of tartaric acid and microscopic visualisation of their resulting enantiomeric crystal formations, he found that the different enantiomers formed opposite handedness crystals.[6, 8, 9]

Biological systems exhibit chiral bias, or homochirality, in the building blocks for life i.e., natural amino acids are found in the L-configuration. Amplification of this chirality up into structures such as peptides, proteins and carbohydrates means that understanding the underlying mechanisms and relationships is incredibly important in research areas such as pharmaceuticals, and agrochemicals.[7] Many examples of enantiomers that exhibit different behaviours within a chiral environment exist, such as the difference in smells of *R*- and *S*-carvone[10] and the pharmaceutical efficacy of *S*-citalopram compared to the less effective *R*-enantiomer.[11] One pertinent example of this is the thalidomide crisis of the late 1950s in which a racemic mixture of the drug was marketed irrespective of differences in biological activity in humans between the *R*- and *S*- enantiomers.[10, 12] As the use of biologics such as peptides and proteins, both large and small becomes more widespread in pharmaceuticals with more than 80 peptide drugs having been approved as of 2022,[13, 14] increasing understanding of the chirality inherent in these systems would aid in their design and development. The prevalence of chirality also spans into the inorganic space, gaining attention in areas such as materials science[15] and nanotechnology,[16] particularly in the synthesis and uses of chiral nanostructures[17] and chiral surfaces.[18] A significant quantity of this research utilises an organic chiral auxiliary to induce chirality in the final self-assembled structures.

As a means of elucidating principles behind chiral induction across length scales, peptides have been chosen to act as a model system. Their inherent chirality in their amino acid subunits transfers up to their secondary structure, most notably in the formation of right-handed α-helical units. The mechanisms responsible for this are well understood and further translate into the formation of super secondary structures, in this case left-handed coiled coils. Following from this, the work in this thesis aims to investigate a further step in the length scale by synthesising a series of coiled coils featuring different metal binding sites. These peptides can self-assemble into supramolecular peptide assemblies both before and after metal is introduced to the system, and through varying the attachment site of the metal chelator, distance from a chiral centre, and identity of the metal, different enantiomers of the metal complex can be obtained.

1.2 Peptide Structure

Peptides are small biological polymers which play significant and versatile roles in many of natures essential processes, from facilitating the transfer of molecules around the body to regulation of cellular processes. Their versatility, specificity, basis in nature, and relatively simple synthesis have led peptides to become increasingly popular targets in drug development, mimicking and adapting natural hormones such as oxytocin and insulin, or being used as delivery agents in which cell targeting or penetrating peptides are attached to a drug payload.[13, 19] The behaviour exhibited by peptides is a direct result of their molecular structure and composition, folding and whether they have associated metal ions and/or cofactors. Some examples of the structure-function relationship include the association of Fe^{2+} in the quaternary structure of haemoglobin, the secondary structure of α-helical DNA binding transcription factors, and the folding of zinc finger proteins by the coordination of a Zn^{2+} ion to His and Cys residues.[20, 21]

Peptide structure can be separated into four levels, with each level impinging on the next, these are commonly known as the primary, secondary, tertiary and quaternary structures. These terms describe not only the molecular structure of the peptide, but also the behaviour of this peptide in 3D space and its relationship to other molecules, for example the formation of dimers, trimers, etc, or the association of a metal ion.[22]

1.2.1 Primary Structure

The primary structure of a peptide describes the sequence of its basic polymer units, amino acids (AA), linked together by condensation reactions forming amide bonds and conventionally depicted right to left from C- to N-terminus. There are 20 proteinogenic amino acids each with a unique side chain or R-group (**Figure 1.1**) which living organisms utilise to synthesise their peptides and proteins. A rare 21st proteinogenic AA does exist which is an analogue of cysteine, called selenocysteine (Sel) however it is outwith the scope of this work.[23] The R-groups of the AAs are ultimately responsible for determining the final shape, charge and functionality of the resulting peptide as a consequence of non-covalent interactions such as hydrogen bonding and π-stacking between their functional groups. As shown in **Figure 1.1**, R-groups can be classified into four groups; polar neutral, polar charged, hydrophobic, and other, with a separate category for glycine and proline, whose

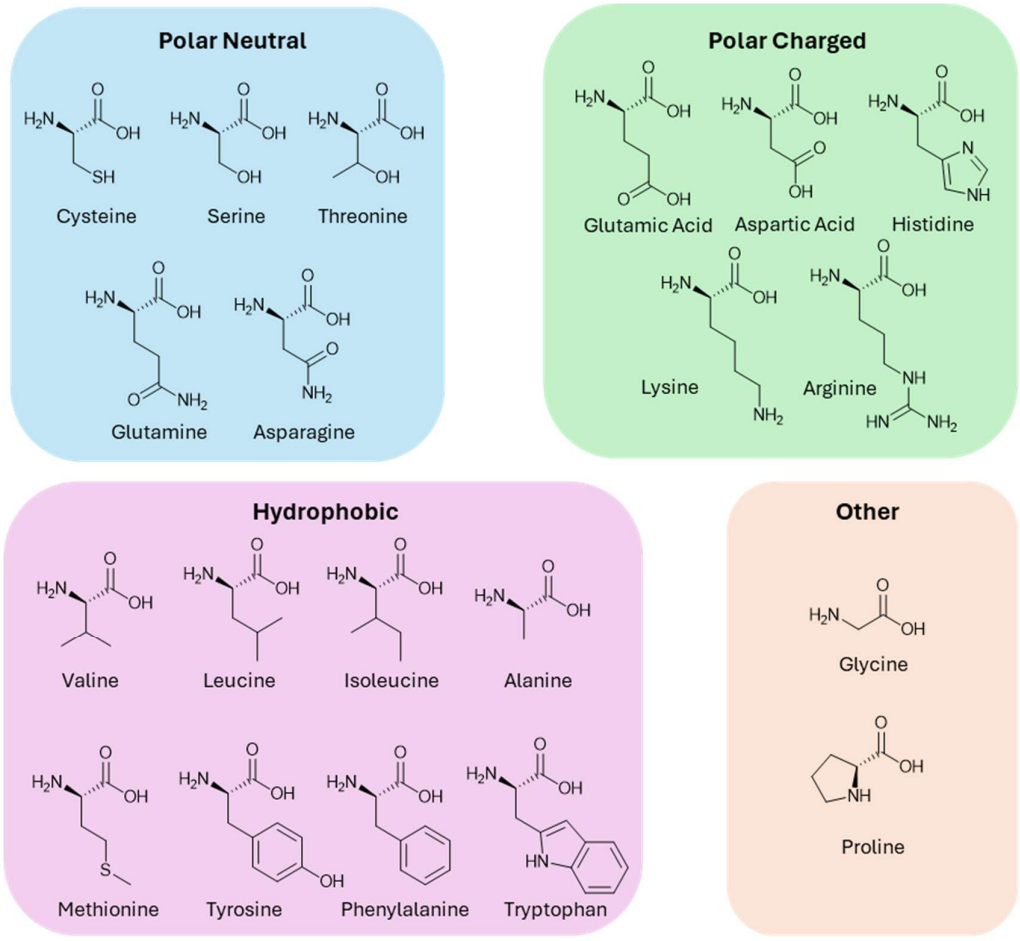

Figure 1.1 - Structures of the 20 proteinogenic amino acids, categorised by their side chains, polar neutral, polar charged, hydrophobic and other. All are shown as the L-enantiomer.

structures cannot be definitively held within the specific restraints of the other three. Proteinogenic amino acids (excluding glycine) can also be characterised by their chirality, which is biased to the L-enantiomer. Signalled by the presence of an asymmetric carbon (the α-carbon), the proteinogenic AAs are defined as being 'point chiral', i.e. asymmetric about a single atom (point) in the molecule. Homochirality in the primary structures of peptides directly influences that of the secondary structure that will ultimately be adopted by the final molecule.

1.2.2 Secondary Structure

Secondary structure of a peptide or protein refers to the folding of the AA chain into more complex 3D conformations when solvated. This folding occurs as a result of non-covalent interactions, mainly hydrogen bonding, between AAs intramolecularly. Common secondary structures adopted by peptides include *α*-helices, *β*-sheets and *β*-turns, all of which will contribute to the overall topology and resulting functionality of the peptide.[22, 24] The secondary structure of a peptide is characterised by repeating dihedral (φ and ψ) angles. The correlation between the dihedral angles and the secondary structure of a peptide is summarised in the Ramachandran plot (**Figure 1.2**).[25]

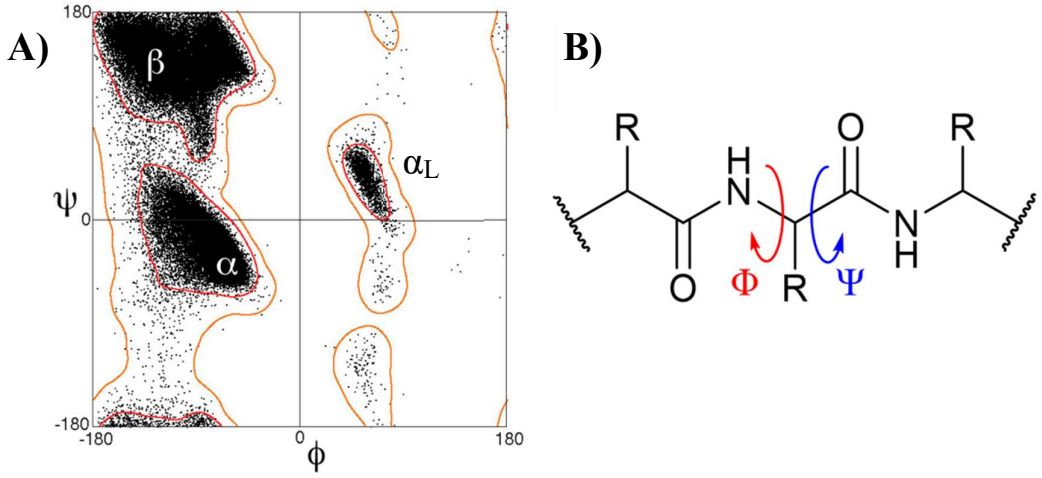

Figure 1.2 - A) General Ramachandran plot reproduced from Lovell *et al* 2003[25] **B)** ChemDraw representation of the dihedral angles of the amide bond which form the basis of the Ramachandran plot.

1.2.2.1 α-Helices

The *α*-helix is the most common secondary structures adopted by peptides and proteins.[22] First described by Pauling in 1951,[26] their structure is characterised by 3.6 AA (5.6 Å) repeating units known as helical turns, with average dihedral angles of φ = -61°, ψ = -41°.[27-29] These turns are stabilised by *i-i+4* H-bonding interactions with a distance of approximately 2.75 Å, between the carbonyl oxygen and the amide hydrogen of the peptide backbone, forming the characteristic spiral (**Figure 1.3**). In designing an α-helix, AAs such as alanine, glutamic acid, leucine and methionine are typically favoured. Whereas proline, glycine, tryptophan and tyrosine are avoided as they tend to be 'helix-breaking'. These unfavoured amino acids can cause destabilisation of the helix as a result of side chain steric clash, or in the case of proline, have incompatible dihedral angles, likely rendering that conformation thermodynamically unstable. Proline can be tolerated in some cases, but these tend to include that AA at an N- terminus.[24, 30] Due to the entropic mismatch of the beneficial H-bonding interactions and the steric interactions associated with folding, typically short peptide based α-helical structures are not observed outside of larger protein structures. Typically, upwards of 15 AAs are required for a short *α*-helical peptide, unless other stabilising interactions are present within the structure.[31]

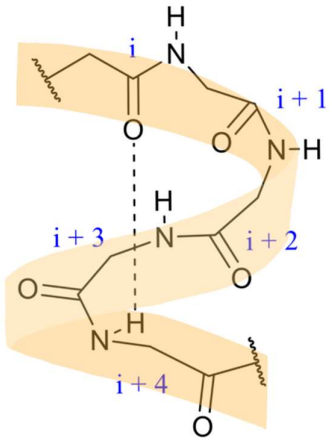

Figure 1.3 - Representation of the H-bonding *i* – *i*+ 4 interaction in an α-helical turn unit, side chains omitted for clarity.

In relation to asymmetry, as a result of homochirality, typically natural α-helices favour the right-handed or *P*-conformation. Visualisation of the Ramachandran plot shows that the α_L

(left-handed α-helix) region is scarcely populated (**Figure 1.2**).[25, 28, 32, 33] Theoretically, formation of an α_L-helix would lead to a large energetic penalty due to steric interactions between the peptide backbone and the R-groups of the L-AAs, which is what makes them rare in nature.[34, 35] Synthesis of left-handed or *M*-helices is possible using oppositely handed AAs, but those that have been reported tend to feature majority glycine residues.[36]

Regarding terminology, the asymmetry of the secondary structure is no longer fixed about a single point like its substructure, now it is topological and fixed about an axis, termed helical or axial symmetry, and labelled as either, *P* or + (right-handed), or *M* or – (left-handed). Distinguishing between these two isomers can be done relatively simply using the 'rule of thumb' depicted in **Figure 1.4**.

By using the thumb as an axis and following the direction of the fingers as if they were the helix, the direction the fingers are pointed represents the direction that the helix is coiling.

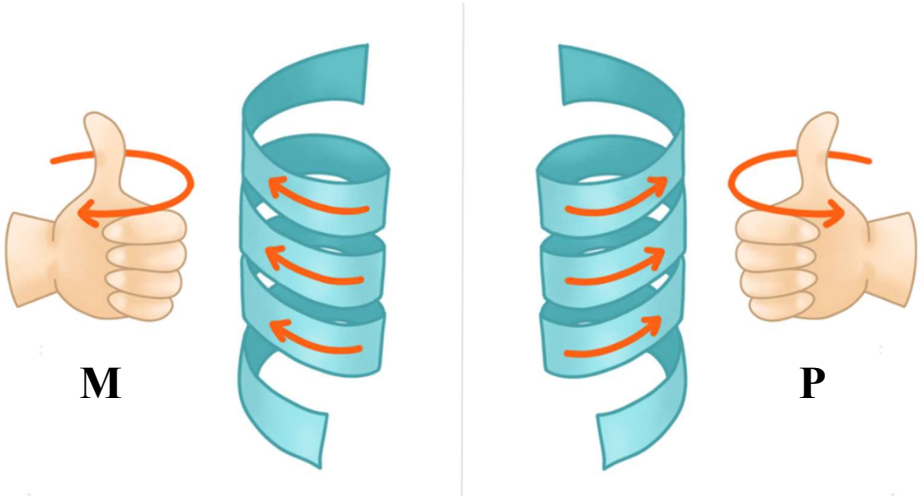

Figure 1.4 - Cartoon representation of helical chirality and enantiomer determination by 'rule of thumb' with an M-helix depicted on the left and a *P*-helix depicted on the right.

1.2.2.2 Coiled Coils

A subset of the structural degrees of peptides discussed earlier in Section 1.2 is the super-secondary structure. This intermediate stage of peptide structure falls between the secondary and tertiary structures and involves the specific arrangement of two or more secondary structural elements, for example, coiled-coils (CCs), helix-turn-helix motifs and leucine

zippers.[37, 38] Comparatively, the tertiary structure, as will be discussed, describes the overall folding leading to the 3D conformation of the final peptide or protein.

As mentioned, CCs are an example of one of these structural motifs (**Figure 1.5**). First described by Crick in 1952, coiled-coils form due to self-assembly processes which coil together multiple helices by packing side chains like 'knobs' into adjacent 'holes' of an another strand.[39] Formation of these structures relies on solvophobic interactions and are routinely stabilised by inter-strand salt-bridges. Typically, in design of a CC the heptad repeat (*abcdefg*) is used with its composition generally following a pattern of HPPHPPP (H = Hydrophobic, P = Polar). This generates an amphipathic helix displaying both a polar, solvent exposed face, and a hydrophobic face. During the self-assembly process the hydrophobic faces of the helices will align, with the hydrophobic *a* and *d* residues of the adjacent strands packing together in the manner described above.[40, 41]

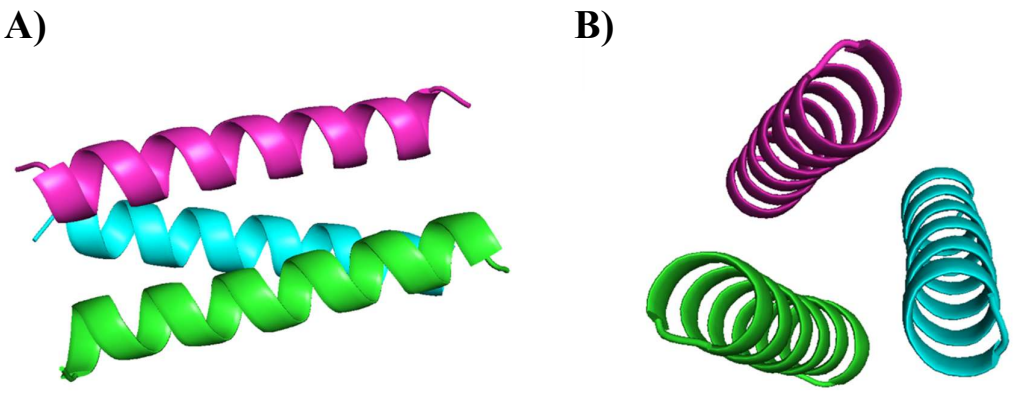

Figure 1.5 - Cartoon depiction of a short trimeric coiled coil assembly **A)** Side-View **B)** End-View looking from the N-terminus.

A common and simple representation of the interactions governing the CC are helical wheel diagrams (**Figure 1.6**), which can be used as a design tool. When designing a synthetic CC sequence, the content of each position of the heptad is of vital importance. Early studies by Harbury *et al,* in 1993 found that altering the content of the *a* and *d*-positions of the heptad repeat of a leucine zipper peptide (GNC4-p1) between different combinations of Isoleucine (Ile) and Leucine (Leu), could lead to the preferential formation of dimers, trimers and tetramers. By including Ile at an *a*-position and Leu at *d*-position, dimer preference was observed. Changing this such that both positions were altered to Ile, trimers were preferred. Tetramer formation was preferred when expressing Leu at an *a*-position and Ile at a *d*-position.[42] Further investigation reported by Fletcher *et al.* in 2012 found that despite the reproducibility of the trimeric and tetrameric systems with their *de novo* sequence, the dimer

system instead resulted in trimer formation both in solution and when in its crystal state, suggesting Harburys findings were particular to the GCN4 sequences. It was found within Fletchers work that to obtain preference for the dimeric system that substitution of a central *a*-position Ile for an asparagine (Asn) residue would lead to the desired dimeric CC. This substitution acts to destabilise the trimer formation forcing the dimer formation as an alternative and indicates the close energetic relationship.[43]

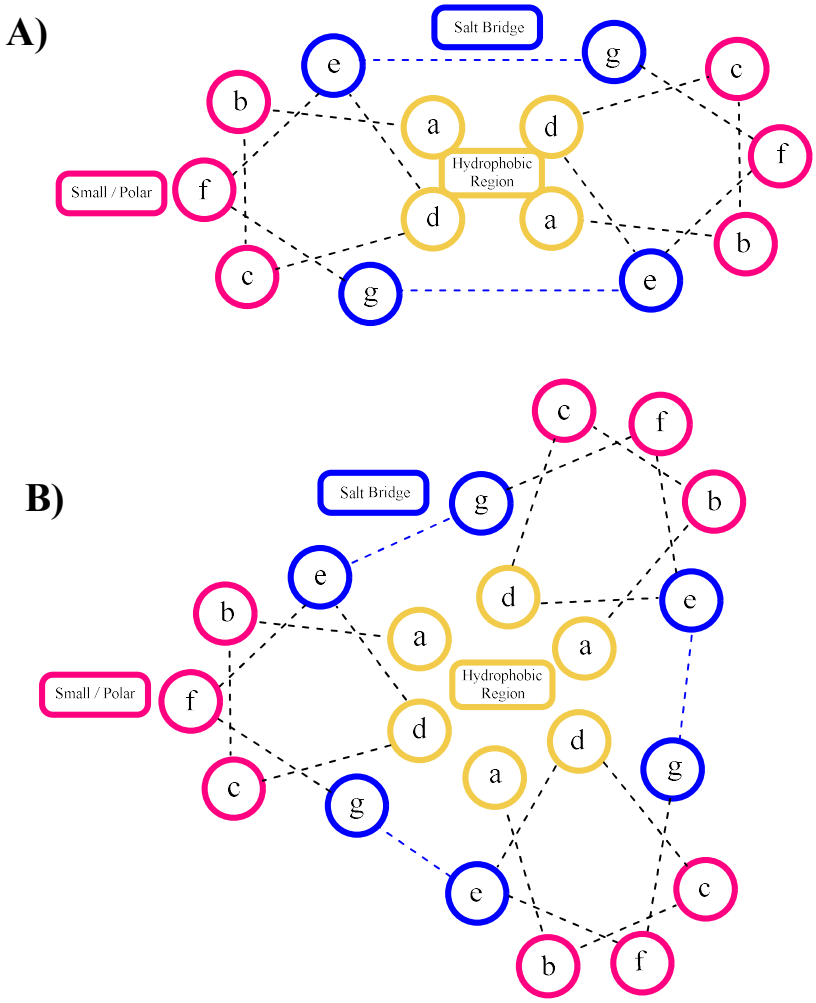

Figure 1.6 - Helical wheel representations of the interactions occurring in coiled coil assemblies. **A)** dimeric coiled coil **B)** trimeric coiled coil.

With respect to the asymmetry displayed by these conformations, generally a CC which follows the heptad repeat design will exhibit supercoiling of the opposite helical-handedness to the helices that comprise it, i.e. a CC made up of *P*-helices will result in an *M*-supercoiling of the CC.[44] Despite this, *P*-supercoiling has been reported in sequences that follow an eleven AA repeat format.[45] The supercoiling that occurs in CC structures leads to a shorter periodicity of 3.5 AAs (5.1 Å), than what is typically found for *α*-helices, 3.6 AAs.[26] This

comes about due to bending of the helices to allow for the side chain packing between strands and ultimately leading to the supercoiling as the helices wind around each other forming the favourable interstrand contacts.[46]

1.2.3 Tertiary and Quaternary Structures

Further folding of larger peptides and proteins results in the formation of tertiary and quaternary structures.

Tertiary structures are the result of peptide or protein folding in response to non-covalent interactions, i.e. hydrophobic/solvophobic, charge-charge and π-stacking interactions. The interactions that lead to tertiary structures occur over a larger area than the close-proximity side chain and backbone interactions that result in secondary and supersecondary structures and are therefore more applicable to larger peptides.[47, 48] Examples of tertiary structures include globular and fibrous conformations.

The quaternary structure is more common among larger peptides and proteins. These structures are characterised by the association of two or more peptide/protein subunits. These multimer peptides can exist as either homo- or hetero-conformations, depending on their composition. Quaternary structure also can include the association of a metal to a protein.

1.3 Non-Covalent Interactions and Self Assembly

Non-covalent interactions (NCIs) are vitally important for the control of self-assembly processes. Self-assembly involves the directed organisation of a system relying on interactions between the component parts of that system.[49] The direction of the organisation is dependent on NCIs such as, hydrogen bonding, π-stacking, charge-charge interactions and solvophobic interactions, acting individually or in concert.

The most relevant example to this work is the self-assembly of peptide sequences into their primary, secondary, tertiary and quaternary structures. As has been covered thus far it is well documented that these assemblies rely on a combination of NCIs to act synergistically in order for the formation of the final ordered structure. The interactions act in unison to allow the system to reach a favourable, energetic minima, reducing the free energy of the system while simultaneously maximising the attractive interactions between the components.

Additionally, because self-assembled systems are typically governed by NCIs their assembly is reversible, and therefore can be controlled by external stimuli such as pH or temperature.[50]

1.3.1 Hydrogen Bonding

Hydrogen bonding is an electrostatic, dipole-dipole interaction which arises between a hydrogen bond donor (δ+) and a hydrogen bond acceptor (δ-). First defined by Pauling in 1931 the hydrogen bond has been an important consideration in both biological systems and synthetic chemistry.[29, 51, 52] When a hydrogen atom is bound to an electronegative atom such as a nitrogen, oxygen or one of the halogens, this creates a δ+ pole on the H as the electron density is drawn towards the more electronegative atom. This δ+ H can act as a H-bond donor to an electronegative atom with a δ- pole, such as a N, O or halogen lone pair. Comparative to most other NCIs that will be discussed (with the exception of charge-charge interactions), H-bonding interactions are considered strong, with this strength dependant on the identity of the donor/acceptor pair and their relative electronegativity or pK_a values as well as the environment in which the system exists.[51, 53] In aqueous solutions of peptides and proteins the H-bonds that contribute to the secondary structures have been reported to have a strength of between 0.5-1.5 kcalmol^{-1}, however this is dependent on solvent and is theoretically larger in magnitude in non-aqueous environments as a result of less competition with the solvent for H-bonding.[54]

In biological systems H-bonds will typically form between H, O, N and S atoms, however, these interactions can occur with any atoms which have a strong enough dipole. As has been discussed earlier, H-bonds are the foundation of the secondary structure of peptides and proteins, forming between the amide NH and carbonyls of the backbone resulting in folding in structures such as α-helices and β-sheets. In addition to this they are responsible for the selectivity of the coupling of the DNA base pairs, A/T and C/G together forming the characteristic double helix (**Figure 1.7**).

H-bonds will typically have a bond distance between 2.7–3.3 Å measured between the heavy atoms (N–O). The stronger of these bonds having a shorter bond distance and *vice versa* for the weaker H-bonds.[51, 54, 55]

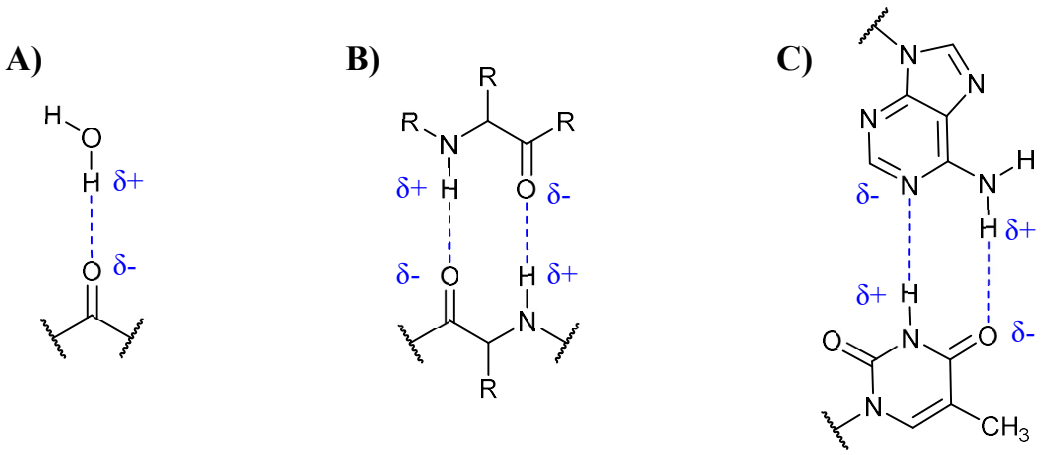

Figure 1.7 - Examples of H-bonding **A)** carbonyl to water molecule **B)** H-bonding interactions in peptide backbones **C)** DNA base pairs A and T.

1.3.2 π-Stacking

Aromatic interactions are widely used in the construction of self-assembling supramolecular assemblies. These interactions are attractive forces which occur between the δ- and δ+ poles of aromatic structures, depending on their orientations (see **Figure 1.8**). Aromatic stacking is typically reported in three different orientations; stacked, off-set stacked and edge-to-face. The order of stability of these orientations is generally reported as; edge-to-face ≈ offset stacked > stacked. This order of stability occurs as a result of the electrostatic orbital interactions.[56] From **Figure 1.8** it can be seen that the stacked conformation contains a repulsive interaction between the electron rich π-orbitals of the two rings being in close proximity to one and other. To combat this, the offset stacked orientation aligns the electron rich (δ-) π-orbitals with the electron poor (δ+) H-orbitals, forming a favourable attractive interaction.[53] Edge-to-face stacking is considered the most favourable interaction in theory, due to the favourable overlap of the π-orbital of one ring and the σ*-orbital of the other, whilst having the two π-orbitals as far from each other as possible but still close enough for the attractive interaction to occur. In practise the stability of the offset stacked and the edge-to-face orientations tend to be quite similar. The relative stability of these interactions depends on the identity of the aromatics included in the system, with the above interpretation being based on simple benzene rings.[56]

With heteroaromatic systems such as bipyridine, phenanthroline and hydroxyquinoline which will be the focus of this thesis, these interactions will occur differently. Using pyridine

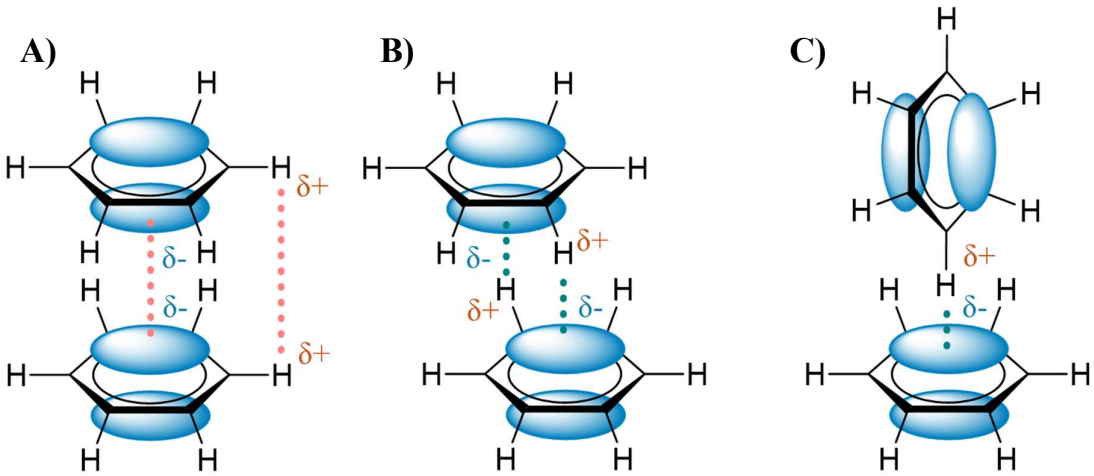

Figure 1.8 - Orbital interactions of common aromatic stacking interactions. **A)** Stacked arrangement **B)** Offset stacked orientation **C)** Edge-to-face orientation.

as a simple example the presence of a heteroatom, in this case nitrogen, in the aromatic ring results in a dipole within ring due to the relative electronegativities of N (3.05) and C (2.55).[57] This results in the electron density being oriented towards the N atom, reducing the repulsive interactions between the π-orbitals of adjacent rings. This ultimately makes the relative stabilities of each of the geometries of π-π interactions more comparable in the case of heteroaromatics.[58] An extreme example of this is the stability of the stacked conformations of hexafluorobenzene with benzene. Due to the substitution of electronegative fluorine atoms at each carbon of the benzene ring, the quadrupole moment of the benzene is completely reversed, resulting in a favourable interaction between the two when directly stacked or in the offset conformation.[56]

Similar to H-bonding, aromatic interactions play important roles in the structural arrangements of peptides and proteins as well as the formation of the DNA double helix. With respect to peptides, there are four proteinogenic AAs with the capacity for aromatic interactions; histidine, phenylalanine, tryptophan and tyrosine.[59] These residues can frequently be found in the interior of globular proteins such as parvalbumin, which have been suggested to form structurally stabilising aromatic interactions and likely contribute to their folding.[60, 61] Studies by Serrano *et al*. found that solvent exposed Tyr residues on an α-helical segment of the barnase protein interacted in a stabilising edge-to-face configuration contributing a stability of -1.3 kcalmol^{-1}.[62] Another study by Butterfield *et al.* included the design of short (19-24 AA) peptides with designed *i*-*i*+4 aromatic interactions between a

series of natural and non-natural aromatic AA sidechains. The data in this study suggested that the π-stacking interactions between the aromatic AAs stabilised the α-helicity of the peptides and in some cases could double the overall helicity of the peptide when measured by circular dichroism.[61]

1.3.3 Charge-Charge interactions

Charge-charge or ionic interactions were mentioned briefly in the context of peptide super-secondary and tertiary structures. They are often associated with CC structures as charged side chain interactions hold the CCs together and make their formation more thermodynamically favourable.[63]

In peptides and proteins, charged side chain interactions can occur between positively charged side chains of residues such as, Arg, His or Lys, and negatively charged side chains of residues Asp or Glu (**Figure 1.9**). These interactions form stabilising interactions intra- and inter-molecularly and directing folding. Charge-charge interactions are dependent on the pK_a values of the side chain groups, with these values ranging from 3.9 for the carboxylic acid side chain of Asp, to 12.5 for the guanidinium type side chain of Arg.[64] As a result of the dependence on pK_a, charge-charge interactions are highly dependent on the environment (solvent) and the pH of the system. These variables can play a large part in determining if charge-charge interactions even occur at all. Many biological systems rely on these charged interactions to form complex structures, bind metals and stabilise the folding of proteins.[65,66]

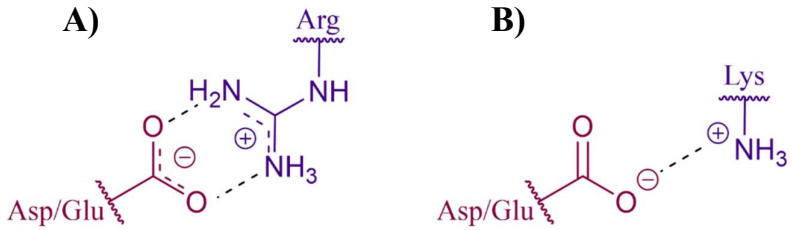

Figure 1.9 – Two examples of charge-charge interactions that can occur between peptide/protein sidechains. **A)** Interaction between an Asp or Glu carboxylate, and the Arg guanidinium side chain. **B)** Interaction between the Asp or Glu carboxylate and the Lys amine.

Outside of peptide side-chain interactions, electrostatic bonding between charged residues and metal ions are also incredibly important in biological systems, for example in the protein transferrin, which facilitates Fe(III) transport in the body.[65] The transferrin protein allows for the transport of typically insoluble Fe(III) ions within the plasma by tight binding of the Fe(III) ions to a His, Asp and two Tyr residues within its structure, solubilising it for transport.[67]

An example of charge-charge interactions in a synthetic system can be seen between 8-hydroxyquinoline N-functionalised peptiods and Co(II) or Cu(II) ions stabilising the helical secondary structure of the foldamer which were reported on by Maayan *et al.* in 2008.[68] A peptoid is a peptidomimetic, which lack amide bonds in their backbones as they are comprised of N-functionalised (typically methylated) Glycine residues.[69] By coordinating the transition metal (TM) ions the peptoid foldamer helicity increased significantly, and interestingly, this helicity was transferred onto the TM-8-hydroxyquinoline complex as evidenced by the presence of a positive exciton couplet in the CD spectrum consistent with the absorbance band observed for the 8-hydroxyquinoline unit.

Another example of the power of charge-charge interactions can be found in the Burkhard *et al*. study on improving CC stability found that by including a complex network of intermolecular salt bridge interactions they could stabilise the trimeric CC formation of a short two-heptad repeat sequence.[45]

1.3.4 Solvophobic Interactions

Solvophobic/hydrophobic effects are governed by entropic principles, often related back to the basic concept of ‘like dissolves like’, with positive entropies associated with polar molecules being dissolved in polar solvents and vice versa. In order for a system to be thermodynamically favourable an amphiphilic molecule in a polar solvent for example will try and arrange itself such that its polar regions are solvent exposed and its non-polar regions pack together minimising the unfavourable enthalpic effects associated with the non-polar region interacting with the polar solvent.[70] This is the same phenomenon that can be observed when mixing oil and water.

These interactions are commonly discussed in the context of hydrophobic packing which hold particular importance in biological systems and form the basis of much of protein and peptide folding behaviours in aqueous and biological media. As was mentioned in the section on peptide structure, amino acid side chains can be categorised as polar (hydrophilic) or non-polar (hydrophobic) reflecting their interactions within aqueous media. The side chains of alanine (Ala), leucine (Leu), isoleucine (Ile), valine (Val) and methionine (Met) all exhibiting aliphatic hydrophobic behaviours and phenylalanine (Phe), tyrosine (Tyr) and tryptophan (Trp) exhibiting aromatic hydrophobicity. Globular tertiary structure is primarily energetically guided by hydrophobic interactions, minimising the unfavourable interactions with the solvent by forming spherical structures containing a hydrophobic core and a hydrophilic/polar surface. This behaviour is also employed for the design of coiled coils.[45] The alignment of the hydrophobic faces of the amphiphilic peptide sequences is the main driving force for coiled coil packing (**Figure 1.10**).

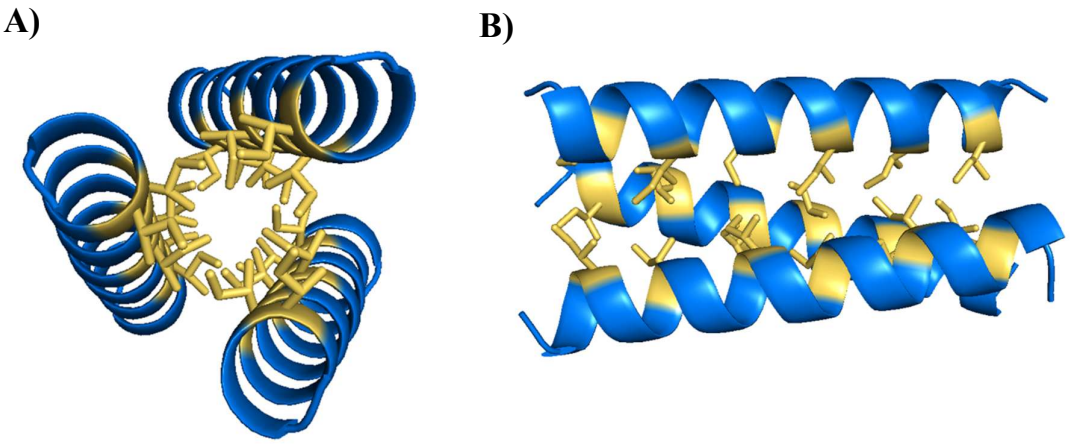

Figure 1. 10 - Hydrophobic packing in a 3-heptad trimeric CC. **A)** Top-down view through the centre of the CC. **B)** Side-view of the CC.

An important example of solvophobic interactions highlighting self-assembly processes in biological systems is the formation of the cytoplasmic membrane of the cell. The structure of this cell component is a phospholipid bilayer, in which the polar, phosphate heads point outwards into the aqueous environment and the hydrophobic, lipid tails pack together forming the characteristic bilayer as is depicted in **Figure 1.11**.[71] This process occurs as a result of solvophobic driven self-assembly in a biological (aqueous) environment.

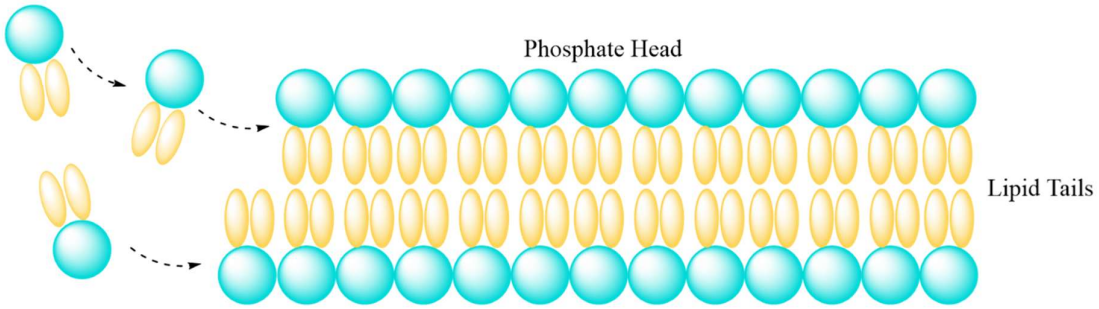

Figure 1. 11 - Cartoon representation of the self-assembly of the phospholipid bilayer. Blue circles depict the hydrophilic phosphate heads; yellow oblongs depict the hydrophobic lipid tails which pack together as a result of interactions with the polar solvent.

These same principles have been applied synthetically by chemists to influence the assembly of large structures as a result of interactions with the solvent. Typically, these interactions will occur alongside other NCIs such as H-bonding. Types of structures which have been investigated include hydrogels,[72] micelles,[73] vesicles,[74] nanotubes,[75] and nanosheets[76] for applications including materials/surface development for tissue scaffolds and as capsules for drug delivery.[50, 77]

Peptide amphiphiles (PAs) or lipopeptides have been an attractive component for many of these systems.[71, 77-80] Similar to the phospholipids discussed above, PAs have a polar head, in this case the peptide which generally contains a bioactive component (e.g. cell adhesion - RGD, matrokine - KTTKS),[81, 82] attached to a hydrophobic (lipid) tail, directing self-assembly by hydrophobic interactions with solvent.[83] Additionally, surfactant-like peptides (SLPs) have also been used in this context. Similarly to PAs, SLPs have regions of hydrophobicity and hydrophilicity, making them amphipathic, however this is achieved through the side chains of the AAs rather than an appended lipid. SLPs will typically have 1-2 charged residues which comprise the hydrophilic head group.

The self-assembly of PAs has been found to have applications in regenerative medicine, for example, through assembly of nanofibril gels containing the IKVAV cell adhesion motif.[76] In these structures the IKVAV motif serves as the hydrophilic head-group which is attached to a Ala_4Gly_3 linker and finally a 16 carbon alkyl chain, comprising the hydrophobic tail part of the subunits (**Figure 1.12**). When self-assembled the nanofibril structure features the hydrophilic head-group on the surface, and the hydrophobic tails packed into the inner cavity of the cylindrical fibre. These PA subunits were found to self-assemble into nanofibril hydrogels in aqueous environments of cell media, as well as *in vivo* and showed promising results in promoting cell differentiation for the formation of neurons.[84]

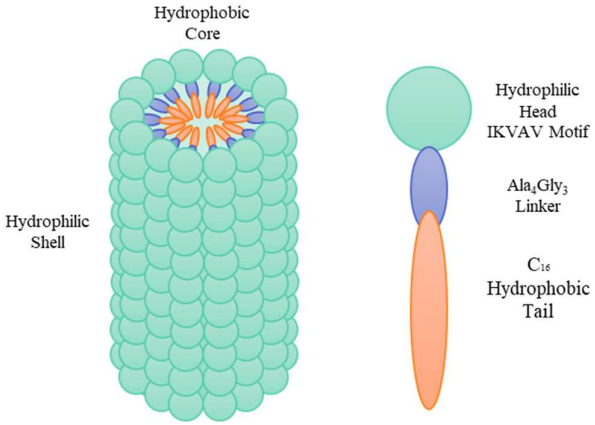

Figure 1.12 - Construction of nanofibers from peptide amphiphiles (PAs). Amphiphilic peptide structure comprised of the hydrophilic head group which is a IKVAV cell adhesion motif, attached to a flexible Ala_4Gly_3 linker and a hydrophobic alkyl chain (C_{16}). These peptides self-assemble as a result of hydrophobic self-assembly such that the hydrophilic head groups (green) form the surface of the cylindrical structure and the alkyl chains (orange) pack in the central pore.[76,84]

1.4 Supramolecular Assemblies and Coordination Chemistry

Supramolecular assemblies form as a result of the self-assembly principles and NCIs discussed in the previous section. Defined as the 'chemistry beyond the molecule' supramolecular chemistry is the study of molecular assemblies combining component molecules which are stabilised by intra- and inter- molecular NCIs.[85, 86] Synthetically these assemblies take a vast amount of inspiration from biological systems and even utilise biological building blocks such as amino acids, nucleic acids and peptides within their structures to govern the self-assembly.

Having already discussed the other NCIs above, this section aims to discuss specifically metal-ligand interactions, a subset of charge-charge interactions and their use for templating assemblies which have only been referenced briefly.

Metal-ligand interactions typically occur as an electrostatic interaction between a positively charged metal ion (electron acceptor), and a negatively charged, or electron rich organic molecule (electron donor), resulting in an ionic bond strength between that of covalent interactions and other NCIs, approximately 15-50 kcalmol^{-1} depending on the content of the M-L pair.[87] These are also referred to as Lewis acid/base interactions where the metal acts as the Lewis acid, accepting electrons, and the ligand acts as the Lewis base, donating electrons. The main reason coordination type bonding is used is due to the directionality of the bonds as a result of the coordination through p- and d-orbitals leading to the formation of predictable geometries (**Figure 1.13**).

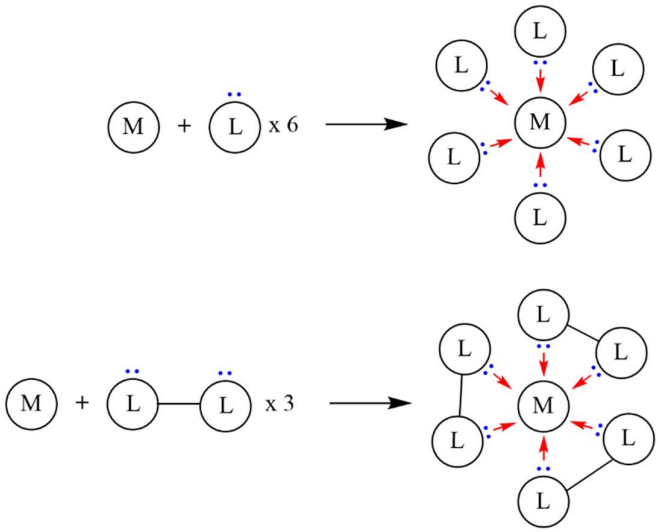

Figure 1.13 - Illustration of dative bonds with both monodentate and bidentate ligands for the formation of octahedral type geometries.

There are many options when it comes to deciding on the components of a coordination complex; composition of the ligands and identity of the metal being the main two considerations. The choice of the aforementioned components is highly dependent on what the desired final structure is to be, as well as the function, with different metal ions having propensities for certain geometries as a result of their electronic configurations, for example. Synthesis of supramolecules using metal coordination to template is a very well documented topic across the literature, with these supramolecules having structures such as rotaxanes, catenanes and knots.[86, 88, 89]

Due to the sheer volume of content within this topic of chemistry, this section of the review will focus on bidentate chelating units and coordination to metals in the d- and p-blocks of

the periodic table. Alongside a summary of these components, reference to relevant applications from the literature have also been mentioned.

1.4.1 Chelating Units

Chelate, from the Greek *'chele'* which translates to 'claw' refers to ligands which can coordinate with two or more of their atoms to form a coordination sphere (**Figure 1.14**). This atom donation from the chelator results in a ring of electrons which is accepted and shared with the positively charged metal ion.[90, 91]

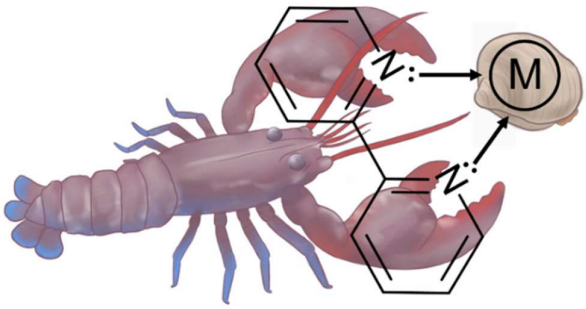

Figure 1.14 - Illustrative representation of a bidentate chelating unit (bpy) as a lobster with two claws '*chele'*, pinching its prey (clam) which represents the metal ion that is receiving the lone pairs.

Chelating units are all polydentate in nature with frequently cited examples including; ethylenediamine (en, bidentate),[92] bipyridine (bpy, bidentate),[93, 94] phenanthroline (phen, bidentate),[95] terpyridine (tpy, tridentate)[96] and ethylenediaminetetraacetic acid (EDTA, hexadentate) (**Figure 1.15**). These ligands mostly interact with metal cations through dative bonding, with the exception of the carboxylic acids of EDTA. The term dative means that each donor atom contributes a pair of electrons. Ionic ligands, like those in EDTA, which contribute a single electron per donor atom via a negative charge can also be used for the formation of metal-ligand complexes. Examples of ligands which participate in ionic bonding include 8-hydroxyquinoline, oxalates, halides (Cl^-, F^-, Br^-) and hydroxide ions OH^-, however many of these are monodentate.[97]

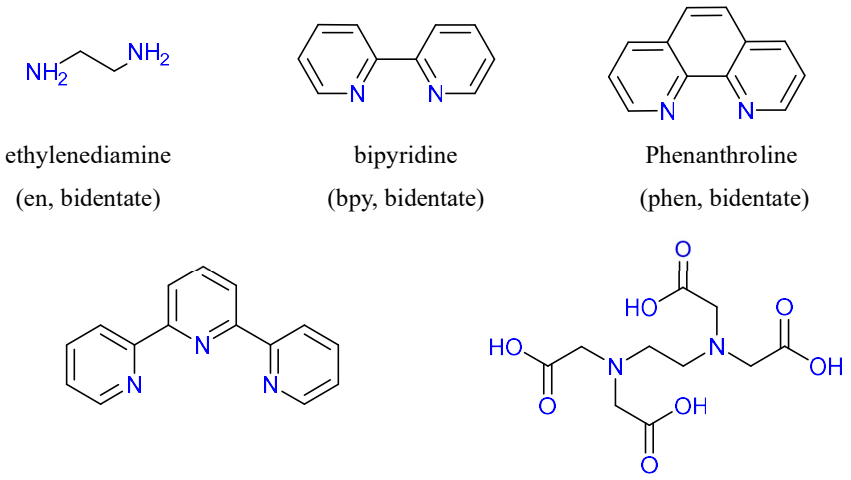

ethylenediamine (en, bidentate) | bipyridine (bpy, bidentate) | Phenanthroline (phen, bidentate)

terpyridine (tpy, tridentate) | ethylenediaminetetraacetic acid (EDTA, hexadentate)

Figure 1.15 - Structures of common chelating units with the donor atoms highlighted in blue.

The popularity of chelating ligands in the supramolecular chemistry literature is largely attributed to the chelate effect. The chelate effect is used to describe the increased thermodynamic stability of chelate complexes compared to their analogous monodentate complex. To better describe this concept the following example is often used; comparison of the $[M(en)_3]^{2+}$ and $[M(NH_3)_6]^{2+}$ complexes which have been provided in **Figure 1.16**.

A) $[M(OH_2)_6]^{2+} + 6NH_3 \leftrightharpoons [M(NH_3)_6]^{2+} + 6H_2O$

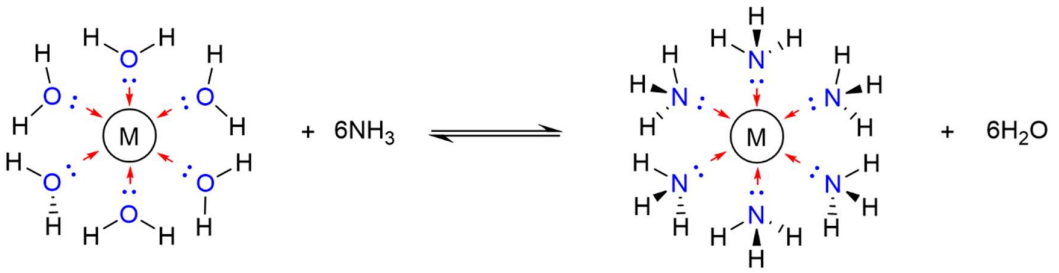

B) $[M(OH_2)_6]^{2+} + 3en \leftrightharpoons [M(en)_3]^{2+} + 6H_2O$

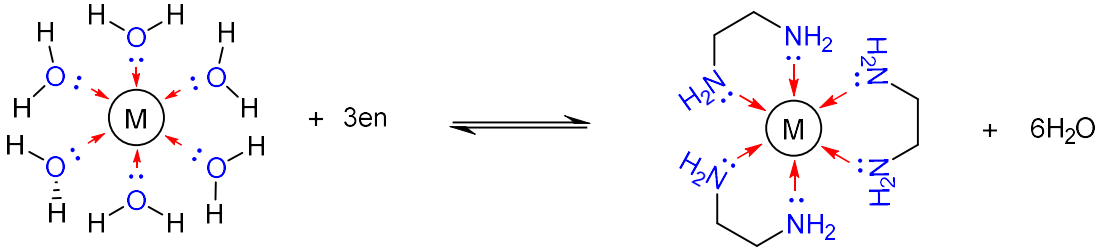

Figure 1.16 - A) Equilibrium between the $[M(H_2O)_6]^{2+}$ complex and the $[M(NH_3)_6]^{2+}$ complex. **B)** Equilibrium between the $[M(H_2O)_6]^{2+}$ complex and the $[M(en)_3]^{2+}$ complex.

The disparity in the stability of these two complexes occurs as a result of differences in the entropy of these systems, reflected in the equilibrium constants of the equations provided in **Figure 1.16**. In equation **A)** the six H_2O ligands are replaced with six NH_3 ligands, resulting in a negligible change in the entropy of the system, however, in equation **B)** the six H_2O ligands are replaced with three en ligands, which results in an increase in the entropy of this system. From the Gibbs free energy equations provided below (1), (2), it can be seen that a larger value of ΔS° will result in a larger, negative value of ΔG°, and therefore a larger value of equilibrium constant *K*, making this reaction more favourable thermodynamically.

$$\Delta G° = -RT\,lnK \qquad (1)$$

$$\Delta G° = \Delta H° - T\Delta S° \qquad (2)$$

Another interesting facit of chelating units that has contributed to their prevalence in the literature is their use in the formation of chiral complexes. All of the chelating units provided in **Figure 1.15** have a plane of symmetry, however, by introducing asymmetry to these molecules, for example with 2,2′-bipyridine-4-carboxylic acid (**Figure 1.17**), four different isomers of their octahedral metal complexes can be obtained.

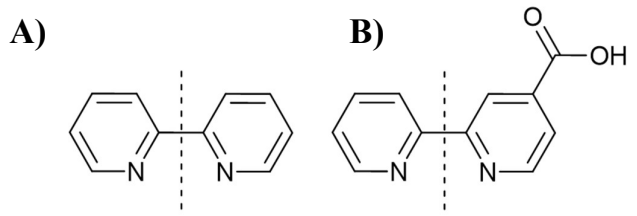

Figure 1.17 - Structure of **A)** 2,2′-Bipyridine comparative to **B)**2,2′-Bipyridine-4-carboxylic acid.

The formation of different isomers of this system results from different approaches of the ligands to the metal centre. Continuing with the example of 2,2′-bipyridine-4-carboxylic acid, the possible isomers have been provided in **Figure 1.18**. In this figure the four isomers depicted are *fac*-Δ, *fac*-Λ, *mer*-Δ, and *mer*-Λ. First, identification of the Δ- and the Λ-isomers can be performed by following the direction of rotation of the ligands, as is represented in the figure with the green (right-handed, clockwise) and blue (left-handed, anticlockwise) arrows. Additionally, the asymmetry also leads to two further isomers, the *fac* (facial) and *mer*-(meridian) isomers. These two isomers can be distinguished from each other in this case by determining if the carboxylic acid groups of the 2,2′-bipyridine-4-carboxylic acid ligands are situated on the 'face' or along the 'meridian' of the complex. Looking at the *fac*-Δ complex in the figure for example, the 3 carboxylic acid groups are all pointing into the page, taking up one face of the complex, however, comparison to the *mer*-Δ complex situated around the metal centre in a T-shape, characteristic of a *mer*-complex.

These different types of chirality, along with others will be discussed further in Section 1.5.

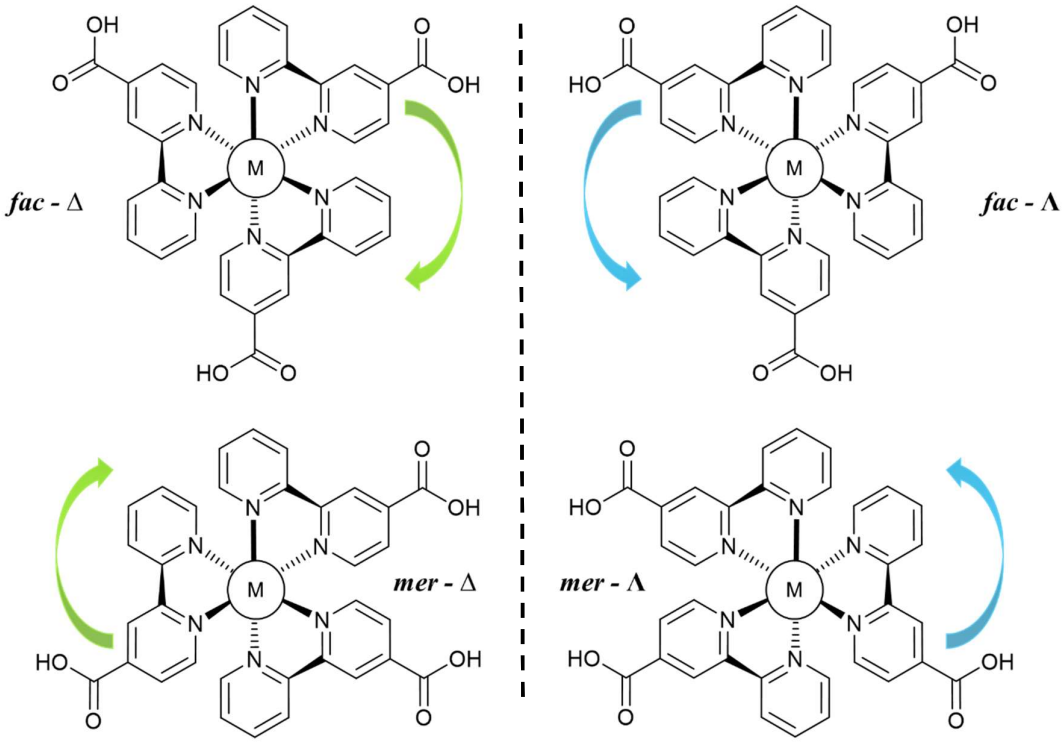

Figure 1.18 – The different isomers of the tris-[M]-2,2′-bipyridine-4-carboxylic acid complex. The right-handed or Δ-isomers are shown on the left, with the dashed line in the middle representing the mirror plane, on the right the left-handed or Λ-isomer

1.4.1.1 Bipyridine

Bipyridine (in its 2,2′- form) is first cited as being discovered in 1888 by Blau in his work on its synthesis and subsequent coordination to Fe(II) ions.[93] The bipyridine molecule is a bi-heterocyclic compound in which the nitrogen atoms can feature in six different configurations around the rings, with the most common of these being the chelating 2,2′-regioisomer (**Figure 1.19**).[98] The 2,2′ regioisomer will be the subject of this section due to its well documented behaviour as a chelate.

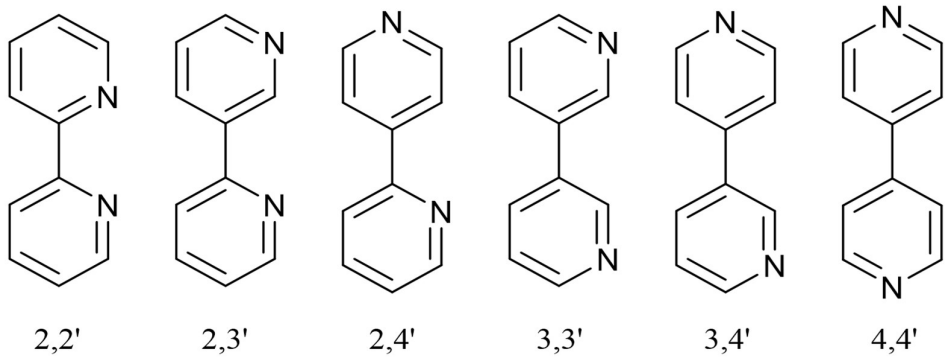

Figure 1.19 - The structures of the six different regioisomers of bipyridine.

2,2′-bipyridine is one of the most widely used chelating units across supramolecular and coordination chemistry and even has applications in biochemistry and drug discovery. The popularity can likely be attributed to a range of synthesis routes, for example via metal catalysed cross-coupling reactions, and functionalisation, making them relatively cheap to buy comparative to other large chelators,[98] along with well characterised coordination behaviour. The bpy ligand is a neutral ligand, contributing two donor nitrogen atoms to the coordination sphere and forming a five-membered chelate ring with the metal. It is categorised as a strong-field ligand and generally will coordinate to metal with a bite angle of approximately 80° (**Figure 1.20**).[99]

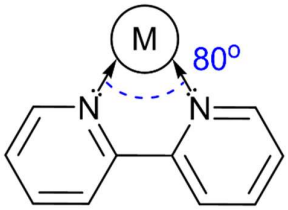

Figure 1.20 – Typical, theoretical bite angle of 2,2′-bipyridine.

Experimentally, the magnitude of the bite angle is variable and dependant on the identity of the metal centre. Crystal structures from the Cambridge Structural Database (CSD) of tris-bipyridine complexes have been compared in **Figure 1.21**. Crystal structures of the Co^{2+},[100] Ni^{2+},[101] Cu^{2+},[102] and Zn^{2+}[103] complexes have been provided, showing the range of bond angles adopted by the complexes, resulting in the apparent trend of Co < Ni > Cu > Zn. This suggests that the Ni^{2+} complex is the closest to an ideal octahedron, with angles of 90°. It is important to note that in the case of $[Cu(bpy)_3]^{2+}$ the bite angle is varied as a result of high

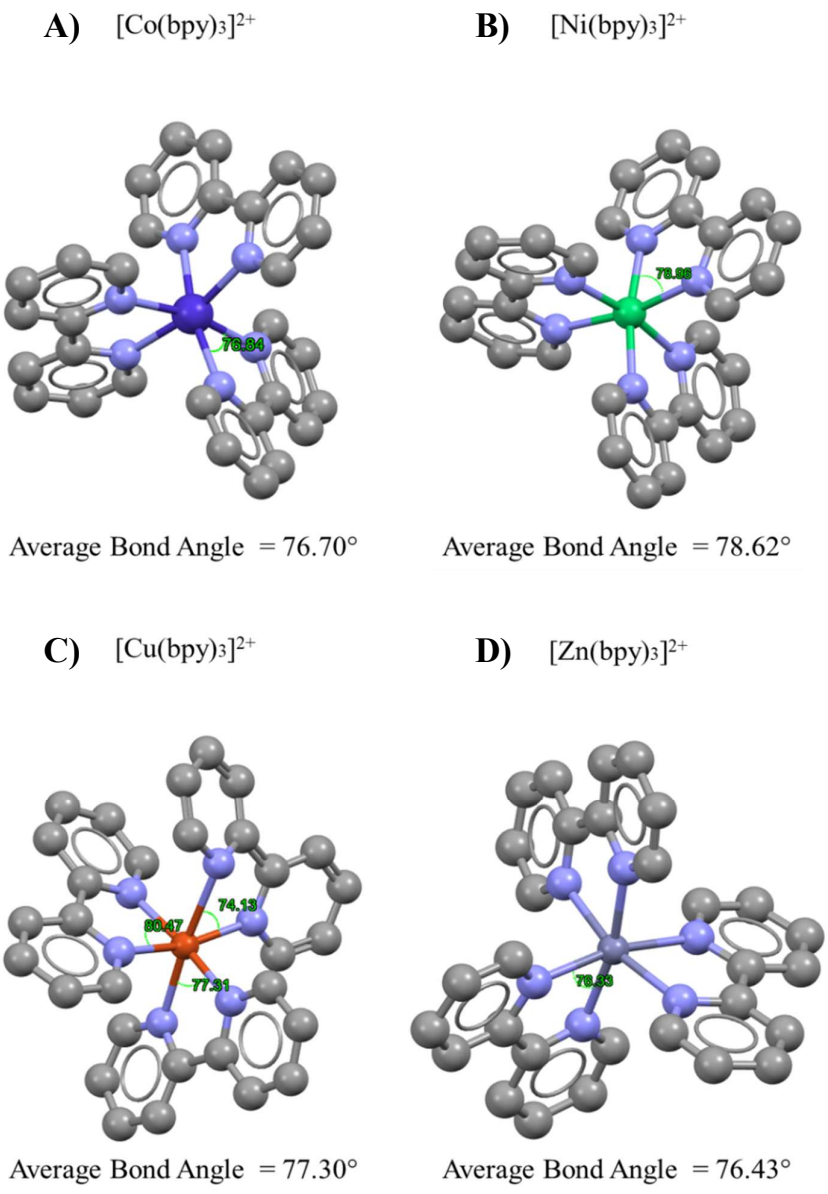

Figure 1.21 - Crystal structures and bond angles of **A)** $[Co(bpy)_3]^{2+}$, CSD code (KOKDUM)[100] **B)** $[Ni(bpy)_3]^{2+}$ CSD code (BPYNIS)[101] **C)** $[Cu(bpy)_3]^{2+}$, CSD code (RIGTEH)[102] **D)** $[Zn(bpy)_3]^{2+}$, CSD code (OREHEZ)[103]. The counter ions were excluded for clarity.

levels of distortion in this complex, and ranges from 74.13° – 80.47°, these distortions will be covered in more detail in Section 1.4.1.3.

The term 'strong-field ligand' comes from ligand field theory and describes a ligand which contributes a larger orbital splitting energy or Δ_{oct} through its interactions with the metal ion (see **Figure 1.22**). Other factors such as the metal oxidation state and a higher charge will typically correspond with larger Δ_{Oct}, and the identity of the metal and ligand will influence the magnitude of Δ_{Oct}.[97]

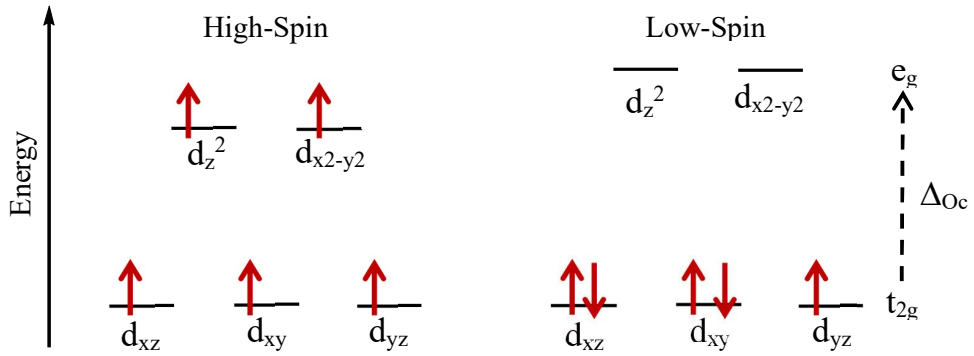

Figure 1. 22 - Orbital splitting diagrams for a low and high spin d^5 complex. Dashed arrow shows the orbital splitting energy between the t_{2g} and the e_g orbital sets.

Experimentally, bpy-complexes can be characterised by UV-Vis absorption spectroscopy. Prior to complexation with a metal ion, bipyridine exhibits a strong π-π* transition typically around 280 nm. However, once in a complex the absorbance wavelength of this band will appear between 290 – 340 nm (**Figure 1.23**). The exact values of the absorbance wavelengths of the π-π* transition are dependent on the identity of the metal within the complex and any functionalisation of the bpy moieties as these can influence the electronic transitions which cause these spectroscopic bands.[104] Additionally, upon complexation, transitions will also be observed at longer wavelengths in the visible region of the electromagnetic spectrum, between 500–700 nm. These absorption bands occur as a result of metal ligand charge transfer (MLCT) electron transitions from the metal ion d-orbital to the bipyridine π*-orbital.[16, 105]

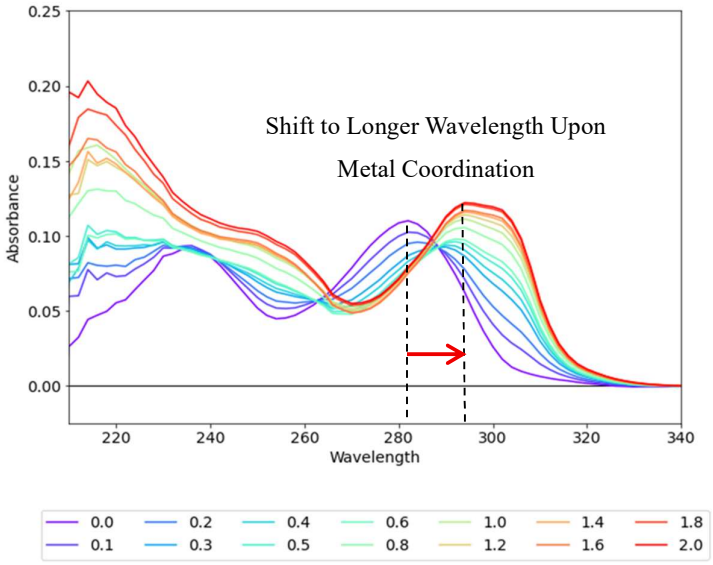

Figure 1.23 - Example $CoCl_2$ UV-Vis absorption titration with [2,2′-Bipyridine]- 4,4′-dimethanol performed in H_2O. Increasing the equivalents of Co^{2+} ions in solution in 0.1 increments up to 1.0 eq and then 0.2 eq up to 2.0 eq of Co^{2+} with respect to [2,2′-Bipyridine]- 4,4′-dimethanol.

Complexes of bpy have a wide range of practical applications, ranging from anti-bacterial, -fungal and -viral applications, to materials for renewable energy, to optically active and luminescent materials.[106] One such example of the application of complexes of bpy ligands includes a 2020 study by Gençkal.[107] This study found that heteroleptic (containing 2 or more different ligands around a single metal ion), square planar, Cu(II) complexes with both 2,2′-bipyridine (or 1,10-phenanthroline) and chrysin (flavonoid) type ligands exhibited a higher level of antioxidant activity comparative to chrysin alone (**Figure 1.24**). Furthermore, another study from 2021 by Shchegolkov *et al.* found antifungal and antibacterial activity of heteroleptic Co(II) and Cu(II) complexes of 2,2′-bipyridine (or 1,10-phenanthroline) and trifluorosalicylate ligands.[108]

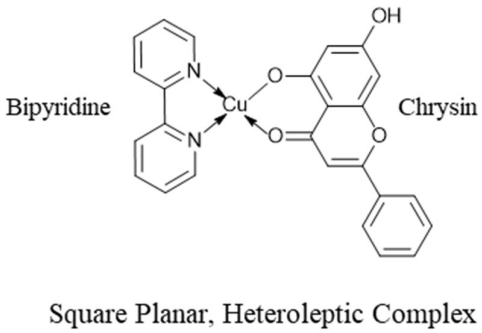

Figure 1.24 - Heteroleptic, square planar complex of Cu(II) with 2,2′-bipyridine and chrysin ligands[107].

Bpy units have precedent in the literature as components in self-assembled peptide supramolecules, mediating the assembly by coordination to metals.[109] One pertinent example with interesting applications comes from the Chmielewski Group and the use of bpy ligands to synthesise higher order collagen bundles, with radial elongation.[110-112] This work focuses on the formation of type II polyproline helices (PPII) for the formation of collagen bundles. These structures differ from the typical α-helix in that they assume a left-handed conformation and exhibit dihedral angles of φ = -75°, ψ = 145° and do not feature intramolecular hydrogen bonds, instead folding as a result of steric interactions between the proline residues.[113] This work has included the incorporation of one or more bipyridine moieties to a PPII strand. The bipyridine moieties have been incorporated through amide coupling to a lysine side chain in a central position within the PPII helices, protruding from the solvent exposed face of the helices. The PPII helices self-assemble into the trimeric bundles, and upon introduction of metal ions, in this case Fe^{2+} the bundles undergo radial expansion (**Figure 1.25**). These structures were assessed by transition electron microscopy (TEM) and atomic force microscopy (AFM) which demonstrated that the structures were expanding radially, as they only appeared as tall as a single triple helix bundle.[112] These structures have since been applied to the formation of 3D gels for cell scaffolding.[110]

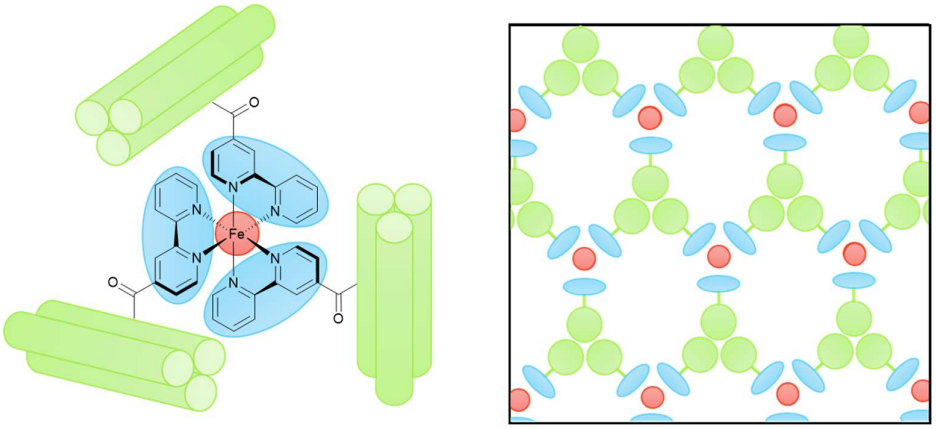

Figure 1.25 – Structure of octahedral tris-bipyridine complex formed as a result of Fe^{2+} coordination. The coordination then results in radial expansion of the collagen bundles[109-112].

1.4.1.2 Phenanthroline

1,10-Phenanthroline (phen) is another popular chelating unit with very similar characteristics to the bpy ligand (**Figure 1.26**). These similarities include the denticity and the bite angle, however the inclusion of the third aromatic ring at the rear of the structure prevents rotations which are possible in the bpy ligand, introducing an increased rigidity which the bpy chelate does not exhibit.[114, 115]

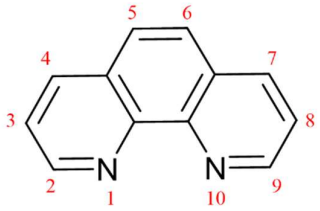

Figure 1.26 - ChemDraw representation of 1,10′-phenanthroline

As a result of the lack of rotation in phen, this ligand acts as a stronger chelate than the 2,2′-bipyridine discussed previously. This is a result of the principles related to the chelate effect which were discussed previously, and the rigidity of phen making the coordination more entropically favourable.[116] The bite angle of the phen chelate in theory should also be approximately 80°, however, experimentally, this value appears between 77–80° in tris-phen complexes, depending on the metal. For example, a series of tris-phen complexes with first row TMs, Co^{2+},[117] Ni^{2+},[118] Cu^{2+},[119] and Zn^{2+},[120] were examined in **Figure 1.27**. From this it can be observed that, like the tris-bpy complexes, the Ni^{2+} complex results in the least distorted octahedral structure, with the bite angles closer to 80°. Comparatively to the tris-bpy complexes, the bite angles are all larger in magnitude by approximately 1° as a result of the increased rigidity of the phen compared to the bpy units.

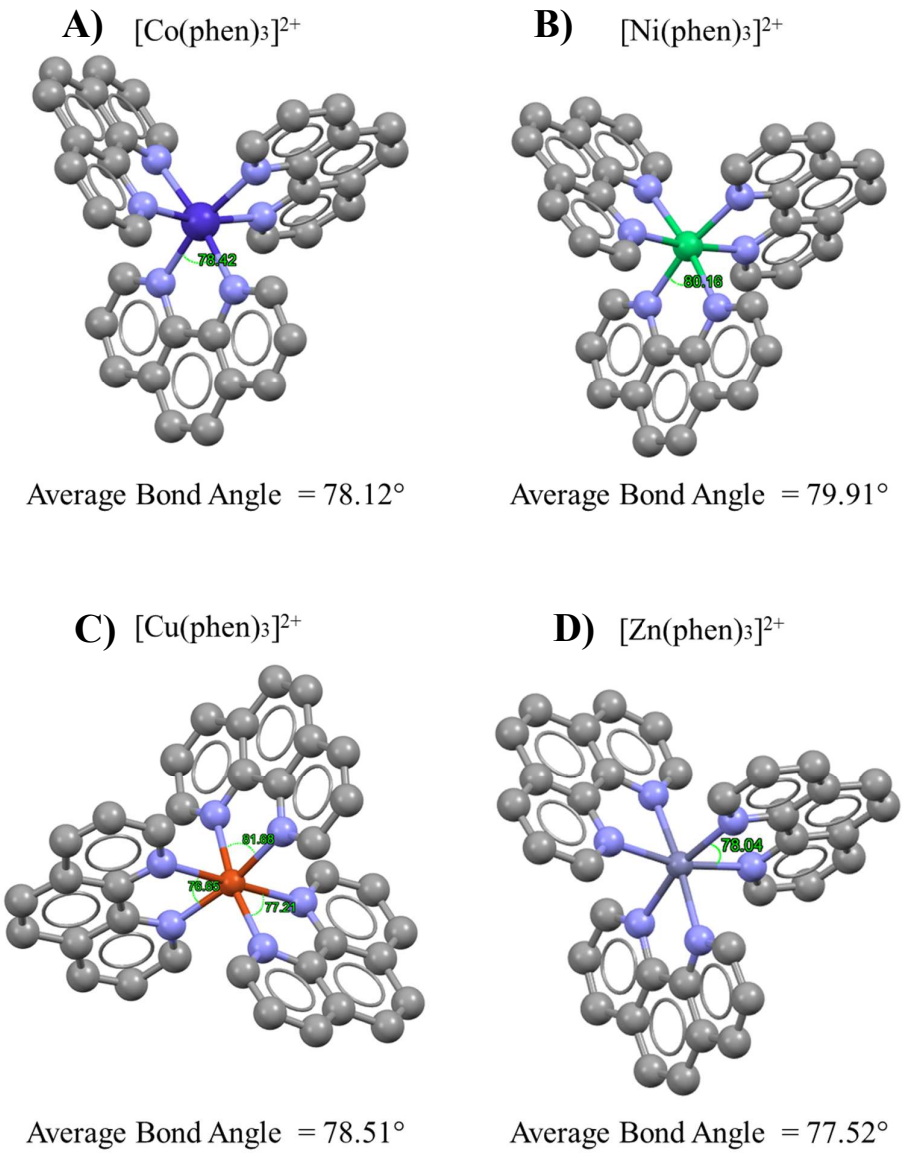

Figure 1.27 - Crystal structures and bond angles of **A)** $[Co(phen)_3]^{2+}$, CSD code (WAWRAR)[117] **B)** $[Ni(phen)_3]^{2+}$ CSD code (SIRKOT)[118] **C)** $[Cu(phen)_3]^{2+}$, CSD code (PENCUC)[119] **D)** $[Zn(phen)_3]^{2+}$, CSD code (EPIBUC), 120. The counter ions were excluded for clarity.

With respect to the spectroscopic properties of the phen chelating unit, an absorption band associated with the π-π* transition can be observed for the uncoordinated ligand in the UV-Vis spectra between 265–270 nm, subtly red-shifting by around 5 nm upon introduction and coordination of a metal ion. The identity of the metal is important for determining the intensity of this shift, as well as any functional groups present on the phen moiety and the pH of the environment of the complex.[121] An example of this shift in the λ_{max} shift upon metal coordination is provided in **Figure 1.28**. This example specifically is a phen-appended peptide with the structure of (Phen-GQEIAAIKKEIAAIKKEIAAIKYG-NH_2) which exhibits a λ_{max} of 270 nm in its uncoordinated state and then shifts towards 275 nm upon coordination to Co^{2+} ions.

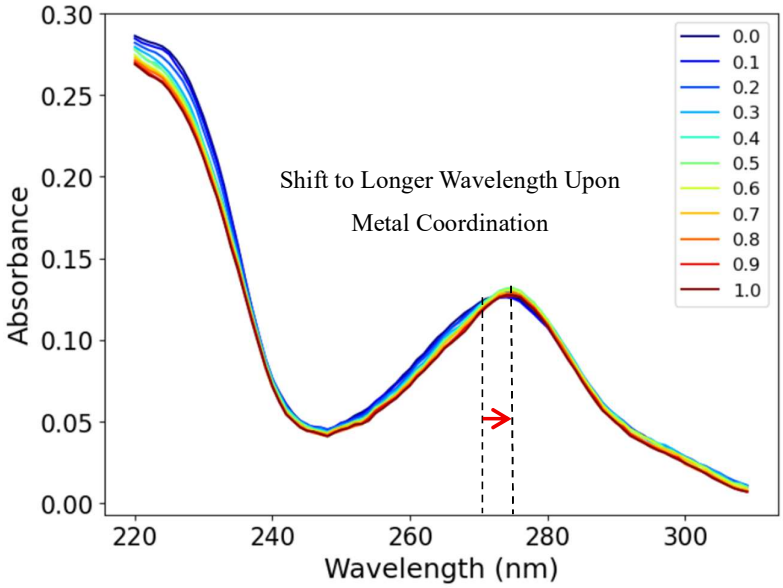

Figure 1.28 - Example $CoCl_2$ UV-Vis absorption titration with a phen-appended peptide (Phen-GQEIAAIKKEIAAIKKEIAAIKYG-NH_2) from this thesis, performed in 20 mM MOPs buffer. Increasing the equivalents of Co^{2+} ions in solution in 0.1 increments up to 1.0 eq with respect to a singular phen-peptide. A shift from a λ_{max} of ~270 nm to ~275 nm is observed upon coordination to the Co^{2+} ions.

The extended aromatic structure of phen and its ability to coordinate to a vast range of metal cations gives it desirable properties in areas of research such as the synthesis of luminescent compounds, medicinal applications[107, 108], DNA groove binding and intercalation,[116] and as optical and chemical sensors.[114, 122] The aromaticity, planarity and chelation also make it an attractive component for metal templated synthesis of supramolecular structures such as catenanes and knots.[89]

1.4.1.3 8-Hydroxyquinoline

8-Hydroxyquinoline (8-HQ) (**Figure 1.29**) has gained a significant amount of popularity as a chelating unit in the past 20 years.[123] Its popularity can be attributed to its high affinity as a chelate and vast range of applications in areas such as drug discovery, [124-126] agriculture, [123] and materials science, with tris-(8-HQ)-Al(III) having been used as a component of OLEDs previously.[127]

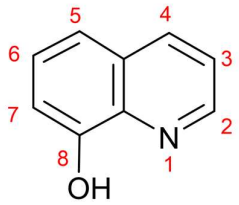

Figure 1.29 - Structure of 8-Hydroxyquinoline

Structurally, 8-HQ consists of a pyridine ring fused to a phenol, with the hydroxyl group attached at the 8-position. It's structure is rigid and planar, akin to the 1,10-phenanthroline, and coordinates to metal with the same theoretical bite angle (~80°) as bpy and phen.[128] Experimentally, as was observed for the bpy and the phen complexes, these values are variable. An example of a tris-8-HQ complex with Ga^{3+} from the literature is shown in **Figure 1.30**.[129]

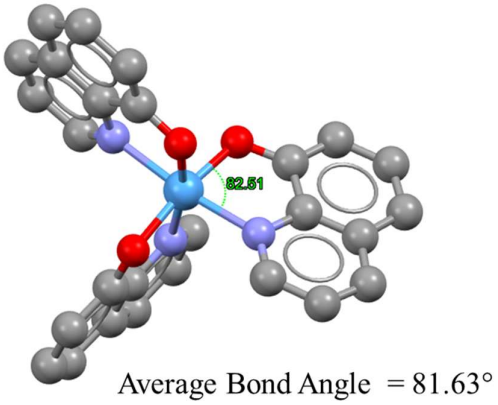

Figure 1.30 – Tris-8-HQ complex with Ga^{3+}. The average of the three bite angles was measured as 81.63°. CSD code (ETELAQ)[129].

The pK_a of the hydroxyl group of 8-HQ is cited from the literature as having a value of approximately 10 in aqueous solutions, similar to other phenols.[130]

Spectroscopically, the free 8-HQ moiety is reported in the literature as having an absorption band at 245 nm from a π-π* transition, which red-shifts to 262 nm upon coordination to metal ions. An example of this transition and the effect of metal coordination can be seen in **Figure 1.31**. This example is from an 8-HQ appended peptide sequence (8-HQ-GEIAAIKKEIAAIKKEIAAIKKYG-NH_2) which has been titrated against Ga^{3+} ions in 0.1 eq increments up to 0.8 eq with respect to the peptide sequence. From this it can be observed that the π-π* transition in this instance at 0.0 eq of Ga^{3+} occurs at ~250 nm, upon addition of Ga^{3+} this signal red-shifts towards ~265 nm. This matches with the values quoted from the literature.

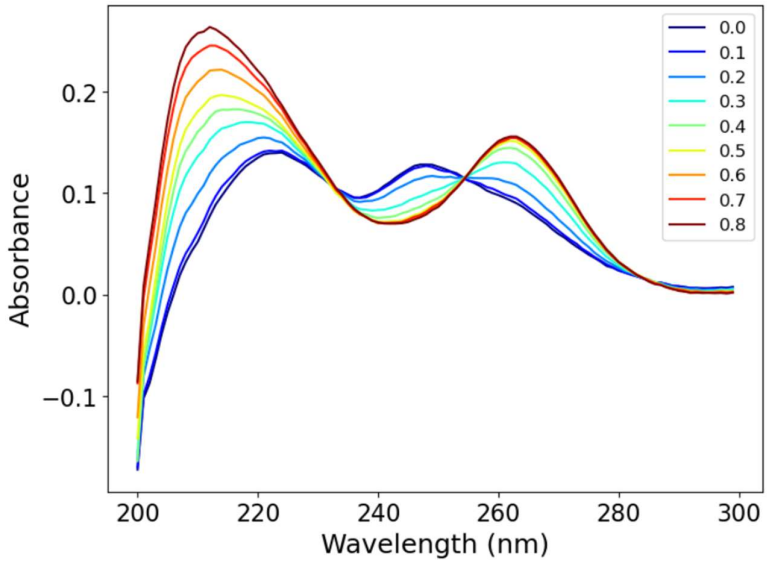

Figure 1.31 - Example $Ga(NO_3)_3$ UV-Vis absorption titration with an 8-HQ-appended peptide (8-HQ-GEIAAIKKEIAAIKKEIAAIKKYG-NH_2)from this thesis, performed in 20 mM MOPs buffer. Increasing the equivalents of Ga^{3+} ions in solution in 0.1 increments up to 0.8 eq with respect to a singular 8-HQ-peptide. The π-π* transition is originally observed at ~250 nm which then shifts to ~265 nm upon coordination to the Ga^{3+} ions.

For chiral complexes of 8-HQ this signal is reflected as either a positive or negative exciton couplet in the CD spectra centred around ~262 nm, depending on the chirality of the complex.[68, 131] An example of the expected spectral pattern can be found in the work of Maayan *et al* and their synthesis of metallo-peptoids (peptides with tertiary amides) functionalised with 8-HQ chelating groups.[68] In this example the peptoid assembles into a helical structure, directed by π-stacking interactions between the (*S*)-1-phenylethyl groups (Nspe) forming a helical structure akin to a polyproline-I helix with 3-residues per turn. This

is exhibited in the CD spectrum as the characteristic double minima (208 nm and 222 nm), stabilised by metal chelating to the two 8-HQ moieties. It is also observed in this experiment that the stereogenic information from the helical peptoid is projected onto the tetra-coordinated complex. This is visualised in the CD spectrum as an exciton couplet signal with a minimum at 260 nm and a maximum at 272 nm, making it a positive exciton couplet.

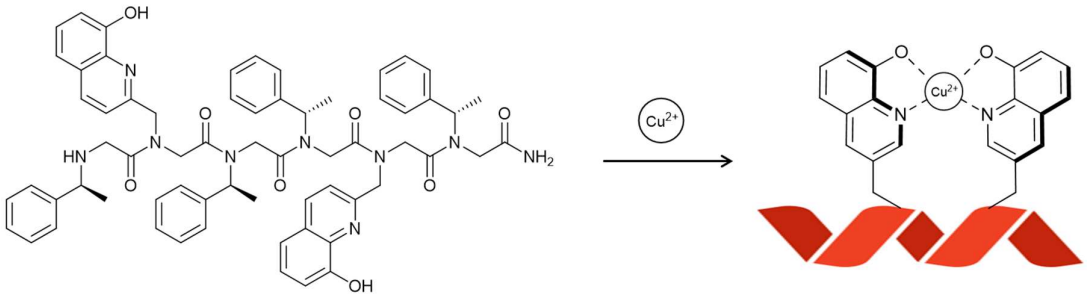

Figure 1.32 – Formation of an intra-molecular tetracoordinated Cu^{2+} complex with two appended 8-HQ residues on the peptoid sequence (*i*-*i*+3 interaction). The sequence assembles into a helical structure which preorganises the 8-HQ moieties for coordination to the Cu^{2+} ions upon coordination to the Cu^{2+} ions. Coordination is hypothesised to be pseudo-tetrahedral[68].

1.4.2 d- and p-Block Metals

Alluded to in the sections up to this point the choice of metal for the formation of coordination complexes can have a significant effect on its geometry and properties.

First row transition metals (d-block) are a common choice for the formation of complexes, which is likely as a result of their relevance to biological applications due to their abundance in the human body, contributing to the formation of minerals to the function of enzymes.[132] Metals from the latter half of this series include Co, Mn, Zn, Fe and Cu and are found in significant quantities in the human body and considered vital for life, playing roles in enzyme activity, oxygen transport, and cell signalling. Interestingly Fe is more abundant in the human body (ppm) than the ocean.[97] Furthermore, complexes of these metals can form naturally in the body, as shown with the Fe(II)-haemoglobin and -transferrin complexes. Due to their biocompatibility these metals are often incorporated into biomimetic structures, in order to mimic the structures and functions of native proteins.

The d-block elements are found in rows 3-12 of the periodic table. Their properties are well studied and many reviews on the different properties of this group of elements as well as more focused studies on specific metals in the series can be found in the literature.[133-137] For the purposes of this thesis some of the more relevant properties of the first row TMs have been summarised below (**Figure 1.33**). In this figure the difference between the electronic configurations in the gas-phase and when the element is in a coordination complex have been addressed. When in the gas-phase the 4s orbital is filled first, however, when in a complex, the 3d orbital is filled first, making the electronic configurations appear differently. It is worth also noting that beyond Mn, oxidation states exceeding 3^+ are uncommon. This is due to increased nuclear charge going across the period with increasing atomic number, which results in a higher energy required to remove an electron.[97] Atomic and ionic radii are also important considerations with respect to complex formation with these metals. In the periodic table, generally, the atomic radius will decrease across the rows such that Sc > Ti > V > Cr > Mn > Fe > Co > Ni > Cu > Zn. This trend is a result of the increasing nuclear charge of the metals, resulting in the nucleus of the atom pulling the outer electrons closer and, hence decreasing the size. The ionic radii of these elements are more complicated however and is dependent on the charge of the ion, with cations being smaller than the neutral atoms (due to loss of electrons) and anions being larger (gain of electrons). Generally, in their most common ionic states, the ions have been calculated to follow the trend of, $Sc^{3+} > Ti^{3+} < V^{2+} < Cr^{2+} < Mn^{2+} > Fe^{2+} > Co^{2+} > Ni^{2+} < Cu^{2+} < Zn^{2+}$ across the first row of transition

metals.[138] The differences occur as a result of a combination of electron–electron repulsions making certain configurations have a larger radii than others, and increasing nuclear charge across the row pulling the electrons closer and making those configurations smaller. It is worth noting however that the values all range between 83 pm (Mn^{2+}) to 67 pm (Ti^{3+}).

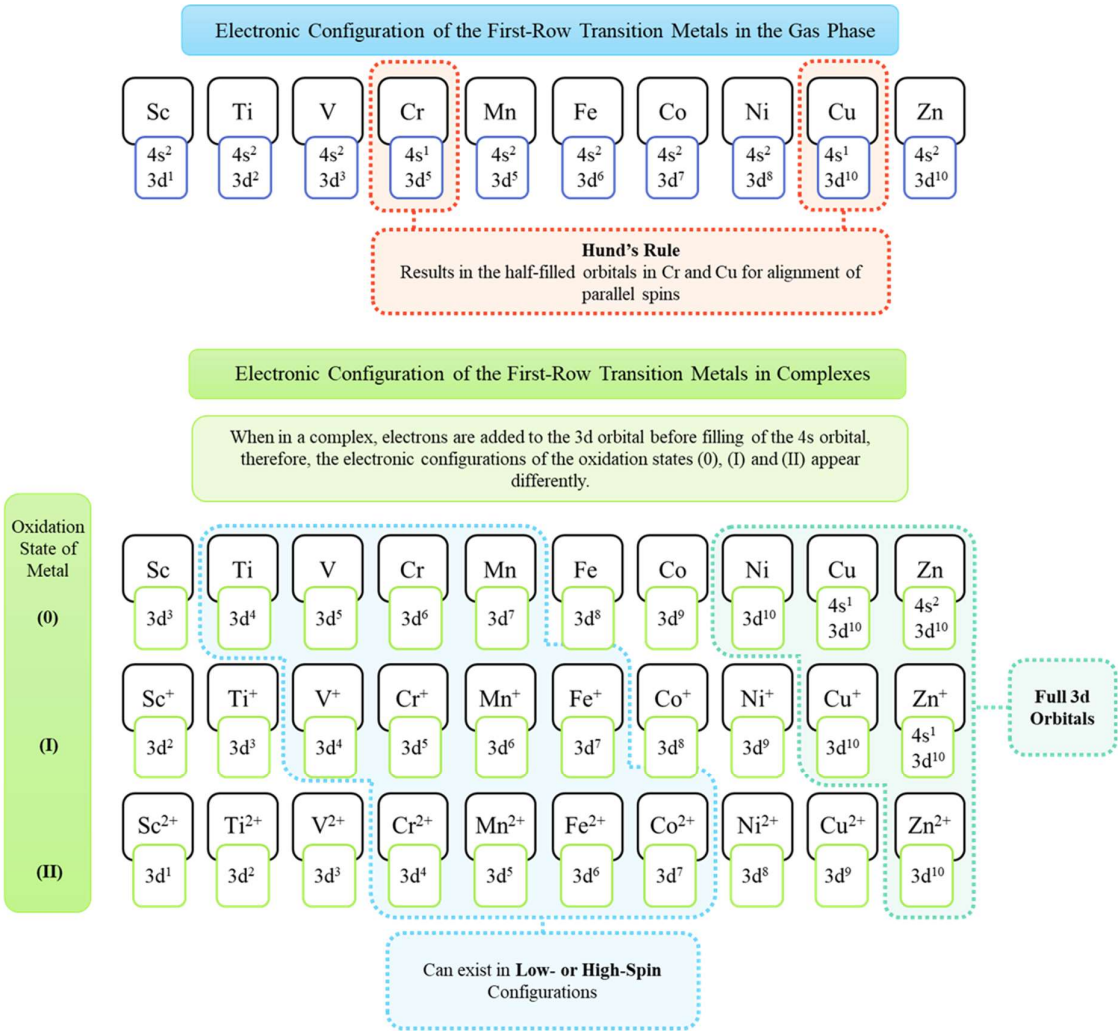

Figure 1.33 - Electronic configurations of first row transition metal (d-block) elements, in the gas phase, as well as when complexed in (0), (I) and (II) oxidation states. Highlighted in the figure are the ions which can form high- and low-spin orbital configurations (blue) as well as those with a filled 3d orbital (teal), and the unusual behaviour of Cr and Cu in their gas phase configurations (orange).

Outside of the d-block transition metals, the attractive properties of p-block (or post-transition) metals for synthesising complexes with well-defined geometries including tetrahedral and octahedral structures has also been well documented.[139]

The p-block metals reside in groups 13-16 (**Figure 1.34**), and include Al and Ga, which have been used within this work. These metal elements, like the transition metals, have attractive

properties, such as reliable formation of octahedral and tetrahedral complexes with both monodentate and polydentate ligands.[127, 131, 137, 140]

Unlike the d-block metals, the p-block metals have a filled d-orbital and rely on their p- and s- orbitals for bonding. As a result of this, they are less geometrically diverse.

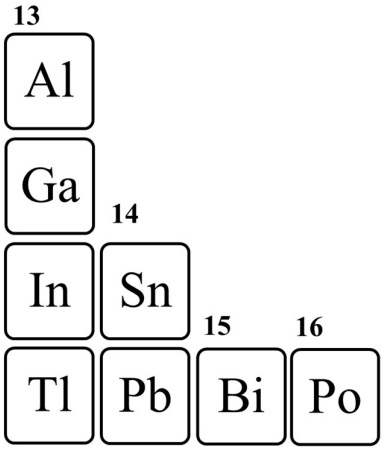

Figure 1.34 – Main group (p-block) metals.

A comparison of the d- and p-orbitals can be found in **Figure 1.35** which helps to illustrate this point. All of the p-orbitals (**Figure 1.35 – B**)) are coincident with either the *x*, *y* or *z*-axis, this allows for good orbital overlap with ligands in an octahedral or tetrahedral orientation. However, looking at the d-orbitals (**Figure 1.35 – A**)), not only are there two orbitals coincident with *x, y* and *z*-axis (d_x^2-$_y^2$, d_z^2), but there are an additional three orbitals, the d_{xy}, d_{xz} and d_{yz} orbitals, which point in between these axis, allowing more structural diversity when coordinating to a d-orbital, as ligands can have good orbital overlap from more directions. Despite this difference there are still many well documented examples of both p-block and d-block metal complexes, most relevantly, octahedral geometries with polydentate ligands.[95, 125, 131, 141, 142]

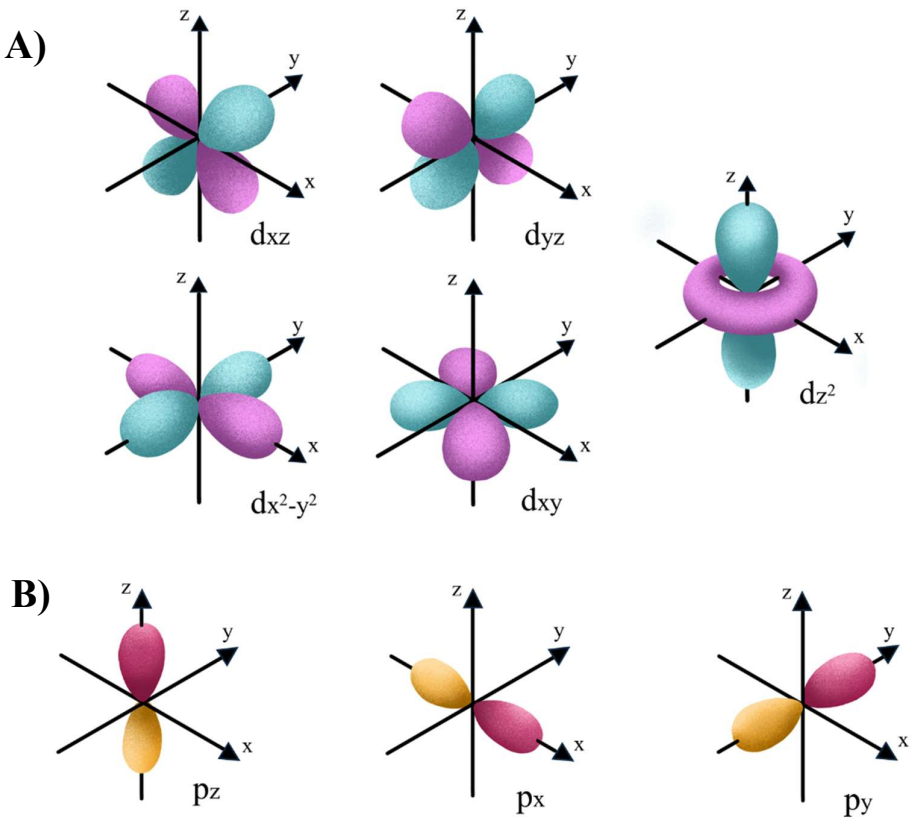

Figure 1.35 - Orbital diagrams; **A)** the five d-orbitals represented in blue and purple, and **B)** the three p-orbitals are represented in pink and yellow.

1.4.2.1 Jahn-Teller Distortions

An important effect to consider is the occurrence of distortions within complexes. One common example found in the d-block metals is the Jahn-Teller distortion which arises from electronic degeneracy in the d-orbitals. This occurs when an electron can be placed in two or more different orbitals, creating asymmetry. Jahn-Teller effects can be observed in metal ions with electronic compositions of d^1, d^2, d^4 (low-spin), d^5 d^7 and d^9 and will exhibit as either an elongation or compression of the *z*-axis.

Elongation is most frequently observed in d^9 complexes, such as complexes with Cu^{2+} ions. The asymmetry of the e_g set of orbitals occurs due to the presence of an uneven number of electrons, with the final electron being placed into the d_z^2 orbital. In this case, the d_z^2 orbital becomes destabilised, and to compensate for this, is lowered in energy. Additionally, all other orbitals with a *z*-component will be lowered in energy as well (**Figure 1.36 – A)**). As a

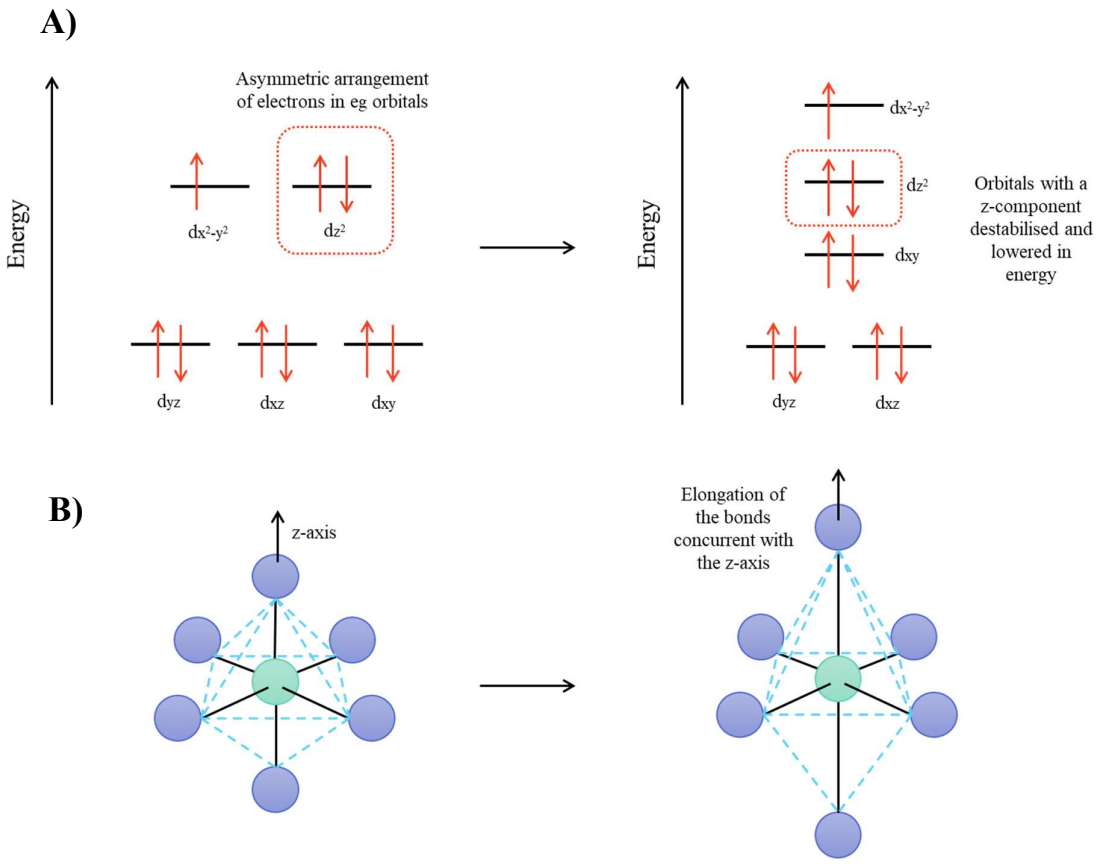

Figure 1.36 – A) Orbital diagram showing the consequence of asymmetrical arrangements of electrons within the orbitals. If the electron in a d^9 system is in the dz^2 orbital, this orbital and other orbitals with a z-component lower in energy. **B)** The lower energy of these orbitals results in elongation of bonds coincident with the z-axis.

consequence of the destabilization of these orbitals, bonds concurrent with the z-axis elongate, resulting in the distorted structure shown in **Figure 1.36 – B)**.

An example of this structural distortion in Cu^{2+} of bpy and phen can be seen in **Figure 1.37**. By measuring the bond lengths of the crystal structures, it can be observed that for the tris-bpy complex of Cu^{2+} the bonds along the *x*- and *y*-axis are on average 2.028 Å whereas the bonds that lie along the *z*-axis are on average 2.345 Å, exhibiting this elongation. The same can be observed in the tris-phen complex of Cu^{2+} with the bonds along the *x*- and *y*-axis exhibiting an average bond length of 2.037 Å and those along the *z*-axis having an average bond length of 2.328 Å.[102, 119]

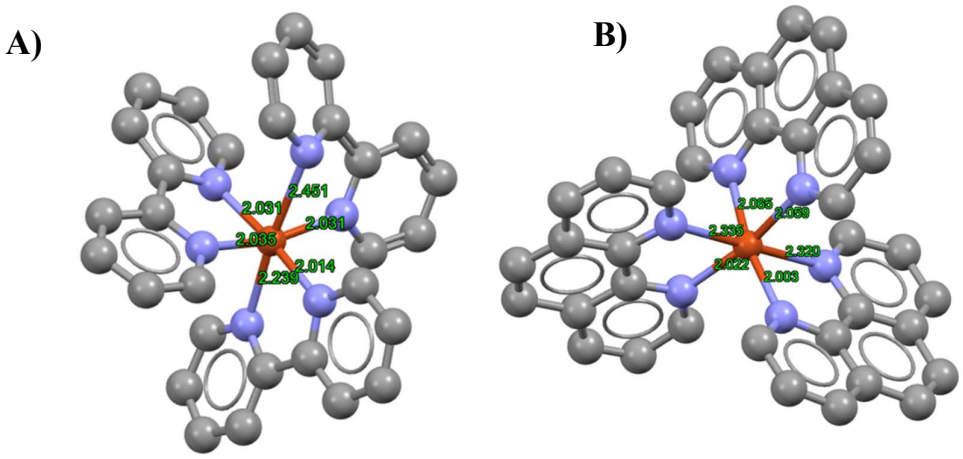

Figure 1.37 – Crystal structures of **A)** $[Cu(bpy)_3]^{2+}$, CSD code (RIGTEH)[102] **B)** $[Cu(phen)_3]^{2+}$, CSD code (PENCUC)[119]. Measured bond lengths are displayed in green for both complexes.

If the asymmetry arises however, due to the final electron being placed in the $d_{x^2-y^2}$ orbital, this results in destabilisation of orbitals with an *x*- or *y*-component, lowering their energy. In this instance the bonds along the *z*-axis are compressed and as the lobes of the $d_{x^2-y^2}$ orbital points directly at the ligands, these bonds become elongated. These effects are less commonly observed than the elongation effects.[97]

1.5 Chirality

Chirality is a term that is used to describe the handedness or asymmetry of an entity. A structure that is chiral or asymmetric is defined by its non-superimposable nature with respect to its mirror image. An easy visualisation of this concept is to attempt to superimpose your hands, no matter how you move them in space this should not be possible, they are non-superimposable mirror images of one and other.

As a concept, chirality is applicable to all conceivable length scales, from the atomic to the macroscopic and has a strong prevalence and importance in nature and across the scientific fields.[4, 5] The prevalence of chirality across many fields of science and technology makes it incredibly important to understand the underlying mechanisms in which chiral information is passed across different length scales, yet despite this, little is currently understood.[6] Particularly important in studies of biology and drug discovery, biological systems display homochirality in their basic building blocks, favouring L-amino acids (AAs) and D-nucleic acids for synthesis of proteins and DNA respectively. The chiral bias in life's very basic subunits, through chiral information transfer, leads to chiral bias in larger biological structures, on a smaller scale this can look like right-handed α-helices, but on a larger scale this leads to the asymmetry in human organs, [3] the helicity of snail shells,[2] and the chiral gyroid chitin arrangements in the Green Hairstreak butterfly.[143-145] These examples of macroscopic chirality indicate how the chirality of specific proteins can direct the chiral assembly of molecules, including achiral, inorganic components, in a way which is visible to the naked eye. From these natural phenomenon scientists have been inspired to observe these biological processes to gain understanding on the underlying mechanisms and apply them to artificial systems such that large chiral assemblies can be synthesised with desirable functionalities.

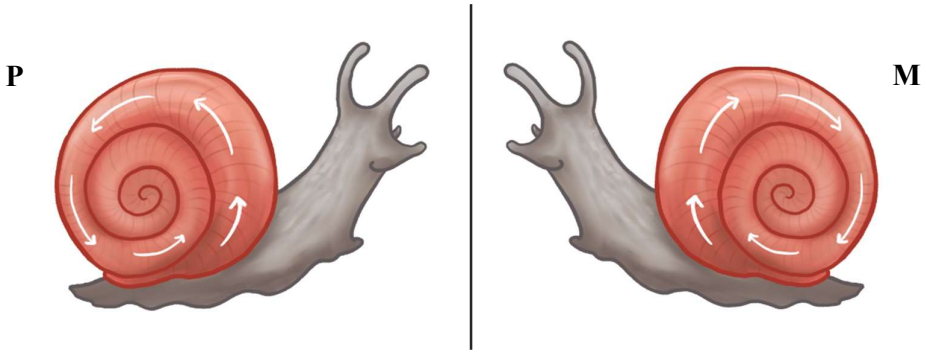

Figure 1.38 - Cartoon representation of chirality in nature - example is of the mirror image of a snail, showing the non-superimposable nature of their helical shells. *P*-helical snail shells are more common in nature, with the M-shell often occurring as a result of a genetic mutation.

1.5.1 Molecular Chirality

At a molecular level, chirality can occur about a point (point-chirality), about an axis (axial chirality) or about a plane (planar chirality).[34] The simplest of these is point chirality in which the molecule features an asymmetrically substituted sp^3 tetrahedral centre.[146] Typically this will be a chiral carbon, and can be nicely demonstrated by the two enantioforms of α-amino acids (**Figure 1.39**) which feature an asymmetrically substituted α-carbon.

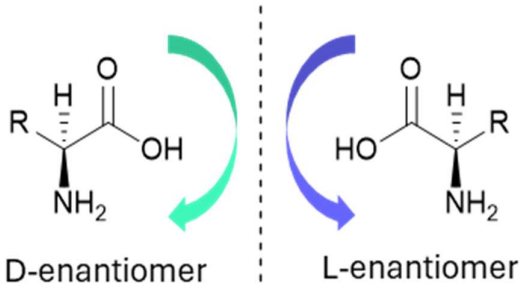

Figure 1.39 - Enantioforms of amino acids.

Point chiral molecules are typically labelled as *S*- (sinister) or *R*- (rectus) following the Cahn-Ingold-Prelog naming convention, in which *S* denotes the left-handed (anti-clockwise) conformation and *R* the right (clockwise). The rules for the prioritisation of different *R*-groups ultimately determine the handedness assigned to the molecule. Prioritisation is assigned by the atomic number of the substituent, for example sulfur (atomic number = 16) being awarded higher priority than oxygen (atomic number = 8). Higher priority sidechains are counted first and then moving either left or right towards the next highest priority group, the directionality can be assigned.

The Cahn-Ingold-Prelog naming convention can also be applied to AAs, however, the result of this is that all AAs, with the exception of cysteine, are labelled as the *S*-configuration. This occurs due to the higher prioritisation of sulfur comparative to oxygen for the reason described above. Despite having the same spatial arrangement and optical rotation, cysteine is labelled as the opposite enantiomer, therefore it is common for biological molecules to be labelled in the L-(*laevus*)/D-(*dexter*) notation to conserve consistency across all AAs (**Figure 1.40**).[147]

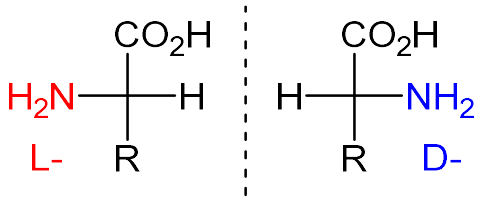

Figure 1.40 - Fischer projections of amino acids

Planar, axial and helical chirality differ from point chirality in that the molecule itself does not require a chiral centre. Instead of exhibiting their asymmetry around a single atom their asymmetry occurs about an axis or plane, and therefore the atoms (points) in the molecule themselves can be achiral but instead arranged in a chiral sense. Typically, on a molecular level these structures feature rotational restrictions such as double/triple bonds or rings which allow for the formation of structural isomers. It is generally this lack of flexibility that results in the mirror image being non-superimposable as rotation is not available to this structure. These types of asymmetries which occur about an axis, or a plane will be discussed more in the context of supramolecularly chiral molecules as they are important for chiral assemblies of molecules.

1.5.2 Supramolecular Chirality

Supramolecular chirality terms are used to describe structures that have been formed by non-covalent interactions.[5, 34] Within the lens of this thesis, this terminology will be used to describe the super-secondary structures of peptides along with metal-peptide complexes. Supramolecules rely on self-assembly of their components as governed by non-covalent interactions such as hydrogen bonding, solvophobic effects and aromatic stacking (Section 1.3). The components or subunits which comprise these structures can be chiral or achiral, all with the ability to form chiral superstructures as a result of asymmetric arrangements of these component parts. The control of this chirality and the preferential formation of one enantiomer over another is often orchestrated by a chiral auxiliary molecule. These auxiliary molecules can direct the folding and association of the supramolecular components by biasing the structure one way or another by covalent and non-covalent interactions with the original structure. Chirality in supramolecular assemblies has gained interest due to the structures often exhibiting dynamic and stimuli responsive behaviours, making them interesting targets for applications such as catalysis and mimicking of enzymes.[148,149]

Notation for supramolecularly chiral structures depends on the type of structure that is being dealt with. In the context of helically chiral structures, such as the α-helices and CCs, the chirality is noted as being either left- or right-handed, depending on the direction in which the helix curls around the axis. These isomers have been reported in this simplistic manner with the directionality being determined by following the vector as depicted in **Figure 1.41**.

More commonly the notation for these isomers will be *P*- or (+) for a right-handed helix, or *M*- or (-) for a left-handed helix.

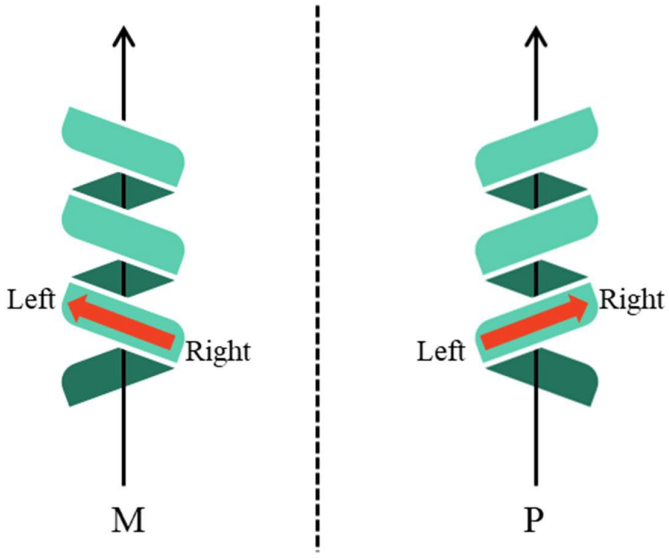

Figure 1.41 – *P*- and *M*- helices, directionality can be determined by following the rotation around the axis either from left to right (*P*-) or right to left (*M*-).

Similarly, for supramolecularly chiral complexes, such as the octahedral complexes that are the main focus of this thesis, the naming conventions for uncoordinated assemblies will be (+) or (-), but when coordinated will follow the Δ-/Λ- notation where Δ-notates a right-handed structure and Λ- a left-handed structure. To determine the handedness of octahedral complexes, the propellor diagram is often utilised (**Figure 1.42).**

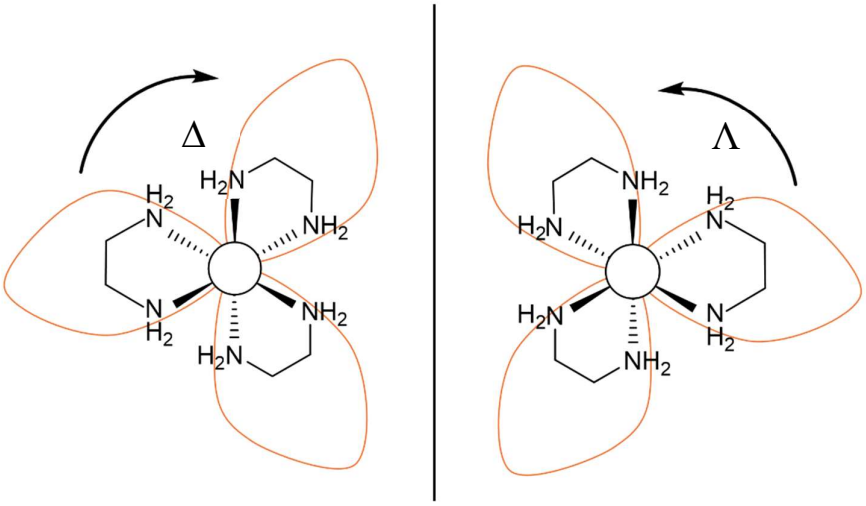

Figure 1.42 - Propellor diagram of a tris-chelate octahedral complex (using en ligands as an example) with the viewpoint along the C_3 axis. Assigning chirality of an ML_3 octahedral complex using this diagram requires following the clockwise or anticlockwise directions of the 'out-of-the-page' facing ligands, as indicated by the arrows in the figure.

These supramolecular assemblies can take many forms such as nanoparticles, nanotubules, MOFs, lattices, hydrogels, and metal-peptide catenanes and typically feature an organic chiral auxiliary in the synthesis to template the self-assembly process.[6, 16, 131, 150, 151] Use of chiral auxiliaries, often referred to as 'chiral sergeants', can direct the formation of globally chiral supramolecular assemblies by amplifying their chirality onto the achiral soldiers.[152] This type of chiral amplification has been observed in polymeric systems with as low as 0.5% chiral monomers still exhibiting a chiral sense.[153]

Due to their biological propensity to self-assemble, biocompatibility and easy synthesis peptides have become a popular choice as chiral auxiliaries when generating self-assembled super-structures.[154] Generally, these peptides will be short, linear sequences which vary in the handedness of the AA content, but some studies also include longer sequences with little variation in the AA content, for example polyproline helices.[155] The self-assembly of these short peptides into larger structures often relies on hydrophobic interactions that guide the packing in aqueous media, H-bonding between AA side-chains and/or ligation to a metal binding motif.[71, 142]

The chiral amplification during self-assembly eluded to in this section has been discussed in more detail with reference to relevant examples in the next section (1.5.3).

1.5.3 Chiral Information Transfer in Self-Assembly

The self-assembly of supramolecular systems is a widely studied topic among the scientific disciplines and has been gaining interest in the eyes of chemists and biologists alike for the last 40 years.[156] From the perspective of the synthetic chemist, studying these systems allows insight into how information is communicated from molecule to molecule with increasing complexity. By synthesising model systems using a bottom-up approach, the complexity increases with scale. These model systems can allow chemists and biologists to investigate the various communications between molecules in complex systems, from the transfer of stereochemical information to the origins of life and prebiotic chemical evolution. Peptides and amino acids, due to their well-documented stereochemical information transfer and ability to form large assemblies, are frequently used in these model systems.[156]

Although the exact mechanisms of chiral information transfer on large scales are not well investigated, some of the principles involved in short scale chiral information transfer have been elucidated through the use of the model systems described above. Simplistically, chiral information transfer is governed by self-assembly processes occurring as a result of non-covalent interactions between the component parts, with directionality imparted on the system as a result of chirality in the components.

One example of well documented chiral information transfer on this relatively small scale is in the super-secondary structure that is a common feature of peptides and proteins, the coiled coil. CCs form due to intermolecular, non-covalent, H-bonding, hydrophobic and ionic interactions between two or more α-helices and exhibit a left-handed supercoiling as a result of the off-set between the α-helices which is required for packing. If the α-helices comprising the CC were instead replaced with α_L-helices, this packing arrangement would result in right-handed supercoiling of the new CC, because of the sidechain steric interactions. This higher-level chiral information begins at the molecular level with the AAs. Point chiral L-AAs when self-assembling into α-helices favour *P*-helices. This favourability is summarised neatly by the Ramachandran plot (Section 1.2) which shows that as a result of the *phi (Φ)* and *psi (Ψ)* angles of the AAs, the right-handed (α) helix is the dominant conformation afforded by L-AAs. As before, if the chirality of the AA was switched to the D-conformation, the opposite will hold true. The chiral information from the AA determines the conformation of the secondary structure and then as mentioned above, the secondary structure chirality influences that of the super-secondary structure.

It has been demonstrated that altering the point chirality of even a single AA in a short peptide sequence can drastically alter the architecture of the resulting aqueous self-assembly.[72, 157] This has been shown in the work of Marchesan, for example, through synthesis of homo- and heterochiral tripeptide sequences. It was found in this work that homochiral sequences of Phe-X-Phe (where X = Ala, Val, Nva, Leu, Ile or Nle) did not self-assemble into hydrogels, however, altering these sequences to feature the opposite chirality AA in the as the central residue resulted in the formation of hydrogels, with the exception of Phe-^{D}Ala-Phe. The assembly of these heterochiral sequences into hydrogels was monitored by CD spectroscopy and it was observed that the signals increased over time throughout gel formation, and that the gel stability was temperature dependant (thermoreversible gels). X-ray diffraction of the tripeptides uncovered the structural relationship between the chirality of the AAs and the resulting assembly that is formed (**Figure 1.43**). It was observed that the

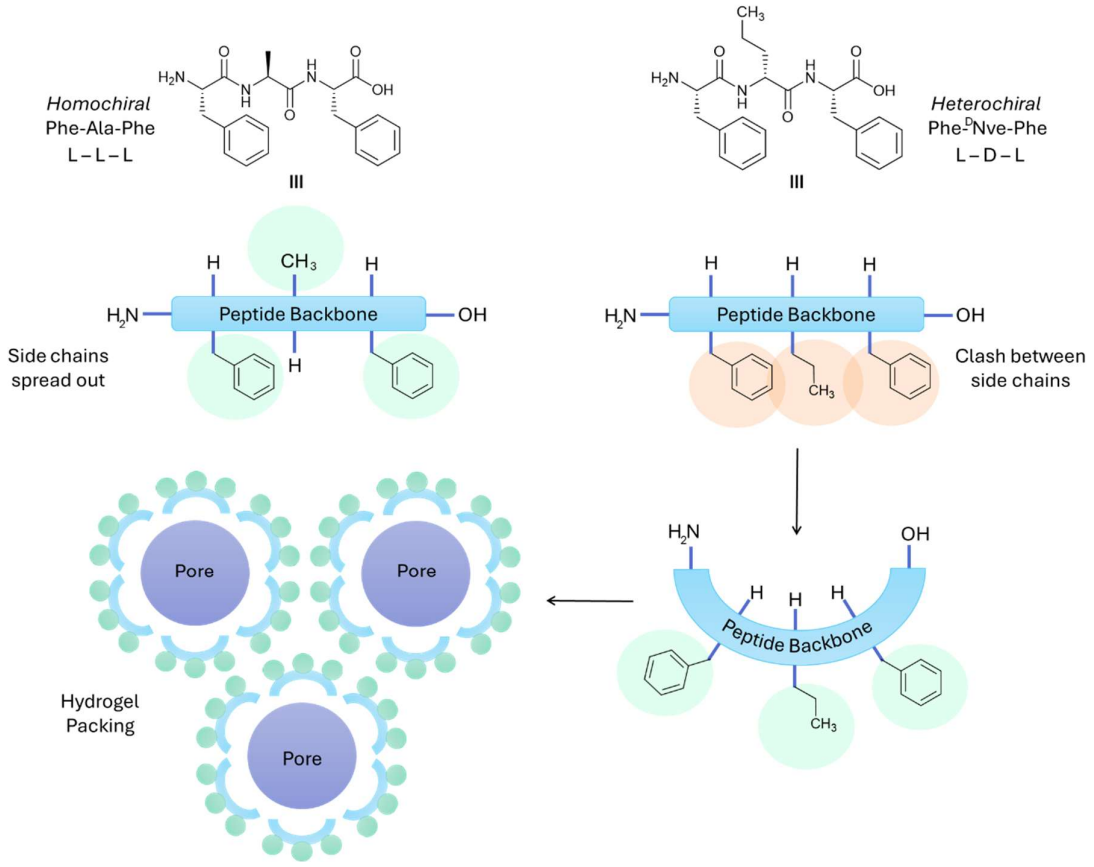

Figure 1.43 - Homochiral and Heterochiral tripeptide packing work performed by Marchesan *et al.* The structural differences of the homo- and heterochiral peptides are shown, with the 'bending' of the peptide backbone occurring in the case of the heterochiral species to account for the large amount of steric bulk resulting from the hydrophobic side chains all being present on the same face. The amphipathic nature of the heterochiral species results in the hydrophobic packing which forms the hydrogel.[157]

heterochiral sequences form amphipathic structures, which bend, forming an 'arc shape' in order to account for the additional steric bulk from the hydrophobic side chains all being present on the same face. This leads to the formation of the hydrogel, as the hydrophobic groups pack together in a hexagonal fashion, as demonstrated in **Figure 1.43**.

Chiral information transfer or amplification was briefly discussed in the previous section with mention of the 'sergeants and soldiers' principle which is employed frequently to generate chirality in a mostly achiral system. One example of this phenomenon taken from the literature focuses on the induction of chirality in 3_{10} helical peptides comprised of alternating achiral Z-dehydrophenyalanine (ΔPhe) and 2-Aminoisobutyric acid (Aib) residues (**Figure 1.44**). These residues are commonly used in these systems as they are 'helix favouring', specifically, their presence is commonly used in the synthesis of the secondary structure known as the 3_{10} helix. 3_{10} helices are similar in structure to α-helices, however, they are more tightly wound. Their turns are 3-AA long instead of the α-helices 3.6, and their H-bonding interaction occurs between the *i*–*i*+3 residues instead of the *i*–*i*+4 interactions seen in α-helices.

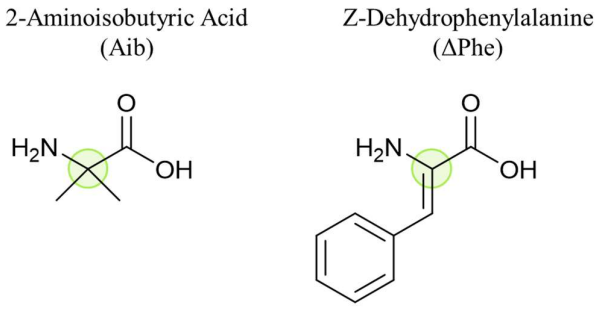

Figure 1.44 - Chemical structures of 2-aminoisobutyric acid and z-dehydrophenylalanine with the achiral carbon highlighted in green.

This study involved the synthesis of a series of six peptides: I–VI (**Figure 1.45**). By varying the position and chiral content of the peptide sequence by inclusion of an L- or D-Leu residue, either at the N- or C-terminus, the chirality of the resulting 3_{10} helix could be controlled. Peptides I, II and III which include an L-Leu in their structures were found to direct the 3_{10} helix to a left-handed screw sense, as observed by the presence of a positive exciton couplet in the CD spectra. Furthermore, sequence III, which features two Leu residues, one at each end of the sequence, exhibits the strongest CD signal which suggests it has a stronger chiral preference for the left-handed screw sense as a result of having two chiral soldiers in the sequence. On the other hand, sequences IV and V exhibit a negative exciton couplet in their

CD spectra. Sequence V which has a D-Leu at the N-terminus has exhibits the strongest preference for the right-handed screw sense. Sequence IV has both an L and D-Leu in the sequence, with the D-Leu situated at the N-terminus and the L-Leu at the C-terminus.

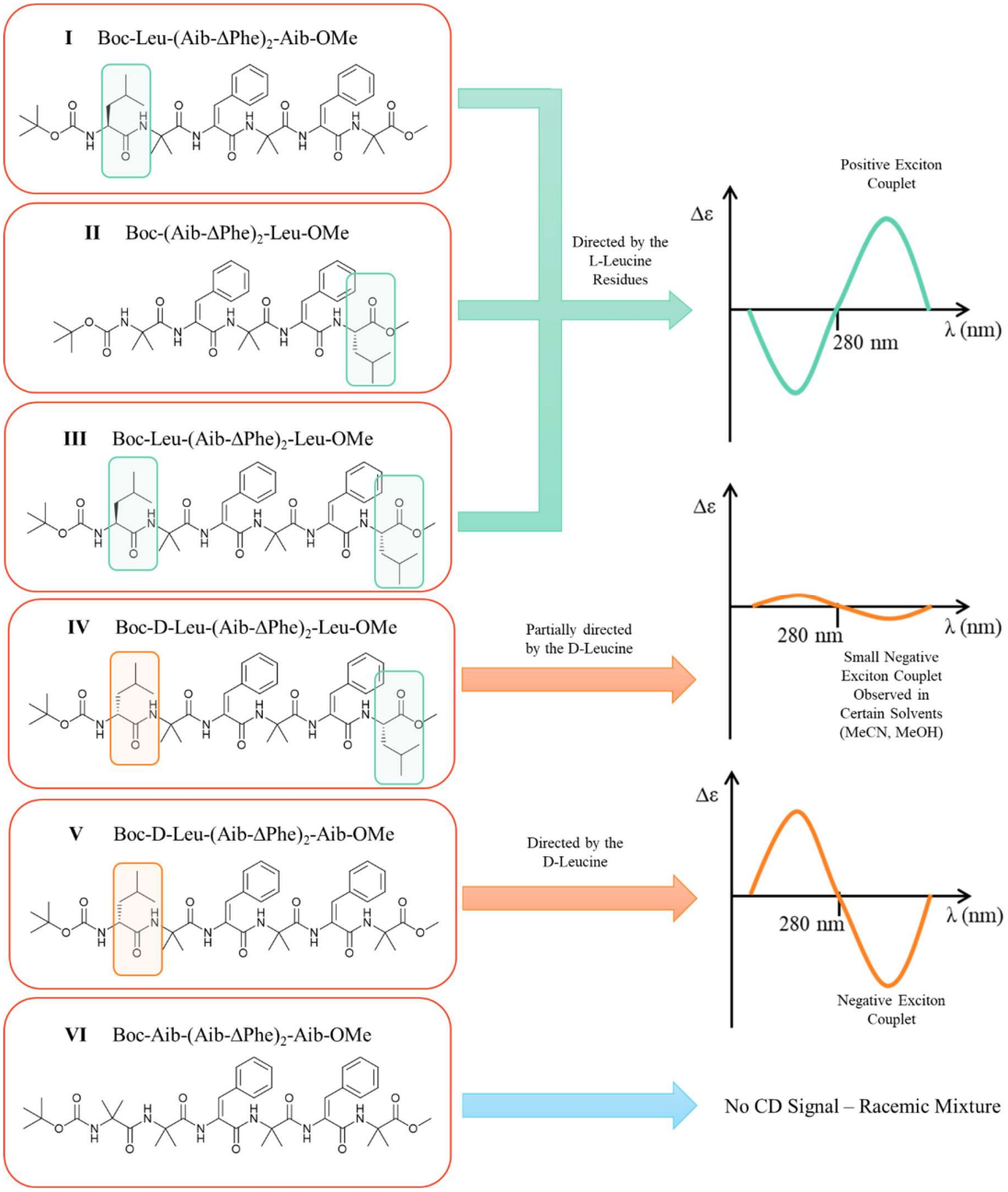

Figure 1.45 - Helical Screw Sense directing by inclusion of a chiral amino acid at the C- or N-terminus of the peptide. Peptides I-III direct the folding into the 3_{10} helix to favour a left-handed screw sense, as exhibited by a positive exciton couplet centred around 280 nm in the CD spectra. Peptide IV and V direct the folding to favour folding into the right-handed screw-sense, characterised by the presence of the negative exciton couplet in the CD. Peptide VI is a control sequence which contains no chiral auxiliaries.[133]

Interestingly, rather than exhibiting no signal, indicative of a racemic mixture, these peptides showed a small preference for the right-handed screw sense, with the D-Leu dominating the chiral information transfer. Sequence VI was a control sequence to show that the 3_{10} helix formed a racemic mixture in the absence of a chiral auxiliary.

It was concluded by the authors that this was a result of positioning, with chiral sergeants at the N-terminus having more influence than those at the C-terminus. These systems exhibit the 'sergeants and soldiers' behaviour that was discussed above and demonstrate cooperative behaviour between the chiral and achiral components during their self-assembly (**Figure 1.45**). A later study by the same research group indicated that natural 3_{10} helices may have inbuilt chiral recognition abilities through the N-terminus and highlights the importance of the N-terminal position for biological recognition and interaction.[158] This study also highlights a different type of chiral information transfer known as Non-Covalent Chiral Domino Effect (NCDE). By synthesis of a sequence comprised of achiral AAs; Aib, β-Ala and ΔPhe (**Figure 1.46**), a racemic mixture of 3_{10} helices is generated, exhibiting no preference for either screw sense when analysed by CD. Though introduction of a chiral amino acid to this system, i.e. L-Pro or D-Pro, it was discovered that the chiral preference

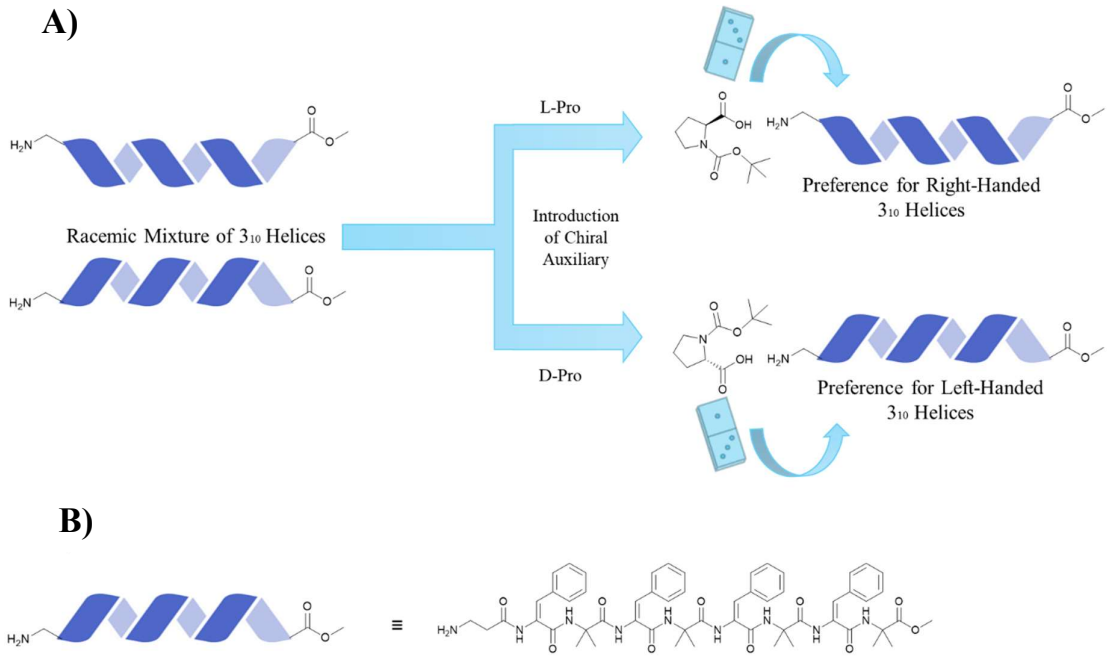

Figure 1.46 - A) Non-covalent chiral domino effect (NDCE) in 3_{10} helices. To a racemic mixture of 3_{10} helices, comprised of achiral amino acids, a chiral 'domino' or auxiliary, is added, directing the folding of the 3_{10} folding. If an L-AA is introduced, the helices favour the right-handed screw sense, however, if the D-AA is introduced instead, the left-handed screw sense was found to be more preferable. **B)** The sequence of the 3_{10} helices used in this study.[158]

of the helical screw sense could be controlled. In more detail, the results showed that L-Pro induced a right-handed screw sense in the helices, whereas D-Pro induced the left-handed screw sense (**Figure 1.46**).

It was hypothesised that the mechanism for this information transfer occurred through a non-covalent interaction between the chiral domino (Pro) and the N-terminal residues of the peptide sequence. By forming two H-bonds, first between the carbonyl group on the Boc group of the Pro and first amide of the peptide backbone and second between the Pro carbonyl group and the second amide of the peptide backbone. Additionally, there is a proposed ionic interaction between the amide of the peptide N-terminus and the carboxylate of the Pro (**Figure 1.47**).

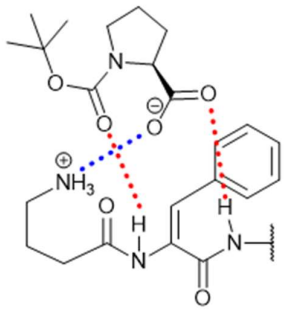

Figure 1.47 - Proposed interaction between the chiral 'domino' (L-Pro) and the N-terminal amino acids of the peptide. The red dotted lines indicate the proposed H-bonds between the backbone amides and the Pro carboxylates, and the blue dotted line shows the proposed ionic interaction between the carboxylic acid of the Pro and the terminal amine.[158]

Foldamers and helicates (metal coordinating foldamers) are oligomeric structures which have been used successfully as synthetic, biomimetic structures, these include mimics of protein secondary structures, and most often, these will be of a helical nature.[159-161] Foldamers are 'folding oligomers', synthetic molecules which through external stimuli fold into ordered states. Helicates are a specific subset of foldamers which coordinate metal ions to form repeating helical structures.[160]

Foldamers are a very common way of analysing the factors influencing the amplification of chirality and the limitations of such system. Typical examples of the short chains comprising foldamers will only feature a very small chiral unit which can determine the chirality of the whole system via a sergeants and soldiers type mechanism. This mechanism is also sometimes referred to as Covalent Chiral Domino Effect (CCDE).[158] In theory, this concept is very similar to the sergeants and soldiers' principle, however, CCDE is more narrowly focused on chiral information amplification along a chain of achiral subunits. The chiral

information that is transferred in this way is typically helical and is passed down the chain inducing a helical chirality across the length of the molecule.[6] Foldamer chemistry and the conformational restraints in these systems related to their chiral induction has been subject to much investigation.[162, 163] One such example of this research published by Byrne *et al.* discussed the long-range (over 60 chemical bonds) chiral induction of an achiral peptide foldamer by featuring either monomers or dimers of chiral L-α-methylvaline units at the N-terminus inducing helicity in the system.[164] This system again took advantage of the propensity for oligomers of achiral subunits, Aib, ΔPhe and 1-aminocyclohexane carboxylic acid (Ac_6c) (**Figure 1.48**) to form 3_{10} helices.[165] To investigate the ability to control the stereochemistry of these sequences, two sequences of these achiral AAs were synthesised. The first of these sequence in **Figure 1.48** is I), which features a singular L-methylvaline residue at the N-terminus (Z-L-(αMe)ValAib_4Aib*Aib_4-OtBu), and the second, II), features an L-methylvaline dimer at the N-terminus (Z-L-(αMe)Val_2Aib_4Aib*Aib_4-OtBu), asterisk (*) symbols in the sequences indicate presence of a ^{13}C label on that residue for NMR. Analysis of the CD spectra of these two peptides in organic solvents found a preferential formation of the right-handed screw sense of the helices. Furthermore, through observation of the ^{13}C NMR it was found that peptide II) biased the folding with a helical excess up to 98% in THF. Following the success of controlling the helical screw sense down the chain,

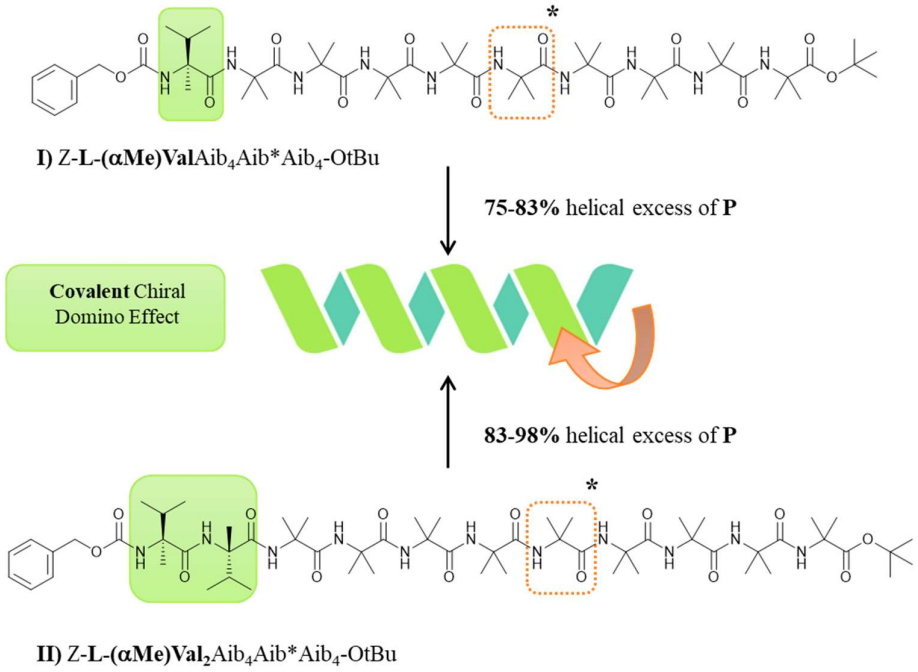

Figure 1.48 - The chiral communication from the N-terminal L-(αMe)Val residues propagates down the chain directing the folding to favour a right-handed (P) screw sense in a 75-83% helical excess for I) and 83-98% helical excess for II).[165]

the ability of these motifs to result in the formation of a new stereogenic centre by controlling an asymmetric reaction was investigated.

To do this sequence III) Z-L-(αMe)Val_2Aib_4Δ $PheAib_4$-OtBu, in **Figure 1.39** was synthesised. This sequence has a ΔPhe residue as the central residue. As this AA is unsaturated and reactive, when exposed to Crabtree's catalyst it is hydrogenated. It was found that the helicity of this sequence (P, right-handed) resulted in a 95% preferable formation of the L-Phe residue following hydrogenation, as opposed to the D-Phe.

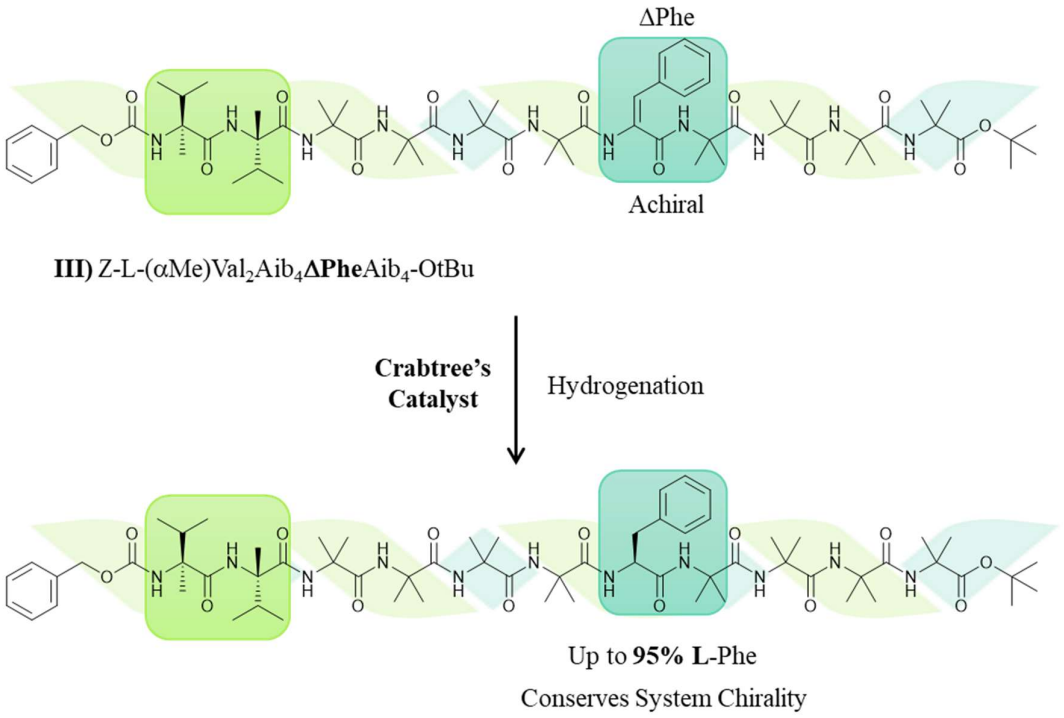

Figure 1.49 - Demonstrates the ability of sequence III) to conserve the chiral information conducted by the terminal L-(αMe)Val residues, favourably forming the L-Phe during hydrogenation with Crabtree's catalyst.[165]

Remote control of chiral induction on terminal residues by the foldamer helicity was then investigated. Three comparable sequences of increasing length containing repeating units of (Aib_4Ac_6c), were synthesised. The longest of these sequences; IV) Z-L-(αMe)$Val_2Aib_4Ac_6cAib_4Ac_6cAib_4Ac_6cAib_4$-$NHCH{=}CHCH_3$, in **Figure 1.50** was synthesised. In order to investigate remote stereocontrol by the residues at the N-terminus on the reactive group, $NHCH{=}CHCH_3$ at the C-terminus, these peptides were reacted with a nucleophilic arene. The result of this reaction was stereochemical control of the reaction, conserving the screw sense of the foldamer, into the new component, over 60 bonds.

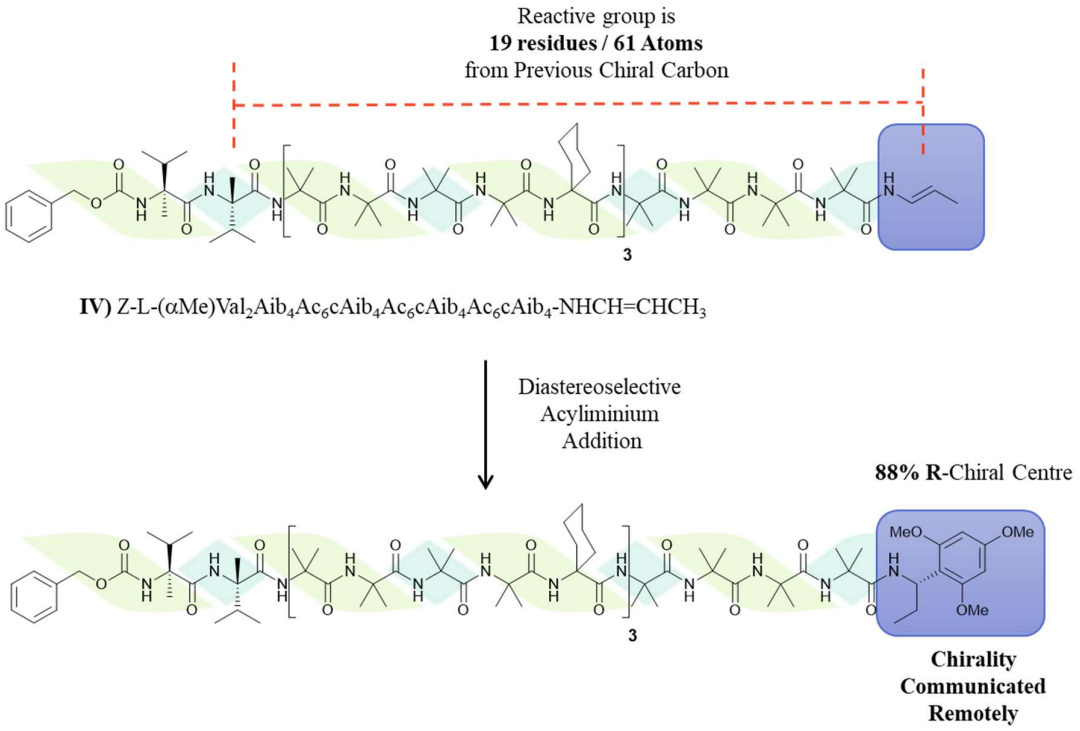

Figure 1.50 - The long-range chiral communication (over 60 bonds) conducted by the terminal L-(αMe)Val residues.[165]

Another aspect of chiral amplification is the idea of the 'Majority Rules' principle. Experiments that utilise this principle involve addition of an enantiomeric excess (ee) of one of the components as a means of controlling the chirality of the entire system. This slight ee results in an imbalance in the chirality of the system which then directs the overall chirality of the assembly of the components to follow that of the majority determining the final global chirality.[6, 148] This principle has been employed to generate a chiral bias in systems such as helical sense of polyisocyanates,[166-168] and chiral aggregates of polythiophenes.[169]

In more detail, the 'Majority Rules' principle has been employed in the literature to bias the chirality of the helical structure polyisocyanates by introducing a slight enantiomeric excess of either the *R*- or *S*-isomers of the polymer subunits (**Figure 1.51).** This study investigated the helicity of the helical products of 2,6-dimethylheptyl isocyanate polymers in their homo and heterogenous forms. Synthesis of the homopolymer of *(R)*-2,6-dimethylheptyl isocyanate results in a signal which is consistent with M-helical chirality for these structures, and *vice versa* for the *(S)*-2,6-dimethylheptyl isocyanate. Interestingly, by synthesising a copolymer of *(R)*- and *(S)*- 2,6-dimethylheptyl isocyanate with a slight ee of the *(R)*-isomer (56%) results in a chiroptic signal indistinguishable from that of the *(R)*-homopolymer. This demonstrates the Majority Rules principle. The slight excess (8%) of one enantiomer dictates

the chirality of the entire structure, resulting in a complete chiral bias of the helical structure. This principle, however, is sensitive to the magnitude of the ee. In this same study an ee of 51% of the *(S)*-isomer is copolymerised with the *(R)*-isomer (49%), resulting in a 2% excess of the *(S)*-isomer within the structure. The result is a chiral bias towards the *P*-helix, however, the magnitude of the chiroptical signal is approximately half that of the *(S)*-homopolymer, demonstrating that there is still some chiral control elicited by the *(R)*-isomer.[168]

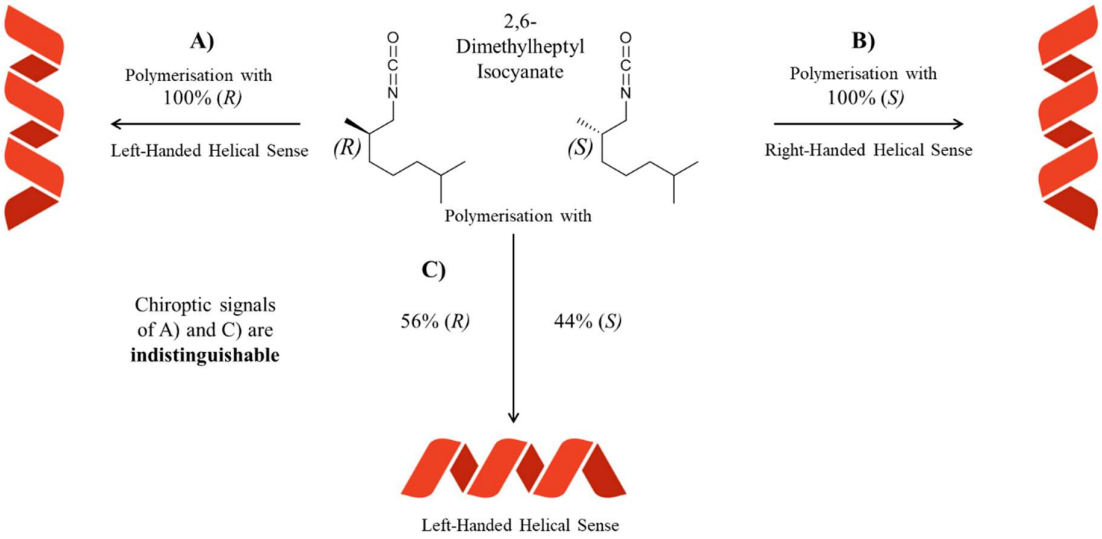

Figure 1.51 - **A)** Result of polymerisation of 100% (*R*)-2,6-dimethylheptyl isocyanate found that there was a chiral information transfer to the 3_{10} helix of a left-handed screw sense. **B)** Result of polymerisation of 100% (*S*)-2,6-dimethylheptyl isocyanate found that there was a chiral information transfer to the 3_{10} helix of a right-handed screw sense. **C)** Result of Copolymerisation of (*R*)-2,6-dimethylheptyl isocyanate and (*S*)-2,6-dimethylheptyl isocyanate with a 12% ee of the *(R)*-2,6-dimethylheptyl isocyanate. Despite only being in slight excess the *(R)*-enantiomer dominated the chiral control leading to a left-handed helical sense.[168]

A further example of the use of stereochemical information transfer comes from the work of the Nitschke group.[170] By reaction of flexible trialdehyde components with *R*- or *S*-1-phenylethylamine, enantiopure L_Λ and L_Δ ligands were generated respectively (**Figure 1.52)**. Coordination of each of these ligands with Zn^{2+} in a 4:4 ratio led to the formation of either the Λ or Δ tetrahedral cages, with the L_Λ/L_Δ ligands occupying the faces of the tetrahedron and the Zn^{2+} ions at the vertices. It was therefore shown that the chirality of the tetrahedral cages could be controlled, and that the resulting cages were enantiopure. Furthermore, in this work the same trialdehyde unit was reacted with an achiral amine, 4-methoxyaniline, to yield the product in **Figure 1.53**. The result of the coordination of this unit with Zn^{2+} in a 4:4 ratio is a racemic mixture of the Λ and Δ enantiomers, as may be anticipated. Interestingly, however, is the host-guest behaviour of this cage-structure. Upon introduction of chiral guest,

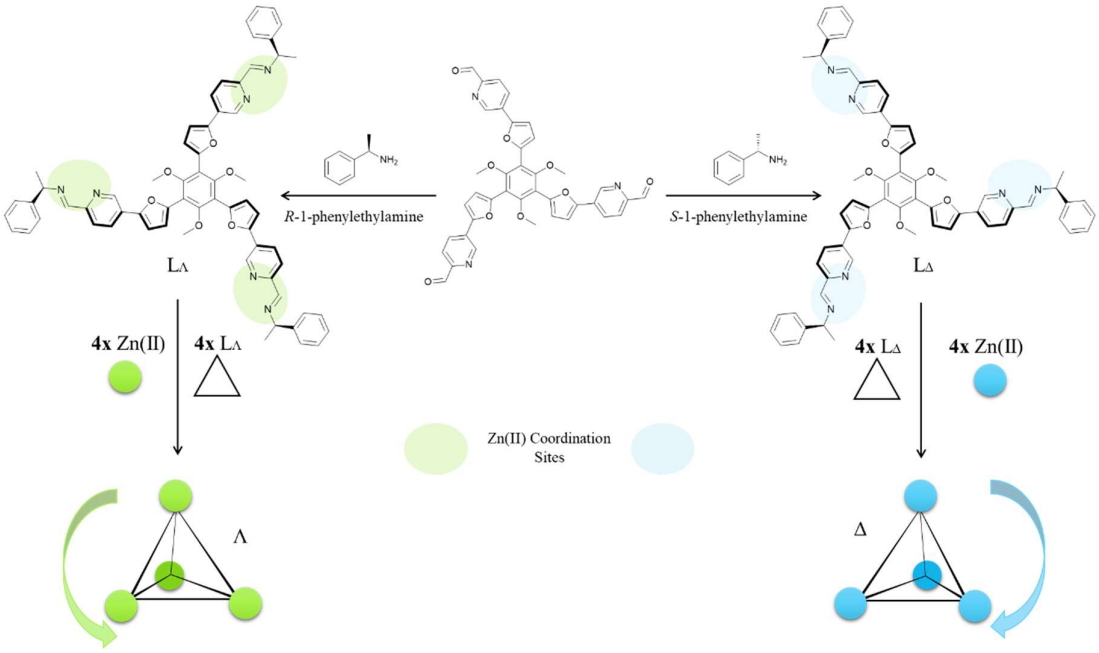

Figure 1.52 -Transfer of stereochemical information by reaction of the flexible trialdehyde with *R*- or *S*-1-phenylethylamine resulting in two stereochemically distinct molecules, L_Λ and L_Δ respectively. When reacted in a 4:4 ratio with Zn^{2+} this led to the formation of enantiopure tetrahedral cages.[170]

natural product (+)-podocarpic acid in the presence of DIPEA as a base, the result is chiral conversion to 100% of the Δ-enantiomer of the cage, with the (+)-podocarpic acid within the cavity, an enantiopure host-guest complex. Interestingly, stereoinversion of the 100% Λ-Zn-cage from the L_Λ ligands was also found to occur when the (+)-podocarpic acid (as the

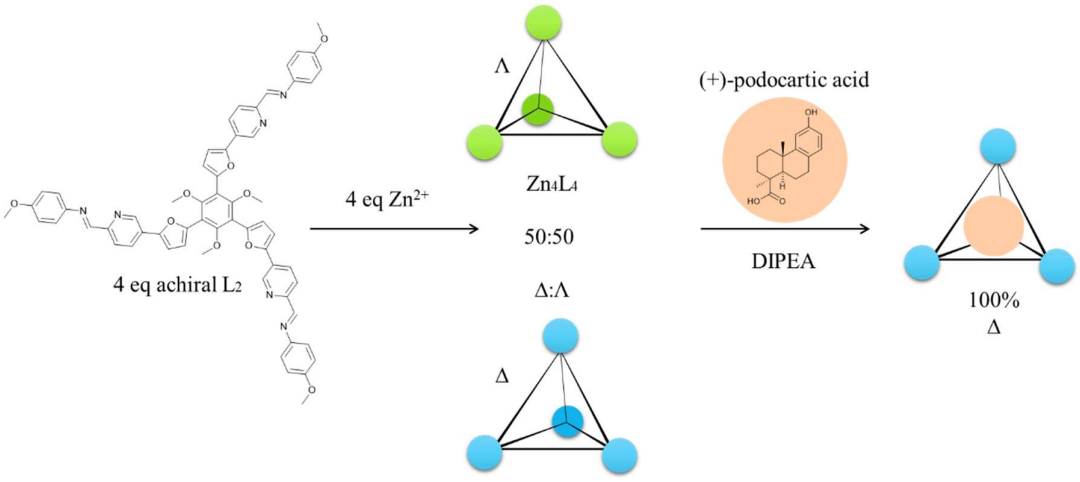

Figure 1.53 – 4 equivalents of achiral ligand L_2 is mixed with 4 equivalents of Zn^{2+} resulting in a 50:50 racemic mixture of the Δ and Λ tetrahedral cages. Introduction of the chiral guest molecule (+)-podocartic acid in the presence of DIPEA resulted in the stereochemical inversion of the cages, leading to a 100% Δ-chirality.[170]

carboxylate) was introduced as the guest. This is suggestive that the chirality of the guest is very influential to the overall chirality of the system.

This group has also investigated a similar tetrahedral cage molecule with peptide based ligands, coordinating to metal ions through thiols of cysteine residues for the formation of cage-based gels.[171] It was also observed in this study that the chirality of the cage could be controlled by tuning the chirality of the peptide ligands, however the stereochemical control was less pronounced than the previous example.

1.5.4 Visualising Chirality

Characterisation of chiral compounds requires techniques such as circular dichroism (CD) or X-ray diffraction (XRD) for determination of absolute configuration.[172] Because the chirality of peptide secondary and super-secondary structures relies on solvent interactions and are typically dynamic, they therefore require the assembly to occur in aqueous solution. This precludes X-ray diffraction as this technique requires the sample to be prepared either as a single crystal (SCXRD), or to be loaded as a power (PXRD), which would not be applicable for monitoring a peptide assembly, nor any dynamic, cooperative interactions between peptide components. More recent work into the cryogenic loading of frozen, aqueous, biological samples for electron diffraction techniques has been performed, this allows for the formation of the secondary structures and molecular assemblies in aqueous solution which are then frozen such that they can be imaged.[173]

Circular dichroism (CD) is the most common method of structural determination for chiral compounds and is pertinent in determining the secondary and tertiary structures of peptides and proteins and monitoring their behaviours in response to external stimuli (pH, temperature, etc).[174] It is also frequently used for elucidating the chirality of octahedral (paddle-wheel complexes) metal complexes.[4,175] This technique uses the principles of UV-Vis absorption spectroscopy by systematically changing the wavelength of the beam and measuring the absorbance of light by the sample. Some CD spectroscopes can be found to take UV-Vis measurements in tandem with the CD ellipticity measurement due to them being dictated by the same principal techniques.

CD, unlike UV-Vis, is a difference method. This means that the measurement that is being reported in the spectra is the difference of two absorbance values for each wavelength. In this case it is the difference in the absorbance of left- and right-handed circularly polarised light, noted as ellipticity. A source of unpolarised light travels towards a monochromator, where it linearly polarises. Following this it enters a modulator, from which it leaves as left and right circularly polarised light which is then directed through the sample. The detector then measures the difference in the absorbance by the sample of the left and right circularly polarised light (**Figure 1.54**).

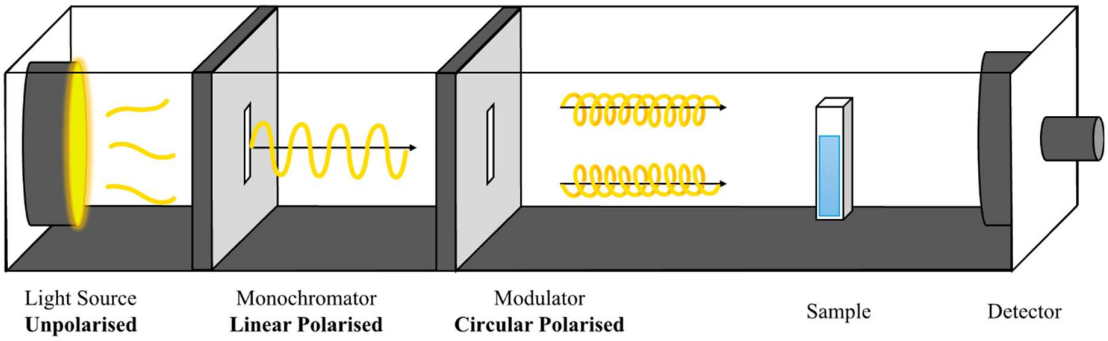

Figure 1.54 - Schematic of the basic principles of CD spectroscopy. From left to right, the light source emits unpolarised light, which then passes through a monochromator becoming linearly polarised. The light then passes through a modulator and becomes circularly polarised. Finally, the light passes through the sample, and that which is not absorbed hits the detector.

CD is commonly used for the structural characterisation of peptides and proteins. The characteristic CD line shapes of the common structural motifs exhibited by peptides and proteins (α-helix, β-sheet) are well documented across the literature and supported by crystal structures.[26, 176]

For all proteinogenic peptides and proteins, the signals corresponding to secondary structures which can be observed in the CD spectra are found in the far-UV region (approximately 190–240 nm) and exhibit a majority negative ellipticity. Peptides comprised of D-AAs on the other hand, lead to secondary structures which exhibit majority positive ellipticity signals. These signals arise from the high energy amide absorbance in this region. Peptides and proteins can also exhibit CD signals in the near-UV region through chiral arrangements of the aromatic AAs, Tyr, Trp and Phe, these absorbance signals are often found at wavelengths between 250-300 nm.[177]

β-sheets are one of the common structural motifs that can be characterised using CD spectroscopy. They exhibit a negative ellipticity signal at approximately 218 nm (from a n-π* transition), and a positive signal at 195 nm (π-π* transition). Similarly, α-helices exhibit a double minima in the CD absorbance, with the first of these minima arising at 222 nm (n-π* transition) and the second at 208 nm as well as a positive signal at ~195 nm (exciton splitting π-π* transition).[176] The ratio of the signals at 222 nm and 208 nm are typically used to qualitatively determine the degree of α-helical character in the peptide sample. If this ratio is skewed towards 222 nm, this signal is considered more helical than one that is skewed towards 208 nm, for example. Methods exist for the quantitative determination of the percentage folding of the α-helix using the ellipticity values at these wavelengths. However, these rely on an assumption for the value of 100% *α*-helical.[178] Another important CD signal when it comes to characterising the structure, or lack-there-of, of peptides and proteins is the random coil. This non-structure exhibits a negative signal in the CD at wavelengths below 200 nm. A graphical representation of a characteristic α-helical signal and random coil have been shown below in **Figure 1.55**. *β*-sheet signal is not provided as it is not relevant to the scope of the project, however there are numerous examples that can be found in the literature.[176]

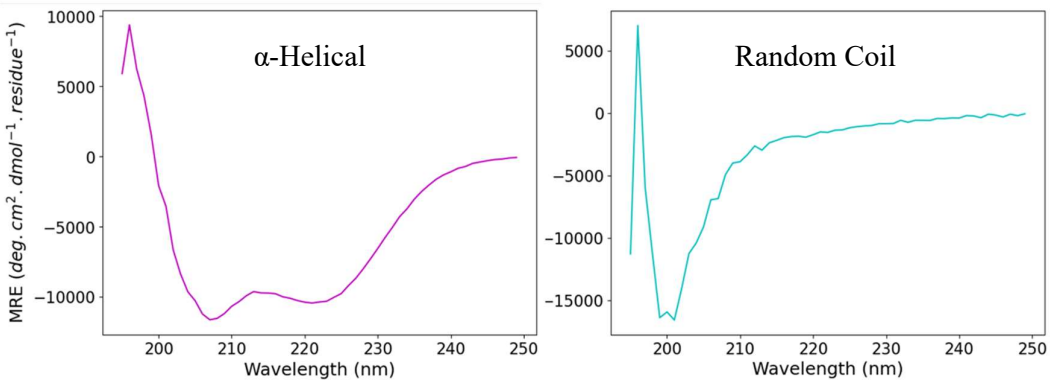

Figure 1.55 - Characteristic line shapes and expected wavelengths for an α-helical structured peptide (purple) and an unstructured peptide (blue). Units of the y-axis are Mean Residual Ellipticity (MRE) which normalises the elliptical absorbance for number of AA residues, concentration and pathlength such that different peptide solutions can be compared.

Circular dichroism is also fundamental for the characterisation of octahedral and tetrahedral chiral metal complexes. Often these complexes feature chelating units with extended chromophores (e.g. bipyridine, phenanthroline, 8-hydroxyquinoline, terpyridine) which exhibit chiral signals in the near-UV region (250 – 300 nm) from their π-π* transitions. The CD signals of these complexes are described as an exciton couplet surrounding the

absorption wavelength, which appears as a bisignate curve, characterised by an area of negative ellipticity and on of positive ellipticity (**Figure 1.56**).[95, 179] Also referred to as an exciton couplet, these signals are the result of close proximity chromophores exhibiting delocalisation of an electronic exciton state across said chromophores, with a larger effect being exuded by degenerate chromophores, e.g. tris-phen.[175] The bisignate nature of this signal arises from attractive and repulsive interactions between the electronic dipoles of the proximal chromophores, with the attractive interactions resulting in the longer wavelength signal, and the repulsive interactions leading to the shorter wavelength signal.[180] The sign of this curve at the two wavelengths is dependent on the handedness of the species being investigated. For a Δ-conformation, the signal will appear as a negative ellipticity at lower energy, and positive at higher energy, and vice versa for the Λ-conformer.[16, 175] An example of an exciton couplet of either handedness is provided in **Figure 1.56.**

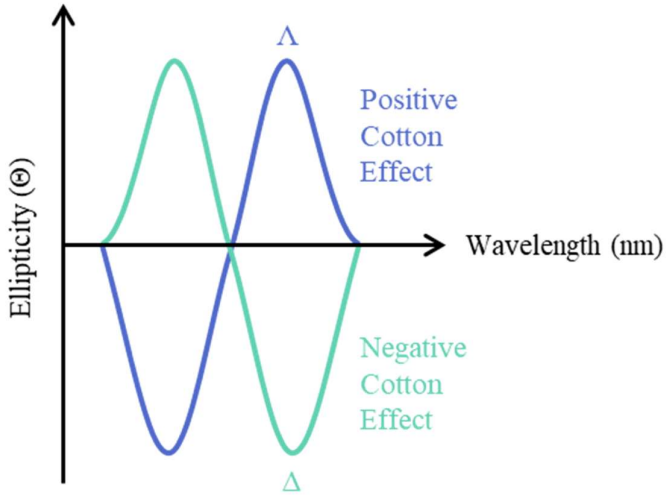

Figure 1.56 - Cartoon representation of two opposite chirality conformations of an exciton couplet type signal in a CD spectrum. The colours denote the assignment of an ML_3 octahedral complex, with blue representing the left-handed complex and the green representing the right handed complex.

1.6 Supramolecular Peptide Assemblies

Using the principles of peptide structural design, coordination chemistry and non-covalent interactions discussed thus far, a wide range of peptide based supramolecular assemblies with various applications have been documented across the literature.

Enzymatic behaviour encapsulates much of the topics discussed throughout this introduction so far. Firstly, they are biological, proteinogenic molecules comprised of mainly amino acids. The exhibit a variety of secondary, tertiary and quaternary structures which define their biological functionalities. Their behaviour with respect to these functionalities is often facilitated by NCIs. They associate cofactors, which are often necessary for their functionality, these include organic molecules such as pyridoxal phosphate (Vit. B6) (**Figure 1.57**) or inorganic, metal ions such as Zn^{2+}, Fe^{2+}, Cu^{2+} and Co^{2+}.

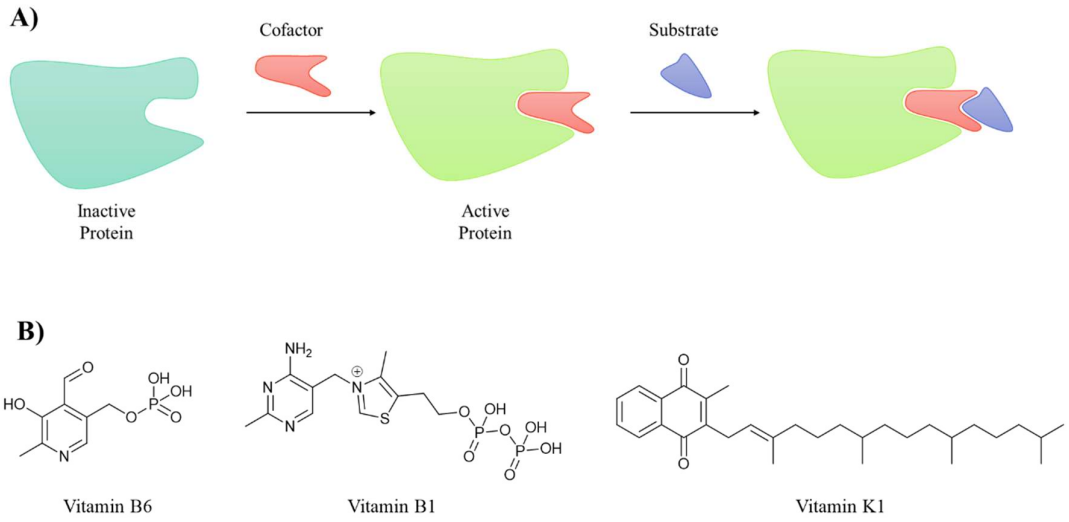

Figure 1.57 - A) Function of Cofactors in Enzymes. Cofactor (orange) associates to the inactive protein (dark green) which activates the protein (light green), now the substrate can bind. **B)** Examples of organic cofactors, vitamin B6, vitamin B1 and vitamin K1 which are vital for enzymatic processes in the body.

Finally, they exhibit specificity, meaning that their activity is dependent on the recognition of chiral components in the biological environment.[181] This combination of different principles encapsulated in a single system makes them incredibly interesting topics for inspiring the designs of artificial systems. Artificial metalloenzymes are an example of *de novo* designed peptide scaffolds using this bottom-up type approach for developing biomimetic systems. By designing a structural motif using the bottom-up approach, the

activity of a specific structural feature or binding region of a larger peptide can be studied.[182] The bottom-up approach is often desirable for designing such systems due to the ability to incorporate non-biological subunits, both organic and inorganic into the structures which can enhance their activity.[183] Such work has focused on the design and synthesis of helical-peptide based biomimetics which assemble into bundles and have the ability to incorporate heme units allowing them to mimic the redox behaviour of oxidoreductase enzymes, for example.[149, 184] This work by the Dutton Group utilised simplistic helical peptide models forming 4-α-helical bundle, known as a maquette. The aim of this work was to mimic the structure and function of the cytochrome b562 enzyme by incorporating heme cofactor B into the synthesised maquettes by interactions with bis-histidine regions in the core of the bundle **(Figure 1.58)**. Of the five synthetic peptides that were prepared and tested, maquette B was found to have heme association rates of the same order as the natural cytochrome b562. This result was a consequence of the flexibility of this maquette compared to the other four structures, with the more flexible structures encountering an entropic barrier, and those which are too rigid encountering an enthalpic barrier to heme uptake. Uptake of the heme was monitored using stopped flow kinetics which measured a full UV-Vis spectrum every millisecond. From this a change in absorption from 395 nm to 412 nm associated with the

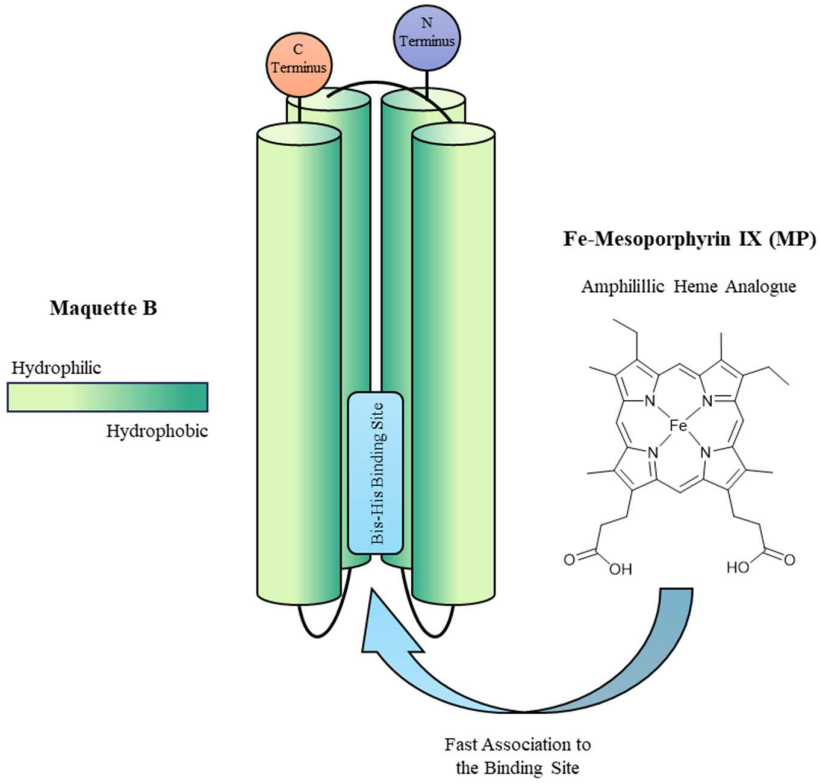

Figure 1.58 – Maquette B folds after association of amphiphilic heme analogue, Fe-Mesoporphyrin IX into a 4-α-helical-bundles with a hydrophilic core and hydrophilic outer region.[149]

porphyrin π-π* transitions as the heme is taken up by the maquette. Other heme analogues were tested in this work and it was found that amphiphilicity of this unit was also important, too hydrophobic and they would experience aggregation before reaching the binding site, and too hydrophilic and they wouldn't enter the binding site.[149]

Another, more general, example of these type of large self-assembling structures comes from metallopeptides. These assemblies have been studied for numerous applications, from materials and nanoscience to drug discovery.[185,186] Examples include the folding of dendrimer type peptides in the work done by Ousaka *et al.*[16] In this work peptides containing a single chiral AA were synthesised and attached to either end of a bipyridine moiety **(Figure 1.59**). The sequences of these peptides were specifically designed to self-assemble into 3_{10} helices, which when they contain an L-Val, favour the *P*-conformation and when containing a D-Val, favour the M-conformation.[16] It was observed that when these peptide ligands were coordinated to Fe^{2+} ions that the chirality of the complex was controlled, with M-helices resulting in Λ-complexes, and vice versa for *P*-helices. Sequence C3 was found to

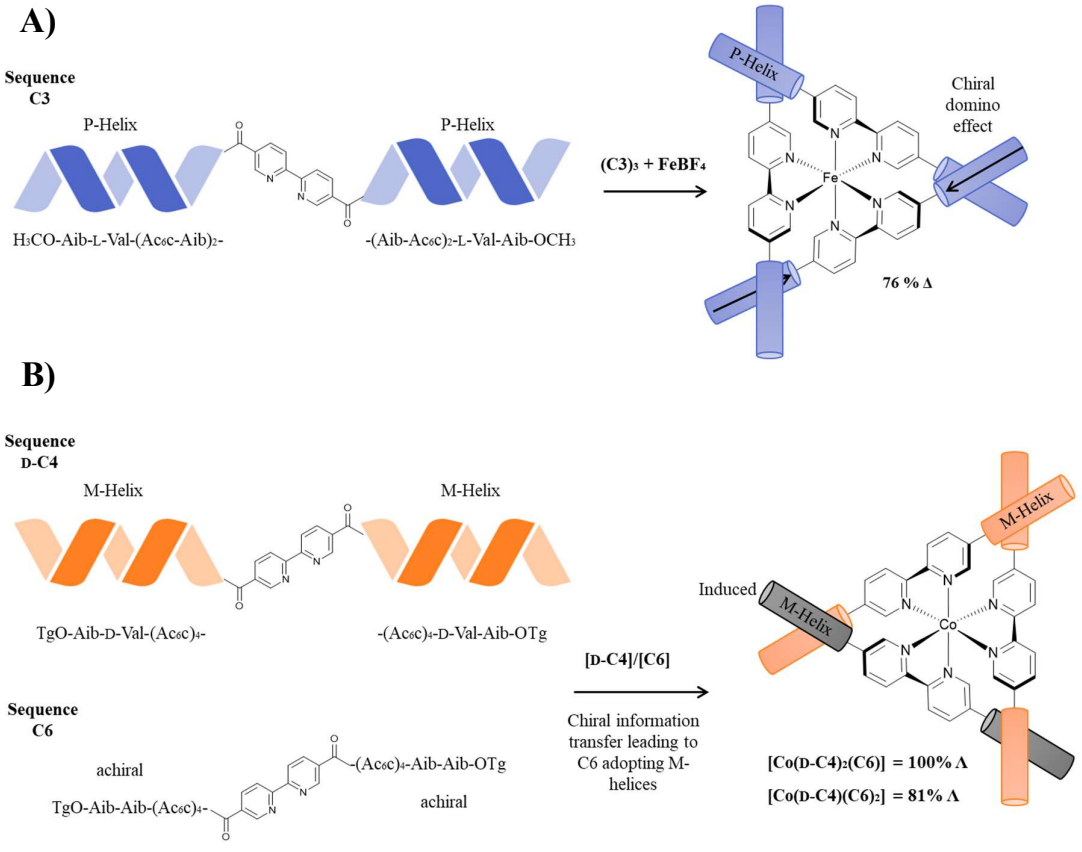

Figure 1.59 – **A)** Chiral domino effect from the P-helices of sequence C3 onto the Fe^{2+} complex resulting in 76% preference for Δ-isomer. **B)** Chiral induction observed when D-C4 is mixed with C6 (achiral) in the presence of Co^{2+} ions. Preference for the Λ-isomer of the complex observed as well as M-helicity being induced in the achiral C6 sequences.[16]

preferentially form Δ-complexes up to 76%. However, when tert-butyl ammonium chloride (TBAC) was introduced, the preference for this chirality over time increased to 100%. This was determined to be a result of Cl^- ions stabilising the assemblies by coordination to the N-terminal amides of the peptide segments. Furthermore, it was found that mixing sequence D-C4 with achiral C6 in the presence of Co^{2+} ions resulted in chiral induction from the D-C4 M-helices, through the Λ-Co^{2+} complex and resulting in induced M-helices in the achiral C6 sequences. The ratio of [D-C4]/[C6] had an impact on the magnitude of the chiral induction, with higher values of [D-C4] leading to more chiral preference.[16]

Looking specifically at coiled coil assemblies, there are numerous examples across the literature. As natural, self-assembling systems, CC's have been used to synthesise and investigate various systems including peptide-based hydrogels and fibres,[187] as MRI contrast agents,[188-190] and also synthesising mimics of biological structures to further understanding on their mechanisms and structural tolerances.[191, 192]

One such example of these studies includes work performed by the Woolfson group, generating biocompatible hydrogels using self-assembling CC-based fibres. The groups previous studies, inspired by nature, focused on the formation of self-assembling fibres (SAFs) and featured sequences including a 28-residue CC heterodimeric system which was synthesised by following CC design principles of the heptad repeat, *abcdefg* (**Figure 1.60**). The design features an Asn-Asn interaction, highlighted in green in the figure, between the complimentary strands. This interaction allows for the offset between the two strands and results in the 'sticky ends', which are highlighted in **Figure 1.60**. As a result of the offset, the negatively charged portion (blue) of one strand aligns with the positively charged portion of another complimentary strand, forming ion bridges between the Lys and Glu residues. Additionally, these structures feature charged residues in the exposed *b* and *c*-positions (Asp, His, Arg) which allow inter-fibre interactions, leading to the thickening of the assemblies of

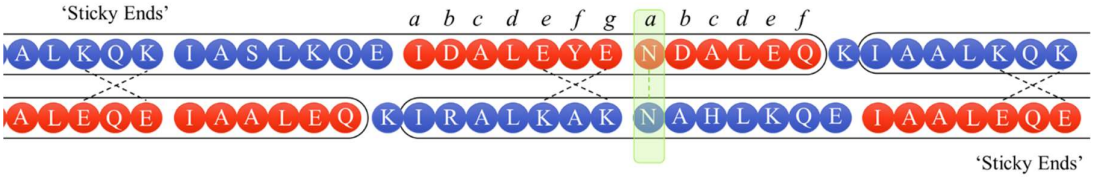

Figure 1.60 - Interactions between the heterodimeric CCs which lead to the formation of fibrous structures. Highlighted in yellow are the 'sticky end' areas of the peptide helices which allow for longitudinal association of further helices. Highlighted in green is the Asn-Asn interaction which results in the offset of the complimentary strands. The *e-g* position salt-bridges are indicated by a black dotted line (- - -).[187]

fibres. The 'sticky ends' are these same negative or positively charged portions, which will favour longitudinal assembly of further strands resulting in the long (>100 μm long, 20 nm wide) fibrous structures.[187]

A more recent study within the group found that fine-tuning of the interactions in the *b, c* and *f* positions of the α-helices could result in either stabilisation and thickening producing the SAFs discussed above, or formation of peptide-based fibrous hydrogels (hSAFs) (**Figure 1.61**). As before the *a, d, e, g* positions are responsible for the dimerization of the complimentary strands, however, altering the exposed *b, c* and *f* positions to feature Ala and Gln residues weakens the inter-fibre interactions and promote H-bonding, which is crucial for hydrogellation. hSAFs with sequences in which the *b, c* and *f* positions were changed to QQQ, AAA and AAQ were compared. For the sequences $hSAF_{QQQ}$ and $hSAF_{AAA}$ both were found to self-assemble into gel structures, with the former hydrogellating at low temperature (20 °C) and melting with increased temperature and the latter forming weak gels at low temperatures and strengthening with heat (≤ 95 °C). Furthermore, $hSAF_{AAQ}$ did not gel. Following from this data, the application of these gels for cell-growth were tested. It was

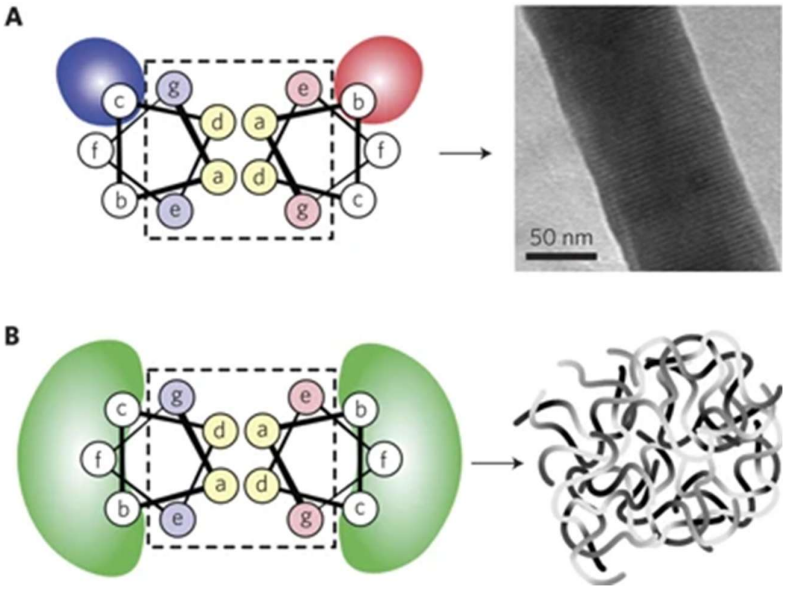

Figure 1.61 - Design principles of SAFs amd hSAFs. A) Helical wheel diagram showing the interactions between the complimentary strands leading to the formation of the SAFs B) Helical wheel diagram showing the interactions between the complimentary strands leading to the formation of hSAFs. The green area represents the exposed surface in which the *b, c,* and *f* positions have been altered to polar uncharged residues.[193] This figure was reproduced with permission from Springer Nature, (See Appendix E for Permissions)

found that they could support the growth and that the cells also exhibited differentiation on these hSAF gel surfaces.[193]

Design of self-assembling metal coordinating peptide CCs for use as MRI contrast agents has been the focus of the Peacock group. This research utilises the natural affinity of peptides for metal association to associate different lanthanide ions within the hydrophobic core of an α-helical peptide CC. Previous studies by the group lead to the development of the first Gd^{3+} coordinating coiled coil which demonstrated increased MRI relaxivity comparative to commercially available MRI agents.[188] To further this work a systematic study based around the original sequence testing a variety of positions within the hydrophobic core of the trimeric CC as binding sites for various lanthanide ions was performed. Four different sequences were produced, systematically moving the binding residues, Asn, Trp and Asp, from the *d, f* and *a*-positions of the 1st and 2nd heptads in MB1-1, down to the *d, f* and *a*-positions of the 4th and 5th heptads in MB1-4 (**Figure 1.62**). The self-assembly of these systems was analysed by circular dichroism, both in the absence and presence of $GdCl_3$. From this data it was observed that MB1-1 forms the most folded structures and is least

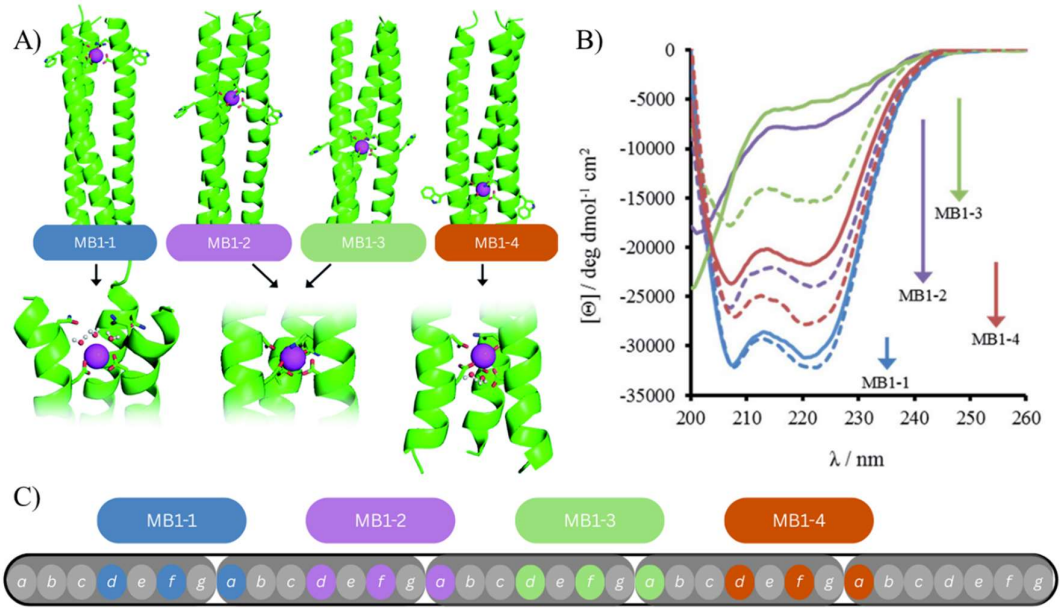

Figure 1.62 – Altering the lanthanide binding site within the hydrophobic core of the CC. **A)** Computational representations of the coordination sphere of peptides MB1-1 (blue), MB1-2 (purple), MB1-3 (green) and MB1-4 (red) **B)** Circular dichroism traces of MB1-1 (blue), MB1-2 (purple), MB1-3 (green) and MB1-4 (red) both in the absence (solid line) and presence (dotted line) of 10 μM $GdCl_3$ **C)** Positions of the Asn (*d*-position), Trp (f-position) and Asp (*a*-position) residues within the heptad repeats of the CC peptides. – Parts **A)** and **B)** of this figure have been reproduced with permissions (Creative Commons Attribution 3.0 Unported Licence) from The Royal Society of Chemistry.[189]

affected by the presence of the Gd^{3+} coordination, followed by MB1-4, MB1-2 and finally MB1-3. This suggests that the coordination is more tolerable at the termini of the CC. [189, 190, 194]

By luminescence experiments it was found that the binding sites which were more buried within the hydrophobic core (MB1-2 and MB1-3) which do not associate water within the coordination sphere are better designed as luminescence probes. In contrast, MB1-1, which features the coordination site at the N-terminus, can associate water in the coordination sphere results in a highly promising MRI contrast agent, with 4-fold MRI relaxivity comparative to the original design, MB1-2. These results highlight the importance of systematic design studies for metallopeptides, showing that there is a significant structure-function relationship between the coordination site and the peptide stability. [189, 190, 194]

The De Grado Group have long focused on the nuances of peptide and protein design, coining the term '*de novo* design' describing the bottom-up approach of protein design.[191, 195, 196] They have harnessed the self-assembling capabilities of α-helical peptides for the formation of larger, functional structures, in this case, ion channels. Heptad repeat sequences of polar AAs Leu and Ser were synthesised into three different sequences, **A)** $(LSSLLSL)_3$ (21-mer), **B)** $(LSSLLSL)_2$ (14-mer) and **C)** $(LSLLLSL)_3$ (21-mer) to test the formation of ion channels in a lipid bilayer (**Figure 1.63**). The helicity of these three sequences was analysed by circular dichroism finding that all of the sequences showed the characteristic double minima at 208 and 222 nm, and the maximum at 190 nm consistent with an α-helical

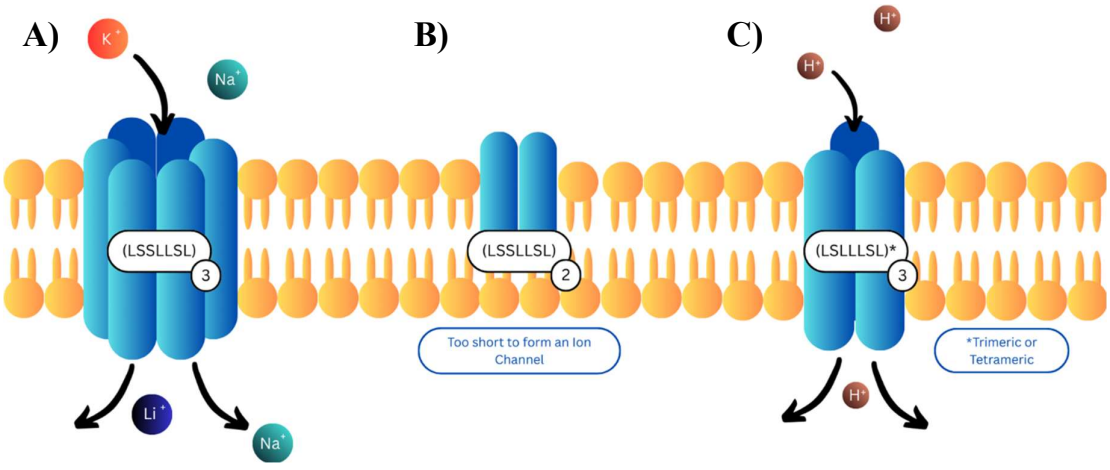

Figure 1.63 - Schematic of the formed ion channels of peptides $(LSSLLSL)_3$, $(LSSLLSL)_2$ and $(LSLLLSL)_3$. **A)** The hypothesised hexameric $(LSSLLSL)_3$ peptide bundle, where the blue represents the α-helices, forming an ion channel of between 5–8Å. **B)** The shorter peptide sequence $(LSSLLSL)_2$ fails to span the membrane but shows some character of membrane disruption. **C)** Altering the sequence to $(LSLLLSL)_3$ is suggested to form either trimeric or tetrameric bundles which embed in the membrane forming ion channels with a pore size of ≤ 1Å.[191]

structure with a more pronounced folding observed for the 21-mer peptides than the 14-mer peptide, as would be expected. By using the Mueller-Montral planar bilayer method the assembly of these sequences into ion channels was analysed.[191]

By analysis of the current across the bilayer it was found that when the $(LSSLLSL)_3$ sequence is incorporated into the bilayer there are current pulses consistent with that of an ion channel. Further analysis found that this behaviour was also seen with a variety of metal salts (HCl, LiCl, NaCl, KCl, CsCl). Interestingly, when the $(LSLLLSL)_3$ sequence was incorporated, it was found to form proton selective channels, due to the smaller diameter of the pore. In contrast, when the $(LSSLLSL)_2$ sequence was incorporated analysis of the current showed behaviour consistent with membrane disruption but not pulse-like behaviour which is expected for an ion channel. The differences between the $(LSSLLSL)_3$ and the $(LSLLLSL)_3$ sequences are a result of a single residue substitution from a Ser residue in the *c*-position to a Leu resulting in different oligomerisation states between the two sequences, with the forming leading to the larger oligomers and the former the smaller. This substitution replaces the polar side chain of Ser with the hydrophobic side chain of Leu, which influences the packing by stabilising the 'knobs into holes' hydrophobic packing between the bundles (**Figure 1.64**). The presence of the Ser in this position would lead to unfavourable interhelical interactions between a hydrophobic (leu) and polar (ser) side chain. To account for this the helices will pack to form a larger, polar pore, in which the Ser side chain can favourably interact with the aqueous environment.[191]

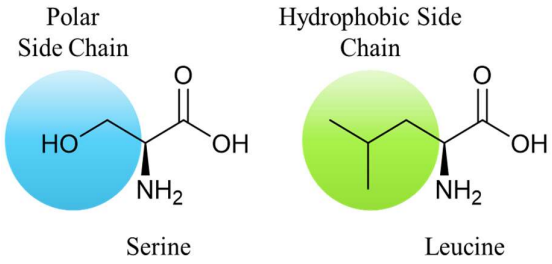

Figure 1.64 - Serine and Leucine side chains

These systems again highlight the importance of developing understanding of the self-assembly of these larger biological systems and the nuances of peptide *de novo* design.

Another example of the applications of CC assemblies comes from the Thomson group and their *de novo* Ubiquitin binding motifs.[192] In order to study the protein-protein interactions (PPIs) that are involved in Ubiquitin recognition a truncated E/K-heterodimeric-CC forming

pair of sequences (18-mer) which was rationally designed to feature a known Ubiquitin interacting motif (UIM) on the solvent exposed face of one of dimer strands (E), placing the residues key for the ubiquitin interaction (Leu, Ile, Ala and Ser) in the *b, c* and *f*-positions of the sequence. Initially, sequences **4** (E-strand) and **5** (K-strand) which had been N-terminally capped were analysed by CD as a reference for folding. These results found that independently these sequences had CD signals consistent with random coils, suggesting no folding. Furthermore, when mixed, only a small amount of helicity was observed indicating no self-assembly. After crosslinking the peptides using CuAAC, forming a triazole bridge at the N-terminus, peptide **3** was generated. The CD signal shows that this peptide is now capable of forming the desired helical-CC structure (**Figure 1.65**) despite only being 18-residues long. Following the success of the crosslinking, the UIM residues were substituted into the sequence for the the E-strand of the dimer which was subsequently mixed with the K-strand to form crosslinked peptide **9** (**Figure 1.65-C)**). The CD of this sequence comparative to that of the reference UIM-1 sequence was found to be similar, with a slight increase in folding observed in peptide **9**. Finally, to observe the ability of these CCs to bind to Ubiquitin, a fluorescence polarisation (FP) titration was performed (**Figure 1.65-D)**).

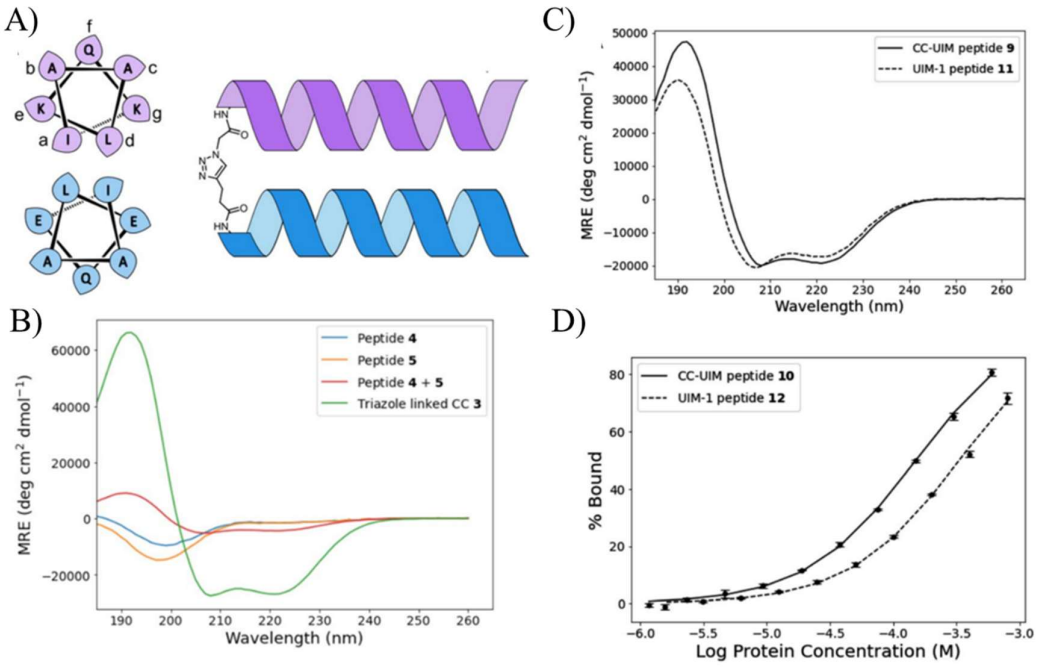

Figure 1.65 – **A)** Representation of the triazole crosslink formed by CuAAC at the N-terminus of the CC peptide **3. B)** Circular dichroism traces of control peptides **4**, **5**, a mixture of **4** and **5** and crosslinked CC peptide **3. C)** Circular dichroism traces of UIM containing CC peptide **9** (solid line) comparative to native control peptide UIM-1 (dashed line). **D)** FP binding assay results of UIM containing fluorescently labelled peptide **10** (solid line) comparative to fluorescently labelled native control peptide UIM-1 (dashed line). This figure has been reproduced with permissions (Creative Commons Attribution 3.0 Unported Licence) from The Royal Society of Chemistry.[192]

In order to visualise the CCs by fluorescence, the K-strand of peptide **9** was fitted with a fluorescent label, fluorescein. Again, this was mixed with the E-strand containing the UIM residues, resulting in peptide **10**. Titration of both peptide **10** and UIM-1 reference peptide **12** yielded the results in (**Figure 1.65-D)**). From this it was observed that designed CC-peptide **12** had a lower value of K_d (K_d =138.8 ± 5.0 μM) than the native UIM-1 reference sequence (K_d = 311.3 ± 15.5 μM), indicating a stronger affinity for Ubiquitin.[192]

Further work on developing new ubiquitin binding motifs and understanding their selectivity is currently being undertaken within the group.

The works discussed in this section aim to highlight the importance of developing understanding and toolkit of knowledge which can be utilised by researcher when employing a *de novo* design approach to generate a functional peptide sequence. Understanding the structural tolerances, binding residues, selectivity and self-assembly of these systems can make rational design of peptides into functional materials much easier in future generations of scientists.

With respect to chirality in these systems, it is quite typical for the inbuilt chirality of peptides and amino acids to be used as chiral auxiliaries in such systems, imparting their chirality onto metal complexes. Because of this, several AA-like chelating units with their own inbuilt chirality have been synthesised. Two examples include valabipy and [(2,2′-bipyridin)-5-yl]-D-alanine (D-Bpa5) (**Figure 1.66**) for easy incorporation into peptide sequences.[142 197] Both of these bipyridyl AAs have been used for the preferential formation of one enantiomer of a tris-bpy metal complexes by their incorporation into peptide backbones. Metal binding to peptides does not necessarily require a chelating unit. Amino acids and peptide/protein chains are capable of coordination to metals through the amide backbone. Additionally, several of the proteinogenic AAs feature functionalities on their side chains (indole,

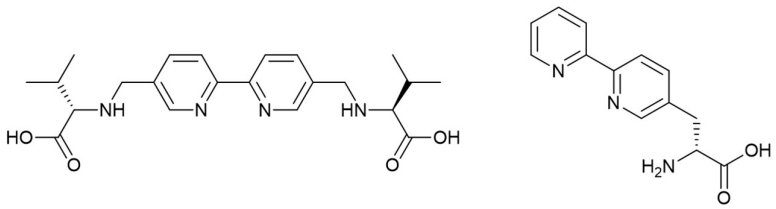

L-Valabipy D-Bpa5

Figure 1.66 - Structures of some unnatural bipyridyl amino acids, L-valabipy (left) and [(2,2′ -bipyridin)-5-yl]-D-alanine (D-Bpa5) (right).

imidazole, phenol, thiol, carboxylate) which are capable of coordination to metal ions and vital for many biological processes.[198]

The principles discussed in this introduction have been applied to larger topologically chiral interlocked structures including peptide based catenanes and knots.[185, 199-201] Peptides are often used in these assemblies due to the straightforward design principles for structural elements such as *β*-turns, as well as their inbuilt chirality for directing the topological chirality of the assemblies. This type of chemistry, has utilised the turn structure of *β*-hairpin motifs to facilitate the turns of a metal (lanthanide) coordinated peptide-based trefoil knot, for example (**Figure 1.67**).[199] This work utilised the self-assembly of the β-turn motif to initiate the turns of a trefoil knot during self-assembly with Ln^{3+} ions. Coordination to the Ln^{3+} ions was found to be tricapped trigonal prismatic through the 2,6-pyridinecarboxyamide groups within the knot strand. The knotted structure during self-assembly is favourably formed as a result metal directing and further favoured due to the presence of aromatic structures which exhibit π-π stacking interactions. This example incorporates the principles of protein secondary structures (β-turn), metal coordination and NCIs into one structure, and also favourably forms the over-hand knot with the (Δ) chirality.[199]

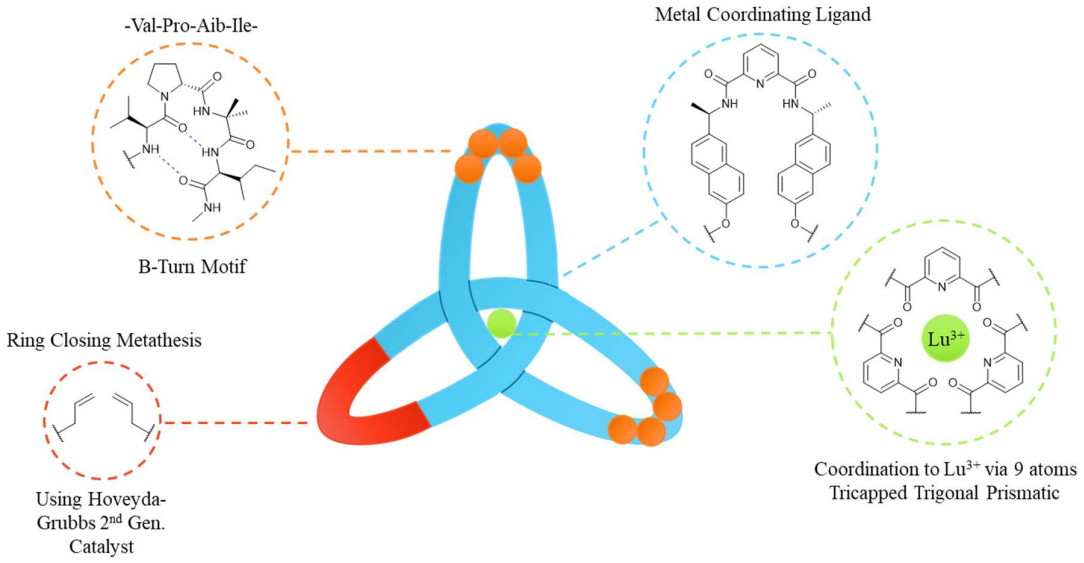

Figure 1.67 - Over-hand (Δ) trefoil knot formed from a single strand, with the turns comprised of four AA residues, Val, Pro, Aib and Ile, which self-assembles into a β-turn motif (orange) which assemble around a Lu^{3+} ion by coordination through 2,6-pyridinedicarboxamide groups (green). The coordination is directed by favourable aromatic, π-π stacking interactions (blue). The structure is closed, creating the trefoil knot, through ring closing metathesis (red) using Hoveyda-Grubbs 2nd generation catalyst.[199]

1.7 Thesis Aims

The aims of this thesis are to construct a model system of chiral induction to a supramolecular peptide assembly which exhibits cooperative folding upon metal ion coordination. By understanding the mechanisms which determine the formation of right-handed *α*-helices and their subsequent packing into left-handed supercoils, and by fitting these sequences with bidentate chelating units at the N-terminus the overarching aim is to understand and control the chirality of these terminal complexes.

The work in Chapter 2 aims to display the cooperative relationship of homotrimeric coiled coil folding with the formation of chiral N-terminally bound complexes with aromatic chelating units (bpy and phen). This has been done by synthesis and comparison of a bpy functionalised, 3-heptad homotrimeric CC, to two negative control peptides. The first negative control features an acetyl cap at the N-terminus to prove the effects of the chelating unit. The second is a 1-heptad repeat bpy-functionalised peptide sequence which was designed to show the dependence of the folding on the chiral complex preference. In this chapter a selection of first row transition metals (Co^{2+}, Ni^{2+}, Cu^{2+} and Zn^{2+}) are also tested, to assess any differences in the coordination and folding behaviours.

Chapter 3 aims to further the understanding of the cooperative relationship discovered in the previous chapter by probing the spatial tolerances of the chiral information transfer. By design and synthesis of three different series of peptides, the reliance on the distance from a chiral centre and location in the heptad repeat have been tested. The first series of 3-heptad homotrimeric peptides was designed to tests the effect of increasing the distance between the bpy units and a chiral centre. The second series was synthesised in response to the results from this series, these were 4-heptad repeat homotrimeric sequences to reduce the effect of the terminal residues on the unfolding of the peptide. The final series was designed to test how altering the pseudo-register position of the bpy chelating unit would affect the chirality of the complex and whether or not the position could bias the chiral preference which is observed.

Chapter 4 focuses on testing an alternate bidentate chelating unit, 8-hydroxyquinoline, to further the understanding that has already been developed and identifying if the principles discovered in the previous chapters are applicable to other systems. This has been done by design and synthesis of three homotrimeric coiled coils and varying the register position such that the chelate features at the *a, d* and *e* positions in the heptad.

2 Chiral Effects in Metal Binding Motifs at the N-Terminus of Trimeric Coiled Coils

This chapter covers the design and synthesis of short trimeric coiled coils which have been N-terminally functionalised with metal binding motifs 2,2′-bipyridine and 1,10-phenanthroline to investigate the degree of chiral information transfer from the trimeric peptide system to the supramolecular assembly as a function of metal binding to first row transition metals. Furthermore, this chapter discusses the relationship between the helicity of the synthesised trimeric peptide system and the resulting complex that is formed at the N-terminus.

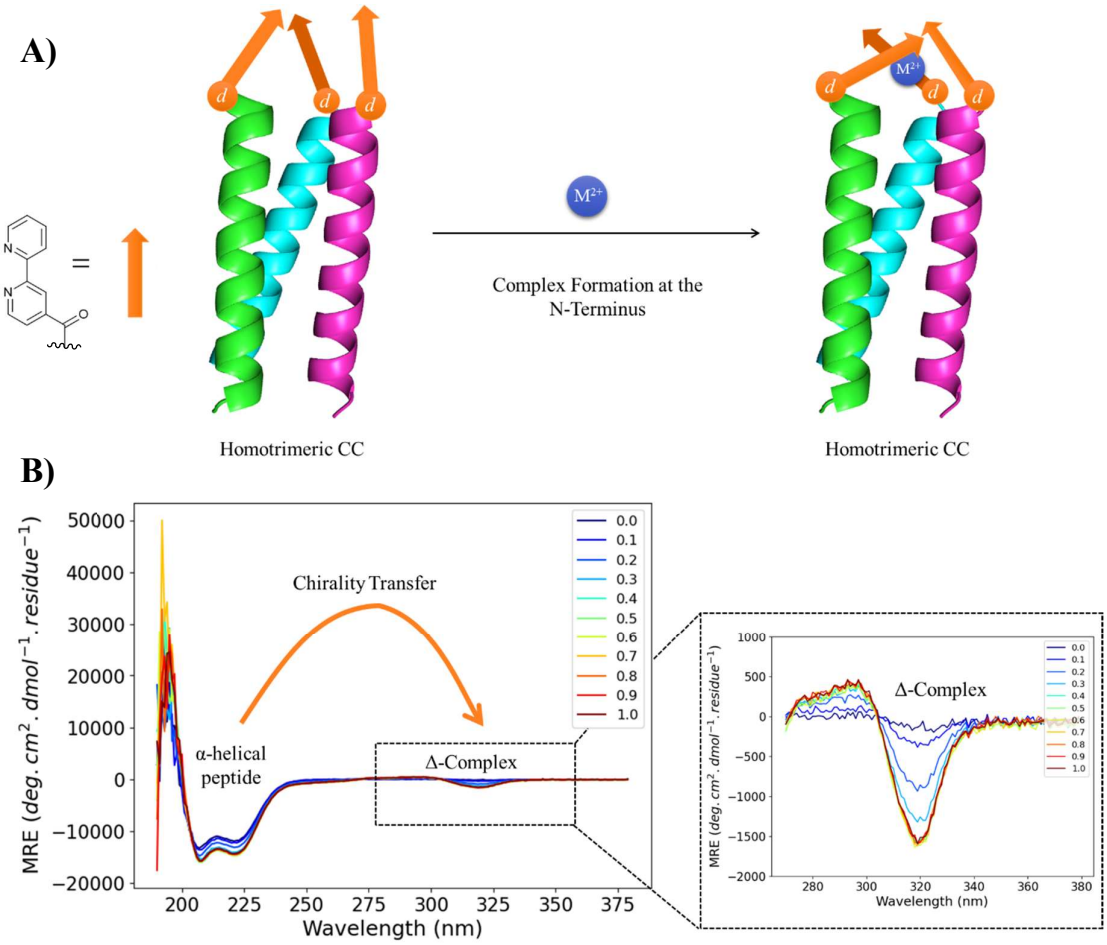

Figure 2.1 – Graphical Abstract showing the functionalised N-termini of a CC homotrimer binding to a M^{2+} ion via bipyridine units in right-handed orientation as evidenced by the negative exciton couplet in the CD spectrum. **A)** Coupling of 2,2′-bipyridine-4-carboxylic acid to the N-termini with orange vectors representing the bpy moiety **B)** Evidence of chiral information transfer from the peptide onto the metal centre from the CD spectroscopy.

2.1 Aims

Understanding the underlying principles of chiral information transfer by use of short peptide coiled-coils as chiral auxiliaries to assess their ability to transfer their chiral information onto a terminal chelate complex could potentially aid in design of peptide-inorganic hybrid systems. Therefore, understanding how to design these systems to control the chirality could be beneficial across a range of specialities, such as synthesis of 'man-made' enzymes or to aid design principles of nanostructures.

The aim of this chapter is to discuss the preferential formation of Δ-tris-(bpy-peptide) and Δ-tris-(phen-peptide) complexes in response to a series of first row transition metals, Fe^{2+}, Co^{2+}, Ni^{2+}, Cu^{2+} and Zn^{2+}. The experiments involved in this work aim to show that this preference is in response to the attachment of the chelating moiety to the helically chiral trimers testing whether the helicity of the peptide and the chirality of the resulting complex are coupled, or whether the effects occur as a result of attachment to inherently chiral subunits.

2.2 Design and Synthesis of Bipyridine Functionalised Trimeric Coiled Coils

2.2.1 Sequence Design

The three heptad repeat peptide sequence (**1a**, **1b**) used in the experiments detailed in this chapter was designed to fold in aqueous environments based on the principles of coiled-coil design described in the introduction (Section 1.2.2). The sequences are tabulated below in **Table 2.1**. These sequences were designed to fold in response to neutral pH (aqueous MOPS buffer) for all experiments in this chapter. Regarding the design of this sequence, the heptad repeat (*abcdefg* = IAAIKKE) follows the HPPHPPP formula, with small helix favouring residues in the *b* and *c* positions and charged residues in the *e* and *g* positions to allow for inter-strand salt-bridge formation. Additionally, this sequence should favour trimer formation due to the presence of two Ile residues in the hydrophobic positions of the heptad repeat. The final heptad features a Tyr residue replacing a Lys residue in the *f* position which has been included for easier spectroscopic visualisation and concentration calculations from its characteristic absorbance at 280 nm.[202] A Gly residue was included at the N-terminus to cap the helix and add flexibility for the bpy.

Table 2.1 – Peptide sequences of **1a**, **1b**, **2a** and **2b**

Peptide No.	Capping Moiety	Sequence	C-Terminus
1a	Bpy	GQEIAAIKKEIAAIKKEIAAIKYG	NH_2
1b	Ac	GQEIAAIKKEIAAIKKEIAAIKYG	NH_2
2a	Bpy	GQEIAAIKYG	NH_2
2b	Ac	GQEIAAIKYG	NH_2

In addition to the three heptad CC sequence, a single heptad sequence was also included (**2a** and **2b**). The purpose of this sequence was to serve as a negative control. Due to the thermodynamic penalty of folding, the short nature of this sequence means that it should not fold as there are limited contacts between the strands. The behaviour of the tris-bipyridine complex in response to attachment to a random coil peptide will help uncover the relationship between the secondary structure of the peptide and the resulting chiral preference of the terminal metal complex.

2.2.2 Bipyridine Placement

2,2′-bipyridine-4-carboxylic acid was chosen as the chelating unit in these experiments due to its prevalence in the literature and ease of ligation to a peptide system (**Figure 2.2**). The placement of the bpy on the N-terminus of the peptide was decided due to literature precedent for the formation of chiral complexes with the bpy at this position.[203] This work aims to build on the discovery of the chiral information transfer from CC to complex by understanding the coupling relationship between the two and the spatial constraints of the system. The spectroscopic and binding behaviour of bpy have also been well documented therefore making comparison of any signals resulting from the CD and UV absorbance

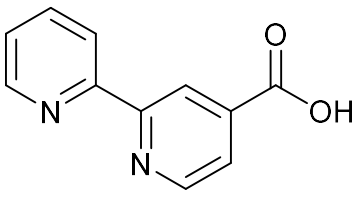

Figure 2.2 - Structure of 2,2'-bipyridine-4-carboxylic acid.

spectrometry easily identified without obtaining a crystal structure of the tris-(bpy-peptide) complex.

Synthetically, it is possible to install a bpy moiety at either terminus of a peptide, or for it to be chemically attached to an AA side chain, for example, 2,2′-bipyridine-4-carboxylic acid can be coupled to a Lysine amine. For the purpose of this investigation the bpy, in the form of 2,2′-bipyridine-4-carboxylic acid, was chemically attached to the N-terminus by standard amide coupling reaction performed on resin. This placement was chosen in order to probe the influence of the helicity of the CC, in this case *P*-helices with *M*-supercoiling, on the resulting tris-bpy complex occurring at the N-terminus. Ascertaining whether the chiral information from the peptides could influence the chiral preference at the metal centre. In addition to this it is also a very straightforward method for generating a peptide capable of binding transition metal ions.

In terms of register position, the bpy falls at a *d*-position in this sequence, the effect of altering the register position of the chelator will be further investigated in Chapter 3.

2.2.3 Preparation of **1a, 1b, 2a** and **2b** by SPPS

Solid phase synthesis methods were used to generate the peptides used throughout this work (**Figure 2.3**). This was performed using a microwave assisted peptide synthesiser (CEM Liberty Blue). This equipment allows for the longest of the sequences discussed to be prepared in approximately 4 hours. The same principles for SPPS apply as have been presented in **Figure 2.3,** which focuses on the principles of manual SPPS. However, reaction times for automated synthesis are shorter as reagents are prepared in larger excesses and elevated temperatures (75–80°) are used.

For coupling of the chelating groups that have been used in this work the manual procedure presented in **Figure 2.3** is used. This material is much more expensive than standard Fmoc-AAs and therefore the large excesses which are required for the microwave assisted method were not desirable and therefore they were coupled manually using only 4 equivalents of the chelating group. The same coupling agents (DIC/Oxyma) were used for these amide coupling reactions.

After synthesis of the peptides, they are cleaved from the resin using a mixture of TFA:H_2O:TIPS (ratio 95:2.5:2.5). The TFA is then removed under a stream of $N_2(g)$ and then precipitated into (cold) diethyl ether. They are then filtered and redissolved in MeCN:H_2O (50:50) before lyophilising.

Crude peptide solutions were analysed by LC-MS before purification by reverse phase HPLC on a 20-80% MeCN gradient over 20 minutes. Following this the resulting purified peptides were analysed by reverse-phase HPLC on a 50-minute gradient, 20-80% MeCN method to assess purity, followed by HR-MS for characterisation.

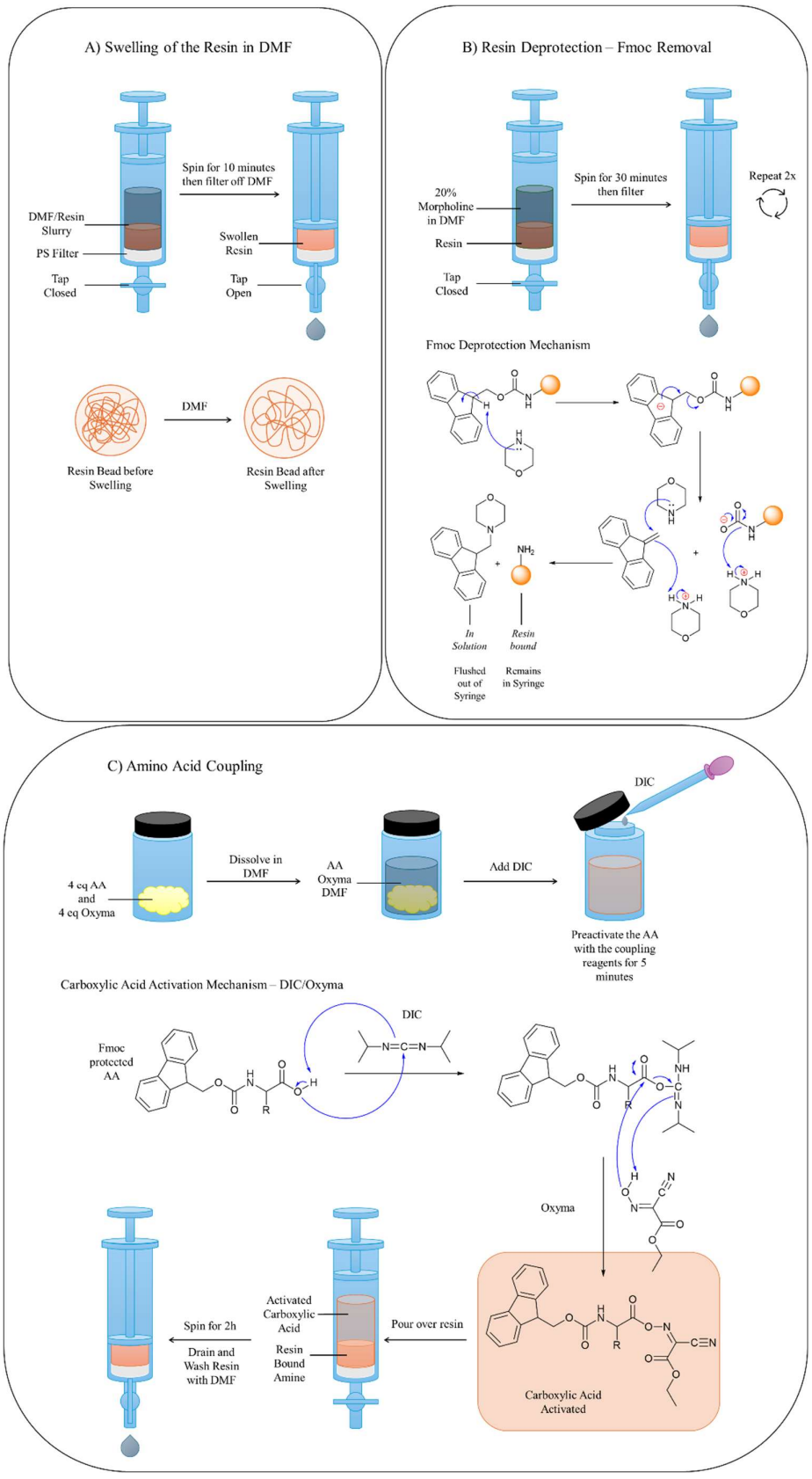

Figure 2.3 – Principles of Solid Phase Peptide Synthesis (SPPS) **A)** Resin must be swollen in organic solvent (DMF) before coupling can occur. **B)** Removal of Fmoc groups from resin or AA to allow for coupling. **C)** Manual AA coupling on resin.

2.3 The Effect of an N-terminal 2,2′-bipyridine on the Self-Assembly of a Trimeric Coiled Coil

2.3.1 Comparison to an Acetyl-Capped Homotrimeric CC

In order to investigate if the presence of a 2,2′-bipyridine moiety at the N-terminus influenced the self-assembly and stability of the homotrimeric coiled-coil system in an apo environment (with no metal ions to influence coordination), peptides **1a** and **1b** were synthesised by microwave assisted SPPS and their self-assembly assessed by circular dichroism (CD). **1a** (bpy-GQEIAAIKKEIAAIKKEIAAIKYG-NH_2) was N-terminally functionalised on resin by manual amide coupling of 2,2′-bipyridine-4-carboxylic acid. **1b** (Ac-GQEIAAIKKEIAAIKKEIAAIKYG-NH_2) was synthesised to act as a control sequence with a standard acetyl capping moiety installed at the N-terminus.

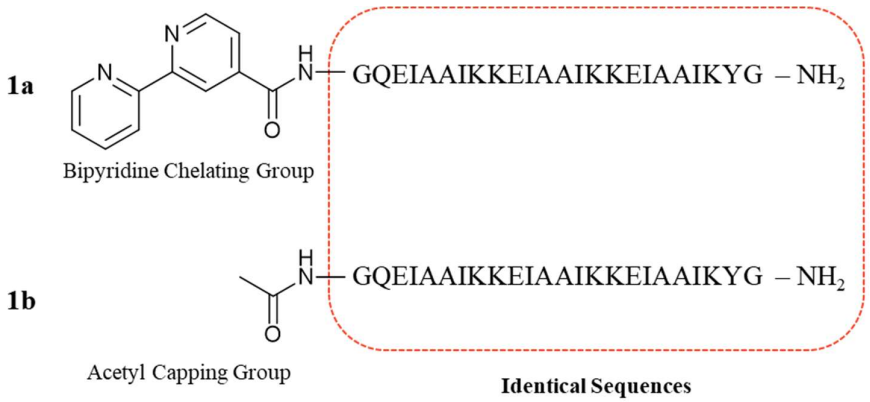

Figure 2.4 – Comparison of **1a** and **1b**. The AA sequences are identical, both with a NH_2 C-terminal cap. However, the N-terminal caps are different, with **1a** having a bipyridine chelating group for metal coordination, and **1b** having an acetyl capping group such that it can act as a negative control sequence which should not coordinate to the added metal ions.

CD traces of **1a** and **1b (Figure 2.5)** were recorded between 180 – 400 nm to account for the signal which is exhibited by a chiral octahedral tris-bipyridine complex, which arises between 280–330 nm.[175,16] The data from the measurements have been converted into molar residual ellipticity (MRE) (deg.cm^2.dmol^{-1}.residue^{-1}), normalising the data for concentration and amino acid content. This allows for comparison of different sequences as well as different concentrations for folding ability.

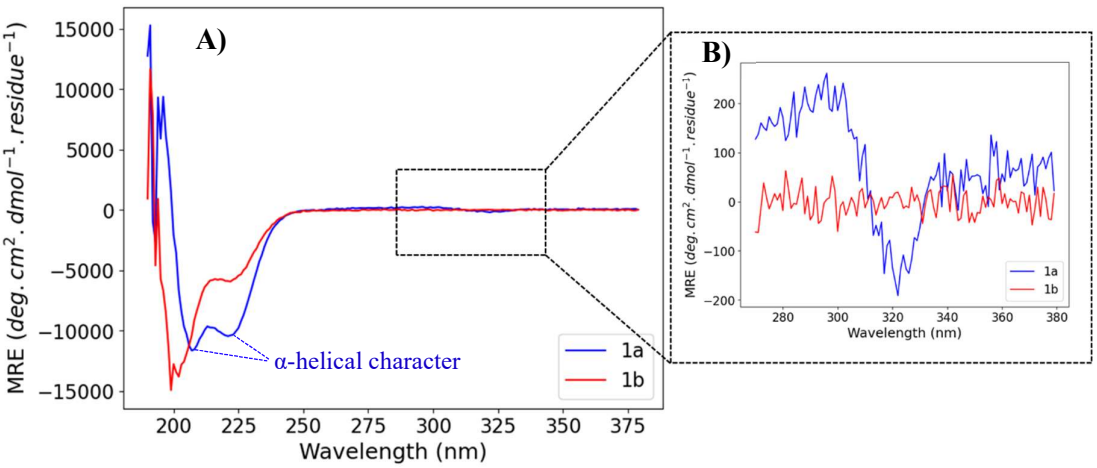

Figure 2.5 - CD spectra of **1a** (blue line - 10 μM in 20 mM aqueous MOPS buffer, pH 7) and **1b** (red line - 10 μM in 20 mM aqueous MOPS buffer, pH 7). **A)** Full spectrum in which the ellipticity consistent with the peptide secondary structure is measured. Peptide **1a** exhibits characteristic double minima at 222 nm and 202 nm, whereas **1b** exhibits minima closer to 190 nm, consistent with a random coil. B) Zoomed in near UV-region in which the ellipticity from the chromophore interactions is measured.

Comparison of the **1a** and **1b** spectra suggested that presence of bipyridine at the N-terminus increases the α-helical content of **1a** compared to **1b**. This is indicated in the far-UV (**Figure 2.5 A)**) trace of **1a** displaying α-helical character, contrary to that of **1b**, which has a trace in the far-UV showing that a greater proportion of this structure behaves as a random coil.[177] This behaviour indicates that the bipyridines of **1a** could be interacting intermolecularly, likely as a result of intermolecular π-stacking interactions leading to the cooperative relationship observed. These interactions could be serving as a self-assembly mechanism to favourably bring the three strands of the trimer together, inducing the helicity and therefore forming the desired coiled-coil trimer in **1a** but not **1b** where these interactions cannot occur due to the lack of bpy units.

The cooperative behaviour discussed above is further supported by the negative Cotton-effect at 320 nm (**Figure 2.5 – B)**) which is observed in **1a** but not **1b**. This is suggestive of exciton coupling from the pre-arranged conformation of the bipyridines in proximity to one another as a result of intermolecular interactions. The band is consistent with a π-π* transition made possible by having the bpy chromophores closely arranged in space.[175, 179] Additionally, the presence of both the signal at 222 nm and that at 320 nm in combination suggests that the ligands are pre-arranged in a *fac*-conformation, with all the peptide strands centred around one face of the complex allowing them to make the contacts they require to form the trimeric coiled-coil, a *mer* conformation would result in less contact between the strands of the trimer and lead to a loss of helicity, therefore it is unlikely that this conformation would occur at all (**Figure 2.6**).[204]

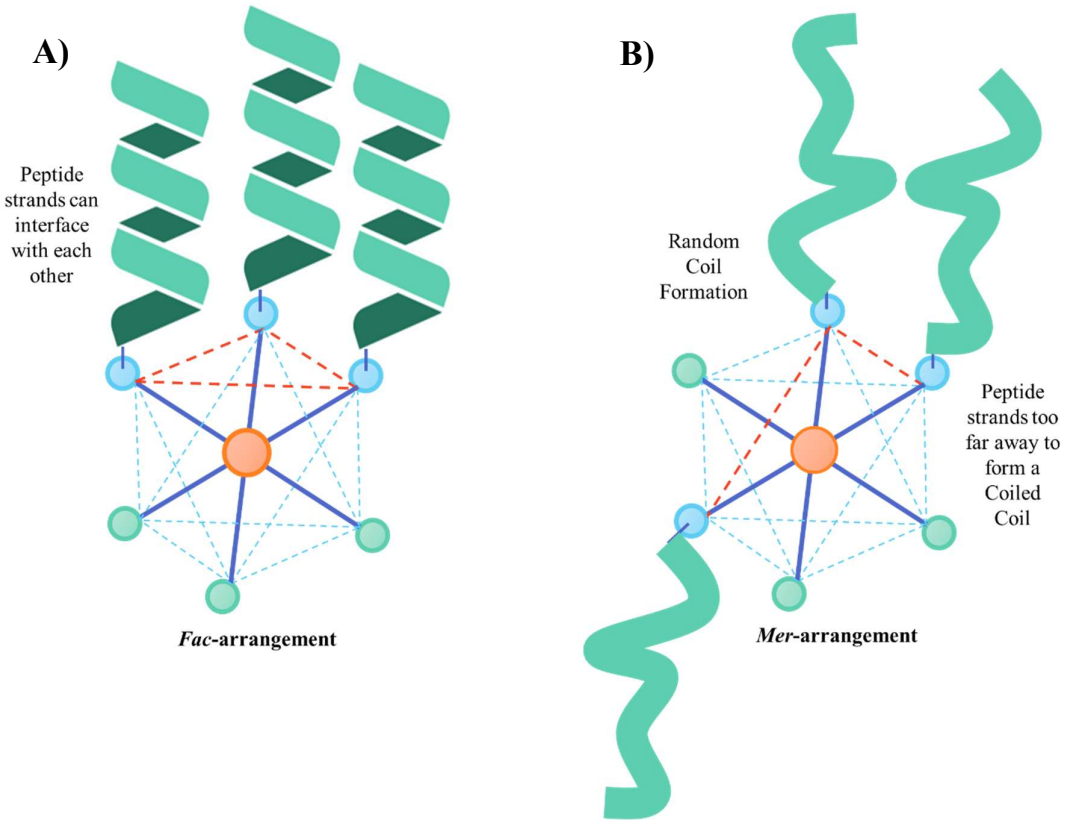

Figure 2.6 – Differences in the arrangements of the *fac*- and *mer*-configurations of the tris-(bpy-peptide) complexes. **A)** *fac-arrangement* results in all peptide strands being present on the same face of the octahedron allowing them to interface and fold into a CC. **B)** *mer*-arrangement of the ligands however leads to one of the peptide strands to be too far away to form the CC.

2.3.2 Comparison to a Random-Coil Bpy-Capped Peptide

To further the understanding of the cooperative relationship between the folding of the CC and the formation of a chiral terminal complex, single heptad peptide **2a** and its control sequence **2b** were also subjected to CD spectroscopy analysis.

The behaviour observed in the CD-trace here (**Figure 2.7)** and in Section 2.3.1 - **Figure 2.5** is again suggestive of the cooperative relationship between the folding of the CC and the formation of the Δ-tris-(bpy-peptide) conformation that was discussed in the previous section. In the absence of the bpy, as seen in **1b,** the CC is not formed, which is likely due to the lack of secondary interactions at the N-terminus shown to influence the folding in the previous section by the comparison of the traces of **1a** and **1b**. Peptides **2a** and **2b** both result in trace consistent with random coils even in the presence of the bpy as seen in **2a**. It also follows in the single heptad peptides that no exciton couplet at 320 nm is found.

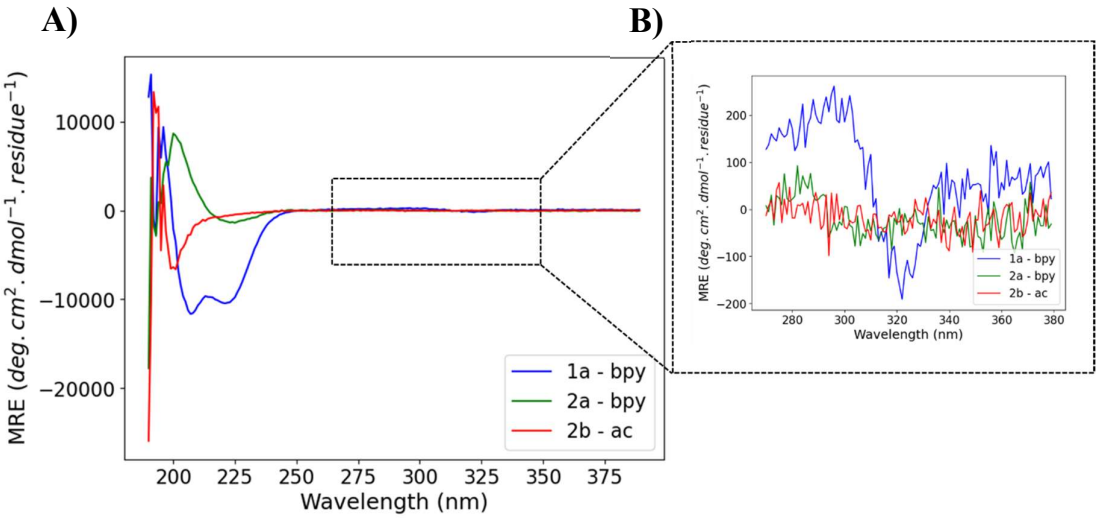

Figure 2.7 - CD Trace of **1a** (blue), **2a** (green) and **2b** (red). All 10 µM in 20 mM aqueous MOPS buffer, pH 7. **A)** Full spectrum showing the peptide folding of the three peptides, **1a** exhibiting helical character and **2a** and **2b** both exhibiting random coil behaviour. **B)** Zoomed in segment of the near UV-region showing that **1a** is the only sequence which exhibits a chiral signal from the bpy moieties.

These two behaviours together indicate that the formation of the prearranged chiral Δ-tris-(bpy-peptide) at the N-terminus relies on the rigidity and self-assembly of the CC. This was shown as **2a** which cannot form a CC, also does not exhibit any chiral signal from the bpy moieties, despite the bpy being attached to chiral AAs. However, the stability of the CC also in turn relies on the presence of the bpy and its π-stacking interactions to stabilise the secondary structure. This was demonstrated by comparison of **1a** and **1b**. These two

behaviours can therefore be described as cooperative in this system. In order to remove the reliance on the bpy for peptide folding into a CC, the sequence can be made longer, increasing the strand-to-strand contacts and therefore lowering the energetic penalty of folding.

2.4 The Effect of the Addition of First Row TMs to 2,2′-bipyridine Functionalised Peptides on their Ability to Self-Assemble into Chiral Complexes

2.4.1 UV Absorbance Titrations of 2,2′-Bipyridine with First Row TMs

Preliminary UV absorbance titrations of [2,2′-bipyridine]-4,4′-dimethanol with first row transition metals Co^{2+}, Cu^{2+} and Zn^{2+} were performed (**Figure 2.8**). This bpy moiety was chosen due to its solubility in aqueous media to be used as an indication of where the UV-transitions would occur in the spectra. Further controls for these systems with bpy-appended random coil peptides were discussed in **Figure 2.7** such that the chiral information transfer

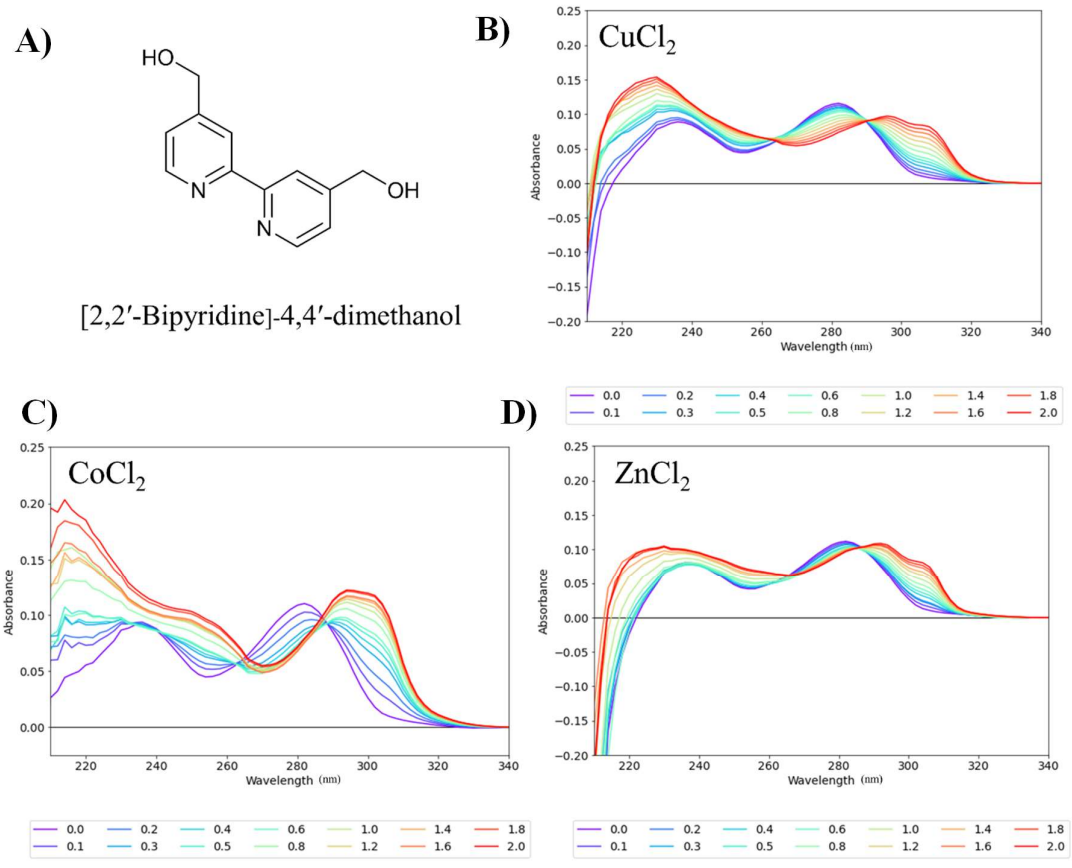

Figure 2.8 - UV-Vis absorbance titrations of [2,2'-Bipyridine]-4,4'-dimethanol (10 μM) against increasing concentrations of B) Cu^{2+}, C) Co^{2+} and D) Zn^{2+} in H_2O. M^{2+} ions titrated into solution as 4 μL (1 μM) increments up to 2.0 eq with respect to bpy concentration.

could be attributed to the helicity and not the attachment to a chiral AA. These data indicated that in the absence of peptide, the bipyridine when in an unbound state will have an absorbance at 280 nm, but when bound this will shift to 300 nm. The spectra show that in all three titrations the bipyridines display a two-state transition, and the point at which this change occurs for both the Co^{2+} and the Zn^{2+} titrations is at approximately 0.3 eq of metal commensurate with formation of an octahedral complex. Cu^{2+} however reaches this point after 0.6 eq, indicating that the complex formed is not octahedral as desired (bpy units in 2:1 ratio with Cu^{2+}). This was anticipated for Cu^{2+} due to its propensity for Jahn-Teller effects in octahedral arrangements, making them unfavourable.[205, 206]

2.4.2 UV Absorbance Titrations of N-Terminally Bound 2,2′-Bipyridine with First Row TMs

Titrations of Cu^{2+}, Co^{2+} and Zn^{2+} were also performed on **1a** to determine any spectroscopic differences which could occur when the bpy moiety is conjugated to a peptide strand (**Figure 2.9**). When conjugated directly to the N-terminus of **1a** by an amide linkage, the signal of

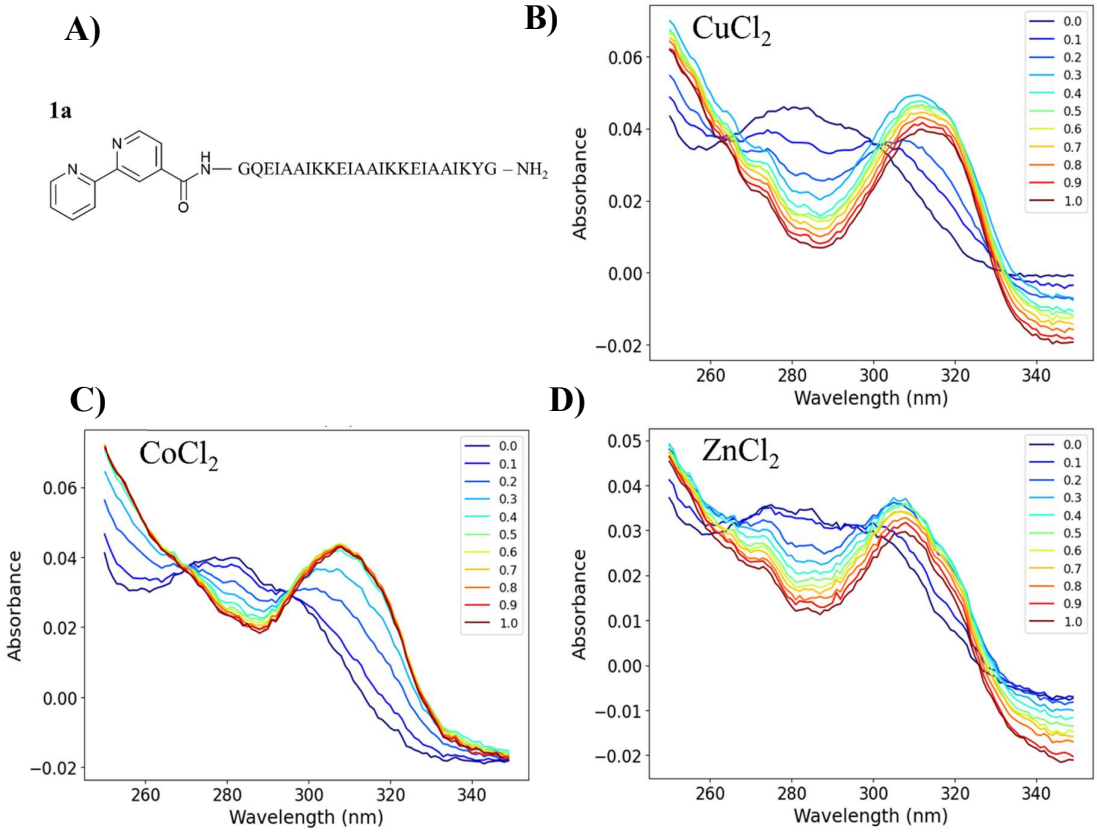

Figure 2.9 - Trace of the UV-Vis absorbance titrations of **A) 1a** (10 μM) in 20 mM aqueous MOPS buffer against increasing concentrations of **B)** Cu^{2+}, **C)** Co^{2+} and **D)** Zn^{2+}. M^{2+} ions added in 4 μL (1 μM) increments. Negative values of absorbance have likely occurred due to dilute samples increasing the effect of noise in the readings.

the bound bipyridine, and the isosbestic point is red-shifted to a longer wavelength, from approx. 290 nm in the free bipyridine to 300 nm in the N-terminally conjugated bipyridine. Furthermore, the transition to the bound state for the Cu^{2+} ion titration is reached much earlier in the peptide conjugated bpy, at 0.3 eq. This behaviour is hypothesised to be a result of the prearranged bipyridines from their CC attachment making this tris-octahedral conformation more thermodynamically favourable. For the free bpy units this behaviour cannot be observed due to the lack of stabilising interactions which prearrange the bpy-moieties to favour an octahedral conformation. This is the only metal in which this effect was observed as the other tested metals already showed preference for the octahedral conformation with the un-appended bpy units.

2.4.3 CD Titrations of N-Terminally Bound 2,2′-Bipyridine with First Row TMs

To further investigate the relationship between the chirality of the secondary structure and that of the supramolecular complex formed at the N-terminus, a series of first row TMs (Fe^{3+}, Fe^{2+}, Co^{2+}, Ni^{2+}, Cu^{2+} and Zn^{2+}) were titrated into 10 µM solutions of **1a** and **1b** in 0.1 eq increments up to 1 eq with respect to one strand of peptide (or bipyridine).[203] The complex formation was monitored by CD and UV spectroscopy. Plots of the signals recorded at 222 nm (peptide helicity) and at 320 nm (bpy chromophore) presents the relationship between the MRE of the secondary structure of **1a** and of the supramolecular assembly, as a function

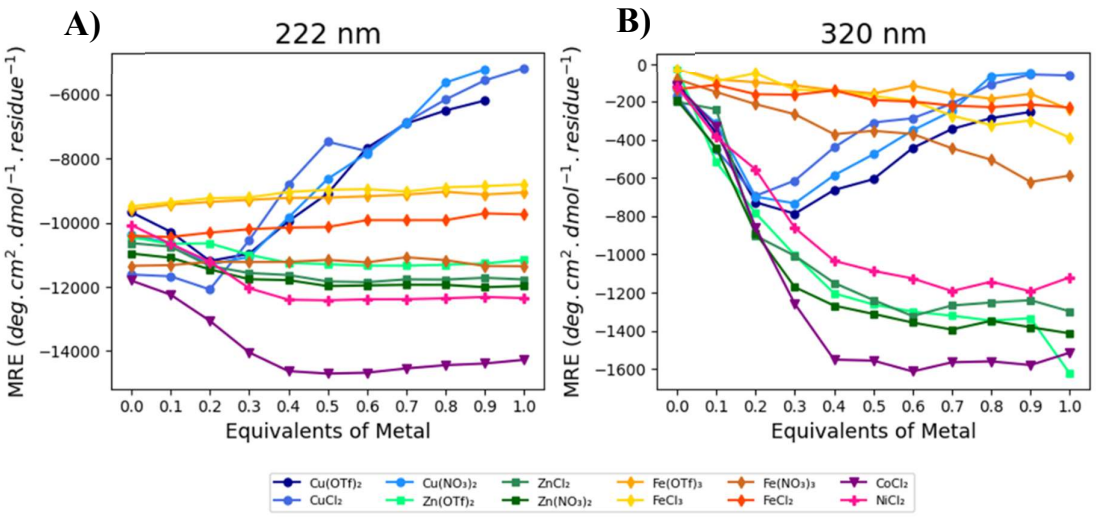

Figure 2.10 - Plot of Molar Ellipticity of **1a** as a function of concentration of TM ion in solution. Equivalents of metal were calculated with respect to the concentration of bipyridine in solution. **A)** Change in MRE with increasing concentration of TM at 222 nm, indicating a change in the helical content of the peptide. **B)** Change in MRE with increasing concentration of TM at 320 nm, indicating change in the chiral conformation of the bpy arrangement.

of concentration of the TM ions (**Figure 2.10**). Various counterions (Cl^-, NO_3^-, $CF_3SO_3^-$) were also tested to assess if competitive binding with the counterion was an important factor in this system.

Initial observations of these plots highlight a relationship between the helicity shown by the peptide and the resulting complex that is formed at the N-terminus in response to addition of metal ions. From this data it can also be concluded that counterion has a negligible effect on the resulting signals and does not participate in any significant manner to the resulting tris-(bpy-peptide) complexes, it therefore will not be discussed further.

The behaviour of **1a** in response to increasing concentration of Cu^{2+} ions shows that the formation of the Δ-**1a** isomer in this instance was concentration dependant. The magnitude of the signal at 320 nm increases in response to the increasing concentration of Cu^{2+} ions until 0.3 eq where it reaches its greatest intensity. Following this point the signal then begins to diminish, indicating a loss of chirality due to the loss of the octahedral complex, where the Cu^{2+} ions adopt a more favourable conformation. The signal at 222 nm appears to confirm this theory, as the concentration of Cu^{2+} ions increase in solution the helicity of **1a** is lost, demonstrating cooperative behaviour.

Examination of the full CD trace of these titrations **(Figure 2.11)** makes this behaviour more apparent. Initially, as the concentration of Cu^{2+} approaches 0.3 eq, the helicity increases with the signal from the complex, however, as this concentration is exceeded, the line shape changes to that characteristic of a random coil. This behaviour in the presence of Cu^{2+} ions is theorised to be a consequence tetragonal elongation distortion from the Jahn-Teller effect, decreasing the stability of forming these complexes.[97] As the concentration of Cu^{2+} increases in solution, the ratio of bpy:Cu^{2+} increases towards a 1:1 relationship. As such, the bpy moieties may be forming up to three Cu^{2+} complexes at the N-terminus utilising hydrate or nitrate (from the counterions) ligands from the sample solution to fill the coordination sphere. Having multiple Cu^{2+} ions coordinated to the N-terminus would result in repulsive interactions to account for the additional charge. This could explain the decrease in helicity observed in the CD with increasing concentration of Cu^{2+}, as the repulsive interactions could lead to fraying of the CC, pulling the strands apart from the N-terminus. This theory is further confirmed by the loss of the exciton-couplet signal at 320 nm, which indicates that a chiral octahedral complex is originally formed and subsequently lost. This observation would likely be a result of changes to the coordination sphere due to the lability of the octahedral complex formed up to 0.3 eq of Cu^{2+}.

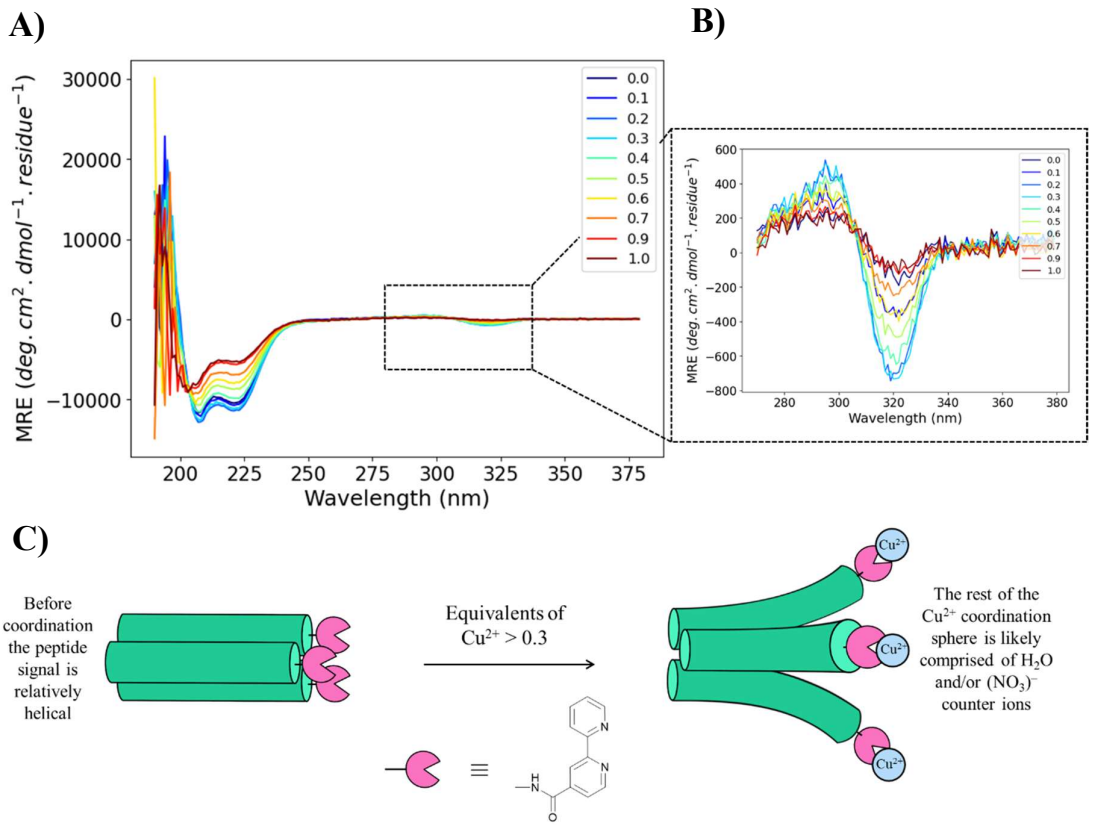

Figure 2.11 - CD trace of titration of **1a** (10 μM) against $Cu(NO_3)_2$ in 20 mM aqueous MOPS buffer, pH 7. **A)** Full spectrum plot for increasing equivalents of Cu^{2+} showing the increase and then subsequent decrease in helicity with increasing equivalents of Cu^{2+}. **B)** Zoomed in segment of the spectrum showing the increase and then subsequent decrease in the chiral signal from the bpy coordination to Cu^{2+} **C)** Cartoon representation of the hypothesised response of the **1a** trimers to increasing concentrations of Cu^{2+} in solution, it can be suggested that the bpy moieties will tend towards a 1:1 ratio with the Cu^{2+} resulting in fraying of the N-terminus which leads to the loss of helicity observed in **A)**. The rest of the coordination sphere will be likely comprised of H_2O and counterions from solution, in this case $(NO_3)^-$.

Comparison of the end point of this titration of **1a** against Cu^{2+} to the signal which was observed for **1b** under the same conditions shows that despite losing much of its α-helical content, as the concentration of Cu^{2+} increased in solution, **1a** does not quite reach the level of unfolding observed in the acetyl capped **1b** control sequence (**Figure 2.12**). It is worth noting that the signal from **1b** does not change in response to increasing concentrations of Cu^{2+} therefore meaning that the comparison to the 1.0 eq results in the same signal intensities as a comparison to the 0.0 eq spectra for **1b**. (Appendix A)

In contrast to the dynamic behaviour observed for Cu^{2+}, titrations against metal ions that form octahedral complexes with bpy ligands, such as Zn^{2+}, Ni^{2+}, and Co^{2+},[104, 105, 142] displayed increased stability compared to Cu^{2+} when incorporated into the helices. This

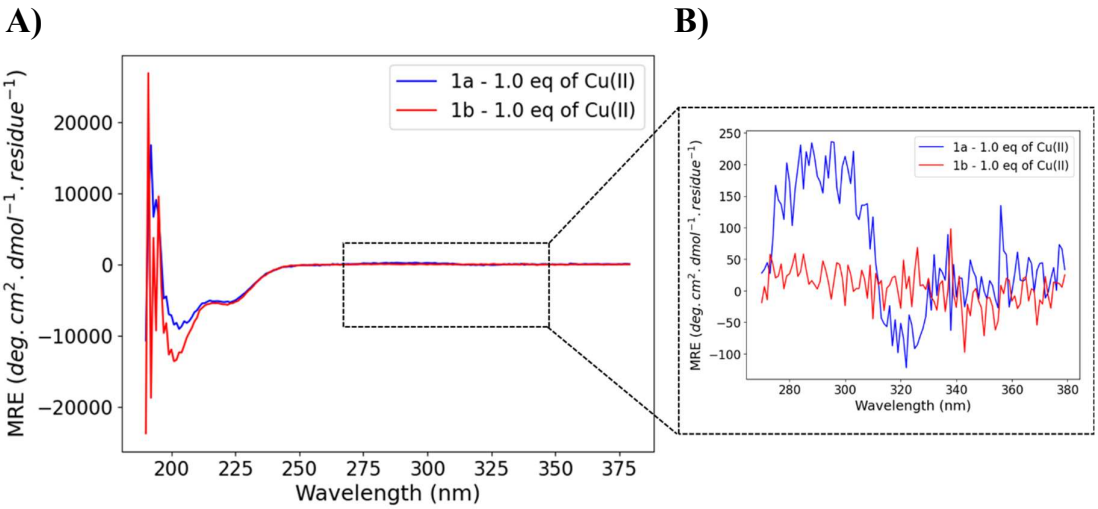

Figure 2. 12 - Comparison of CD traces of the end point of titrations of **1a** and **1b** against Cu^{2+} (1.0 eq). Both solutions were 10 µM peptide in 20 mM aqueous MOPS buffer. **A)** Full spectrum showing that **1a** in the presence of 1.0 eq of Cu^{2+} still has some helical character when compared to the random coil signal that was observed for **1b**. **B)** Zoomed in segment of the region with the bpy signals showing that **1a** with 1.0 eq of Cu^{2+} still shows a small amount of chiral preference for the Δ-isomer.

includes at concentrations higher than 0.3 eq. Additionally they were found to exhibit stronger signals at 320 nm (**Figure 2.13**).[93]

The data in **Figure 2.10** demonstrates that the signal at 320 nm reaches its greatest intensity at approximately 0.3 eq of M^{2+} ion with all three of the metal salts. In the case of the Ni^{2+} and Co^{2+} titrations, the addition of M^{2+} ions not only results in an increase in the magnitude of the signal at 320 nm, but also that at 222 nm, indicating that as a result of binding to metals, the helicity of **1a** is stabilised. As with the signal at 320 nm, this 222 nm signal also reaches a minimum at 0.3 eq of M^{2+}, with the stronger effect seen in response to Co^{2+}. Typically, the ionic radius of these ions will follow Co^{2+} (~90 pm) > Ni^{2+} (~83 pm) < Cu^{2+} (~88 pm) < Zn^{2+} (~89 pm). In this instance, the bpy, is a strong field ligand which increases the energy of the e_g orbitals and results in low-spin configurations being adopted by the ions. However, from this set of ions, the Co^{2+} (d^7) is the only one which can adopt a low-spin electronic conformation, resulting in less repulsions due to increased electron pairing and a smaller ionic radius of ~ 78 pm. The differences in ionic radius between their complexes with bpy could offer an explanation for the order of stabilisation of the helices.[97, 138] This effect would likely be subtle however as the differences in the ionic radii are of the order of tens of picometers. It is also a possibility that as a result of these titrations taking place in an aqueous environment that differences in the CD could be attributed to the cation hydration, and competition with H_2O as a ligand which could result in the slow association that is

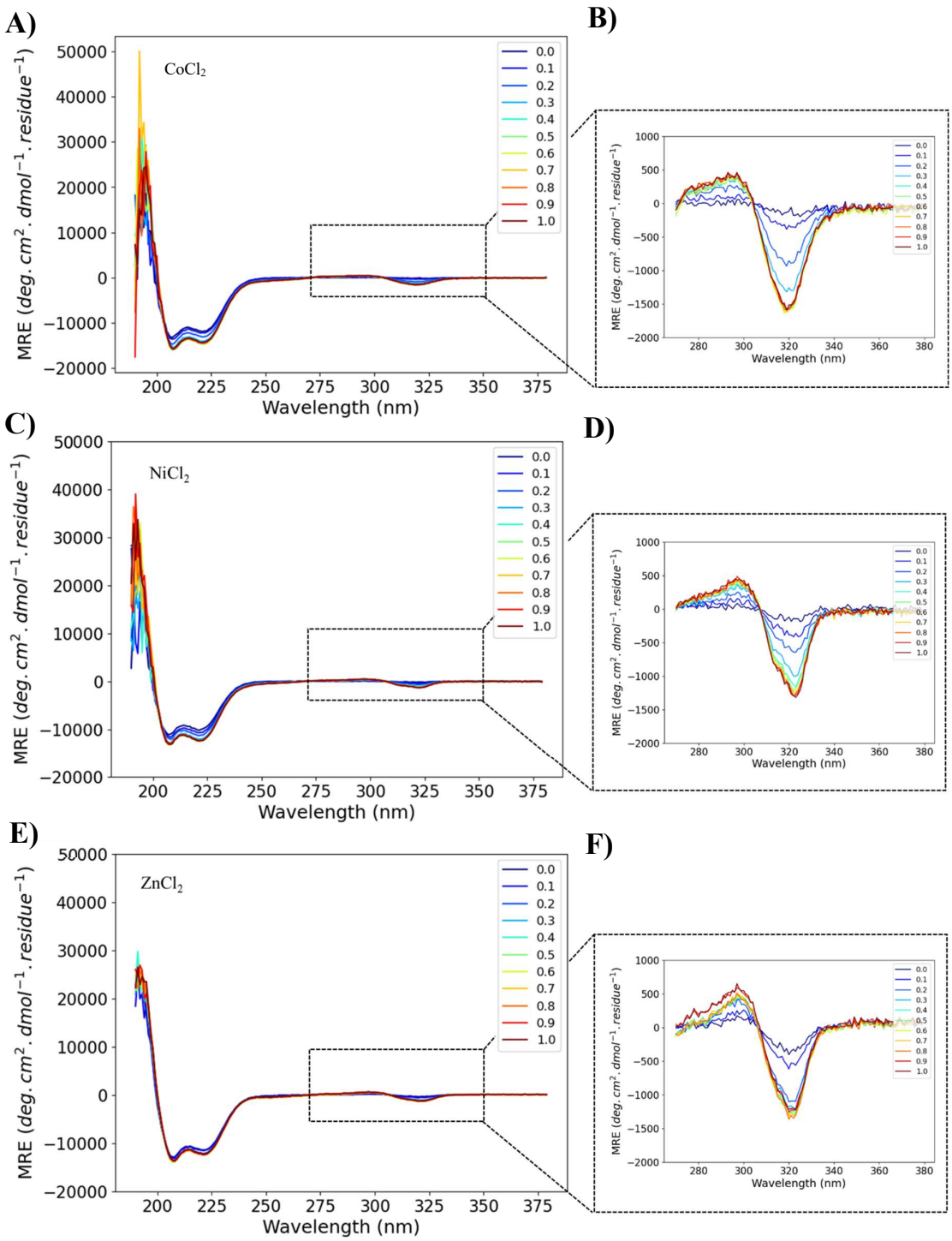

Figure 2.13 - CD traces of **1a** (10μM) titrations against **A)** $CoCl_2$, full spectrum showing the peptide folding behaviour with increasing eq of Co^{2+} **B)** $CoCl_2$, zoomed segment showing the bpy response to increasing eq of Co^{2+} **C)** $NiCl_2$, full spectrum showing the peptide folding behaviour with increasing eq of Ni^{2+} **D)** $NiCl_2$, zoomed segment showing the bpy response to increasing eq of Ni^{2+} **E)** $ZnCl_2$, full spectrum showing the peptide folding behaviour with increasing eq of Zn^{2+} **F)** $ZnCl_2$, zoomed segment showing the bpy response to increasing eq of Zn^{2+}. All were performed in 20 mM aqueous MOPS buffer.

observed for Zn^{2+} for example. The exact reasoning for the differences between the cations tested (with the exception of Cu^{2+}) is not obvious.

The Fe^{3+} and Fe^{2+} titrations displayed CD traces consistent with the behaviour of the Zn^{2+} complexes, however, the signal observed at 320 nm was much weaker This was determined to be a result of Fe^{2+}/Fe^{3+} cations being exhibiting solubility issues in the aqueous media used, resulting in inconsistent equivalents across the experiments. This was visible as orange Fe^{3+} precipitate forming as the experiment continued due to oxidation of the Fe^{2+} ions in solution and formation of Fe_2O_3 (iron oxide). For these reasons and after having success with the other metal ions, Fe^{3+} and Fe^{2+} binding in these complexes was not explored further.

2.4.4 Variable Temperature CD

As mentioned previously, to investigate the stability of both the CCs and the TM-complexes that have been formed in these systems, variable temperature experiments were performed and monitored by CD and UV spectroscopy. In all of the following experiments the temperature in the sample stage was ramped from 5 – 80 °C with measurements being taken every 5 °C, following this the temperature was cooled back to 5 °C and a final measurement was taken.

To begin with, **1a** was monitored without any metal ions present in solution to provide a baseline for comparison to the further experiments. From this experiment it can be observed (**Figure 2.14**) that as the temperature increases toward 80 °C, the secondary structure of peptide **1a** is lost as the ellipticity signal shifts towards that of a random coil.

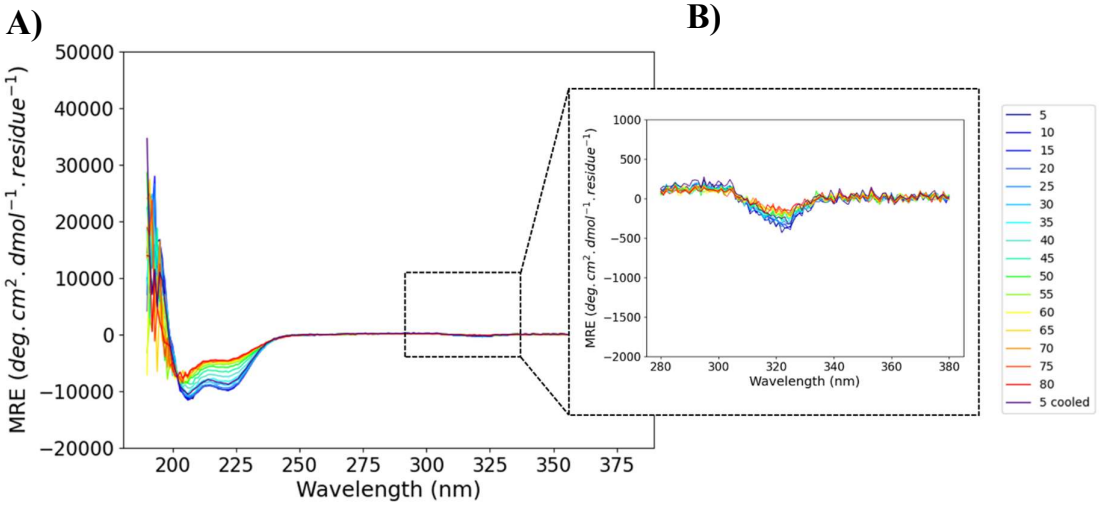

Figure 2.14 - CD Trace of the variable temperature measurements of **1a** (10 μM) in 20 mM aqueous MOPS buffer (pH 7) in the absence of metal ions. **A)** Full spectrum showing effect of increasing temperature on peptide folding **B)** Zoomed in trace showing the effect of temperature on the bpy conformation.

Comparison to the stability of **1b** (**Figure 2.15**) which does not benefit from the aromatic interactions stabilising the secondary structure, indicates that the presence of the bpy does in fact stabilise the CC. Upon cooling of **1a** at the end of the experiment however, it appears that the folding is reinstated. The signal does not return to the same magnitude that it reaches at the starting point of the experiment however the signal shape is still characteristic of a CC.

With respect to the bpy signal (**Figure 2.14 - B)**), the rise in temperature has a small effect with the magnitude of the signal reducing. The signal returns back to the initial ellipticity upon cooling to 5 °C. This suggests that this conformation of the bpy is more thermodynamically stable. The loss of this signal alongside the loss of α-helical content as the experiment progresses also confirms the coupled relationship between the chiral bpy conformation and the secondary structure of the peptide. As there is no metal to hold the strands of the trimeric CC together, the increase in temperature results in unfolding of the CC. The fact that the signal from the bpy interactions are not entirely lost indicates that this unfolding is likely happening away from the N-terminus, and the presence of the bpy units at the N-terminus is 'protecting' the trimer from completely unfolding in response to temperature. The stabilising intermolecular interactions between the bpy strands also means that re-folding of the secondary structure of **1a** is much more thermodynamically stable.

In addition to variable temperature of **1a**, the same experiment was run for the control, ac-capped peptide **1b**. This experiment was mainly to show the difference in stability of the functionalised peptide (**1a**) when compared to **1b**, and to determine if the most unfolded state reached during the variable temperature of **1a** matched that of **1b** which allows analysis of how much stabilisation the bpy unit is allowing (**Figure 2.15).**

From this spectrum it can be observed, as has been shown before, that there is no apparent defined secondary structure of this peptide sequence in the absence of the bpy units at the N-terminus. The lineshape of the spectrum is consistent with a random coil. The degree of folding for this peptide in comparison to the end point which was seen for **1a** shows that **1a** is more stabilised due to the presence of the bpy units that reinforce the secondary structure.

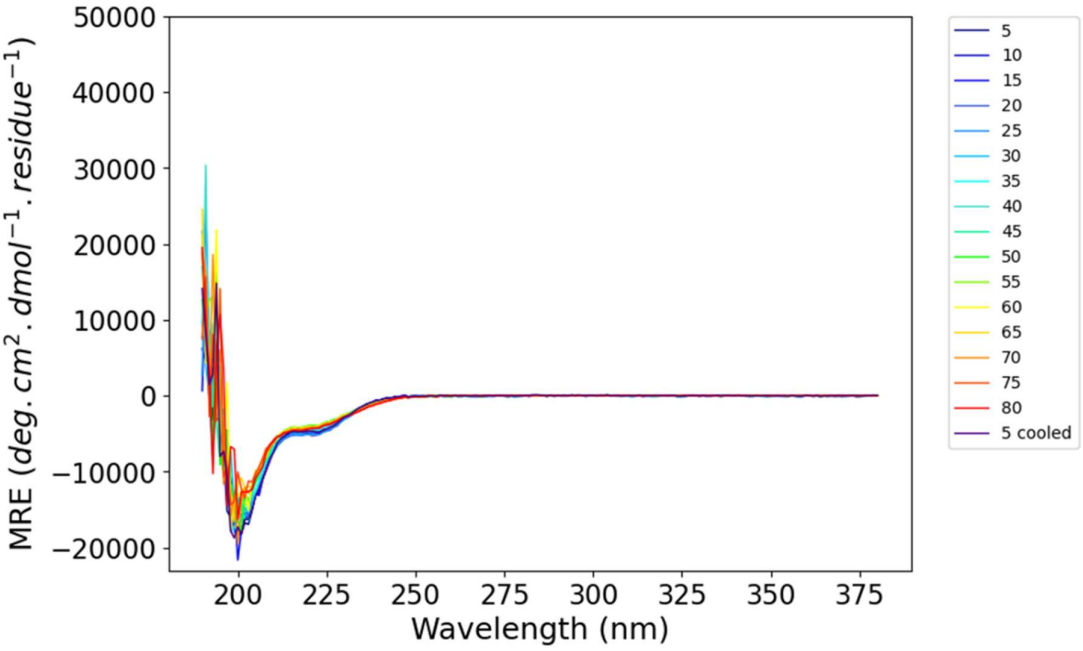

Figure 2. 15 - CD Trace of the variable temperature measurements of **1b** (10 μM) in 20 mM aqueous MOPS buffer (pH 7) in the absence of metal ions.

This trace was then compared to samples of **1a** which had been pre-equilibrated with 0.3 eq of either Co^{2+}, Ni^{2+}, Cu^{2+} or Zn^{2+} to analyse any effects on the stability of the system. The samples were pre-equilibrated at room temperature (rt) for approximately 60 min with 0.3 eq of each M^{2+} ion before CD measurements were obtained.

First, **1a** in the presence of Co^{2+} (**Figure 2.16**) exhibits unfolding as the temperature increases. When compared to the same sample (**1a**) with no metal, the behaviour in this experiment appears consistent, with no extra stabilisation afforded by the presence of Co^{2+} ions in the sample, despite evidence from the UV absorbance at lower temperatures that they are still associated to the bpy units. The UV absorbance **(Figure 2.16 C)**) shows that as the temperature of the sample increases however, the λ_{max} of the bpy shifts back to 280 nm, thus indicating that the Co^{2+} ions are dissociating from the complexes with the increasing temperature.

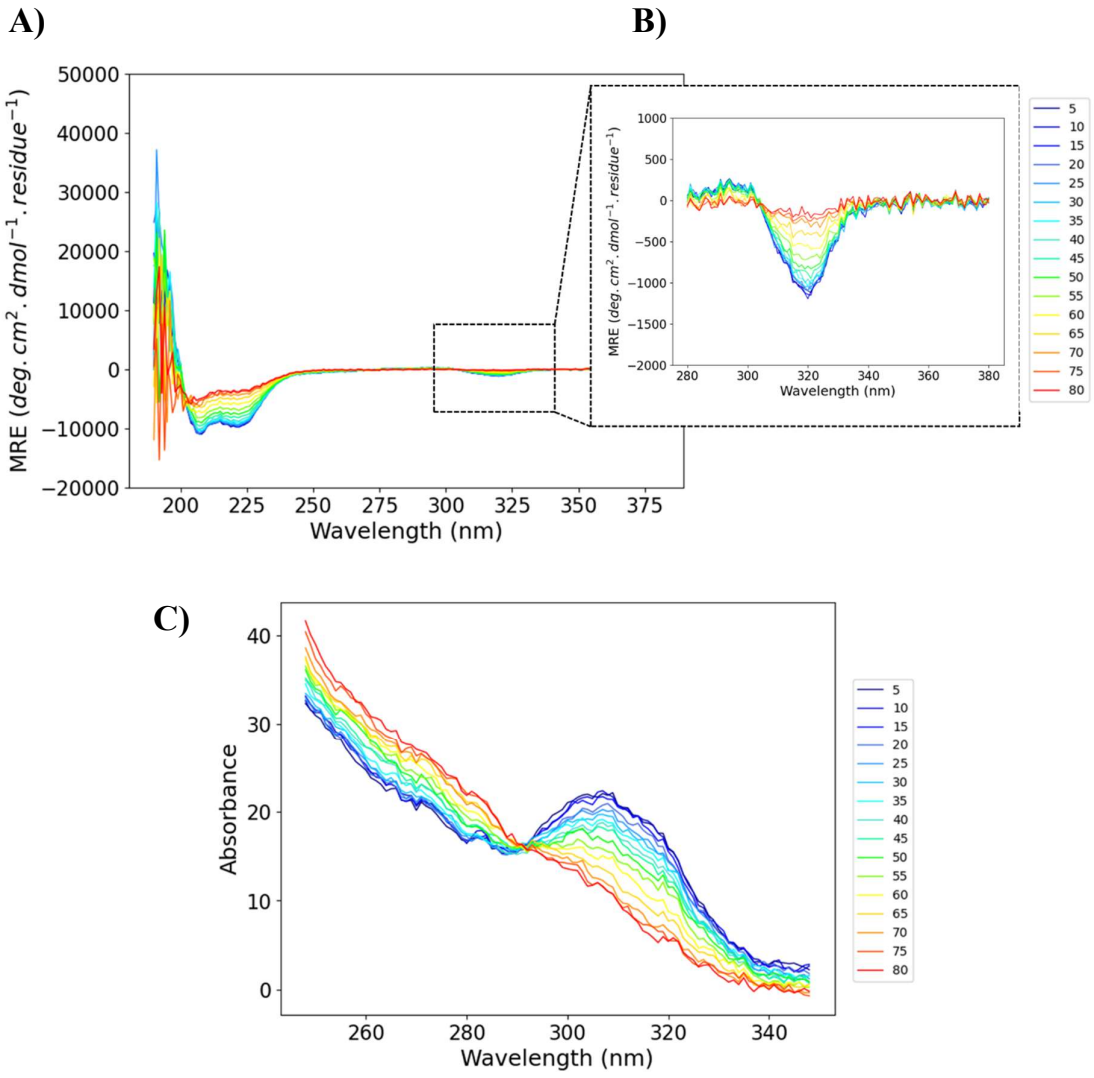

Figure 2.16 - CD and UV absorbance traces of the variable temperature measurements of **1a** (10 μM) in the presence of 0.3 eq Co^{2+} in 20 mM aqueous MOPS buffer, pH 7. **A)** Full CD trace showing the effect of temperature on the peptide folding of **1a** with 0.3 eq of Co^{2+} **B)** Zoomed segment of the full trace showing the impact of temperature on bpy conformation **C)** UV-Absorbance spectrum of **1a** + 0.3 eq of Co^{2+} and the effect of increasing temperature.

With respect to the complex formation, at low temperatures, consistent with the Co^{2+} titration there is a strong negative Cotton effect at approximately 320 nm. This indicates the preferential formation of the Δ-tris-(bpy-**1a)** complex. As the temperature increases, a reduction in magnitude of this signal is observed as was also seen for the metal free system in **Figure 2.14**. In that case it was thought that this was a result of the loss of the α-helical content of the peptide, however, in this case, the UV absorbance indicates that heating the solution causes the Co^{2+} to dissociate from the bpy as was mentioned above. The resulting loss in the signal at 320 nm is likely a result of both the dissociation of the Co^{2+} ions from

the bpy units as the temperature increases towards 55 °C and the unfolding of **1a** at higher temperatures. From the UV absorbance as the temperature reaches 55 °C the trace appears more indicative of uncoordinated **1a**, with the λ_{max} shifted back towards 280 nm, at which point it can be seen that both the peptide helicity and the bpy signal at 320 nm start to diminish with the increasing temperature. In comparison the metal free sample of **1a** (**Figure 2.14**) shows the helicity and the bpy signal at 320 nm decrease at a relatively stable rate across the experiment.

Interestingly, the behaviour of the Ni^{2+} sample of **1a** suggests that the Ni^{2+} ions form a much stronger complex with the bpy units. What can be observed from the thermal melt CD of peptide **1a** in the presence of Ni^{2+} (**Figure 2.17**) is that as the temperature is increased the helical signal corresponding to the secondary structure of **1a** does decrease, but not to the

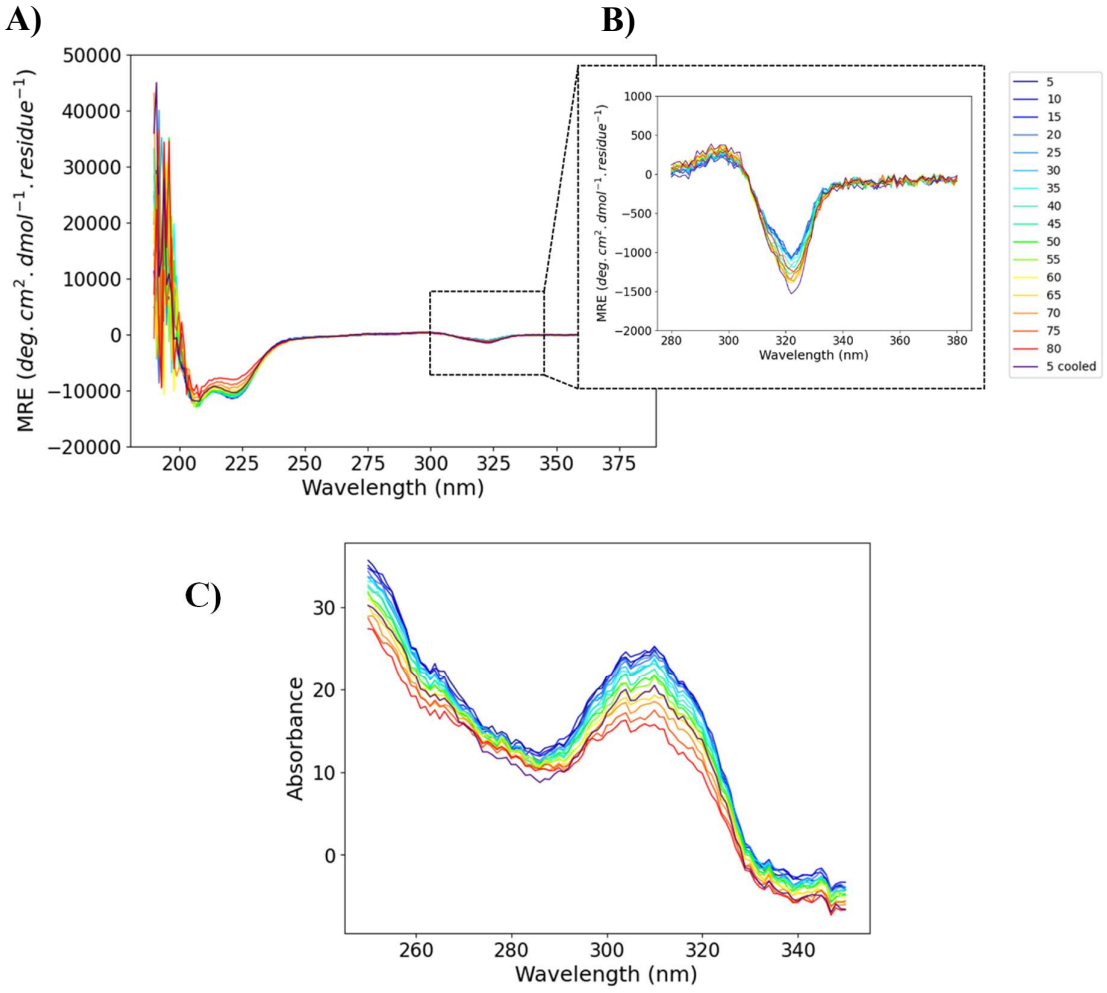

Figure 2.17 - CD and UV absorbance traces of the variable temperature measurements of **1a** (10 μM) in the presence of 0.3 eq Ni^{2+} in 20 mM aqueous MOPS buffer, pH 7. **A)** Full CD trace showing the effect of temperature on the peptide folding of **1a** with 0.3 eq of Ni^{2+} **B)** Zoomed segment of the full trace showing the impact of temperature on bpy conformation **C)** UV-Absorbance spectrum of **1a** + 0.3 eq of Ni^{2+} and the effect of increasing temperature.

same extent as any of the other metals described below. Thermodynamically, the secondary structure is stabilised by the presence of the bound Ni^{2+} and despite the slight reduction in magnitude of the signal corresponding to the secondary structure at higher temperatures, upon cooling **1a** folds back into its CC super-secondary structure. Again, the signal does not return to the magnitude it reached at the starting point of the experiment.

Additionally, the Δ-tris-(bpy-peptide)-Ni^{2+} complex is not lost as the temperature increases but instead appears to stabilise at the higher temperatures. The signal at approximately 322 nm has an initial value of approximately -1000 deg·cm^2·dmol^{-1}·residue^{-1} which when heated to approximately 70 °C now reaches a minimum of -1250 deg·cm^2·dmol^{-1}·residue^{-1}. Past this point the measurements at 75 and 80 °C indicate that the structure is beginning to break down, however, the following measurement at 5 °C shows that the Δ-tris-(bpy-peptide)-Ni^{2+} complex now has a chiral signal with a magnitude of -1500 deg·cm^2·dmol^{-1}·residue^{-1}, having decreased from the start value by 50%. The annealing of this sample has allowed it to reach a product with increased stability which in this case is a chiral complex favouring a Δ-conformation. The UV absorbance from this experiment shows that in this case, the metal does not dissociate from the bpy with increasing temperature, indicating that this complex is stable and provides an explanation as to why the super-secondary structure is not entirely lost upon heating.

The Cu^{2+}-**1a-**complex behaviour is as expected following its observed dynamic behaviour in the Cu^{2+} titration in Section 2.4.3. Initially, as the temperature is increased, both the signal arising from the bpy complex and the helical signal from **1a** are reduced (**Figure 2.18**). The bpy signal going close to zero, indicating dissociation of the metal which is again reflected by the reduction of the UV-max absorbance at 310 nm. The helical signal from **1a** is also shifted towards random coil with the increasing temperature, as was observed for the Co^{2+} sample, but as the sample is cooled it returns to the signal corresponding to a CC.

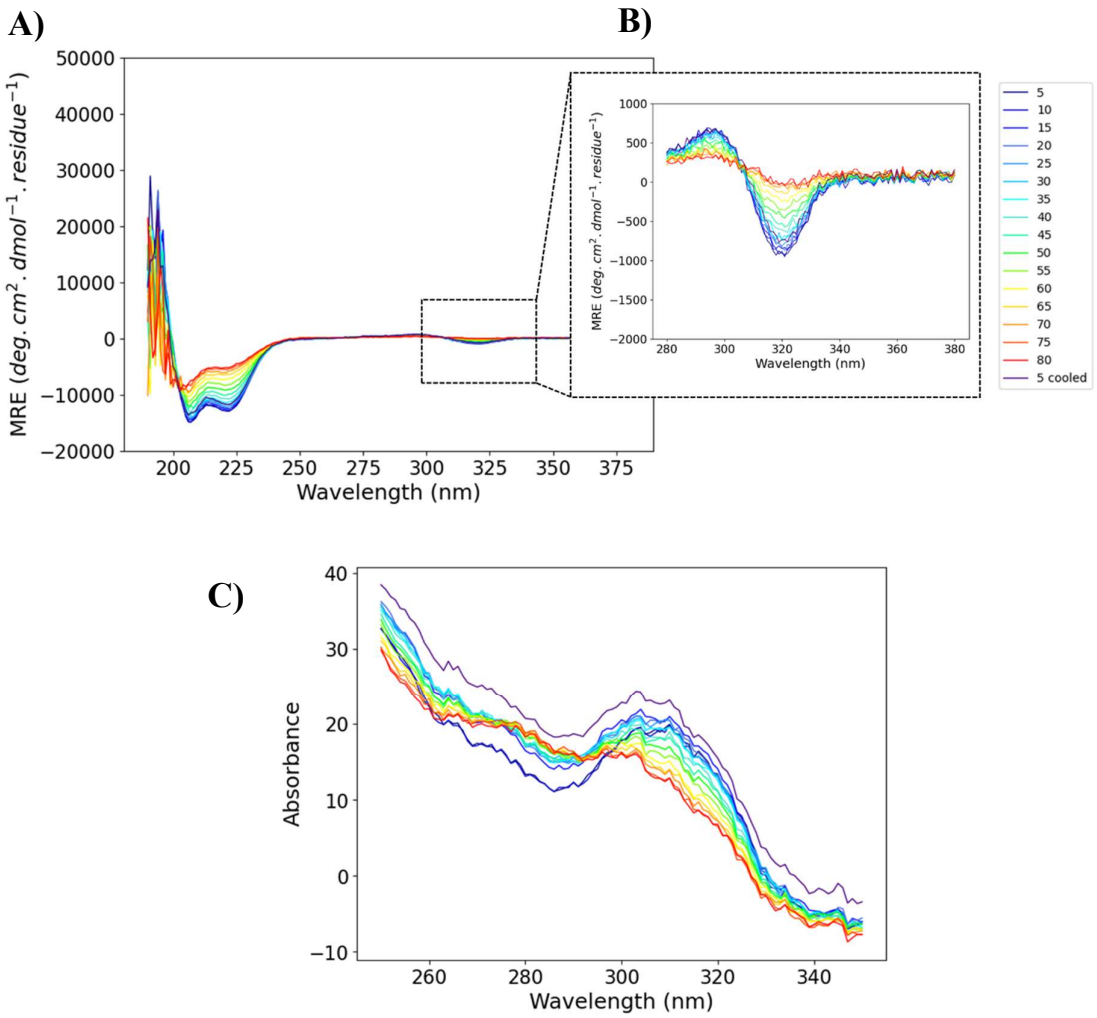

Figure 2.18 - CD and UV absorbance traces of the variable temperature measurements of **1a** (10 μM) in the presence of 0.3 eq Cu^{2+} in 20 mM aqueous MOPS buffer, pH 7. **A)** Full CD trace showing the effect of temperature on the peptide folding of **1a** with 0.3 eq of Cu^{2+} **B)** Zoomed segment of the full trace showing the impact of temperature on bpy conformation **C)** UV-Absorbance spectrum of **1a** + 0.3 eq of Cu^{2+} and the effect of increasing temperature.

Variable temperature CD measurements of the Zn^{2+} sample shows the same behaviour as the Cu^{2+} sample (**Figure 2.19**). As the temperature increases, the signal corresponding to the CC super-secondary structure of **1a** is lost, becoming more characteristic of the random coil and the signal from the Δ-tris-(bpy-peptide) complex also tends towards 0 deg·cm^2·dmol^{-1}·residue^{-1}. Despite the loss of the exciton couplet from the complex, like the other metal samples and even when the sample is absent of metal, the signal is not completely eradicated. This is a consequence of the aromatic stacking interactions still stabilising the conformation at the N-Terminus.

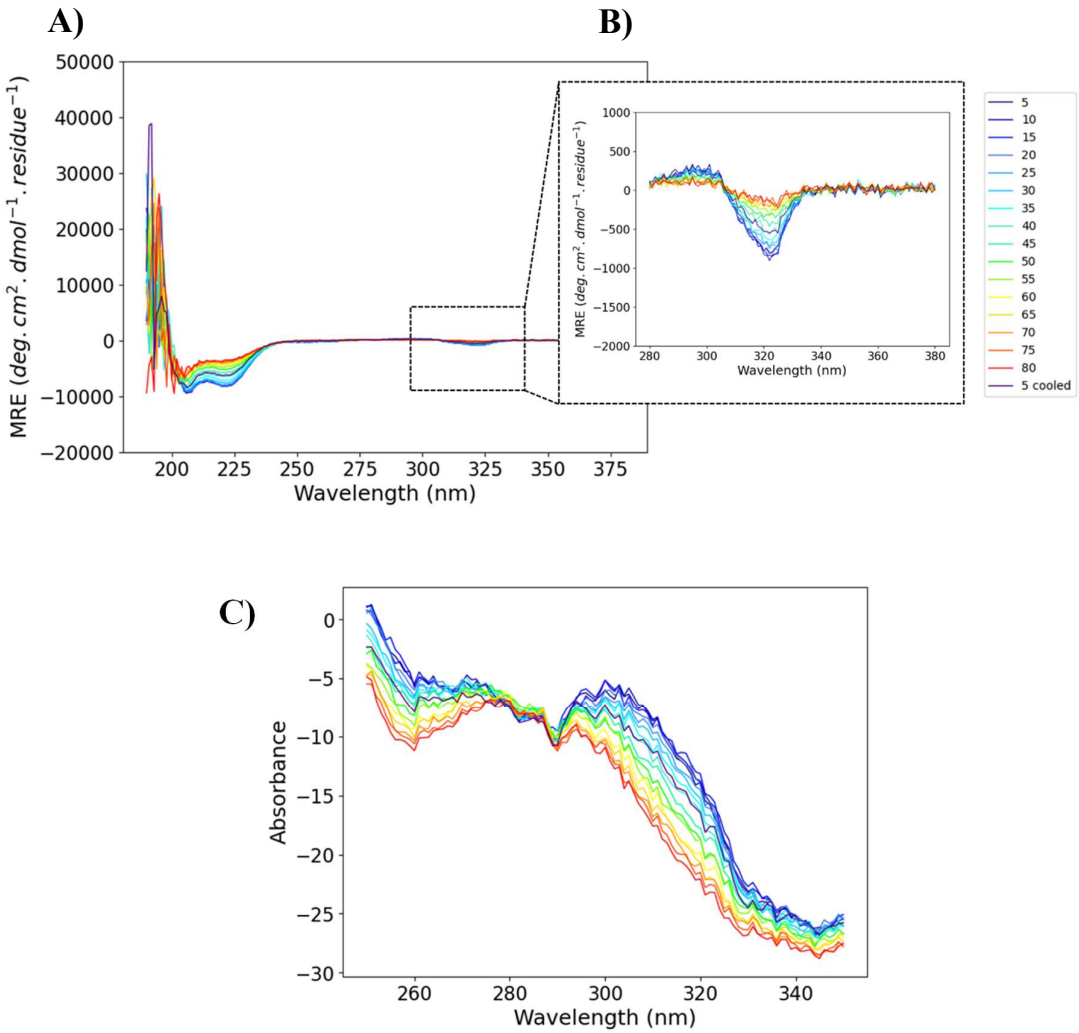

Figure 2.19 - CD and UV absorbance traces of the variable temperature measurements of **1a** (10 μM) in the presence of 0.3 eq Zn^{2+} in 20 mM aqueous MOPS buffer, pH 7. **A)** Full CD trace showing the effect of temperature on the peptide folding of **1a** with 0.3 eq of Zn^{2+} **B)** Zoomed segment of the full trace showing the impact of temperature on bpy conformation **C)** UV-Absorbance spectrum of **1a** + 0.3 eq of Zn^{2+} and the effect of increasing temperature.

To summarise, the presence of first row TMs Co^{2+}, Cu^{2+} and Zn^{2+} in **1a** does not appear to significantly stabilise the super-secondary structure as at high temperatures the metal ions dissociate from the bpy units. Conversely, Ni^{2+} ions were found to stabilise the CC super-secondary structure. Additionally, in all cases the Δ-conformation of the bpy units in **1a** was found to be the favoured conformation, even after annealing.

2.5 Ligation of Rigid Chelating Molecule 1,10-phenanthroline to a Homotrimeric Coiled Coil

To further probe the relationship discovered between the CC helicity and the conformational bias in the N-terminal complex with the bpy chelating units, 1,10-phenanthroline (phen) was investigated as an example with increased rigidity and conjugation.

2.5.1 Sequence Design

For sake of comparison to the previous bpy studies the sequences used in the following study feature the same 3-heptad repeat sequence as **1a** with alteration of the N-terminus resulting in **3a.** The sequences are shown in **Table 2.2**.

Table 2.2 -Sequences of **3a** and **1b**

Peptide No.	Capping Moiety	Sequence	C-Terminus
3a	Phen	GQEIAAIKKEIAAIKKEIAAIKYG	NH_2
1b	Ac	GQEIAAIKKEIAAIKKEIAAIKYG	NH_2

Sequence **1b** is also used as a negative control in this study as it has the same base sequence but features no chelating units, therefore we can attribute any differences in the CD and UV absorbance traces to differences caused by the presence of the chelating unit at the N-terminus.

2.5.2 The Effect of the Presence of an N-terminal 1,10-Phenanthroline on the Self-Assembly of a Trimeric Coiled Coil

1,10-phenanthroline-4-carboxlic acid was investigated as an alternative chelating unit that could also be easily installed at the N-terminus using standard amide coupling methods. It was hypothesised that the larger conjugated system of the phenanthroline would result in stronger π-stacking interactions between the strands, thus stabilising the CC-structure of the peptides.

3a was synthesised by SPPS and functionalised at the N-terminus by standard amide coupling of 1,10-phenanthroline-4-carboxylic acid on resin. After cleavage and purification **3a** was then titrated against Cu^{2+}, Zn^{2+} and Co^{2+} respectively and monitored by CD and UV absorbance spectroscopy.

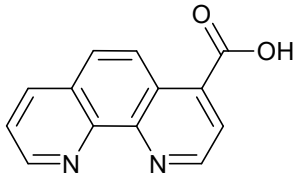

Figure 2.20 – Structure of 1,10-phenanthroline-4-carboxylic acid

The CD traces comparing the phen-functionalised peptide **3a** with the bpy-(**1a**) and Ac-(**1b**) capped versions can be found in **Figure 2.21**. These results show that the presence of phenanthroline at the N-terminus does not have a similar effect on the stability of the CC as the bpy moiety. It would appear instead that the addition of the phenanthroline at the N-terminus has a detrimental effect on the helicity of the CC. This is likely due to its increased rigidity compared to bpy resulting in steric repulsion at the N-terminus. It is possible that the lack of flexibility means that the phen cannot form the same stabilising aromatic interactions as the bpy was found to have, and as a consequence, the steric repulsion leads to a fraying

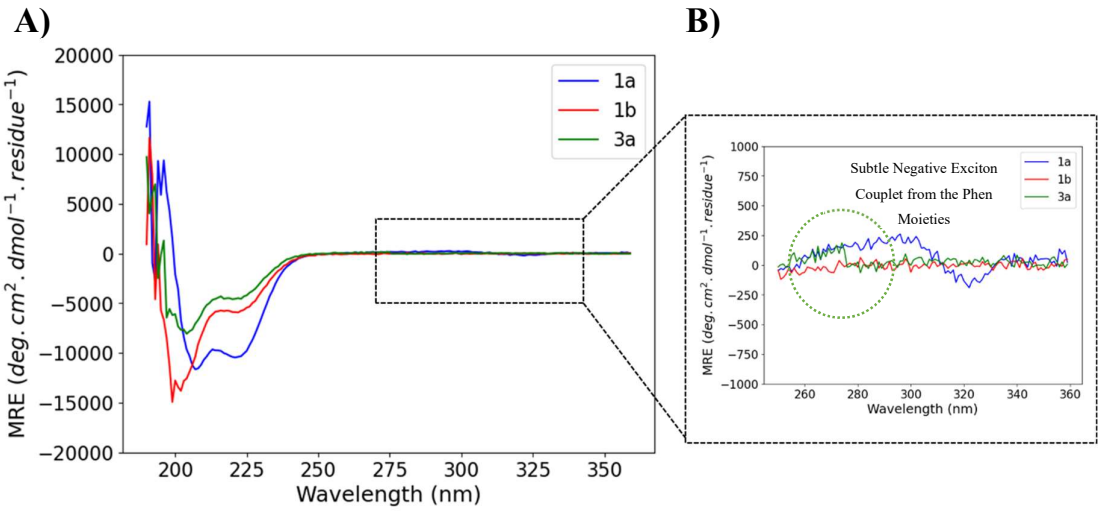

Figure 2.21 - CD trace comparison of **1a** (blue), **1b** (red) and **3a** (green), all 10 µM in 20 mM aqueous MOPs buffer, pH 7. **A)** Full CD spectrum comparison showing the differences in peptide folding between **1a**, **1b** and **3a**. **B)** Zoomed segment of the CD spectrum showing the differences between the bpy and phen conformations when attached to the same peptide sequence.

of the CC, pushing the strands apart. As a result of this, the signal corresponding to a chiral-phen complex is very small. With the lack of secondary or super-secondary structure rigidity and resulting conformational bias from the CC onto the complex, there is little control of the handedness of the resulting complex. The slight CC helicity, however, does result in a small favourability for the Δ-tris-(phen-peptide) complex which can be seen in **Figure 2.21 B)** where the green trace is displaying a small negative exciton couplet centred around approximately 270 nm (circled in green in **Figure 2.21 B)**). The UV absorbance of the phen coupled peptide **3a** can be found in **Figure 2.22**. From this spectrum it can be seen that the change in absorbance between a metal free **3a** and a Cu^{2+} coordinated **3a** is subtle, with the absorbance wavelength red-shifting from 273 nm to 277 nm.

Three different TM ions were titrated into 10 μM solutions of **3a** in 0.1 eq (4 μL) increments up to 1.0 eq with respect to the peptide (and likewise the phenanthroline). In the case of all three metals (Co^{2+}, Cu^{2+} and Zn^{2+}) tested, only small effects were observed in both the CD and the UV absorbance.

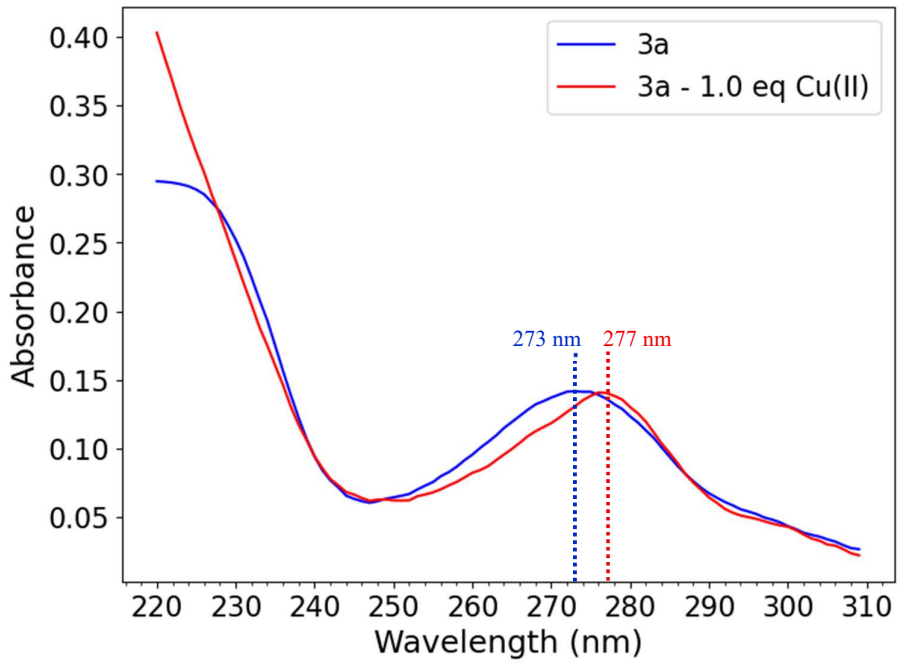

Figure 2.22 – UV absorbance of **3a** both in the absence of metal ions and with 1.0 eq of Cu^{2+} to show the difference in absorbance between metal free (blue) and coordinated phenanthroline. There is a subtle red-shift to 277 nm upon coordination of Cu^{2+} (red).

From the Co^{2+} experiment, no discernible change is apparent in the helical signal which arises from **3a** (**Figure 2.23**). The magnitude of the negative exciton couplet from the phen decreases as the experiment progresses, indicating that the complex is either experiencing no chiral preference or due to saturation of the phen binding sites as was hypothesised with

Cu^{2+} in Section 2.4.1. The UV absorbance measurements from this experiment shows that as the concentration of Co^{2+} increases in solution the expected change in absorbance from 273 nm to 277 nm occurs, indicating complex formation (**Figure 2.23**).

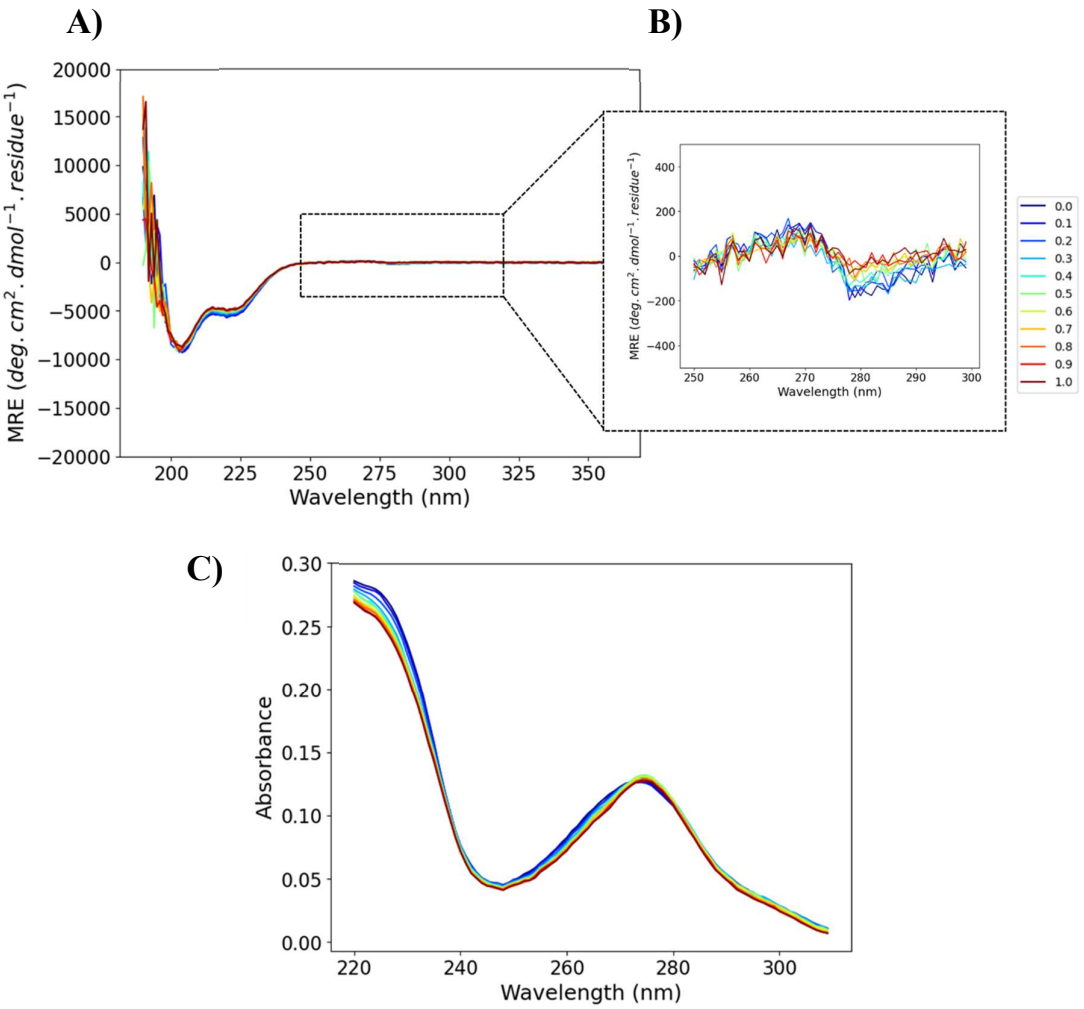

Figure 2.23 - CD Trace of the titration of **3a** (10µM) against Co^{2+} in 20 mM aqueous MOPS buffer, pH 7. **A)** Full CD spectrum showing the response of **3a** peptide folding with increasing equivalents of Co^{2+} **B)** Zoomed segment of the full CD trace showing the changes in phen conformation with increasing Co^{2+} equivalents, a small loss of ellipticity is observed **C)** UV-Absorbance trace showing the difference in absorbance with increasing equivalents of Co^{2+}, red-shift from 273 nm to 277 nm indicative of Co^{2+} coordination.

The signals from the Cu^{2+} experiments indicate a slight unfolding of the CC super-secondary structure as the concentration of Cu^{2+} increases in solution as well as loss of the exciton couplet from the phenanthroline, as observed for Co^{2+}. In addition, the trace from the UV-absorbance indicates the transition from uncoordinated to coordinated ligands with increasing equivalents of Cu^{2+}, with the transition occurring at 0.3 eq of Cu^{2+} (**Figure 2.24**).

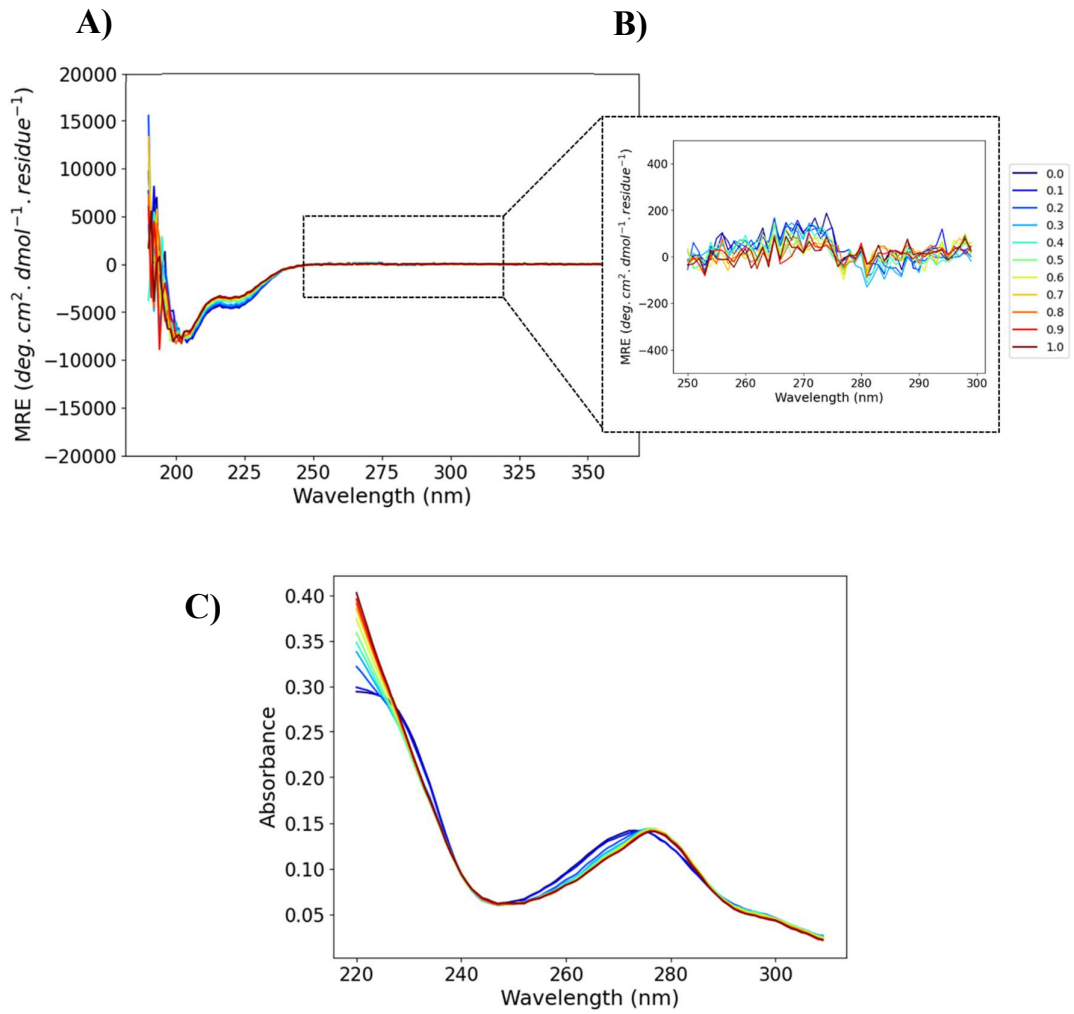

Figure 2.24 - CD Trace of the titration of **3a** (10μM) against Cu^{2+} in 20 mM aqueous MOPS buffer, pH 7. **A)** Full CD spectrum showing the response of **3a** peptide folding with increasing equivalents of Cu^{2+} **B)** Zoomed segment of the full CD trace showing the changes in phen conformation with increasing Cu^{2+} equivalents, a small loss of ellipticity is observed **C)** UV-Absorbance trace showing the difference in absorbance with increasing equivalents of Cu^{2+}, red-shift from 273 nm to 277 nm indicative of Cu^{2+} coordination.

The results from the Zn^{2+} experiment can be found in **Figure 2.25**. From this it can be seen that **3a** exhibited no changes to the helicity of the peptide and only a slight reduction in the exciton couplet from the phenanthroline with increasing equivalents of Zn^{2+}. Interestingly, however, the exciton couplet from the phen exhibits the opposite sign as has been observed for all the previous experiments with this peptide. As the concentration of Zn^{2+} in solution tends towards 0.3 eq, the magnitude of the Λ-phen exciton couplet increases, beyond this, the magnitude gradually decreases. In addition to this from the UV absorbance the two-state transition from free phen to bound phen can now be seen, with this transition taking place at approximately 0.3 eq of Zn^{2+}.

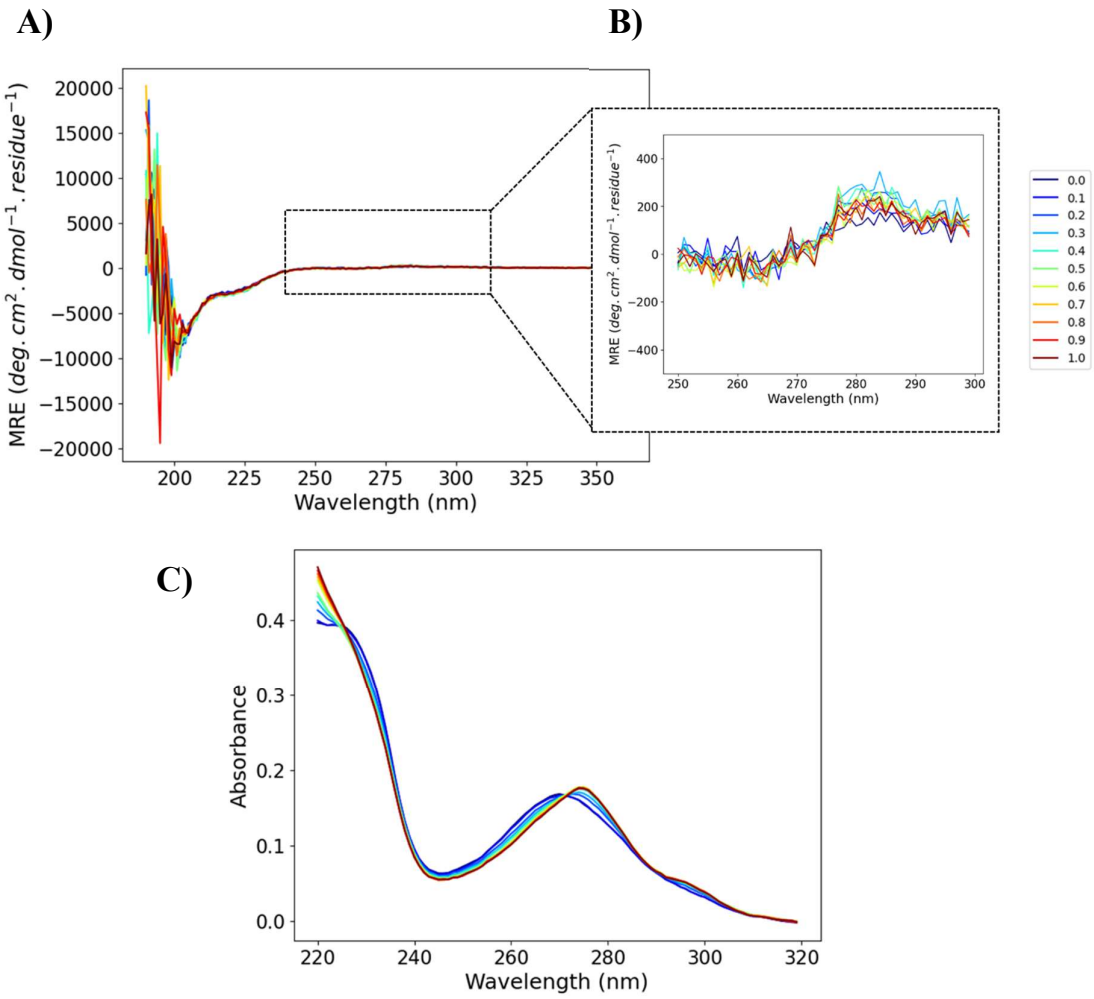

Figure 2.25 - CD Trace of the titration of **3a** (10μM) against Zn^{2+} in 20 mM aqueous MOPS buffer, pH 7. **A)** Full CD spectrum showing the response of **3a** peptide folding with increasing equivalents of Zn^{2+} **B)** Zoomed segment of the full CD trace showing the changes in phen conformation with increasing Zn^{2+} equivalents, a small loss of ellipticity is observed **C)** UV-Absorbance trace showing the difference in absorbance with increasing equivalents of Zn^{2+}, red-shift from 273 nm to 277 nm indicative of Zn^{2+} coordination.

The difference in handedness of the complex here shows that this system exhibits less preference in chirality upon complexation and is much more poised to form either handedness of the complex. The magnitude of the signals in comparison to what was observed for the bpy conjugated peptide **1a** shows that the chiral information transfer from the peptide to the complex is much less pronounced for the phen system. This could be a result of the increased rigidity of the phen structure. Where the bpy can rotate to accommodate the helicity of the peptide at the N-terminus whilst also forming aromatic interactions and coordinating to the metal ion in a Δ-tris(bpy-peptide) conformation, the phen is rigid and cannot rotate as freely. Given that these rotations are not available within the phen structure itself, it is likely to form the tris(phen-peptide) complex requires distortion

of the peptide structure at the N-terminus. This could explain why there is a loss in the helicity of the peptide comparative to the bpy appended sequence **1a**. The lowered helicity of the peptide, therefore, could present an explanation to the lack of chiral information transfer onto the complex. If the CC was unfolding to accommodate the phen at the N-terminus, when the metal is introduced, the ligands for the complex are not prearranged in a chiral conformation, and therefore when the metal is introduced, a racemic mixture is formed. This is backed up by the loss of chirality as the metal is introduced in all three titrations.

Variable temperature CD measurements of **3a** were also performed. These were done both in the absence of metal and in the presence of 0.3 eq of Co^{2+} (**Figure 2.26**).

Comparison of these two traces suggests that the Co^{2+} coordination of the phen at the N-terminus does marginally stabilise the super-secondary structure of **3a**. This is apparent as with the increase in temperature, **3a** + 0.3 eq of Co^{2+} remains stable up to 50 °C, approximately 10 °C higher than the metal free equivalent thus suggesting a partial stabilisation when the TM is bound to the phen. The zoomed portion of the data in the range of 250 – 300 nm (**Figure 2.26 B)** and **D)**) shows the exciton couplet from the phen units reducing as the temperature increases and the super-secondary structure of the peptide is reduced.

Evidence from the variable temperature UV absorbance trace of **3a** in the presence of 0.3 eq of Co^{2+} suggests that as the temperature increases, the Co^{2+} ions do not dissociate from the phen units, indicating that they are more strongly bound than in the bpy functionalised peptide **1a** where dissociation was observed.

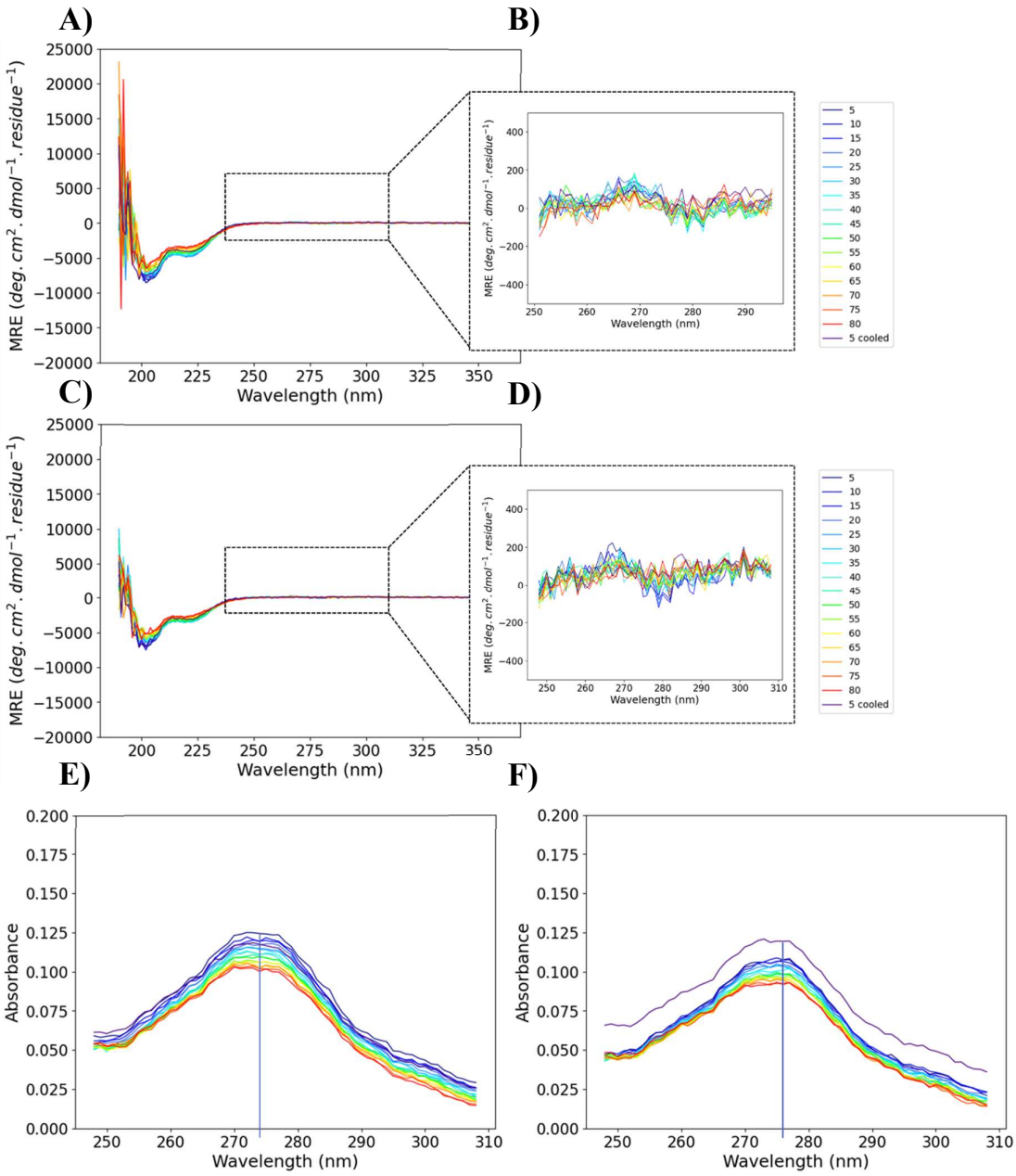

Figure 2.26 - CD and UV absorbance of the variable temperature measurements of **3a A)** Full variable temperature CD spectra of **3a** (10 μM) in the absence of metal ions **B)** Zoomed segments of variable temperature CD spectra of **3a** (10 μM) in the absence of metal ions **C)** Full variable temperature CD spectra of **3a** (10 μM) in the presence of 0.3 eq Co^{2+}. **D)** Zoomed segments of variable temperature CD spectra of **3a** (10 μM) in the presence of 0.3 eq Co^{2+}. **E)** Variable temperature UV absorbance of **3a** in the absence of metal. **F)** Variable temperature UV absorbance of **3a** in the presence of 0.3 eq of Co^{2+}. All were performed in 20 mM aqueous MOPS buffer, pH 7.

2.6 Conclusions

In conclusion, through amide coupling of 2,2′-bipyridine-4-carboxylic acid to the N-terminus of a 3-heptad CC sequence at the *d*-position can lead to reliable preferential formation of the Δ-tris-(bpy-**1a)** complex.

Through synthesis and subsequent analysis by CD and UV absorbance spectroscopy of peptides **1a**, **1b**, **2a** and **2b**, the relationship between the helicity of the peptide and the preferential formation of these chiral complexes has been addressed. Comparison of peptides **1a** and **1b** both in the absence and presence of M^{2+} ions showed the cooperative nature of the degree of α-helicity of the peptide and the resulting magnitude of the exciton couplet arising from the bpy-units. From this data it can be concluded that the presence of the bpy-unit at the N-terminus results in a higher degree of α-helicity, most likely as a result of intermolecular π-interactions between the bpy moieties. Furthermore, 1-heptad repeat peptide **2a** which also features a bpy at the N-terminus in a *d*-position indicates no chiral preference in the resulting bpy-conformation either in the absence or presence of M^{2+} ions. Comparing this to the observations for **1a** shows the reliance of the chiral complex formation on the helical content of the peptide.

The results in this chapter also demonstrate the different behaviours of this system in response to different first row TMs (Co^{2+}, Ni^{2+}, Cu^{2+}, Zn^{2+}). A dynamic relationship was found for Cu^{2+} titrations in which concentrations exceeding 0.3 eq with respect to the peptide resulted in loss of α-helicity and reduction in the magnitude of the bpy exciton couplet. This further demonstrated the cooperative relationship between the helicity of the peptide and the preferential chiral complex formation.

Titrations against the other metals in this series indicated preferential formation of *fac*-Δ-octahedral complexes between the bpy units and the M^{2+} ions, with the Ni^{2+} and Co^{2+} titrations showing increased folding in response to the binding of the metal ions. These effects were suggested as being attributed to electronic differences in the metal cations, i.e. ionic radii which increase across the series, differences in molecular binding orbitals or the different hydration enthalpies of the cations resulting in differing levels of competition with the H_2O in the samples. Although these suggestions were made the exact reasoning for the difference was not obvious and it is likely a combination of factors that contribute to the differences that are observed.

Variable temperature measurements of these complexes showed that presence of the TM-complex at the N-terminus only thermally stabilised the secondary structure in the case of the Ni^{2+} complex, indicating that this forms the strongest complexes with the bpy groups of **1a**. This was further supported by the UV absorbance from this experiment which indicated much less Ni^{2+} dissociation with the increasing temperature than was observed for the other metals in this series.

Alternative chelating unit 1,10-phenanthroline-4-carboxylic acid was also tested under the same conditions. Presence of the phen at the N-terminus of **3a** did not have the same stabilising effect on the α-helicity of the peptide as was observed for the bpy-peptide (**1a**). This was thought to be a result of its bulkier structure potentially leading to slight fraying of the N-terminus. The results from titrations of Co^{2+}, Cu^{2+} and Zn^{2+} into peptide **3a** showed much less pronounced chiral information transfer than was observed for the bpy-equivalent of this peptide. Additionally, peptide **3a** showed much less preference for one handedness of the complex over another, exhibiting a small preference for both the Δ- and the Λ-conformations during different experiments. This inconsistency combined with the reduced magnitude of the phen exciton couplet in both cases suggest that this system is much more poised to form either handedness of the complex. This was suggested to be a result of the reduced helicity which is likely a result of the more rigid structure of the phen units when compared to the bpy alternative.

3 Spatial Constraints of the Chiral Preference in N-terminally Functionalised Supramolecular Peptide Assemblies

This chapter explores the tolerance of the self-assembled trimeric CCs for the formation of chiral N-terminal complexes. It is divided into two main vs, the first discussing addition of chiral and achiral spacers to the N-terminus and the second discussing the position of the chelating unit with respect to the helical register.

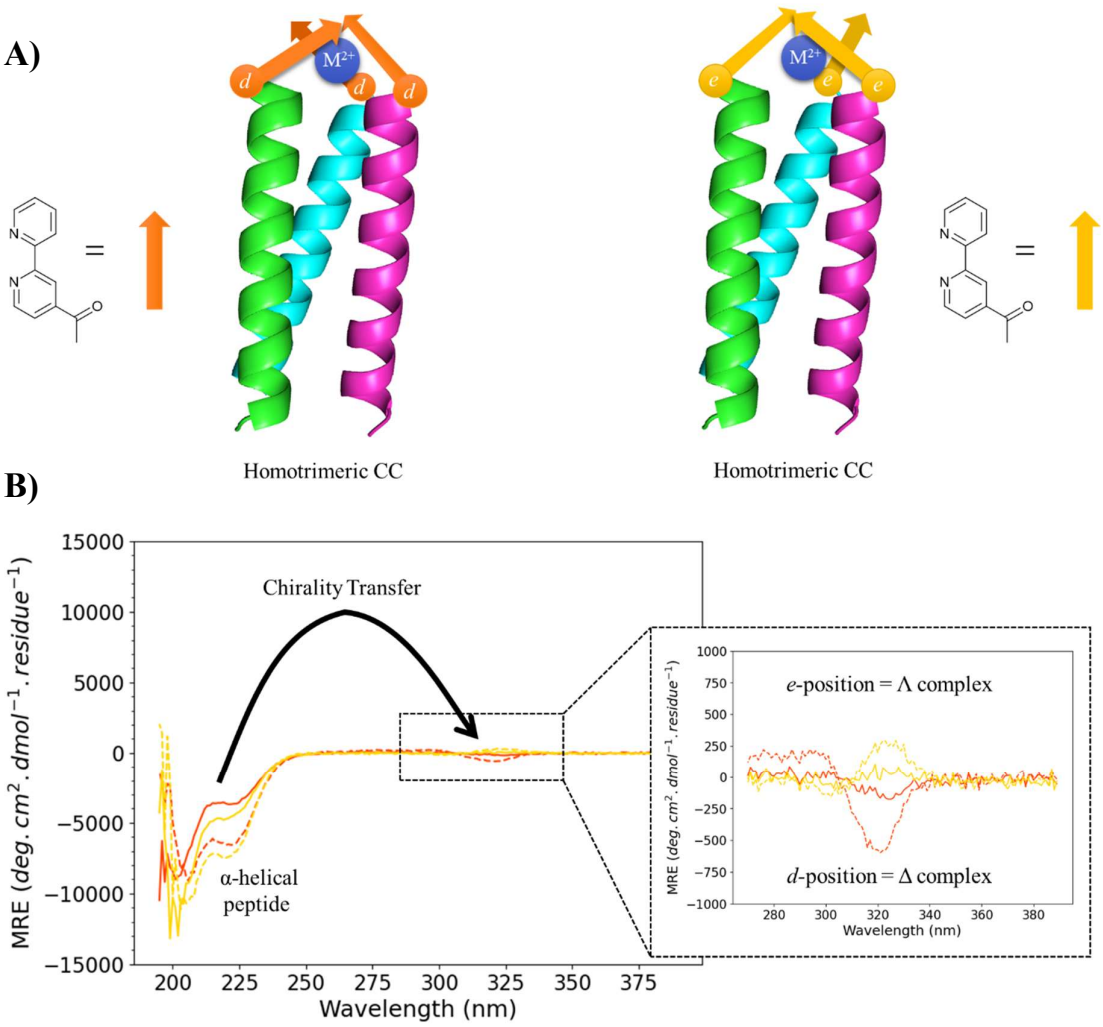

Figure 3.1 – Graphical abstract showing the formation of opposite handedness complexes at the N-terminus of a left-handed supercoiling CC by changing the position of the bpy unit within the helical register. **A)** Cartoon homotrimeric CCs showing the bpy in the *d*-position (orange) or the *e*-position (yellow) represented by a vector. The directionality indicates the handedness of the complexes formed. **B)** CD spectrum showing the chiral information transfer from the peptide helicity onto the complex, with the peptide featuring the bpy at the *d*-position exhibiting a negative exciton couplet (Δ) and the peptide with the bpy at the *e*-position exhibiting a positive exciton couplet (Λ).

Through the design and synthesis of two sets of trimeric CC peptides the relationship between the distance of the chelating molecule (bpy) from a chiral residue and the resulting preferential formation of a chiral tris-bpy complex is probed.

A further set of trimeric CCs was also prepared to investigate the tolerance of the system for the formation of chiral tris-bpy complexes when the bpy falls at different positions in the helical register.

3.1 Aims

This chapter is to investigate the spatial tolerances governing the preferential formation of Δ-tris-(bpy-peptides) or Λ-tris-(bpy-peptides). This is investigated by preparation of 17 different CC forming peptides functionalised at the N-terminus with bpy units. These peptides vary in length, helical content, register position of the bpy and distance of bpy from a chiral centre. By altering these variables, the understanding of the relationship between the helicity of the CC and the resulting chiral complex formation at the N-terminus can be furthered.

The experiments aim to show that a preference for one isomer over the other can be in fact be controlled by altering the register position of the chelating unit (**Figure 3.1**), and that the strength of this preference is further controlled by proximity of the chelator to a chiral centre.

3.2 Design and Synthesis of 3- and 4-Heptad Homotrimeric Coiled Coils Featuring Increasing Distance from a Chiral Centre

3.2.1 Sequence Design

Sequences **1a** and **1b** were modified to feature achiral spacers (Gly, GlyGly and PEG) (**Figure 3.2**) of increasing length at the N-terminus preceding the attachment site of the bipyridine. The aim of varying this structural aspect was to probe the limits of the chiral information transfer from the CC homotrimer to the terminal metal complex by systematically increasing the distance between the bipyridine and a chiral residue. In addition to the achiral spacers, peptide **4a** which exhibits a direct attachment to a chiral residue (alanine) was also synthesised to assess if this amplifies the chiral effects demonstrated in Chapter 2.

In designing these sequences care was taken where possible to ensure that the register position of the bpy wasn't altered across the 4 different sequences. Alongside the bpy functionalised peptides, control sequences (labelled ***b***) were synthesised for each, all of which were acetyl capped at the N-terminus (**Table 3.1**), to ensure that effects observed in the CD and UV absorbance spectroscopy occurred because of bpy-chelation and not that of nonspecific binding to the CC via a side chain group.

Table 3.1 - Sequences of **1a, 1b, 4a, 4b, 5a, 5b, 6a** and **6b**

Peptide No.	Capping Moiety	Sequence and Register	C-Terminus
1a	**bpy**	**G**QEIAAIKKEIAAIKKEIAAIKYG *efg**a**bc**d**efg**a**bc**d**efg**a**bc**d**efg*	NH_2
1b	Ac	**G**QEIAAIKKEIAAIKKEIAAIKYG *efg**a**bc**d**efg**a**bc**d**efg**a**bc**d**efg*	NH_2
4a	**bpy**	**A**QEIAAIKKEIAAIKKEIAAIKYG *efg**a**bc**d**efg**a**bc**d**efg**a**bc**d**efg*	NH_2
4b	Ac	**A**QEIAAIKKEIAAIKKEIAAIKYG *efg**a**bc**d**efg**a**bc**d**efg**a**bc**d**efg*	NH_2
5a	**bpy**	**GG**EIAAIKKEIAAIKKEIAAIKYG *efg**a**bc**d**efg**a**bc**d**efg**a**bc**d**efg*	NH_2
5b	Ac	**GG**EIAAIKKEIAAIKKEIAAIKYG *efg**a**bc**d**efg**a**bc**d**efg**a**bc**d**efg*	NH_2
6a	**bpy**	**PEG**-QEIAAIKKEIAAIKKEIAAIKYG *e fg**a**bc**d**efg**a**bc**d**efg**a**bc**d**efg*	NH_2
6b	Ac	**PEG**-QEIAAIKKEIAAIKKEIAAIKYG *e fg**a**bc**d**efg**a**bc**d**efg**a**bc**d**efg*	NH_2

Sequence **1a** (four atom distance from chiral residue) was altered by changing the terminal *e*-position Gly to an Ala, producing sequence **4a** to investigate if direct attachment to a chiral residue increases the effects seen in Chapter 2.

Similarly, for **5a** the *f*-position Gln preceding the terminal Gly was also changed to a Gly, resulting in a distance from a chiral residue to the bpy of seven-atoms.

In sequence **6a** the terminal Gly was replaced with Fmoc-amino-3,6 dioxaoctanoic acid (labelled PEG), which was subsequently deprotected and coupled to the bpy moiety by an amide coupling reaction using DIC/Oxyma reagents (See Chapter 6). This PEG spacer

introduces 10 atoms in between the bpy and the last chiral residue and is the furthest distance explored in this study.

A structural representation of the distance (in no. of atoms) between the bpy unit and its nearest chiral centre has been included in **Figure 3.2**.

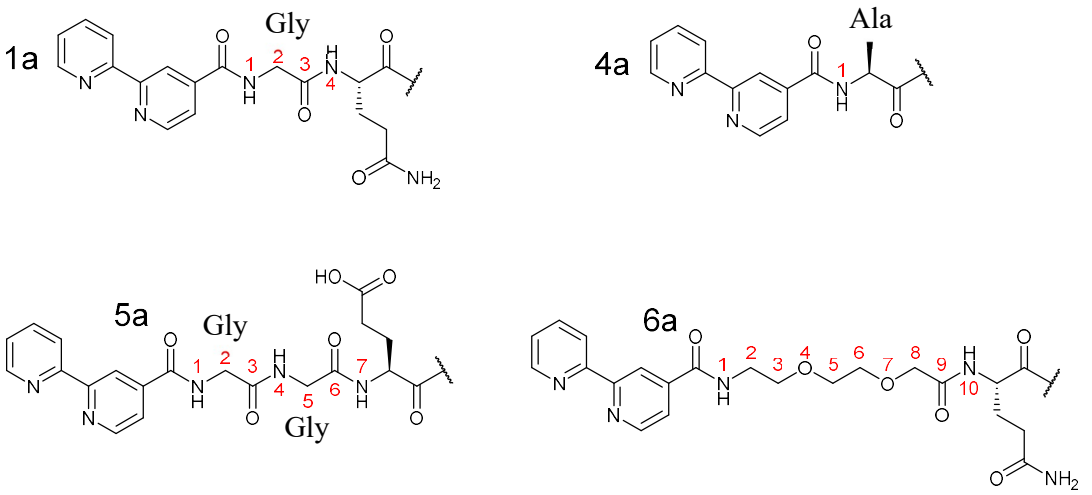

Figure 3.2 – Structures of the chiral and achiral spacers used in sequences **1a**, **4a**, **5a** and **6a**, showing the distance of the bpy units from a chiral centre in number of atoms

Reference CD and UV absorbance studies of the control **b** sequences found that as with **1a** and **1b**, in the absence of bpy at the N-terminus, the sequences **4b**, **5b** and **6b** fail to produce a signal characteristic of an α-helix, instead producing the line shape of a random coil. Furthermore, titration of these controls against both Zn^{2+} and Cu^{2+} show no change in the CD trace in response to the addition of metal (Appendix B).

Alongside this set of peptides an additional series of 4-heptad repeat sequences were also synthesised (**Table 3.2**). This series was hypothesised to form more stable CCs due to more interactions between the helices making them more thermodynamically stable, therefore, alteration of the residues at the N-terminus should not influence the helicity to the same extent as the shorter, 3-heptad, counterparts. The increased stability should allow us to distinguish whether any differences in the resulting complexes arise from the loss in helicity, in the case of the shorter CCs, or if it occurs as a result of the distance of the chelator from a chiral centre.

The sequences of these 4-heptad CCs are included in **Table 3.2** below. Design of the sequences simply involved repetition of the middle heptad one more time to generate the 4-heptad sequences used.

Table 3.2 - Sequences of **7a**, **7b**, **8a**, **8b**, **9a**, **9b**, **10a** and **10b**

Peptide No.	Capping Moiety	Sequence and Register	C-Terminus
7a	**bpy**	**A**QEIAAIKKEIAAIKKEIAAIKKEIAAIKYG *efg**a**bc**d**efg**a**bc**d**efg**a**bc**d**efg**a**bc**d**efg*	NH_2
7b	Ac	**A**QEIAAIKKEIAAIKKEIAAIKKEIAAIKYG *efg**a**bc**d**efg**a**bc**d**efg**a**bc**d**efg**a**bc**d**efg*	NH_2
8a	**bpy**	**G**QEIAAIKKEIAAIKKEIAAIKKEIAAIKYG *efg**a**bc**d**efg**a**bc**d**efg**a**bc**d**efg**a**bc**d**efg*	NH_2
8b	Ac	**G**QEIAAIKKEIAAIKKEIAAIKKEIAAIKYG *efg**a**bc**d**efg**a**bc**d**efg**a**bc**d**efg**a**bc**d**efg*	NH_2
9a	**bpy**	**GG**EIAAIKKEIAAIKKEIAAIKKEIAAIKYG *efg**a**bc**d**efg**a**bc**d**efg**a**bc**d**efg**a**bc**d**efg*	NH_2
9b	Ac	**GG**EIAAIKKEIAAIKKEIAAIKKEIAAIKYG *efg**a**bc**d**efg**a**bc**d**efg**a**bc**d**efg**a**bc**d**efg*	NH_2
10a	**bpy**	**PEG**–QEIAAIKKEIAAIKKEIAAIKKEIAAIKYG *e fg**a**bc**d**efg**a**bc**d**efg**a**bc**d**efg**a**bc**d**efg*	NH_2
10b	Ac	**PEG**–QEIAAIKKEIAAIKKEIAAIKKEIAAIKYG *e fg**a**bc**d**efg**a**bc**d**efg**a**bc**d**efg**a**bc**d**efg*	NH_2

Comparison of the CD data from the **7a**, **8a**, **9a** and **10a** to their ***b*** controls showed that even in the absence of the bpy unit at the N-terminus there was still a large degree of folding within these sequences, these spectra can be found in Appendix B.

3.3 The Effect of Increasing Distance Between Chelate and a Chiral Centre in 3-Heptad Coiled Coils on the Formation of Chiral Supramolecular Peptide Assemblies

To investigate the limits of the chiral information transfer from the trimeric coiled coil to the N-terminal octahedral complex, peptides **1a**, **4a**, **5a** and **6a** were titrated against both Zn^{2+} and Cu^{2+} and analysed by CD and UV absorbance spectroscopy. Cu^{2+} allows the coupled relationship between the metal complex and the helicity of the CC as the concentration of Cu^{2+} increases in solutions to be observed and Zn^{2+} forms more stable complexes up to 1.0 eq of metal ion.

3.3.1 Alanine Spacer

Comparison of the helicity of **1a**, **1b**, **4a** and **4b** has been made in **Figure 3.3**. From this it can be observed that for **1b** and **4b** (without the stabilising effects of the bpy), replacement of the final Gly in the sequence with an Ala results in a marginal increase in the helicity of the CC. This is evidenced by a change in the magnitude of the **4b** signal at 222 nm approximately -1500 deg·cm^2·dmol^{-1}·residue^{-1}. The presence of bpy at the N-terminus of these sequences, **1a** and **4a**, results in increased helicity in both instances. In **1a** this is observed as a change in magnitude at 222 nm of approximately -4500 deg·cm^2·dmol^{-1}·residue^{-1} and for **4a** this change in magnitude at 222 nm is approximately -5500 deg·cm^2·dmol^{-1}·residue^{-1}.

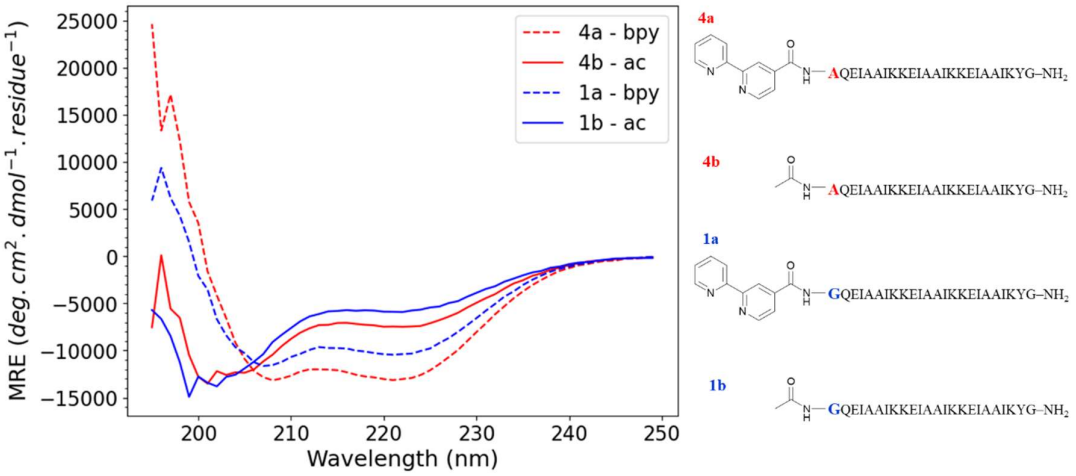

Figure 3.3 - Comparison of the helical region of the CD traces of **4a, 4b, 1a** and **1b** (all 10 μM) in 20 mM aqueous MOPS buffer, pH 7. Structures (in sequence format) provided to the right of the figure to show that the only difference is the alteration of the terminal residue from Gly in **1a** and **1b** to Ala in **4a** and **4b**.

Initial comparison of the CD traces of the Cu^{2+} titrations of **4a** and **1a** shows that replacement of the terminal Gly (**1a**) with an L-Ala residue (**4a**) results in a stronger negative Cotton-effect centred around 310 nm, indicating a stronger preference from this sequence for the Δ-isomer of the terminal complex (**Figure 3.4**). This signal from **1a** exhibits its largest magnitude at 0.3 eq of Cu^{2+} with a value of approximately -750 deg·cm^2·dmol^{-1}·residue^{-1}. In comparison, **4a** exhibits a signal at 0.3 eq of Cu^{2+} of approximately -1300 deg·cm^2·dmol^{-1}·residue^{-1}. The increase in concentration of Cu^{2+} ions above 0.3 eq led to loss of the Δ-bpy signal as the bpy sites become saturated with Cu^{2+} ions and move away from the octahedral geometry. In contrast to **1a** however, **4a** exhibits a negative Cotton effect which does not reduce completely back to the starting point upon reaching 1.0 eq of Cu^{2+}, instead this signal

appears to plateau at -500 deg·cm^2·dmol^{-1}·residue^{-1}. This behaviour is again an indication of the stronger preference of **4a** for the Δ-bpy complex. With respect to the change in helicity of **4a** in response to increasing concentrations of Cu^{2+} both **1a** and **4a** were found to behave similarly, with a tendency to lose helicity in response to quantities of Cu^{2+} above 0.3 eq. The increased helicity in **4a** compared to **1a**, as shown in **Figure 3.3** could explain the increased chiral amplification shown by **4a**.

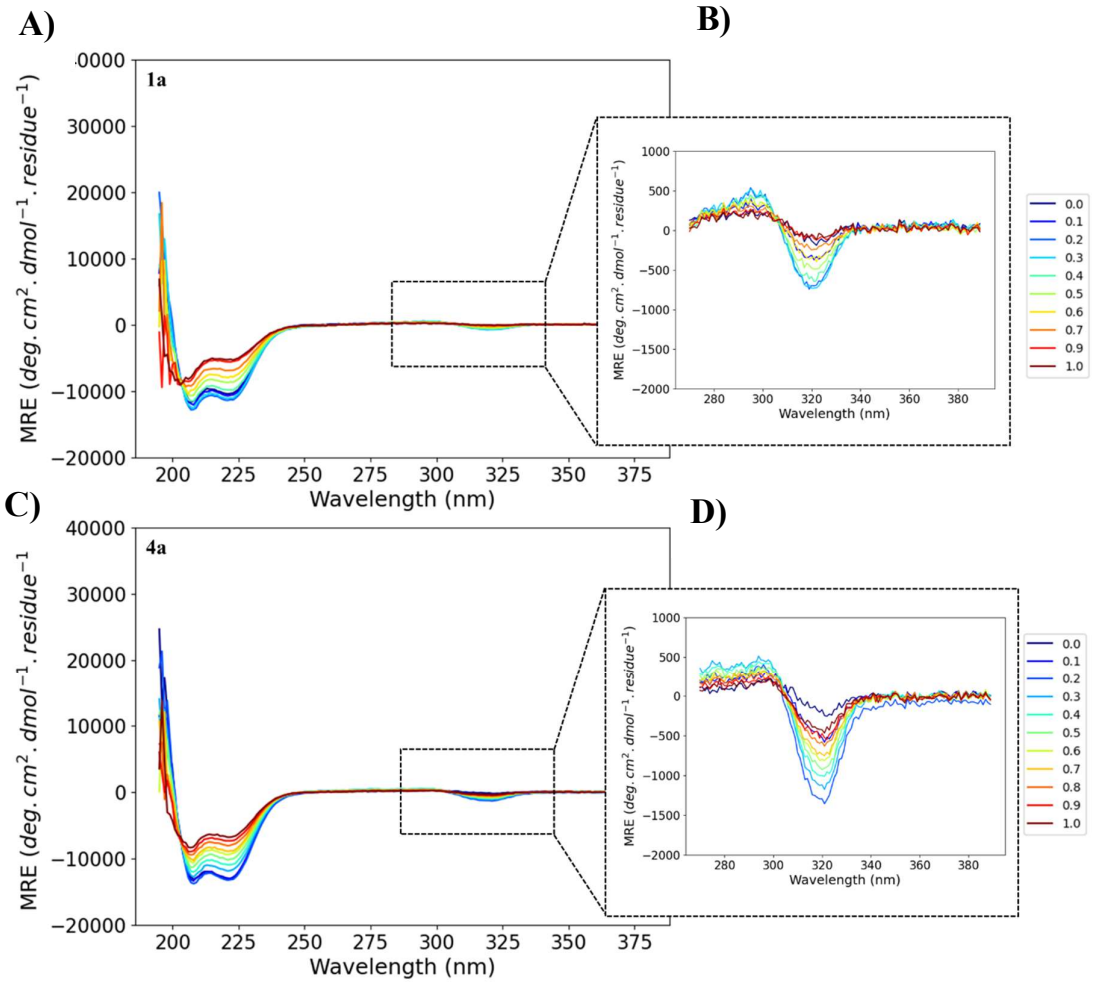

Figure 3.4 - CD traces of **1a** (10 µM) and **4a** (10 µM) in response to increasing concentrations of Cu^{2+} in 20 mM aqueous MOPS buffer, pH 7. **A)** Full CD spectrum of **1a** titration with Cu^{2+} **B)** Zoomed segment of **1a** CD spectrum showing the response in the ellipticity of bpy with increasing concentration of Cu^{2+}. **C)** Full CD spectrum of **4a** titration with Cu^{2+} **B)** Zoomed segment of **4a** CD spectrum showing the response in the ellipticity of bpy with increasing concentration of Cu^{2+}.

The titrations of **1a** and **4a** against Zn^{2+} ions again behaved similarly but the effect of direct attachment to a chiral amino acid appeared reduced in comparison to the Cu^{2+} titrations (**Figure 3.5**). The helicity of **4a** remained stable throughout the titration and the Δ-bpy signal rapidly decreased towards a minimum of approximately -1400 deg·cm^2·dmol^{-1}·residue^{-1} as a response to metal binding. This increase in magnitude of the signal continues up until 0.5

eq of Zn^{2+} where it stabilises and begins to plateau with increasing equivalents. The change in MRE at 320 nm of **4a** was found to be greater in magnitude, approximately -2000 deg·cm^2·dmol^{-1}·residue^{-1} than that of **1a**, approximately -1500 deg·cm^2·dmol^{-1}·residue^{-1}. This is indicative that the change in sequence from **1a** to **4a**, in which the bpy has direct attachment to the chiral L-Ala residue, leads to a stronger effect with respect to chiral induction onto the complex. To determine whether this difference occurs as a result of increased helicity of the CC by substitution of Gly for Ala or if it is due to the closer proximity of the bpy to a chiral centre the negative controls of these sequences, **1b** and **4b**, can be analysed as was shown in **Figure 3.3**. From the CD of these Ac-capped sequences (**Figure 3.3**) it can be concluded that the substitution of the terminal Gly residue for an Ala residue leads to a small increase in the helical content of the peptide even in the absence of the bpy unit. This suggests that altering the sequence in this way increases its helical character, and in turn increases the chiral bias in the formation of the terminal complex.

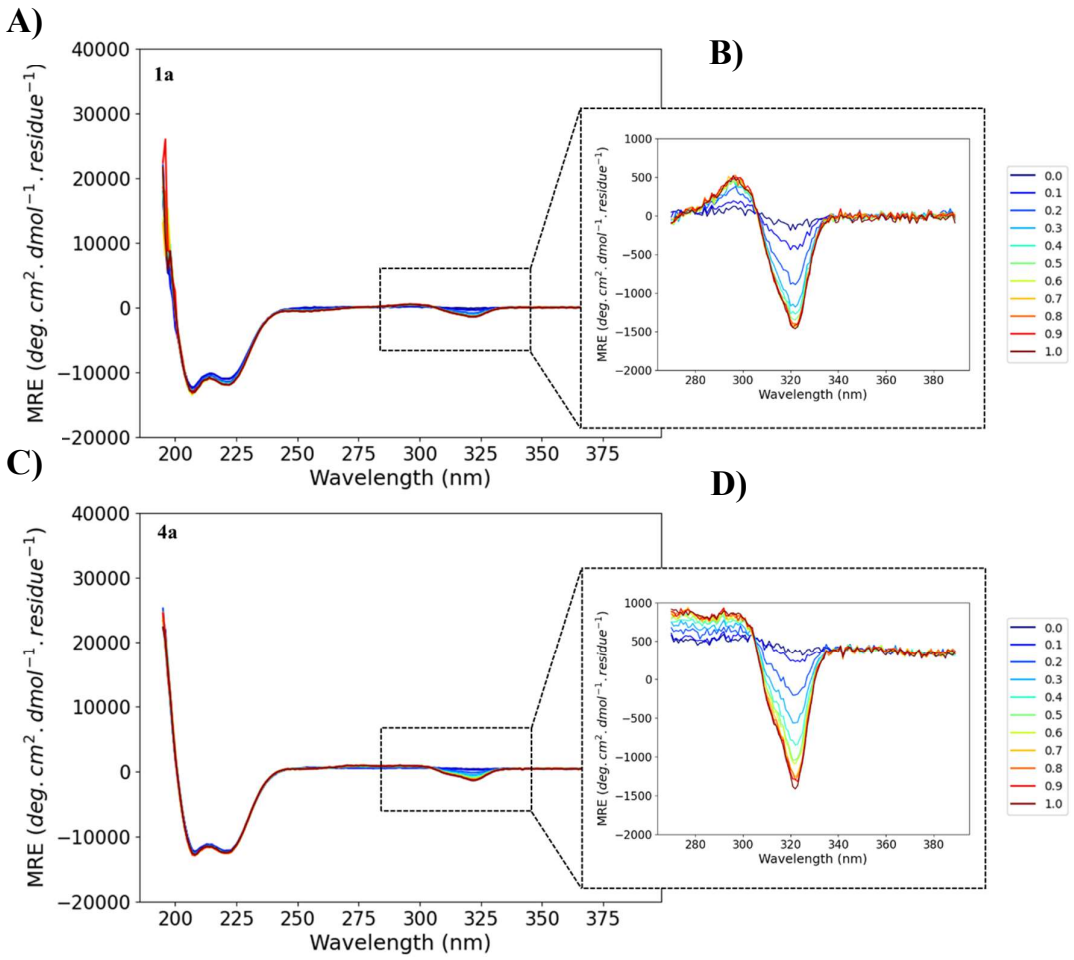

Figure 3.5 - CD traces of **1a** (10 µM) and **4a** (10 µM) in response to increasing concentrations of Zn^{2+} in 20 mM aqueous MOPS buffer, pH 7. **A)** Full CD spectrum of **1a** titration with Zn^{2+} **B)** Zoomed segment of **1a** CD spectrum showing the response in the ellipticity of bpy with increasing concentration of Zn^{2+}. **C)** Full CD spectrum of **4a** titration with Zn^{2+} **B)** Zoomed segment of **4a** CD spectrum showing the response in the ellipticity of bpy with increasing concentration of Zn^{2+}.

3.3.2 GlyGly Spacer

Alteration of the sequence to feature two Gly residues as the preceding AAs to the bpy unit should theoretically increase the rotational freedom of the terminus and therefore reduce the preference for one handedness of the complex over the other.

CD data from the titrations of **5a** appear to confirm the disruptive effect of increasing the distance of the bpy from a chiral residue on the preferential formation of the N-terminal Δ—tris-(bpy-peptide) complex. First looking at the titrations against Cu^{2+} ions (**Figure 3.6**) it can be seen that the behaviour reflects that of **1a** and **4a** with the initial stabilisation of the CC and formation of the Δ—tris-(bpy-peptide) up until 0.3 eq of Cu^{2+} after which the signal at 320 nm reduces back to the starting point and the signal from the CC tends to a more random-coil-like shape. Contrary to **1a** and **4a** however a much smaller change in MRE at 320 nm of approximately -600 $deg \cdot cm^2 \cdot dmol^{-1} \cdot residue^{-1}$ is observed possibly due to the higher degree of rotational freedom of the N-terminus of **5a**.

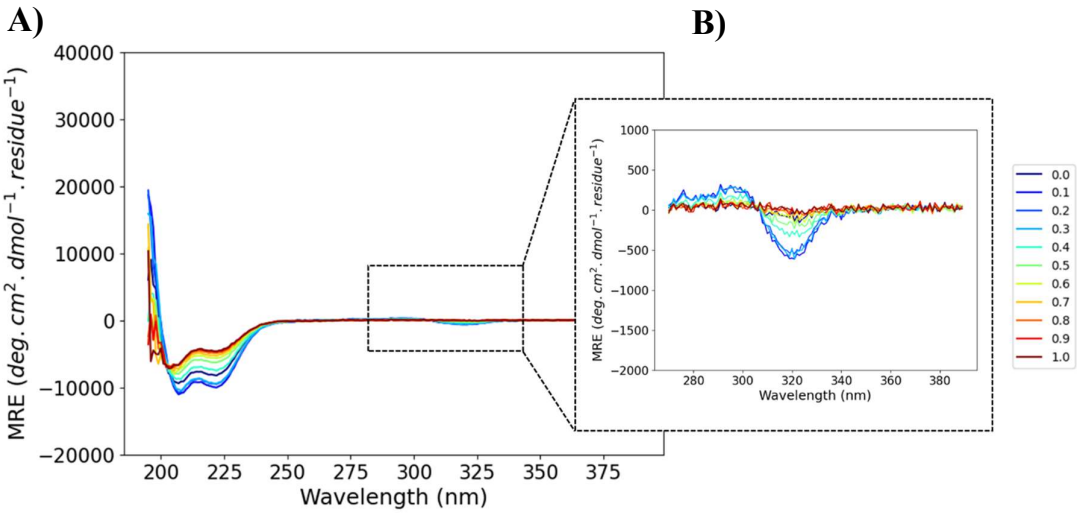

Figure 3.6 - CD trace of **5a** (10 μM) with increasing concentrations of Cu^{2+} in 20 mM aqueous MOPS buffer, pH 7. **A)** Full CD spectrum of **5a** titration with Cu^{2+} **B)** Zoomed segment of **5a** CD spectrum showing the response in the ellipticity of bpy with increasing concentration of Cu^{2+}.

Looking at the titration of **5a** against Zn^{2+} ions, the behaviour is as expected (**Figure 3.7**). With respect to the CC helicity there is no change as the concentration of Zn^{2+} ions increases in solution, as was the case with **1a** and **4a**. Similarly, the signal from the Δ—tris-(bpy-peptide) increases with the increasing concentration of Zn^{2+} ions up until 0.5 eq where the signal levels off. This signal reaches a strength of approximately -800 $deg \cdot cm^2 \cdot dmol^{-1} \cdot residue^{-1}$, which is significantly reduced when compared to the signals obtained for **1a** and **4a**.

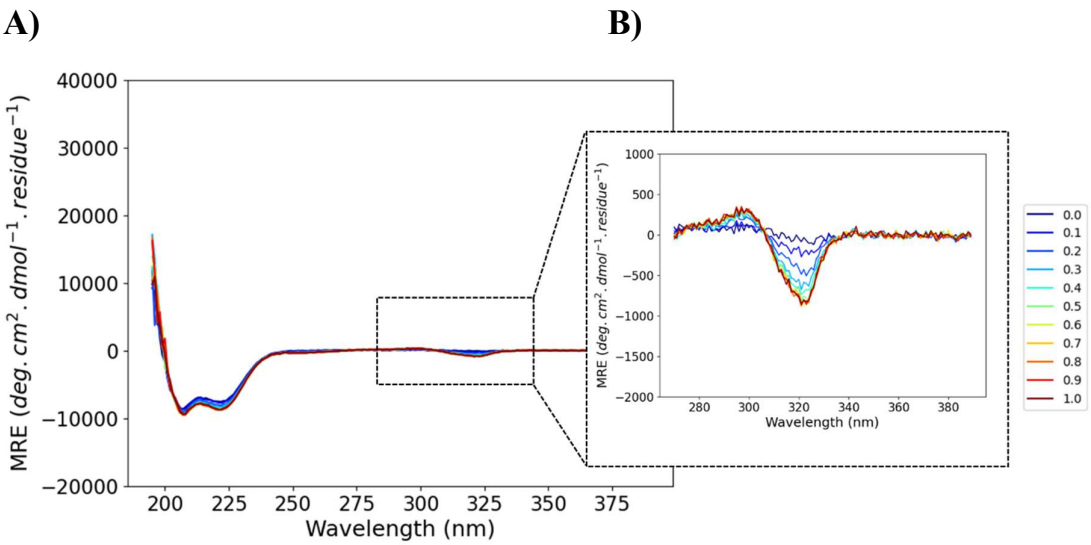

Figure 3.7 - CD Trace of **5a** (10 μM) in response to increasing concentrations of Zn^{2+} in 20 mM aqueous MOPS buffer, pH 7. **A)** Full CD spectrum of **5a** titration with Zn^{2+} **B)** Zoomed segment of **5a** CD spectrum showing the response in the ellipticity of bpy with increasing concentration of Zn^{2+}.

The reduction in the magnitude of the tris-(bpy-peptide) complex signal again can be attributed to the cooperative relationship between the complex formation and the helical content of the CC. Comparison of the CD traces of the Ac-capped control peptides demonstrates a small loss in α-helical character with the change in sequence from **1b** to **5b** (**Figure 3.8**). This is further revealed by comparison of the bpy substituted versions which also demonstrate this reduction in α-helical character as the N-terminal residue is altered.

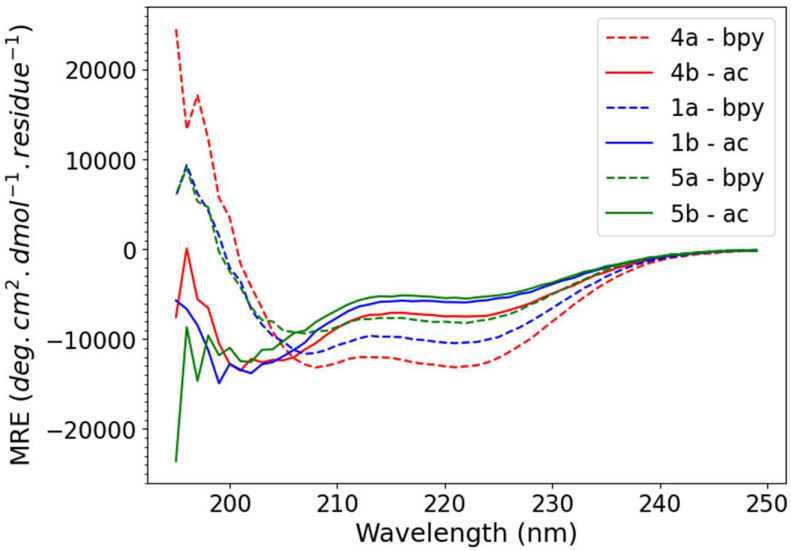

Figure 3.8 - Comparison of the CD Traces of Ac-capped **1b**, **4b** and **5b** and bpy functionalised **1a**, **4a** and **5a.** All peptide samples at a concentration of 10 μM in 20 mM aqueous MOPS buffer, pH 7.

3.3.3 PEG Spacer

Increasing the distance from a chiral residue to 10 atoms by inclusion of the PEG spacer in sequence **6a** resulted in a complete loss for the preference of the Δ-tris-(bpy-peptide) complex, with the signal at 320 nm showing no indication of chirality. This was the case for both the titration against Cu^{2+} ions and the titration against Zn^{2+} ions **(Figure 3.9).**

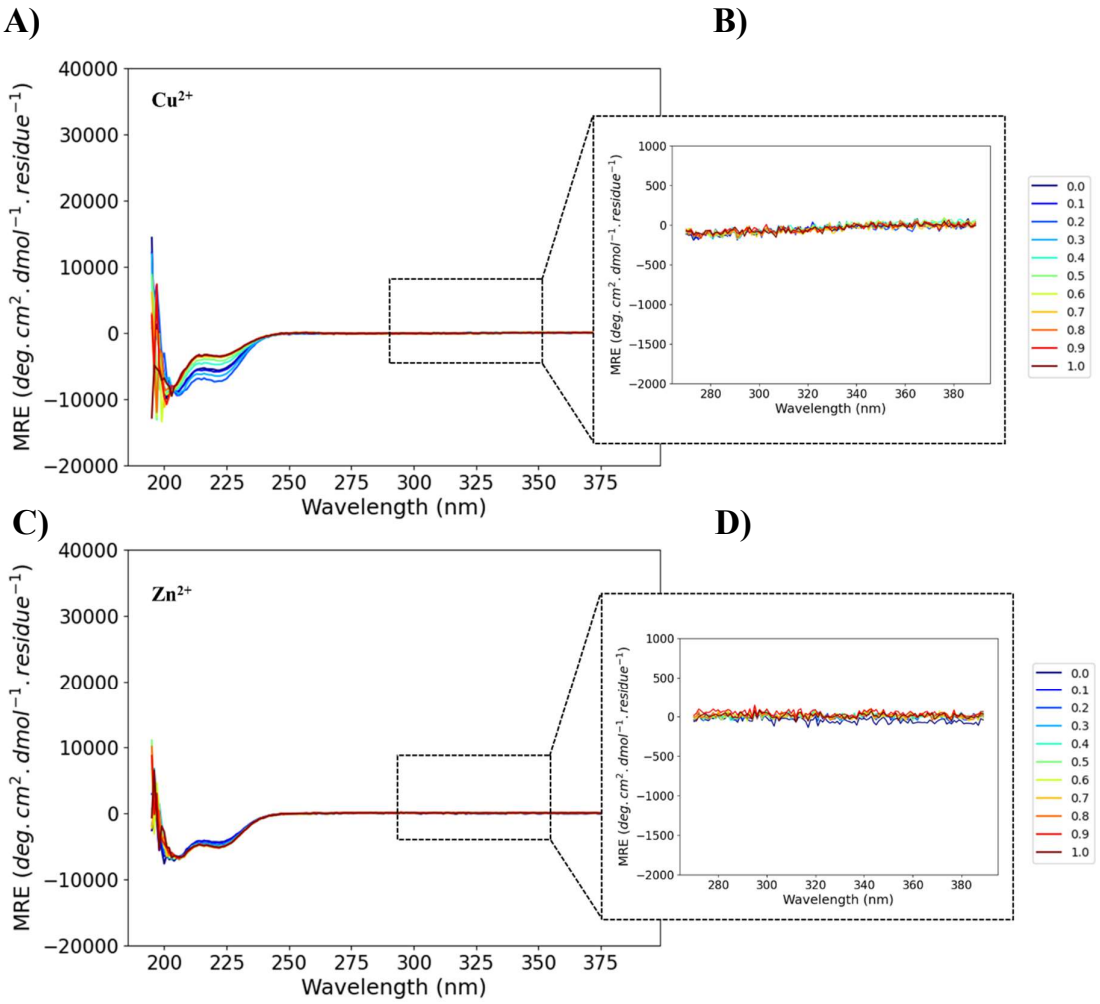

Figure 3.9 - CD Traces of **6a** (10 μM) titrations against Cu^{2+} and Zn^{2+} **A)** Full CD spectrum of the titration of **5a** with Cu^{2+} **B**) Zoomed segment of the titration of **5a** with Cu^{2+} **C)** Full CD spectrum of the titration of **5a** with Zn^{2+} **D**) Zoomed segment of the titration of **5a** with Zn^{2+}. Both performed in 20 mM aqueous MOPS buffer, pH 7.

Closer inspection of the two titrations shows that the signal corresponding to the helices behaves in the same manner as in the previous experiments, with the response to increasing concentration of Cu^{2+} being the loss of α-helical character and the response to increasing concentrations of Zn^{2+} being a slight stabilisation of the helices.

UV absorbance measurements confirmed the transition of the bpy from its unbound to its bound state with increasing concentration of both Cu^{2+} and Zn^{2+} (**Figure 3.10**).

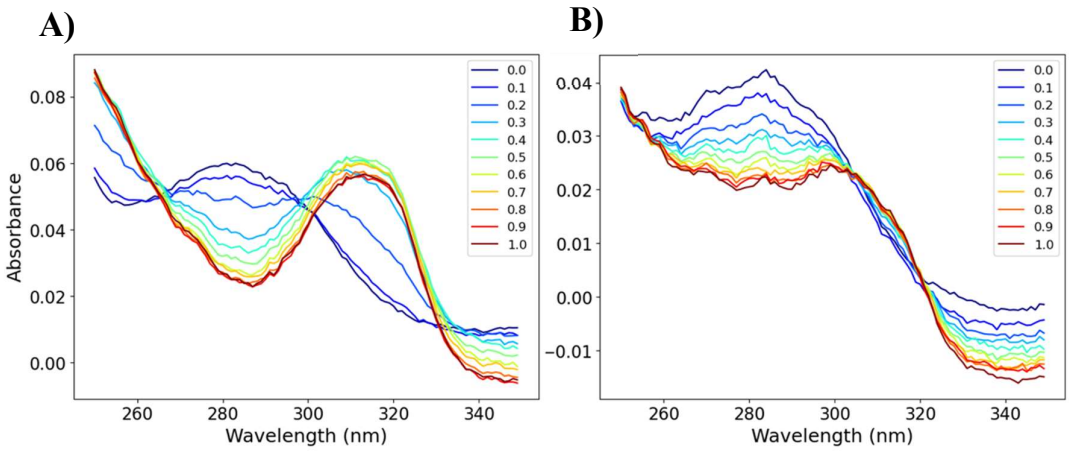

Figure 3.10 - UV- Vis Absorbance of **6a** (10 μM) titration against **A)** Cu^{2+} and **B)** Zn^{2+} in 20 mM aqueous MOPS buffer, pH 7.

The trace from the Cu^{2+} titration shows a transition from unbound to bound after 0.2 eq of metal ion, indicating the formation of the tris-(bpy-peptide) complex. This is characterised by the shift in λ_{max} from approximately 283 nm to 312 nm. The Zn^{2+} titration trace however transitions much more gradually to the absorbance indicating coordination. This suggests that the transition from **5a** to Zn^{2+} coordinated **5a** is less favourable as the system is not pre-organised like **1a** or **4a**.

3.3.4 Comparison

Comparison of the results from the CD and the UV absorbance of **1a**, **4a**, **5a** and **6a** from the previous section in this chapter demonstrates the cooperative relationship between the α-helical content of the peptides and the ability to form a chiral complex at the N-terminus. As the number of atoms from a chiral residue is increased from **4a** < **1a** < **5a** < **6a** the preference for the formation of Δ-(bpy-peptide) complex is reduced until being completely lost between 7 and 10 atoms distance from a chiral centre. In this delicately balanced system, it follows that this behaviour arises from the helical content of the peptide. As the distance between the bpy units and a chiral residue was increased the initial helicity of the peptides before addition of any TM ions was as follows, **4a** > **1a** > **5a** > **6a**. They clearly display a reduction in the α-helical content as the number of residues in the sequence that were substituted for an achiral alternative increases (**Figure 3.11**). Furthermore, comparison to the control sequences, **1b**,

4b, **5b**, and **6b** again shows that the helicity of the sequence increases upon conjugation of the bpy unit to the N-terminus.

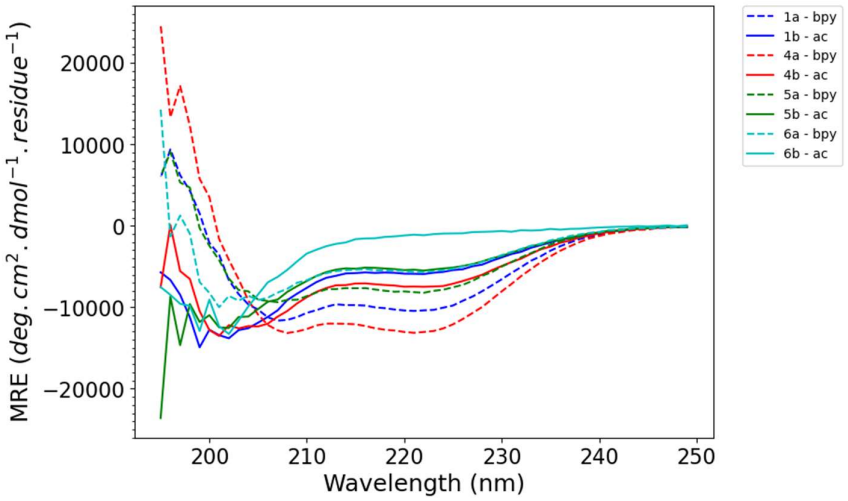

Figure 3.11 - Comparison of the CD traces of **1a**, **4a**, **5a** and **6a** in the absence of TM ions. All peptides 10 µM in 20 mM aqueous MOPS buffer, pH 7. This spectrum is zoomed in on the signal corresponding to the helicity of the peptides, to highlight the difference in helicity when the N-terminus of the peptide sequence is altered.

This behaviour is reflected in the bpy exciton couplet signal at 320 nm, which has the largest magnitude when directly attached to a chiral AA residue in **4a**, and no exciton couplet at 320 nm when the PEG spacer is used in **6a** (**Figure 3.12**).

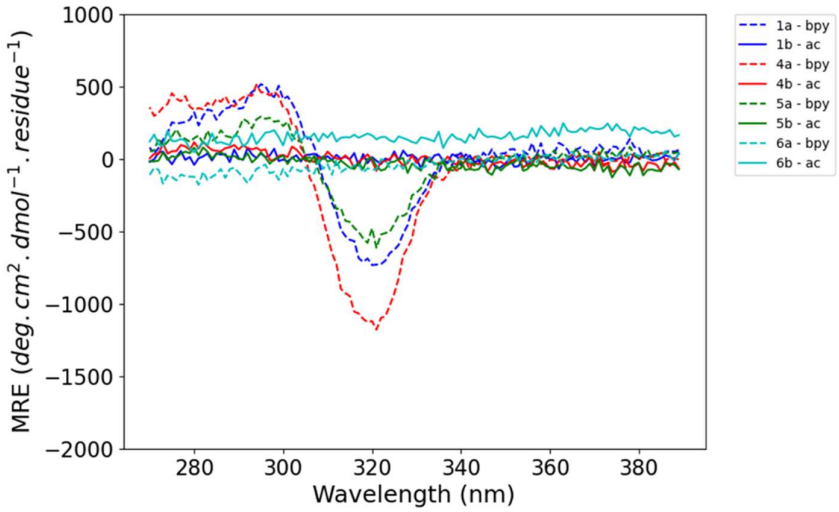

Figure 3.12 - Comparison of the CD traces of **1a**, **4a**, **5a** and **6a** in the presence of 0.3 eq of Cu^{2+} ions. All peptides 10 µM in 20 mM aqueous MOPS buffer, pH 7. This spectrum is zoomed in on the signal corresponding to the conformation of the bpy units to highlight the difference in chirality when the N-terminus of the peptide sequence is altered.

The α-helical content of **1a**, **4a**, **5a**, and **6a** throughout these experiments has been examined. It is possible that the ability of the AA spacers used in **1a** (Gly) and **5a** (GlyGly) to form the desired *α*-helical hydrogen bonding pattern increases the α-helical content of these peptides when compared to the structure of the spacer in **6a**, which does not have the ability to hydrogen bond in this same *i*-*i*+4 pattern as it continues down the chain of the spacer towards the bpy unit.

3.4 The Effect of Increasing Distance Between Chelate and a Chiral Centre in 4-Heptad Coiled Coils on the Formation of Chiral Supramolecular Peptide Assemblies

To decipher the effect of altering the distance of the bpy from a chiral centre, the relationship between the CC helicity and the complex needed to be disentangled (**Table 3.2**).

3.4.1 Alanine Spacer

Comparison of **4a** and **7a** in the absence of metal shows the increased helicity of **7a** through addition of a further heptad repeat to the sequence of **4a** (**Figure 3.13**). The increase in the helicity can be quantified by observation of the signal at 222 nm, with **4a** having a magnitude of approximately -13000 deg·cm^2·dmol^{-1}·residue^{-1} and **7a** having a magnitude of 222 nm of approximately -26000 deg·cm^2·dmol^{-1}·residue^{-1}, therefore exhibiting a 100% increase in

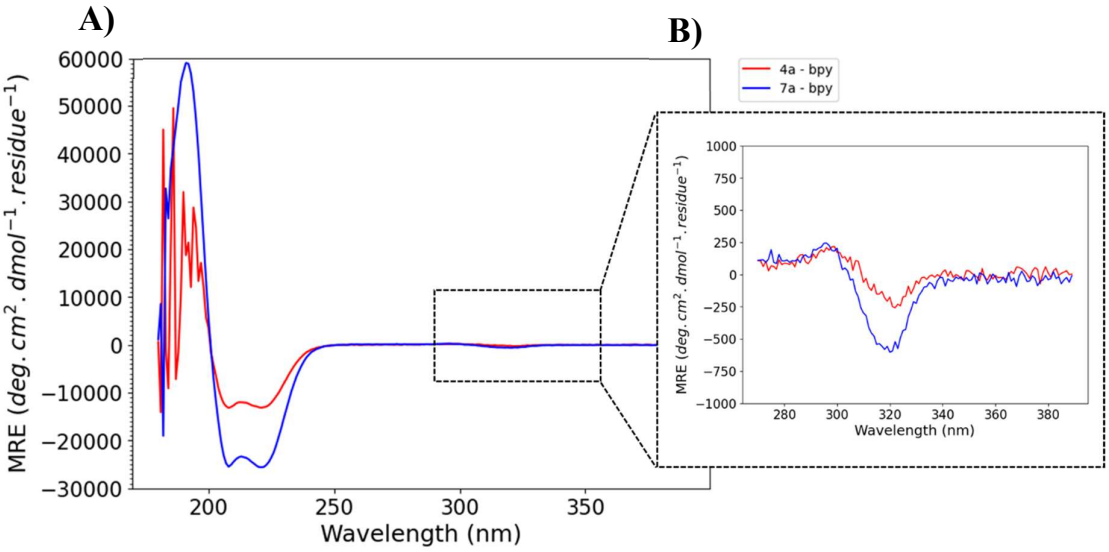

Figure 3.13 – Comparison of the traces of **4a** (three heptad repeats) and **7a** (four heptad repeats). **A)** Comparison of the helical conformations of peptides **4a** and **7a** showing the increase in helicity observed for **7a**. **B)** Zoomed segment of the spectrum showing the increased chirality of the bpy conformation in **7a** compared to **4a**. All peptides 10 μM in 20 mM aqueous MOPS buffer, pH 7

helicity comparative to its 3-heptad equivalent. Additionally, the signal at 320 nm corresponding to the bpy conformation, shows an increase in magnitude for **7a** compared to **4a** with an increase of approximately -350 deg·cm^2·dmol^{-1}·residue^{-1}.

The CD of the titrations of **7a** against both Zn^{2+} and Cu^{2+} can be seen in **Figure 3.14**. They demonstrate that addition of another heptad to the sequence results in a significant increase in the α-helical content of the peptide. Furthermore, unlike the previous titrations against Cu^{2+} ions, **7a** does not exhibit a loss in α-helical character as the concentration of Cu^{2+} increases past 0.3 eq. This behaviour is suggestive that the helicity is no longer reliant on the interactions between the bpy units as the additional heptad increases the stability of forming

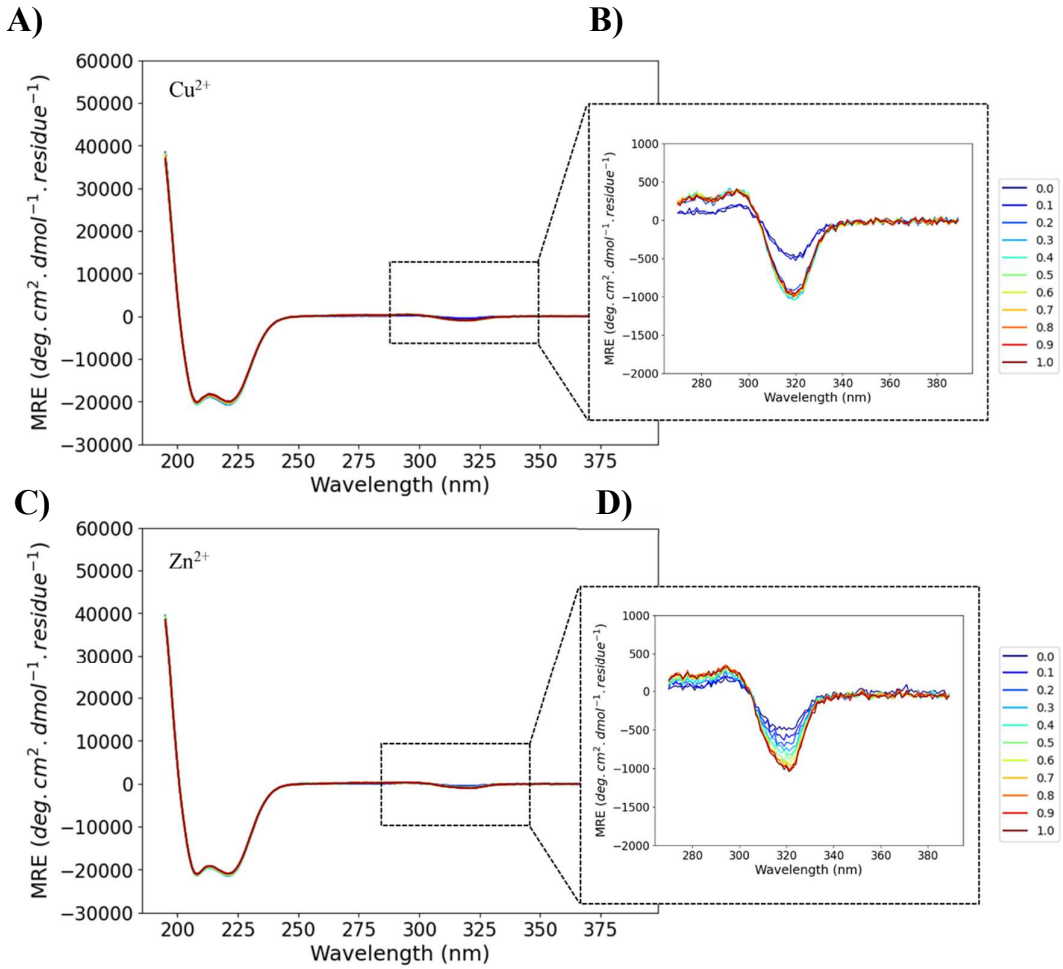

Figure 3.14 - CD of titrations of **7a** (10 μM) against Cu^{2+} and Zn^{2+} **A)** Full CD spectrum of the Cu^{2+} titration against **7a** showing how the peptide helicity changes with increasing equivalents of Cu^{2+} **B)** Zoomed segment of the full spectrum of the Cu^{2+} titration of **7a** showing the changes in the bpy conformation with increasing equivalents of Cu^{2+} **C)** Full CD spectrum of the Zn^{2+} titration against **7a** showing how the peptide helicity changes with increasing equivalents of Zn^{2+} **D)** Zoomed segment of the full spectrum of the Zn^{2+} titration of **7a** showing the changes in the bpy conformation with increasing equivalents of Zn^{2+}. All spectra were run in 20 mM aqueous MOPS buffer, pH 7.

the CC irrespective of the bpy unit. This was not observed in the 3-heptad version of this peptide, **4a**.

Additionally, with respect to the complex formation, preference is still observed for the Δ-tris-(bpy-peptide) complex, with no reduction in the signal magnitude as the Cu^{2+} concentration exceeds 0.3 eq. This behaviour suggests that the increased stability of this 4-heptad CC comparative to its 3-heptad counterpart (**4a**). Previous discussion in Chapter 2 suggested that the bpy coordination sites were becoming saturated with Cu^{2+} ions as the experiment progressed, resulting in the coincidental loss of the chirality observed for the complex, and the loss of the helicity of the peptide. Having now increased the stability of the CC and reducing the flexibility of the N-terminus by increasing the sequence by a heptad and thus increasing the NCI between the strands, the behaviour of the bpy is restricted and can no longer influence the helicity of the CC. Instead, full control of the chirality of the tris-(bpy-peptide) complex by the CC is observed.

Despite the increased stability of the self-assembled system, the magnitude of the bpy-complex signal is slightly less than that of the shorter **4a** and **1a** peptides but remains within the same range as observed in the previous experiments.

The titration against Zn^{2+} ions in **Figure 3.14 C)** and **D)** shows the same behaviour in the peptide helicity, with no change observed as the concentration of Zn^{2+} in solution increases. The complex formation, however, appears slower than was observed in the Cu^{2+} titration in **Figure 3.14 A).** The ellipticity corresponding to the complex with Zn^{2+} doesn't appear to stabilise until the end of the experiment, at approximately 0.8 eq of Zn^{2+}.

3.4.2 Gly Spacer

Peptide **8a** features a Gly residue at the position preceding the bpy, replacing the chiral Ala residue, and increasing the distance between the bpy and a chiral centre to four atoms. The CD exhibits similar behaviour as before with the helical content of the peptides remaining the same independent of the concentration of Cu^{2+} or Zn^{2+} in solution and the AAs comprising the last three AAs of the sequence.

Comparing the CD traces of **7a** and **8a** (**Figure 3.14** and **Figure 3.15**) little difference is observed between the helicity of **7a** and **8a**, showing that at this sequence length, alteration of these terminal AAs has little effect on the overall helicity of the peptide. This is unlike the behaviour observed with **4a** and **1a**, where it was observed that altering these residues resulted in differences in the α-helical content of the peptides. The stabilised nature of the

super-secondary structures of **7a** and **8a** means that the effects on the N-terminal complexes can be attributed to the distance from a chiral centre, rather than the α-helical content of the peptide. The complexes exhibit similar behaviour with the signal magnitude increasing up to 0.3 eq of $Cu^{2+}$and 0.6 eq of Zn^{2+}.

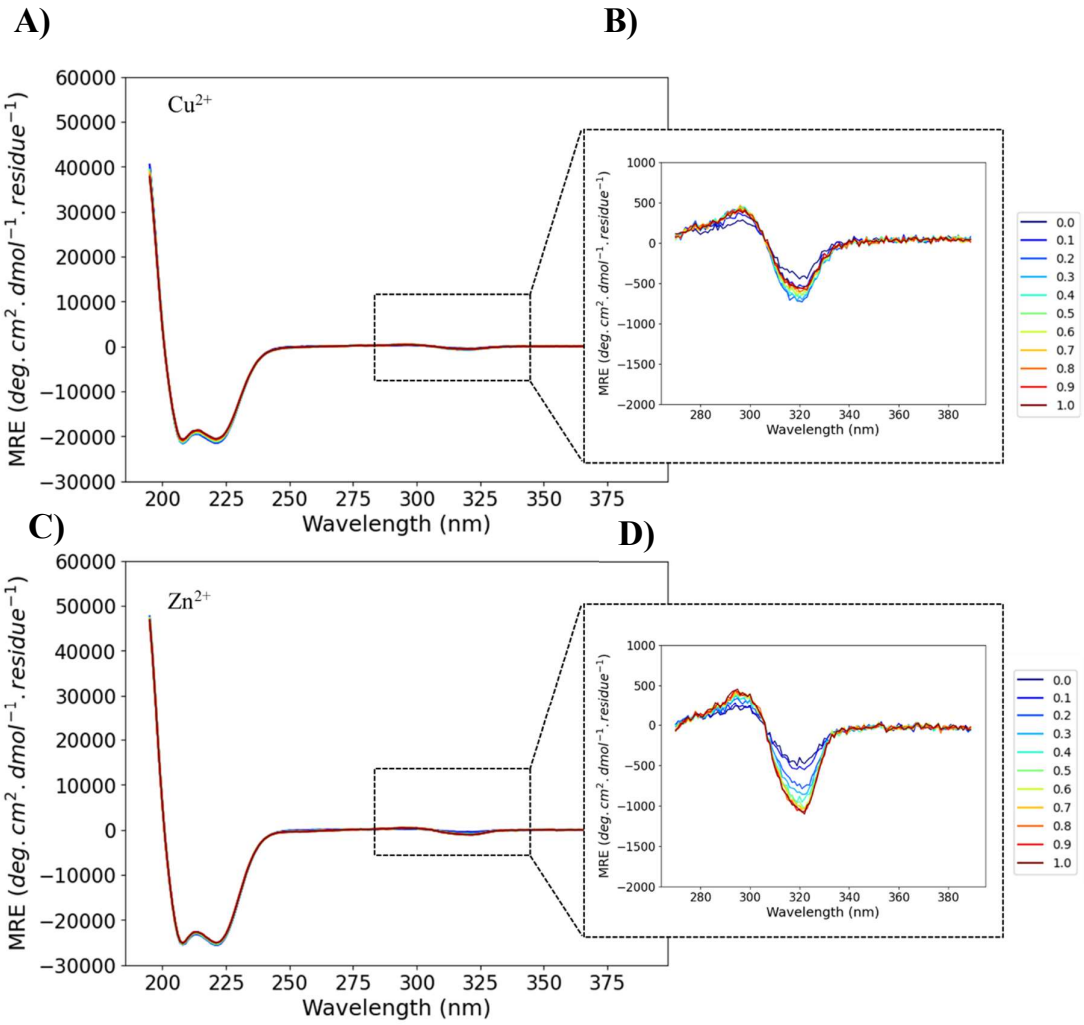

Figure 3.15 - CD of titrations of **8a** (10 μM) against Cu^{2+} and Zn^{2+} **A)** Full CD spectrum of the Cu^{2+} titration against **8a** showing how the peptide helicity changes with increasing equivalents of Cu^{2+} **B)** Zoomed segment of the full spectrum of the Cu^{2+} titration of **8a** showing the changes in the bpy conformation with increasing equivalents of Cu^{2+} **C)** Full CD spectrum of the Zn^{2+} titration against **8a** showing how the peptide helicity changes with increasing equivalents of Zn^{2+} **D)** Zoomed segment of the full spectrum of the Zn^{2+} titration of **8a** showing the changes in the bpy conformation with increasing equivalents of Zn^{2+}. All spectra were run in 20 mM aqueous MOPS buffer, pH 7.

Interestingly, the exciton couplet around 320 nm in the Cu^{2+} titration shows a reduction in magnitude after 0.3 eq, similar to what was found in the 3-heptad peptides (Section 3.3). This indicates that the Gly residue in the terminal position instead of the Ala, allows the bpy units more rotational freedom to deviate from the desired tris-(bpy-peptide) structure and instead begin to saturate the bpy binding sites.

The behaviour of the complex with respect to the Zn^{2+} concentration remains as before with the signal levelling off and remaining up to 1.0 eq of Zn^{2+}. The magnitude of this signal is comparable to that of **7a**.

3.4.3 GlyGly Spacer

Increasing the distance between the bpy units and a chiral residue to seven atoms by altering the sequence so that the two AAs preceding the bpy are both achiral, results in peptide **9a**. The CD traces of the titrations of **9a** against both Cu^{2+} and Zn^{2+} can be seen in **Figure 3.16**.

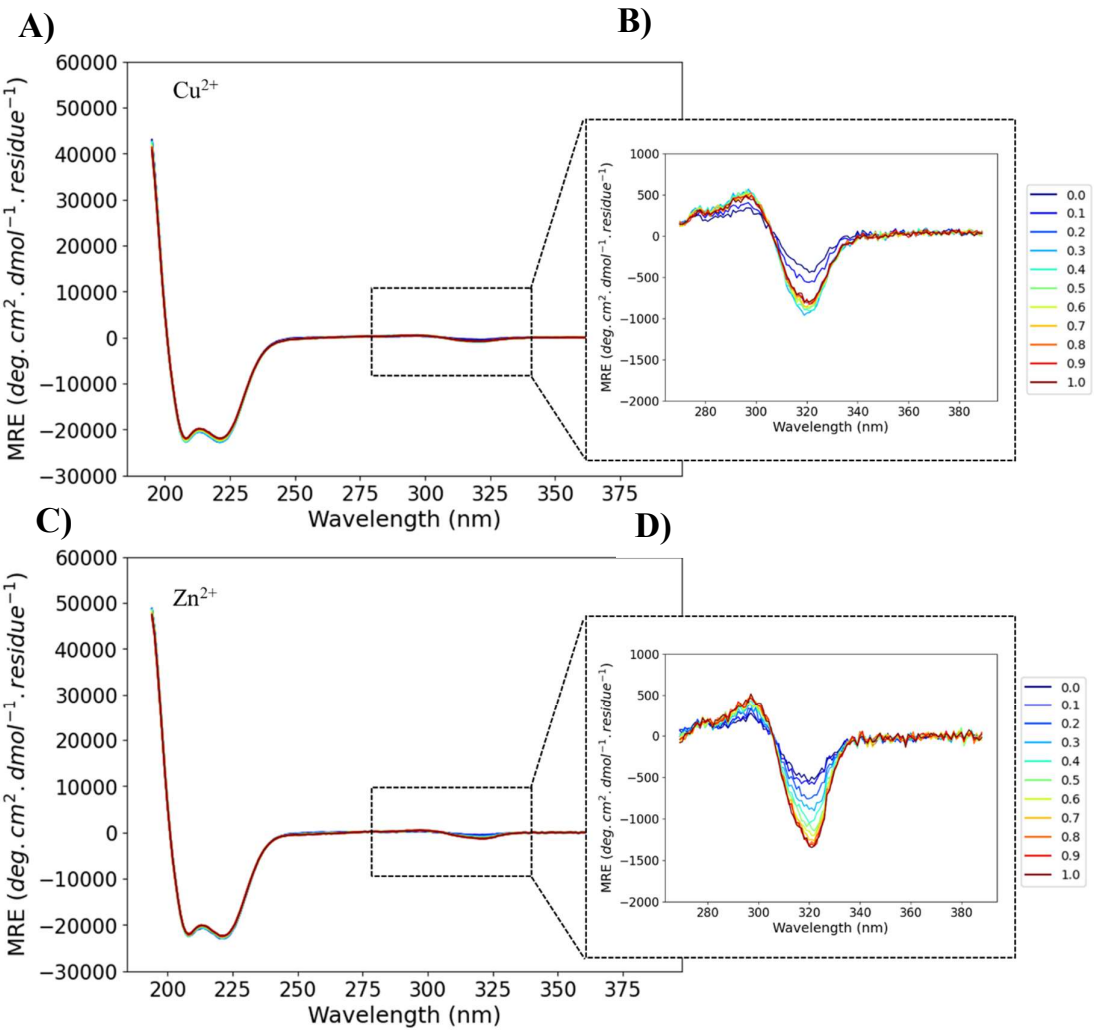

Figure 3.16 - CD of titrations of **9a** (10 μM) against Cu^{2+} and Zn^{2+} **A)** Full CD spectrum of the Cu^{2+} titration against **9a** showing how the peptide helicity changes with increasing equivalents of Cu^{2+} **B)** Zoomed segment of the full spectrum of the Cu^{2+} titration of **9a** showing the changes in the bpy conformation with increasing equivalents of Cu^{2+} **C)** Full CD spectrum of the Zn^{2+} titration against **9a** showing how the peptide helicity changes with increasing equivalents of Zn^{2+} **D)** Zoomed segment of the full spectrum of the Zn^{2+} titration of **9a** showing the changes in the bpy conformation with increasing equivalents of Zn^{2+}. All spectra were run in 20 mM aqueous MOPS buffer, pH 7.

From these it can be observed that this change in sequence again has no significant effect on the α-helical content of **9a** as was seen with the 3-heptad counterpart **5a**. As with **8a** the effect of the increasing concentration of Cu^{2+} on the exciton couplet arising from the bpy units in **9a** is that the magnitude increases up to 0.3 eq of Cu^{2+} before beginning to reduce again. With respect to the titration against Zn^{2+} the data is similar to what was observed for **8a**, however, it appears that the signal doesn't reach the maximum magnitude until 0.8 eq of Zn^{2+}. Like with **8a**, there is an increase in the rotational freedom at the N-terminus without the restrictions of AA sidechains. This could explain the reduction in signal magnitude. Conversely, there is also the ability for these Gly residues to exhibit H-bonding interactions giving the N-terminus more stability than a spacer without this capacity.

3.4.4 PEG Spacer

The final peptide in this series is **10a**, which has the same PEG spacer as **6a** as the preceding residue to the bpy units. Inclusion of this spacer results in a distance between the bpy units and a chiral residue of ten atoms. As stated previously, this spacer does not have the capacity to H-bond in the *i*-*i*+4 pattern required for the continuation of the α-helix. This therefore reduces this peptides (**10a**) capability to assemble into a more ordered structure at the N-terminus and therefore have less control over the chirality of the tris-(bpy-peptide) complexes which form. This is reflected in the CD spectra from the titrations of **10a** against Cu^{2+} and Zn^{2+} ions (**Figure 3.17**). Although the helicity of the CC is not impacted by the PEG group at the N-terminus as evidenced by the characteristic double minima at 202 nm and 222 nm, no exciton couplet signals corresponding to the formation of a chiral tris-(bpy-peptide) complex is observed around 320 nm. This suggests that no chiral information transfer from the helical sense of the peptide onto the complex when this spacer is used occurs, likely as a result of the linker flexibility. Consistent with the other peptides in this 4-heptad series, the α-helical content of peptide **10a** does not change over the course of the experiment with increasing concentrations of metal ions, and the magnitude of the signal is also consistent with **7a**, **8a** and **9a.** This indicates that the difference in the chiral information observed for **10a** is a direct result of the inclusion of the PEG spacer.

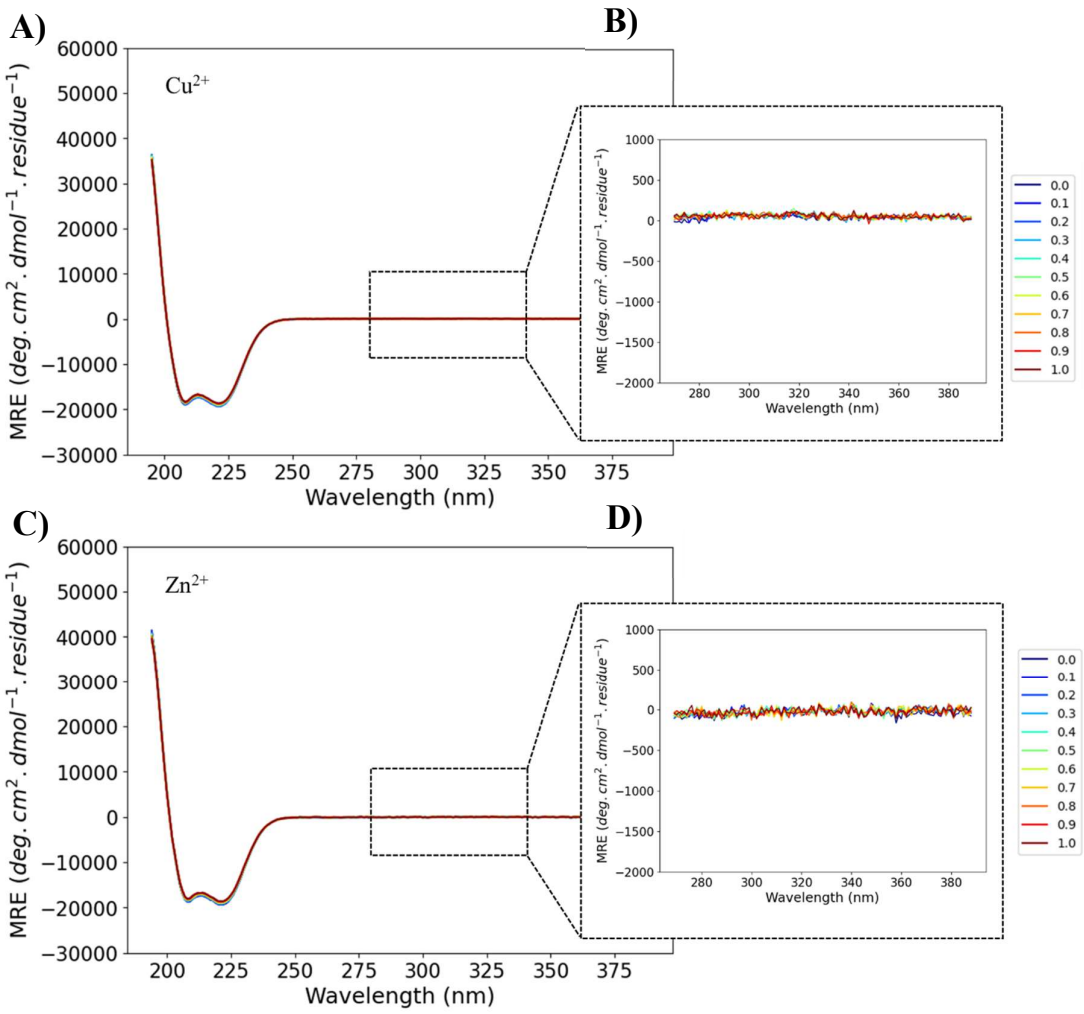

Figure 3.17 - CD of titrations of **10a** (10 μM) against Cu^{2+} and Zn^{2+} **A)** Full CD spectrum of the Cu^{2+} titration against **10a** showing how the peptide helicity changes with increasing equivalents of Cu^{2+} **B)** Zoomed segment of the full spectrum of the Cu^{2+} titration of **10a** showing the changes in the bpy conformation with increasing equivalents of Cu^{2+} **C)** Full CD spectrum of the Zn^{2+} titration against **10a** showing how the peptide helicity changes with increasing equivalents of Zn^{2+} **D)** Zoomed segment of the full spectrum of the Zn^{2+} titration of **10 a** showing the changes in the bpy conformation with increasing equivalents of Zn^{2+}. All spectra were run in 20 mM aqueous MOPS buffer, pH 7.

3.4.5 Comparison

Comparison of the CD spectra of the 4 peptides in this series, **7a**, **8a**, **9a**, and **10a** demonstrates the effect of distance of the bpy units from a chiral centre on the magnitude of the chiral information transfer onto the terminal TM complex (**Figure 3.18**). Comparison of these spectra shows that there are only subtle differences in the helicity of these sequences, with the order of degree of α-helicity following; **10a** < **7a** < **8a** < **9a**. The magnitude of the helicity ranges from -19000 deg·cm^2·dmol^{-1}·residue^{-1} for **10a** to -23000 deg·cm^2·dmol^{-}

^{1}·residue^{-1} for **9a**. With the extra stability of **9a** being attributed to substitution of both the Ala and Glu residues at the N-terminus of the sequence with GlyGly.

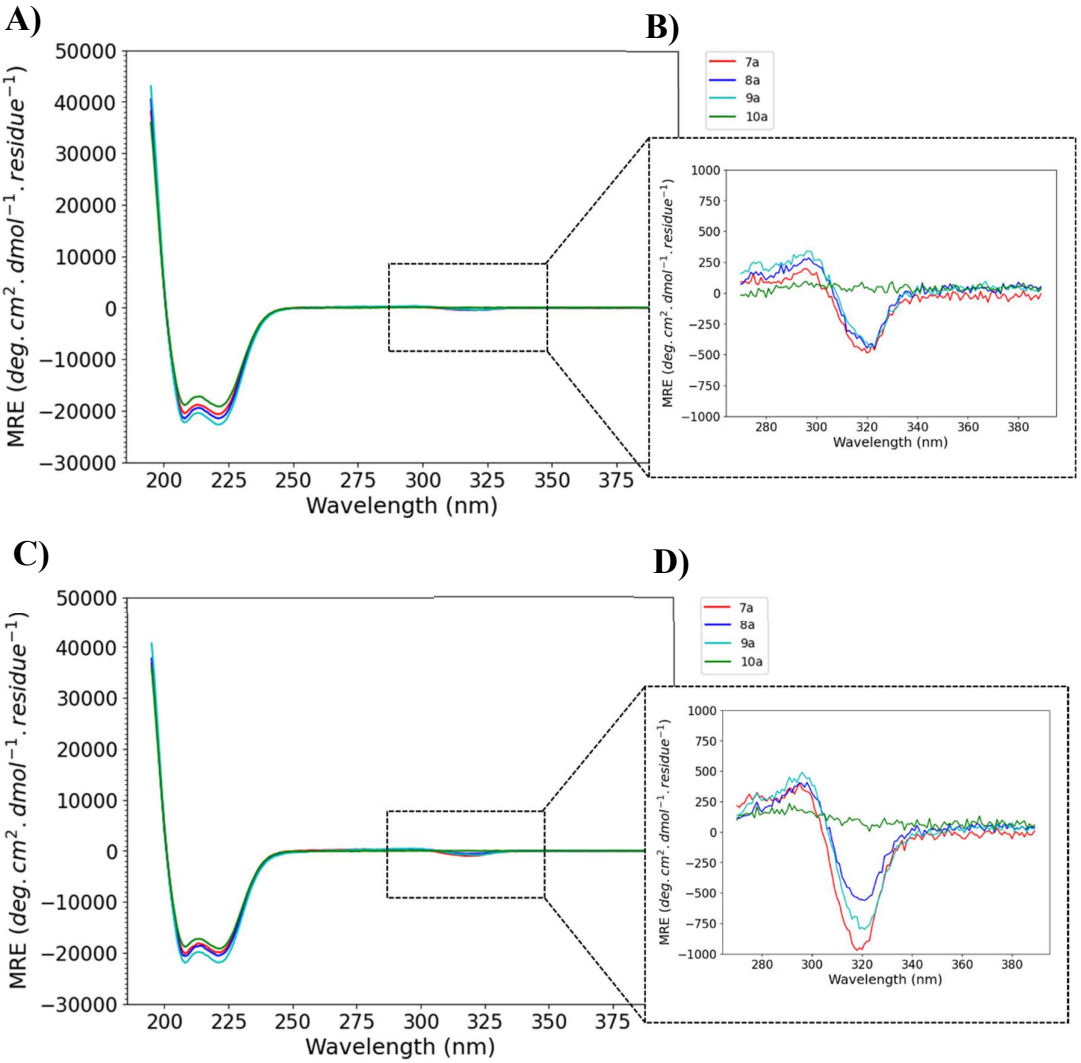

Figure 3.18 – Overlayed CD spectra of **7a**, **8a**, **9a** and **10a** (10 μM) **A)** Full CD spectrum showing the subtle difference in the peptide helicity between **7a**, **8a**, **9a** and **10a** in the absence of metal ions **B)** Zoomed segment showing the differences in the bpy conformation between **7a**, **8a**, **9a** and **10a** in the absence of metal ions **C)** Full CD spectrum showing the subtle difference in the peptide helicity between **7a**, **8a**, **9a** and **10a** in the presence of 1.0 eq of Cu^{2+} **D)** Zoomed segment showing the differences in the bpy conformation between **7a**, **8a**, **9a** and **10a** in the presence of 1.0 eq of Cu^{2+}. All were run in 20 mM aqueous MOPS buffer, pH 7.

From this data it can also be concluded that direct attachment to a chiral AA, i.e. Ala (**7a**), leads to the most significant chiral effects in the tris-(bpy-**7a**) complex once coordinated to Cu^{2+} ions, however, in the metal free environment the magnitude of the chiral bpy signal of **7a, 8a** and **9a** are comparable. Peptide **7a** was also found to exhibit increased stabilisation with respect to the formation of a chiral tris-(bpy-**7a**) complex in the presence of high concentrations of Cu^{2+}.

Increasing the distance between the bpy and a chiral centre by inclusion of an achiral AA, i.e. Gly (**8a**) or GlyGly (**9a**), exhibited comparable effects despite increasing the distance from a chiral centre from four to seven atoms. This was hypothesised to be a result of the ability for the Gly residues to still contribute to the H-bonding interactions comprising the α-helices (**Figure 3.19**). The lack of stabilising side chain interactions in these positions however result in the reduction in magnitude of the Δ-tris-(bpy-peptide) complex signal as the concentration of Cu^{2+} increases in solution and the bpy units become saturated.

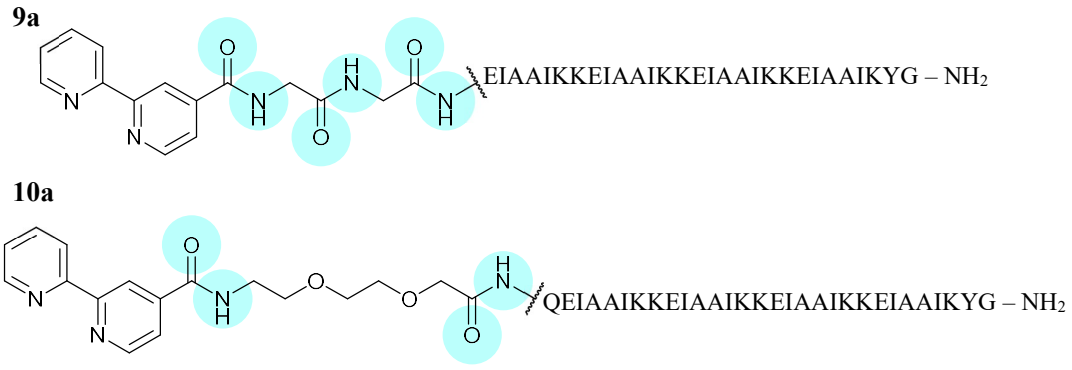

Figure 3.19 – Structure of **9a** and **10a** showing the available H-bonding sites in the **9a** and **10a** spacers, GlyGly and PEG.

Furthering this the addition of the PEG spacer in **10a** resulted in no chiral information transfer to the complex despite the indication of binding from the UV absorbance data in the instance of the Cu^{2+} titration. The higher degree of freedom afforded by the PEG spacer due to its lower capacity for H-bonding in the *i*-*i*+4 pattern required for continuation of the α-helix results in a less defined super-secondary structure at the N-terminus. The lack of rigidity from the spacer preceding the bpy units is likely what causes the loss in chiral information transfer in this case.

The results of the 3-heptad series and the 4-heptad series shows that the chiral information transfer onto the complex relies more on the α-helical content of the peptide, rather than the distance from a chiral centre. Additionally, the H-bonding ability of the spacers preceding the bpy-units is likely important in continuing the helical structure which defines the handedness of the complex.

3.5 Design and Synthesis of 3-heptad Repeat Homotrimeric Coiled Coils Featuring various chiral spacers.

3.5.1 Sequence Design

Following the results from Section 3.3, a selection of other chiral spacers (D-ala and L-Pro) were investigated to further test the constraints of this system (**Table 3.3**). Peptides **11a** (**11b**) and **12a** (**12b**) follow the same 3-heptad repeat sequence as those investigated for the achiral spacers in Section 3.3. The only alteration being the final AA in the sequence preceding the bpy-unit, substituting in a D-ala in **11a** and an L-pro in **12a**.

Table 3.3 - Sequences of **11a**, **11b**, **12a** and **12b.**

Peptide No.	Capping Moiety	Sequence and Register	C-Terminus
11a	**Bpy**	**a**QEIAAIKKEIAAIKKEIAAIKYG *efg**a**bc**d**efg**a**bc**d**efg**a**bc**d**efg*	NH_2
11b	Ac	**a**QEIAAIKKEIAAIKKEIAAIKYG *efg**a**bc**d**efg**a**bc**d**efg**a**bc**d**efg*	NH_2
12a	**Bpy**	**P**QEIAAIKKEIAAIKKEIAAIKYG *efg**a**bc**d**efg**a**bc**d**efg**a**bc**d**efg*	NH_2
12b	Ac	**P**QEIAAIKKEIAAIKKEIAAIKYG *efg**a**bc**d**efg**a**bc**d**efg**a**bc**d**efg*	NH_2

D-ala was chosen due to its opposite chirality as the final AA residue of the sequence. This means that sequence **11a** can be directly compared to **4a** to observe the effects of altering the chirality of the residue attached to the bpy.

Proline was chosen because of its rotational rigidity about the amide compared to all other proteinogenic amino acids. Typically, when included in a helical sequence a Pro residue sits at a terminal position where the loss of H-bonding to the amide is not as disruptive to the structure. It was thought that inclusion of this rigid residue at the terminal AA position in the sequence would have a significant effect on the conformation of the resulting complex and allow more insight into the spatial constraints of this system.

3.6 The Effect of Addition of Chiral Spacers on the Formation of Chiral Supramolecular Peptide Assemblies

3.6.1 D-Alanine

A comparison of **4a** (L-Ala) to **11a** (D-Ala) can be seen in **Figure 3.20**, showing the difference in the peptide helicity and chiral information transfer onto the bpy when the terminal AA is substituted with its isomer both in the absence and presence of both Cu^{2+} and Zn^{2+}.

Initially, prior to the addition of any Cu^{2+} ions, it can be seen that the helical signal from **4a** has a larger magnitude than that of **11a**. As the only difference in the sequences is the alteration of the final AA residue, the reduced helical content can be attributed to featuring a non-natural D-AA at the N-terminus. The signal from the tris-(bpy-peptide) complex appears to be of a similar magnitude for both **11a** and **4a**.

Following the titration through to 0.3 eq of Cu^{2+} the helicity of **4a** is now slightly reduced, and the lineshape is more comparable to that of **11a**. The exciton couplet arising from the tris-(bpy-peptide) complex is more telling of the effect of the D-Ala on the chiral information transfer. In peptide **11a** at 0.3 eq of Cu^{2+} the magnitude of the signal at 320 nm changes by approximately -400 $deg \cdot cm^2 \cdot dmol^{-1} \cdot residue^{-1}$. Conversely, the magnitude of this signal from peptide **4a** changes by approximately -1000 $deg \cdot cm^2 \cdot dmol^{-1} \cdot residue^{-1}$. This indicates that the preference for the Δ-handedness is stronger when the bpy is attached to a natural L-Ala and changing this AA to a D-Ala results in a lower chiral preference.

Finally, moving to 1.0 eq of Cu^{2+} ions in solution the α-helical content of the two peptides appears to be the same, having reduced due to saturation of the bpy-binding sites resulting in the fraying of the N-termini of the CC that was discussed in Chapter 2. The exciton couplet signals from the tris-(bpy-peptide) complexes of **11a** and **4a** both reduce as the concentration of Cu^{2+} increases to 1.0 eq. **11a** reduces past the starting point value and has a change of approximately +500 $deg \cdot cm^2 \cdot dmol^{-1} \cdot residue^{-1}$, whereas the signal from **4a** reduced by approximately +750 $deg \cdot cm^2 \cdot dmol^{-1} \cdot residue^{-1}$. This behaviour indicates the importance of the helicity of the peptide on the resulting chirality of the complex. Despite exhibiting a stronger chiral preference at 0.3 eq, the chiral preference of **4a** reduces significantly as the helical content is reduced.

Similar to above a comparison of the Zn^{2+} titrations of peptide **11a** against **4a** (L-Ala) can be found in **Figure 3.20 – C), D).** Initial comparison of the three different eq of Zn^{2+} shows very similar CD behaviour of **11a** and **4a**.

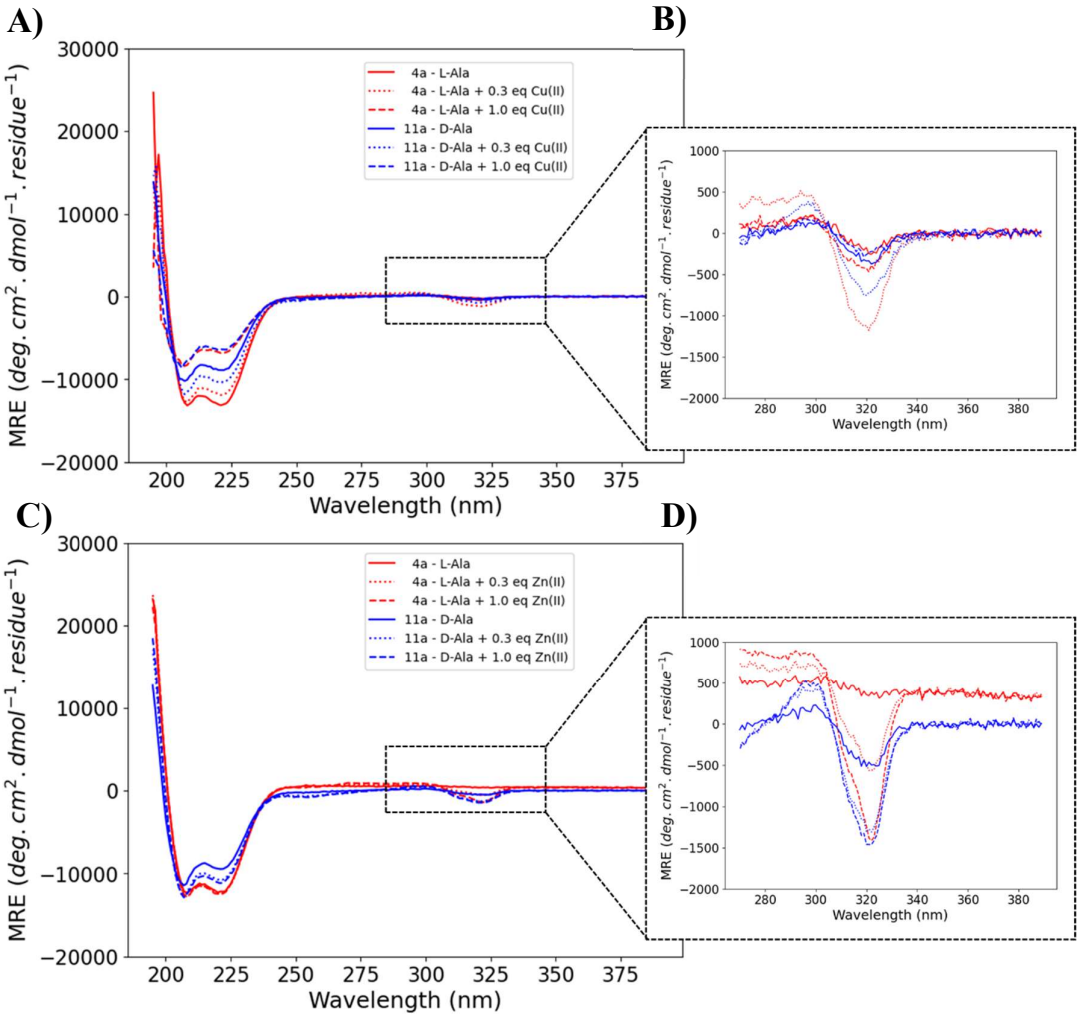

Figure 3.20 - Overlayed CD spectra of **4a** and **11a** (10 μM) **A)** Full CD spectrum showing the decrease in helicity of **11a** compared to **4a** at 0.0, 0.3 and 1.0 eq of Cu^{2+} **B)** Zoomed segment showing the differences in the bpy conformation of **11a** compared to **4a** at 0.0, 0.3 and 1.0 eq of Cu^{2+} **C)** Full CD spectrum showing the decrease in helicity of **11a** compared to **4a** at 0.0, 0.3 and 1.0 eq of Zn^{2+} **D)** Zoomed segment showing the differences in the bpy conformation of **11a** compared to **4a** at 0.0, 0.3 and 1.0 eq of Zn^{2+}. All were run in 20 mM aqueous MOPS buffer, pH 7.

At the beginning of both of these experiments the helicity of **4a** and **11a** is again comparable, with **4a** (L-Ala) exhibiting a slight degree more α-helicity. The bpy-exciton couplets at this stage are different however, with **11a** exhibiting a larger signal.

Moving to 0.3 eq of Zn^{2+} again, the helical content of the two peptides remains similar with a slight increase in helicity observed for **11a** as the metal is introduced. Additionally, there is an increase in magnitude in the negative exciton couplet in both instances, although not

immediately obvious at first glance, this increase in magnitude is similar for **11a** and **4a**, increasing in magnitude by approximately 800 deg·cm^2·dmol^{-1}·residue^{-1} comparative to the approximate 900 deg·cm^2·dmol^{-1}·residue^{-1} change that is observed for **4a**.

Comparison of the final measurements of these titrations after the addition of 1.0 eq of Zn^{2+} shows that although the final signals appear similar, the overall change in ellipticity as a response to the addition of the metal ions is quite different. **4a** (L-ala) between 0.0 eq and 1.0 eq of Zn^{2+} exhibits an overall change in ellipticity of approximately 1800 deg·cm^2·dmol^{-1}·residue^{-1} whereas the D-ala alternative **11a** only experiences a change of approximately 960 deg·cm^2·dmol^{-1}·residue^{-1}, just over 50% of the change observed for **4a**. The difference between these two peptides suggests that the L-AA at the terminus is beneficial, however, the global chirality of the α-helical peptide dominates that chiral transfer onto the terminal complex. Although the terminal AA handedness has an effect on the outcome of the chiral preference in the complex, what is observed is that the complex chirality is much more dependent on the helical content or global chirality of the assembly as a whole.

Looking at the full titration of **11a** against Cu^{2+} ions by CD spectroscopy (**Figure 3.21**) it is shown that changing the handedness of the penultimate residue in the sequence (from L-ala (**4a**) to D-ala (**11a**)) resulted in a slight loss in the initial α-helical content of the peptide and a reduced magnitude of the signal resulting from the Δ-tris-(bpy-peptide) complex as was shown previously in **Figure 3.20**. As the titration progresses, the signal corresponding to the helicity of peptide **11a** increases in magnitude alongside the signal from of the Δ-tris-(bpy-peptide) complex exciton couplet up to 0.3 eq of Cu^{2+} ions where reduction of this signal is then observed as was observed for **4a**.

With respect to the full titration of **11a** against Zn^{2+} ions there is minimal change to the helicity of the peptide as the experiment progresses other than a slight increase in the α-helical content upon addition of Zn^{2+} again up to 0.3 eq. This behaviour is stronger than what was observed for the Zn^{2+} titration of **4a.** Additionally, the strength of the exciton couplet from the bpy units is comparable to that of the L-Ala counterpart. This behaviour indicates that the chirality of the final AA in this sequence makes negligible difference to the chiral preference of the N-terminal complex, and that the conformational preference is much more dependent on the global chirality of the helices.

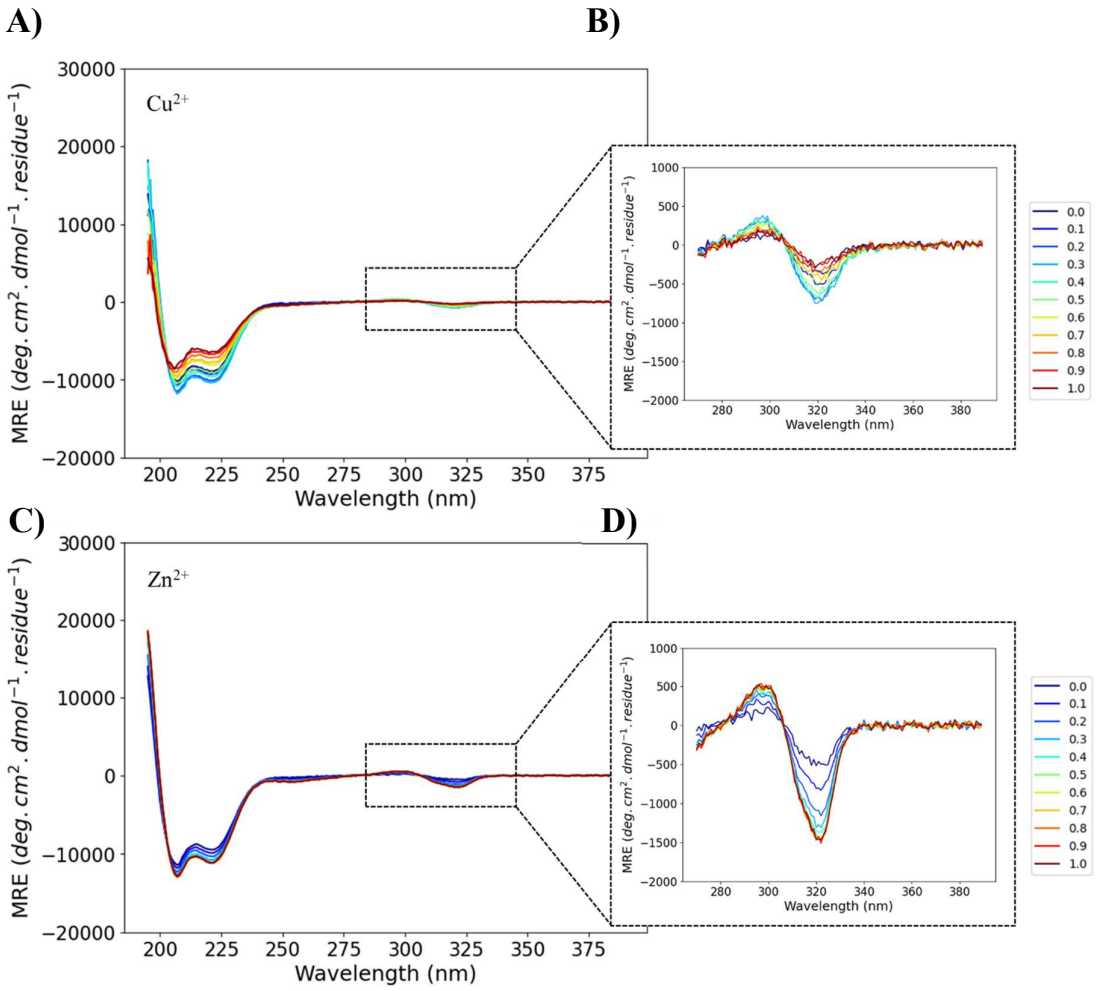

Figure 3.21 - CD of titrations of **11a** (10 μM) against Cu^{2+} and Zn^{2+} **A)** Full CD spectrum of the Cu^{2+} titration against **11a** showing how the peptide helicity changes with increasing equivalents of Cu^{2+} **B)** Zoomed segment of the full spectrum of the Cu^{2+} titration of **11a** showing the changes in the bpy conformation with increasing equivalents of Cu^{2+} **C)** Full CD spectrum of the Zn^{2+} titration against **11a** showing how the peptide helicity changes with increasing equivalents of Zn^{2+} **D)** Zoomed segment of the full spectrum of the Zn^{2+} titration of **11a** showing the changes in the bpy conformation with increasing equivalents of Zn^{2+}. All spectra were run in 20 mM aqueous MOPS buffer, pH 7.

3.6.2 L-Proline

Peptide **12a** featuring an L-Pro as the terminal AA was titrated against increasing concentrations of $Zn^{2+}$and Cu^{2+} and analysed by CD and UV absorbance spectroscopy.

For the titration of **12a** with Cu^{2+} ions (**Figure 3.22**), the beginning of the experiment shows a partially helical peptide. In comparison to peptide **11a** from the previous section, this is a considerably less helical assembly, with the signal at 222 nm for **11a** being approximately -10000 deg·cm^2·dmol^{-1}·residue^{-1}, compared to **12a** exhibiting a signal with magnitude of approximately -5000 deg·cm^2·dmol^{-1}·residue^{-1} at this wavelength. . This behaviour shows

that featuring the L-Pro residue at the N-terminus has a disruptive effect on the self-assembly of the helices into a CC formation.

As the titration proceeds, as has been observed previously with Cu^{2+} and initial increase in the α-helical content is observed up to 0.3 eq of Cu^{2+} which after this point begins to reduce and tend towards a line shape consistent with a random coil.

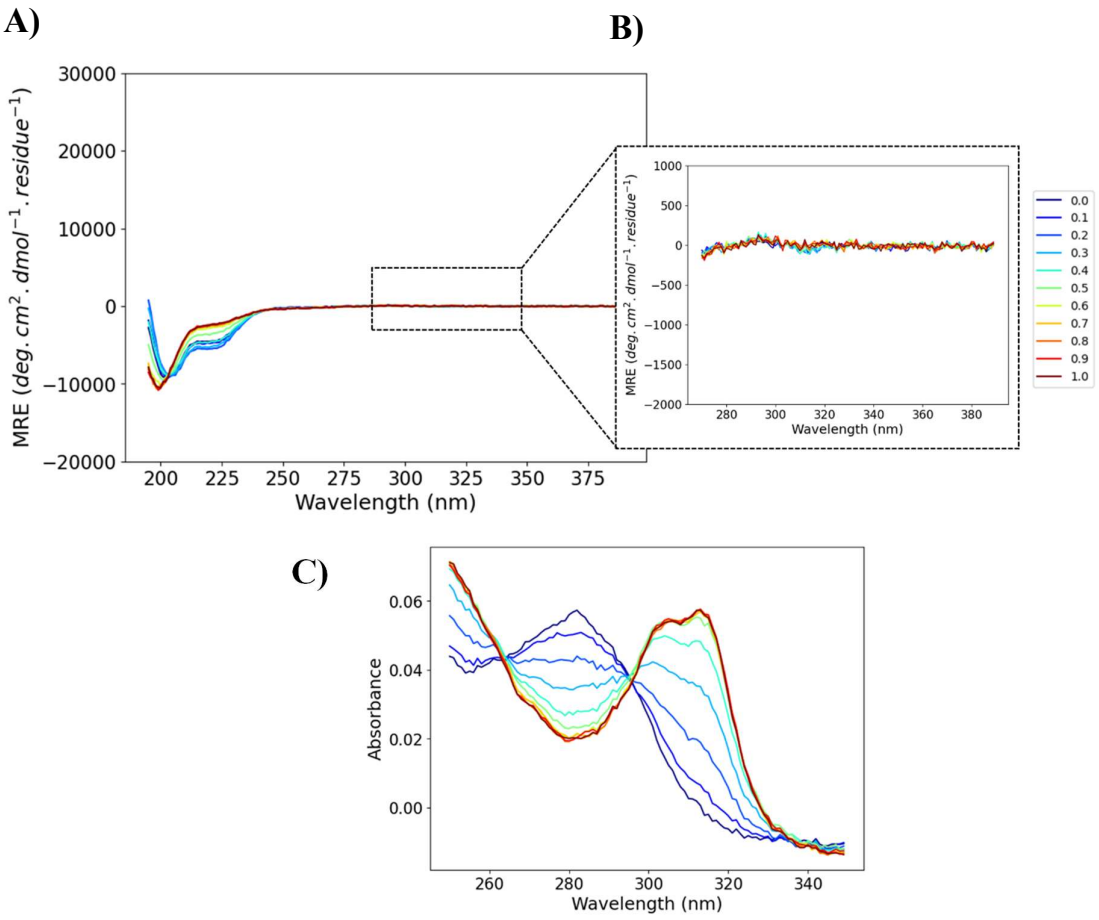

Figure 3.22 - CD and UV-Vis titrations of **12a** (10 μM) against Cu^{2+} ions in 20 mM aqueous MOPS buffer, pH 7. **A)** Full spectrum of **12a** titration with Cu^{2+} showing the change in helicity with increasing equivalents of Cu^{2+} **B)** Zoomed segment of the **12a** titration with Cu^{2+} showing the lack of chiral information transfer onto the bpy-complex **C)** UV absorbance spectra of the titration of **12a** with Cu^{2+} showing the two-state transition of unbound bpy to Cu^{2+} coordinated bpy with the change occurring at 0.3 eq of Cu^{2+} indicating a tris-(bpy-**12a**) complex.

With respect to the bpy conformation, there is a small negative exciton couplet at the expected wavelength, however little change is observed as the titration progresses. Despite this there is a strong two-state transition in the UV absorbance indicating the association of the Cu^{2+} ions to the bpy units.

Moving to the titration of **12a** against Zn^{2+} ions (**Figure 3.23**), looking at the helicity there is little change in magnitude as the experiment proceeds, however a slight stabilising effect is observed. As the Zn^{2+} associates to the bpy at increasing equivalents there no observable change in the magnitude of the negative exciton couplet from the bpy units, suggesting that this system is not set up for chiral complex formation. Again, the UV absorbance exhibits the two-state transition as the experiment proceeds, but this transition appears weak.

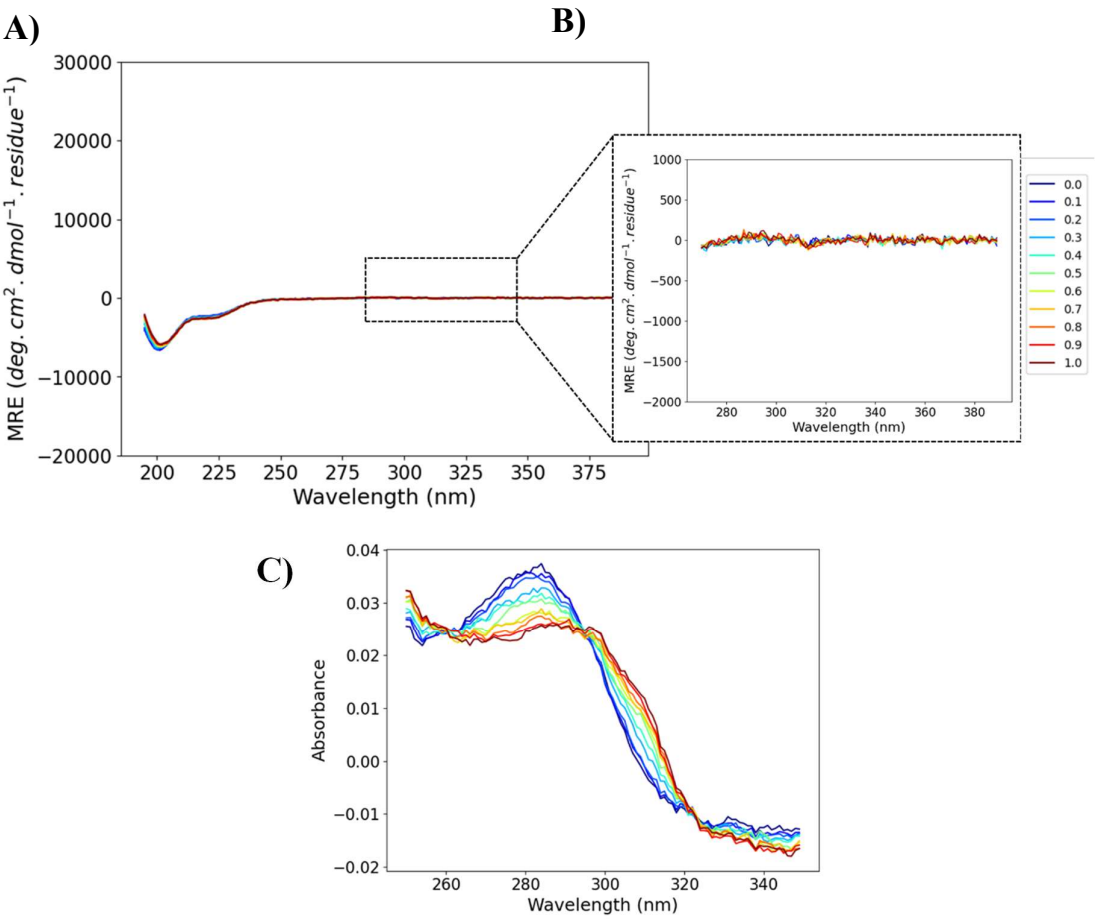

Figure 3. 23- CD and UV-Vis titrations of **12a** (10 µM) against Zn^{2+} ions in 20 mM aqueous MOPS buffer, pH 7. **A)** Full spectrum of **12a** titration with Zn^{2+} showing the change in helicity with increasing equivalents of Zn^{2+} **B)** Zoomed segment of the **12a** titration with Zn^{2+} showing the lack of chiral information transfer onto the bpy-complex **C)** UV absorbance spectra of the titration of **12a** with Zn^{2+} showing the two-state transition of unbound bpy to Zn^{2+} coordinated bpy.

To summarise, changing the terminal AA of the peptide sequence can have a significant effect on the chiral information transfer from the helical peptides onto the bpy conformation. Changing this residue to the more rotationally restricted L-Pro led to a reduction in the α-helical content of peptide **12a** and a subsequent reduction in chiral preference for the Δ-conformation of the bpy units despite evidence of binding to the Cu^{2+} and Zn^{2+} ions. Conversely, altering the handedness of the terminal AA as was investigated with **11a** showed

little change to the overall helicity and some change to chiral preference of the bpy conformation. The change from L-AA to D-AA could have a more pronounced effect however with AAs that feature larger side chains, in which steric interactions between the side chains might have more of a negative effect on the H-bonding pattern at the N-terminus The loss of this repeating helical, *i*-*i*+4 H-bonding pattern has been hypothesised earlier in this chapter with respect to the PEG spacers in **6a** and **10a** to have a pronounced effect on the chiral information transfer onto the complex. Therefore, by substituting D-Ala for example with D-Arg, which has a much larger side chain, may lead to steric clash between the D-AA and the peptide backbone, resulting in a loss of helicity at the N-terminus. This hypothesis would have to be tested in future experiments.

3.7 Design and Synthesis of Homotrimeric Coiled Coils Featuring Systematic Variation of Register Position at the N-terminus

To investigate the implications on the chirality of the terminal complex by changing the bpy unit position within the helical register, a series of seven peptides featuring the bpy at all available register positions were synthesised.

3.7.1 Sequence Design

Design of this series of peptides used the same base sequence as peptide **1a** for consistency. Consideration was taken while altering the register position to keep the AA content of the peptides the same, allowing them to form the same inter-strand contacts and therefore exhibiting minimal change in the stability of the peptide and its resulting secondary structure. Therefore, any differences in the observed structure should be a result of the bpy-positioning. The only exception is **13a** where the penultimate residue should be a Lys, however, this was switched to a Gln to avoid the amine group of the Lys sidechain contributing to the coordination sphere.

Sequences of this peptide series can be found in **Table 3.4** along with their corresponding register, highlighting the pseudo-register position of the terminal bpy. Alongside this the control sequences of these peptides (**-b**) are also included, all of which contain the same peptide sequence as their bpy counterpart but instead feature and acetyl (Ac) capping moiety at the N-terminus such that changes in the spectra can be attributed to the bpy units.

Table 3.4 - Sequences of peptides **13a/b**, **14a/b**, **15a/b**, **16a/b**, **17a/b**, **18a/b** and **19a/b** and the register of the sequences.

Peptide No.	Capping Moiety	Sequence and Register	C-Terminus
13a	**Bpy** ***e***	QEIAAIKKEIAAIKKEIAAIKYG *fg**a**bc**d**efg**a**bc**d**efg**a**bc**d**efg*	NH_2
13b	Ac *e*	QEIAAIKKEIAAIKKEIAAIKYG *fg**a**bc**d**efg**a**bc**d**efg**a**bc**d**efg*	NH_2
14a	**Bpy** ***f***	EIAAIKKEIAAIKKEIAAIKKYG *g**a**bc**d**efg**a**bc**d**efg**a**bc**d**efga*	NH_2
14b	Ac *f*	EIAAIKKEIAAIKKEIAAIKKYG *g**a**bc**d**efg**a**bc**d**efg**a**bc**d**efga*	NH_2
15a	**Bpy** ***g***	IAAIKKEIAAIKKEIAAIKKEYG ***a**bc**d**efg**a**bc**d**efg**a**bc**d**efgab*	NH_2
15b	Ac *g*	IAAIKKEIAAIKKEIAAIKKEYG ***a**bc**d**efg**a**bc**d**efg**a**bc**d**efgab*	NH_2
16a	**Bpy** ***a***	AAIKKEIAAIKKEIAAIKKEIYG *bc**d**efg**a**bc**d**efg**a**bc**d**efg**a**bc*	NH_2
16b	Ac *a*	AAIKKEIAAIKKEIAAIKKEIYG *bc**d**efg**a**bc**d**efg**a**bc**d**efg**a**bc*	NH_2
17a	**Bpy** ***b***	AIKKEIAAIKKEIAAIKKEIAYG *c**d**efg**a**bc**d**efg**a**bc**d**efg**a**bc**d***	NH_2
17b	Ac ***b***	AIKKEIAAIKKEIAAIKKEIAYG *c**d**efg**a**bc**d**efg**a**bc**d**efg**a**bc**d***	NH_2
18a	**Bpy** ***c***	IKKEIAAIKKEIAAIKKEIAAYG ***d**efg**a**bc**d**efg**a**bc**d**efg**a**bc**d**e*	NH_2
18b	Ac *c*	IKKEIAAIKKEIAAIKKEIAAYG ***d**efg**a**bc**d**efg**a**bc**d**efg**a**bc**d**e*	NH_2
19a	**Bpy** ***d***	QKEIAAIKKEIAAIKKEIAAIYG *efg**a**bc**d**efg**a**bc**d**efg**a**bc**d**ef*	NH_2
19b	Ac *d*	QKEIAAIKKEIAAIKKEIAAIYG *efg**a**bc**d**efg**a**bc**d**efg**a**bc**d**ef*	NH_2

3.7.2 Visualising the Bipyridine Direction

Mapping the bpy directionality on a CC template could indicate some of the effects that maybe observed during the CD titration experiments provided the terminal AA and the carbonyl of the bpy-chelating unit contribute to the helical H-bonding pattern (**Figure 3.24**).

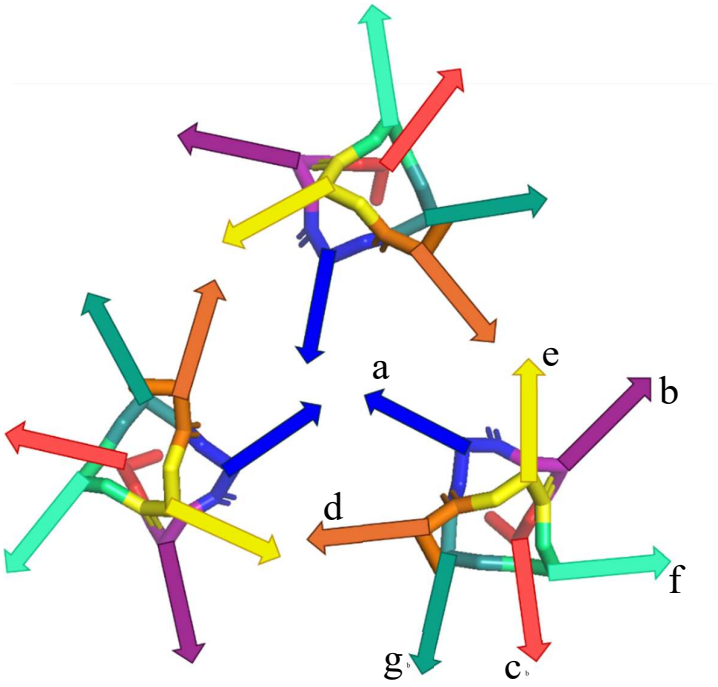

Figure 3.24 - Top down view of a trimeric coiled coil with vectors representing the directionality of the bpy units if attached at this register position.

In this figure, the arrows, or vectors, represent the general directionality that the bpy will follow when at that register position. The vector encapsulates the directionality of the amide bond connection to the helix assuming all H-bonding interactions in the chain are formed correctly. A schematic of the vector content has been included for ease of understanding in **Figure 3.25**.

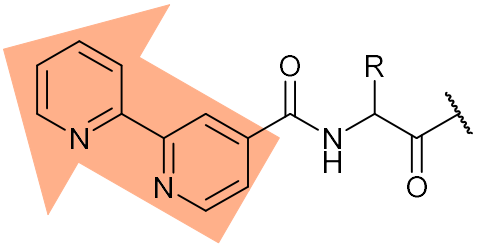

Figure 3. 25- Structure defining the content of the vector representations for CC mapping.

From these representations, it can be seen that sequences with the bpy at an *a*, *d* or *e* will have the bpy units in proximity to each other and set up for interstrand binding. Sequences where the bpy falls at a *b*, *c*, *f* or *g* position would not be prearranged for binding in the tris-(bpy-peptide) arrangement between the 3-strands and therefore negative cooperativity could be observed for these peptides.

In addition to this, the bpy vectors in the CC mapping, **Figure 3.24**, also suggest that complexes formed with the bpy in the *d*-position (orange) are preorganised to favour the opposite conformation compared to when the bpy is in the *e*-position (yellow). The directionality of these vectors suggests that if the H-bonding interactions at the terminal residues remain then a *d*-position bpy will preferably form a Λ-conformation and those in the *e*-position will preferably form in the Δ-conformation. This however does not fit with what has been observed for the tris-(bpy-peptide) complexes formed in Chapters 2 and 3. The peptides used so far in these chapters feature the bpy-moiety at the *d*-position of the heptad, which as suggested, would form a Λ-conformation complex, however, the opposite has been observed with preferential formation of the Δ-conformation in all cases. This therefore suggests that the terminal residues of the sequence do not follow the helicity, potentially a result of the presence of the bpy unit.

Those in the *a*-position (blue) point inwards, this arrangement suggests that the ligands will be in close proximity to one and other and therefore may experience detrimental steric effects.

3.8 The Effect of Changing Chelator Register Position on the Formation of Chiral Supramolecular Peptide Assemblies

Titrations of peptides **13a** – **19a** against both Cu^{2+} and Zn^{2+} ions were performed and the results monitored by CD and UV absorbance spectroscopy.

3.8.1 Bpy in positions *b, c, f* or *g*

Featuring the bpy in one of the solvent facing positions of the CC, as the mapping suggested, resulted in no formation of the chiral bpy complexes at the N-terminus in any of the tested conditions (Cu^{2+} or Zn^{2+}) with any of the sequences; **14a, 15a, 17a** or **18a**. CD spectroscopy and UV absorbance of the titrations of these four (**14a, 15a, 17a** and **18a**) peptides against Cu^{2+} can be found in **Figures 3.26** – **3.30**.

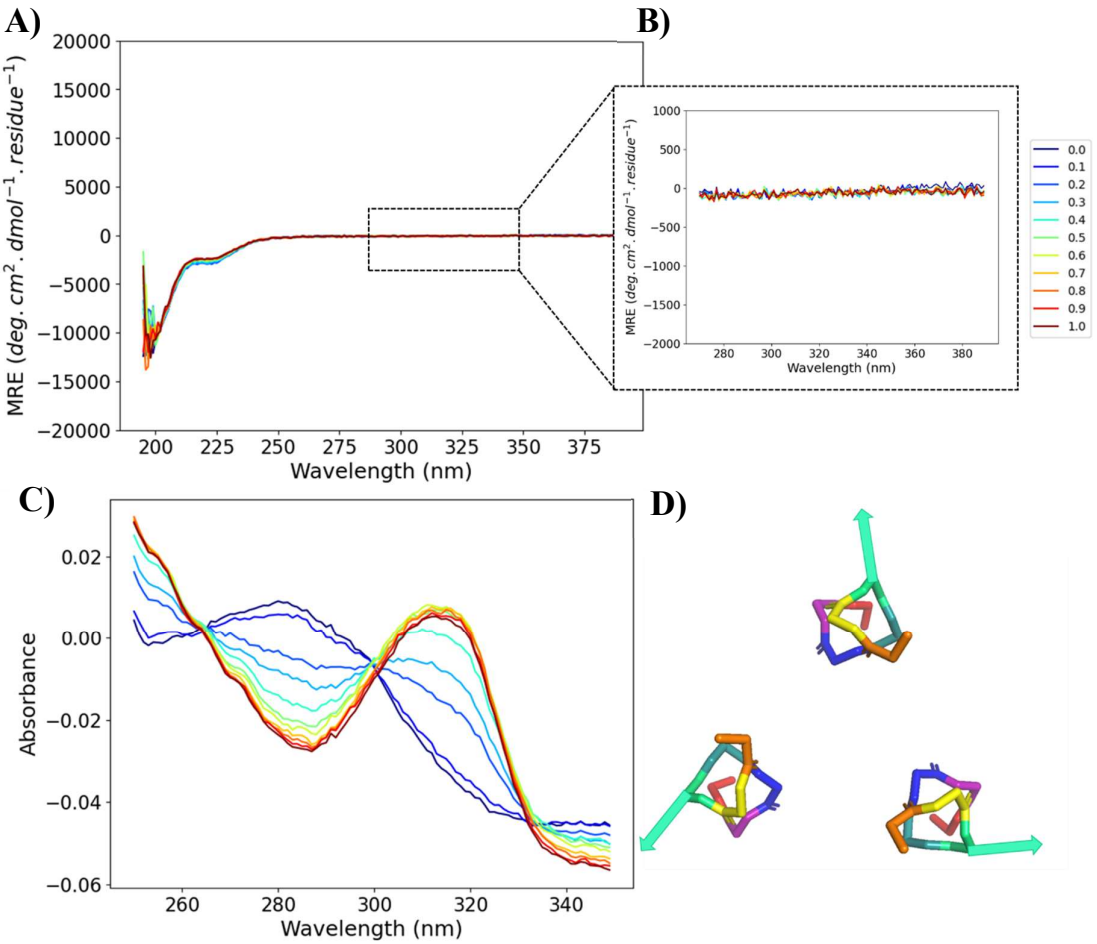

Figure 3.26 - CD and UV titrations of **14a** (10 μM) against Cu^{2+} ions in 20 mM aqueous MOPS buffer, pH 7. **A)** Full spectrum of **14a** titration with Cu^{2+} showing the change in helicity with increasing equivalents of Cu^{2+} **B)** Zoomed segment of the **14a** titration with Cu^{2+} showing the lack of chiral information transfer onto the bpy-complex **C)** UV absorbance spectra of the titration of **14a** with Cu^{2+} showing the two-state transition of unbound bpy to Cu^{2+} coordinated bpy. **D)** View of CC showing predicted bpy directionality.

The titrations of **14a**, **15a**, **17a** and **18a** all indicate minimal self-assembly of the helices into α-helical structures, instead the lineshapes of all four of these peptides are more characteristic of a random coil, exhibiting a large minima at 190 nm.

This data suggests that featuring the bpy units at one of the back, solvent facing positions (*b, c, f* or *g*) does not facilitate the CC assembly that has been observed in the previous chapter when the bpy has been at an inward facing position (*d*-position). Furthermore, the concentration of Cu^{2+} in solution no longer has an influence on the structure of the peptide. As the concentration of Cu^{2+} in solution increases, there is no observed change in the helicity of the peptide in any of the tested sequences (**14a**, **15a**, **17a** and **18a**). If the strands are being brought together by the metal binding of the terminal bpy unit, the spatial arrangement of bpy means that the strands are not interfacing correctly to form the helices.

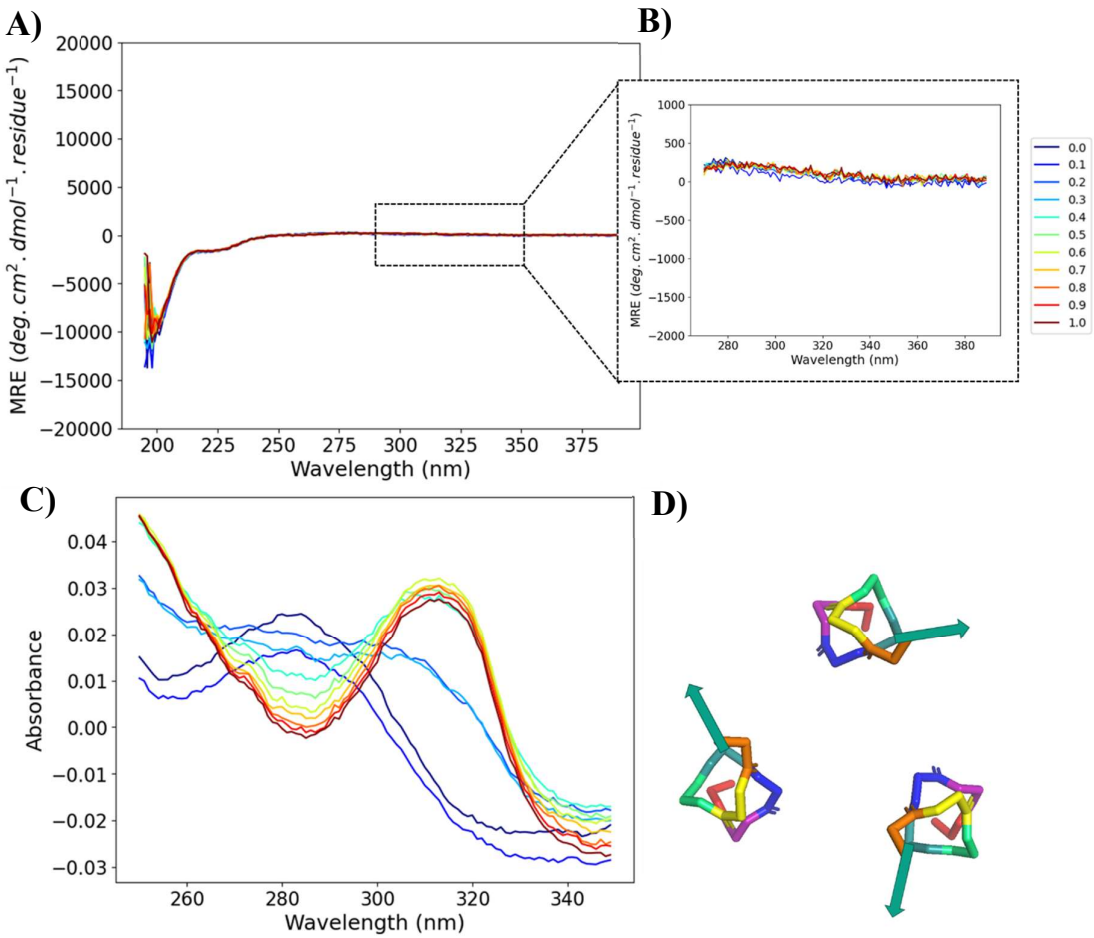

Figure 3.27 - CD and UV titrations of **15a** (10 μM) against Cu^{2+} ions in 20 mM aqueous MOPS buffer, pH 7. **A)** Full spectrum of **15a** titration with Cu^{2+} showing the change in helicity with increasing equivalents of Cu^{2+} **B)** Zoomed segment of the **15a** titration with Cu^{2+} showing the lack of chiral information transfer onto the bpy-complex **C)** UV absorbance spectra of the titration of **15a** with Cu^{2+} showing the two-state transition of unbound bpy to Cu^{2+} coordinated bpy. **D)** View of CC showing predicted bpy directionality.

As a result of the lack of super-secondary or secondary structure observed in these experiments, there is no chiral information transfer onto the resultant bpy complexes for **14a** (**Figure 3.26**), **15a** (**Figure 3.27**), **17a** (**Figure 3.28**) and **18a** (**Figure 3.29**). This is indicated by no chiral signal being observed at 320 nm for any of the sequences, where the value of the exciton couplet from the bpy-conformation has been found to appear previously.

The UV absorbance of these peptides indicates that in the cases of **14a**, **15a**, **17a** and **18a** the bpy units are binding to the Cu^{2+} as they are exhibiting a two-state transition from an absorbance at 280 nm to 320 nm as the concentration of Cu^{2+} increases past 0.3 eq in solution. This indicates that the bpy units could be forming intermolecular complexes and given the stoichiometry, they should be tris-(bpy-peptide) complexes. This could indicate that the complex is forming on a partially unfolded peptide, with negligible chiral information

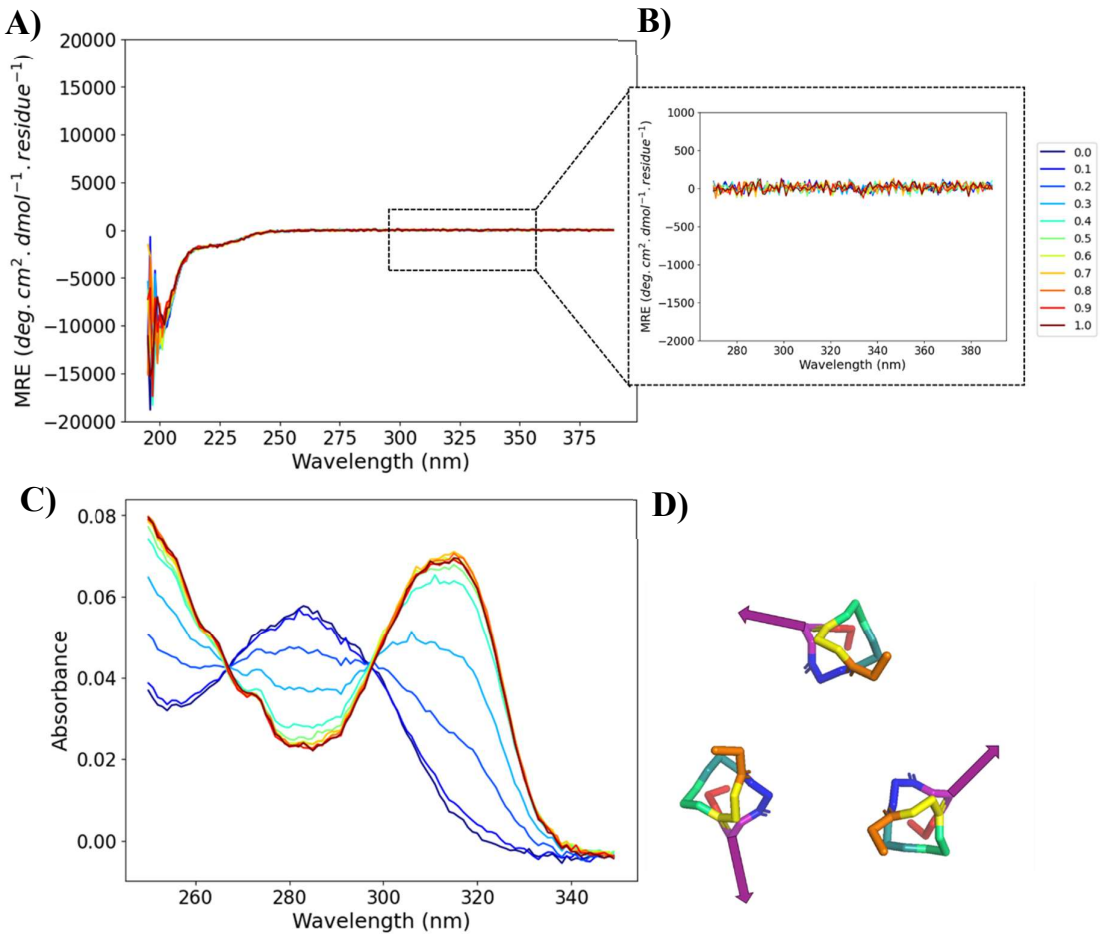

Figure 3.28 - CD and UV titrations of **17a** (10 μM) against Cu^{2+} ions in 20 mM aqueous MOPS buffer, pH 7. **A)** Full spectrum of **17a** titration with Cu^{2+} showing the change in helicity with increasing equivalents of Cu^{2+} **B)** Zoomed segment of the **17a** titration with Cu^{2+} showing the lack of chiral information transfer onto the bpy-complex **C)** UV absorbance spectra of the titration of **17a** with Cu^{2+} showing the two-state transition of unbound bpy to Cu^{2+} coordinated bpy. **D)** View of CC showing predicted bpy directionality.

transfer from the lack of ordered helicity in the peptide structure. It is likely a feature of the bpy placement that causes this reduction in α-helical content, these register positions likely do not hold the bpy units in a preferable conformation for the formation of a chiral complex.

The data from the Zn^{2+} titrations against these peptides shows similar behaviour, with no indication of strong helical signals from the peptide strands and no chiral information being observed for the complexes. However, from the UV absorbance, there is no strong indication of the two-state transition from the binding of the bpy to the Zn^{2+} ions (**Figure 3.30**). Only the Cu^{2+} titrations have been included here as representative spectra due to the similarities

with the Zn^{2+} titration behaviour. The Zn^{2+} CD data from these titrations are found in Appendix B.

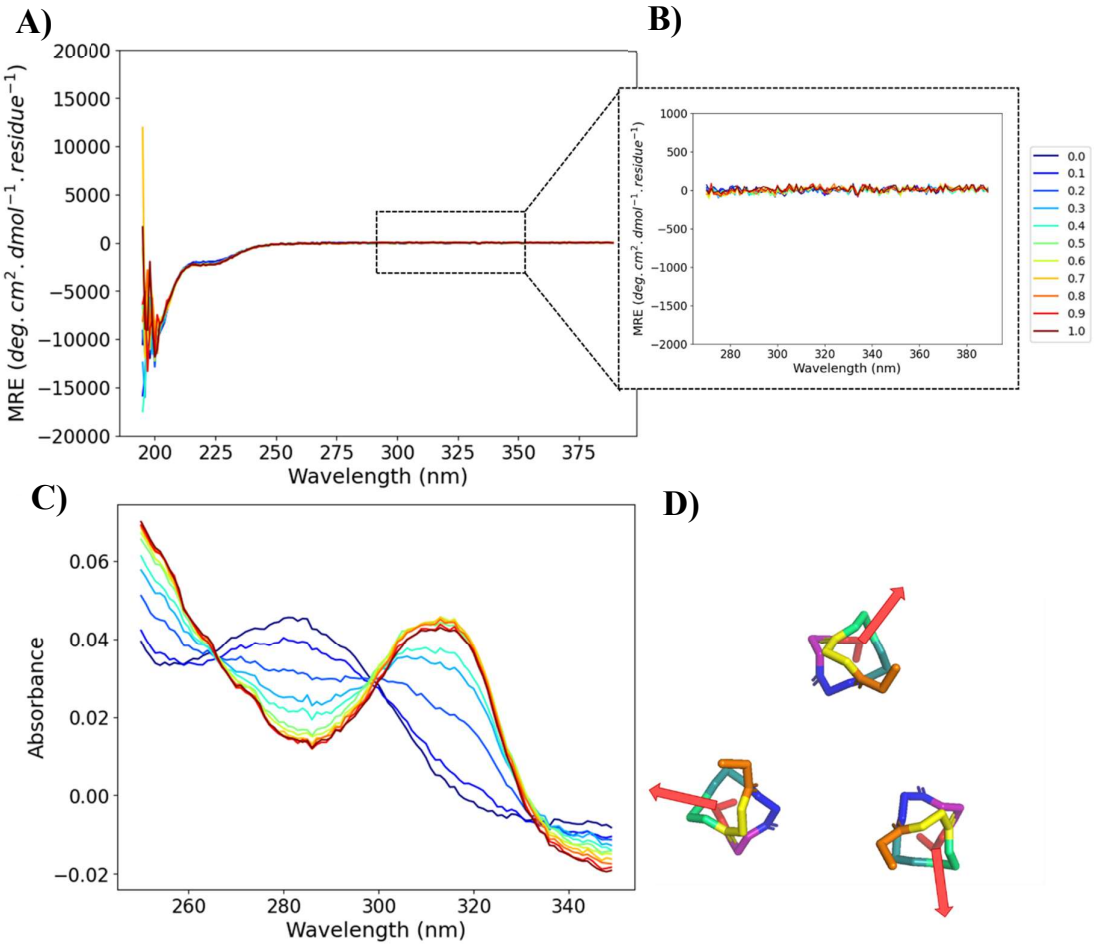

Figure 3.29 - CD and UV titrations of **18a** (10 μM) against Cu^{2+} ions in 20 mM aqueous MOPS buffer, pH 7. **A)** Full spectrum of **18a** titration with Cu^{2+} showing the change in helicity with increasing equivalents of Cu^{2+} **B)** Zoomed segment of the **18a** titration with Cu^{2+} showing the lack of chiral information transfer onto the bpy-complex **C)** UV absorbance spectra of the titration of **18a** with Cu^{2+} showing the two-state transition of unbound bpy to Cu^{2+} coordinated bpy. **D)** View of CC showing predicted bpy directionality.

As mentioned, from the UV absorbance of the Zn^{2+} titrations (**Figure 3.30**) of **14a**, **15a**, **17a** and **18a** there is evidence that the bpy is binding to the TM ions in solution, as there is an isosbestic point just before 310 nm, but the transition is relatively weak in comparison to what has been observed previously.

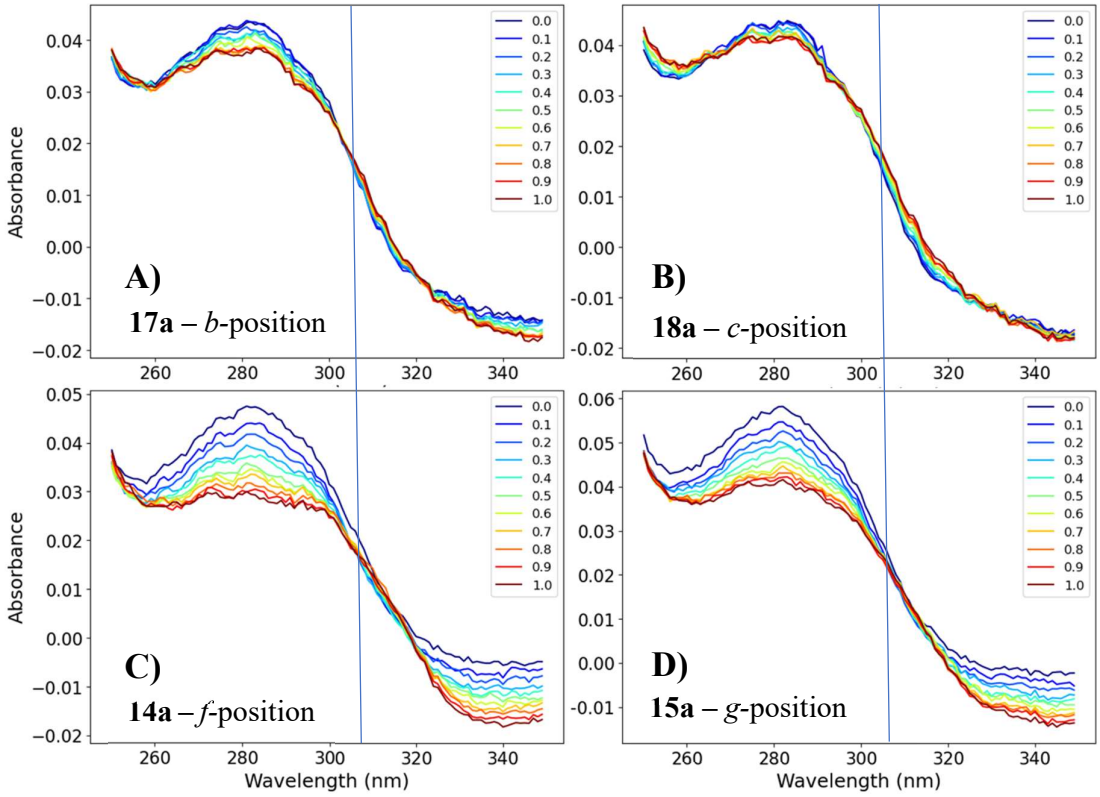

Figure 3.30 - UV absorbance spectra of **A) 17a**, **B) 18a**, **C) 14a** and **D)15a** titrations against Zn^{2+}. All peptides 10 μM in 20 mM aqueous MOPS buffer, pH 7.

This transition is much more prominent in the spectra of **14a** (*f*-position*)* and **15a** (*g*-position) than **17a** (*b*-position) and **18a** (*c*-position). The reasoning for this difference is not known. Further experiments probing these positions could illuminate the reasoning for this behaviour, however, given the lack of chiral information transfer onto the complex from these peptides, these positions were not investigated further as part of this research.

3.8.2 Bpy in positions *a*, *d*, or *e*

Coupling of the bpy to one of the inward facing positions of the CC lead to interesting results regarding the handedness of the terminal complex and the spatial positioning of the bpy unit. CD spectroscopy and UV absorbance of the titrations of these three peptides (**13a, 16a** and **19a**) against Cu^{2+} and Zn^{2+} can be found in **Figures 3.31 – 3.37**.

As all the experiments in the earlier chapter has been run with the bpy in a *d*-position of the helical register, using variations of the same sequence, coupling of the bpy unit to a *d*-position in this experiment (**19a**) results in CD behaviour the same as has been shown in the previous chapters. Having the bpy in this position allows for stabilisation of the super-

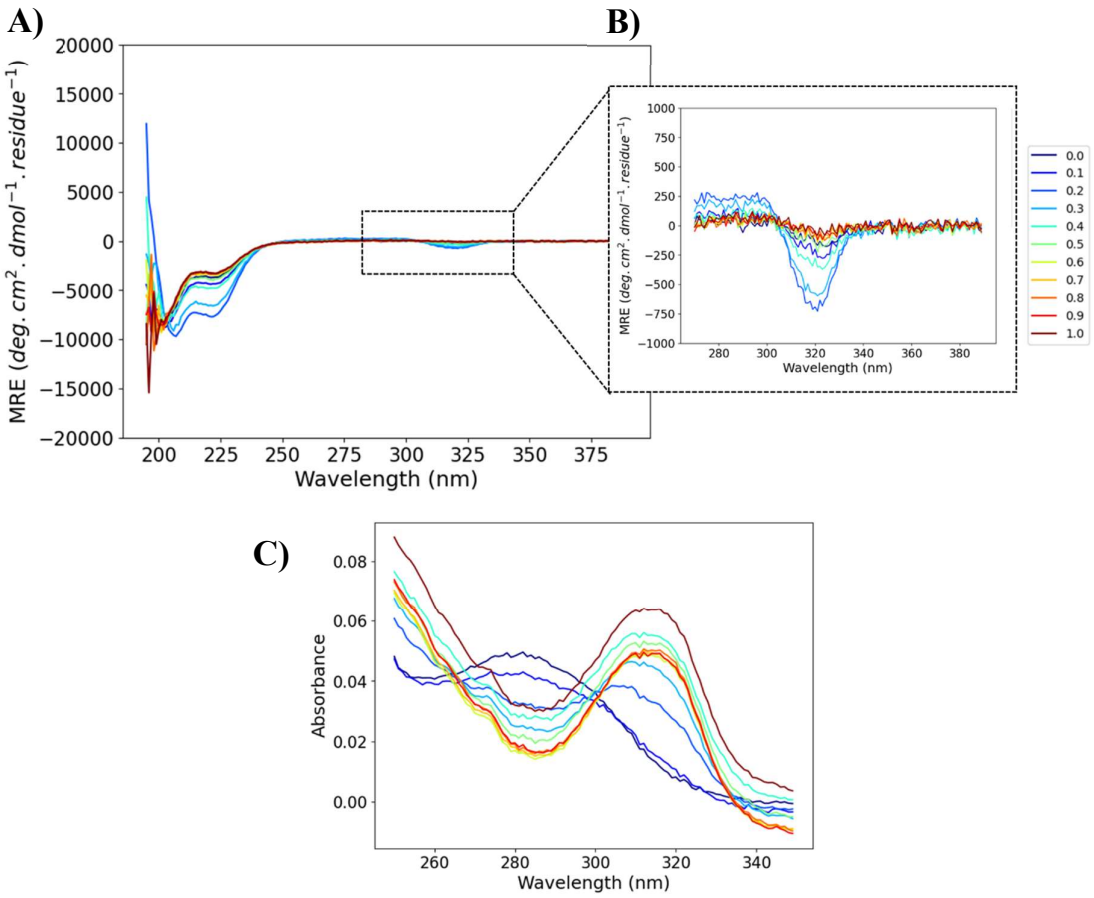

Figure 3.31 - CD and UV titrations of **19a** (10 μM) against Cu^{2+} ions in 20 mM aqueous MOPS buffer, pH 7. **A)** Full spectrum of **19a** titration with Cu^{2+} showing the change in helicity with increasing equivalents of Cu^{2+} **B)** Zoomed segment of the **19a** titration with Cu^{2+} showing the chiral information transfer onto the bpy-complex **C)** UV absorbance spectra of the titration of **19a** with Cu^{2+} showing the two-state transition of unbound bpy to Cu^{2+} coordinated bpy.

secondary structure by intermolecular π-stacking interactions between the terminal bpy units. The helicity of **19a** (see **Figure 3.31**) then increases as the concentration of Cu^{2+} moves towards 0.3 eq with respect to the bpy units. Beyond this, the helical content of the peptide reduces with the increasing concentration of Cu^{2+} ions, as was observed in Chapter 2.

The titration of **19a** against Zn^{2+} is shown in **Figure 3.32**. The helical behaviour is as to be expected with a slight stabilisation of the secondary structure (signal at 222 nm) occurring due to the coordination of the CC to Zn^{2+} ions via the bpy-moieties. Again, the signal at 320 nm is exhibited as a negative exciton couplet, indicative of the Δ-tris-(bpy-peptide) complex. The exciton couplet at 320 nm increases in magnitude as the experiment progresses to a value of approximately -300 deg·cm^2·dmol^{-1}·residue^{-1} at 1.0 eq of Zn^{2+}. The UV absorbance trace of this titration indicates a weak two-state transition from unbound bpy (280 nm) to

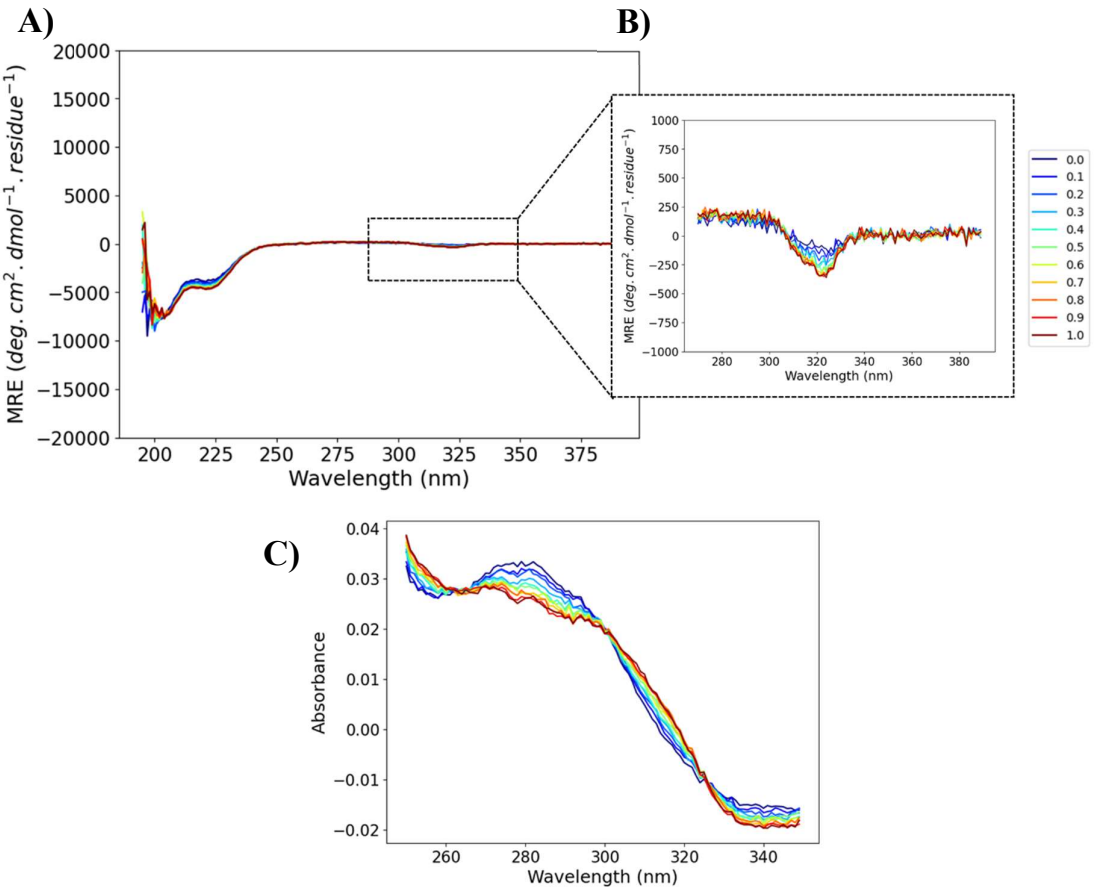

Figure 3.32 - CD and UV titrations of **19a** (10 μM) against Zn^{2+} ions in 20 mM aqueous MOPS buffer, pH 7. **A)** Full spectrum of **19a** titration with Zn^{2+} showing the change in helicity with increasing equivalents of Zn^{2+} **B)** Zoomed segment of the **19a** titration with Zn^{2+} showing the chiral information transfer onto the bpy-complex **C)** UV absorbance spectra of the titration of **19a** with Zn^{2+} showing the two-state transition of unbound bpy to Zn^{2+} coordinated bpy.

Zn^{2+} coordinated bpy (320 nm). This weak transition was also observed previously in Section 3.3 with the Zn^{2+} titrations.

Comparison to CD of the peptide **13a** with the bpy now being featured at an *e*-position shows that moving the position of the bpy in the sequence can result in formation of the opposite handedness, Λ-tris-(bpy-peptide) complex at the N-terminus without altering the chirality of any of the AAs in the sequence (**Figures 3.33** and **3.34**).

Interestingly, formation of the complex by addition of Cu^{2+} to this system (**Figure 3.33**) does influence the helicity of peptide **13a** to the same extent as was exhibited by featuring the bpy at the *d*-position with peptide **19a,** despite the difference in directionality of the terminal complex. Additionally, the magnitude of the exciton couplet at 320 nm for **13a** (approximately +250 deg·cm^2·dmol^{-1}·residue^{-1}) is less than half the magnitude of **19a**

(approximately –750 deg·cm^2·dmol^{-1}·residue^{-1}) suggesting that the Δ-conformation may be more favourable in this instance.

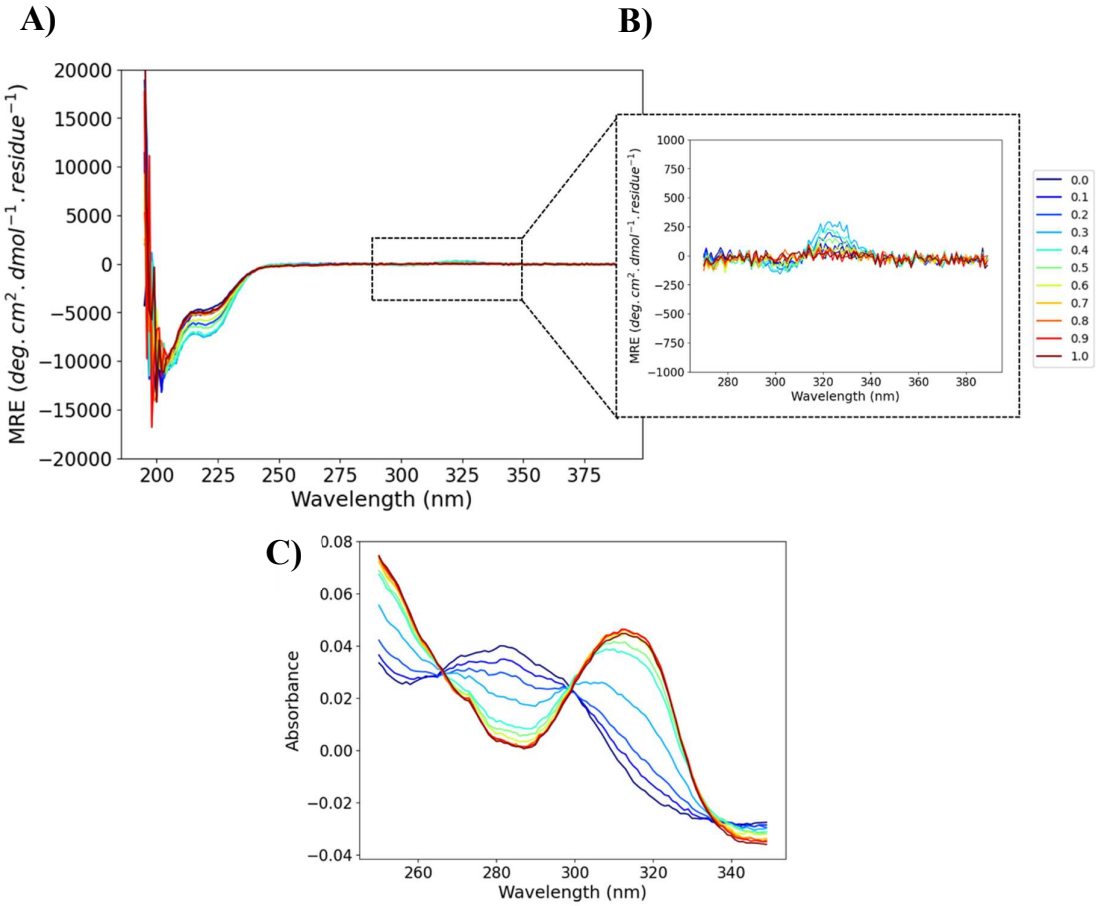

Figure 3.33 - CD and UV titrations of **13a** (10 μM) against Cu^{2+} ions in 20 mM aqueous MOPS buffer, pH 7. **A)** Full spectrum of **13a** titration with Cu^{2+} showing the change in helicity with increasing equivalents of Cu^{2+} **B)** Zoomed segment of the **13a** titration with Cu^{2+} showing the chiral information transfer onto the bpy-complex **C)** UV absorbance spectra of the titration of **13a** with Cu^{2+} showing the two-state transition of unbound bpy to Cu^{2+} coordinated bpy.

The CD of the titrations of **13a** with Zn^{2+} can be found in **Figure 3.34**. This data shows that as the concentration of Zn^{2+} increases in solution, the α-helical content of **13a** increases slightly, as was observed for **19a**. Furthermore, the positive exciton couplet detected in **13a** at 1.0 eq of Zn^{2+} (approximately +400 deg·cm^2·dmol^{-1}·residue^{-1}) has a similar magnitude to the negative exciton couplet shown for **19a** (approximately -375 deg·cm^2·dmol^{-1}·residue^{-1}). In both cases the magnitude of this exciton couplet increases as the experiment progresses and the concentration of Zn^{2+} ions increases.

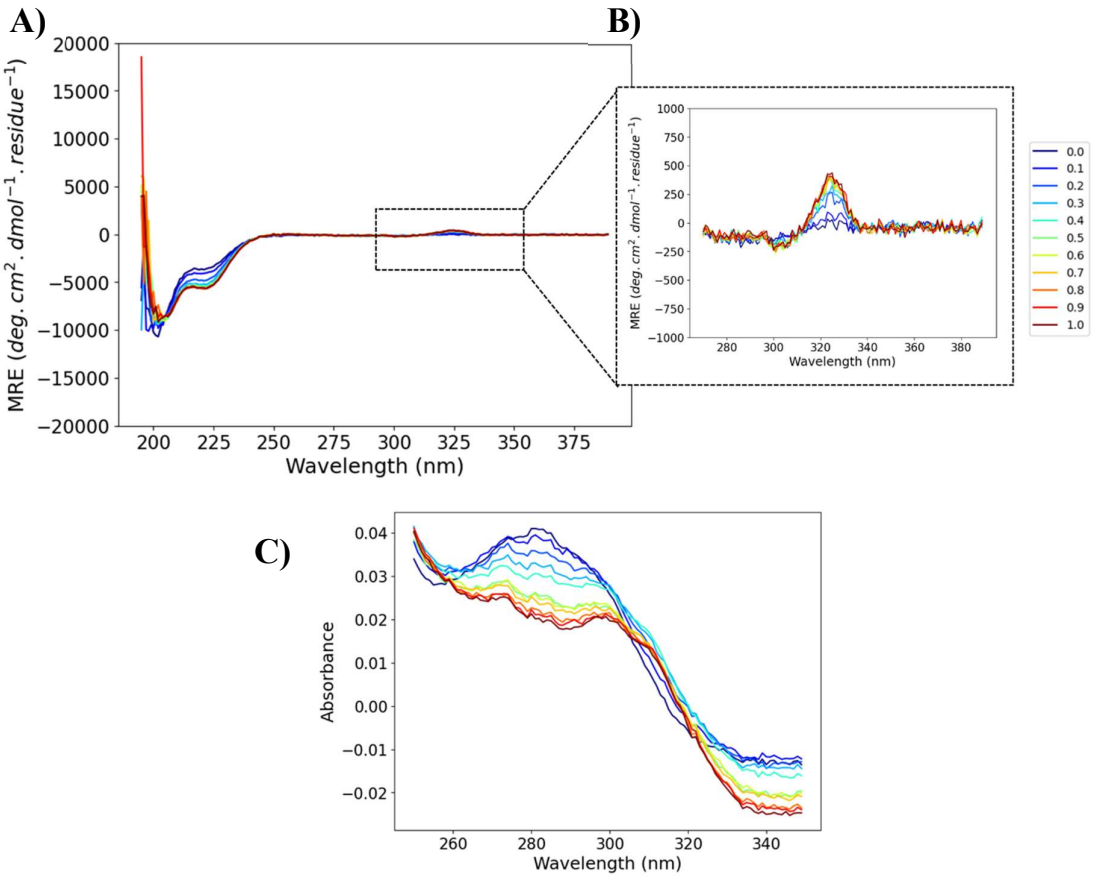

Figure 3.34 - CD and UV titrations of **13a** (10 μM) against Zn^{2+} ions in 20 mM aqueous MOPS buffer, pH 7. **A)** Full spectrum of **13a** titration with Zn^{2+} showing the change in helicity with increasing equivalents of Zn^{2+} **B)** Zoomed segment of the **13a** titration with Zn^{2+} showing the chiral information transfer onto the bpy-complex **C)** UV absorbance spectra of the titration of **13a** with Zn^{2+} showing the two-state transition of unbound bpy to Zn^{2+} coordinated bpy.

A direct comparison of the CD traces of **13a** and **19a** can be found in **Figure 3.35**. From this it can be seen that the initial helicity of the two peptides with no metal ions in the systems are similar, with magnitudes at 222 nm of approximately -5000 deg·cm^2·dmol^{-1}·residue^{-1} and approximately -4000 deg·cm^2·dmol^{-1}·residue^{-1}, respectively. At 0.3 eq of Cu^{2+} these values increase to approximately -7500 deg·cm^2·dmol^{-1}·residue^{-1} for **13a** and approximately -6500 deg·cm^2·dmol^{-1}·residue^{-1}. Therefore, the increase in helicity upon coordination is consistent across both sequences with an increase of approximately -2500 deg·cm^2·dmol^{-1}·residue^{-1} for both sequences. Looking at the signal at 320 nm the difference in ellipticity is apparent, with **13a** exhibiting a positive exciton couplet with a value of approximately +250 deg·cm^2·dmol^{-1}·residue^{-1} and **19a** exhibiting a negative exciton couplet with a value of approximately -600 deg·cm^2·dmol^{-1}·residue^{-1}, indicating a Λ- and Δ-conformations respectively.

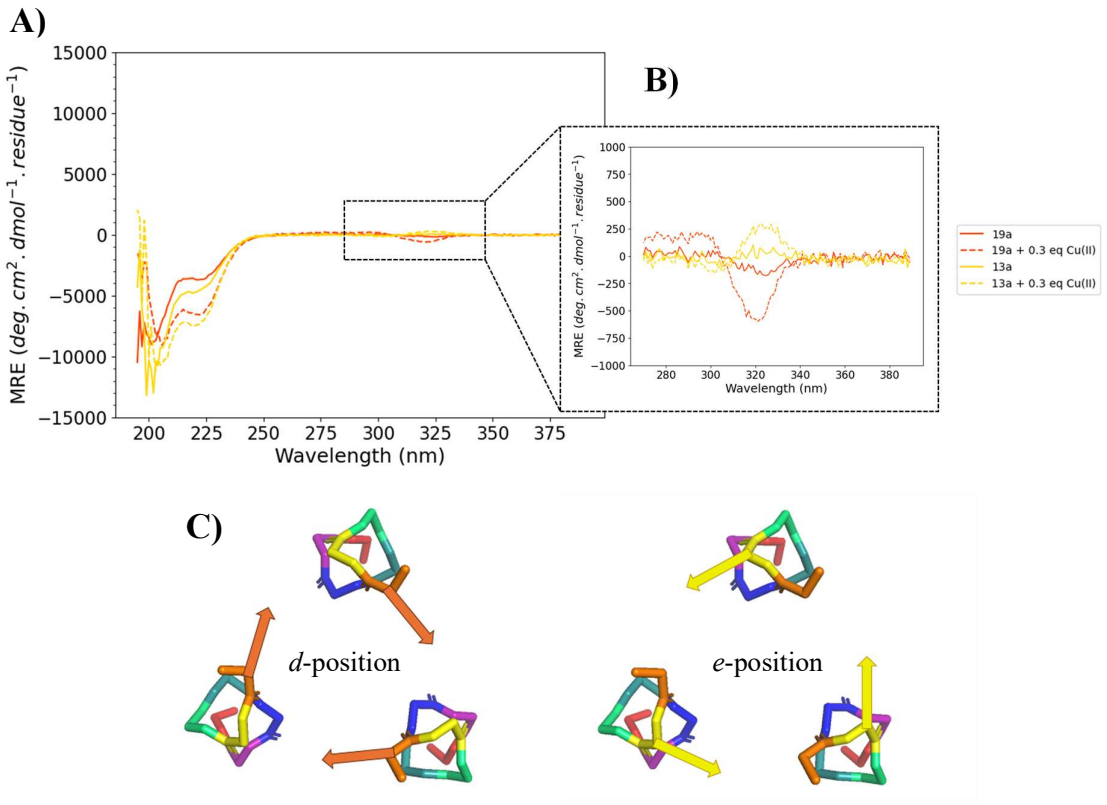

Figure 3.35 – Comparison of the CD traces of **13a** (yellow) and **19a** (orange) in the absence of metal (solid lines) and in the presence of 0.3 eq of Cu^{2+} (dashed lines). **A)** Full spectrum comparison of **13a** and **19a** showing the differences in helicity in both the absence of metal and the presence of 0.3 eq of Cu^{2+} **B)** Zoomed segment of the full spectra showing the difference in the bpy-conformations for **13a** and **19a**, with **13a** exhibiting a positive exciton couplet and **19a** exhibiting a negative exciton couplet, both of which increase in magnitude upon introduction of Cu^{2+}. **C)** Comparison of the *d*- and *e*-position models used to indicate the approximate bpy-directionality excluding the effects of NCIs.

Peptide **16a** features the bpy at the *a*-position. The CD and UV absorbance spectroscopy of the titration of this **16a** with Cu^{2+} (**Figure 3.36**) shows that having the bpy in this position is detrimental to the formation of the CC. The signal observed for the Cu^{2+} titration is characteristic of a random coil, and this is not changed by addition of the Cu^{2+} ions to the system. From this behaviour it can be hypothesised that the bpy in this position results in energetically unfavourable steric interactions between the strands of the peptide meaning that it cannot form the desired CC structure, even in the presence of TM ions which in **13a** and **19a** were found to enhance the α-helical content of the peptide.

Despite this, a small positive exciton couplet in the expected region of UV for the bpy complex is observed. This signal indicates the bpy units are in a Λ-handedness arrangement and somewhat in proximity to one and other, and that this relationship is not influenced by the addition of TM ions to the solution. The lack of change to exciton couplet paired with

the evidence of the two-state transition in the UV absorbance suggests that despite the binding of the Cu^{2+} ions to the bpy this chiral arrangement of the bpy units is independent of TM concentration.

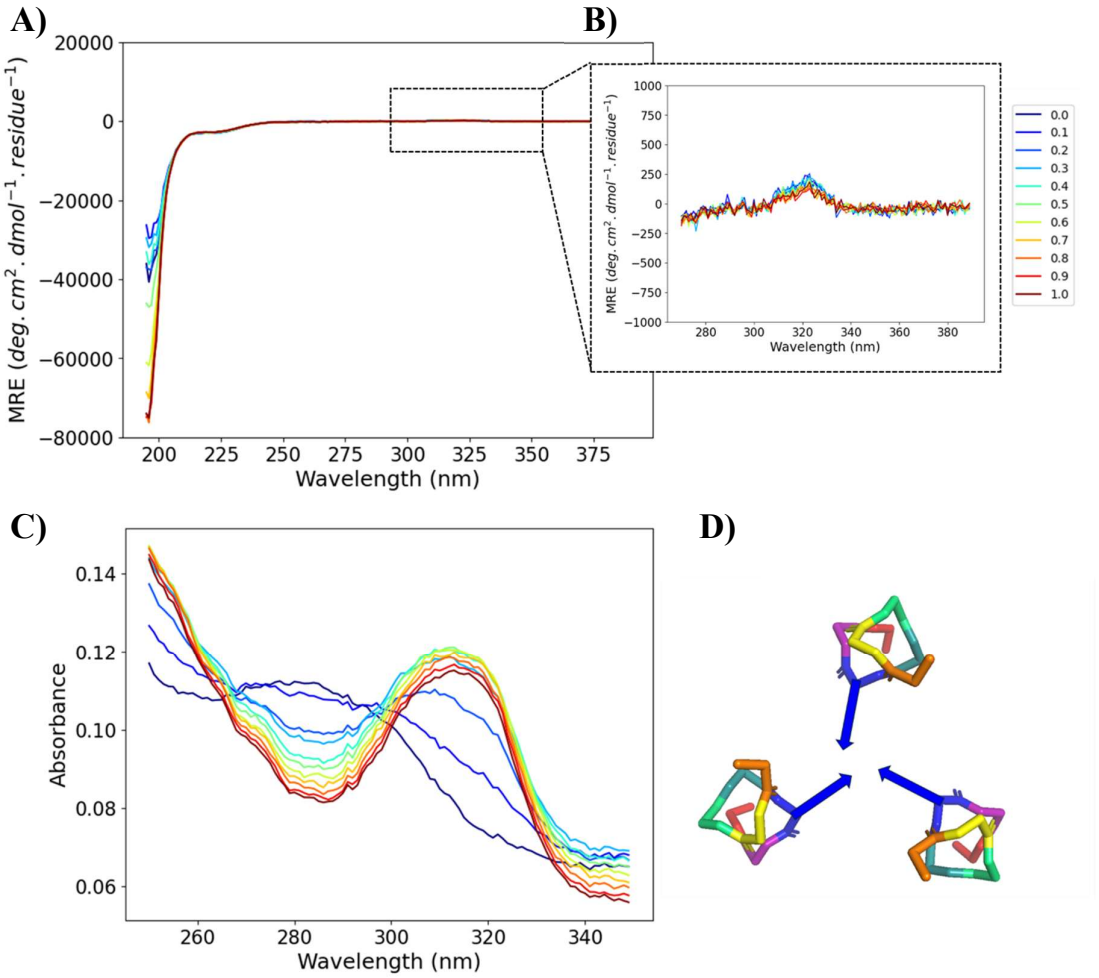

Figure 3.36 - CD and UV titrations of **16a** (10 μM) against Cu^{2+} ions in 20 mM aqueous MOPS buffer, pH 7. **A)** Full spectrum of **16a** titration with Cu^{2+} showing that there is no change in helicity with increasing equivalents of Cu^{2+} **B)** Zoomed segment of the **16a** titration with Cu^{2+} showing the lack of chiral information transfer onto the bpy-complex, however a small positive exciton couplet can be observed at 320 nm **C)** UV absorbance spectra of the titration of **16a** with Cu^{2+} showing the two-state transition of unbound bpy to Cu^{2+} coordinated bpy. **D)** View of CC showing predicted bpy directionality.

The titration of **16a** against Zn^{2+} reflects what was seen in the Cu^{2+} titration of this peptide (**Figure 3.37**). The initial behaviour of the peptide in the absence of metal ions shows that again, this peptide resembles a more random coil structure, and there is presence of a positive exciton couplet around 309 nm. Upon addition of Zn^{2+} ions to the solution there is no change with respect to the α-helical content of the peptide, nor the magnitude of the exciton couplet.

Again, the two-state transition from the UV absorbance of this titration is weak but still observed.

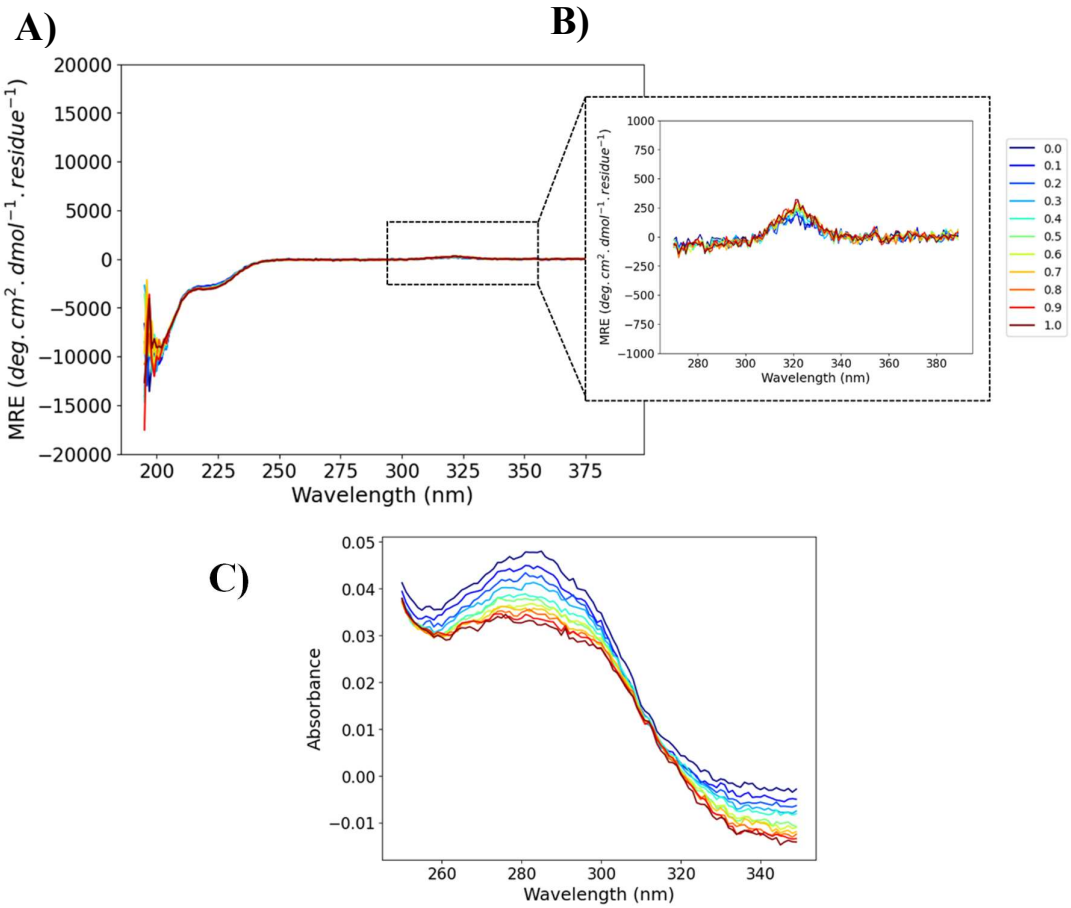

Figure 3.37 - CD and UV titrations of **16a** (10 μM) against Zn^{2+} ions in 20 mM aqueous MOPS buffer, pH 7. **A)** Full spectrum of **16a** titration with Zn^{2+} showing that there is no change in helicity with increasing equivalents of Zn^{2+} **B)** Zoomed segment of the **16a** titration with Zn^{2+} showing the lack of chiral information transfer onto the bpy-complex, however a small positive exciton couplet can be observed at 320 nm **C)** UV absorbance spectra of the titration of **16a** with Zn^{2+} showing the two-state transition of unbound bpy to Zn^{2+} coordinated bpy.

3.8.3 Comparison

Comparison of all the register positions suggests that in order for chiral information transfer from the helices onto the complex to occur, the bpy must be coupled such that it is featured at an *a*- *d*- or *e*- position in the sequence. Having the bpy units in one of the solvent facing positions does not allow for the stabilising intermolecular π-stacking interactions that are afforded by having it in one of the central positions. This results in the peptides with the bpy

units in these positions adopting a structure characteristic of a random coil, due to the balanced nature of this system.

From the comparison in **Figure 3.38**, the Cu^{2+} and the Zn^{2+} titrations indicate that only in **13a** (*e*-position) and **19a** (*d*-position) is the α-helical content increased by the binding of the TM to the bpy units. All other tested positions α-helical content remains consistent across the entirety of the titration, independent of the concentration of TM in solution.

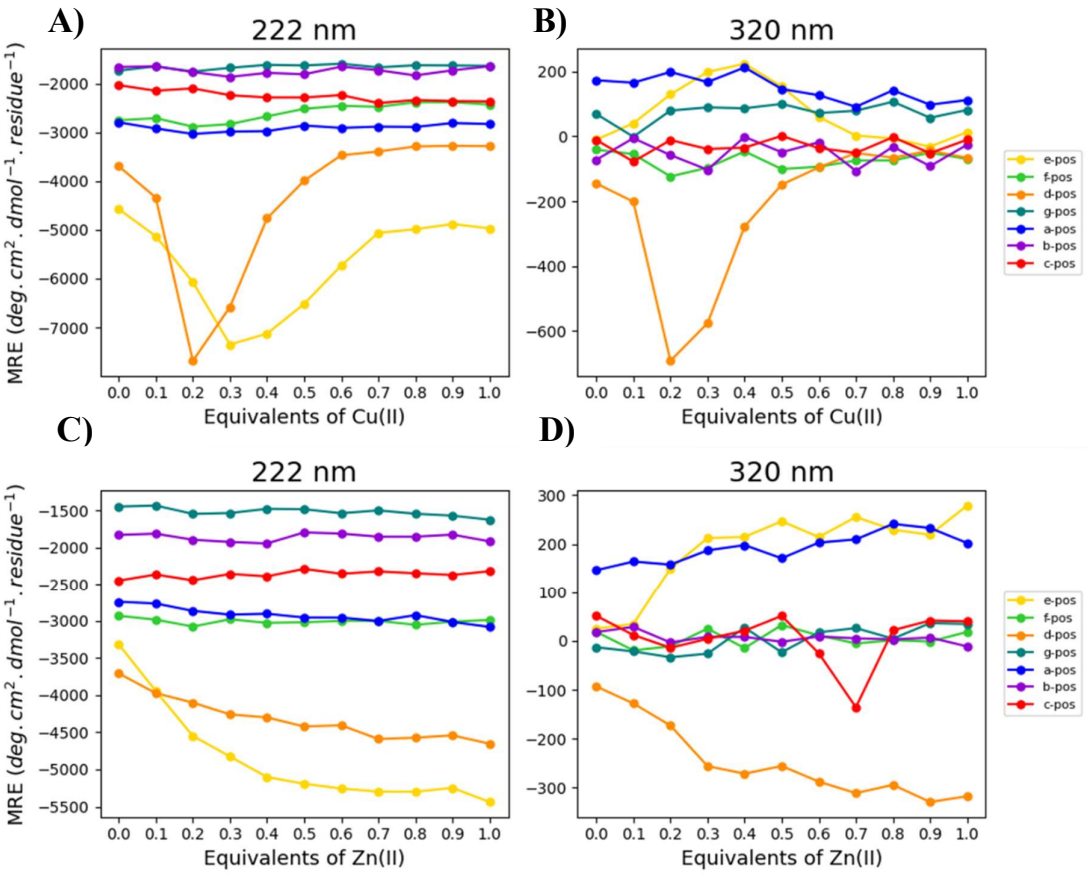

Figure 3.38 - Comparison of all register positions by plotting the MRE at 222 nm (helical signal) and 320 nm (bpy complex signal) against the concentration of **A)** Cu^{2+} CD titration readings at 222 nm **B)** Cu^{2+} CD titration readings at 320 nm **C)** Zn^{2+} CD titration readings at 222 nm and **D)** Zn^{2+} CD titration readings at 320 nm.

Changes in the signal from the bpy complex exciton couplet at 320 nm are only significant again in the *d*- and *e*-positions, displaying opposite effects for the two peptides. Additionally, there is a small concentration dependence observed for the *a*-position Zn^{2+} titration, but the changes in ellipticity are not significant.

Despite attempt to map the directionality of the bpy units with respect to the helices the resulting chiral preferences from the experimental spectra show the opposite helicity to what

is anticipated. This could suggest that the terminal residues of the helices no longer follow the amide H-bonding pattern which would project the bpy unit in the direction suggested by the map. Furthermore, a biological molecular modelling tool called Chai-1 was used in an attempt to predict the bpy-unit orientation upon conjugation to the N-terminus of a CC. This programme allows modelling of biological molecules such as proteins and nucleotides by input of the sequence into the terminal. It can also account for non-biological modifications by inputting a SMILES string. This allows the modified biological molecule to be modelled with the relationship between the biological component and the modification being accounted for. Modelling with the Chai-1[207] resource was performed for these sequences to attempt to explain the differences that have been observed in the CD. It was found that these models strongly predicted helical folding in the orientation consistent with a CC, even with the sequences which were found experimentally to not form the CC structures.

Unfortunately, as well as these models tending to over predict the helix formation they also did not appear to couple the behaviours of the attached ligand to the helix. The over prediction of the helicity meant that these models could be used qualitatively, to observe how the spatial arrangements might look for these systems, however any information on the energetics of the system, metal coordination and preferential formation of the different handedness complexes cannot be inferred.

This work is ongoing within the group. Additional information on how these models were run can be found in Section 6.2.

3.9 Conclusions

In conclusion through design and synthesis of 17 variations of a CC trimeric design featuring the bpy chelating unit in different spatial environments with respect to the peptide strand, the spatial restraints of chiral information transfer on this system have been investigated.

By increasing the distance between the bpy chelating unit and the last chiral centre in two different sets of peptides it was shown that there is a correlative relationship occurring between the content of the N-terminus and the chiral preference of the complex.

In the case of the 3-heptad repeat series of peptides (**1a**, **4a**, **5a** and **6a**) it was found that the inclusion of these spacers at the N-terminus resulted in more of an effect on the α-helicity of the peptide which then resulted in the loss of chiral information transfer as the achiral spacer increased in length. It was concluded that as the distance from a chiral centre increased in

these sequences from **4a** < **1a** < **5a < 6a** (1 atom < 4 atoms < 7 atoms < 10 atoms) it followed that the α-helical content of these peptides was **4a** > **1a** > **5a > 6a**. Therefore, the resulting chirality of the bpy arrangement could be attributed to loss of α-helical content. In addition to this the idea that the AA spacers (Ala, Gly and GlyGly) had the ability to H-bond was presented as a possible explanation for the complete loss of chiral preference in the instance of the PEG spacer (**6a**).

To investigate the distance from a chiral centre by inclusion of an achiral spacer further the series of 4-heptad repeat peptides were also investigated. The additional heptad resulted in the helicity of the peptide having less dependence on the content of the final three AAs of the sequence. Therefore, little difference between the α-helical content of these four peptides was observed. Having established a comparable starting point with respect to the helicity of these peptides, the experiments showed that increasing the distance from a chiral centre by addition of an AA spacer (Gly and GlyGly) resulted in comparable magnitudes of bpy exciton couplet, suggesting no effect on the chiral preference. This has been suggested to be a result of the H-bonding ability of these spacers allowing the helicity to be carried through. Conversely, when the PEG spacer was used no chiral preference was observed. This spacer is both longer and has a reduced capacity for H-bonding which could explain this difference.

By inclusion of two more sequences (**11a** and **12a**) featuring different chiral terminal AAs the spatial tolerances of this system were further probed. Addition of a D-Ala residue prior to the bpy resulted in very minimal change in the helical content of the peptide but an observable difference in the chiral information transfer to the complex, both L- and D-Ala, however, exhibit a Δ-tris-(bpy-peptide) conformation. This relationship further confirmed the reliance on the helicity rather than the specific peptide content for the chiral information transfer. Furthermore, having L-Pro as the terminal AA of the sequence led to a loss in α-helical content of **12a** and a resulting loss in chiral preference in the bpy conformation.

Finally, investigation into changing the register position of the bpy within the peptide sequence led to the conclusion that the chiral preference of the bpy complex can be controlled by changing the bpy between the *d*- and *e*-position of the sequence.

Featuring the bpy in a more solvent facing position (*b, c, g, f*) resulted in no chiral information transfer leading to the conclusion that the bpy units are not held in close enough proximity. This was further confirmed by the reduction in α-helical content observed with the bpy in these positions.

Placing the bpy at one of the inward facing positions of the CC (*a, d, e*) led to the most dramatic effects in the CD spectra. When at an *a*-position the helicity of the peptide was compromised, likely a result of steric clash between the bpy units leading to fraying of the N-terminus. Conversely, featuring the bpy at a *d*-position lead to the reliable formation of the Δ-bpy conformation whereas for the *e*-position the Λ-bpy conformation was preferred.

4 Chiral Effects of Metal Binding to 8-HQ Binding Motif at the N-terminus

This chapter follows the synthesis and subsequent analysis of 8-hydroxyquinoline (8-HQ) N-terminally functionalised CC homotrimers. Using the principles determined in the previous chapters, three peptides were synthesized with an 8-HQ unit at either an *a*-, *d*-, or *e*- position. Chiral induction into the 8-HQ complexes from the peptides was then studied by CD and UV absorbance during titrations against Ga^{3+}, Al^{3+} and Co^{2+}.

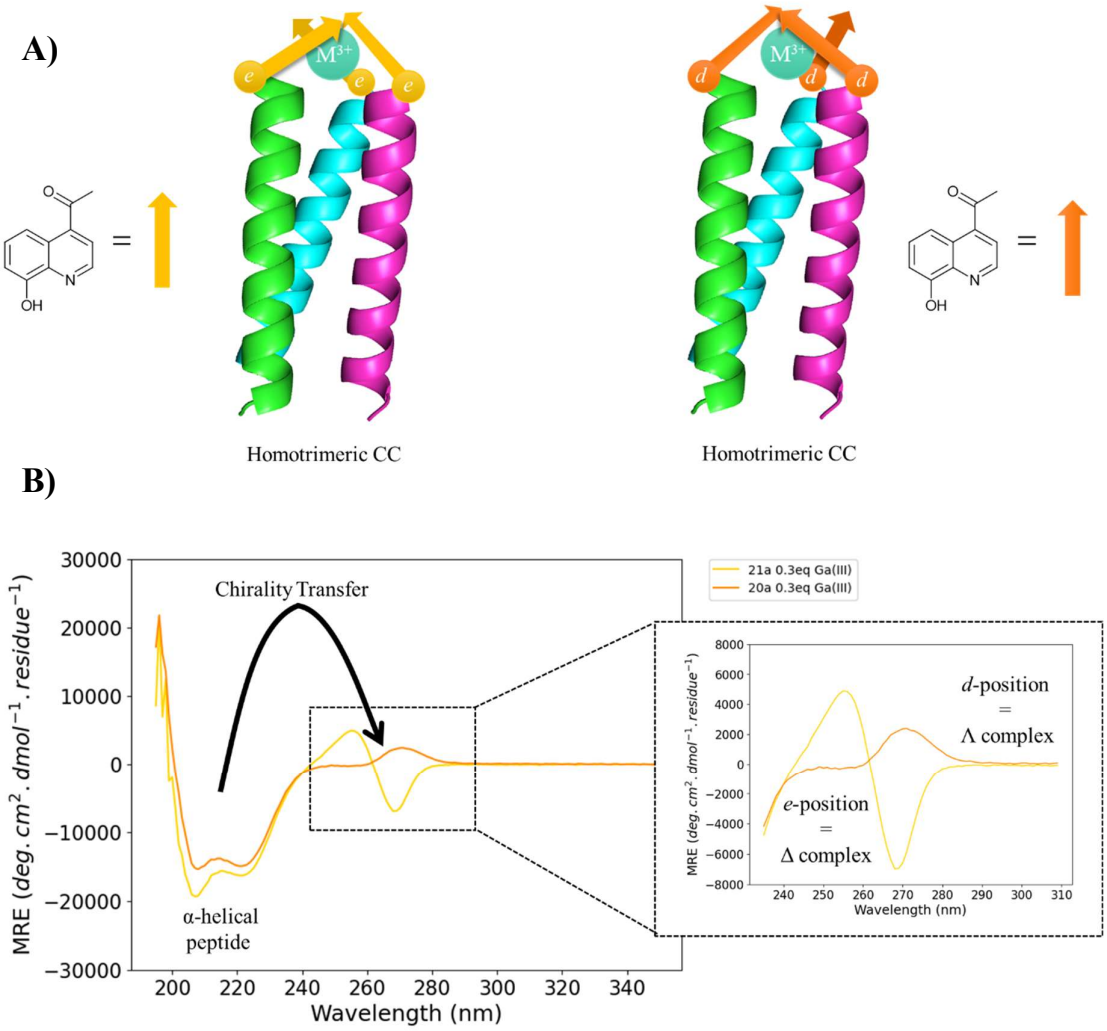

Figure 4.1 - Graphical abstract showing the formation of opposite handedness complexes at the N-terminus of a left-handed supercoiling CC by changing the position of the 8-HQ unit within the helical register. **A)** Cartoon homotrimeric CCs showing the bpy in the *d*-position (orange) or the *e*-position (yellow) represented by a vector. The directionality indicates the handedness of the complexes formed. **B)** CD spectrum showing the chiral information transfer from the peptide helicity onto the 8-HQ complex, with the peptide featuring the 8-HQ at the *d*-position exhibiting a positive exciton couplet (Λ) and the peptide with the 8-HQ at the *e*-position exhibiting a negative exciton couplet (Δ).

4.1 Aims

The aim is to explore the preferential formation of Λ-tris-(8HQ-peptide) and Δ-tris-(8HQ-peptide) complexes in response to binding to p-block metals Ga^{3+} and Al^{3+} and TM Co^{2+}. It was thought that preferential formation of one isomer over the other could be controlled by altering the position in the sequence of the 8-HQ, similar to the bpy-peptides in Chapter 2.

Furthering this, the chapter discusses the behaviour of these systems in response to changes in pH and aims to prove that the difference in chiral induction comparative to the tris-(bpy-peptide) complexes discussed in Chapters 2 and 3, is as a result of H-bonding between -OH functional groups of the 8-HQ units.

4.2 Design and Synthesis of Homotrimeric Coiled Coils featuring 8-hydroxyquinoline at the N-terminus

4.2.1 Sequence Design

The peptides used in this study were designed to be comparable to the bpy-functionalised peptides in Chapter 2. To this end, the peptide sequence of **20a** is identical to **1a** (and therefore has the same control sequence, **1b**), with the bpy substituted for 8-Hydroxyquinoline (8-HQ) (**Figure 4.2**), which will appear at a *d*-position in the sequence. Following this, the register was altered to synthesise **21a** and **22a** (and their control sequences **21b** and **22b**) in which the 8-HQ residue is featured at the *e*- and *a*-positions respectively. Additionally, a decision was made to include a Gly as the final AA residue in these sequences for flexibility, as the results from Chapter 3 suggested that addition of one

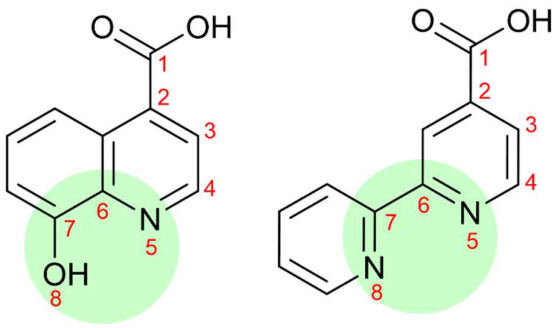

Figure 4.2 - 8-Hydroxyquinoline-4-carboxylic acid structure comparison to 2,2′-bipyridine-4-carboxylic acid showing the similarity in the donor atom placement.

achiral spacer did not have a significant effect on the resulting chiral preference of the final complex.

Following the results from Chapter 3, the solvent-exposed positions in the heptad repeats (*b, c, f,* and *g*) were excluded from this series, as despite evidence of metal binding at the bpy unit, there was no evidence to suggest the formation of chiral complexes with these structures.

Table 4.1 shows the sequences of these peptides, the content of their C- and N-termini and their helical registers.

Table 4.1 - Sequences and helical registers of **20a**, **1b**, **21a**, **21b**, **22a** and **22b.**

Peptide No.	Capping Moiety	Sequence and Register	C-Terminus
20a	**8-HQ** ***d***	GQEIAAIKKEIAAIKKEIAAIKYG *efg**a**bc**d**efg**a**bc**d**efg**a**bc**d**efg*	NH_2
1b	Ac *d*	GQEIAAIKKEIAAIKKEIAAIKYG *efg**a**bc**d**efg**a**bc**d**efg**a**bc**d**efg*	NH_2
21a	**8-HQ** ***e***	GEIAAIKKEIAAIKKEIAAIKKYG *fg**a**bc**d**efg**a**bc**d**efg**a**bc**d**efga*	NH_2
21b	Ac *e*	GEIAAIKKEIAAIKKEIAAIKKYG *fg**a**bc**d**efg**a**bc**d**efg**a**bc**d**efga*	NH_2
22a	**8-HQ** ***a***	GAIKKEIAAIKKEIAAIKKEIAYG *bc**d**efg**a**bc**d**efg**a**bc**d**efg**a**bcd*	NH_2
22b	Ac *a*	GAIKKEIAAIKKEIAAIKKEIAYG *bc**d**efg**a**bc**d**efg**a**bc**d**efg**a**bcd*	NH_2

4.3 Chiral Induction from Coiled Coil Homotrimers on to tris-(8HQ-peptide) Complexes

To investigate the relationship between the structure of the 8-HQ functionalised CC and the resulting N-terminal complexes, titrations of **20a, 21a** and **22a** against Co^{2+}, Ga^{3+} and Al^{3+} were performed, and the resulting behaviour was analysed by CD and UV absorbance spectroscopy. Different metals were chosen for these complexes due to literature precedent

for 8-HQ octahedral complexes with p-block metals.[127, 109] This is likely a consequence of hard-soft acid-base theory, with 8-HQ being a hard base and Ga^{3+} and Al^{3+} being hard acids.

4.3.1 Co^{2+}

Initial CD experiments focused on titrations against Co^{2+} ions. Co^{2+} was chosen due to its observed effectiveness with respect to binding in the titrations with the bpy functionalised peptides in Chapter 2.

Plots of the CD titrations of **20a**, **21a** and **22a** against Co^{2+} ions can be found in **Figure 4.3** and the UV absorbance titration in **Figure 4.4**. Initial observation of these plots strongly indicates the formation of chiral complexes at the N-terminus of these peptides in response to addition of Co^{2+} ions. Interestingly, these complexes appear to express the opposite handedness to their bpy-counterpart, **1a** (*d*-position), **13a** (*e*-position) and **16a** (*a*-position). For example, peptide **1a,** with the chelating unit at the *d*-position has a signal consistent with the Δ-tris-(bpy-peptide) complex. However, peptide **20a**, which has the same sequence, shows a signal with an exciton couplet consistent with the Λ-tris-(8HQ-peptide) complex. This follows with the vector mapping **(Figure 4.5**) which was attempted in Chapter 3 suggesting that the 8-HQ chelating unit allows for the continuation of the α-helical H-bonding pattern of *i*–*i*+4, resulting in the anticipated handedness for the complexes.

The mean residue ellipticity (MRE) in the UV region between 180–250 nm of the titrations shows that the helicity of both **20a** and **21a**, like **1a**, is stabilised by the presence of the aromatic chelating unit at the N-terminus, even in the absence of metal. The peptide structure of **22a** follows its bpy counterpart in this respect as well, with the 8-HQ residues in too close proximity to each other likely resulting in steric clash and therefore having a detrimental effect on the helicity of the peptide. The preorganisation of the 8-HQ residues in **20a** and **21a** leads to a Cotton effect consistent with the Λ- and Δ- isomers, respectively. This observed effect is interesting as the complex formation appears to favour the opposite handed isomers to their bpy counterpart peptides **1a** and **13a**, Section 2.4.3 and Section 3.8.2. This difference in behaviour is suggestive of a continuation of the helical H-bonding pattern required for CC formation and could be attributed to the presence of the hydroxyl group on the 8-HQ unit. The theory that this behaviour is caused by H-bonding interactions is further investigated in Section 4.3.4.

Figure 4.5 revisits the helical mapping discussed in Chapter 3. This representation aims to qualitatively demonstrate the directionality of the chelating unit with respect to the CC chains when helical H-bonding is undisturbed. This figure shows that when the chelating

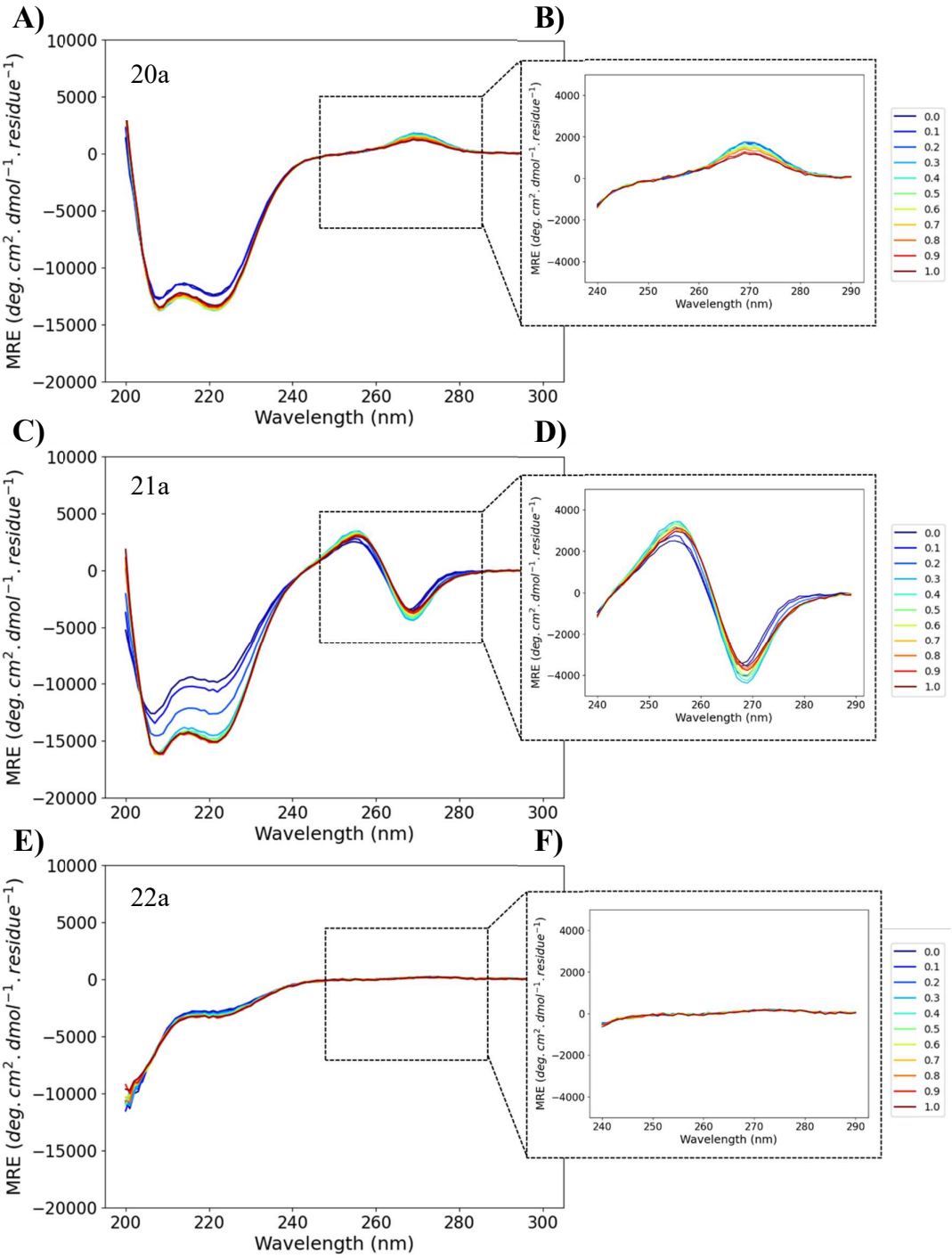

Figure 4.3 - CD and UV absorbance traces of **20a, 21a and 22a** titrations with Co^{2+}. All peptide samples 10 µM in 20 mM aqueous MOPS buffer, pH 7. **A)** Full CD spectrum of **20a** titration with Co^{2+} showing the helicity of the peptide **B)** Zoomed segment of the CD spectrum of **20a** showing the conformation of the 8-HQ units **C)** Full CD spectrum of **21a** titration with Co^{2+} showing the helicity of the peptide **D)** Zoomed segment of the CD spectrum of **21a** showing the conformation of the 8-HQ units **E)** Full CD spectrum of **22a** titration with Co^{2+} showing the helicity of the peptide **F)** Zoomed segment of the CD spectrum of **22a** showing the conformation of the 8-HQ units.

group is present in the *d*-position (orange) a left-handed complex is predicted, however in the *e*-position (yellow), the right-handed complex appears to be preferred. Going back to **Figure 4.3** the CD traces of **20a** and **21a** appear to reflect this behaviour, with **20a** exhibiting a positive exciton couplet, suggestive of a left-handed complex, and **21a** exhibiting a negative exciton couplet, suggestive of the right-handed complex.

Looking in more detail at the titration of **20a** against Co^{2+} (**Figure 4.3 – A)** and **B)**) it can be seen that as the concentration of Co^{2+} ions in solution is increased with respect to **20a**, the signal at 270 nm corresponding to the Λ-isomer decreases in magnitude, suggesting that the preferential formation of that isomer is lost. The UV absorbance trace between 230–290 nm indicates a two-state transition which suggests the binding of the Co^{2+} to the 8-HQ units. Therefore, the loss of chirality with the increasing concentration of Co^{2+} may suggest that the complex formation is strained, resulting in the observed loss of chirality as the complex forms. Alternatively, the Co^{2+} ions could be behaving in a similar manner to the Cu^{2+} ions at high concentrations as has been seen in Chapter 2, where the 8-HQ binding sites become

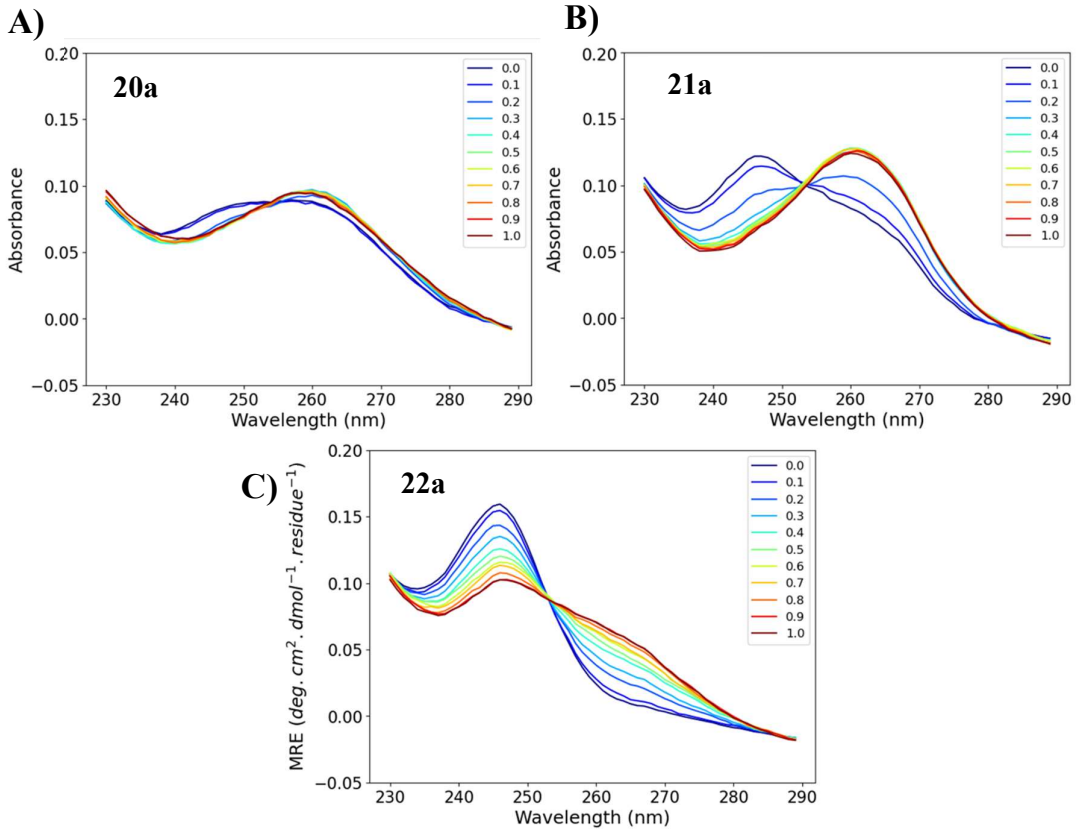

Figure 4.4 – UV absorbance titration traces for **20a**, **21a** and **22a** all 10 μM in 20 mM MOPS, pH 7. **A)** UV absorbance titration of **20a** with Co^{2+} **B)** UV absorbance titration of **21a** with Co^{2+} **C)** UV absorbance titration of **20a** with Co^{2+}.

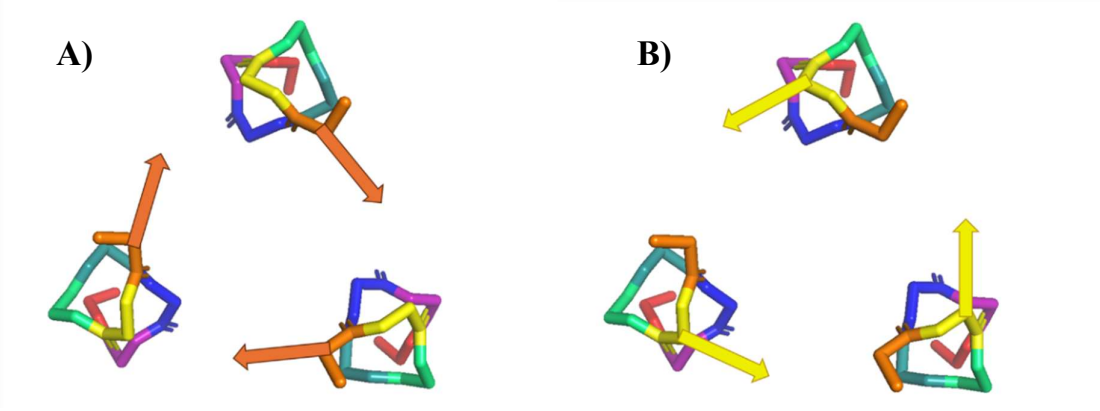

Figure 4.5 – Vector mapping onto a Coiled Coil model with **A)** orange vectors representing the chelating unit in the *d*-position and **B)** yellow vectors representing the chelator in the *e*-position.

saturated as the concentration of the cations increases in solution. However, the CD trace in **Figure 4.3** shows that as the concentration of Co^{2+} is increases there is no loss in the helicity of the peptide unlike what was observed for Cu^{2+} in Chapters 2 and 3. Therefore, the loss in chirality observed in the **20a** complex as the cation concentration increases is likely due to another factor.

Peptide **21a** exhibits an increase in the α-helical content as the concentration of Co^{2+} in solution increases, suggesting that the complex formation supports the inter-strand CC interactions. The negative exciton couplet centred around 260 nm increases in magnitude up to 0.3 eq of Co^{2+}. Beyond this the signal then decreases back to its starting point. Again, there is evidence of the two-state transition in the UV absorbance, with no indication that the Co^{2+} is dissociating from the 8-HQ unit.

As mentioned above the CD trace of the peptide structure of **22a** indicates a high degree of random coil content. As the concentration of Co^{2+} in this titration increases, a slight increase in the helicity can be observed as the signal at 222 nm increases. The signal corresponding to tris-(8-HQ-peptide) complex of **22a** does not change in response to increasing concentrations of Co^{2+}, however, from the UV absorbance we can see the two-state transition from the unbound to bound ligand. This change in the max absorbance signal does however appear much less pronounced than those that were recorded for **20a** and **21a**.

It is worth noting that this point that the magnitude of the exciton-couplets which correspond to the chiral tris-(8HQ-peptide) complexes is significantly larger than those observed for the tris-(bpy-peptide) complexes. The magnitude of **21a** (- 4000 deg·cm^2·dmol^{-1}·residue^{-1}) is approximately 2.6 times larger than the strongest signal observed for the bpy complexes (**1a**

+ Co^{2+}, -1500 deg·cm^2·dmol^{-1}·residue^{-1}). This behaviour could signify that secondary interactions from the 8-HQ units could further bias the chiral preference by stabilising the prearrangement of the units, thus resulting in the stronger Cotton effect that is observed. A comparison of **1a** and **21a** titrations against Co^{2+} can be found in **Figure 4.6**.

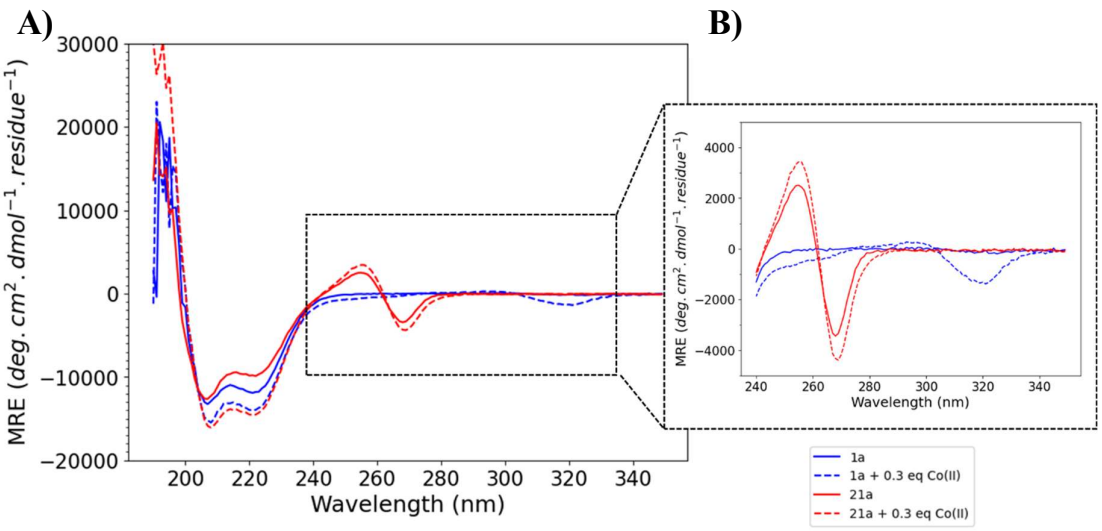

Figure 4.6 - Comparison of the full CD spectra line shapes from the titrations of **A)** Comparison of the full traces of **1a** (blue) and **21a** (red) in both the absence of metal ions (solid lines) and in the presence of 0.3 eq of Co^{2+} (dashed lines) and **B)** Zoomed segment of the full overlayed spectra of **1a** and **21a** absence of metal ions and in the presence of 0.3 eq of Co^{2+} showing the differences in the signals from the bpy and 8-HQ units, respectively.

4.3.2 Ga^{3+}

Literature of 8-HQ complexes is often centred around use of p-block metals and lanthanides in their M^{3+} oxidation states to form the complexes.[131] As a result of this further studies using Ga^{3+} and Al^{3+} salts were undertaken to elucidate any differences in the binding behaviour and resulting chiral complexes. A comparative titration of **1a** against Ga^{3+} was performed to assess if this had any interesting effects however there was no evidence from the UV absorbance or CD signals that the Ga^{3+} was coordinating to the bpy units (see Appendix A).

Titrations of **20a, 21a** and **22a** against Ga^{3+} ions were performed and monitored by CD and UV absorbance spectroscopy (**Figure 4.7** and **Figure 4.8**). At first glance the behaviour of these peptides and their corresponding complexes is consistent with that from their titration against Co^{2+} ions. However, on closer inspection the response from binding to Ga^{3+} ions is much stronger than Co^{2+} in the case of all three peptides in this series, **20a**, **21a** and **22a**. This result is surprising given no coordination was observed for **1a**. Additionally, in the case of **22a** it can also be seen that there is an increase in the α-helical content of the super-secondary peptide structure as the concentration of Ga^{3+} ions increases in solution. This behaviour was not observed in the Co^{2+} ion titrations to the same extent, nor was it observed with the bpy titrations to any notable extent.

It is worth noting that the energy of the exciton couplet corresponding to the isomers of the 8-HQ octahedral complex appears close in wavelength to the signal corresponding to the peptide helicity. This has resulted in a slight additive or subtractive effect in the helical signal which is dependent on the chirality of the resulting complex. The helical signal of a peptide is determined using the ratio of the signals a 208 nm and 222 nm with a larger signal at 222 nm indicating a higher degree of helicity. In this instance the π-π* transition from the 8-HQ moiety interferes slightly with the signal at 222 nm giving an artificially high or low measurement of helicity. For example, the ratio of the signals at 222 nm and 208 nm in **21a** is skewed towards 208 nm. This typically would indicate that this system is less helical, however, the negative exciton couplet centred at 262 nm appears to have a partially cancelling effect on the signal at 222 nm as it would have a positive ellipticity around this wavelength. Comparison to the trace of **20a**, which features a positive exciton couplet shows the ratio of signal at 208 nm to that at 222 nm to be slightly in favour of the 222 nm. This indicates a higher α-helical content, but again, it cannot be interpreted as a more helical system due to the proximity of the exciton couplet arising from the 8-HQ. This behaviour

could help to explain the dramatic increase in helicity with increasing Ga^{3+} concentration in the titration of **22a**.

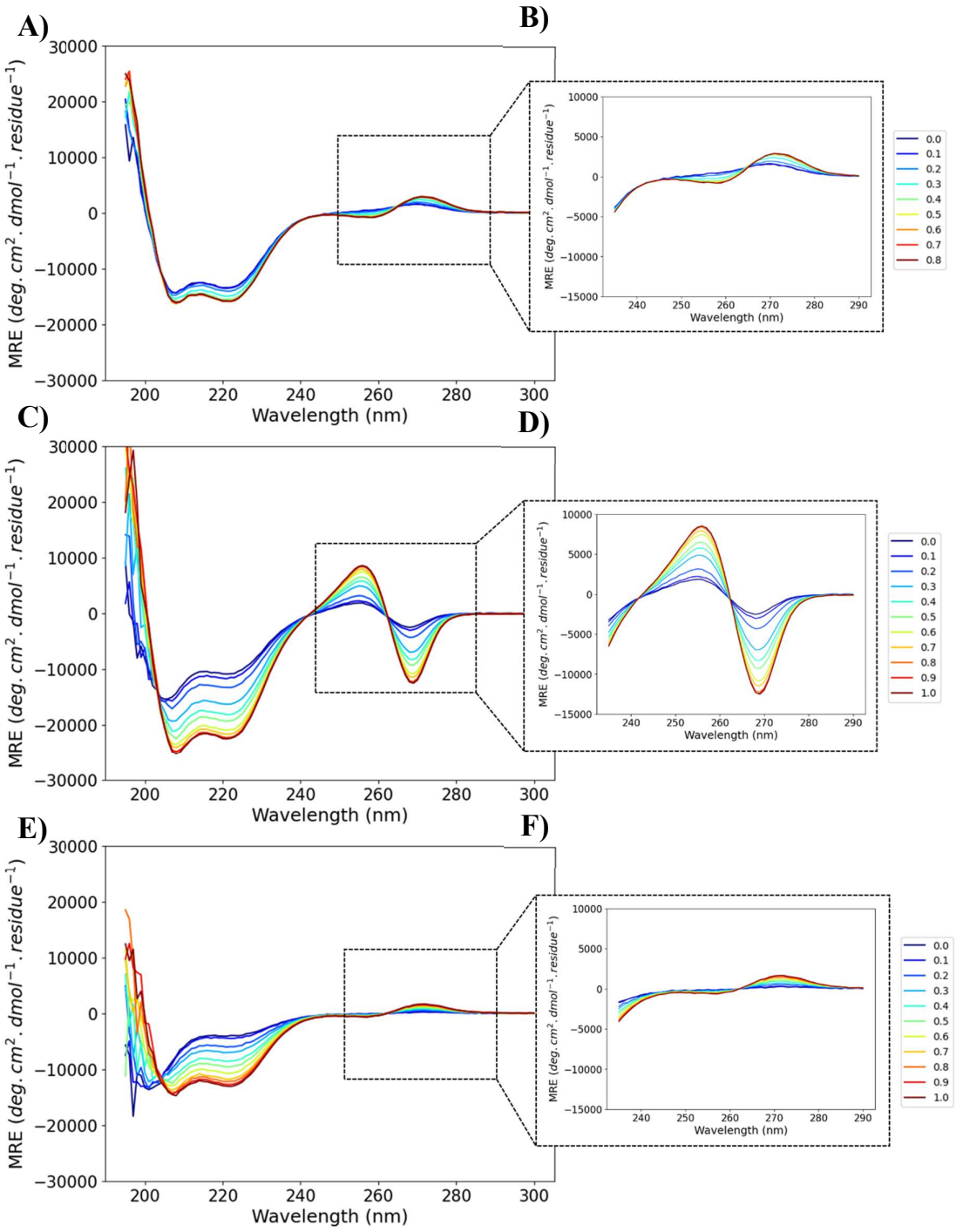

Figure 4.7 - CD and UV absorbance traces of **20a, 21a and 22a** titrations with Ga^{3+}. All peptide samples 10 µM in 20 mM aqueous MOPS buffer, pH 7. **A)** Full CD spectrum of **20a** titration with Ga^{3+} showing the helicity of the peptide **B)** Zoomed segment of the CD spectrum of **20a** showing the conformation of the 8-HQ units **C)** Full CD spectrum of **21a** titration with Ga^{3+} showing the helicity of the peptide **D)** Zoomed segment of the CD spectrum of **21a** showing the conformation of the 8-HQ units **E)** Full CD spectrum of **22a** titration with Ga^{3+} showing the helicity of the peptide **F)** Zoomed segment of the CD spectrum of **22a** showing the conformation of the 8-HQ units.

Closer observation of the CD titration of **20a** against Ga^{3+} shows that as the concentration of Ga^{3+} increases, so does the exciton couplet signal from the 8-HQ. This signal tends to increase until approximately 0.4 eq of Ga^{3+} where it begins to plateau . Similar can be said for the signal from the peptide which shows an increase in magnitude at 222 nm as the titration progresses until 0.4 eq as well. Looking at the UV absorbance (**Figure 4.8**) this behaviour can be explained. The change in absorbance band from 248–262 nm starts to occur at 0.3 eq of Ga^{3+}, which would have the metal in an approximate 1:3 ratio to **20a**. The strength of the UV absorbance signal then continues to increase as the concentration of Ga^{3+} in solution increases rapidly up to 0.5 eq where the signal begins to plateau , reflecting the similar changes observed in the ellipticity, and indicating a slow association of the Ga^{3+} cation. The slower transition from free 8-HQ to bound 8-HQ observed in the spectra above could indicate that the association is slow at the low concentrations used in these experiments (maximum concentration of Ga^{3+} is 10 µM in 2 mL at 1.0 eq) and there could be a kinetic effect occurring which could be rectified by repetition of these experiments at higher concentrations. This concept of kinetic effects in these systems is explored more in relation

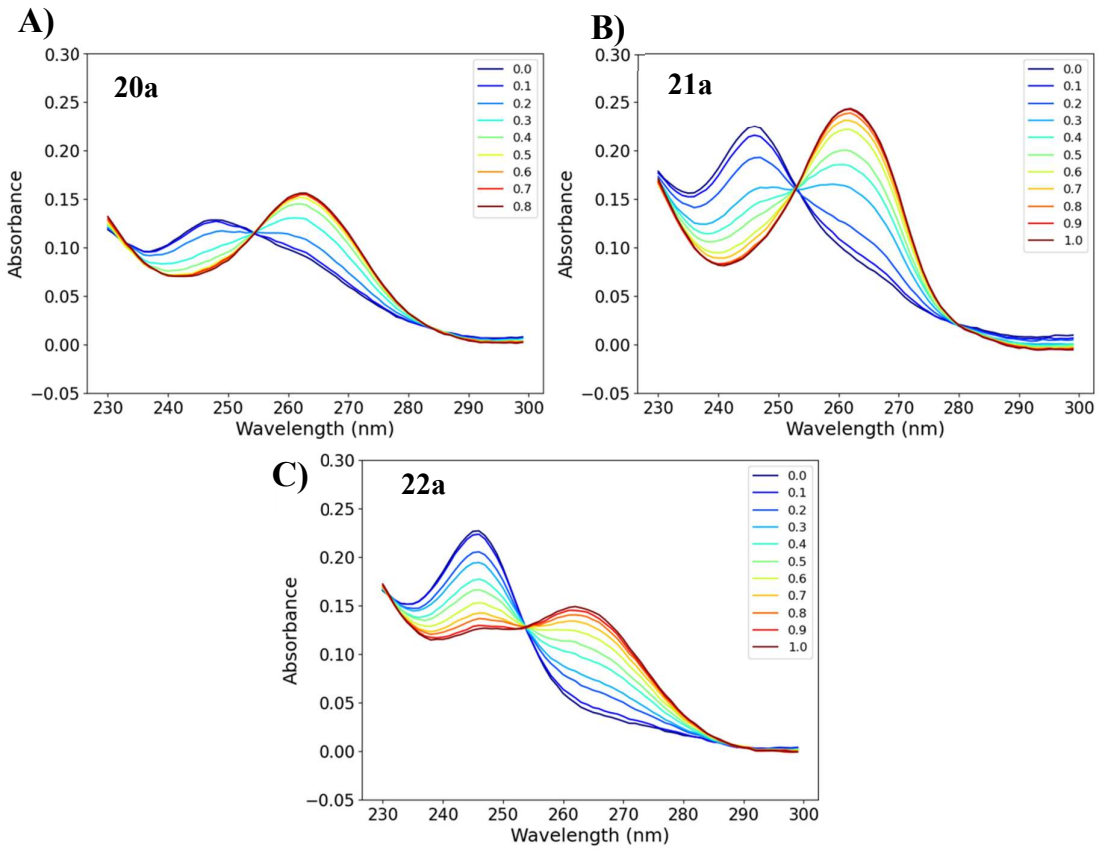

Figure 4.8 – UV absorbance titration traces for **20a**, **21a** and **22a** all 10 µM in 20 mM MOPS, pH 7. **A)** UV absorbance titration of **20a** with Ga^{3+} **B)** UV absorbance titration of **21a** with Ga^{3+} **C)** UV absorbance titration of **20a** with Ga^{3+}.

to $AlCl_3$ (Section 4.3.3) in which it has more of a prominent effect. In the instance of Ga^{3+} max. binding is reached within the timeframe of the experiment and therefore the kinetics were not investigated further due to time constraints and would be beneficial as further work on this project.

The positive exciton couplet that is seen here is consistent with a Λ-tris-(8HQ-peptide) complex, again, showing favourability for the opposite chirality than its bpy counterpart (**Figure 4.9**). Furthermore, the strength of this signal is approximately twice as strong (+2200 deg·cm^2·dmol^{-1}·residue^{-1}) than observed for the bpy complexes.

21a exhibits the strongest effects of all three of the peptides which have been investigated in this chapter as well as this thesis. The exciton couplet signal from the 8-HQ reaches approximately half the strength of the signal from the peptide, exhibiting a magnitude nearly 10 times larger than any of the bpy-functionalised peptides. As was observed with the Co^{2+} titration, **21a** displays stabilisation of the super-secondary structure in response to the addition of Ga^{3+} indicating that this binding favourably stabilises the CC. Both the signal from the peptide region and that of the 8-HQ complex appear to rapidly increase up until 0.6 eq of metal where the signals begin to plateau with further equivalents . The UV absorbance again indicates that the two-state transition from unbound to bound 8-HQ occurs at 0.3 eq of Ga^{3+} consistent with the formation of an octahedral complex. The slow increase in the signals as the concentration increases is likely a feature of kinetics, as mentioned previously

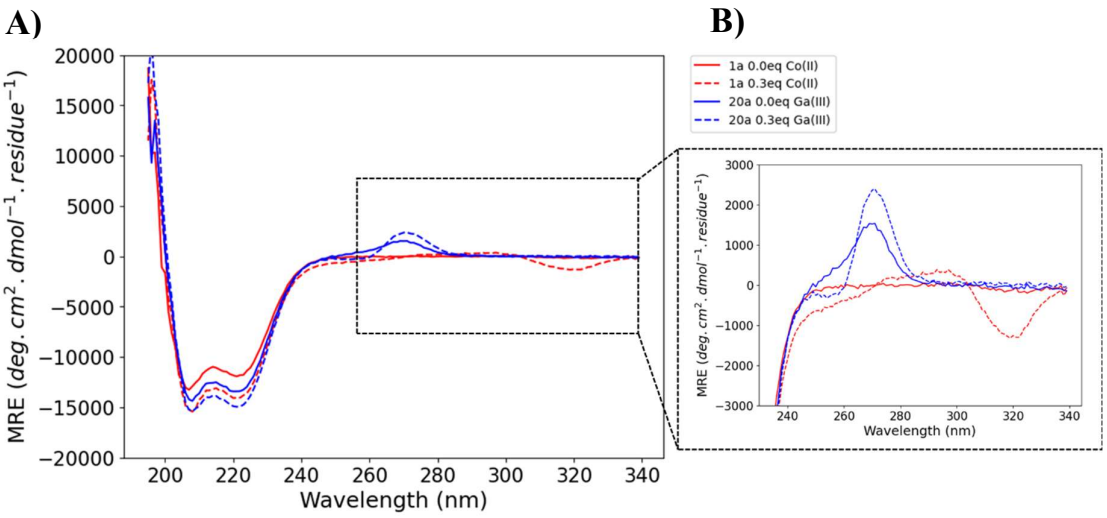

Figure 4.9 - Comparison of the CD traces of peptides **1a** (bpy) (red) and **20a** (8-HQ) (blue) at 0.0 eq of metal ions (Co^{2+} or Ga^{3+}) (solid lines) and 0.3 eq of metal ions (Co^{2+} or Ga^{3+}) (dashed lines). **A)** Full CD overlayed CD spectra of **1a** and **20a** in the absence of metal ions and the presence of 0.3 eq of metal ions, Co^{2+} and Ga^{3+}, respectively **B)** Zoomed segment of the overlayed spectra showing the differences in the chiral information transfer onto the bpy complex in **1a** and the 8-HQ complex in **20a**.

with respect to peptide **20a,** and again would be interesting to investigate as further work. With respect to the chirality of this system, the negative exciton couplet indicates the formation of a Δ-tris-(8HQ-peptide) complex, consistent with the behaviour demonstrated in response to Co^{2+} in Section 4.3.1 but again, the opposite chirality to that of the complex on the N-terminus of peptide **13a** which features a bpy at the *e*-position during its titration against Zn^{2+} as was investigated in Section 3.8.2.

A comparison of the bpy-*e*-position-peptide (**13a**) with increasing concentrations of Zn^{2+} ions with the 8-HQ-*e*-position-peptide (**21a**) titration against Ga^{3+} is made in **Figure 4.10**. This comparison highlights the intensity of the 8-HQ exciton couplet in comparison to what was observed for a bpy in this same position. It also aims to show the difference in chiral preference between the two. In the metal free systems shown in **Figure 4.10 A)** there is an initial difference in α-helical content between the two peptides due to their different sequences with **13a** containing one less AA than **21a**. Despite the absence of Ga^{3+} in the **21a** sample at this point a large negative exciton couplet is still observed around 265 nm indicating the relative strength of the 8-HQ non-covalent interactions in comparison to what was observed for bpy at this position in the sequence. As the Ga^{3+} titration against **21a** proceeds an increase in both the α-helical content of the peptide and more significantly the 8-HQ exciton couplet is observed. This behaviour continues to 1.0 eq where the magnitude of the exciton couplet is approximately half the size of the signal arising from the peptide. Comparatively to what is observed for the bpy-peptide at this point with the exciton couplet

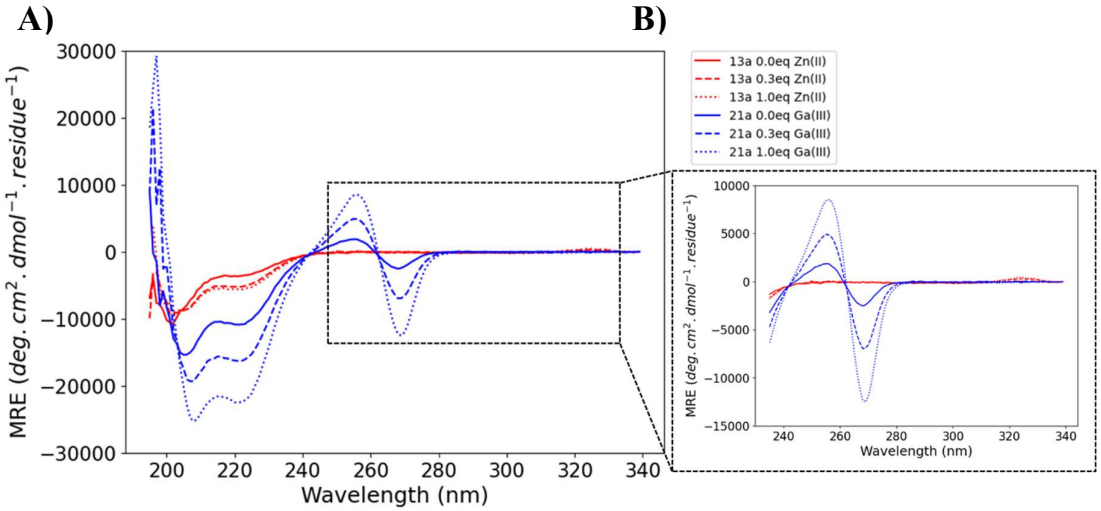

Figure 4.10 - Comparison of the CD traces of peptides **13a** (bpy) (red) and **21a** (8-HQ) (blue) at 0.0 eq of metal ions (Co^{2+} or Ga^{3+}) (solid lines), 0.3 eq of metal ions (Co^{2+} or Ga^{3+}) (dashed lines) and 1.0 eq of metal ions (Co^{2+} or Ga^{3+}) (dotted lines) . **A)** Full CD overlayed CD spectra of **13a** and **21a** in the absence of metal ions and the presence of 0.3 eq of metal ions, Co^{2+} and Ga^{3+}, respectively **B)** Zoomed segment of the overlayed spectra showing the differences in the chiral information transfer onto the bpy complex in **13a** and the 8-HQ complex in **21a**.

from the bpy conformation at is largest only reaching a 20th of the magnitude of the signal from the peptide, the significance of the magnitude observed from peptide **21a** can be put into context.

The behaviour of **22a** in response to Ga^{3+} ions follows the same pattern as with the Co^{2+} titration but with a stronger influence from the Ga^{3+} binding on the final structure of the peptide. Interestingly, as was the case with the Co^{2+} titration, the chiral preference displayed by the complex is Λ. This means that **22a** exhibits the same directionality as the bpy functionalised *a*-position peptide **16a**. This behaviour does not follow that of the other two peptides of this series, **20a** and **21a**, which has been discussed. Peptides **20a** and **21a** exhibit opposite chirality when compared to their bpy-functionalised positional counterparts **1a** and **13a** respectively. The *a*-position peptides **16a** and **22a** does not exhibit this change in chirality upon altering the chelating group (**Figure 4.11**).

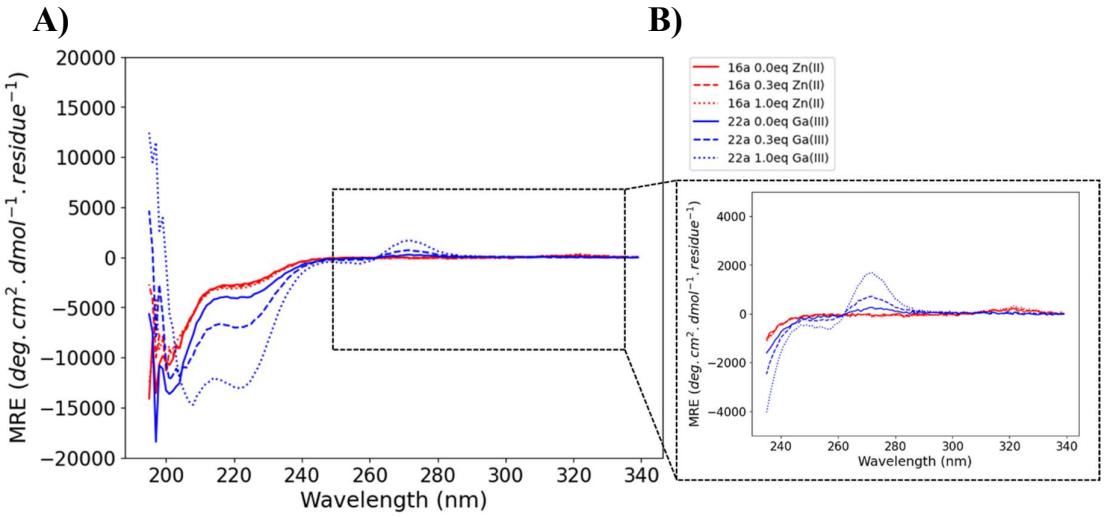

Figure 4.11 - Comparison of the CD traces of peptides **16a** (bpy) (red) and **22a** (8-HQ) (blue) at 0.0 eq of metal ions (Co^{2+} or Ga^{3+}) (solid lines), 0.3 eq of metal ions (Co^{2+} or Ga^{3+}) (dashed lines) and 1.0 eq of metal ions (Co^{2+} or Ga^{3+}) (dotted lines) . **A)** Full CD overlayed CD spectra of **16a** and **22a** in the absence of metal ions and the presence of 0.3 eq of metal ions, Co^{2+} and Ga^{3+}, respectively **B)** Zoomed segment of the overlayed spectra showing the differences in the chiral information transfer onto the bpy complex in **16a** and the 8-HQ complex in **22a**.

4.3.2.1 Variable Temperature CD – 0.3 eq of Ga^{3+}

Variable temperature CD measurements of these three peptides (**20a, 21a, 22a**) in the presence of 0.3 eq of Ga^{3+} were also performed to probe the thermal stability of these systems. The variable temperature CD data from **20a** can be seen in **Figure 4.12**. This data shows that as the peptide is heated towards 80 °C the signal corresponding to the helicity of the peptide slowly reduces in magnitude and tends towards a more random coil, however, helicity is not completely lost like can be seen with the control peptide **1b.** Additionally, the α-helical content increases back to the starting point upon cooling back to 5 °C. The behaviour of this peptide in response to temperature indicates that the helical structure of **20a** is stabilised by the presence of the complex at the N-terminus.

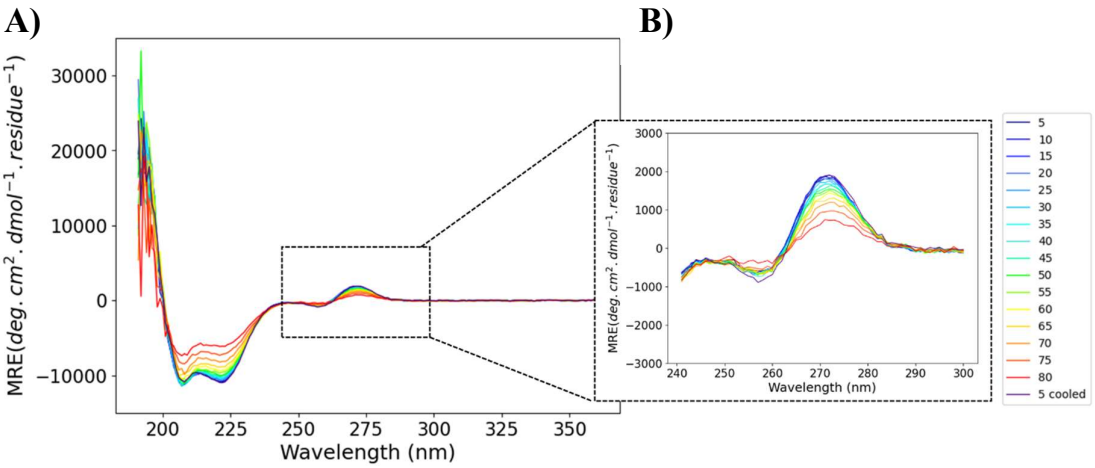

Figure 4.12 - Variable temperature CD spectroscopy of **20a** (10 μM) with 0.3 eq of Ga^{3+} in 20 mM aqueous MOPS buffer, pH 7. **A)** Full variable temperature CD spectrum showing how the peptide structure changes with increasing temperature and after cooling. **B)** Zoomed segment of the full spectrum showing the conformation of the 8-HQ moieties with increasing temperature and after cooling.

With respect to the exciton couplet signal from the complex centred around 262 nm, as the solution is heated the signal from the complex is also lost. Upon cooling back to 5°C, the signal is reinstated back to its original magnitude. The UV absorbance data from this variable temperature experiment indicated that the loss in the magnitude of the chiral signal from the complex occurs as a result of Ga^{3+} dissociation from the binding sites of the 8-HQ units (**Figure 4.13**). This trace shows that as the temperature increases past 60°C the absorbance band at 262 nm begins to reduce in magnitude and shifts to an absorbance band at 245 nm. This indicates that the Ga^{3+} dissociates from the 8-HQ units at these high temperatures. This data also shows that once the temperature is cooled down to 5 °C the Ga^{3+} re-associates as

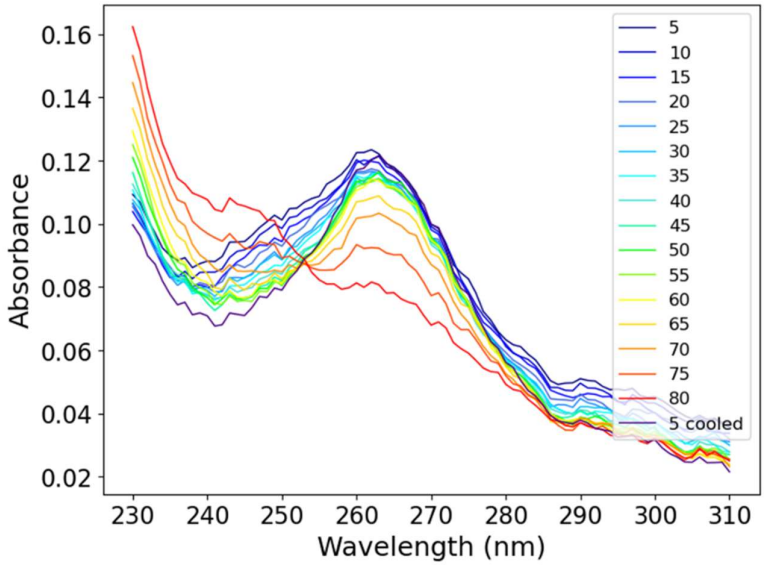

Figure 4.13 – UV absorbance of the variable temperature CD experiment of **20a** (10 μm) with 0.3 eq of Ga^{3+} in 20 mM aqueous MOPS buffer, pH 7.

the absorbance band is again at 262 nm. The UV absorbance data therefore confirms that the reduction in magnitude of the 8-HQ exciton couplet that is observed at higher temperatures occurs as a result of dissociation of the Ga^{3+} ions.

The variable temperature CD of **21a** is displayed in **Figure 4.14**. From this it can be observed that the response of the peptide to the increasing temperature is much less detrimental than what was observed for **20a**. It appears that the formation of the complex at the N-terminus

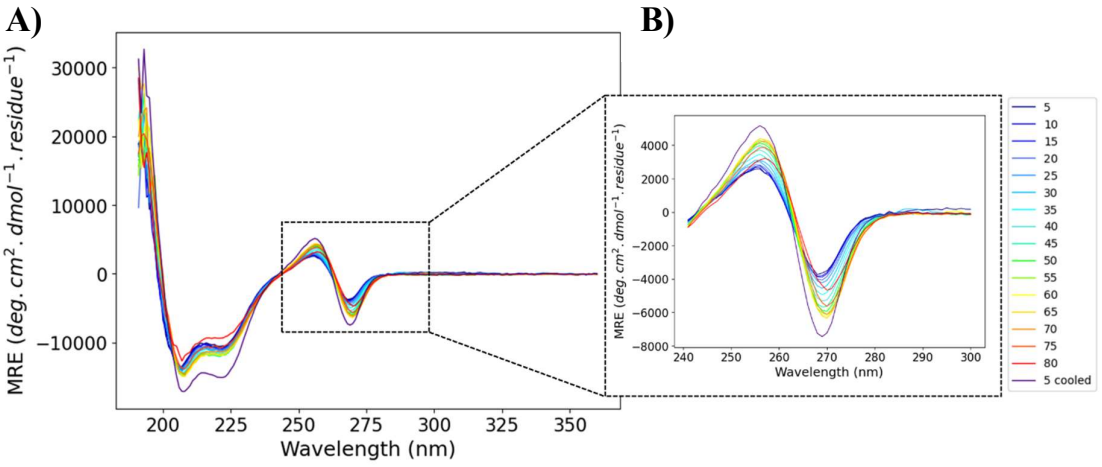

Figure 4.14 - Variable temperature CD spectroscopy of **21a** (10 μM) with 0.3 eq of Ga^{3+} in 20 mM aqueous MOPS buffer, pH 7. **A)** Full variable temperature CD spectrum showing how the peptide structure changes with increasing temperature and after cooling. **B)** Zoomed segment of the full spectrum showing the conformation of the 8-HQ moieties with increasing temperature and after cooling.

of **21a** results in increased stability of the super-secondary structure with very little reduction in the α-helical content as the temperature increases towards 80°C. Additionally what is observed is that up to 60°C the structure is stabilised, with the α-helical content exhibiting an increase. It is only after 60°C that the structure appears to exhibit unfolding of the CC.

Upon cooling back to 5°C the α-helical content of **21a** increases further, showing an increased magnitude when compared to the starting measurement. This behaviour is also exhibited by the CD signal at 262 nm. This signal, as before, increases in magnitude with the increasing temperature up to 60°C, past this point the magnitude decreases as the peptide unfolds. Again, cooling to 5°C at the end of this experiment afforded a significantly larger magnitude in the exciton couplet from the 8-HQ complex. The UV absorbance of this variable temperature CD fully explains this difference in behaviour compared to that of **20a** (**Figure 4.15**). From this data it appears that in the beginning of the experiment, the Ga^{3+} ions are not yet associated to the 8-HQ units, as evidenced by the absorbance band at 245 nm. The discussion of the titration experiment with Ga^{3+} for this peptide alluded to the idea that the Ga^{3+} could be slow kinetically when associating to the 8-HQ units. Upon performing this experiment, the Ga^{3+} was added immediately before the first measurement was taken, therefore it appears that the Ga^{3+} doesn't begin to associate with the 8-HQ units until at approximately 40°C. This has been addressed in Chapter 4.3.2.2.

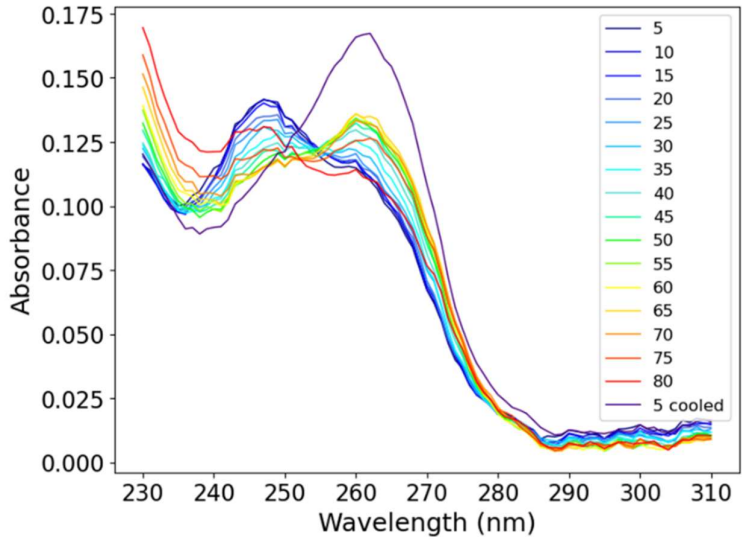

Figure 4.15 - UV absorbance of the variable temperature CD experiment of **21a** (10 μm) with 0.3 eq of Ga^{3+} in 20 mM aqueous MOPS buffer, pH 7

As the experiment progresses and the temperature increases, the Ga^{3+} binds to the 8-HQ units as the two-state transition can be observed as occurring at around 40–45°C. The Ga^{3+} ions then remain bound up to 60°C where the ions begin to dissociate again. Following this,

cooling back to 5°C results in the bound state being reinstated with a relatively large absorbance. This behaviour combined with what is observed in the CD trace and indicates that the implied increase in stability comparative to **20a** cannot be attributed to an increased stability as a result of chelation, as the UV absorbance demonstrates that no chelation has occurred until the temperature was increased. This variable temperature experiment has been re-run at a higher starting concentration of Ga^{3+} with 30 minutes allowed for equilibration in solution in the next section (4.3.2.2).

The variable temperature CD of **22a** has been plotted and shown in **Figure 4.16**. This data shows that in this peptide, increasing the temperature to 80°C has very little effect on the folding and the 8-HQ binding. The increase in temperature does not reduce the α-helical content of **22a**, however, the structure of this peptide is largely unfolded to begin with. The signal at 270 nm from the 8-HQ exciton couplet does show an increase in magnitude upon cooling however and this could indicate that binding has only taken place after the annealing process has concluded. The UV absorbance from this experiment (**Figure 4.17**) shows that as was seen with **21a**, the 8-HQ units remain entirely unbound at the beginning of the experiment and actually appears to remain in this state throughout the experiment. Following the cooling stage the signal does appear to shift with a slight increase in the absorbance between 255–290 nm. This lineshape post-cooling is somewhat reminiscent of what was observed previously during the Ga^{3+} titration of **22a** as the 8-HQ transitioned from unbound to bound.

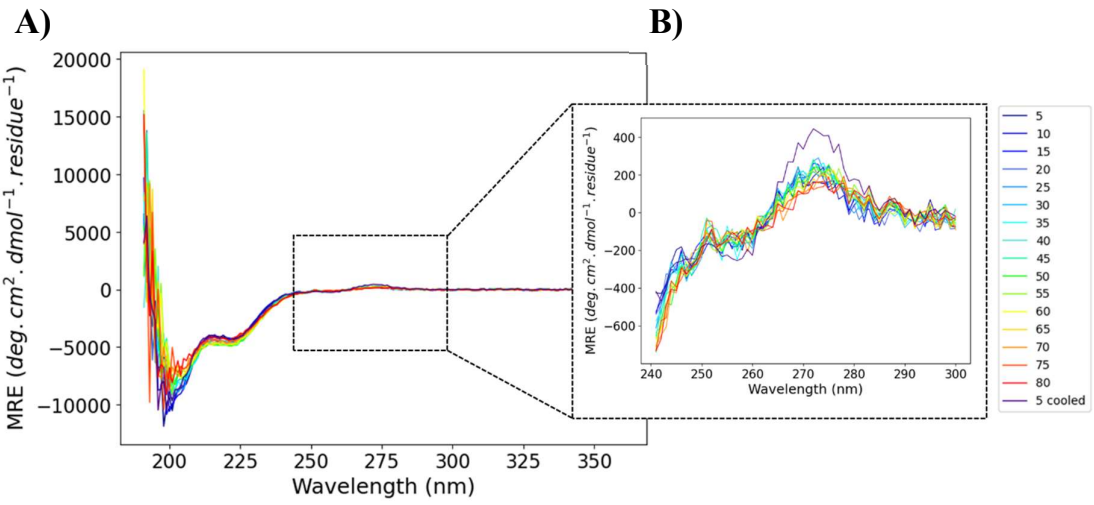

Figure 4.16 - Variable temperature CD spectroscopy of **22a** (10 μM) with 0.3 eq of Ga^{3+} in 20 mM aqueous MOPS buffer, pH 7. **A)** Full variable temperature CD spectrum showing how the peptide structure changes with increasing temperature and after cooling. **B)** Zoomed segment of the full spectrum showing the conformation of the 8-HQ moieties with increasing temperature and after cooling.

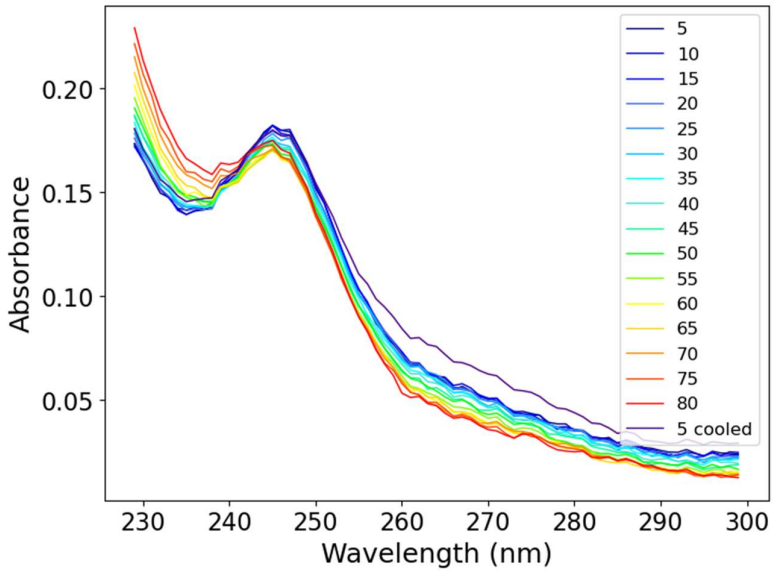

Figure 4.17 - UV absorbance of the variable temperature CD experiment of **22a** (10 μm) with 0.3 eq of Ga^{3+} in 20 mM aqueous MOPS buffer, pH 7

In an attempt to eliminate some of the issues encountered in these experiments regarding the unbound Ga^{3+} at the start point of the experiment, these experiments were repeated at a higher concentration of Ga^{3+} and were allowed to pre-equilibrate before beginning the variable temperature experiment for 30 min.

4.3.2.2 Variable Temperature CD – 1.0 eq of Ga^{3+}

As stated previously, the variable temperature experiments of **20a**, **21a**, and **22a** were repeated using 1.0 eq of Ga^{3+} and were allowed to pre-equilibrate for 30 min.

The variable temperature CD and UV of the **20a** sample under the above stated conditions is plotted in **Figure 4.18**. The behaviour exhibited in this experiment is similar to what was seen in the 0.3 eq of Ga^{3+} version in Section 4.3.2.1. The main difference is the strength of the signals with the α-helicity increasing in magnitude comparative to the system with 0.3 eq of Ga^{3+} as well as the exciton couplet from the 8-HQ increasing to almost twice the intensity in this sample as a result of the increased complex formation with 1.0 eq Ga^{3+}.

As the temperature increases, the α-helicity of the peptide starts to slowly reduce which then occurs more rapidly as the sample reaches 60 °C. However, even at the highest measured temperature, **20a** still exhibits some degree of α-helicity, indicating the stability of the system due to the terminal tris-(8-HQ-peptide) complex with Ga^{3+}. The exciton couplet signal from

the 8-HQ conformation exhibits similar behaviour to this, with the signal reducing relatively consistently as the temperature increases.

Interestingly, upon cooling back to 5°C , unlike the 0.3 eq of Ga^{3+} sample, the exciton couplet signal from this sample of **20a** does not quite return to the observed starting point. Despite this, the signal from the UV absorbance does return to the max. absorbance that was observed at the first measurement. This UV absorbance behaviour suggests the Ga^{3+} returns to being fully associated to the 8-HQ units. Additionally, the signal corresponding to the α-helicity of peptide **20a** does return to the same magnitude observed during the first measurement. The combination of these three pieces of data suggests that after heating and subsequent cooling, some of the observed chiral preference in the 8-HQ complex is lost. From the UV absorbance it can be seen that as the sample is heated towards 75°C, the signal suggests that the Ga^{3+} is

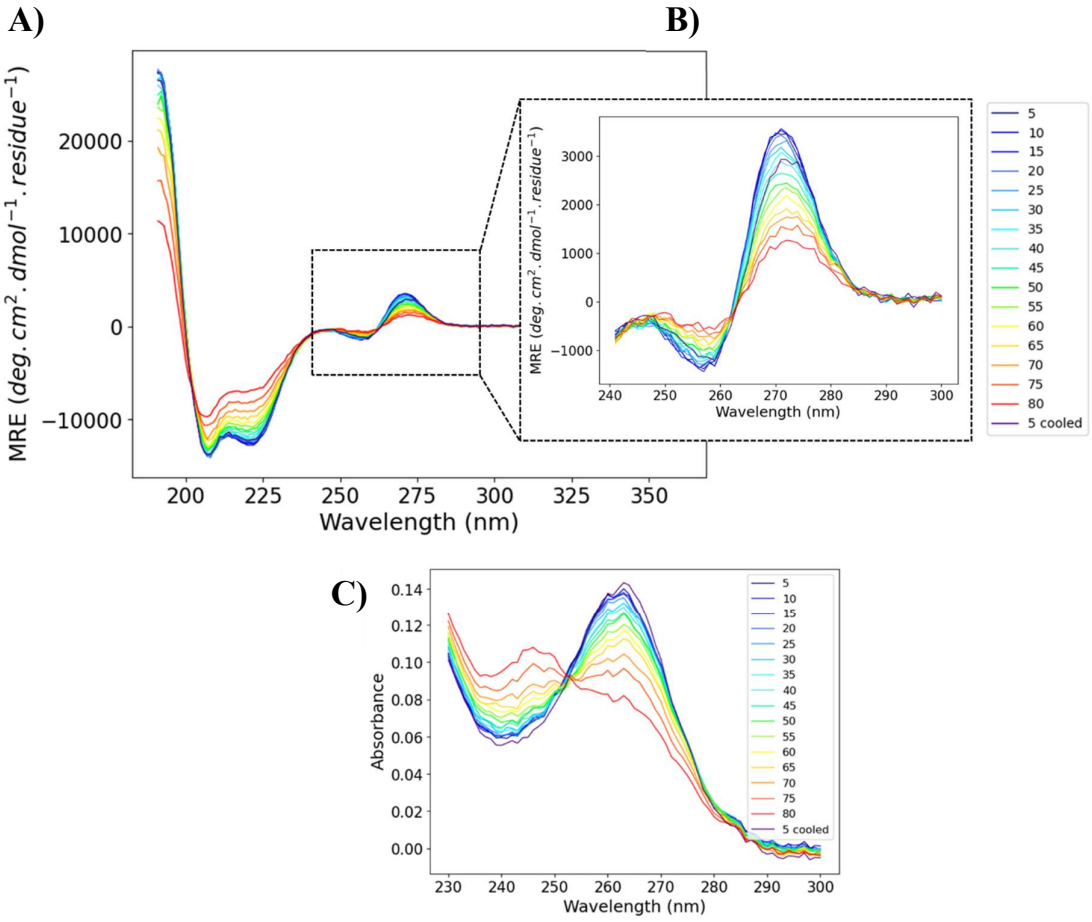

Figure 4. 18 - Variable temperature CD and UV absorbance spectroscopy of **20a** (10 μM) with 1.0 eq of Ga^{3+} in 20 mM aqueous MOPS buffer, pH 7. **A)** Full variable CD spectrum of **20a** preequilibrated with 1.0 eq of Ga^{3+} showing the change in structure with increasing temperature. **B)** Zoomed segment of the full spectrum of **20a** showing the changes in the 8-HQ complex conformation with increasing temperature. **C)** UV-absorbance of the variable temperature CD experiment showing the change in absorbance with increasing temperature.

dissociating from the 8-HQ. It could be that as the sample is cooled past this point and the Ga^{3+} re-associates that it does so initially in a way which saturates more of the 8-HQ binding sites as a result of the higher concentration of Ga^{3+} in solution. Allowing the sample to equilibrate longer before taking the final measurement could mitigate this if the system and complex formation exhibits dynamic behaviour.

The data from the variable temperature CD and UV absorbance experiment for **21a** is plotted in **Figure 4.19**. From this data it can be observed that re-running this experiment at the higher concentration of 1.0 eq of Ga^{3+} and allowing time for equilibration eliminated the issues encountered in Section 4.3.2.1.

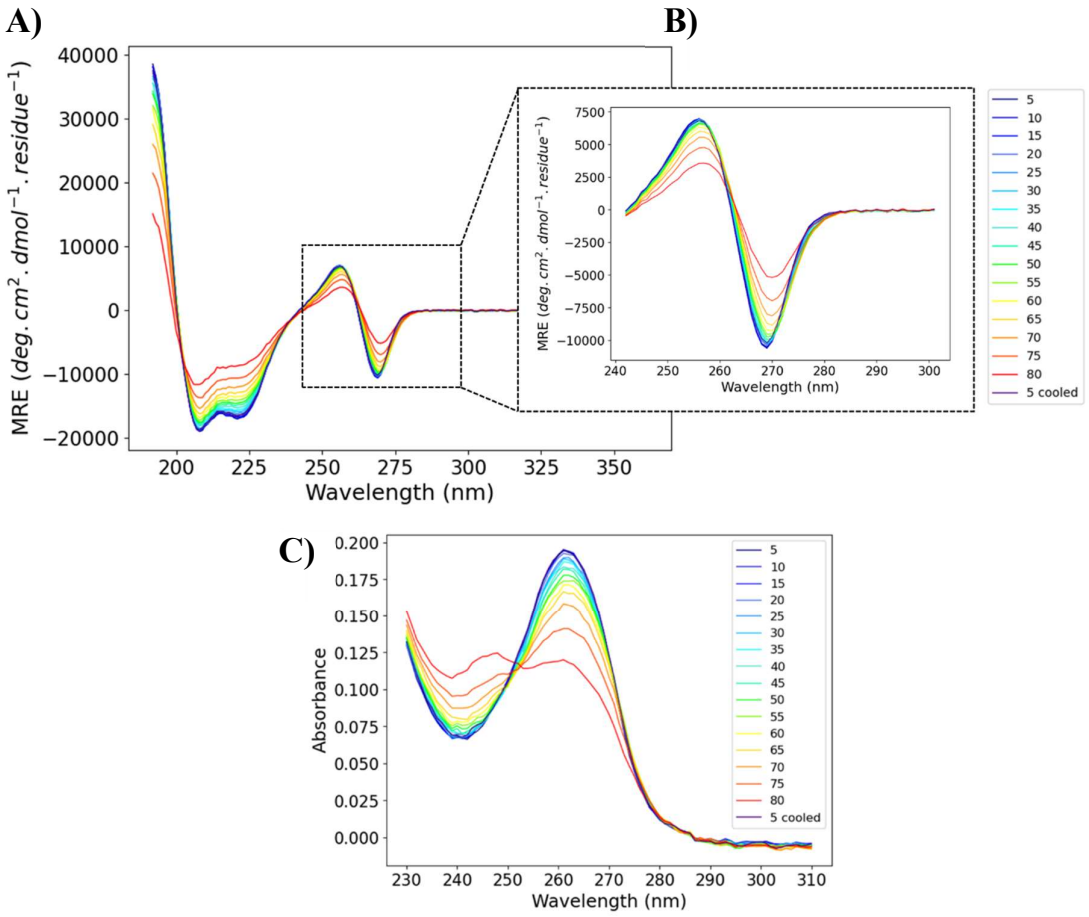

Figure 4.19 - Variable temperature CD and UV absorbance spectroscopy of **21a** (10 μM) with 1.0 eq of Ga^{3+} in 20 mM aqueous MOPS buffer, pH 7. **A)** Full variable CD spectrum of **21a** preequilibrated with 1.0 eq of Ga^{3+} showing the change in structure with increasing temperature. **B)** Zoomed segment of the full spectrum of **21a** showing the changes in the 8-HQ complex conformation with increasing temperature. **C)** UV-absorbance of the variable temperature CD experiment showing the change in absorbance with increasing temperature.

The data here shows that as the temperature of the **21a** + 1.0 eq of Ga^{3+} sample is increased the helicity of the peptide remains relatively stable up to 60°C, following this point it begins to decrease more rapidly. As was observed for the sample of **20a**, there is still a degree of α-helicity observed after heating to 80°C, indicating the stability of this system. The behaviour of the 8-HQ exciton couplet reflects what has been observed for the helicity. As the sample is heated the magnitude of the exciton couplet stays relatively consistent up to about 70°C. Following this point again the more rapid reduction in magnitude is observed. Observation of the UV absorbance shows that above 70°C the Ga^{3+} begins to dissociate from the 8-HQ units. The UV absorbance behaviour could indicate two possiblities. First, it could be that the dissociation of the Ga^{3+} ions from the 8-HQ units reduces the stability of the CC resulting in the loss of α-helical content at higher temperatures. Alternatively, the opposite could be true, at the higher temperatures the CC may become so unstable that it begins to unfold forcing the 8-HQ units apart. Given the dissociation in the UV absorbance it is more likely that the former of these suggestions is true. This could be tested by comparing to a variable temperature CD of a metal free sample of **21a** and assessing its stability at higher temperatures.

Finally, looking at the variable temperature CD experiment of **22a** + 1.0 eq Ga^{3+} the temperature dependant behaviour can be observed (**Figure 4.20**). From these spectra it can be seen that as the temperature increases there is no significant change in the peptide structure as at the beginning of the experiment the CD trace of **22a** resembles a relatively unstructured peptide. The exciton couplet from the 8-HQ units starts with a magnitude of approximately +200 $deg \cdot cm^2 \cdot dmol^{-1} \cdot residue^{-1}$, as the experiment progresses and the temperature increases this signal tends towards zero, becoming completely flat at a temperature of approximately 55°C. The behaviour of the UV absorbance from this experiment reflects this with the 8-HQ-bound signal (265 nm) reducing with the increasing temperature transitioning to the 8-HQ-free signal (242 nm) at approximately 50°C.

Comparatively to both **20a** and **21a**, **22a** shows decreased stability. This is likely a feature of having the 8-HQ at the *a*-position as was discussed in Section 3.8.2 with respect to a bpy unit. The data in that section suggested that having the chelating unit at that central position in the sequence led to unfavourable steric interactions which resulted the reduced folding comparative to having the chelating unit for example in a *d*-position.

The data in this section reflects what was observed in Section 3.8.2 with the *a*-position resulting in the least stabilising interactions and the least chiral preference in the resulting complexes. Interestingly, unlike the bpy-peptides where the *d* and *e*-positions showed

comparable magnitudes in the CD, with the 8-HQ-peptides the *e*-position shows a significant increase in magnitude compared to the *d*-position.

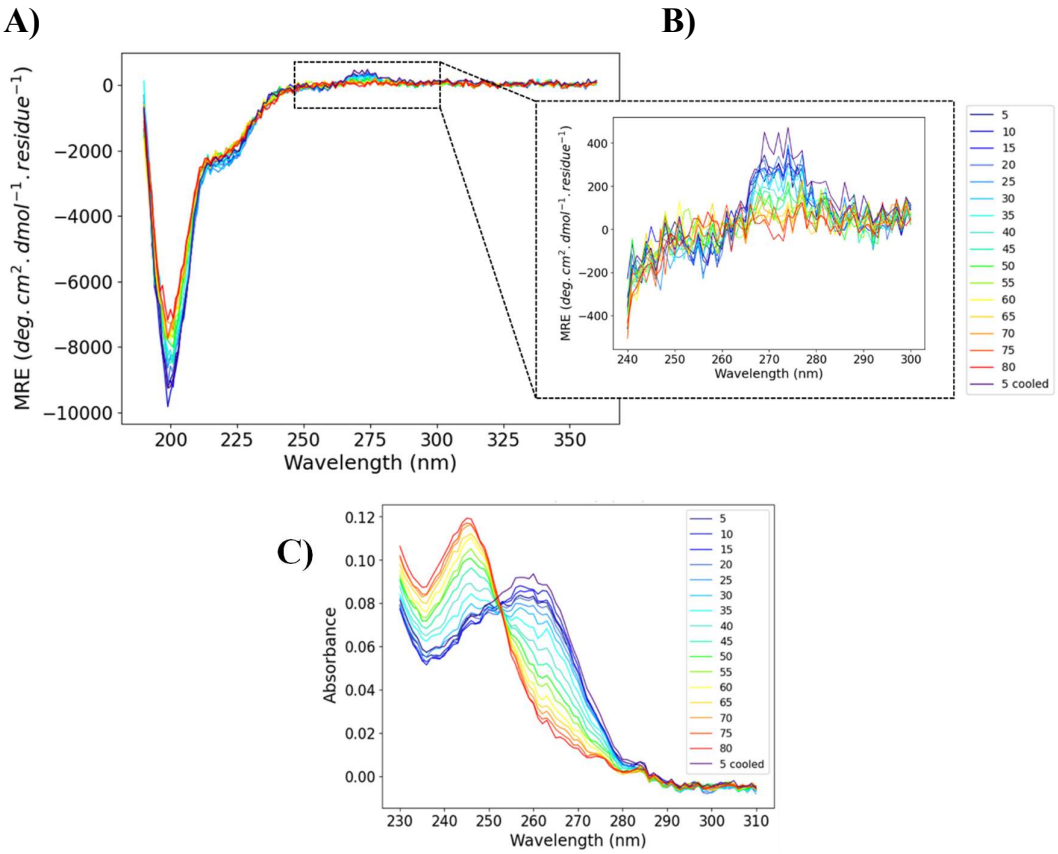

Figure 4.20 - Variable temperature CD and UV absorbance spectroscopy of **22a** (10 μM) with 1.0 eq of Ga^{3+} in 20 mM aqueous MOPS buffer, pH 7. **A)** Full variable CD spectrum of **22a** preequilibrated with 1.0 eq of Ga^{3+} showing the change in structure with increasing temperature. **B)** Zoomed segment of the full spectrum of **22a** showing the changes in the 8-HQ complex conformation with increasing temperature. **C)** UV-absorbance of the variable temperature CD experiment showing the change in absorbance with increasing temperature.

4.3.3 Al^{3+}

Al^{3+} was also explored as the metal for the formation of these complexes. Al^{3+} is another p-block metal (Group 13) like Ga^{3+}, which was hypothesised to have a stronger preference than first row TMs for the formation of octahedral complexes with 8-HQ moieties.[127]

This titration against Al^{3+} ions was only performed for peptide **20a** (**Figure 4.21**). The behaviour exhibited in this titration was similar to what was observed for the Ga^{3+} titration for peptide **20a**. However, in this titration there is no significant change in the α-helical content as the concentration of metal ion increases in solution. Additionally, the magnitude of the Cotton effect observed around 262 nm at the end of the titration is about 500 $deg \cdot cm^2 \cdot dmol^{-1} \cdot residue^{-1}$ less than that from the Ga^{3+} titration despite it being the same

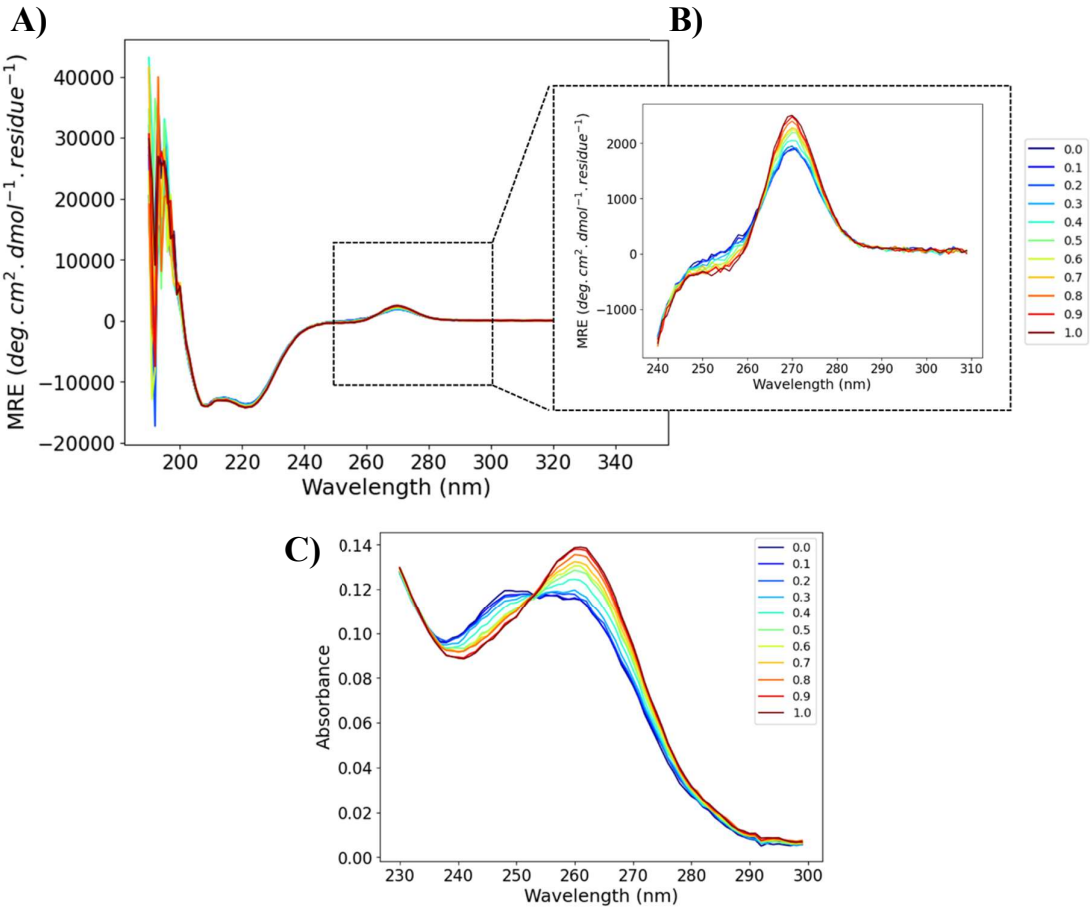

Figure 4.21 - CD and UV absorbance spectroscopy of **20a** (10 μM) titration with Al^{3+} in 20 mM aqueous MOPS buffer, pH 7. **A)** Full CD spectrum of **20a** with increasing concentration of Al^{3+} showing there is no change in peptide structure with increasing equivalents of Al^{3+}. **B)** Zoomed segment of the full spectrum of **20a** showing the changes in the 8-HQ complex conformation with increasing equivalents of Al^{3+}. **C)** UV-absorbance of the CD experiment showing the change in absorbance with equivalents of Al^{3+} exhibiting the transition from uncoordinated 8-HQ to Al^{3+} coordinated 8-HQ.

peptide. From the UV absorbance spectra it can be seen that the two-state transition indicating the binding of the Al^{3+} to the 8-HQ appears to transition more slowly than was observed for the Ga^{3+}. This suggests that the rate of association of the Al^{3+} is slower than the Ga^{3+}.

Because of this observation a short time-based analysis of this peptide was performed in which 0.3 eq of Al^{3+} was pipetted into a 10 µM solution of peptide **20a**. A CD measurement was performed immediately, and then a second measurement was recorded after letting the sample equilibrate for 120 min. The results of this study can be seen in **Figure 4.22**. From this it can be seen that over time the Cotton effect from the 8-HQ units increases significantly, indicating there is some kinetic effects occurring in this system.

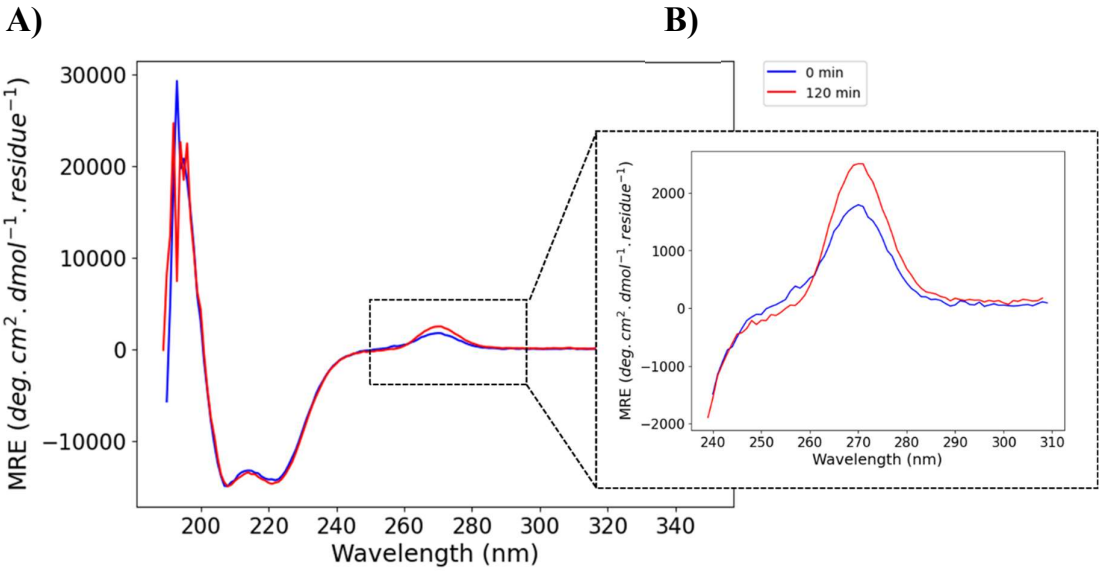

Figure 4.22 - CD traces of **20a** (10 µM) with 0.3 eq of Al^{3+} at 0 min (blue line) and 120 min after addition of Al^{3+} (red line). Measurements taken at room temperature in 20 mM aqueous MOPS buffer, pH 7. **A)** Full CD spectrum showing the difference between measurement taken of **20a** with 0.3 eq of Al^{3+} after 0 min and 120 min. **B)** Zoomed segment showing the difference in the 8-HQ conformation after 0 min and 120 min with 0.3 eq of Al^{3+}.

From these results a longer study in which 0.3 eq of Al^{3+} was added to a 10 µM solution of **20a** and CD measurements recorded at 0, 15, 30, 60, 120 and 240 min was performed. The aim of this experiment was to determine the optimal time of equilibration with the metal before recording CD measurements (**Figure 4.23**). From this data it can be observed that similar to the earlier experiment (**Figure 4.22**), the initial Cotton effect around 262 nm has a magnitude of approximately +1700 $deg \cdot cm^2 \cdot dmol^{-1} \cdot residue^{-1}$. After 15 minutes the second measurement shows an increase in this signal by approximately 800 $deg \cdot cm^2 \cdot dmol^{-}$

^{1}·residue^{-1} which then settles after 30 min at a signal magnitude of approximately +2700 deg.cm^{2}.dmol^{-1}.residue^{-1} increasing by a further 200 deg.cm^{2}.dmol^{-1}.residue^{-1}. From this data it can be stated that an optimal equilibration time of 30 min at room temperature would be required for any further experiments with Al^{3+}. Alternatively, heating the sample with the Al^{3+} for a period of time before running the CD measurements could reduce the time taken for the equilibration, but this could be at the detriment of the peptide structure depending on the temperature required.

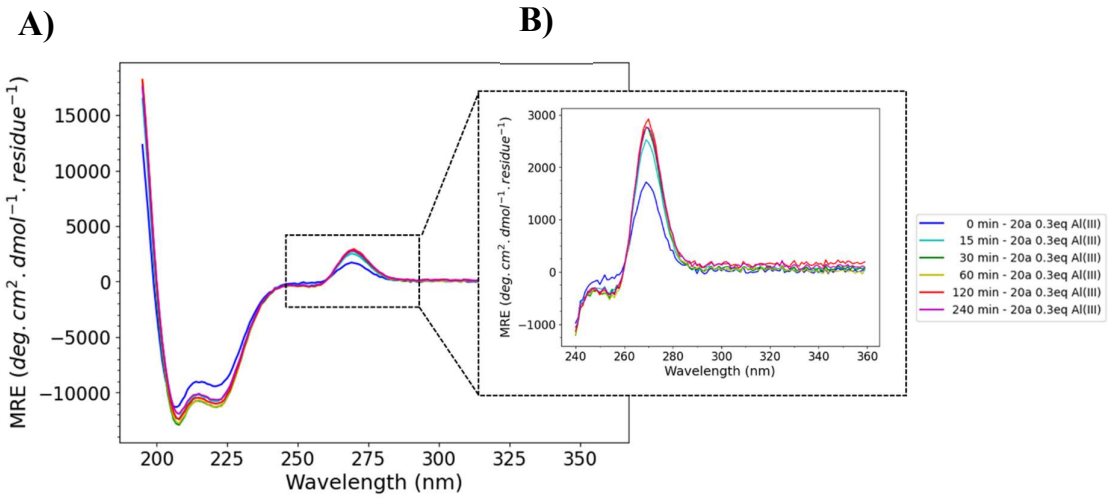

Figure 4.23 – Overlay of the CD traces of **20a** (10 μM) with 0.3 eq of Al^{3+} at 0 min (blue line), 15 min (cyan), 30 min (green), 60 min (yellow), 120 min (red) and 240 min (magenta) after addition of Al^{3+}. Measurements taken at room temperature in 20 mM aqueous MOPS buffer, pH 7. **A)** Full CD spectrum showing the difference between measurement taken of **20a** at these time points. **B)** Zoomed segment showing the difference in the 8-HQ conformation at these time points.

Comparison of the signal after 30 min in the presence of 0.3 eq of Al^{3+} and the signal from the Ga^{3+} titration with **20a** shows that these signals now have a comparable magnitude (**Figure 4.24**).

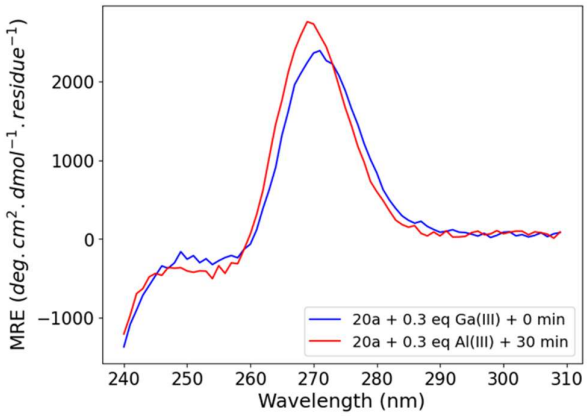

Figure 4.24 – Comparison of the 8-HQ region of the CD spectra of **20a** with 0.3 eq of Ga^{3+} (blue) with the CD spectra of **20a** with 0.3 eq of Al^{3+} after 30 min equilibration (red).

4.3.4 pH Study

The difference in chirality observed for the 8-HQ functionalised peptides compared to the analogous bpy functionalised peptides lead to the hypothesis that the 8-HQ units H-bonding capability might strengthen inter-strand interactions resulting in the opposite handedness complex being the more stable conformation. In order to test this, the pH of the buffer solution for the samples was changed and CD measurements taken both in the absence and presence of metal was undertaken.

An initial analysis of an unbuffered 10μM solution of peptide **20a** in the presence of 1.0 eq of NaOH resulted in the CD spectra plotted in **Figure 4.25** alongside comparison to the MOPS buffered solution of **20a**. After taking a measurement in the absence of Ga^{3+} ions a measurement was also recorded once 0.3 eq of Ga^{3+} was added.

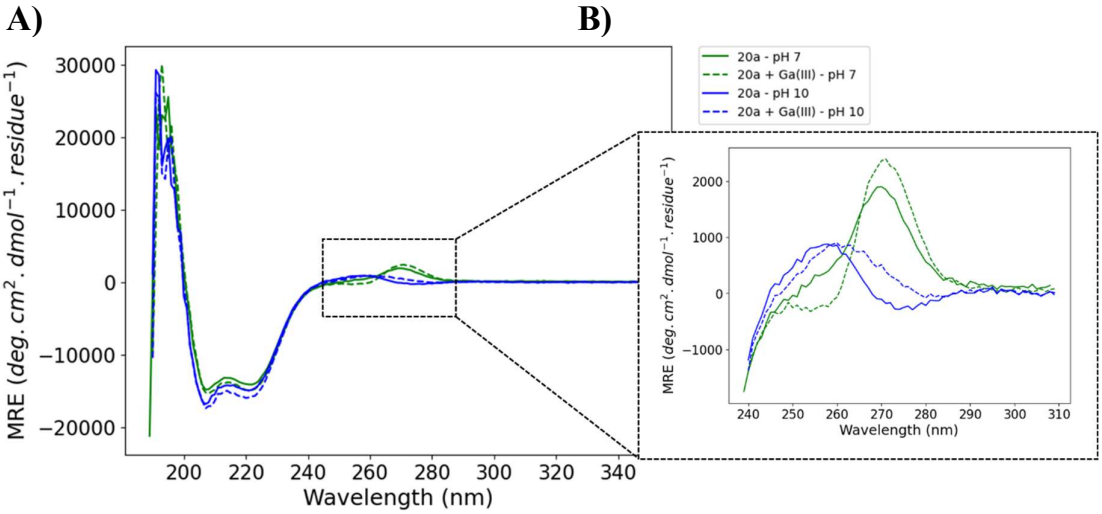

Figure 4.25 - CD traces of **20a** (10 μM) in 20 mM MOPS buffer, pH 7 (solid green line = metal free, dotted green line = 0.3 eq Ga^{3+}) and **20a** (10 μM) in H_2O with 1.0 eq of NaOH (solid blue line = No Ga^{3+}, dotted blue line = 0.3 eq Ga^{3+}). **A)** Full CD spectrum comparison **B)** Zoomed segment highlighting the region where the signal for the 8-HQ appears.

From this data it can be seen that raising the pH of this system using NaOH resulted in the loss of the signal indicating the Λ-tris-(8HQ-**20a)** arrangement and instead displaying a weak signal more consistent with the Δ-tris-(8HQ-**20a)** arrangement. The pK_a of the 8-HQ -OH functionality is 9.8,[130] therefore in this solution of pH 10, the 8-HQ should be partially deprotonated. The spectra indicates that at this high pH the loss of H-bonding capability of the 8-HQ units results in a slight favourability of the opposite handed arrangement. However, it is worth noting that in this experiment, NaOH was used, introducing OH^- ions into the system, which can contribute to the coordination sphere of the 8-HQ-metal-complex.

Additionally, introduction of the Na^+ ions could interfere with the binding to Ga^{3+}. Introduction of Ga^{3+} to this system does strengthen the Λ-tris-(8HQ-**20a)** signal in the pH 7 system as has been observed previously, but in the case of the pH 10 system the Δ-tris-(8HQ-**20a)** signal appears to shift to a longer wavelength.

Following these preliminary results a small series of buffer solutions of pH 4, 6 and 8 were made up and used for samples of **20a**, **21a** and **22a** to analyse the effects of changing the pH on the observed chirality of the chelating units at the N-terminus (**Table 4.2**).

Table 4.2 – Buffers and measured approximate pH values.

Buffer	pH
Ammonium Acetate	4
MOPS	6
Ammonium Bicarbonate	8

The CD measurements of **20a** under these conditions can be seen in **Figure 4.26**. From this it can be seen that moving towards a more acidic pH results in a stronger Cotton effect from the 8-HQ units, additionally, a stronger signal is visible from the peptide. Conversely, at higher pH, this signal is shifted to resemble the weak Δ-tris-(8HQ-**20a)** signal that was observed in the previous study with NaOH. The pK_a of the quinoline is 5.1[130], this suggests

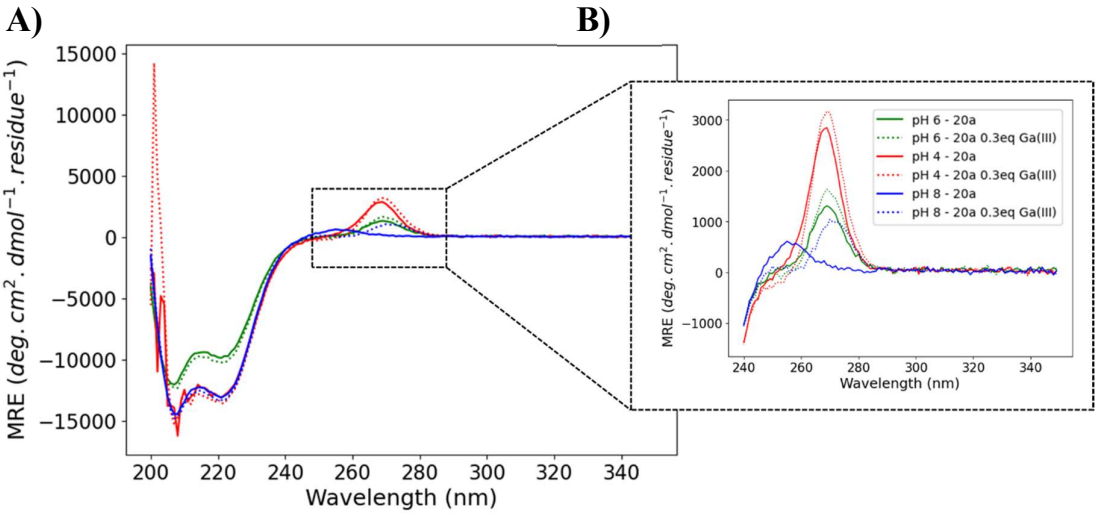

Figure 4.26 - CD traces of **20a** (10 μM) in 20 mM aqueous MOPS buffer, pH 6 (solid green line = No Ga^{3+}, dotted green line = 0.3 eq Ga^{3+}) and **20a** (10 μM) in 20 mM aqueous NH_4HCO_3 buffer, pH 8 (solid blue line = No Ga^{3+}, dotted blue line = 0.3 eq Ga^{3+}) and **20a** (10 μM) in 20 mM aqueous NH_4OAc buffer, pH 4 (solid red line = No Ga^{3+}, dotted red line = 0.3 eq Ga^{3+}). **A)** Full CD spectrum comparison **B)** Zoomed segment highlighting the region where the signal for the 8-HQ appears.

that at the lower pH, both the hydroxyl and the quinoline nitrogen of the 8-HQ functionalities should be partially in their protonated forms.

From the UV absorbance of this experiment (**Figure 4.27**) from pH 6 to pH 8 the absorbance band appears at 246 nm which then shifts to 265 nm upon the addition of Ga^{3+} ions. This transition is understandably more prominent in the pH 8 system, as the functional groups of the 8-HQ should be in equilibrium of protonated/deprotonated at this pH making them more susceptible to complexation.[127] The UV absorbance of the pH 4 solution of **20a** shows different behaviour, with a broad absorbance band of between approximately 250–261 nm with the absorbance band being observed at 250 nm. Addition of Ga^{3+} results in the absorbance band red-shifting towards 262 nm indicating the formation a bound species.

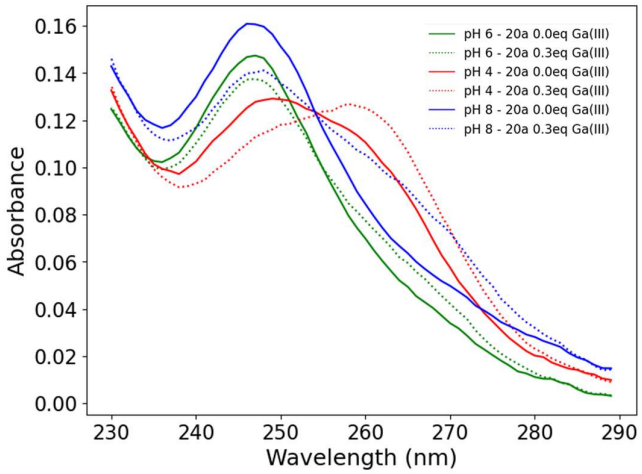

Figure 4.27 - UV absorbance traces of **20a** (10 μM) in 20 mM aqueous MOPS buffer, pH 6 (solid green line = No Ga^{3+}, dotted green line = 0.3 eq Ga^{3+}) and **20a** (10 μM) in 20 mM aqueous NH_4HCO_3 buffer, pH 8 (solid blue line = No Ga^{3+}, dotted blue line = 0.3 eq Ga^{3+}) and **20a** (10 μM) in 20 mM aqueous NH_4OAc buffer, pH 4 (solid red line = No Ga^{3+}, dotted red line = 0.3 eq Ga^{3+}).

The same experiment using peptide **21a** yielded the results in **Figure 4.28**. From this a similar behaviour as was seen for **20a** can be observed, with the smallest magnitude Cotton effect at 270 nm occurring in the pH 6, MOPs buffered system, and the largest occurring from the pH 4 system.

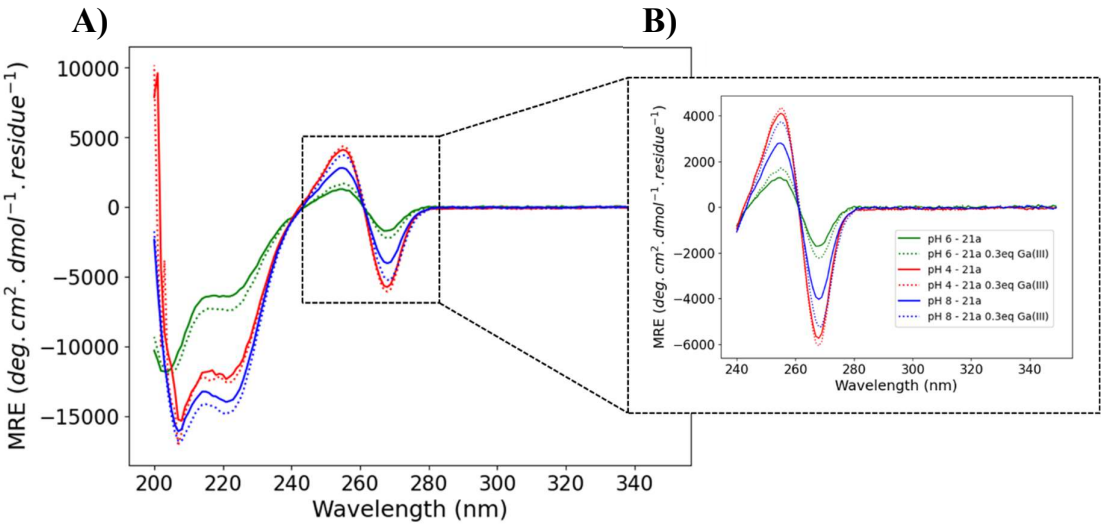

Figure 4.28 - CD traces of **21a** (10 μM) in 20 mM aqueous MOPS buffer, pH 6 (solid green line = No Ga^{3+}, dotted green line = 0.3 eq Ga^{3+}) and **21a** (10 μM) in 20 mM aqueous NH_4HCO_3 buffer, pH 8 (solid blue line = No $Ga^{3+,}$ dotted blue line = 0.3 eq Ga^{3+}) and **21a** (10 μM) in 20 mM aqueous NH_4OAc buffer, pH 4 (solid red line = No Ga^{3+}, dotted red line = 0.3 eq Ga^{3+}). **A)** Full CD spectrum comparison **B)** Zoomed segment highlighting the region where the signal for the 8-HQ appears

The UV absorbance of **21a** under these conditions can be found in **Figure 4.29**. This data is very similar to that from **20a** however, the pH 8, 0.0 eq Ga^{3+} signal is reminiscent of the signal observed for pH 4 with a broad band which almost appears to have two maxima.

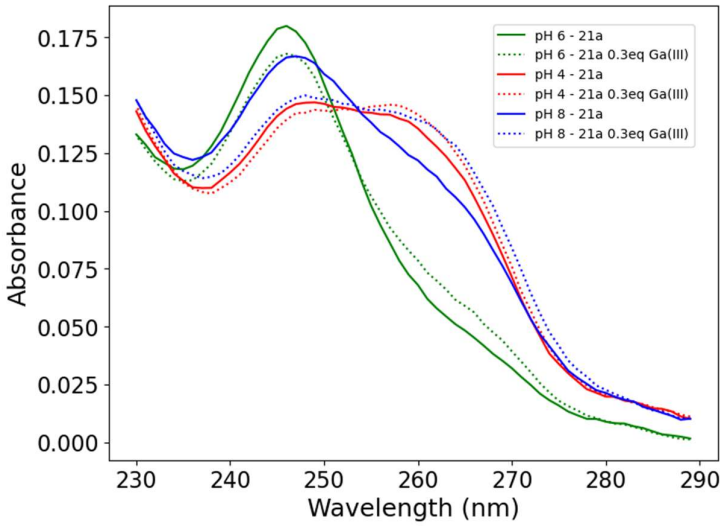

Figure 4.29 – UV absorbance traces of **21a** (10 μM) in 20 mM aqueous MOPS buffer, pH 6 (solid green line = No Ga^{3+}, dotted green line = 0.3 eq Ga^{3+}) and **21a** (10 μM) in 20 mM aqueous NH_4HCO_3 buffer, pH 8 (solid blue line = No $Ga^{3+,}$ dotted blue line = 0.3 eq Ga^{3+}) and **21a** (10 μM) in 20 mM aqueous NH_4OAc buffer, pH 4 (solid red line = No Ga^{3+}, dotted red line = 0.3 eq Ga^{3+}).

Finally, looking at the same conditions for peptide **22a** in **Figure 4.30** it can be seen that the lower pH sample has a Cotton effect resembling the Λ-tris-(8-HQ-**22a**) arrangement, but only after addition of 0.3 eq of Ga^{3+}. Conversely, the higher pH sample exhibits a Cotton effect more characteristic of the Δ-tris-(8HQ-**22a**) before and after addition of Ga^{3+} to the sample. The neutral pH sample does not exhibit any Cotton effect in this UV region either before nor after addition of Ga^{3+}.

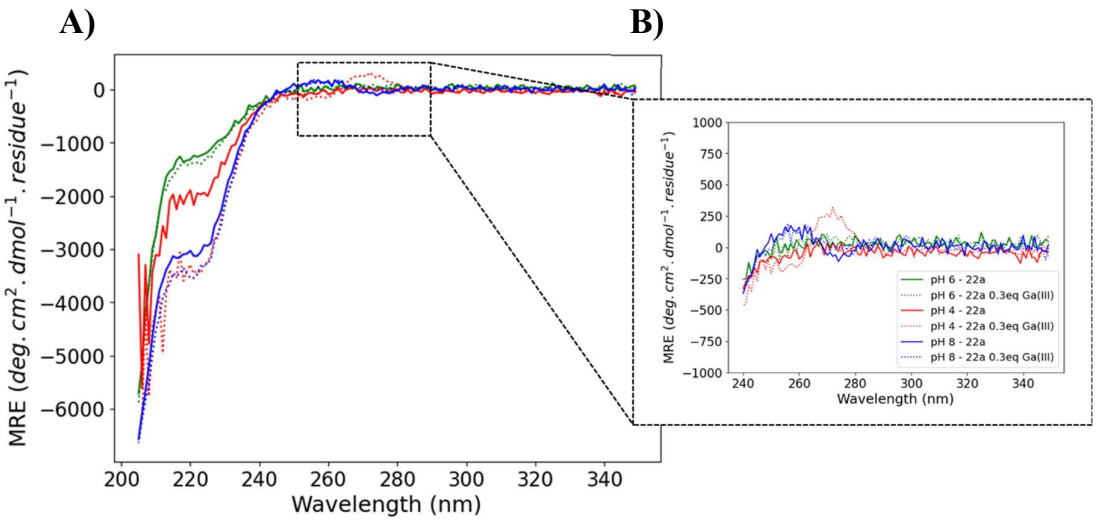

Figure 4.30 - CD traces of **22a** (10 μM) in 20 mM aqueous MOPS buffer, pH 6 (solid green line = No Ga^{3+}, dotted green line = 0.3 eq Ga^{3+}) and **22a** (10 μM) in 20 mM aqueous NH_4HCO_3 buffer, pH 8 (solid blue line = No Ga^{3+}, dotted blue line = 0.3 eq Ga^{3+}) and **22a** (10 μM) in 20 mM aqueous NH_4OAc buffer, pH 4 (solid red line = No Ga^{3+}, dotted red line = 0.3 eq Ga^{3+}). **A)** Full CD spectrum comparison **B)** Zoomed segment highlighting the region where the signal for the 8-HQ appears

The UV absorbance of this experiment (**Figure 4.31**) indicates that for all three of the tested buffers the absorbance band before addition of Ga^{3+} appears at a wavelength of approximately 246 nm with a broad absorption band around 265–270 nm at higher pH. Upon addition of Ga^{3+} this band is also observed in the lower pH sample, however it is slightly blue shifted in comparison. It is not clear what causes this difference.

From the data presented in this section what can be stated is that pH can have a significant effect on the resulting chiral signal in this system. Increasing the pH towards a value of approximately 8 could be hypothesised to enhance the complexation by pushing the equilibrium to favouring the deprotonated form of the 8-HQ ligand, however, it will reduce the inter-ligand H-bonding which is thought to be the reason that peptides featuring the 8-HQ units instead of the bpy units express opposite handedness complexes at the N-terminus. From the variable pH measurements of **22a** it was demonstrated that increasing the pH from 4 to 10 resulted in a change in the favoured arrangement indicated by the Cotton effect at

270 nm. This further indicates that reducing the H-bonding capacity of the 8-HQ ligand results in the formation of an arrangement more reminiscent of what was observed for the bpy peptides in Chapter 2 and Chapter 3.

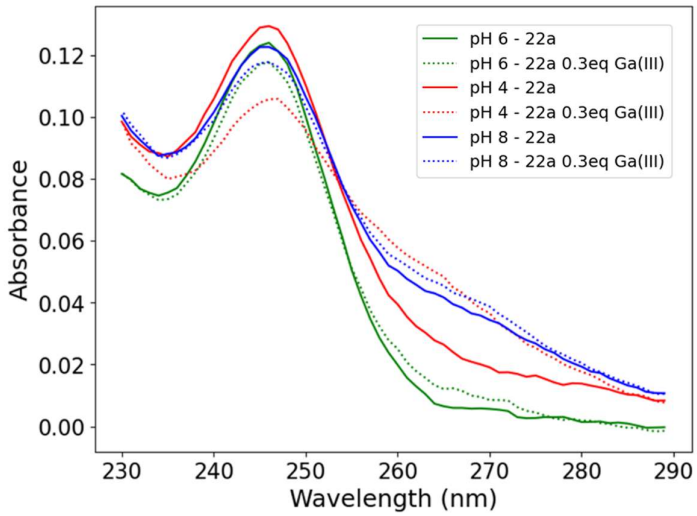

Figure 4.31 - UV absorbance traces of **22a** (10 μM) in 20 mM aqueous MOPS buffer, pH 6 (solid green line = No Ga^{3+}, dotted green line = 0.3 eq Ga^{3+}) and **22a** (10 μM) in 20 mM aqueous NH_4HCO_3 buffer, pH 8 (solid blue line = No Ga^{3+}, dotted blue line = 0.3 eq Ga^{3+}) and **22a** (10 μM) in 20 mM aqueous NH_4OAc buffer, pH 4 (solid red line = No Ga^{3+}, dotted red line = 0.3 eq Ga^{3+}).

4.4 Conclusions

In conclusion investigation of three peptide sequences **20a**, **21a** and **22a**, featuring an 8-HQ chelating unit at the *d*-, *e*- and *a*-positions of the heptad repeat respectively showed chiral preference in the terminal chelate conformation.

Featuring the 8-HQ chelating unit at a *d*- or *e*-position resulted in oppositely handed initial conformations and their subsequent complexes after addition of metal ions (Co^{2+}, Ga^{3+} and Al^{3+}), with the *d*-position favouring the Λ-conformation and the *e*-position favouring the Δ-conformation. The same conformational preference was observed for all 3 of the tested metals and interestingly the chiral preference of the *d*- and *e*-positions were the opposite to what had been observed previously for the bpy-conjugated peptides in Chapters 2 and 3. This did however appear to match more closely with the CC-vector mapping diagram which suggested (provided continuation of the helical H-bonding pattern) that chelating units in the *d*-position will favour the Λ-conformation and those in the *e*-position will favour the Δ-conformation.

These results are much more pronounced when the complex is formed with Ga^{3+} ions, with the strongest chiral preference being obtained for peptide **21a** which has the 8-HQ unit at an *e*-position and shows the Δ-conformation preference. Additional to the chiral preference observed when featuring the 8-HQ unit at this position a strong helical stabilisation is observed when Ga^{3+} associates to **21a**. The same result is not obtained for **20a.** This suggests that the Δ-conformation is more stabilising to the helices than the Λ-conformation for these sequences and this chelating molecule. Additional stabilisation is observed in the Ga^{3+} titration with peptide **22a** featuring the 8-HQ unit at the *a*-position however this is not to the same extent which can be seen for **21a**.

Titration of **20a** against Al^{3+} gave comparable results to what was observed for Ga^{3+}. Additionally, from this titration a kinetic effect was observed. This indicated that the Al^{3+} ions were slow to associate at room temperature. The time dependant experiment showed that full association of the ions to the chelating unit would occur after 30 min at room temperature, however this time could probably be reduced if the sample was heated.

Finally, in an attempt to understand the observed difference in chiral preference between the bpy-conjugated peptides and the 8-HQ-conjugated peptides a variable pH experiment was performed. The results from this experiment suggested that the ability to form H-bonds at

lower pH in samples of **20a**, **21a** and **22a** led to an increased chiral preference for the same conformation as was attained at pH 7. Lowering the pH of **20a** (*d*-position) led to an increase in the Λ-signal, for example. However, increasing the pH towards the pK_a of the 8-HQ -OH functional group led to a decrease in this chiral preference and in fact in the case of **22a** (*a*-position) a switch in the observed chiral preference. This could suggest that this H-bonding pattern within the sequences is somewhat responsible for the structural differences between the bpy-conjugated- and the 8-HQ-conjugated peptides observed in the CD. These results suggest a clear reliance of this system on the pH of the environment. Increasing the pH to 8 could increase the binding to the metal ion by increasing the charge, however, reducing the H-bonding capacity of the system and potentially changing the self-assembly of the system and subsequent chiral preference in the obtained complex.

5 Summary and Future Work

This chapter aims to summarise the conclusions drawn across the three Results and Discussion Chapters (2, 3 and 4). Additionally, the future work for this project will be presented.

5.1 Summary

To conclude, from the results presented in Chapters 2, 3 and 4 it has been confirmed that through synthesis of designed CC sequences with chelating units at the *d*- or *e*-positions of the heptad repeat that chiral preference can be expressed in the resulting chelate complexes. Through analysis of these chelate-N-terminally-conjugated peptides by CD and UV absorbance it was determined that the degree of chiral preference is determined by a number of factors. These include, α-helical content of the peptide, strength of binding to the metal ion, distance from a chiral centre, identity of the chelating unit, ability of the N-terminus to H-bond, and most prevalently, register position of the chelating unit.

Through analysis of bpy-conjugated peptides, **1a** and **2a** it was discovered that chiral information transfer in this system relies heavily on the α-helical content of the peptide in use. The 3-heptad sequence **1a** compared to the 1-hepad sequence **2a** showed that even though the bpy unit was present in both and within a chiral environment, the chiral information transfer relied on the self-assembly of the helices. The relationship between the bpy conformation and the self-assembly was also uncovered by comparison of **1a** to its acetyl-capped control sequence **1b** which exhibited less α-helical content when analysed by CD. This comparison shows that the 3-heptad sequence relies on the intermolecular bpy interactions at the N-terminus to make the formation of the CC more energetically favourable. In summary, the strength of the chiral information transfer from the helices onto the bpy-conformation relies on the α-helical content of the peptide, but the α-helical content of the peptide also relies on the presence of the bpy for self-assembly; it is a complimentary system. Additional to the sequence content, the choice of TM ion also proved important, with TMs Co^{2+} and Ni^{2+} increasing the α-helical content upon binding to the bpy units and expressing the strongest bpy exciton couplets in the CD. Furthermore, binding of **1a** to Ni^{2+} under variable temperature conditions showed that the binding of this TM resulted in stabilisation of the α-helices at higher temperatures. Association of Cu^{2+} ions in these systems also proved

useful as it allowed for the coupled nature of the helicity and the chiral information transfer to be viewed by changes in the CD with increasing concentrations of Cu^{2+} in solution.

Further investigation into the more analogous phen-conjugated peptide **3a** found that this system is delicately balanced. Comparison of **3a** with **1a** showed that the larger phen group at the N-terminus resulted in less folding of the peptides into the desired CC structure. Furthermore, minimal chiral information transfer was observed. This data showed that there were sensitive spatial constraints in this system which were further investigated in Chapter 3 with respect to bpy-conjugated peptides.

Chapter 3 investigated the spatial tolerances of the chiral information transfer in the bpy-conjugated systems. Analysis of peptides **1a**, **4a**, **5a**, **6a**, **7a**, **8a**, **9a** and **10a**, found that increasing the length of the achiral spacer between the CC and the bpy resulted in a reduced chiral information transfer. More interestingly, the reliance of these systems for H-bonding terminal residues was uncovered. Increasing the achiral spacer length from **8a** (Gly) to **9a** (GlyGly) showed no large change in the α-helical content or the chiral signal exhibited by the bpy conformations. However, when increasing this distance from **9a** to **10a** (PEG) there is a complete loss of chiral information transfer onto the bpy-complex from the helices, despite evidence from the UV absorbance absorbance suggesting binding of the TM ions. It was suggested in the chapter that the PEG spacers reduced ability to form H-bonds like the achiral AA spacers Gly and GlyGly showed the dependence on continuing the helical H-bonding pattern on the chiral information transfer. This was more evident in the 4-heptad sequences due to their increased tolerance for changing the terminal residues, as the 3-heptad sequences exhibited lower α-helical content as the terminal residues in the sequence were substituted for the achiral alternatives, resulting in the reduced chiral bpy signal. Furthermore, substitution for D-ala in sequence **11a** showed that the chiral information transfer was more dependent on the helicity of the peptide than the point chirality of the AA preceding the bpy unit.

Changing the register position of the bpy within the heptad repeat sequence also provided insightful results and allowed for chiral control of the terminal bpy complex. It was found that featuring the bpy in a solvent exposed position, *b, c, f* or *g* resulted in no chiral information transfer and additionally, a reduced α-helical content in the peptide. This has been hypothesised to be a result of the bpy units not being 'prearranged' into a conformation which would allow for the stabilising intermolecular π-stacking interactions which allow for the helicity or formation of the complexes. Conversely, featuring the bpy at an *a, d* or *e*-position resulted in different conformations of the bpy complex being formed. Coupling the

bpy such that it resides at a *d*-position as was seen in Chapter 2 led to the formation of the Δ-conformation of the bpy both in the absence and presence of metal. However, upon coupling the bpy such that it resides at an *e*-position the mirror-image conformation of the complex is obtained (Λ-) despite the chirality of the helices remaining constant. It was hypothesised that coupling of the bpy at the *a*-position led to an unfavourable arrangement of the bpy units which lead to fraying at the N-terminus. This led to a reduced α-helical content as observed by CD, and only weak signals arising from the chiral bpy complex. Despite only being weak, it was expressing a signal consistent with the Λ-conformation of the bpy units.

Through analysis of 8-HQ-conjugated peptides, **20a** *(d)*, **21a** *(e)* and **22a** *(a)* the relationship between the chiral information transfer from the helicity of the peptides was further probed. Interestingly, using 8-HQ as the chelating unit in place of the bpy resulted in oppositely handed conformations at the N-terminus. Investigation of the *d*-position peptide **20a** showed that this sequence resulted in the assembly of 8-HQ units in a Λ-conformation, the opposite to what was observed for the bpy-conjugated in the *d*-position. Furthermore, the same principle followed for the *e*-position with the Δ-conformation of the 8-HQ units being preferred. This change was thought to be a result of the H-bonding ability of the 8-HQ units via its -OH functional group and that this behaviour was pH dependant. Unexpectedly, the *a-position* 8-HQ units did not assemble into the oppositely handed conformations as the other two tested positions did. However, upon raising the pH of the system, the opposite conformer was observed in the CD at approximately 265 nm. This suggests that the *a*-position due to its inward facing directionality, is more poised to form either conformation, however, does not show a strong chiral preference for either. It was also discovered that p-block metals, Ga^{3+} and Al^{3+} formed much stronger complexes with the 8-HQ units than Co^{2+}.

To summarise, the relationship between the α-helical content of the peptides and the resulting chiral information transfer onto an N-terminally bound bidentate chelating unit (bpy, phen and 8-HQ) has been discussed. It has been determined that through careful sequence design that the degree of chiral information transfer can be controlled and additionally, the resulting chiral preference can be controlled by featuring the chelating unit at a *d*- or *e*- register position allowing preference for one handedness over the other. It was also determined that the H-bonding ability of both the terminal residues of the peptide sequences and the chelating unit were important for the chiral information transfer and determination of the resulting chiral preference in the chelate conformation.

5.2 Future Work

The future work for the work presented in this thesis is extensive.

In Chapter 2, the phen-appended peptides were presented. It would be valuable insight into these systems to test the phen unit at the different register positions within the sequences in the same way as was performed for the bpy unit in Section 3.7, additionally testing the phen chelating with a wider variety of metals to assess for better coordination. Furthermore, with respect to the phen unit, it would be interesting to test this unit with a more flexible spacer between the phen and the terminus, this could eliminate the issues that were discussed related to the rigidity of these systems. It would also be beneficial to test the full set of TMs coordination to peptide **13a**, which has the bpy at the *e*-position of the sequence, as this was not investigated due to time constraints. Additional to this it would be interesting to investigate other chelating units and where they have been anchored to the peptide to probe the behaviour further. Mentioned briefly in the sequence design in Section 2.2, there is an option to include the bpy unit at other anchor points within a peptide sequence, for example off the side chains, off the C-Terminus, or featured at both the N- and C-Terminus for a bi-functionalised peptide which could coordinate at each terminus.

Chapter 3 contained discussion of the series of achiral spacers (Gly, GlyGly and PEG) which were used to probe the limits of the chiral information transfer from the CC onto the complex. In order to test this relationship further it would be interesting to investigate a series of achiral spacers without the ability to follow the helical H-bonding pattern, like the AA spacers used in this study. For example, using spacer units such as Fmoc-(Amino(Ethoxy))Acetic Acid (**Figure 5.1**) as an alternative for the 7-atom spacer and N-Fmoc-β-alanine as a 5-atom spacer. This could give a better understanding of the chiral induction effects with increasing distance.

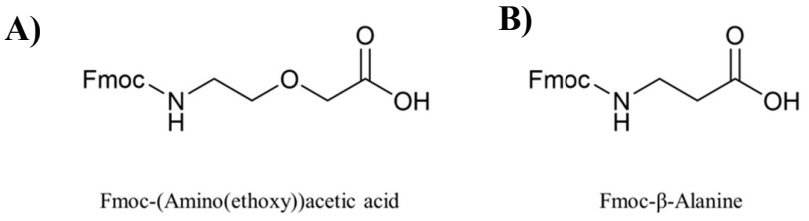

Figure 5.1 – Structures of the suggested alternatives of achiral spacers to test chiral information transfer. **A)** Fmoc-(Amino(ethoxy))acetic acid **B)** Fmoc-β-alanine

It would also be beneficial to do a full study of spatial constraints of the peptides with the bpy in the *e-position*. This could include a comparable study of increasing achiral spacer length like what was performed for the *d*-position.

In Chapter 4 the 8-HQ-appended peptides were discussed. Given the increased signal strength obtained for the 8-HQ-complexes with Ga^{3+} it would potentially be beneficial to synthesise and test the other register positions in the heptad. As the observed effects in this system are more dramatic, more structural information about this system could be attained by analysis of these other positions. Furthermore, a positional study with various chiral and achiral spacers analogous to what was done in Chapter 3 for bpy and has been presented as future work for the phen-units, would allow for further probing of the chiral preference of this system and the limits of the information transfer onto the coordination complex.

It would be helpful in future if molecular dynamics (MD) simulations could be performed to assess the H-bonding of the terminal residues and the chelating units. Given more time this could have provided valuable insight into what was causing the chiral preference and would allow for design of these self-assembling systems and could lead to potential applications for them. Work on MD simulations and molecular modelling is ongoing within the Thomson group.

It has been noted from the literature that complexes of 8-HQ with metal ions such as the Ga^{3+} tested here have fluorescence properties. It would be interesting to test this by performing similar titrations in fluorescence spectroscopy. Additionally, testing these self-assembling systems for circularly polarised fluorescence could be insightful.

Finally, crystallization of these compounds for analysis by either electron diffraction or x-ray crystallography to obtain a crystal structure has been discussed within the group and with our collaborators in the Forgan group. This would likely have to be done with a cryogenic loading procedure given the difficulty with crystallising such peptides and would likely require assistance from an expert in this field. Due to the uncertainty of the enantiomeric excess (ee) in these systems performing in depth NMR experiments to determine the ratio of the different enantiomers of the complexes would be beneficial before crystallisation but again would require an expert in the NMR of biomolecules. Determining the ee of these systems could allow design of future systems which push the ee towards an enantiopure system and therefore make obtaining a crystal structure more likely. In addition to crystallisation of the peptide-complexes it would be interesting and valuable to obtain structures, UV-absorbance and CD data of the 2,2′–bipyridine–4–carboxylic acid complexes

when not ligated to a peptide. This would allow for better comparison to the bpy appended complexes than the tested 2,2–bipyridine–4,4′–dimethanol, which was tested for information about the bpy UV absorbance behaviour. Furthermore, structural information for the phen- and 8-HQ-complexes would be insightful.

All of the future work discussed above is relatively short term, below are some of the potential long-term applications of the work in this thesis, circling back to the scope of this project.

The work in this thesis has demonstrated that through knowledge of the structural design of coiled-coil trimeric peptides, the chirality of an N-terminal chelate complex can be controlled. Some of the principles governing the complex interplay between the structural elements of peptide oligomers and incorporation of a metal interface for the formation of complexes have been elucidated. These principles of chirality control, paired with the ability to use different chelating groups has interesting prospects for future investigations. Chiral control could be interesting for introducing a catalytic element to the peptide structure. This could lead to avenues in the realm of biomimetics with the design of metallopeptides towards artificial enzymes.

Alternatively, to further probe the structural elements of chiral information transfer as a whole, a project could be imagined in which the chiral information is transferred over a longer distance, i.e. introducing an organic foldamer to the other side of the chelating unit, akin to the work performed by Ousaka *et al* in 2011 described in the introduction.[16] This could test if the chiral information which is passed onto the complex, is further communicated down the unfolded helicate/foldamer chain.

6 Experimental

6.1 Chemicals

Unless stated explicitly all the chemicals used in this work were purchased from Sigma Aldrich, Fluorochem, Alfa Aeser or Thermo Fischer Scientific. No further purification or analysis was performed in advance of using these chemicals in experiments.

All of the amino acids used for peptide synthesis were purchased from Fluorochem. These were all in the L-configuration and used Fmoc/tBu protection groups unless otherwise specified.

All solvents used throughout this work were purchased from VWR, Fisher, SLS or Rathburn.

DMF (Rathburn) and TFA (Fluorochem) used in all peptide experiments was of peptide grade (≥99.8% purity) as specified by the suppliers.

6.2 Instruments

For purification of all peptides a Dionex semi-preparative HPLC system was used. The system is fitted with a Dionex P980 pump, Dionex UCV170U UV-Visible detector (recording at 214 nm and 280 nm) and a Luna 5µm, C18, 100 Å, 150 × 10 mm, column which operates at a flow rate of 3 $mL \cdot min^{-1}$. A binary solvent system of buffers A, H_2O + 0.1% TFA, and B, MeCN + 0.1% TFA is used for all purifications.

Analytical HPLC analysis was performed using a Shimadzu reverse-phase HPLC. The system is fitted with Shimadzu LC-20AT pumps, Shimadzu SIL-20A autosampler, Shimadzu SPD-20A UV-Visible detector (recording at 214 nm and 280 nm) and a Phenomenex Gemini 5µm, C18, 110 Å, 150 × 2 mm column, which operates at a flow rate of 0.2 $mL \cdot min^{-1}$. A binary solvent system of buffers A, H_2O + 0.1% TFA, and B, MeCN + 0.1% TFA is used for all analysis. Characterisation of all peptides was performed by running both a 20 min and 50 min gradient.

LC-MS data for crude peptide samples was performed using an Agilent Affinity Lab Liquid Chromatography Mass Spectrometer. This machine is fitted with a Gemini 5µm, C18, 110 Å, 150 × 2 mm column which operates at 0.3 $mL \cdot min^{-1}$. A binary solvent system of buffers A, H_2O + 0.1% TFA, and B, MeCN + 0.1% TFA is used for all analysis. All gradients run occur over 20 minutes.

HR-MS analysis of all purified peptide compounds was provided by the University of Glasgow School of Chemistry Mass Spectrometry Service. The service provides High Resolution Mass Spectrometry using a Bruker microTOF-Q High Resolution Mass Spectrometer instrument for ESI+ measurements. All masses have been reported as the mass to charge (*m/z*) ratio and only nominal masses are reported due to all compounds discussed having a MW above 1 kDa.[208, 209 210]

A Christ Alpha 2-4 LO plus freeze dryer was use for lyophilisation of all peptides. This system typically operates at -80 °C and < 0.5 mbar. Lyophilised samples were prepared in a 1:1 mixture of H_2O and MeCN and then frozen using liquid N_2.

A Thermo Scientific NanoDrop One UV-Visible spectrophotometer was used to measure all peptide concentrations by using 280 nm absorbance. The concentrations were then calculated using the experimental extinction coefficients for bpy functionalised peptides (6696.7 + 1280 (Tyr) $M^{-1}cm^{-1}$), phen functionalised peptides (18061.8 + 1280 (Tyr) $M^{-1}cm^{-}$

[1]) and 8-HQ functionalised peptides (2324.3 + 1280 (Tyr) $M^{-1}cm^{-1}$). Details of the experiments performed to calculate these values can be found in Section 6.4.

All Circular Dichroism measurements were taken using an Applied Photophysics Chirascan VX CD-Spectropolarimeter, with a Quantum Northwest TC temperature controller and a CW-3000 industrial chiller. All samples were prepared in MOPS buffer, pH 7 at a concentration of 10 μM at 25 °C unless otherwise specified.

The UV absorbance measurements of 2,2′-bipyridine-4,4′-dimethanol was performed on a Horiba Duetta Bio UV-Vis-NIR absorption and fluorescence spectrometer. These measurements were performed in deionised water with the bpy unit at a concentration of 10 μM.

6.2.1 Computational Modelling of Peptide Sequences

Models of peptides were generated using Chai-1 version 0.6.1. Each peptide was modelled as a trimer, and the bpy or 8-HQ unit was specified as a SMILES string, as were metal ions when present. Covalent linkages between the bpy or 8-HQ were specified through a .restraints file. Models were generated using 3 trunk steps and 200 diffusion timesteps. Models were built on an Ubuntu Linux workstation equipped with an NVDIA RTX4800 GPU.

All peptide modelling was performed by Dr. Drew Thomson.

6.3 General Procedures for Peptide Synthesis and Functionalisation

All peptides were synthesised on a 0.1 mmol scale on one of the following Rink Amide resins; a ChemMatrix (0.45 mmol·g^{-1} loading), a FluoroChem (0.33 mmol·g^{-1} loading), a TentaGel (0.22 mmol·g^{-1} loading), or a Novabiochem (0.80 mmol·g^{-1} loading).

For all synthesis the resin was swollen with approximately 10 mL DMF for 5 min at room temperature.

6.3.1 Manual Solid Phase Peptide Synthesis

6.3.1.1 Manual Coupling

6.3.1.1.1 PyBOP/DIPEA Coupling

PyBOP (4.5 eq), DIPEA (6.0 eq) and Fmoc-AA_1 (4.0 eq) were dissolved in 5 mL DMF and allowed to preactivate for 5 min at room temperature. The mixture was then transferred into a syringe containing the swollen resin and reacted for 2 h at room temperature. The resin was then washed with 3 × 5 mL DMF.

6.3.1.1.2 DIC/Oxyma Coupling

DIC (4.0 eq), Oxyma (4.0 eq) and Fmoc-AA_1 (4.0 eq) were dissolved in 5 mL DMF and allowed to preactivate for 5 min at room temperature. The mixture was then transferred to a syringe containing the swollen resin and reacted for 2 h at room temperature. The resin was then washed with 3 × 5 mL DMF.

6.3.1.2 Acetyl Capping

The resin bound peptide was suspended in 5 mL DMF. To this suspension acetic anhydride (0.4 mL, 42 eq) and pyridine (0.6 mL, 74 eq) were added and then left to react for 2 h at room temperature. The resin was then washed with 3 × 5 mL DMF followed by 3 × 5 mL DCM.

6.3.1.3 Manual Fmoc Deprotection

For Fmoc deprotection, 5 mL of a 20% morpholine in DMF solution was added to the resin bound peptide and reacted for 15 min. Following this the resin was washed with 3 × 5 mL DMF.

This reaction was repeated twice per deprotection.

6.3.1.4 Manual Cleavage

For cleavage from the resin, 10 mL of a 95 % TFA. 2.5 % H_2O and 2.5 % TIPS mixture was poured over the resin bound peptide. This was then reacted for 2 h at room temperature. The reaction was then filtered into a falcon tube and the excess TFA evaporated under a flow of N_2 gas. Cold Et_2O (40 mL) was then added to the falcon tube and the peptide precipitated out. The precipitate was collected by centrifugation at 40000 rpm for 5 min. The Et_2O was then decanted from the falcon tube and the peptide dissolved in a 1:1 mixture of MeCN/H_2O. Finally, the dissolved peptide was frozen using liquid N_2 and lyophilised.

6.3.2 Automated Solid Phase Peptide Synthesis

All automated peptide synthesis was performed on a Liberty Blue microwave assisted peptide synthesiser. The synthesis all utilised an Fmoc/tBu protecting strategy and morpholine deprotection strategy.

6.3.2.1 Resin Swelling

The automated peptide synthesiser swells the resin by addition of 15 mL DMF and allowing to sit for 5 min at room temperature before draining the excess DMF.

6.3.2.2 Coupling

Coupling of Fmoc-protected AAs was performed by addition of the Fmoc-AA (5 eq, 0.2 M in DMF), DIC (5 eq, 0.5 M in DMF) and Oxyma (5 eq, 1M in DMF) to the reaction vessel. During the coupling the reaction vessel was at ~25 °C, room temperature (0 W) for 5 s, following this the vessel was heated to 80 °C (100 W) for 30 s, 86 °C (70 W) for 20 s, and 90 °C (25 W) for 120 s. Finally, the resin was washed with 5 mL DMF.

6.3.2.3 Fmoc Deprotection

Automated Fmoc deprotection was performed by addition of 4 mL of a 20 % morpholine in DMF solution to the reaction vessel. This was reacted at ~25 °C, room temperature (0 W) for 5 s before heating to 78 °C (100 W) for 30 s, 88 °C (70 W) for 20 s and finally 90 °C (25 W) for 60 s. The deprotection steps are finished by washing with 3 × 4.5 mL DMF.

6.3.3 Coupling of 2,2′-bipyridine-4-carboxylic acid to the N-terminus

2,2′-bipyridine-4-carboxylic acid (4.0 eq), DIC (4.0 eq) and Oxyma (4.0 eq) were dissolved in 5 mL DMF and allowed to preactivate or 5 min at room temperature. The mixture was then transferred into the syringe containing the swollen resin and reacted for 2 h at room temperature. The resin was then washed with 3 × 5 mL DMF and then 3 × 5 mL DCM.

6.3.4 Coupling of 1,10-phenanthroline-4-carboxylic acid to the N-terminus

1,10-phenanthroline-4-carboxylic acid (4.0 eq), DIC (4.0 eq) and Oxyma (4.0 eq) were dissolved in 5 mL DMF and allowed to preactivate or 5 min at room temperature. The mixture was then transferred into the syringe containing the swollen resin and reacted for 2 h at room temperature. The resin was then washed with 3 × 5 mL DMF and then 3 × 5 mL DCM.

6.3.5 Coupling of 8-hydroxyquinoline-4-carboxylic acid to the N-terminus

8-hydroxyquinoline-4-carboxylic acid (4.0 eq, 0.4 mmol), DIC (4.0 eq) and Oxyma (4.0 eq) were dissolved in 5 mL DMF and allowed to preactivate or 5 min at room temperature. The mixture was then transferred into the syringe containing the swollen resin and reacted for 2

h at room temperature. The resin was then washed with 3 × 5 mL DMF and then 3 × 5 mL DCM.

6.4 Extinction Coefficient Determination for bpy, phen and 8-HQ appended peptide sequences

To determine the extinction coefficients of peptide sequences capped with 2,2′-bipyridne, 1,10-phenanthroline and 8-hydroxyquinoline, **1a** (bpy), **3a** (phen) and **20a** (8-HQ) were weighed out and dissolved to a known concentration, serial dilutions were then analysed on the NanoDrop UV-Vis spectrometer and absorbance values plotted.

6.4.1 2,2′-Bipyridine

To determine the extinction coefficient of an N-terminally bound 2,2′-bipyridine, a stock solution of peptide **1a** (2736.57 $g \cdot mol^{-1}$, 12.8 mg, 10 mL, 468 µM) in H_2O was prepared. This solution was then diluted to 300 µM in 1 mL H_2O (641 µL in 1 mL). A two-fold serial dilution was performed resulting in six solutions of concentrations: 300 µM, 150 µM, 75.0 µM, 37.5 µM, 18.8 µM and 9.38 µM.

Absorbance values of these six solutions were then measured on the NanoDrop UV-Vis spectrometer in triplicate and plotted against their concentrations (**Figure 6.1**).

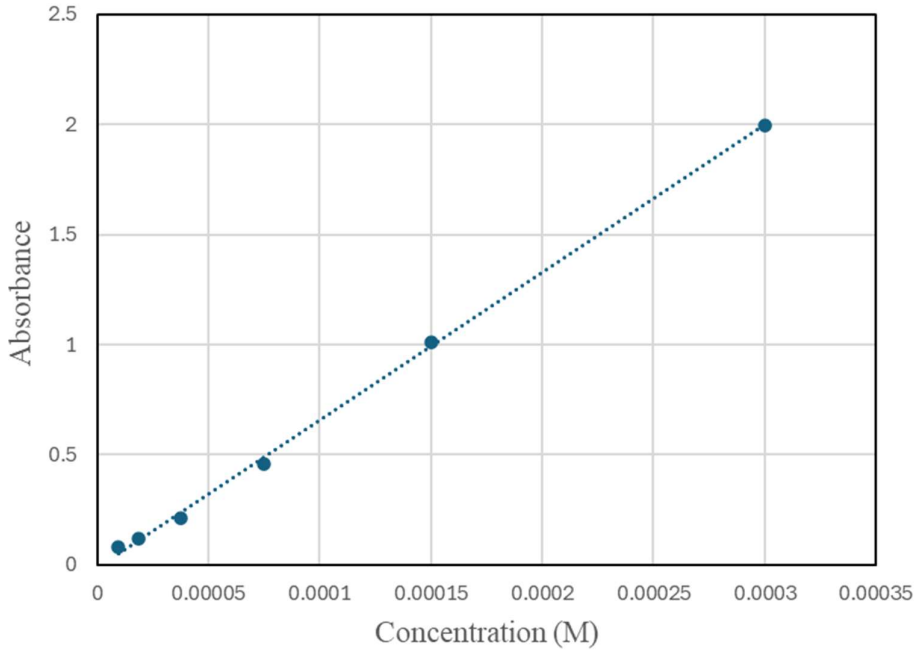

Figure 6.1 - Plot of concentration of **1a** against UV-Vis absorbance at 280 nm (pathlength = 1 cm).

The linear estimation formula (LINEST) in Microsoft Excel was then used to calculate the gradient of the straight line which yielded an ε value of 6696.7 $M^{-1}cm^{-1}$. The value of the Tyr residue (1280 $M^{-1}cm^{-1}$) was then subtracted and the final value of the bpy unit determined to be **ε = 5416.7 $M^{-1}cm^{-1}$**.

6.4.2 1,10-Phenanthroline

To determine the extinction coefficient of an N-terminally bound 1,10-phenanthroline, a stock solution of peptide **3a** (2760.57 $g \cdot mol^{-1}$, 8 mg, 1 mL, 2.9 mM) in H_2O was prepared. This solution was then diluted to 0.73 mM to avoid oversaturation of the detector. A two-fold serial dilution was performed resulting in six solutions of concentrations: 0.73 mM, 0.36 mM, 0.18 mM, 0.09 mM, 0.05 mM and 0.02 mM.

Absorbance values of these six solutions were then measured on the NanoDrop UV-Vis spectrometer in triplicate and plotted against their concentrations (**Figure 6.2**).

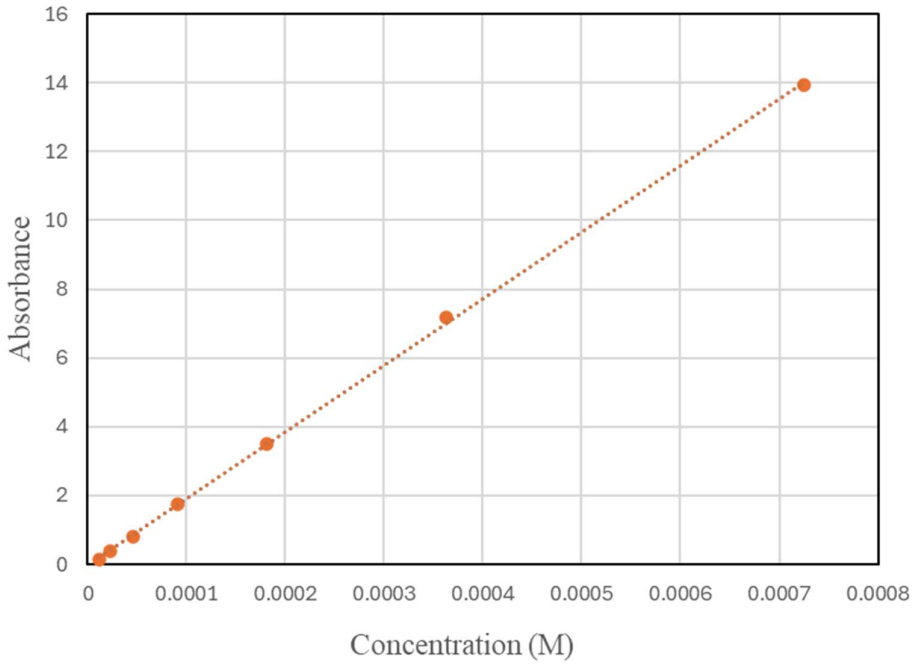

Figure 6.2 - Plot of concentration of **3a** against UV-Vis absorbance at 280 nm (pathlength = 1 cm).

The linear estimation formula (LINEST) in Microsoft Excel was then used to calculate the gradient of the straight line which yielded an ε value of 19341.75 $M^{-1}cm^{-1}$. The value of the Tyr residue (1280 $M^{-1}cm^{-1}$) was then subtracted and the final value of the phen unit determined to be **ε = 18061.75 $M^{-1}cm^{-1}$**.

6.4.3 8-Hydroxyquinoline

To determine the extinction coefficient of an N-terminally bound 8-hydroxyquinoline, a stock solution of peptide **20a** (2725.57 $g \cdot mol^{-1}$, 8.2 mg, 1 mL, 3.0 mM) in H_2O was prepared. This solution was then diluted to 1.5 mM to avoid oversaturation of the detector. A two-fold serial dilution was performed resulting in eight solutions of concentrations: 1.500 mM, 0.750 mM, 0.375 mM, 0.188 mM, 0.094 mM, 0.047 mM, 0.023 mM, and 0.012 mM.

Absorbance values of these eight solutions were then measured on the NanoDrop UV-Vis spectrometer in triplicate and plotted against their concentrations, (**Figure 6.3**).

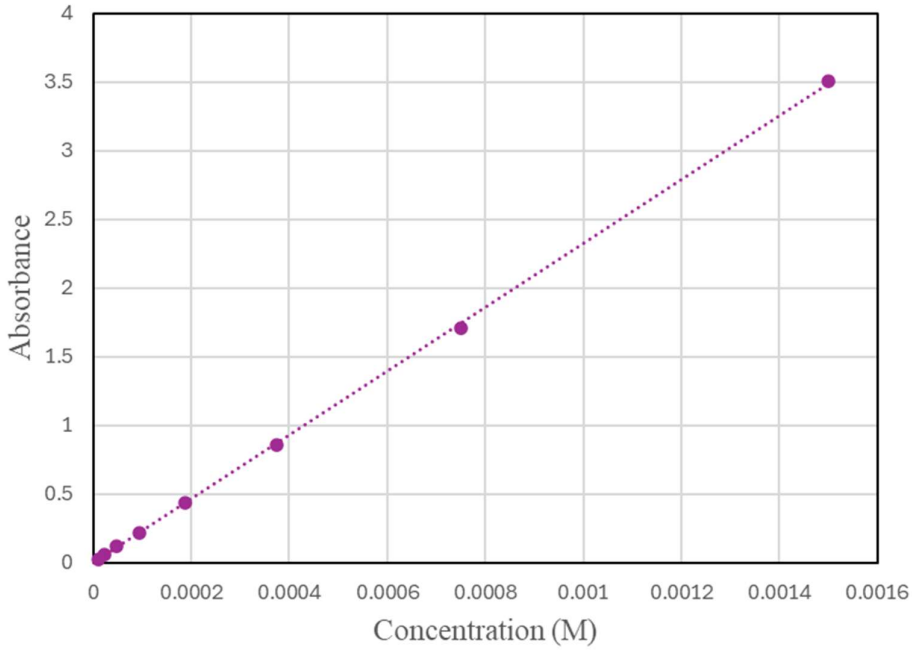

Figure 6.3 - Plot of concentration of **20a** against UV-Vis absorbance at 280 nm (pathlength = 1 cm)

The linear estimation formula (LINEST) in Microsoft Excel was then used to calculate the gradient of the straight line which yielded an ε value of 2324.33 $M^{-1}cm^{-1}$. The value of the Tyr residue (1280 $M^{-1}cm^{-1}$) was then subtracted and the final value of the phen unit determined to be **$\varepsilon = 1044.33\ M^{-1}cm^{-1}$**.

6.5 Chapter 2 Experimental

The experimental section below describes the synthesis and characterisation of peptides **1a**, **1b**, **2a**, **2b** and **3a**, all of which were discussed in Chapter 2.

6.5.1 Peptide Synthesis

Peptides **1a**, **1b**, **2a**, **2b**, and **3a** were all synthesised by microwave assisted SPPS as described in Section 6.3.2 on a 0.1 mmol scale using Rink Amide Resin.

Peptides **1a** and **2a** were modified on resin with 2,2′-bipyridine-4-carboxylic acid coupled to the N-terminus using the method described in Section 6.3.3.

Peptide **1b** and **2b** were acetyl capped on resin using the method described in Section 6.3.1.2.

Peptide **3a** was modified on resin with 1,10-phenanthroline-4-carboxylic acid coupled to the N-terminus using the method described in Section 6.3.4.

Standard cleavage procedure (Section 6.3.1.4) of **1a**, **1b**, **2a**, **2b**, and **3a** was performed. All of these peptides were purified by RP-HPLC using a Phenomenex C18 column.

Peptides **1a–3a** were all obtained as white powders after lyophilisation.

Following lyophilisation, **1a–3a** were characterised by HRMS and analytical HPLC. Details of the characterisation are in Section 6.5.2.

6.5.2 Peptide Characterisation

6.5.2.1 Peptide **1a** – 3-heptad – Bpy Functionalised

Sequence

Bpy	G QEIAAIK KEIAAIK KEIAAIK YG	NH_2

Characterisation

Exact Mass	HPLC Purification Gradient	HPLC Characterisation Gradient	Purity	HRMS Expected	HRMS Detected
2736.57 Da	20-80 % B 20 min	20 - 80% B 50 min	98% RT 23.85 min	$[M+3H]^{3+}$ 913.2	$[M+3H]^{3+}$ 913.6

For all HPLC methods buffers were A = H_2O + 0.1 % TFA, B = MeCN + 0.1% TFA

6.5.2.2 Peptide **1b** – 3-heptad – Ac Capped

Sequence

Ac	G QEIAAIK KEIAAIK KEIAAIK YG	NH_2

Characterisation

Exact Mass	HPLC Purification Gradient	HPLC Characterisation Gradient	Purity	HRMS Expected	HRMS Detected
2596.53 Da	20-80 % B 20 min	20 - 80% B 50 min	89% RT 23.85 min	$[M+3H]^{3+}$ 866.5	$[M+3H]^{3+}$ 866.8

For all HPLC methods buffers were A = H_2O + 0.1 % TFA, B = MeCN + 0.1% TFA

6.5.2.3 Peptide **2a** – 1-heptad - Bpy Functionalised

Sequence

Bpy	G QEIAAIK YG	NH_2

Characterisation

Exact Mass	HPLC Purification Gradient	HPLC Characterisation Gradient	Purity	HRMS Expected	HRMS Detected
1229.62 Da	10-60 % B 20 min	20 - 80% B 50 min	98% RT 22.25 min	$[M+1H]^{1+}$ 1230.6	$[M+1H]^{1+}$ 1230.6

For all HPLC methods buffers were A = H_2O + 0.1 % TFA, B = MeCN + 0.1% TFA

6.5.2.4 Peptide **2b** – 1-heptad – Ac Capped

Sequence

Ac	G QEIAAIK YG	NH_2

Characterisation

Exact Mass	HPLC Purification Gradient	HPLC Characterisation Gradient	Purity	HRMS Expected	HRMS Detected
1089.58 Da	10-60 % B 20 min	20 - 80% B 50 min	99% RT 21.30 min	$[M+1H]^{1+}$ 1090.6	$[M+1H]^{1+}$ 1090.6

For all HPLC methods buffers were A = H_2O + 0.1 % TFA, B = MeCN + 0.1% TFA

6.5.2.5 Peptide **3a** – Phenanthroline Functionalised

Sequence

Phen	G QEIAAIK KEIAAIK KEIAAIK YG	NH_2

Characterisation

Exact Mass	HPLC Purification Gradient	HPLC Characterisation Gradient	Purity	HRMS Expected	HRMS Detected
2760.57 Da	20-80 % B 20 min	20 - 80% B 50 min	90% RT 22.65 min	$[M+3H]^{3+}$ 921.2	$[M+3H]^{3+}$ 921.5

For all HPLC methods buffers were A = H_2O + 0.1 % TFA, B = MeCN + 0.1% TFA

6.5.3 Circular Dichroism of peptides **1a, 1b, 2a, 2b** and **3a**

6.5.3.1 Equipment Set-up

For all experiments with peptides **1a**, **1b**, **2a** and **2b** the wavelength range was set to 400–180 nm, to capture both the signals from the bpy units and the peptide.

For experiments with peptide **3a** the wavelength range was set from 360–180 nm.

6.5.3.2 Sample Preparation

Concentrations of peptide stock solutions were calculated by UV-Vis 280 nm absorbance measurements using the NanoDrop One spectrophotometer.

All peptide samples for the CD were prepared to a concentration of 10 μM in 2 mL, 20 mM aqueous MOPS buffer, (pH 7). These samples were made up in a 2 mL cuvette with a pathlength of 1 cm.

6.5.3.3 Titrations

All metal titrations for peptides **1a**-**3a** were run at room temperature, with 0.25 s time per point and four repeats per titration point.

For all the metal salts used in the titrations ($ZnCl_2$, $Zn(NO_3)_2$, $Zn(OTf)_2$, $CuCl_2$, $Cu(NO_3)_2$, $Cu(OTf)_2$, $FeCl_2$, $FeCl_3$, $Fe(NO_3)_2$, $Fe(OTf)_2$, $NiCl_2$ and $CoCl_2$) stock solutions were made up to 0.5 mM in H_2O.

The titrations of metal salt into the peptide solution were run from 0.0 eq of metal salt to 1.0 eq metal salt. For each point of the titration 4 μL (0.1 eq, 1 μM) of the 0.5 mM metal stock solution was added to the 10 μM peptide solution.

CD titration data was normalised before plotting using the following equation.

[MRE (Mean Residue Ellipticity) = (100 * θ (mdeg) / (C (dmol) * no. of amide * l (cm)]

This normalisation allows for peptides of different compositions to be compared by reporting the ellipticity as a value per residue of the sequence.

6.5.3.4 Variable Temperature

For variable temperature CD experiments, the temperature of the sample stage was set to ramp from 5–80 °C in 5 °C increments. For each temperature measurement, the time per data point was increased to 0.75 s to account for the fact that only 1x measurement was taken per temperature.

6.6 Chapter 3 Experimental

The experimental section below describes the synthesis and characterisation of peptides **4a–19b** all of which were discussed in Chapter 3.

6.6.1 Peptide Synthesis

All peptides (**4a–19b**) were synthesised by microwave assisted SPPS as described in Section 6.3.2 on a 0.1 mmol scale using a Rink Amide Resin and Fmoc/tBu protection strategy. External positions of the synthesiser were used for any non-natural amino acid residues which were coupled.

All **a** peptides (**4a–19a**) had 2,2′-bipyridine-4-carboxylic acid coupled to the N-terminus using the coupling procedure described in Section 6.3.3.

For all **b** peptides (**4b–19b**) acetyl capping procedure (Section 6.3.1.2) was performed.

Standard cleavage procedure (Section 6.3.1.4) of **4a–19b** was performed. All of these peptides were purified by RP-HPLC using a Phenomenex C18 column.

Peptides **4a–19b** were all obtained as white powders after lyophilisation.

Following lyophilisation, **4a–19b** were characterised by HRMS and analytical HPLC. Details of the characterisation are in Section 6.6.2.

6.6.2 Peptide Characterisation

6.6.2.1 Peptide **4a** – 3-heptad - Ala Spacer - Bpy

Sequence

Bpy	A QEIAAIK KEIAAIK KEIAAIK YG	NH_2

Characterisation

Exact Mass	HPLC Purification Gradient	HPLC Characterisation Gradient	Purity	HRMS Expected	HRMS Detected
2750.58 Da	20-80 % B 20 min	20 - 80% B 50 min	95% RT 24.45 min	$[M+2H]^{2+}$ 1376.3	$[M+2H]^{2+}$ 1376.8

For all HPLC methods buffers were A = H_2O + 0.1 % TFA, B = MeCN + 0.1% TFA

6.6.2.2 Peptide **4b** – 3-heptad - Ala Spacer - Ac

Sequence

Ac	A QEIAAIK KEIAAIK KEIAAIK YG	NH_2

Characterisation

Exact Mass	HPLC Purification Gradient	HPLC Characterisation Gradient	Purity	HRMS Expected	HRMS Detected
2610.55 Da	20-80 % B 20 min	20 - 80% B 50 min	93% RT 24.35 min	$[M+2H]^{2+}$ 1306.3	$[M+2H]^{2+}$ 1306.7

For all HPLC methods buffers were A = H_2O + 0.1 % TFA, B = MeCN + 0.1% TFA

6.6.2.3 Peptide **5a** – 3-heptad - GlyGly Spacer - Bpy

Sequence

Bpy	G GEIAAIK KEIAAIK KEIAAIK YG	NH_2

Characterisation

Exact Mass	HPLC Purification Gradient	HPLC Characterisation Gradient	Purity	HRMS Expected	HRMS Detected
2665.53 Da	20-80 % B 20 min	20 - 80% B 50 min	92% RT 23.68 min	$[M+2H]^{2+}$ 1333.8	$[M+2H]^{2+}$ 1334.3

For all HPLC methods buffers were A = H_2O + 0.1 % TFA, B = MeCN + 0.1% TFA

6.6.2.4 Peptide **5b** – 3-heptad - GlyGly Spacer – Ac

Sequence

Ac	G GEIAAIK KEIAAIK KEIAAIK YG	NH_2

Characterisation

Exact Mass	HPLC Purification Gradient	HPLC Characterisation Gradient	Purity	HRMS Expected	HRMS Detected
2525.49 Da	20-80 % B 20 min	20 - 80% B 50 min	98% RT 23.29 min	$[M+2H]^{2+}$ 1263.8	$[M+2H]^{2+}$ 1264.2

For all HPLC methods buffers were A = H_2O + 0.1 % TFA, B = MeCN + 0.1% TFA

6.6.2.5 Peptide **6a** - 3-heptad - PEG Spacer - Bpy

Sequence

Bpy	(PEG) GEIAAIK KEIAAIK KEIAAIK YG	NH_2

Characterisation

Exact Mass	HPLC Purification Gradient	HPLC Characterisation Gradient	Purity	HRMS Expected	HRMS Detected
2824.62 Da	20-80 % B 20 min	20 - 80% B 50 min	95% RT 23.21 min	$[M+2H]^{2+}$ 1413.3	$[M+2H]^{2+}$ 1413.8

For all HPLC methods buffers were A = H_2O + 0.1 % TFA, B = MeCN + 0.1% TFA

6.6.2.6 Peptide **6b -** 3-heptad - PEG Spacer - Ac

Sequence

Ac	(PEG) GEIAAIK KEIAAIK KEIAAIK YG	NH_2

Characterisation

Exact Mass	HPLC Purification Gradient	HPLC Characterisation Gradient	Purity	HRMS Expected	HRMS Detected
2684.58 Da	20-80 % B 20 min	20 - 80% B 50 min	88% RT 23.33 min	$[M+2H]^{2+}$ 1343.3	$[M+2H]^{2+}$ 1343.8

For all HPLC methods buffers were A = H_2O + 0.1 % TFA, B = MeCN + 0.1% TFA

6.6.2.7 Peptide **7a** – 4-heptad – Ala Spacer - Bpy

Sequence

Bpy	A QEIAAIK KEIAAIK KEIAAIK KEIAAIK YG	NH_2

Characterisation

Exact Mass	HPLC Purification Gradient	HPLC Characterisation Gradient	Purity	HRMS Expected	HRMS Detected
3504.06 Da	20-80 % B 20 min	20 - 80% B 50 min	91% RT 26.94 min	$[M+4H]^{4+}$ 877.0	$[M+4H]^{4+}$ 877.5

For all HPLC methods buffers were A = H_2O + 0.1 % TFA, B = MeCN + 0.1% TFA

6.6.2.8 Peptide **7b** – 4-heptad – Ala Spacer - Ac

Sequence

Ac	A QEIAAIK KEIAAIK KEIAAIK KEIAAIK YG	NH_2

Characterisation

Exact Mass	HPLC Purification Gradient	HPLC Characterisation Gradient	Purity	HRMS Expected	HRMS Detected
3364.02 Da	20-80 % B 20 min	20 - 80% B 50 min	85% RT 27.19 min	$[M+3H]^{3+}$ 1122.3	$[M+3H]^{3+}$ 1122.7

For all HPLC methods buffers were A = H_2O + 0.1 % TFA, B = MeCN + 0.1% TFA

6.6.2.9 Peptide **8a** – 4-heptad – Gly Spacer - Bpy

Sequence

Bpy	G QEIAAIK KEIAAIK KEIAAIK KEIAAIK YG	NH_2

Characterisation

Exact Mass	HPLC Purification Gradient	HPLC Characterisation Gradient	Purity	HRMS Expected	HRMS Detected
3490.04 Da	20-80 % B 20 min	20 - 80% B 50 min	90% RT 26.75 min	$[M+4H]^{4+}$ 873.5	$[M+4H]^{4+}$ 874.0

For all HPLC methods buffers were A = H_2O + 0.1 % TFA, B = MeCN + 0.1% TFA

6.6.2.10 Peptide **8b** - 4-heptad – Gly Spacer – Ac

Sequence

Ac	G QEIAAIK KEIAAIK KEIAAIK KEIAAIK YG	NH_2

Characterisation

Exact Mass	HPLC Purification Gradient	HPLC Characterisation Gradient	Purity	HRMS Expected	HRMS Detected
3350.01 Da	20-80 % B 20 min	20 - 80% B 50 min	88% RT 26.91 min	$[M+3H]^{3+}$ 1117.7	$[M+3H]^{3+}$ 1118.0

For all HPLC methods buffers were A = H_2O + 0.1 % TFA, B = MeCN + 0.1% TFA

6.6.2.11 Peptide **9a** - 4-heptad – GlyGly Spacer – Bpy

Sequence

Bpy	G GEIAAIK KEIAAIK KEIAAIK KEIAAIK YG	NH_2

Characterisation

Exact Mass	HPLC Purification Gradient	HPLC Characterisation Gradient	Purity	HRMS Expected	HRMS Detected
3419.01 Da	20-80 % B 20 min	20 - 80% B 50 min	95% RT 26.82 min	$[M+3H]^{3+}$ 1140.7	$[M+3H]^{3+}$ 1141.4

For all HPLC methods buffers were A = H_2O + 0.1 % TFA, B = MeCN + 0.1% TFA

6.6.2.12 Peptide **9b** – 4-heptad – GlyGly Spacer - Ac

Sequence

Ac	G GEIAAIK KEIAAIK KEIAAIK KEIAAIK YG	NH_2

Characterisation

Exact Mass	HPLC Purification Gradient	HPLC Characterisation Gradient	Purity	HRMS Expected	HRMS Detected
3278.97 Da	20-80 % B 20 min	20 - 80% B 50 min	100% RT 26.72 min	$[M+3H]^{3+}$ 1094.0	$[M+3H]^{3+}$ 1094.4

For all HPLC methods buffers were A = H_2O + 0.1 % TFA, B = MeCN + 0.1% TFA

6.6.2.13 Peptide **10a** - 4-heptad – PEG Spacer - Bpy

Sequence

Bpy	(PEG) QEIAAIK KEIAAIK KEIAAIK KEIAAIK YG	NH_2

Characterisation

Exact Mass	HPLC Purification Gradient	HPLC Characterisation Gradient	Purity	HRMS Expected	HRMS Detected
3578.10 Da	20-80 % B 20 min	20 - 80% B 50 min	91% RT 26.39 min	$[M+3H]^{3+}$ 1193.7	$[M+3H]^{3+}$ 1194.4

For all HPLC methods buffers were A = H_2O + 0.1 % TFA, B = MeCN + 0.1% TFA

6.6.2.14 Peptide **10b** – 4-heptad – PEG Spacer – Ac

Sequence

Ac	(PEG) QEIAAIK KEIAAIK KEIAAIK KEIAAIK YG	NH_2

Characterisation

Exact Mass	HPLC Purification Gradient	HPLC Characterisation Gradient	Purity	HRMS Expected	HRMS Detected
3438.10 Da	20-80 % B 20 min	20 - 80% B 50 min	100% RT 26.50 min	$[M+3H]^{3+}$ 1147.0	$[M+3H]^{3+}$ 1147.7

For all HPLC methods buffers were A = H_2O + 0.1 % TFA, B = MeCN + 0.1% TFA

6.6.2.15 Peptide **11a** – D-Ala Spacer – Bpy

Sequence

Bpy	a QEIAAIK KEIAAIK KEIAAIK YG	NH_2

Characterisation

Exact Mass	HPLC Purification Gradient	HPLC Characterisation Gradient	Purity	HRMS Expected	HRMS Detected
2750.58 Da	20-80 % B 20 min	20 - 80% B 50 min	91% RT 23.96 min	$[M+2H]^{2+}$ 1376.3	$[M+2H]^{2+}$ 1376.8

For all HPLC methods buffers were A = H_2O + 0.1 % TFA, B = MeCN + 0.1% TFA

6.6.2.16 Peptide **11b** – D-Ala Spacer - Ac

Sequence

Ac	a QEIAAIK KEIAAIK KEIAAIK YG	NH_2

Characterisation

Exact Mass	HPLC Purification Gradient	HPLC Characterisation Gradient	Purity	HRMS Expected	HRMS Detected
2610.55 Da	20-80 % B 20 min	20 - 80% B 50 min	85% RT 23.98 min	$[M+2H]^{2+}$ 1306.3	$[M+2H]^{2+}$ 1306.7

For all HPLC methods buffers were A = H_2O + 0.1 % TFA, B = MeCN + 0.1% TFA

6.6.2.17 Peptide **12a** – Pro Spacer – Bpy

Sequence

Bpy	P QEIAAIK KEIAAIK KEIAAIK YG	NH_2

Characterisation

Exact Mass	HPLC Purification Gradient	HPLC Characterisation Gradient	Purity	HRMS Expected	HRMS Detected
2776.6 Da	20-80 % B 20 min	20 - 80% B 50 min	87% RT 24.55 min	$[M+2H]^{2+}$ 1389.3	$[M+2H]^{2+}$ 1389.8

For all HPLC methods buffers were A = H_2O + 0.1 % TFA, B = MeCN + 0.1% TFA

6.6.2.18 Peptide **12b** – Pro Spacer – Ac

Sequence

Ac	P QEIAAIK KEIAAIK KEIAAIK YG	NH_2

Characterisation

Exact Mass	HPLC Purification Gradient	HPLC Characterisation Gradient	Purity	HRMS Expected	HRMS Detected
2636.56 Da	20-80 % B 20 min	20 - 80% B 50 min	81% RT 24.89 min	$[M+2H]^{2+}$ 1319.3	$[M+2H]^{2+}$ 1319.8

For all HPLC methods buffers were A = H_2O + 0.1 % TFA, B = MeCN + 0.1% TFA

6.6.2.19 Peptide **13a** – e-position – Bpy

Sequence

Bpy	QEIAAIK KEIAAIK KEIAAIK YG	NH_2

Characterisation

Exact Mass	HPLC Purification Gradient	HPLC Characterisation Gradient	Purity	HRMS Expected	HRMS Detected
2679.55 Da	20-80 % B 20 min	20 - 80% B 50 min	94% RT 23.79 min	$[M+2H]^{2+}$ 1340.8	$[M+2H]^{2+}$ 1341.3

For all HPLC methods buffers were A = H_2O + 0.1 % TFA, B = MeCN + 0.1% TFA

6.6.2.20 Peptide **13b** – e-position - Ac

Sequence

Ac	QEIAAIK KEIAAIK KEIAAIK YG	NH_2

Characterisation

Exact Mass	HPLC Purification Gradient	HPLC Characterisation Gradient	Purity	HRMS Expected	HRMS Detected
2539.51 Da	20-80 % B 20 min	20 - 80% B 50 min	94% RT 23.60 min	$[M+2H]^{2+}$ 1270.8	$[M+2H]^{2+}$ 1271.2

For all HPLC methods buffers were A = H_2O + 0.1 % TFA, B = MeCN + 0.1% TFA

6.6.2.21 Peptide **14a** – f-position - Bpy

Sequence

Bpy	EIAAIK KEIAAIK KEIAAIK K YG	NH_2

Characterisation

Exact Mass	HPLC Purification Gradient	HPLC Characterisation Gradient	Purity	HRMS Expected	HRMS Detected
2679.58 Da	20-80 % B 20 min	20 - 80% B 50 min	90% RT 23.41 min	$[M+2H]^{2+}$ 1340.8	$[M+2H]^{2+}$ 1341.3

For all HPLC methods buffers were A = H_2O + 0.1 % TFA, B = MeCN + 0.1% TFA

6.6.2.22 Peptide **14b** – f-position - Ac

Sequence

Ac	EIAAIK KEIAAIK KEIAAIK K YG	NH_2

Characterisation

Exact Mass	HPLC Purification Gradient	HPLC Characterisation Gradient	Purity	HRMS Expected	HRMS Detected
2539.55 Da	20-80 % B 20 min	20 - 80% B 50 min	97% RT 23.16 min	$[M+2H]^{2+}$ 1270.8	$[M+2H]^{2+}$ 1271.2

For all HPLC methods buffers were A = H_2O + 0.1 % TFA, B = MeCN + 0.1% TFA

6.6.2.23 Peptide **15a** – g-position – Bpy

Sequence

Bpy	IAAIK KEIAAIK KEIAAIK KE YG	NH_2

Characterisation

Exact Mass	HPLC Purification Gradient	HPLC Characterisation Gradient	Purity	HRMS Expected	HRMS Detected
2679.58 Da	20-80 % B 20 min	20 - 80% B 50 min	96% RT 26.39 min	$[M+2H]^{2+}$ 1340.8	$[M+2H]^{2+}$ 1341.3

For all HPLC methods buffers were A = H_2O + 0.1 % TFA, B = MeCN + 0.1% TFA

6.6.2.24 Peptide **15b** – g-position - Ac

Sequence

Ac	IAAIK KEIAAIK KEIAAIK KE YG	NH_2

Characterisation

Exact Mass	HPLC Purification Gradient	HPLC Characterisation Gradient	Purity	HRMS Expected	HRMS Detected
2539.55 Da	20-80 % B 20 min	20 - 80% B 50 min	89% RT 25.38 min	$[M+2H]^{2+}$ 1270.8	$[M+2H]^{2+}$ 1271.2

For all HPLC methods buffers were A = H_2O + 0.1 % TFA, B = MeCN + 0.1% TFA

6.6.2.25 Peptide **16a** – a-position – Bpy

Sequence

Bpy	AAIK KEIAAIK KEIAAIK KEI YG	NH_2

Characterisation

Exact Mass	HPLC Purification Gradient	HPLC Characterisation Gradient	Purity	HRMS Expected	HRMS Detected
2679.58 Da	20-80 % B 20 min	20 - 80% B 50 min	97% RT 25.18 min	$[M+2H]^{2+}$ 1340.8	$[M+2H]^{2+}$ 1341.3

For all HPLC methods buffers were A = H_2O + 0.1 % TFA, B = MeCN + 0.1% TFA

6.6.2.26 Peptide **16b** – a-position - Ac

Sequence

Ac	AAIK KEIAAIK KEIAAIK KEI YG	NH_2

Characterisation

Exact Mass	HPLC Purification Gradient	HPLC Characterisation Gradient	Purity	HRMS Expected	HRMS Detected
2539.55 Da	20-80 % B 20 min	20 - 80% B 50 min	96% RT 24.65 min	$[M+2H]^{2+}$ 1270.8	$[M+2H]^{2+}$ 1271.3

For all HPLC methods buffers were A = H_2O + 0.1 % TFA, B = MeCN + 0.1% TFA

6.6.2.27 Peptide **17a** – b-position - Bpy

Sequence

Bpy	AIK KEIAAIK KEIAAIK KEIA YG	NH_2

Characterisation

Exact Mass	HPLC Purification Gradient	HPLC Characterisation Gradient	Purity	HRMS Expected	HRMS Detected
2679.58 Da	20-80 % B 20 min	20 - 80% B 50 min	93% RT 24.39 min	$[M+2H]^{2+}$ 1340.8	$[M+2H]^{2+}$ 1341.3

For all HPLC methods buffers were A = H_2O + 0.1 % TFA, B = MeCN + 0.1% TFA

6.6.2.28 Peptide **17b** – b-position - Ac

Sequence

Ac	AIK KEIAAIK KEIAAIK KEIA YG	NH_2

Characterisation

Exact Mass	HPLC Purification Gradient	HPLC Characterisation Gradient	Purity	HRMS Expected	HRMS Detected
2539.55 Da	20-80 % B 20 min	20 - 80% B 50 min	93% RT 24.36 min	$[M+2H]^{2+}$ 1270.8	$[M+2H]^{2+}$ 1271.2

For all HPLC methods buffers were A = H_2O + 0.1 % TFA, B = MeCN + 0.1% TFA

6.6.2.29 Peptide **18a** – c-position - Bpy

Sequence

Bpy	IK KEIAAIK KEIAAIK KEIAA YG	NH_2

Characterisation

Exact Mass	HPLC Purification Gradient	HPLC Characterisation Gradient	Purity	HRMS Expected	HRMS Detected
2679.58 Da	20-80 % B 20 min	20 - 80% B 50 min	93% RT 25.54 min	$[M+2H]^{2+}$ 1340.8	$[M+2H]^{2+}$ 1341.3

For all HPLC methods buffers were A = H_2O + 0.1 % TFA, B = MeCN + 0.1% TFA

6.6.2.30 Peptide **18b** – c-position – Ac

Sequence

Ac	IK KEIAAIK KEIAAIK KEIAA YG	NH_2

Characterisation

Exact Mass	HPLC Purification Gradient	HPLC Characterisation Gradient	Purity	HRMS Expected	HRMS Detected
2539.55 Da	20-80 % B 20 min	20 - 80% B 50 min	90% RT 25.51 min	$[M+2H]^{2+}$ 1270.8	$[M+2H]^{2+}$ 1271.2

For all HPLC methods buffers were A = H_2O + 0.1 % TFA, B = MeCN + 0.1% TFA

6.6.2.31 Peptide **19a** – d-position – Bpy

Sequence

Bpy	Q KEIAAIK KEIAAIK KEIAAI YG	NH_2

Characterisation

Exact Mass	HPLC Purification Gradient	HPLC Characterisation Gradient	Purity	HRMS Expected	HRMS Detected
2679.55 Da	20-80 % B 20 min	20 - 80% B 50 min	95% RT 25.69 min	$[M+2H]^{2+}$ 1340.8	$[M+2H]^{2+}$ 1341.3

For all HPLC methods buffers were A = H_2O + 0.1 % TFA, B = MeCN + 0.1% TFA

6.6.2.32 Peptide **19b** – d-position - Ac

Sequence

Ac	Q KEIAAIK KEIAAIK KEIAAI YG	NH_2

Characterisation

Exact Mass	HPLC Purification Gradient	HPLC Characterisation Gradient	Purity	HRMS Expected	HRMS Detected
2539.51 Da	20-80 % B 20 min	20 - 80% B 50 min	97% RT 25.16 min	$[M+2H]^{2+}$ 1270.8	$[M+2H]^{2+}$ 1271.3

For all HPLC methods buffers were A = H_2O + 0.1 % TFA, B = MeCN + 0.1% TFA

6.6.3 Circular Dichroism for Peptides **4a-19b**

6.6.3.1 Equipment Set Up

For all experiments with peptides **4a–19b** the wavelength range was set to 400–180 nm, to capture both the signals from the bpy units and the peptide.

6.6.3.2 Sample Preparation

Concentrations of peptide stock solutions were calculated by UV-Vis 280 nm absorbance measurements using the NanoDrop One spectrophotometer.

All peptide samples for the CD were prepared to a concentration of 10 μM in 2 mL, 20 mM aqueous MOPS buffer, (pH 7). These samples were made up in a 2 mL cuvette with a pathlength of 10 mm.

6.6.3.3 Titrations

All metal titrations for peptides **4a-19b** were run at room temperature, with 0.25 s time per point and four repeats per titration point.

For all the metal salts used in the titrations ($Zn(NO_3)_2$ and $Cu(NO_3)_2$) stock solutions were made up to 0.5 mM in H_2O.

The titrations of metal salt into the peptide solution were run from 0.0 eq of metal salt to 1.0 eq metal salt. For each point of the titration 4 μL (0.1 eq, 1 μM) of the 0.5 mM metal stock solution was added to the 10 μM peptide solution.

CD titration data was normalised before plotting using the following equation.

[MRE (Mean Residue Ellipticity) = (100 * θ (mdeg) / (C (dmol) * no. of amide * l (cm)]

This normalisation allows for peptides of different compositions to be compared by reporting the ellipticity as a value per residue of the sequence.

6.7 Chapter 4 Experimental

The experimental section below describes the synthesis and characterisation of peptides **20a** **21a**, **21b**, **22a** and **22b**, all of which were discussed in Chapter 4.

6.7.1 Peptide Synthesis

All peptides (**20a**, **21a**, **21b**, **22a** and **22b**) were synthesised by microwave assisted SPPS as described in Section 6.3.2 on a 0.1 mmol scale using a Rink Amide Resin and Fmoc/tBu protection strategy.

All **a** peptides (**20a–22a**) had 8-hydroxyquinoline-4-carboxylic acid coupled to the N-terminus using the coupling procedure described in Section 6.3.5.

For all **b** peptides (**21b** and **22b**) acetyl capping procedure (Section 6.3.1.2) was performed.

Standard cleavage procedure (Section 6.3.1.4) of **20a–22b** was performed. All of these peptides were purified by RP-HPLC using a Phenomenex C18 column.

Peptides **20a**, **21a** and **22a** were all obtained as yellow powders after lyophilisation.

Peptides **21b** and **22b** were obtained as white powders after lyophilisation.

Following lyophilisation, **20a–22b** were characterised by HRMS and analytical HPLC. Details of the characterisation are in Section 6.7.2.

6.7.2 Peptide Characterisation

6.7.2.1 Peptide **20a** d-position – 8-HQ

Sequence

8-HQ	G QEIAAIK KEIAAIK KEIAAIK YG	NH_2

Characterisation

Exact Mass	HPLC Purification Gradient	HPLC Characterisation Gradient	Purity	HRMS Expected	HRMS Detected
2725.55 Da	20-80 % B 20 min	20 - 80% B 50 min	96% RT 23.11 min	$[M+3H]^{3+}$ 909.5	$[M+3H]^{3+}$ 909.9

For all HPLC methods buffers were A = H_2O + 0.1 % TFA, B = MeCN + 0.1% TFA

6.7.2.2 Peptide **21a** e-position – 8-HQ

Sequence

8-HQ	G EIAAIK KEIAAIK KEIAAIK K YG	NH_2

Characterisation

Exact Mass	HPLC Purification Gradient	HPLC Characterisation Gradient	Purity	HRMS Expected	HRMS Detected
2725.55 Da	20-80 % B 20 min	20 - 80% B 50 min	98% RT 22.58 min	$[M+2H]^{2+}$ 1363.8	$[M+2H]^{2+}$ 1364.3

For all HPLC methods buffers were A = H_2O + 0.1 % TFA, B = MeCN + 0.1% TFA

6.7.2.3 Peptide **21b** e-position – Ac

Sequence

Ac	G EIAAIK KEIAAIK KEIAAIK K YG	NH_2

Characterisation

Exact Mass	HPLC Purification Gradient	HPLC Characterisation Gradient	Purity	HRMS Expected	HRMS Detected
2596.57 Da	20-80 % B 20 min	20 - 80% B 50 min	97% RT 23.86 min	$[M+2H]^{2+}$ 1299.3	$[M+2H]^{2+}$ 1299.3

For all HPLC methods buffers were A = H_2O + 0.1 % TFA, B = MeCN + 0.1% TFA

6.7.2.4 Peptide **22a** a-position – 8-HQ

Sequence

8HQ	G AIK KEIAAIK KEIAAIK KEIA YG	NH_2

Characterisation

Exact Mass	HPLC Purification Gradient	HPLC Characterisation Gradient	Purity	HRMS Expected	HRMS Detected
2725.59 Da	20-80 % B 20 min	20 - 80% B 50 min	99% RT 23.97 min	$[M+2H]^{2+}$ 1363.8	$[M+2H]^{2+}$ 1364.3

For all HPLC methods buffers were A = H_2O + 0.1 % TFA, B = MeCN + 0.1% TFA

6.7.2.5 Peptide **22b** a-position – Ac

Sequence

Ac	G AIK KEIAAIK KEIAAIK KEIA YG	NH_2

Characterisation

Exact Mass	HPLC Purification Gradient	HPLC Characterisation Gradient	Purity	HRMS Expected	HRMS Detected
2596.57 Da	20-80 % B 20 min	20 - 80% B 50 min	93% RT 24.85 min	$[M+2H]^{2+}$ 1299.3	$[M+2H]^{2+}$ 1299.8

For all HPLC methods buffers were A = H_2O + 0.1 % TFA, B = MeCN + 0.1% TFA

6.7.3 Circular Dichroism for Peptides **20a-22b**

6.7.3.1 Equipment Set Up

For all experiments with peptides **20a**, **21a**, **21b**, **22a** and **22b** the wavelength range was set to 400 – 180 nm, to capture both the signals from the 8-HQ units and the peptide.

6.7.3.2 Sample Preparation

Concentrations of peptide stock solutions were calculated by UV-Vis 280 nm absorbance measurements using the NanoDrop One spectrophotometer.

For all titrations against Co^{2+}, Ga^{3+} and Al^{3+} peptide samples for the CD were prepared to a concentration of 10 μM in 2 mL, 20 mM aqueous MOPS buffer, (pH 7). These samples were made up in a 2 mL cuvette with a pathlength of 10 mm.

For the pH investigation 3 alternate buffer solutions were prepared; ammonium acetate (pH 4), ammonium bicarbonate (pH 8), and MOPS (pH 6). For the samples used in these experiments the peptides were prepared as 10 μM concentrations in 20 mM of the corresponding aqueous buffer (either ammonium acetate, pH 4, ammonium bicarbonate, pH 8, or MOPS, pH 6).

6.7.3.3 Titrations

All metal titrations for peptides **20a–22b** were run at room temperature (approximately 25 °C), with 0.25 s time per point and four repeats per titration point.

For all the metal salts used in the titrations ($CoCl_2$, $Ga(NO_3)_3$ and $AlCl_3$) stock solutions were made up to 0.5 mM in H_2O.

The titrations of metal salt into the peptide solution were run from 0.0 eq of metal salt to 1.0 eq metal salt. For each point of the titration 4 μL (0.1 eq, 1 μM) of the 0.5 mM metal stock solution was added to the 10 μM peptide solution.

CD titration data was normalised before plotting using the following equation.

[MRE (Mean Residue Ellipticity) = (100 * θ (mdeg) / (C (dmol) * no. of amide * l (cm)]

This normalisation allows for peptides of different compositions to be compared by reporting the ellipticity as a value per residue of the sequence.

6.7.3.4 Variable Temperature

For variable temperature CD experiments, the temperature of the sample stage was set to ramp from 5–80°C in 5 °C increments. For each temperature measurement, the time per data point was increased to 0.75 s to account for the fact that only one measurement was taken per temperature.

7 References

1. M. H. Godinho, J. P. Canejo, G. Feio and E. M. Terentjev, *Soft Matter*, 2010, **6**, 5965, DOI: 10.1039/C0SM00427H.
2. F. Maderspacher, *Curr Biol*, 2016, **26**, R215, DOI: 10.1016/j.cub.2016.02.008.
3. M. Inaki, J. Liu and K. Matsuno, *Philos Trans R Soc Lond B Biol Sci*, 2016, **371**, DOI: 10.1098/rstb.2015.0403.
4. A. H. G. David and J. F. Stoddart, *Isr J Chem*, 2021, **61**, 608, DOI: 10.1002/ijch.202100066.
5. J. Dong, Y. Liu and Y. Cui, *Acc Chem Res*, 2021, **54**, 194, DOI: 10.1021/acs.accounts.0c00604.
6. S. M. Morrow, A. J. Bissette and S. P. Fletcher, *Nat Nanotechnol*, 2017, **12**, 410, DOI: 10.1038/nnano.2017.62.
7. B. Ni and H. Cölfen, *SmartMat*, 2021, **2**, 17, DOI: 10.1002/smm2.1021.
8. J. Gal, *Nat Chem*, 2017, **9**, 604, DOI: 10.1038/nchem.2790.
9. G. Vantomme and J. Crassous, *Chirality*, 2021, **33**, 597, DOI: 10.1002/chir.23349.
10. W. Xiao, K.-H. Ernst, K. Palotas, Y. Zhang, E. Bruyer, L. Peng, T. Greber, W. A. Hofer, L. T. Scott and R. Fasel, *Nat Chem*, 2016, **8**, 326, DOI: 10.1038/nchem.2449.
11. J. R. Cossy, in *Comprehensive Chirality*, Elsevier, Amsterdam, 2012, ch.1.1, pp 1-7, DOI: 10.1038/s41598-018-35457-6.
12. E. Tokunaga, T. Yamamoto, E. Ito and N. Shibata, *Sci Rep*, 2018, **8**, 17131, DOI: 10.1038/s41598-018-35457-6.
13. L. Wang, N. Wang, W. Zhang, X. Cheng, Z. Yan, G. Shao, X. Wang, R. Wang and C. Fu, *Signal Transduct and Targeted Ther*, 2022, **7**, 48, DOI: 10.1038/s41392-022-00904-4.
14. D. Al Shaer, O. Al Musaimi, F. Albericio and B. G. de la Torre, *Pharmaceuticals*, 2024, **17**, DOI: 10.3390/ph17020243.
15. M. Denis, J. E. M. Lewis, F. Modicom and S. M. Goldup, *Chem*, 2019, **5**, 1512, DOI: 10.1016/j.chempr.2019.03.008.
16. N. Ousaka, Y. Takeyama, H. Iida and E. Yashima, *Nat Chem*, 2011, **3**, 856, DOI: 10.1038/nchem.1146.
17. N. A. Kotov, L. M. Liz-Marzán and P. S. Weiss, *ACS Nano*, 2021, **15**, 12457, DOI: 10.1021/acsnano.1c06959.
18. A. J. Gellman, *Acc Mater Res*, 2021, **2**, 1024, DOI: 10.1021/accountsmr.1c00145.
19. S. Guo, J. Wang, Q. Wang, J. Wang, S. Qin and W. Li, *Heliyon*, 2024, **10**, e26009, DOI: 10.1016/j.heliyon.2024.e26009.
20. M. Suzuki and M. Gerstein, *Proteins*, 1995, **23**, 525, DOI: 10.1002/prot.340230407.
21. M. Cassandri, A. Smirnov, F. Novelli, C. Pitolli, M. Agostini, M. Malewicz, G. Melino and G. Raschellà, *Cell Death Discov*, 2017, **3**, 17071, DOI: 10.1038/cddiscovery.2017.71.

22. M. M. Gromiha, in *Protein Bioinformatics*, Academic Press, Singapore, 2010, DOI: 10.1016/B978-8-1312-2297-3.50001-1..
23. A. Böck, K. Forchhammer, J. Heider, W. Leinfelder, G. Sawers, B. Veprek and F. Zinoni, *Mol Microbiol*, 1991, **5**, 515, DOI: 10.1111/j.1365-2958.1991.tb00722.x.
24. L. Skipper, in *Encyclopedia of Analytical Science (Second Edition)*, Elsevier, Oxford, 2005, pp. 344-352, DOI: 10.1016/B0-12-369397-7/00493-3..
25. S. C. Lovell, I. W. Davis, W. B. Arendall III, P. I. W. de Bakker, J. M. Word, M. G. Prisant, J. S. Richardson and D. C. Richardson, *Protein*, 2003, **50**, 437, DOI: 10.1002/prot.10286.
26. D. Eisenberg, *Proc Natl Acad Sci USA*, 2003, **100**, 11207, DOI: 10.1073/pnas.2034522100.
27. D. J. Barlow and J. M. Thornton, *J Mol Biol*, 1988, **201**, 601, DOI: 10.1016/0022-2836(88)90641-9.
28. S. A. Hollingsworth and P. A. Karplus, *Biomol Concepts*, 2010, **1**, 271, DOI: 10.1515/bmc.2010.022.
29. G. D. Rose, in *Prediction of Protein Secondary Structure*, Springer US, New York, NY, 2025, pp. 1-17, DOI: 10.1007/978-1-0716-4196-5_1.
30. M. K. Kim and Y. K. Kang, *Protein Sci*, 1999, **8**, 1492, DOI: 10.1110/ps.8.7.1492.
31. H. I. Merritt, N. Sawyer and P. S. Arora, *Pept Sci*, 2020, **112**, DOI: 10.1002/pep2.24145.
32. G. N. Ramachandran, C. Ramakrishnan and V. Sasisekharan, *J Mol Biol*, 1963, **7**, 95, DOI: 10.1016/s0022-2836(63)80023-6.
33. S. W. Robinson, A. M. Afzal and D. P. Leader, in *Handbook of Pharmacogenomics and Stratified Medicine*, Academic Press, San Diego, 2014, ch.13, pp259-287, DOI: 10.1016/B978-0-12-386882-4.00013-X..
34. M. Liu, L. Zhang and T. Wang, *Chem Rev*, 2015, **115**, 7304, DOI: 10.1021/cr500671p.
35. N. E. Shepherd, H. N. Hoang, G. Abbenante and D. P. Fairlie, *J Am Chem Soc*, 2005, **127**, 2974, DOI: 10.1021/ja0456003.
36. S. Annavarapu and V. Nanda, *BMC Struc Biol*, 2009, **9**, 61, DOI: 10.1186/1472-6807-9-61.
37. N. V. Bhagavan and C.-E. Ha, in *Essentials of Medical Biochemistry*, Academic Press, San Diego, 2011, ch.4, pp.29-38, DOI: 10.1016/B978-0-12-095461-2.00004-7..
38. W. T. Godbey, in *An Introduction to Biotechnology*, Woodhead Publishing, 2014, ch. 2, pp. 9-33, DOI: 10.1016/B978-1-907568-28-2.00002-2..
39. F. H. C. Crick, *Nat*, 1952, **170**, 882, DOI: 10.1038/170882b0.
40. L. Truebestein and T. A. Leonard, *BioEssays*, 2016, **38**, 903, DOI: 10.1002/bies.201600062.
41. E. H. Bromley, K. Channon, E. Moutevelis and D. N. Woolfson, *ACS Chem Biol*, 2008, **3**, 38, DOI: 10.1021/cb700249v.
42. P. B. Harbury, T. Zhang, P. S. Kim and T. Alber, *Sci*, 1993, **262**, 1401, DOI: 10.1126/science.8248779.

43. J. M. Fletcher, A. L. Boyle, M. Bruning, G. J. Bartlett, T. L. Vincent, N. R. Zaccai, C. T. Armstrong, E. H. C. Bromley, P. J. Booth, R. L. Brady, A. R. Thomson and D. N. Woolfson, *ACS Synth Biol*, 2012, **1**, 240, DOI: 10.1021/sb300028q.
44. A. N. Lupas, J. Bassler and S. Dunin-Horkawicz, *Subcell Biochem*, 2017, **82**, 95, DOI: 10.1007/978-3-319-49674-0_4.
45. P. Burkhard, R. A. Kammerer, M. O. Steinmetz, G. P. Bourenkov and U. Aebi, *Structure*, 2000, **8**, 223, DOI: 10.1016/s0969-2126(00)00100-3.
46. J. M. Mason and K. M. Arndt, *Chembiochem*, 2004, **5**, 170, DOI: 10.1016/0073-8085(68)80016-6.
47. J. Feher, in *Quantitative Human Physiology (Second Edition)*, Academic Press, Boston, 2017, ch.2.3, pp.130-141, DOI: 10.1016/B978-0-12-800883-6.00012-4..
48. W. T. Godbey, in *Biotechnology and its Applications (Second Edition)*, Academic Press, 2022, ch.3, pp.47-72, DOI: 10.1016/B978-0-12-817726-6.00003-4..
49. G. M. Whitesides and B. Grzybowski, *Sci*, 2002, **295**, 2418, DOI: 10.1126/science.1070821.
50. G. Pandey and D. Datta, in *De Novo Peptide Design*, eds. V. Ramakrishnan, Academic Press, 2023, ch.6, pp.133-171, DOI: 10.1016/B978-0-323-99917-5.00001-9..
51. D. Herschlag and M. M. Pinney, *Biochem*, 2018, **57**, 3338, DOI: 10.1021/acs.biochem.8b00217.
52. P. Ball, *Nat*, 2010, **468**, 1036, DOI: 10.1038/4681036a.
53. C. A. Hunter, K. R. Lawson, J. Perkins and C. J. Urch, *J Chem Soc Perkin Trans 2*, 2001, 651, DOI: 10.1039/B008495F.
54. S. Y. Sheu, D. Y. Yang, H. L. Selzle and E. W. Schlag, *Proc Natl Acad Sci USA*, 2003, **100**, 12683, DOI: 10.1073/pnas.2133366100.
55. D. E. McRee, in *Practical Protein Crystallography (Second Edition)*, Academic Press, San Diego, 1999, ch.3, pp.91-92, DOI: 10.1016/B978-012486052-0/50005-1.
56. T. Chen, M. Li and J. Liu, *Crystal Growth Des*, 2018, **18**, 2765, DOI: 10.1021/acs.cgd.7b01503.
57. PubChem, National Center for Biotechnology Information. Electronegativity in the Periodic Table of Elements https://pubchem.ncbi.nlm.nih.gov/periodic-table/electronegativity, (accessed 13/03/2025, 2025).
58. E. G. Hohenstein and C. D. Sherrill, *J Phys Chem A*, 2009, **113**, 878, DOI: 10.1021/jp809062x.
59. G. B. McGaughey, M. Gagné and A. K. Rappé, *J Biol Chem*, 1998, **273**, 15458, DOI: 10.1074/jbc.273.25.15458.
60. S. K. Burley and G. A. Petsko, *Sci*, 1985, **229**, 23, DOI: 10.1126/science.3892686.
61. S. M. Butterfield, P. R. Patel and M. L. Waters, *J Am Chem Soc*, 2002, **124**, 9751, DOI: 10.1021/ja026668q.

62. L. Serrano, M. Bycroft and A. R. Fersht, *J Mol Biol*, 1991, **218**, 465, DOI: 10.1016/0022-2836(91)90725-L.
63. C. Branden and J. Tooze, *Introduction to protein structure (Second Edition)*, Garland, New York, 1999, DOI: 10.1201/9781136969898.
64. S. Aldrich, Amino Acids Reference Chart, https://www.sigmaaldrich.com/GB/en/technical-documents/technical-article/protein-biology/protein-structural-analysis/amino-acid-reference-chart?srsltid=AfmBOooQZz6IDy1m7bURnL3rFlA46gntYsxIJpiktFjC0mdjCo_FJ2Oq, (accessed 03/04/2025, 2025).
65. E. Frieden, *J Chem Educ*, 1975, **52**, 754, DOI: 10.1021/ed052p754.
66. J. E. Donald, D. W. Kulp and W. F. DeGrado, *Proteins*, 2011, **79**, 898, DOI: 10.1002/prot.22927.
67. J. B. Vincent and S. Love, *BBA Gen Subj*, 2012, **1820**, 362, DOI: 10.1016/j.bbagen.2011.07.003.
68. G. Maayan, M. D. Ward and K. Kirshenbaum, *Chem Comm*, 2009, 56, DOI: 10.1039/B810875G.
69. J. Fetse, S. Kandel, U.-F. Mamani and K. Cheng, *Trends Pharmacol Sci*, 2023, **44**, 425, DOI: 10.1016/j.tips.2023.04.003.
70. Y. Zhao and J. Moore, *Foldamers Based on Solvophobic Effects*, Wiley-VCH, 2007, pp.75-108, DOI: 10.1002/9783527611478.
71. A. C. Mendes, E. T. Baran, R. L. Reis and H. S. Azevedo, *WIREs Nanomed Nanobi*, 2013, **5**, 582, DOI: 10.1002/wnan.1238.
72. J. Wang and B. Xu, *Chem*, 2018, **4**, 1765, DOI: 10.1016/j.chempr.2018.07.011.
73. J. A. Hutchinson, I. W. Hamley, J. Torras, C. Alemán, J. Seitsonen and J. Ruokolainen, *J Phys Chem B*, 2019, **123**, 614, DOI: 10.1021/acs.jpcb.8b11097.
74. A. R. Sapala, S. Dhawan and V. Haridas, *RSC Adv*, 2017, **7**, 26608, DOI: 10.1039/C7RA02746J.
75. J. D. Hartgerink, J. R. Granja, R. A. Milligan and M. R. Ghadiri, *J Am Chem Soc*, 1996, **118**, 43, DOI: 10.1021/ja953070s.
76. C. J. C. Edwards-Gayle and I. W. Hamley, *Org Biomol Chem*, 2017, **15**, 5867, DOI: 10.1039/C7OB01092C.
77. Y.-H. Gao, K. Zhang, M.-R. Ding, X.-F. Gong, H. Cao and L. Wang, *Colloid Interfac Sci Comm*, 2022, **48**, 100622, DOI: 10.1016/j.colcom.2022.100622.
78. J. D. Hartgerink, E. Beniash and S. I. Stupp, *Proc Natl Acad Sci USA*, 2002, **99**, 5133, DOI: 10.1073/pnas.072699999.
79. M. P. Hendricks, K. Sato, L. C. Palmer and S. I. Stupp, *Acc Chem Res*, 2017, **50**, 2440, DOI: 10.1021/acs.accounts.7b00297.

80. R. Booth, I. Insua, S. Ahmed, A. Rioboo and J. Montenegro, *Nat Comm*, 2021, **12**, 6421, DOI: 10.1038/s41467-021-26681-2.
81. V. Castelletto, I. W. Hamley, J. Perez, L. Abezgauz and D. Danino, *Chem Comm*, 2010, **46**, 9185, DOI: 10.1039/C0CC03793A.
82. I. W. Hamley, A. Dehsorkhi and V. Castelletto, *Langmuir*, 2013, **29**, 5050, DOI: 10.1021/la400163q.
83. S. Eskandari, T. Guerin, I. Toth and R. J. Stephenson, *Adv Drug Deliv Rev*, 2017, **110**, 169, DOI: 10.1016/j.addr.2016.06.013.
84. G. A. Silva, C. Czeisler, K. L. Niece, E. Beniash, D. A. Harrington, J. A. Kessler and S. I. Stupp, *Sci*, 2004, **303**, 1352, DOI: 10.1126/science.1093783.
85. M. Malkoch, E. Malmström and A. M. Nyström, in *Polymer Science: A Comprehensive Reference*, Elsevier, Amsterdam, 2012, ch.6.04, pp.113-176, DOI: 10.1016/B978-0-444-53349-4.00162-X..
86. F. Huang and E. V. Anslyn, *Chem Rev*, 2015, **115**, 6999, DOI: 10.1021/acs.chemrev.5b00352.
87. B. Mohan and S. Shanmugaraju, in *Supramolecular Coordination Complexes*, Elsevier, 2023, ch.1, pp.1-25, DOI: 10.1016/B978-0-323-90582-4.00012-9.
88. D. A. Leigh, P. J. Lusby, R. T. McBurney, A. Morelli, A. M. Z. Slawin, A. R. Thomson and D. B. Walker, *J Am Chem Soc*, 2009, **131**, 3762, DOI: 10.1021/ja809627j.
89. C. O. Dietrich-Buchecker, J. P. Sauvage and J. P. Kintzinger, *Tetrahedron Lett*, 1983, **24**, 5095, DOI: 10.1016/S0040-4039(00)94050-4.
90. G. Flora, M. Mittal and S. J. S. Flora, in *Handbook of Arsenic Toxicology*, Academic Press, Oxford, 2015, ch.26, pp.589-626, DOI: 10.1016/B978-0-12-418688-0.00026-5..
91. K. A. Anderson, in *Encyclopedia of Separation Science*, Academic Press, Oxford, 2000, pp.1383-1389, DOI: 10.1016/B0-12-226770-2/02043-3.
92. A. Earnshaw, L. F. Larkworthy and K. C. Patel, *J Chem Soc A*, 1969, DOI: 10.1039/J19690001339.
93. E. C. Constable, *Advances in Inorganic Chemistry*, Academic Press, 1989, pp.1-63, DOI: 10.1016/S0898-8838(08)60014-8.
94. C. Kaes, A. Katz and M. W. Hosseini, *Chem Rev*, 2000, **100**, 3553, DOI: 10.1039/J19690001339.
95. S. F. Mason, *Inorg Chim Acta Rev*, 1968, **2**, 89, DOI: 10.1016/0073-8085(68)80016-6.
96. I. Eryazici, C. N. Moorefield and G. R. Newkome, *Chem Rev*, 2008, **108**, 1834, DOI: 10.1021/cr0781059.
97. M. J. Winter, *d-block Chemistry (Second Edition)*, Oxford University Press, 2023, DOI: 10.1093/hesc/9780198700968.001.0001.
98. A. P. Smith and C. L. Fraser, in *Comprehensive Coordination Chemistry II*, Pergamon, Oxford, 2003, ch.1.1, pp.1-23, DOI: 10.1016/B0-08-043748-6/01103-8..

99. D. Sasi, V. Ramkumar and N. N. Murthy, *ACS Omega*, 2017, **2**, 2474, DOI: 10.1021/acsomega.7b00119.
100. Q.-F. Yang, K. Yue, Z.-H. Wang, X.-Y. Lai, X.-Z. Wang and L. Qin, *CJSC*, 2022, **41**, 2202064, DOI: 10.14102/j.cnki.0254-5861.2011-3266.
101. A. Wada, N. Sakabe and J. Tanaka, *Acta Crystallogr B*, 1976, **32**, 1121, DOI: 10.1107/S0567740876004809.
102. A.-C. Chamayou, C. Biswas, C. Janiak and A. Ghosh, *Acta Crystallogr E*, 2007, **63**, m1936, DOI: 10.1107/S1600536807028863.
103. G. H. Eom, H. M. Park, M. Y. Hyun, S. P. Jang, C. Kim, J. H. Lee, S. J. Lee, S.-J. Kim and Y. Kim, *Polyhedron*, 2011, **30**, 1555, DOI: 10.1016/j.poly.2011.03.040.
104. S. Xu, J. E. T. Smith and J. M. Weber, *Inorg Chem*, 2016, **55**, 11937, DOI: 10.1021/acs.inorgchem.6b02054.
105. C. Verma, I. Y. Yaagoob, L. K. M. O. Goni, S. S. E. Abdelkreem, S. A. Mubarak, H. A. M. Al-Mohsin, A. Alfantazi and M. A. Jafar Mazumder, *Coord Chem Rev*, 2025, **529**, 216433, DOI: 10.1016/j.ccr.2025.216433.
106. A. Salma, M. Fatiha and N. Leila, *Comput Theor Chem*, 2021, **1206**, 113481, DOI: 10.1016/j.comptc.2021.113481.
107. H. Mutlu Gençkal, *J Mol Struc*, 2020, **1209**, 127917, DOI: 10.1016/j.molstruc.2020.127917.
108. E. V. Shchegolkov, I. V. Shchur, Y. V. Burgart, P. A. Slepukhin, N. P. Evstigneeva, N. A. Gerasimova, N. V. Zilberberg, N. V. Kungurov, V. I. Saloutin and O. N. Chupakhin, *Polyhedron*, 2021, **194**, 114900, DOI: 10.1016/j.poly.2020.114900.
109. R. Zou, Q. Wang, J. Wu, J. Wu, C. Schmuck and H. Tian, *Chem Soc Rev*, 2015, **44**, 5200, DOI: 10.1039/C5CS00234F.
110. M. M. Pires, D. E. Przybyla and J. Chmielewski, *Angew Chem Int Ed*, 2009, **48**, 7813, DOI: 10.1002/anie.200902375.
111. D. E. Przybyla and J. Chmielewski, *J Am Chem Soc*, 2008, **130**, 12610, DOI: 10.1021/ja804942w.
112. D. E. Przybyla and J. Chmielewski, *J Am Chem Soc*, 2010, **132**, 7866, DOI: 10.1021/ja103148t.
113. P. Kumar and M. Bansal, *J Struc Biol*, 2016, **196**, 414, DOI: 10.1016/j.jsb.2016.09.006.
114. C. Queffélec, P. B. Pati and Y. Pellegrin, *Chem Rev*, 2024, **124**, 6700, DOI: 10.1021/acs.chemrev.3c00543.
115. P. G. Sammes and G. Yahioglu, *Chem Soc Rev*, 1994, **23**, 327, DOI: 10.1039/CS9942300327.
116. G. Accorsi, A. Listorti, K. Yoosaf and N. Armaroli, *Chem Soc Rev*, 2009, **38**, 1690, DOI: 10.1039/B806408N.
117. P. Kalle and S. I. Bezzubov, *Russ J Inorg Chem*, 2021, **66**, 1682, DOI: 10.1134/S0036023621110103.

118. R. D. Gillard, S. H. Mitchell and W. T. Robinson, *Polyhedron*, 1989, **8**, 2649, DOI: 10.1016/S0277-5387(00)80435-0.
119. O. P. Anderson, *J Chem Soc Dalton Trans*, 1973, 1237, DOI: 10.1039/DT9730001237.
120. Y. Qiu, M. Yang, W. Chen, Y. Su, Z. Ouyang, H. Yan, F. Gao and W. Dong, *J Phys Chem A*, 2013, **117**, 4051, DOI: 10.1021/jp402279k.
121. A. Bencini and V. Lippolis, *Coord Chem Rev*, 2010, **254**, 2096, DOI: 10.1016/j.ccr.2010.04.008.
122. P. Alreja and N. Kaur, *RSC Adv*, 2016, **6**, 23169, DOI: 10.1039/C6RA00150E.
123. C. Bissani Gasparin and D. A. Pilger, *ChemistrySelect*, 2023, **8**, e202204219, DOI: 10.1002/slct.202204219.
124. V. Prachayasittikul, S. Prachayasittikul, S. Ruchirawat and V. Prachayasittikul, *Drug Des Devel Ther*, 2013, **7**, 1157, DOI: 10.2147/dddt.S49763.
125. L. Côrte-Real, V. Pósa, M. Martins, R. Colucas, N. V. May, X. Fontrodona, I. Romero, F. Mendes, C. Pinto Reis, M. M. Gaspar, J. C. Pessoa, É. A. Enyedy and I. Correia, *Inorg Chem*, 2023, **62**, 11466, DOI: 10.1021/acs.inorgchem.3c01066.
126. S.-H. Zhou, W.-H. Liao, Y. Yang, W. Li, Y.-y. Wu, T.-T. Wu, S.-H. Deng, J. Zhou, Z. Li, Q.-H. Zhao, J.-Y. Xu, C. Chen and M.-J. Xie, *ACS Omega*, 2023, **8**, 6945, DOI: 10.1021/acsomega.2c07742.
127. M. L. Ramos, L. L. G. Justino, R. Barata, T. Costa and H. D. Burrows, *Dalton Trans*, 2021, **50**, 16970, DOI: 10.1039/D1DT02858H.
128. J. Palion-Gazda, A. Luz, L. R. Raposo, K. Choroba, J. E. Nycz, A. Bieńko, A. Lewińska, K. Erfurt, P. V. Baptista, B. Machura, A. R. Fernandes, L. S. Shul'pina, N. S. Ikonnikov and G. B. Shul'pin, *Mol*, 2021, **26**, 6364, DOI: 10.3390/molecules26216364.
129. M. Rajeswaran and V. V. Jarikov, *Acta Crystallogr E*, 2004, **60**, m217, 10.1107/S1600536804001242.
130. A. Albert and A. Hampton, *J Chem Soc*, 1954, 505, DOI: 10.1039/JR9540000505.
131. E. Ziegler and G. Haberhauer, *Eur J Org Chem*, 2009, **2009**, 3432, DOI: 10.1002/ejoc.200900250.
132. A. Bera, T. Sarkar, A. Upadhyay and A. Hussain, *Coord Chem Rev*, 2025, **541**, 216847, DOI: 10.1016/j.ccr.2025.216847.
133. D. C. Crans and K. Kostenkova, *Comm Chem*, 2020, **3**, 104, DOI: 10.1038/s42004-020-00341-w.
134. E. C. Constable, *Dalton Trans*, 2019, **48**, 9408, DOI: 10.1039/C9DT00765B.
135. N. Lehnert, E. Kim, H. T. Dong, J. B. Harland, A. P. Hunt, E. C. Manickas, K. M. Oakley, J. Pham, G. C. Reed and V. S. Alfaro, *Chem Rev*, 2021, **121**, 14682, DOI: 10.1021/acs.chemrev.1c00253.
136. A. K. Renfrew, E. S. O'Neill, T. W. Hambley and E. J. New, *Coord Chem Rev*, 2018, **375**, 221, DOI: 10.1016/j.ccr.2017.11.027.

137. C. Wegeberg and O. S. Wenger, *JACS Au*, 2021, **1**, 1860, DOI: 10.1021/jacsau.1c00353.
138. R. D. Shannon, *Acta Crystallogr A*, 1976, **32**, 751, DOI: 10.1107/S0567739476001551.
139. R. R. Maar and J. B. Gilroy, *Chem Eur J*, 2018, **24**, 12449, DOI: 10.1002/chem.201800354.
140. G. H. Robinson, in *Comprehensive Coordination Chemistry II*, Pergamon, Oxford, 2003, ch.3.4, pp.347-382, DOI: 10.1016/B0-08-043748-6/02002-8..
141. D. Nicholls, in *Complexes and First-Row Transition Elements*, Macmillan Education UK, London, 1974, pp.120-127, DOI: 10.1007/978-1-349-02335-6_9..
142. Y. Kobayashi, M. Hoshino, T. Kameda, K. Kobayashi, K. Akaji, S. Inuki, H. Ohno and S. Oishi, *Inorg Chem*, 2018, **57**, 5475, DOI: 10.1021/acs.inorgchem.8b00416.
143. B. Winter, B. Butz, C. Dieker, G. E. Schröder-Turk, K. Mecke and E. Spiecker, *Proc Natl Acad Sci*, 2015, **112**, 12911, DOI: 10.1073/pnas.1511354112.
144. G. E. Schröder-Turk, S. Wickham, H. Averdunk, F. Brink, J. D. Fitz Gerald, L. Poladian, M. C. J. Large and S. T. Hyde, *J Struc Biol*, 2011, **174**, 290, DOI: 10.1016/j.jsb.2011.01.004.
145. M. Saba, B. D. Wilts, J. Hielscher and G. E. Schröder-Turk, *Mater Today Proc*, 2014, **1**, 193, DOI: 10.1016/j.matpr.2014.09.023.
146. G. Roos and C. Roos, in *Organic Chemistry Concepts*, Academic Press, Boston, 2015, ch.3, pp.43-54, DOI: 10.1016/B978-0-12-801699-2.00003-1..
147. H. Jakubowski, Biochemistry Online. A2. Amino Acid Stereochemistry, https://bio.libretexts.org/Under_Construction/Purgatory/Book%3A_Biochemistry_Online_(Jakubowski)/02%3A_PROTEIN_STRUCTURE/2A%3A_Amino_Acids/A02._Amino_Acid_Stereochemistry, (accessed 13th January, 2025).
148. X. Shang, I. Song, M. Han, J. H. Lee, H. Ohtsu, W. Choi, J. C. Kim, J. Ahn, S. K. Kwak and J. H. Oh, *Adv Opt Mater*, 2021, **9**, 2001911, DOI: 10.1002/adom.202001911.
149. L. A. Solomon, G. Kodali, C. C. Moser and P. L. Dutton, *J Am Chem Soc*, 2014, **136**, 3192, DOI: 10.1021/ja411845f.
150. H. Kim, S. W. Im, R. M. Kim, N. H. Cho, H.-E. Lee, H.-Y. Ahn and K. T. Nam, *Mat Adv*, 2020, **1**, 512, DOI: 10.1039/D0MA00125B.
151. J. Dong, Y. Liu and Y. Cui, *J Am Chem Soc*, 2021, **143**, 17316, DOI: 10.1021/jacs.1c08487.
152. T. W. Anderson, J. K. M. Sanders and G. D. Pantoş, *Org Biomol Chem*, 2010, **8**, 4274, DOI: 10.1039/C0OB00027B.
153. L. J. Prins, P. Timmerman and D. N. Reinhoudt, *J Am Chem Soc*, 2001, **123**, 10153, DOI: 10.1021/ja010610e.
154. Y. Shen, Y. Wang, I. W. Hamley, W. Qi, R. Su and Z. He, *Prog Polym Sci*, 2021, **123**, 101469, DOI: 10.1016/j.progpolymsci.2021.101469.
155. Y. Inai, N. Ousaka and Y. Ookouchi, *Biopolymers*, 2006, **82**, 471, DOI: 10.1002/bip.20491.
156. A. Robertson, A. J. Sinclair and D. Philp, *Chem Soc Rev*, 2000, **29**, 141, DOI: 10.1039/A803602K.

157. A. M. Garcia, D. Iglesias, E. Parisi, K. E. Styan, L. J. Waddington, C. Deganutti, R. De Zorzi, M. Grassi, M. Melchionna, A. V. Vargiu and S. Marchesan, *Chem*, 2018, **4**, 1862, DOI: 10.1016/j.chempr.2018.05.016.
158. Y. Inai, N. Ousaka and T. Okabe, *J Am Chem Soc*, 2003, **125**, 8151, DOI: 10.1021/ja035040s.
159. B. A. F. Le Bailly and J. Clayden, *Chem Comm*, 2016, **52**, 4852, DOI: 10.1039/C6CC00788K.
160. D. J. Hill, M. J. Mio, R. B. Prince, T. S. Hughes and J. S. Moore, *Chem Rev*, 2001, **101**, 3893, DOI: 10.1021/cr990120t.
161. M. T. Stone and J. S. Moore, *Org Lett*, 2004, **6**, 469, DOI: 10.1021/ol036238k.
162. T. Boddaert, J. Solà, M. Helliwell and J. Clayden, *Chem Comm*, 2012, **48**, 3397, DOI: 10.1039/C2CC00060A.
163. D. T. J. Morris and J. Clayden, *Chem Soc Rev*, 2023, **52**, 2480, DOI: 10.1039/d2cs00982j.
164. L. Byrne, J. Solà, T. Boddaert, T. Marcelli, R. W. Adams, G. A. Morris and J. Clayden, *Angew Chem Int Ed*, 2014, **53**, 151, DOI: 10.1002/anie.201308264.
165. J. Venkatraman, S. C. Shankaramma and P. Balaram, *Chem Rev*, 2001, **101**, 3131, DOI: 10.1021/cr000053z.
166. M. M. Green, N. C. Peterson, T. Sato, A. Teramoto, R. Cook and S. Lifson, *Sci*, 1995, **268**, 1860, DOI: 10.1126/science.268.5219.1860.
167. M. M. Green, M. P. Reidy, R. D. Johnson, G. Darling, D. J. O'Leary and G. Willson, *J Am Chem Soc*, 1989, **111**, 6452, DOI: 10.1021/ja00198a084.
168. M. M. Green, B. A. Garetz, B. Munoz, H. Chang, S. Hoke and R. G. Cooks, *J Am Chem Soc*, 1995, **117**, 4181, DOI: 10.1021/ja00119a039.
169. B. M. W. Langeveld-Voss, R. J. M. Waterval, R. A. J. Janssen and E. W. Meijer, *Macromol*, 1999, **32**, 227, DOI: 10.1021/ma981349y.
170. W. Xue, E. Benchimol, A. Walther, N. Ouyang, J. J. Holstein, T. K. Ronson, J. Openy, Y. Zhou, K. Wu, R. Chowdhury, G. H. Clever and J. R. Nitschke, *J Am Chem Soc*, 2024, **146**, 32730, DOI: 10.1021/jacs.4c12320.
171. M. Li, H. Zhu, S. Adorinni, W. Xue, A. Heard, A. M. Garcia, S. Kralj, J. R. Nitschke and S. Marchesan, *Angew Chem Int Ed*, 2024, **63**, e202406909, DOI: 10.1002/anie.202406909.
172. J. Gawronski and P. Skowronek, in *Chiral Analysis*, Elsevier, Amsterdam, 2006, DOI: 10.1016/B978-044451669-5/50013-2.
173. B. L. Nannenga and T. Gonen, *Nat Methods*, 2019, **16**, 369, DOI: 10.1038/s41592-019-0395-x.
174. N. Nag, S. Sasidharan, P. Saudagar and T. Tripathi, in *Advanced Spectroscopic Methods to Study Biomolecular Structure and Dynamics*, Academic Press, 2023, ch.1, pp.1-35, DOI: 10.1016/B978-0-323-99127-8.00002-7..
175. S. G. Telfer, T. M. McLean and M. R. Waterland, *Dalton Trans*, 2011, **40**, 3097, DOI: 10.1039/C0DT01226B.

176. D. M. Rogers, S. B. Jasim, N. T. Dyer, F. Auvray, M. Réfrégiers and J. D. Hirst, *Chem*, 2019, **5**, 2751, DOI: 10.1016/j.chempr.2019.07.008.
177. K. Bakshi, M. R. Liyanage, D. B. Volkin and C. R. Middaugh, *Methods Mol Biol*, 2014, **1088**, 247, DOI: 10.1007/978-1-62703-673-3_17.
178. M. Rabe, A. Boyle, H. R. Zope, F. Versluis and A. Kros, *Pept Sci*, 2015, **104**, 65, DOI: 10.1002/bip.22598.
179. B. Bosnich, *Acc Chem Res*, 1969, **2**, 266, DOI: 10.1021/ar50021a002.
180. A. Rodger, in *Encyclopedia of Biophysics*, Springer Berlin Heidelberg, Berlin, Heidelberg, 2013, pp.311-313, DOI: 10.1007/978-3-642-16712-6_646.
181. Y. Yu, C. Hu, L. Xia and J. Wang, *ACS Catal*, 2018, **8**, 1851, DOI: 10.1021/acscatal.7b03754.
182. A. G. Tebo and V. L. Pecoraro, *Curr Opin Chem Biol*, 2015, **25**, 65, DOI: 10.1016/j.cbpa.2014.12.034.
183. Z. Zou, B. Higginson and T. R. Ward, *Chem*, 2024, **10**, 2373, DOI: 10.1016/j.chempr.2024.07.007.
184. F. Rabanal, W. F. DeGrado and P. L. Dutton, *J Am Chem Soc*, 1996, **118**, 473, DOI: 10.1021/ja952831o.
185. X. Kang, L. Wang, B. Liu, S. Zhou, Y. Li, S.-L. Yang, R. Yao, L. Qiao, X. Wang, W. Gong, Y. Liu, L. Shi, J. Dong, Y. Cui and A. P. Davis, *Nat Synth*, 2025, **4**, 43, DOI: 10.1038/s44160-024-00640-3.
186. J. L. Alexander, Z. Thompson and J. A. Cowan, *ACS Chem Biol*, 2018, **13**, 844, DOI: 10.1021/acschembio.7b00989.
187. M. J. Pandya, G. M. Spooner, M. Sunde, J. R. Thorpe, A. Rodger and D. N. Woolfson, *Biochem*, 2000, **39**, 8728, DOI: 10.1021/bi000246g.
188. M. R. Berwick, D. J. Lewis, A. W. Jones, R. A. Parslow, T. R. Dafforn, H. J. Cooper, J. Wilkie, Z. Pikramenou, M. M. Britton and A. F. A. Peacock, *J Am Chem Soc*, 2014, **136**, 1166, DOI: 10.1021/ja408741h.
189. M. R. Berwick, L. N. Slope, C. F. Smith, S. M. King, S. L. Newton, R. B. Gillis, G. G. Adams, A. J. Rowe, S. E. Harding, M. M. Britton and A. F. A. Peacock, *Chem Sci*, 2016, **7**, 2207, DOI: 10.1039/C5SC04101E.
190. A. M. Webster and A. F. A. Peacock, *Chem Comm*, 2021, **57**, 6851, DOI: 10.1039/D1CC02013G.
191. J. D. Lear, Z. R. Wasserman and W. F. DeGrado, *Sci*, 1988, **240**, 1177, DOI: 10.1126/science.2453923.
192. P. Vosbein, P. P. Vergara, D. T. Huang and A. R. Thomson, *Chem Sci*, 2024, **15**, 15776, DOI: 10.1039/D4SC04204B.
193. E. F. Banwell, E. S. Abelardo, D. J. Adams, M. A. Birchall, A. Corrigan, A. M. Donald, M. Kirkland, L. C. Serpell, M. F. Butler and D. N. Woolfson, *Nat Mater*, 2009, **8**, 596, DOI: 10.1038/nmat2479.

194. L. N. Slope, M. G. Hill, C. F. Smith, P. Teare, F. J. de Cogan, M. M. Britton and A. F. A. Peacock, *Chem Comm*, 2020, **56**, 3729, DOI: 10.1039/C9CC08189E.
195. W. F. DeGrado, C. M. Summa, V. Pavone, F. Nastri and A. Lombardi, *Annu Rev Biochem*, 1999, **68**, 779, DOI: 10.1146/annurev.biochem.68.1.779.
196. C. M. Goodman, S. Choi, S. Shandler and W. F. DeGrado, *Nat Chem Biol*, 2007, **3**, 252, DOI: 10.1038/nchembio876.
197. M. Kyakuno, S. Oishi and H. Ishida, *Chem Lett*, 2005, **34**, 1554, DOI: 10.1246/cl.2005.1554.
198. Y. Shimazaki, M. Takani and O. Yamauchi, *Dalton Trans*, 2009, **38,** 7854, DOI: 10.1039/B905871K.
199. Y. Song, F. Schaufelberger, Z. Ashbridge, L. Pirvu, I. J. Vitorica-Yrezabal and D. A. Leigh, *Chem Sci*, 2021, **12**, 1826, DOI: 10.1039/D0SC05897A.
200. C. D. Allen and A. J. Link, *J Am Chem Soc*, 2016, **138**, 14214, DOI: 10.1021/jacs.6b09454.
201. J. Zhong, Z. Sun, L. Zhang, G. F. S. Whitehead, I. J. Vitorica-Yrezabal and D. A. Leigh, *J Am Chem Soc*, 2024, **146**, 21762, DOI: 10.1021/jacs.4c05953.
202. G. H. Beaven and E. R. Holiday, *Advances in Protein Chemistry (Seventh Edition)*, Academic Press, 1952, pp.319-386, DOI: 10.1016/S0065-3233(08)60022-4..
203. M. Lieberman and T. Sasaki, *J Am Chem Soc*, 1991, **113**, 1470, DOI: 10.1021/ja00004a090.
204. M. R. Ghadiri, C. Soares and C. Choi, *J Am Chem Soc*, 1992, **114**, 825, DOI: 10.1021/ja00036a072.
205. M. V. Veidis, G. H. Schreiber, T. E. Gough and G. J. Palenik, *J Am Chem Soc*, 1969, **91**, 1859, DOI: 10.1021/ja01035a051.
206. J. Echeverría, E. Cremades, A. J. Amoroso and S. Alvarez, *Chem Comm*, 2009, **28**, 4242, DOI: 10.1039/B903867A.
207. Chai-1 Discovery Team, J. Boitreaud, J. Dent, M. McPartlon, J. Meier, V. Reis, A. Rogozhonikov and K. Wu, *bioRxiv*, 2024, DOI: 10.1101/2024.10.10.615955.
208. A. G. Brenton and A. R. Godfrey, *J Am Soc Mass Spectrom*, 2010, **21**, 1821, DOI: 10.1016/j.jasms.2010.06.006.
209. M. L. Gross, *J Am Soc Mass Spectrom*, 1994, **5**, 57, DOI: 10.1016/1044-0305(94)85036-4.
210. T. B. K. Webb, M. Sargent, B. Stein Methodology for Accurate Mass Measurement of Small Molecules: Best Practise Guide, https://www.rsc.org/images/MS1_tcm18-102518.pdf, (accessed 07/04/2025, 2025).

8 List of Appendices

Appendix A

Chapter 2 – Chiral Effects in Metal Binding Motifs at the N-Terminus of Trimeric Coiled Coils.

The following appendix contains additional spectral information for the results discussed in Chapter 2 of this thesis. This includes full CD spectra of the control peptides (1b and 2b) titrations against Zn^{2+} and Cu^{2+}, titration data for peptide **1a** against $Ga(NO_3)_3$ and HT measurements for metal titrations against **1a** and **3a**.

Note - only representative HT measurements have been provided.

Contents

A.1 Control Peptide CD Spectra

A.1.1 - **1b**

Sequence

Ac	G QEIAAIK KEIAAIK KEIAAIK YG	NH_2

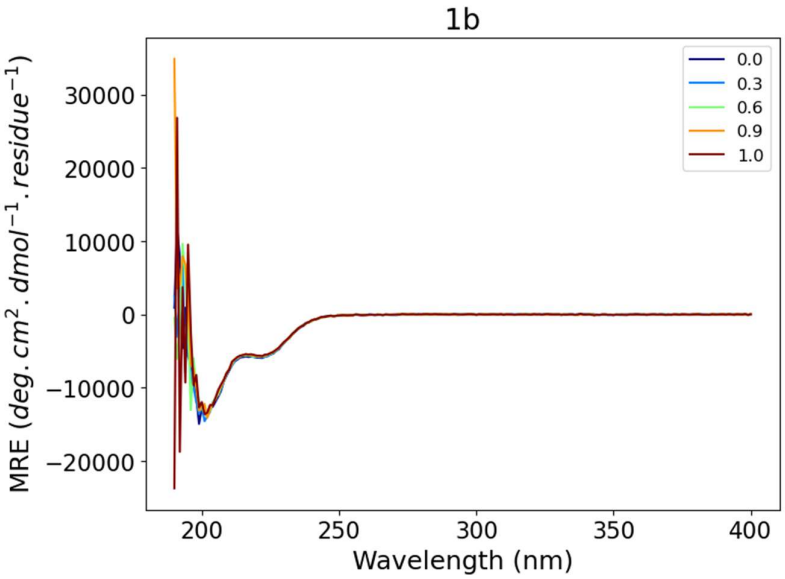

Figure A. 1– CD spectra of **1b** (10 μM) titration against **$Cu(NO_3)_2$** in 20 mM aqueous MOPS (pH 7)

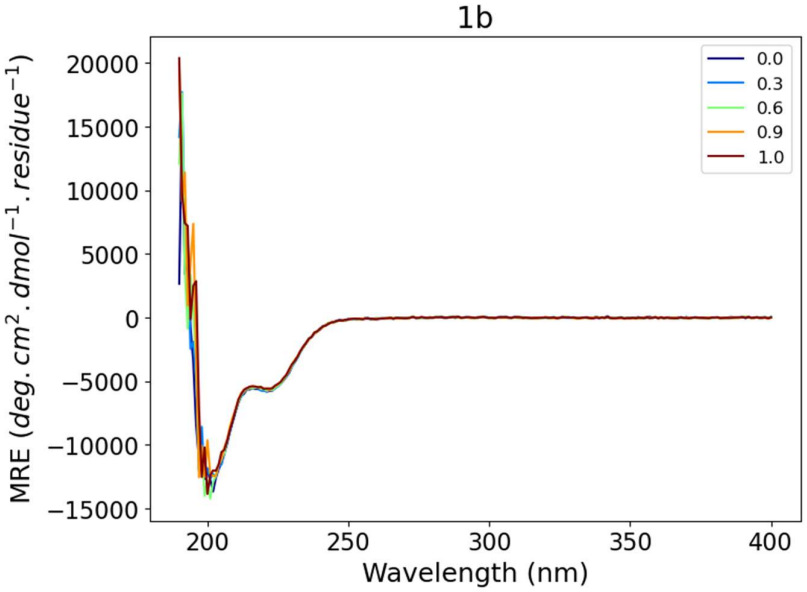

Figure A. 2- CD spectra of **1b** (10 μM) titration against **$Zn(NO_3)_2$** in 20 mM aqueous MOPS (pH 7)

A.1.2 - **2b**

Sequence

Ac	G QEIAAIK YG	NH_2

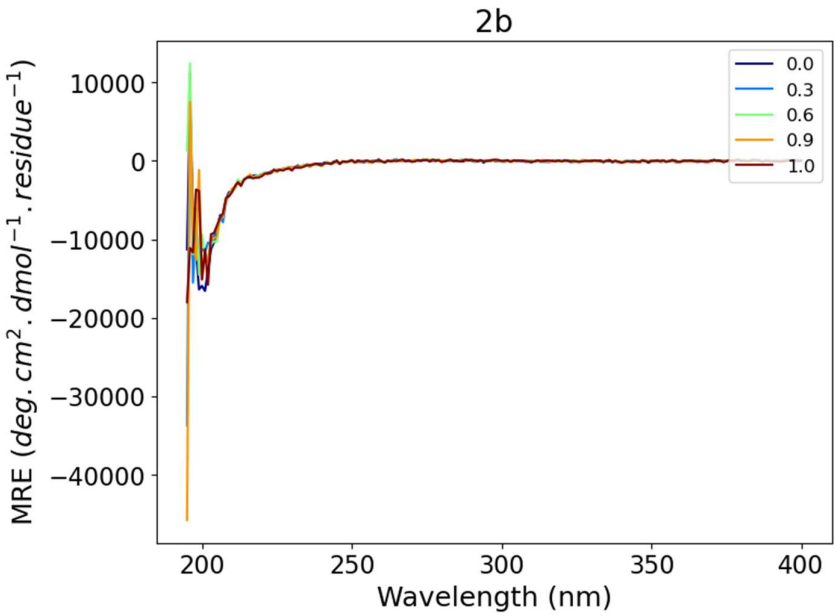

Figure A. 3- CD spectra of **2b** (10 µM) titration against **$Cu(NO_3)_2$** in 20 mM aqueous MOPS (pH 7)

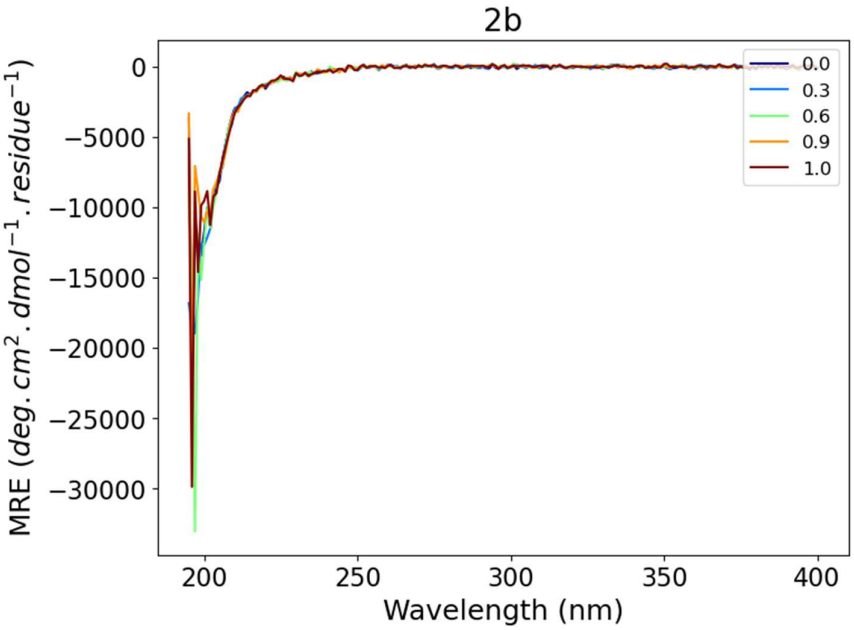

Figure A. 4- CD spectra of **2b** (10 µM) titration against **$Zn(NO_3)_2$** in 20 mM aqueous MOPS (pH 7)

A.2 – CD Spectrum of **1a** titration against $Ga(NO_3)_3$

Sequence

Bpy	G QEIAAIK KEIAAIK KEIAAIK YG	NH_2

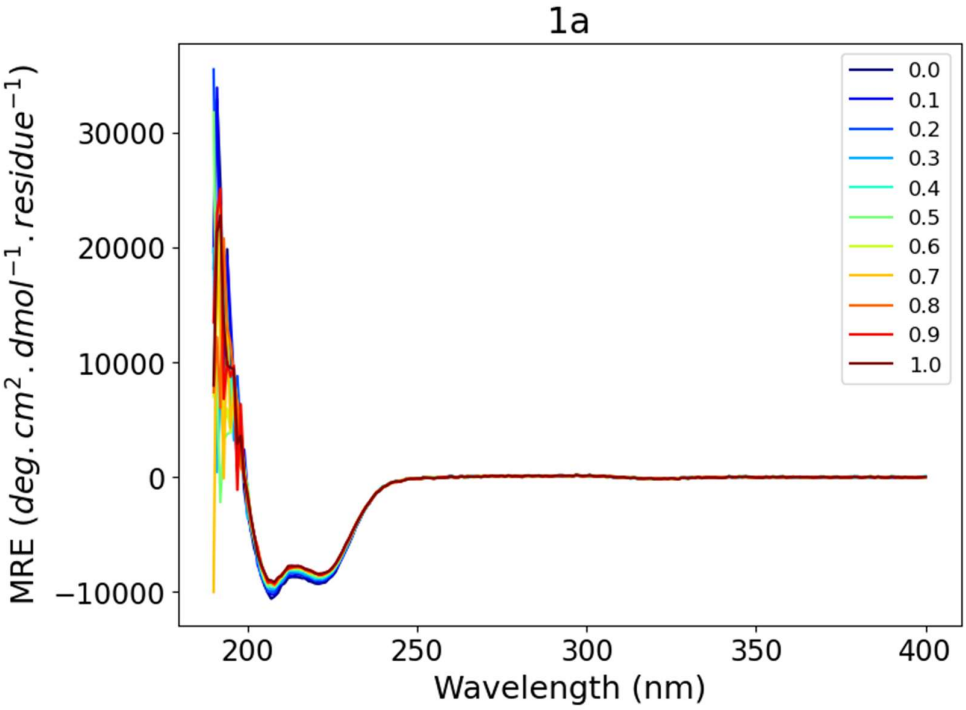

Figure A.5 - CD spectra of **1a** (10 μM) titration against **$Ga(NO_3)_3$** in 20 mM aqueous MOPS (pH 7)

A.3 – HT Measurements

A.3.1 – **1a** + Co(II)

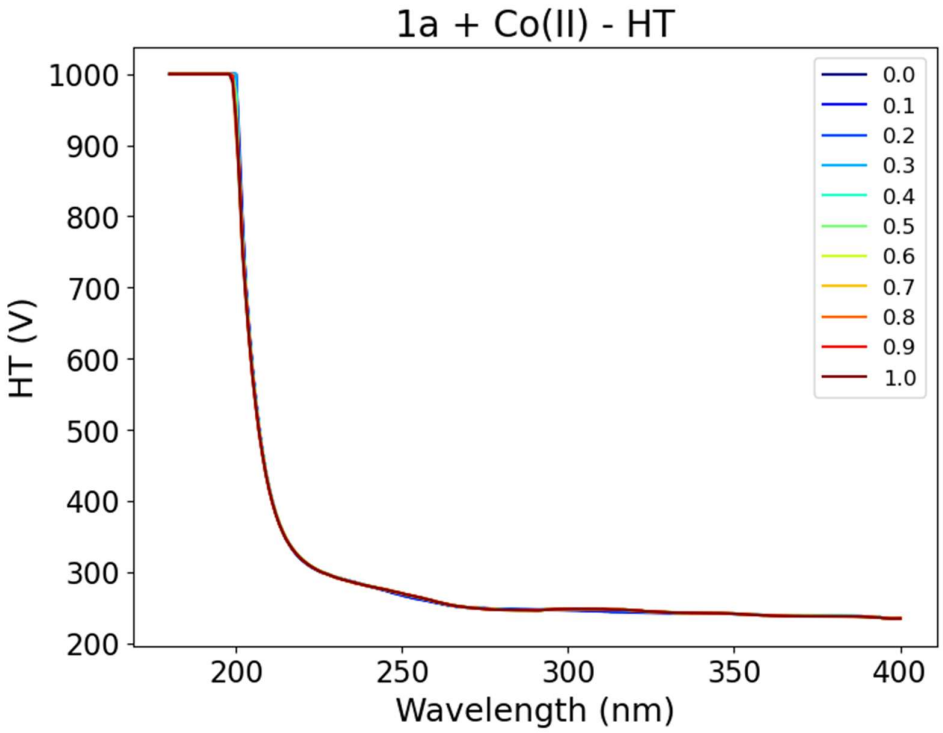

Figure A. 6– High Tension (HT) from the CD of **1a** titration against **$CoCl_2$**, in 20 mM aqueous MOPS buffer (pH 7)

A.3.2 - **1a** + Zn(II)

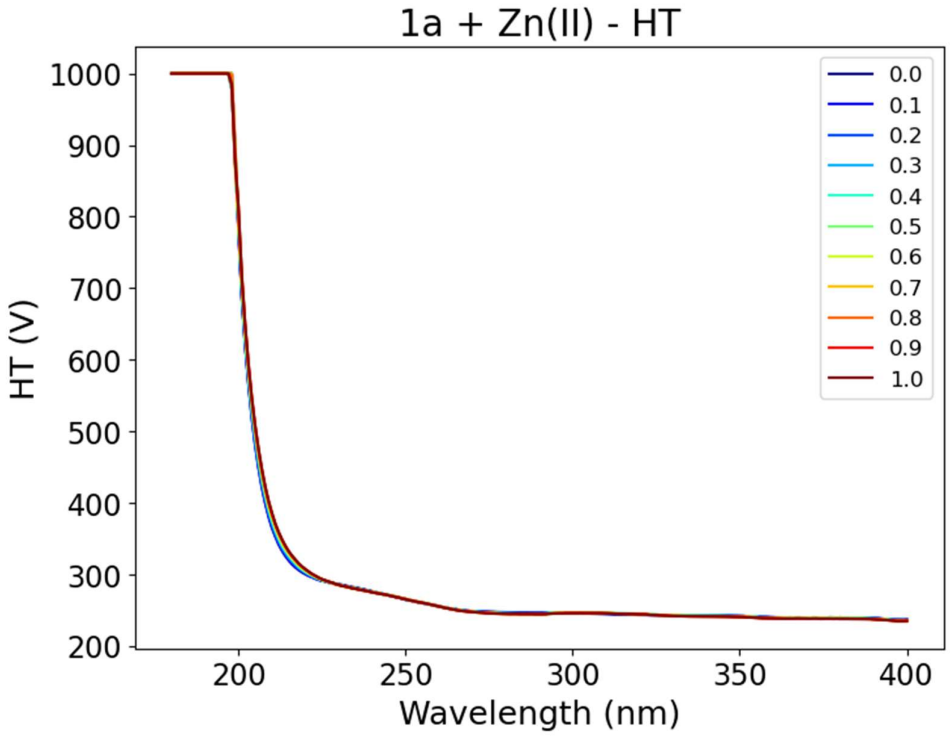

Figure A. 7- High Tension (HT) from the CD of **1a** titration against **$Zn(NO_3)_2$**, in 20 mM aqueous MOPS buffer (pH 7)

A.3.3 - **1a** + Cu(II)

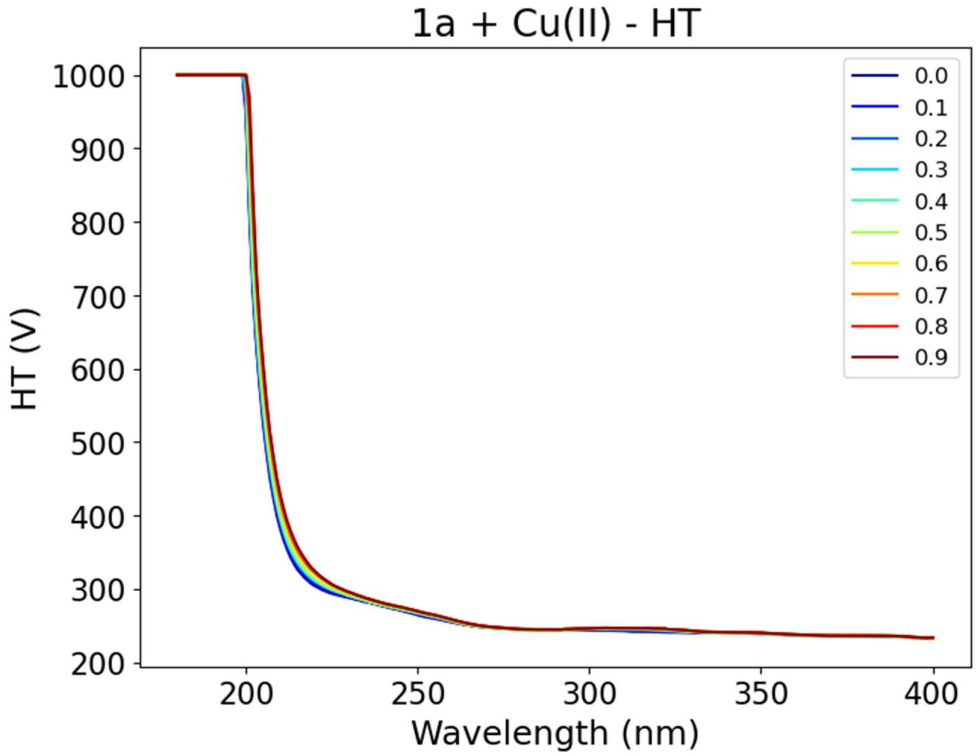

Figure A. 8 - High Tension (HT) from the CD of **1a** titration against **$Cu(NO_3)_2$**, in 20 mM aqueous MOPS buffer (pH 7)

A.3.4 – **1a** + Ni(II)

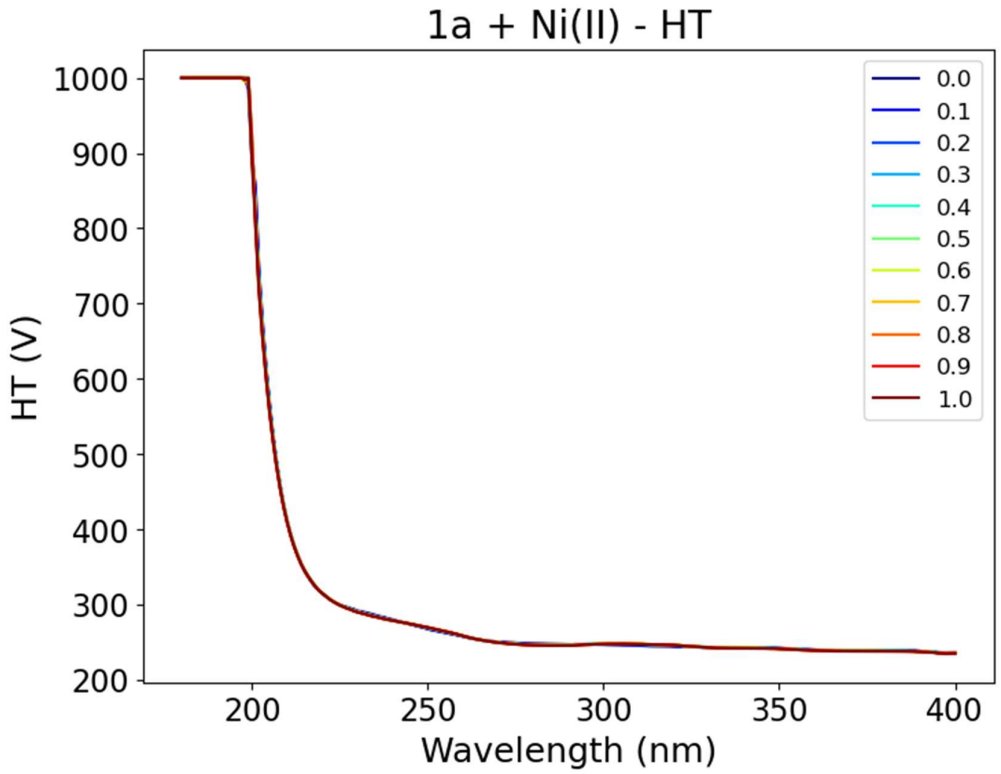

Figure A. 9 - High Tension (HT) from the CD of 1a titration against **$NiCl_2$**, in 20 mM aqueous MOPS buffer (pH 7)

A.3.5 - **1a** + Fe(II)

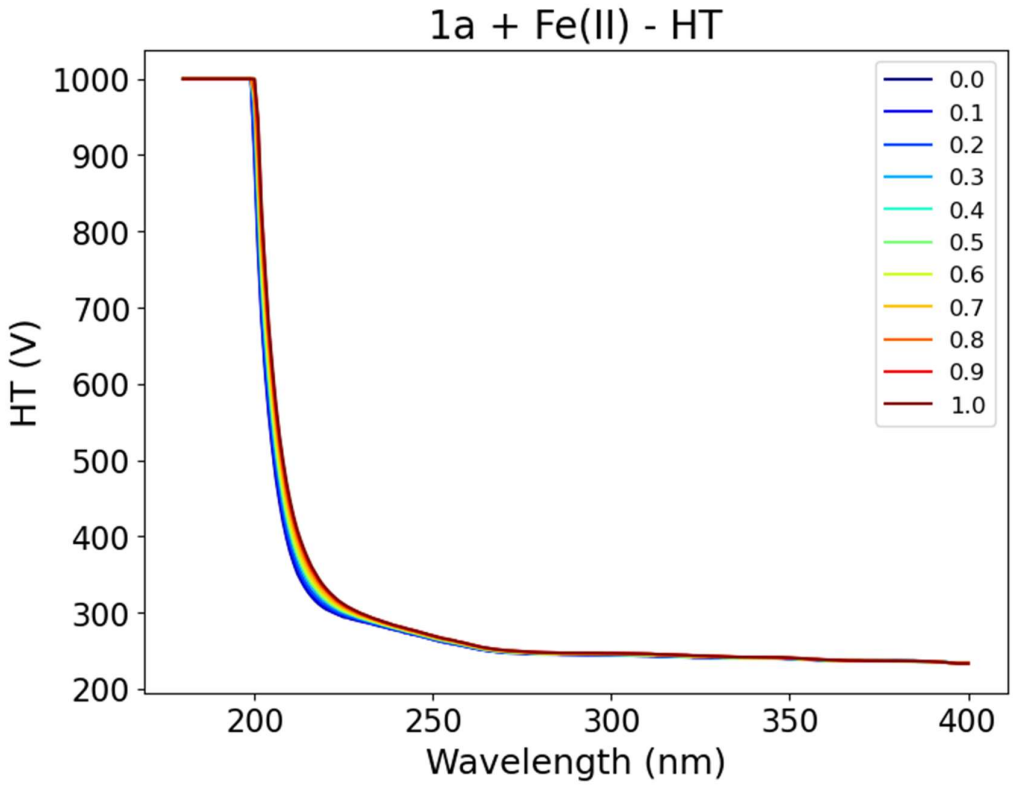

Figure A.10 - High Tension (HT) from the CD of **1a** titration against **$Fe(NO_3)_2$**, in 20 mM aqueous MOPS buffer (pH 7)

A.3.6 - **3a** + Co(II)

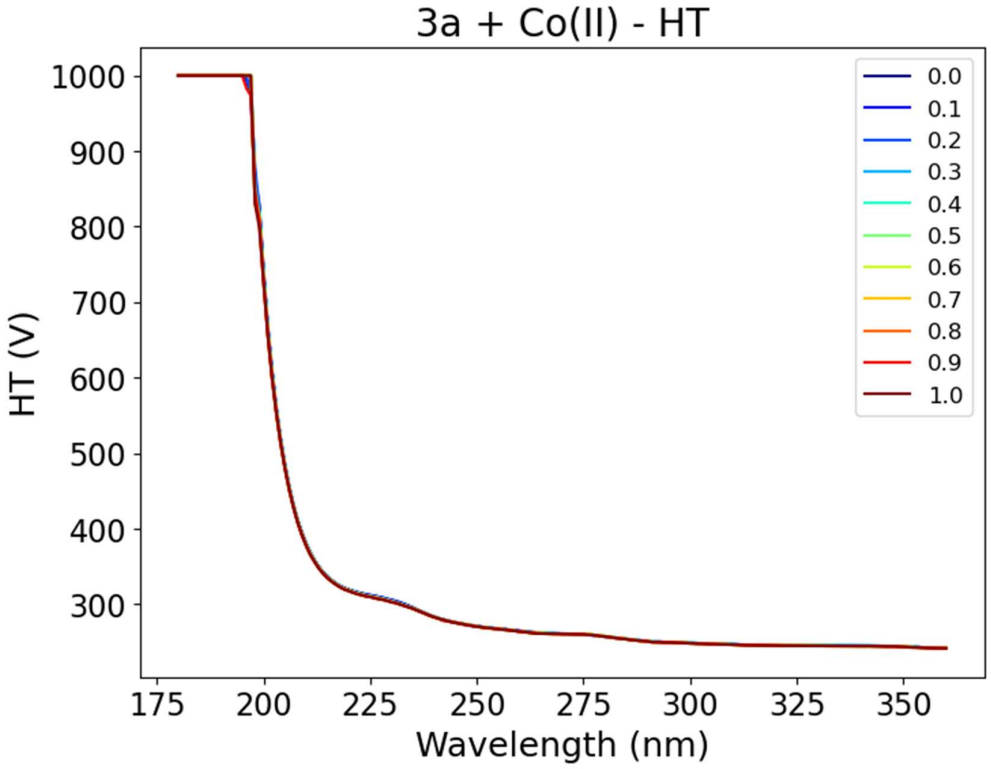

Figure A. 11 - High Tension (HT) from the CD of **3a** titration against $CoCl_2$, in 20 mM aqueous MOPS buffer (pH 7)

Appendix B

Chapter 3 – Spatial Constraints of the Chiral Preference in N-terminally Functionalised Supramolecular Peptide Assemblies.

The following appendix contains additional spectral information for the results discussed in Chapter 3 of this thesis. This includes full CD spectra of the control peptides (**4b–19b**) titrations against $Zn^{2+}$and Cu^{2+} and additional Zn^{2+} titration data for peptides **14a**, **15a**, **17a** and **18a.**

Contents

B.1 – Control Peptide CD Spectra

B.1.1 – **4b**

Sequence

Ac	A QEIAAIK KEIAAIK KEIAAIK YG	NH_2

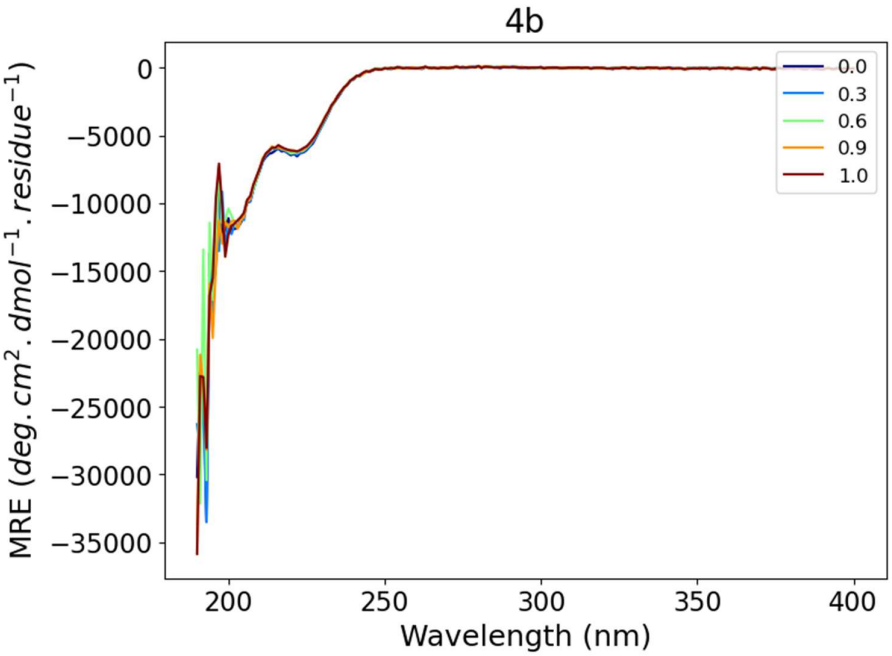

Figure B. 1 - CD spectra of **4b** (10 μM) titration against **Cu(NO₃)₂** in 20 mM aqueous MOPS (pH 7)

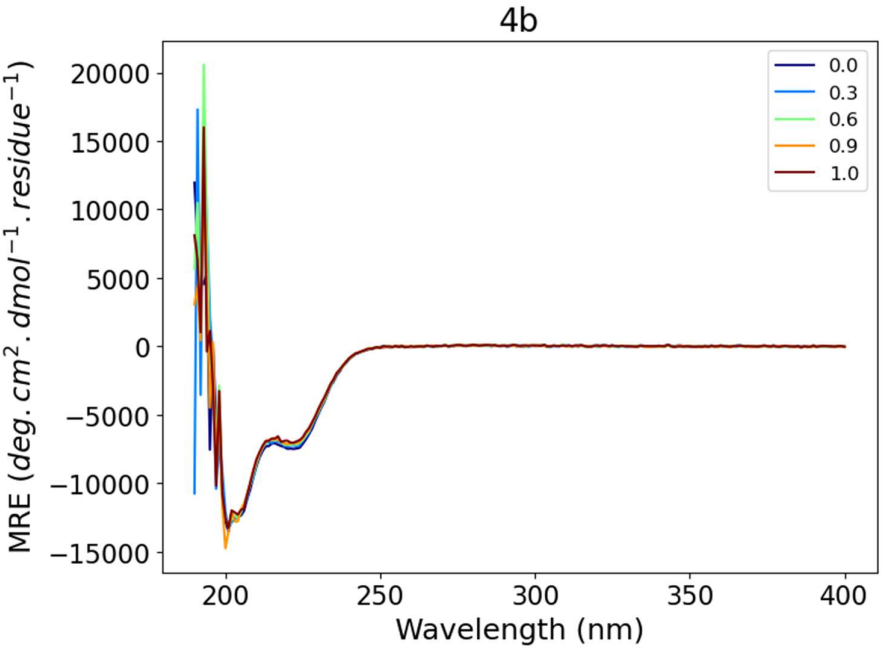

Figure B.2 - CD spectra of **4b** (10 μM) titration against **Zn(NO₃)₂** in 20 mM aqueous MOPS (pH 7)

B.1.2 - **5b**

Sequence

Ac	G GEIAAIK KEIAAIK KEIAAIK YG	NH_2

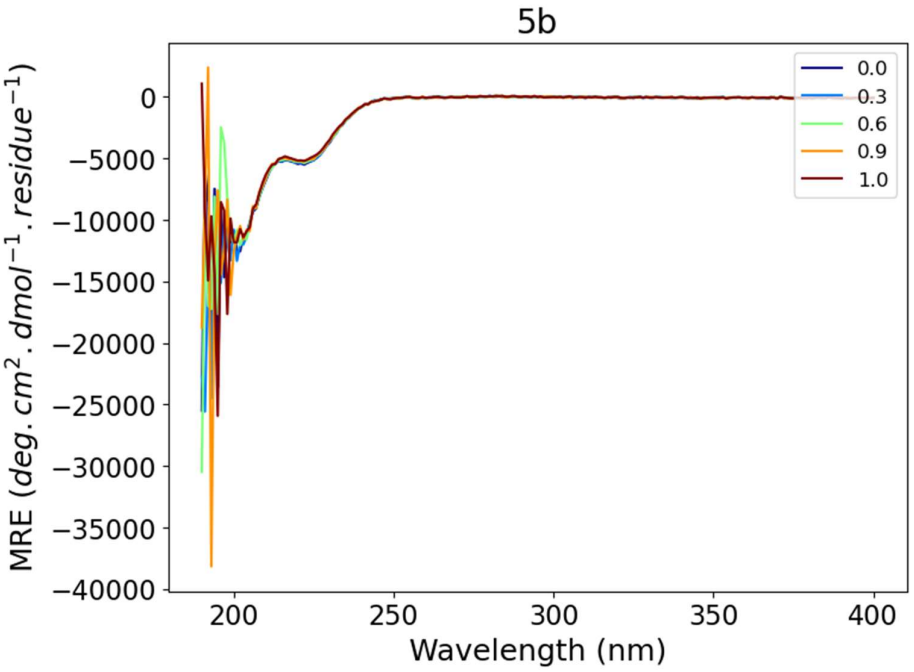

Figure B. 3 - CD spectra of **5b** (10 µM) titration against **$Cu(NO_3)_3$** in 20 mM aqueous MOPS (pH 7)

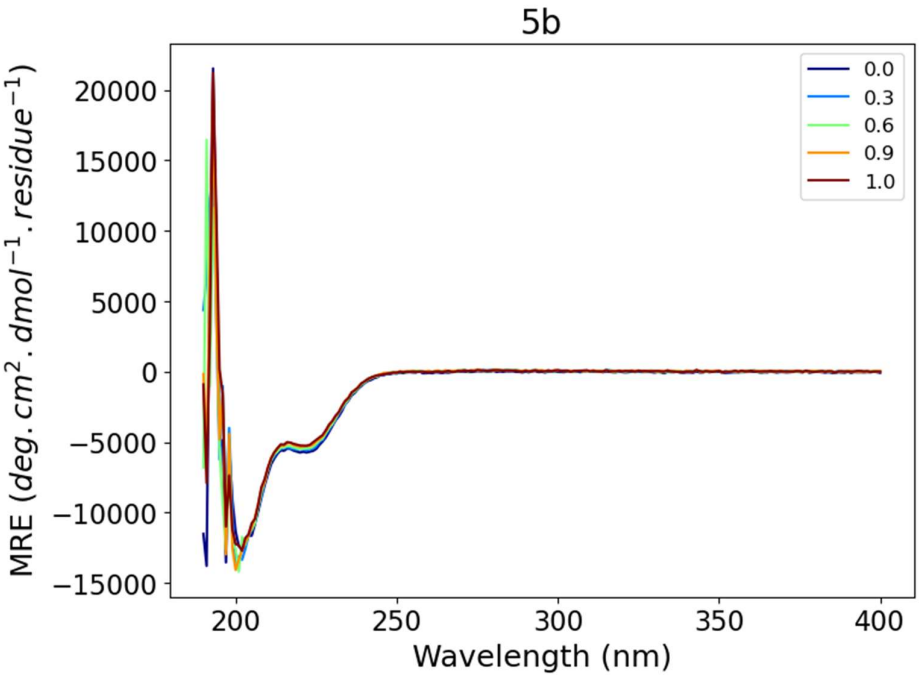

Figure B. 4 - CD spectra of **5b** (10 µM) titration against **$Zn(NO_3)_2$** in 20 mM aqueous MOPS (pH 7)

B.1.3 - **6b**

Sequence

Ac	PEG GEIAAIK KEIAAIK KEIAAIK YG	NH_2

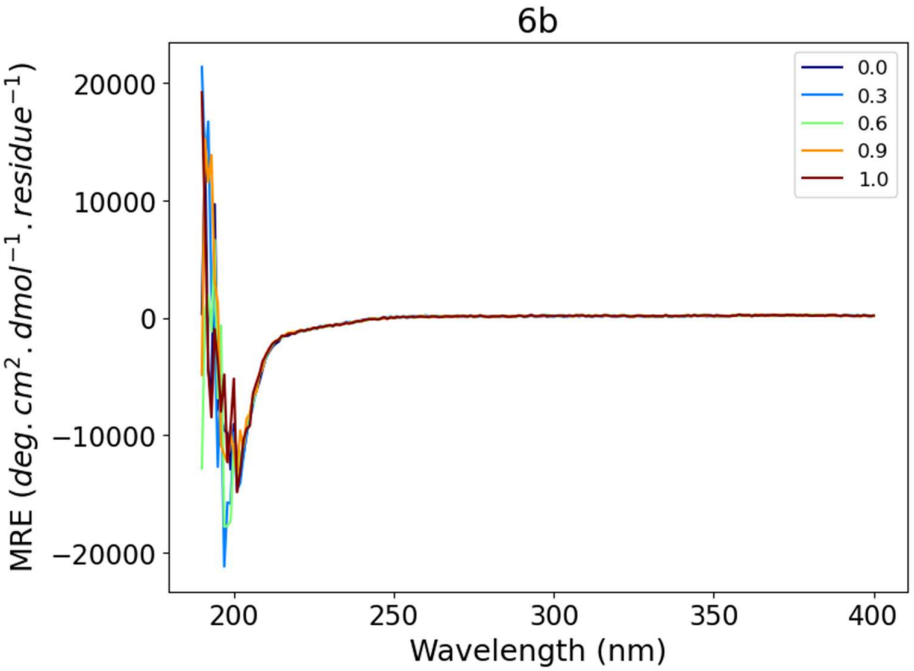

Figure B. 5 - CD spectra of **6b** (10 µM) titration against **$Cu(NO_3)_3$** in 20 mM aqueous MOPS (pH 7)

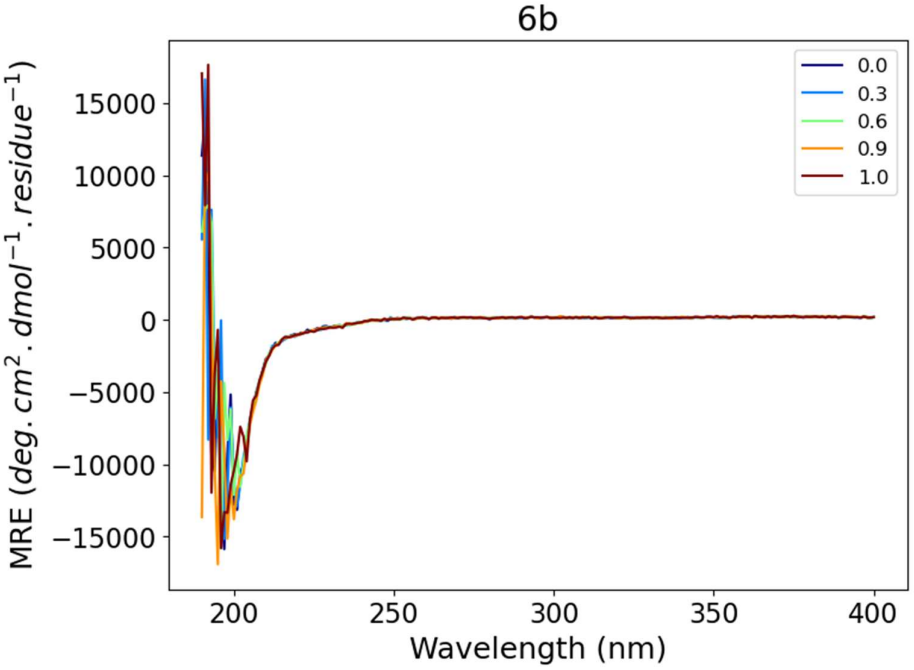

Figure B. 6 - CD spectra of **6b** (10 µM) titration against **$Zn(NO_3)_3$** in 20 mM aqueous MOPS (pH 7)

B.1.4 - **7b**

Sequence

Ac	A QEIAAIK KEIAAIK KEIAAIK KEIAAIK YG	NH_2

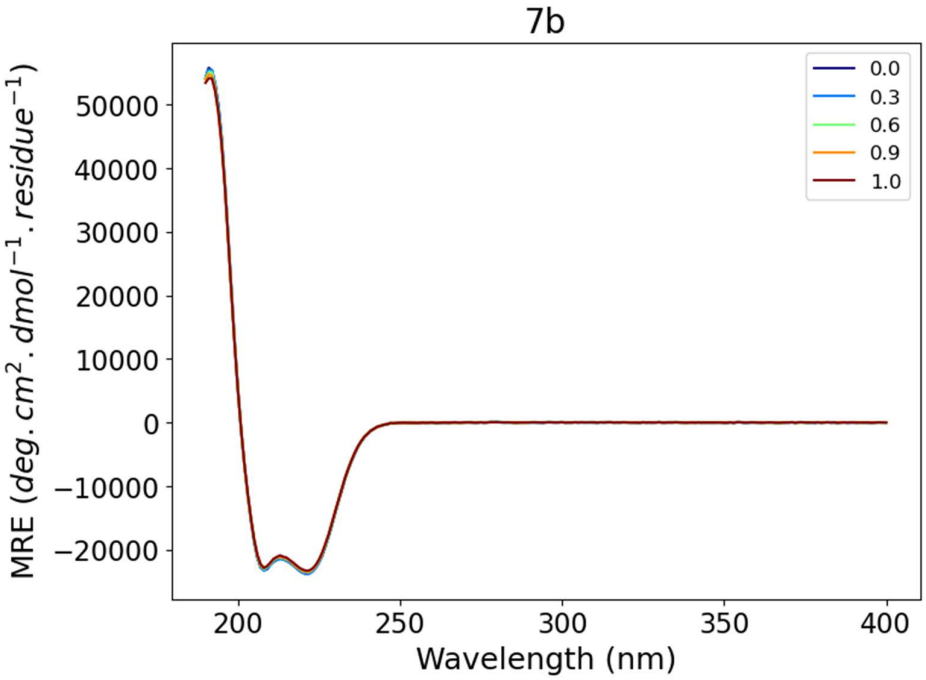

Figure B.7 - CD spectra of **7b** (10 μM) titration against **$Cu(NO_3)_3$** in 20 mM aqueous MOPS (pH 7)

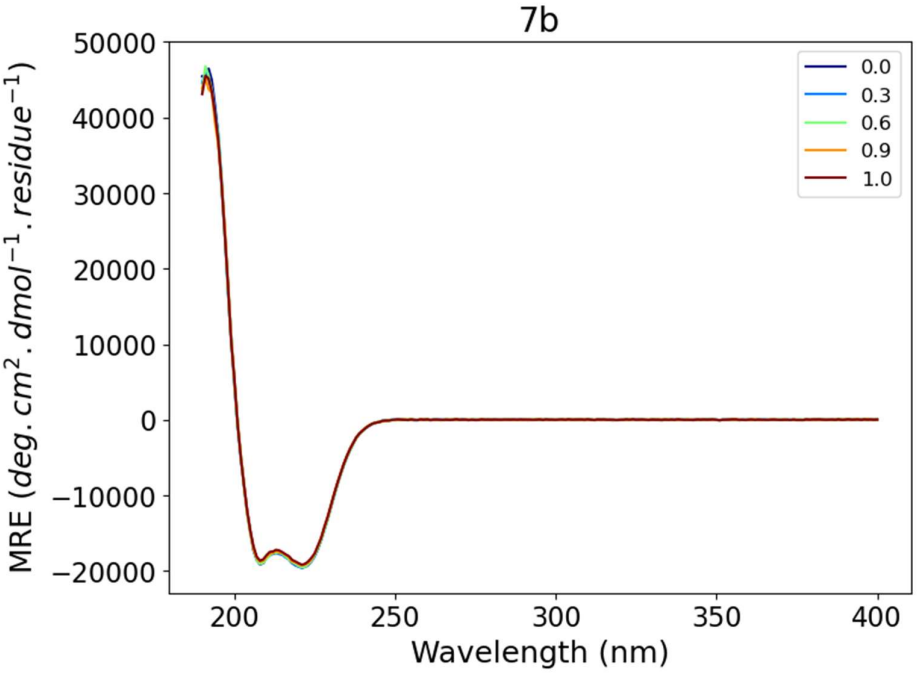

Figure B.8 - CD spectra of **7b** (10 μM) titration against **Zn $(NO_3)_3$** in 20 mM aqueous MOPS (pH 7)

B.1.5 - **8b**

Sequence

Ac	G QEIAAIK KEIAAIK KEIAAIK KEIAAIK YG	NH_2

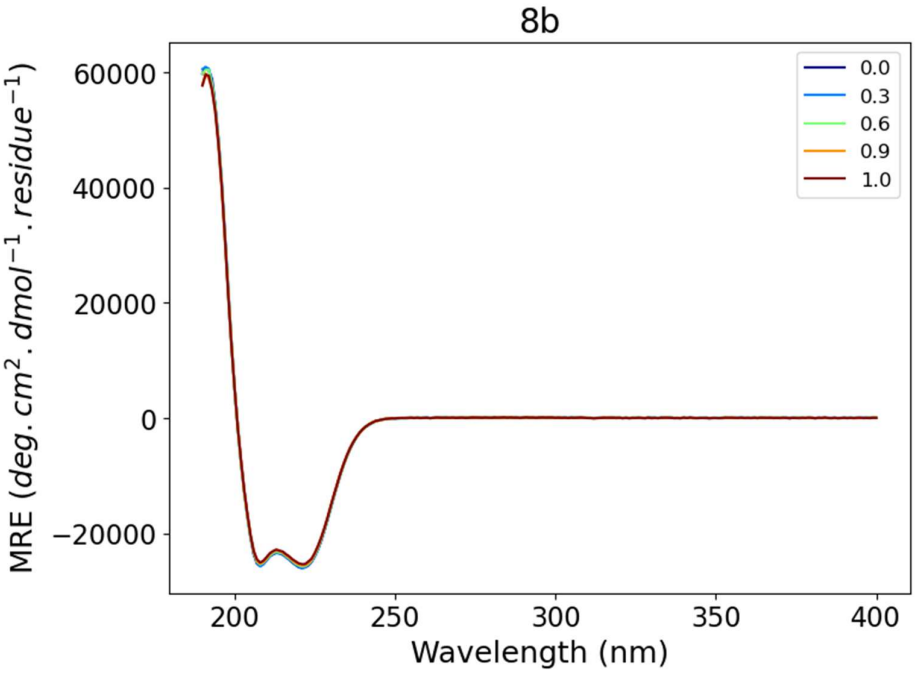

Figure B.9 - CD spectra of **8b** (10 µM) titration against **Cu $(NO_3)_3$** in 20 mM aqueous MOPS (pH 7)

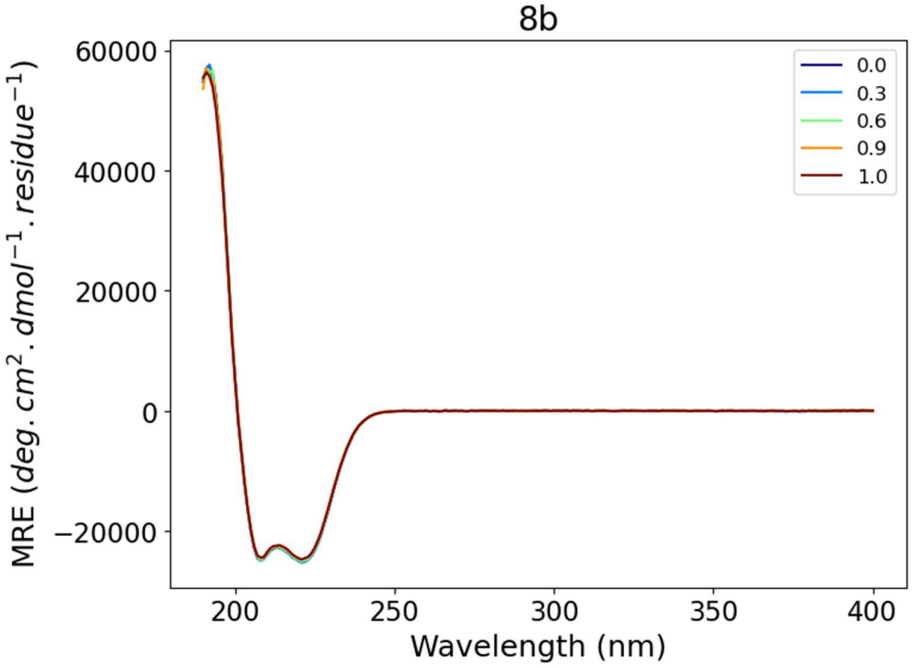

Figure B.10 - CD spectra of **8b** (10 µM) titration against **Zn $(NO_3)_3$** in 20 mM aqueous MOPS (pH 7)

B.1.6 - **9b**

Sequence

Ac	G GEIAAIK KEIAAIK KEIAAIK KEIAAIK YG	NH_2

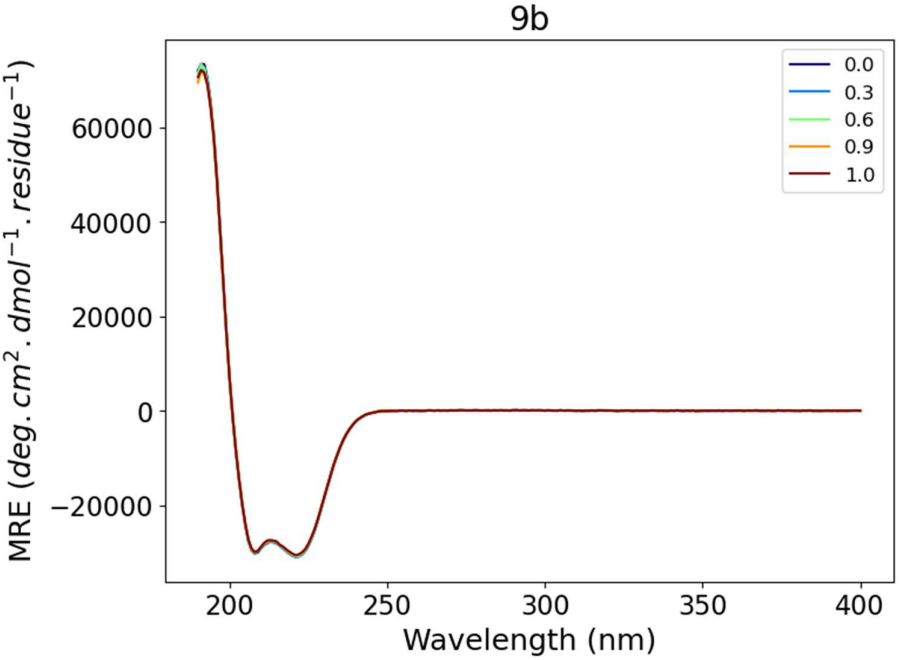

Figure B.11 - CD spectra of **9b** (10 μM) titration against **$Cu(NO_3)_3$** in 20 mM aqueous MOPS (pH 7)

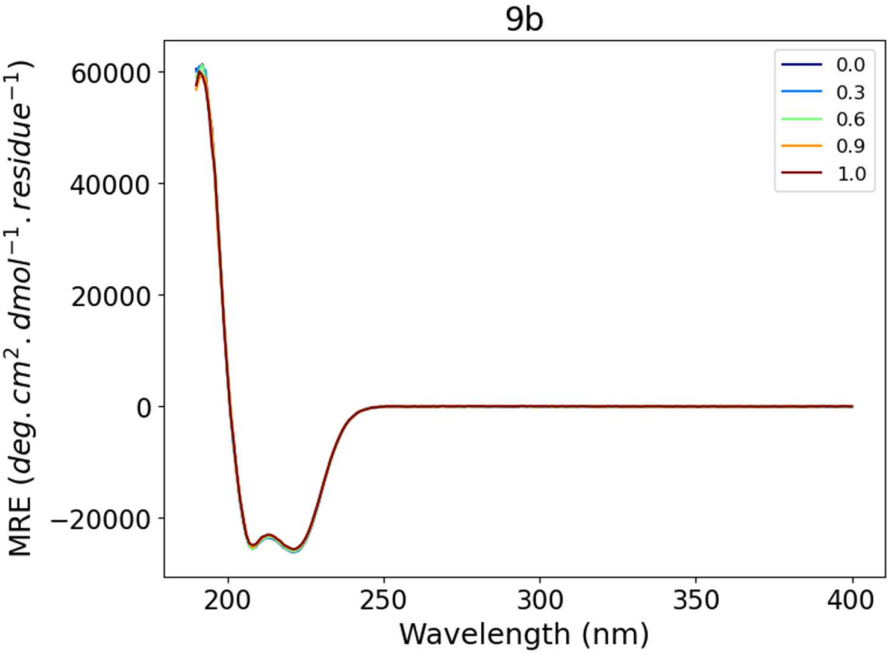

Figure B.12 - CD spectra of **9b** (10 μM) titration against **$Zn(NO_3)_3$** in 20 mM aqueous MOPS (pH 7)

B.1.7 - **10b**

Sequence

Ac	PEG QEIAAIK KEIAAIK KEIAAIK KEIAAIK YG	NH_2

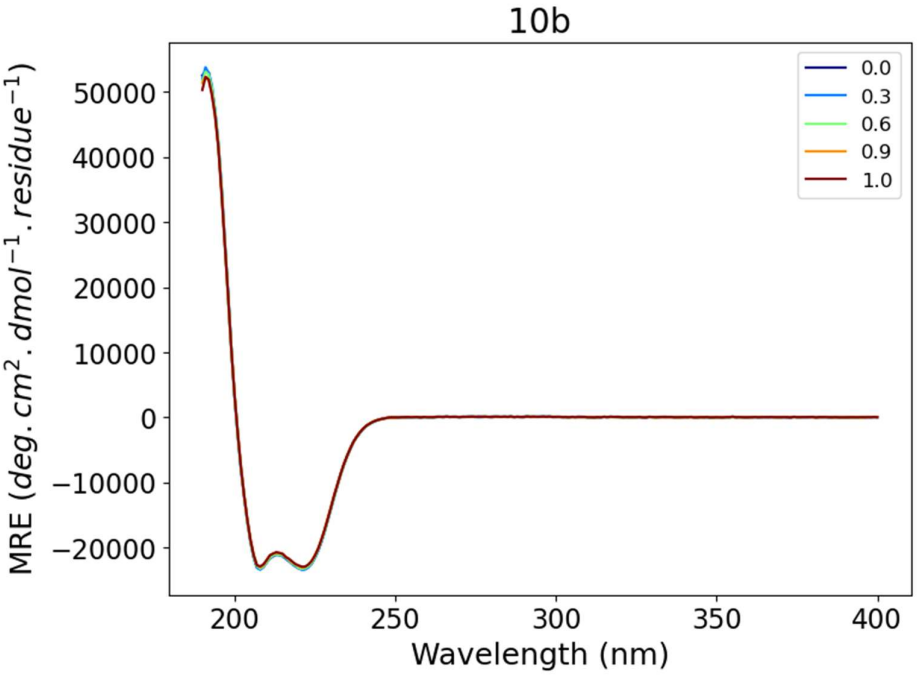

Figure B.13 - CD spectra of **10b** (10 µM) titration against **$Cu(NO_3)_3$** in 20 mM aqueous MOPS (pH 7)

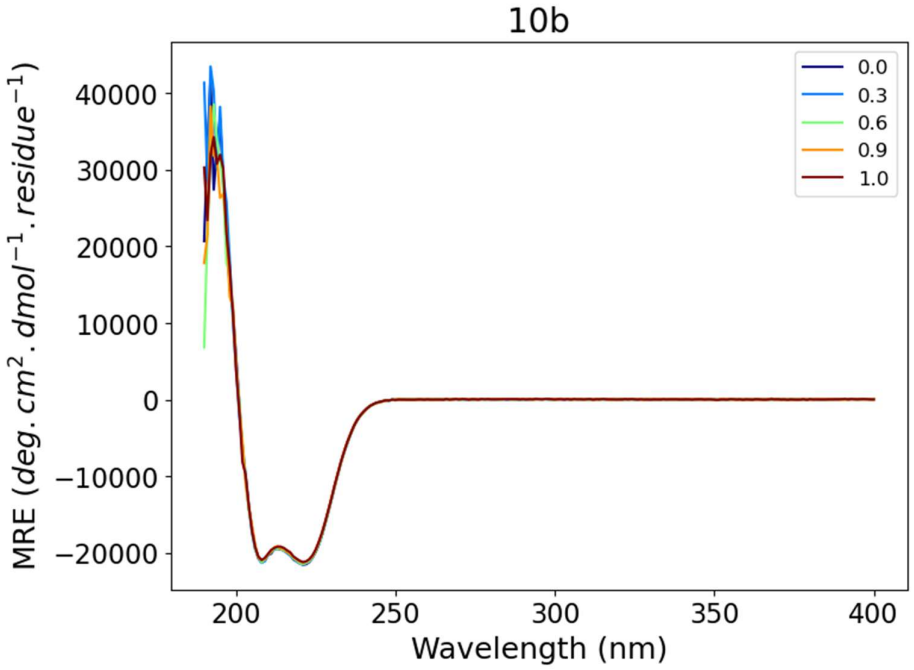

Figure B.14 - CD spectra of **10b** (10 µM) titration against **$Zn(NO_3)_3$** in 20 mM aqueous MOPS (pH 7)

B.1.8 - **11b**

Sequence

Ac	a QEIAAIK KEIAAIK KEIAAIK YG	NH_2

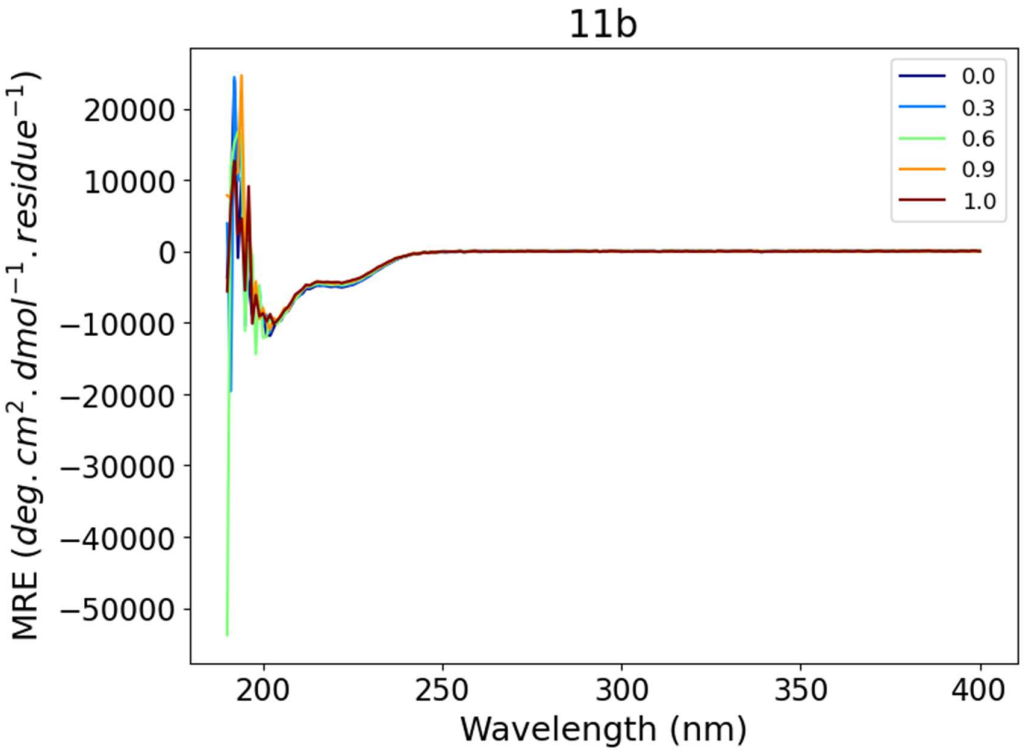

Figure B.15 - CD spectra of **11b** (10 μM) titration against **$Zn(NO_3)_3$** in 20 mM aqueous MOPS (pH 7)

B.1.9 - **12b**

Sequence

Ac	P QEIAAIK KEIAAIK KEIAAIK YG	NH_2

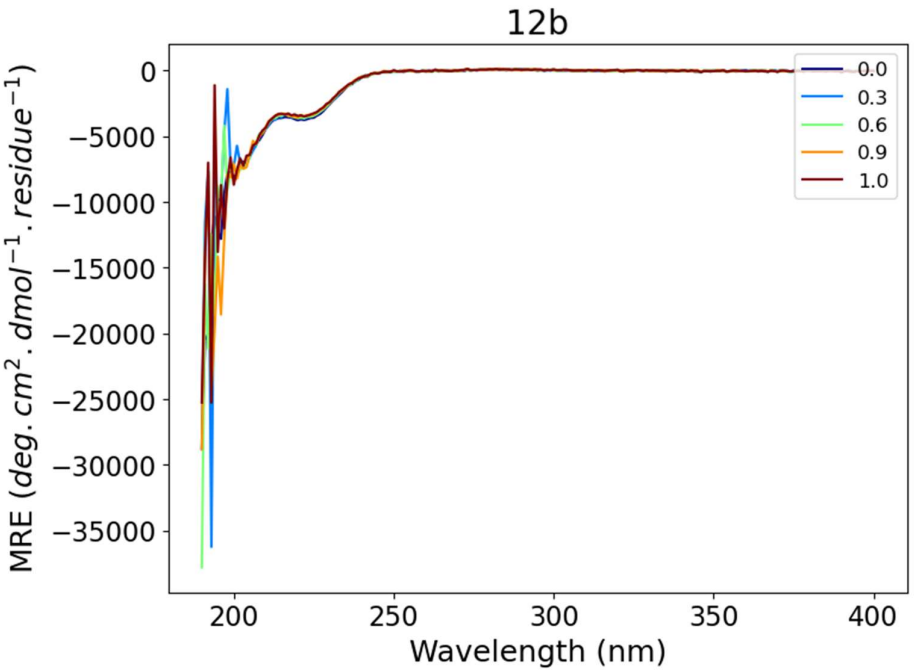

Figure B.16 - CD spectra of **12b** (10 μM) titration against **$Cu(NO_3)_3$** in 20 mM aqueous MOPS (pH 7)

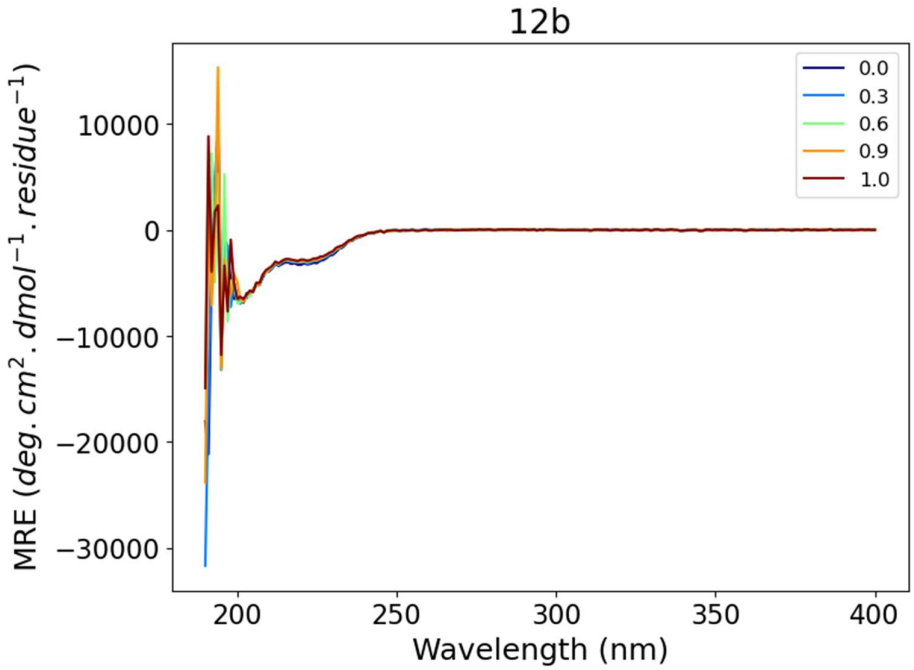

Figure B.17 - CD spectra of **12b** (10 μM) titration against **$Zn(NO_3)_3$** in 20 mM aqueous MOPS (pH 7)

B.1.10 - **13b**

Sequence

Ac	QEIAAIK KEIAAIK KEIAAIK YG	NH_2

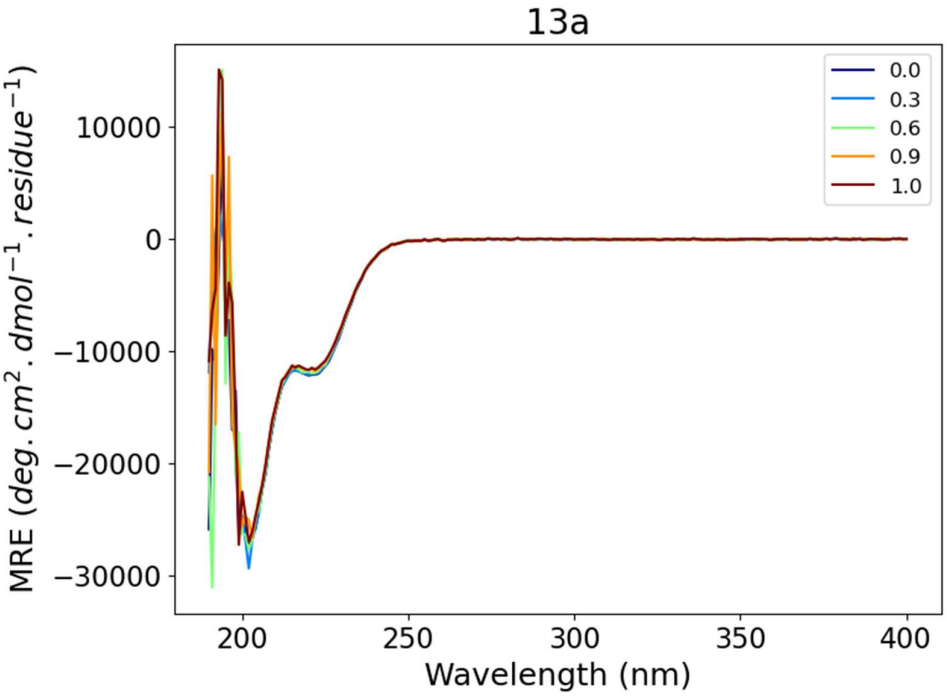

Figure B.18 - CD spectra of **13b** (10 μM) titration against **$Cu(NO_3)_3$** in 20 mM aqueous MOPS (pH 7)

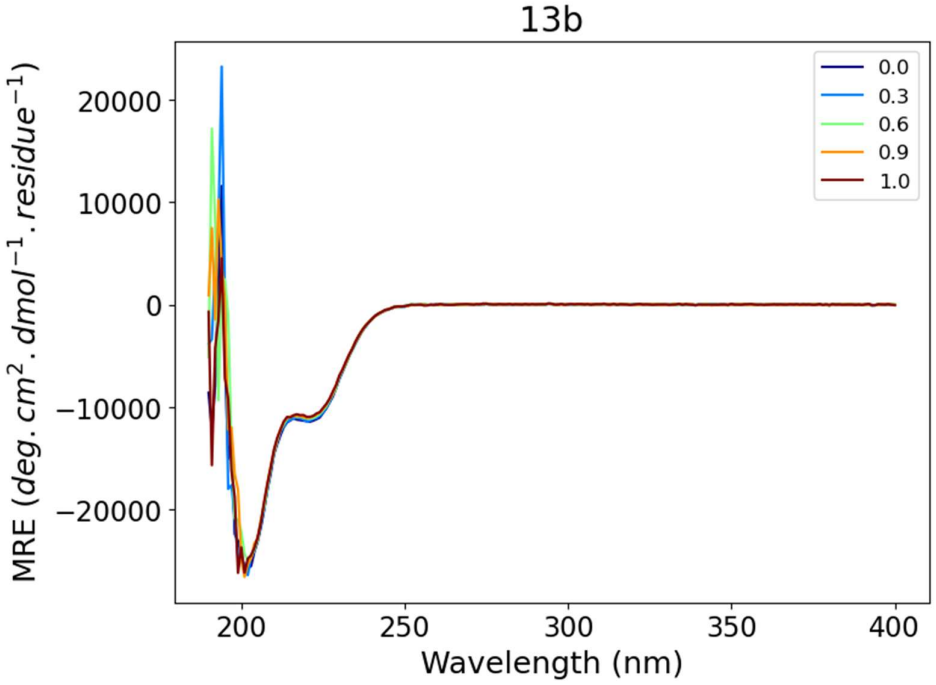

Figure B.19 - CD spectra of **13b** (10 μM) titration against **$Zn(NO_3)_3$** in 20 mM aqueous MOPS (pH 7)

B.1.11 - **14b**

Sequence

Ac	EIAAIK KEIAAIK KEIAAIK K YG	NH_2

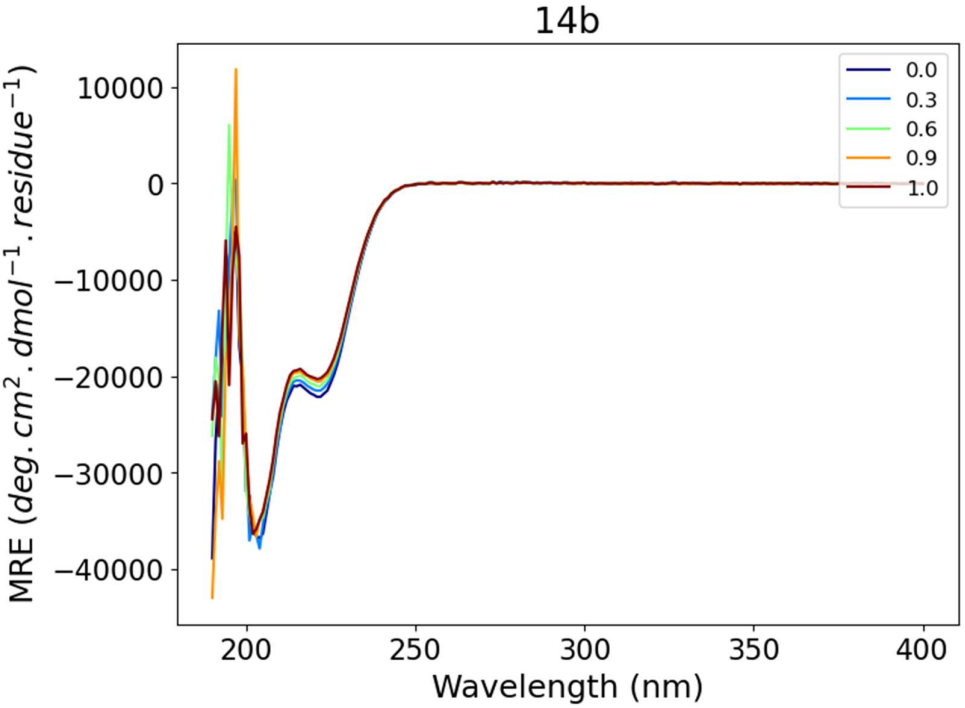

Figure B.20 - CD spectra of **14b** (10 µM) titration against **$Cu(NO_3)_3$** in 20 mM aqueous MOPS (pH 7)

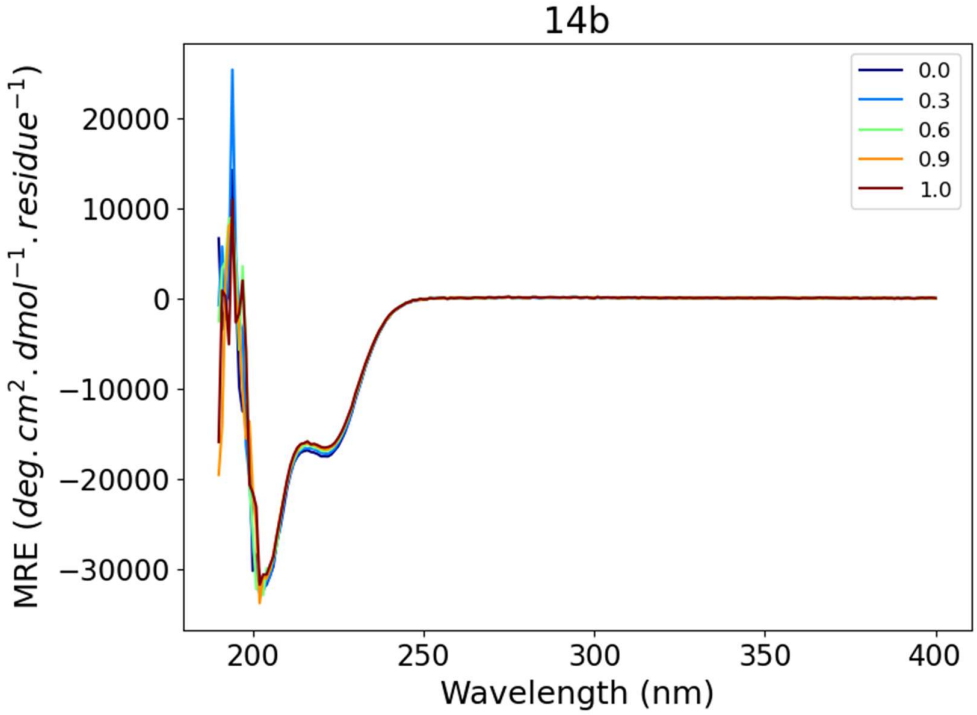

Figure B.21 - CD spectra of **14b** (10 µM) titration against **$Zn(NO_3)_3$** in 20 mM aqueous MOPS (pH 7)

B.1.12 - **15b**

Sequence

Ac	IAAIK KEIAAIK KEIAAIK KE YG	NH_2

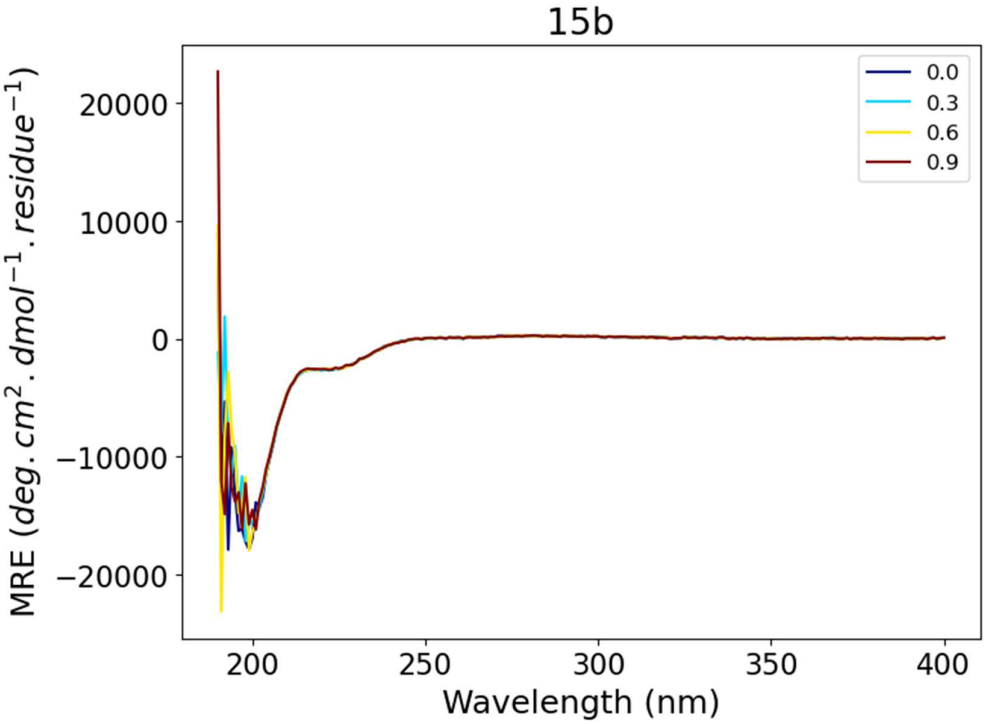

Figure B.22 - CD spectra of **15b** (10 µM) titration against **$Cu(NO_3)_3$** in 20 mM aqueous MOPS (pH 7)

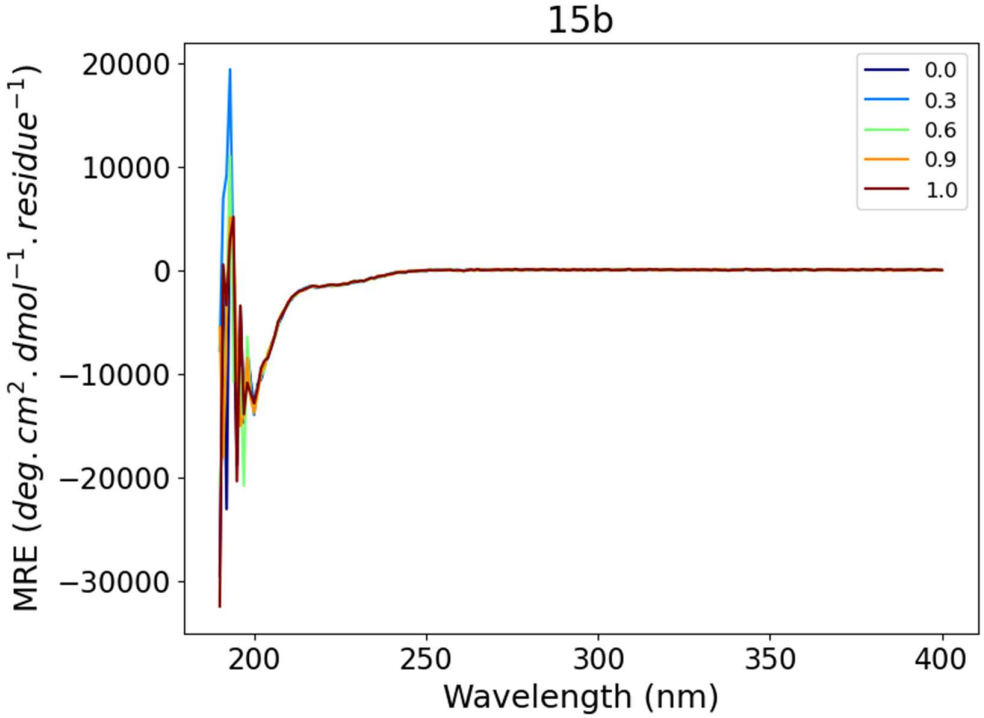

Figure B.23 - CD spectra of **15b** (10 µM) titration against **$Zn(NO_3)_3$** in 20 mM aqueous MOPS (pH 7)

B.1.13 - **16b**

Sequence

Ac	AAIK KEIAAIK KEIAAIK KEI YG	NH_2

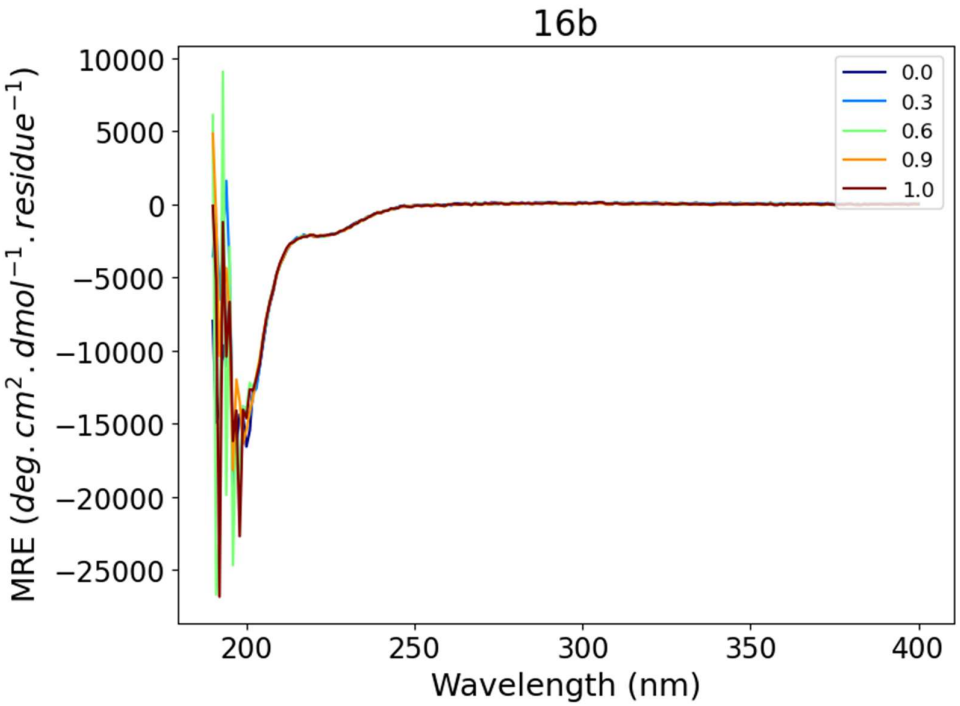

Figure B.24 - CD spectra of **16b** (10 µM) titration against **$Cu(NO_3)_3$** in 20 mM aqueous MOPS (pH 7)

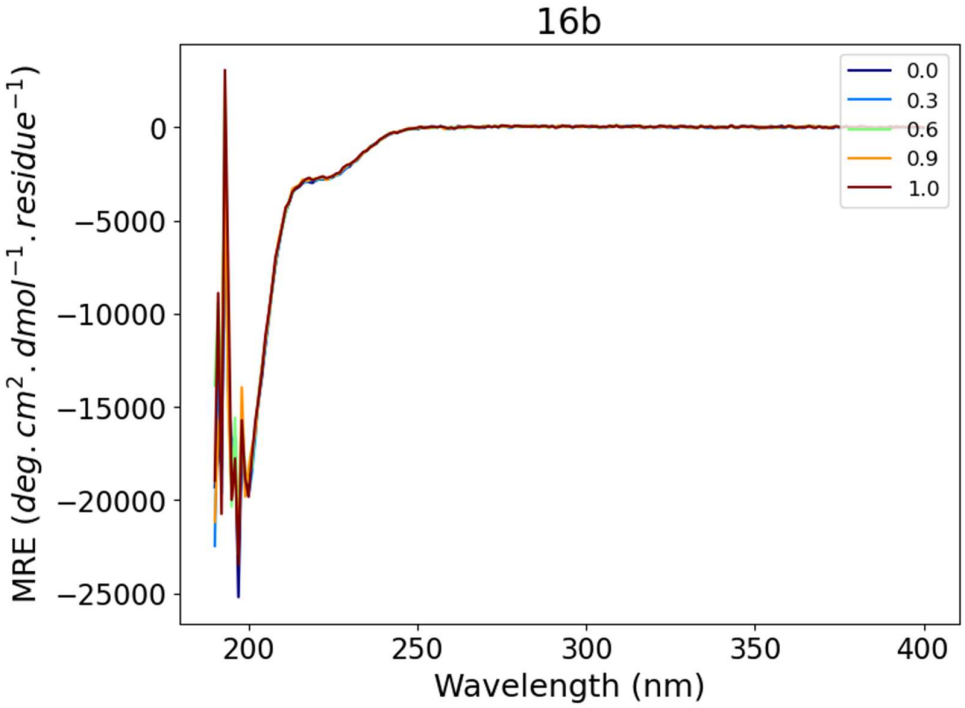

Figure B.25 - CD spectra of **16b** (10 µM) titration against **$Zn(NO_3)_3$** in 20 mM aqueous MOPS (pH 7)

B.1.14 - **17b**

Sequence

Ac	AIK KEIAAIK KEIAAIK KEIA YG	NH_2

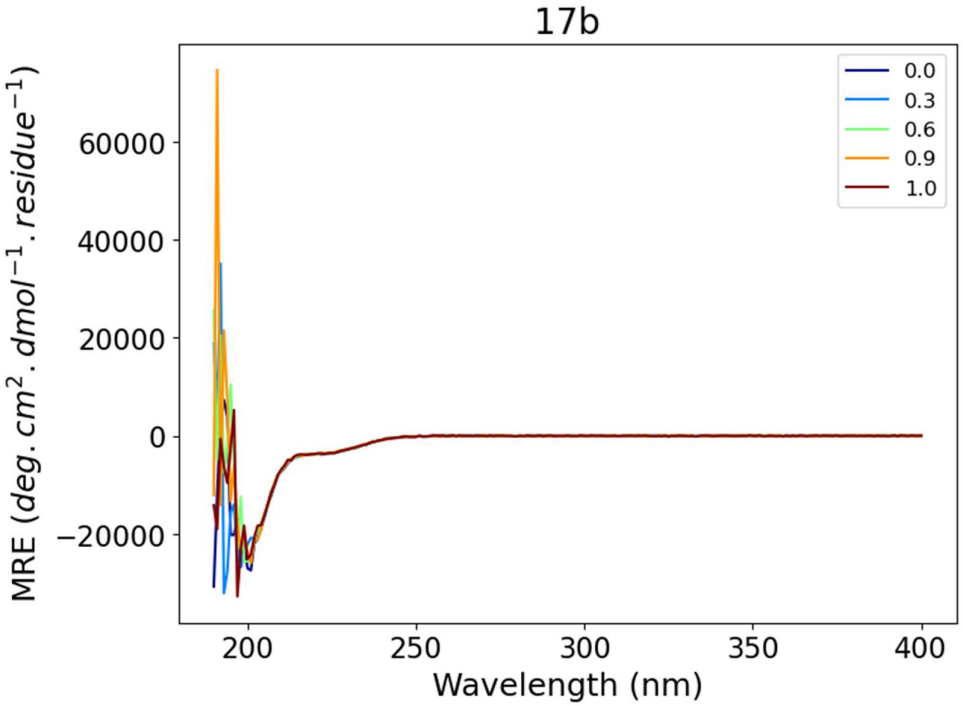

Figure B.26 - CD spectra of **17b** (10 µM) titration against **$Cu(NO_3)_3$** in 20 mM aqueous MOPS (pH 7)

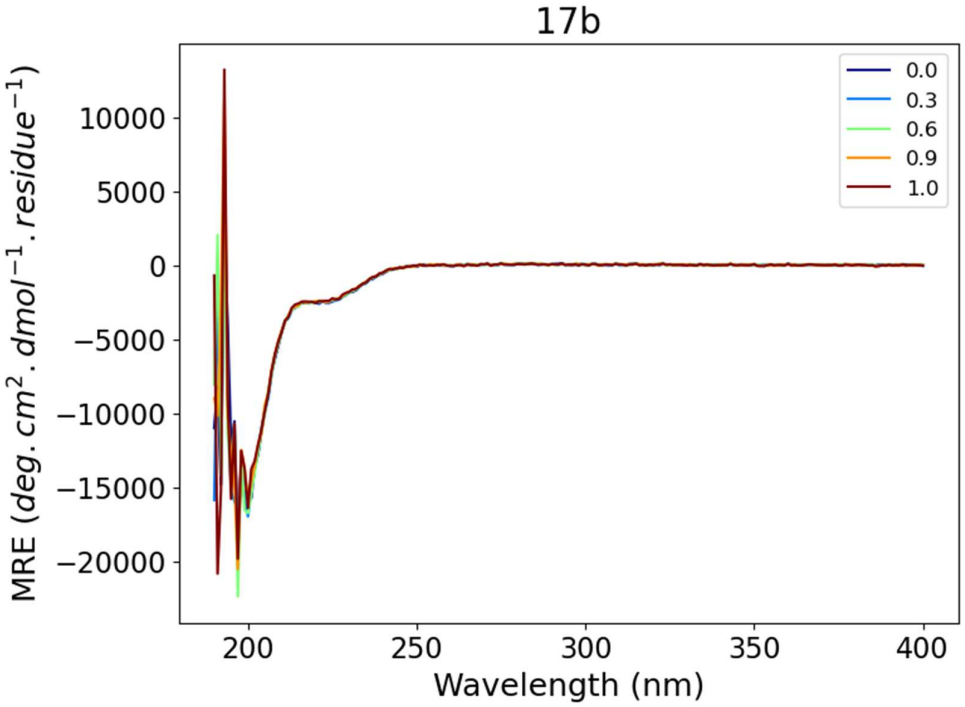

Figure B.27 - CD spectra of **17b** (10 µM) titration against **$Zn(NO_3)_3$** in 20 mM aqueous MOPS (pH 7)

B.1.15 - **18b**

Sequence

Ac	IK KEIAAIK KEIAAIK KEIAA YG	NH_2

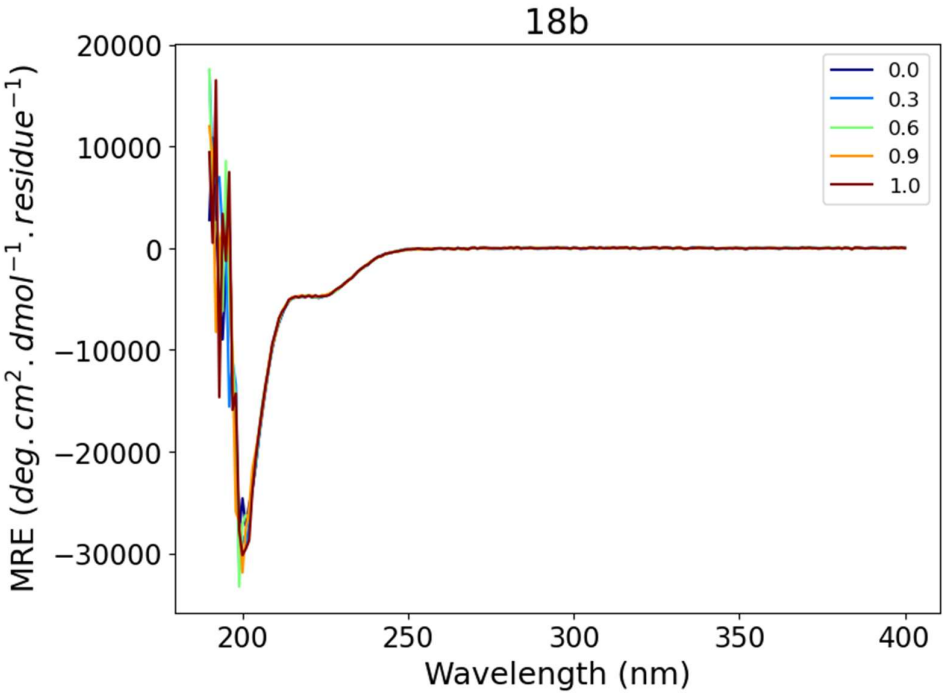

Figure B.28 - CD spectra of **18b** (10 µM) titration against **$Cu(NO_3)_3$** in 20 mM aqueous MOPS (pH 7)

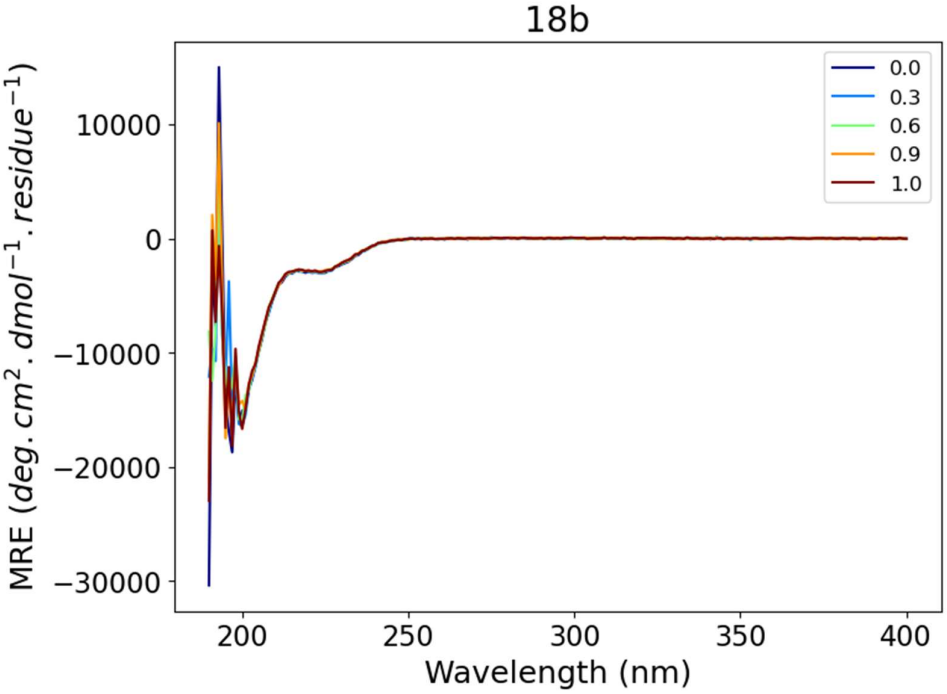

Figure B.29 - CD spectra of **18b** (10 µM) titration against **$Zn(NO_3)_3$** in 20 mM aqueous MOPS (pH 7)

B.1.16 - **19b**

Sequence

Ac	Q KEIAAIK KEIAAIK KEIAAI YG	NH_2

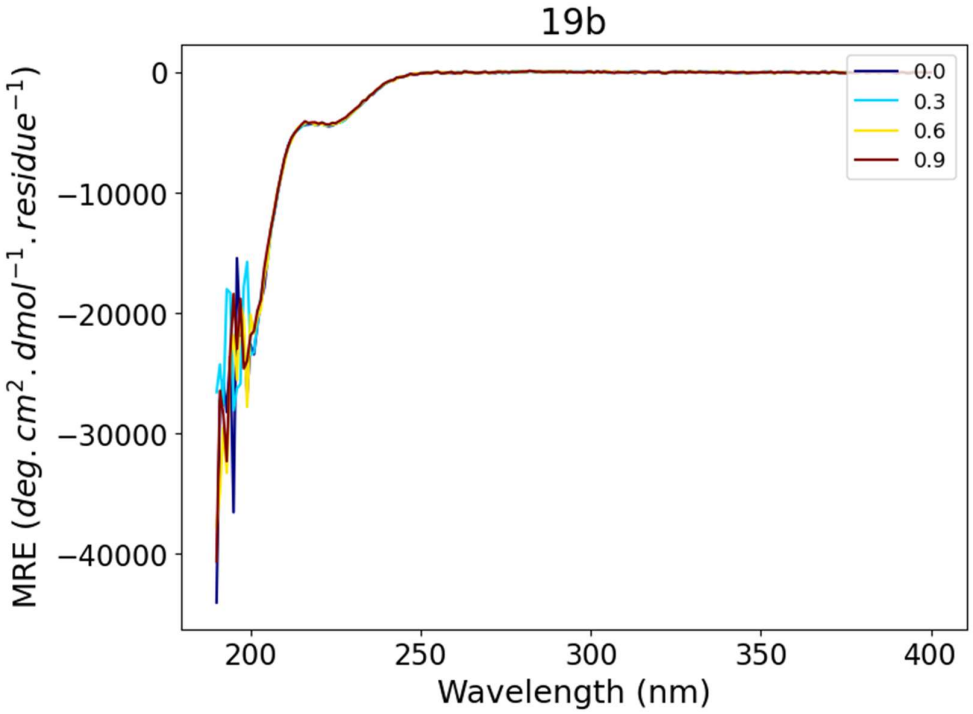

Figure B.30 - CD spectra of **19b** (10 μM) titration against **$Cu(NO_3)_3$** in 20 mM aqueous MOPS (pH 7)

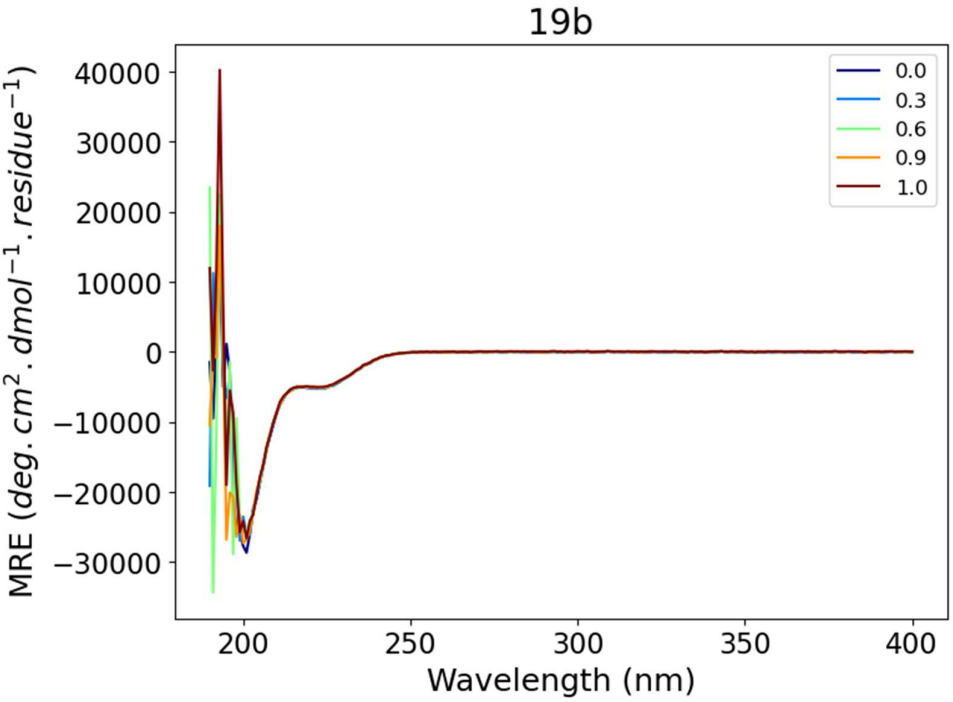

Figure B.31 - CD spectra of **19b** (10 μM) titration against **$Zn(NO_3)_3$** in 20 mM aqueous MOPS (pH 7)

B.2 Additional CD spectra for **14a, 15a, 17a** and **18a**

B.2.1 - **14a**

Sequence

bpy	EIAAIK KEIAAIK KEIAAIK K YG	NH_2

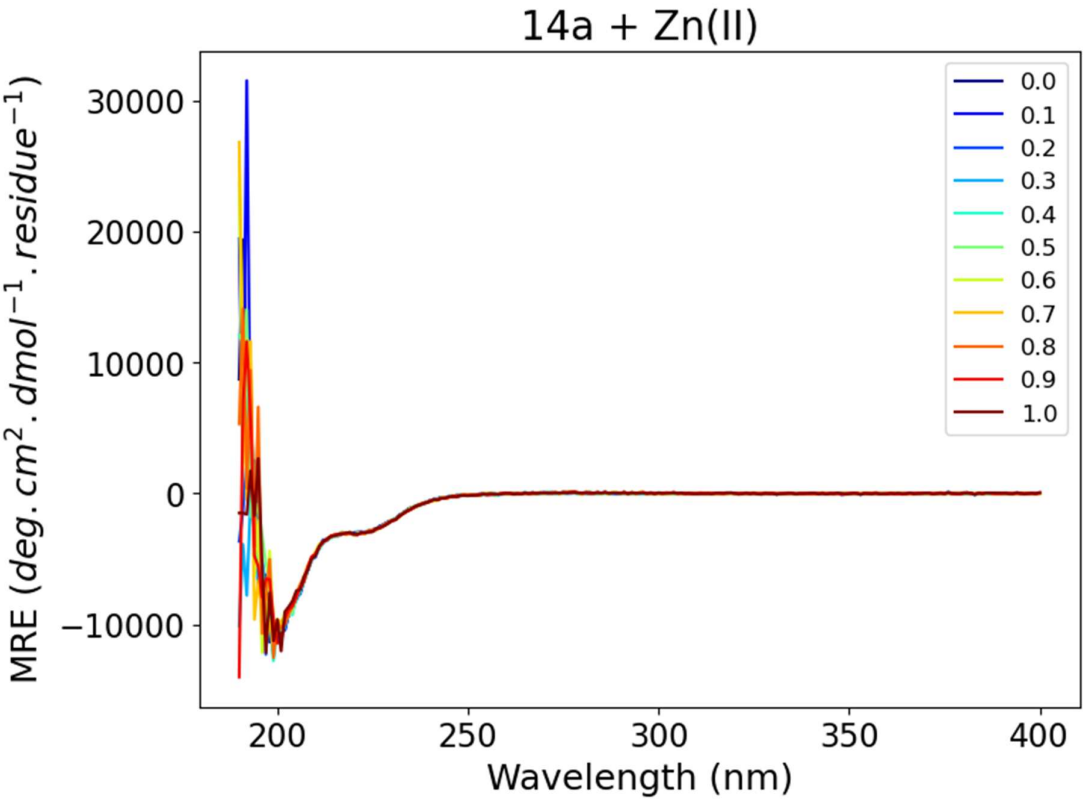

Figure B.32 - CD spectra of **14a** (10 μM) titration against **$Zn(NO_3)_3$** in 20 mM aqueous MOPS (pH 7)

B.2.2 - **15a**

Sequence

bpy	IAAIK KEIAAIK KEIAAIK KE YG	NH_2

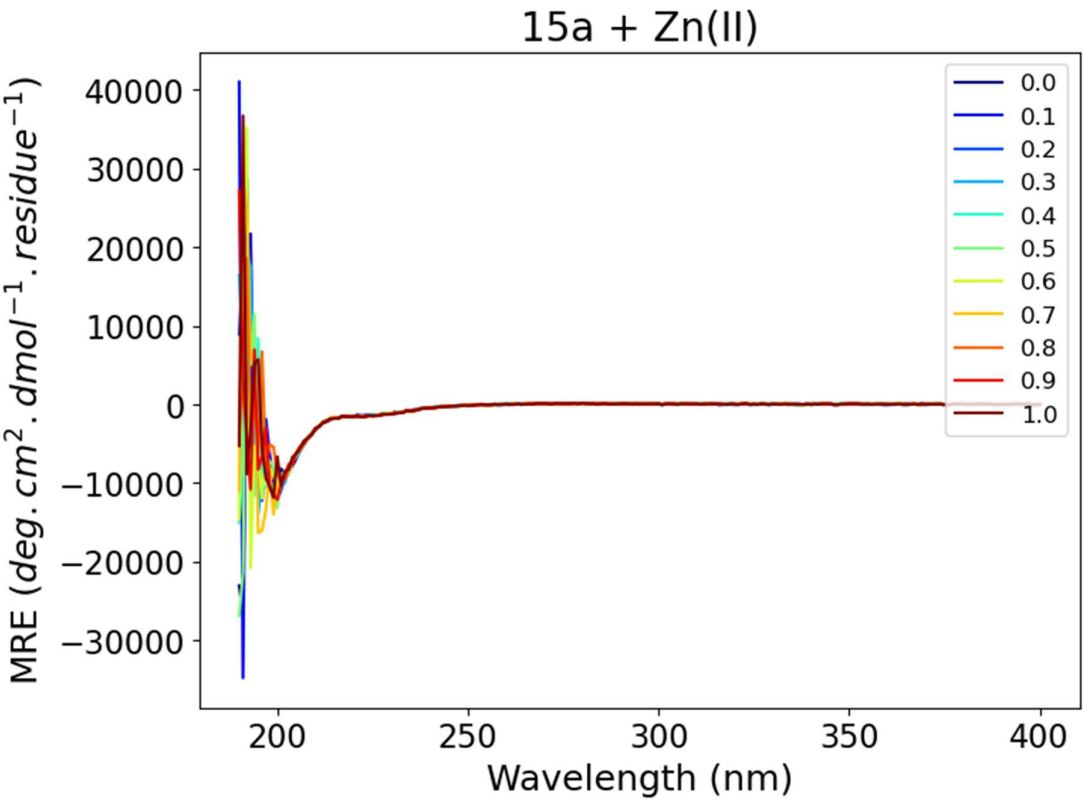

Figure B.33 - CD spectra of **15a** (10 μM) titration against **$Zn(NO_3)_3$** in 20 mM aqueous MOPS (pH 7)

B.2.3 - **17a**

Sequence

bpy	AIK KEIAAIK KEIAAIK KEIA YG	NH_2

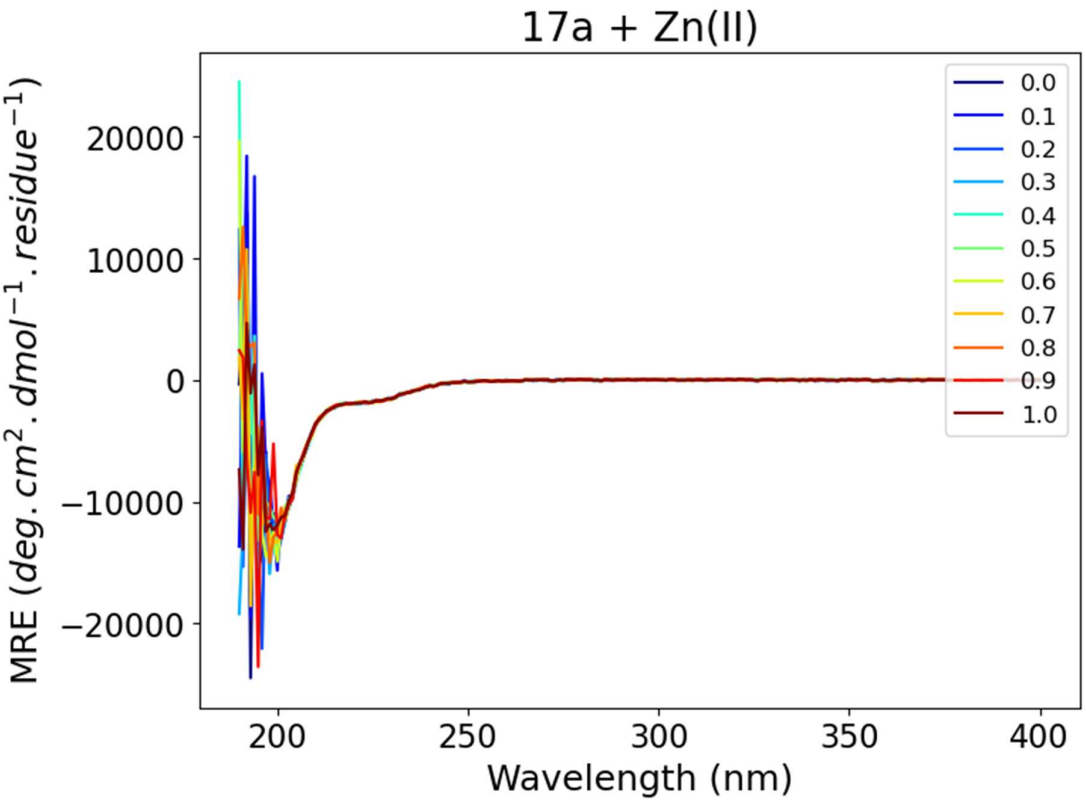

Figure B.34 - CD spectra of **17a** (10 μM) titration against **$Zn(NO_3)_3$** in 20 mM aqueous MOPS (pH 7)

B.3.4 - **18a**

Sequence

bpy	IK KEIAAIK KEIAAIK KEIAA YG	NH_2

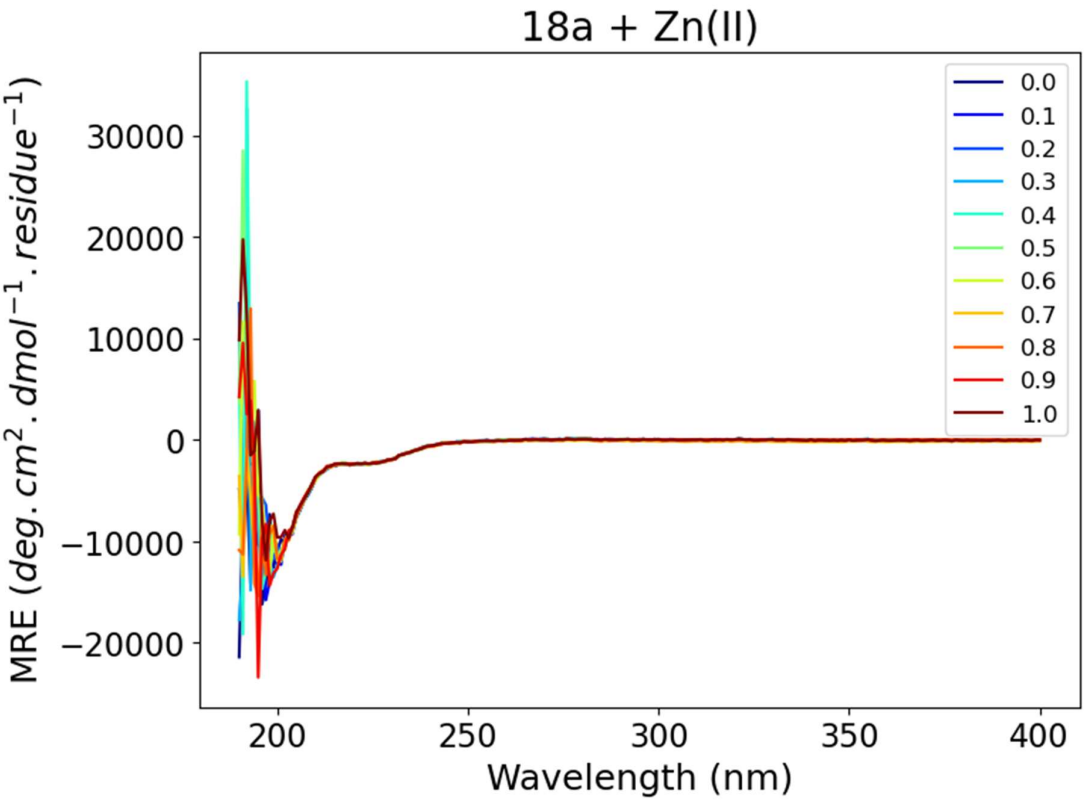

Figure B.35 - CD spectra of **18a** (10 µM) titration against **$Zn(NO_3)_3$** in 20 mM aqueous MOPS (pH 7)

Appendix C

Chapter 4 – Chiral Effects of Metal Binding to 8-HQ at the N-Terminus

The following appendix contains additional spectral information for the results discussed in Chapter 4 of this thesis. This includes full CD spectra of the control peptides (**21a** and **22a**) titrations against Ga^{3+}, HT measurements for the Ga^{3+} titrations of **20a**, **21a** and **22a** in MOPS buffer, and HT measurements for the buffers used in the pH investigation.

Note – Control Peptide for **20a** is **1b** from Chapter 2 (see Appendix A).

Contents

C.1 – Control Peptide Spectra

C.1.1 – **21b**

Sequence

Ac	G EIAAIK KEIAAIK KEIAAIK K YG	NH_2

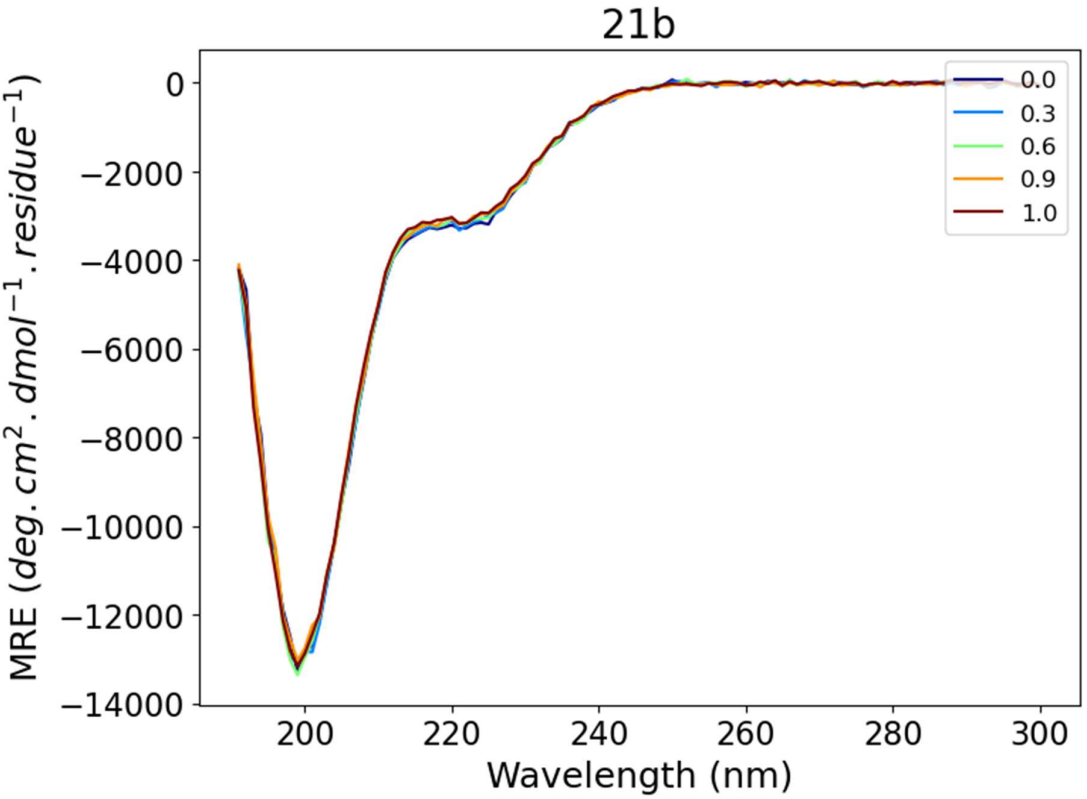

Figure C. 1 - CD spectra of **21b** (10 μM) titration against **$Ga(NO_3)_3$** in 20 mM aqueous MOPS (pH 7)

C.1.2 - **22b**

Sequence

Ac	G AIK KEIAAIK KEIAAIK KEIA YG	NH_2

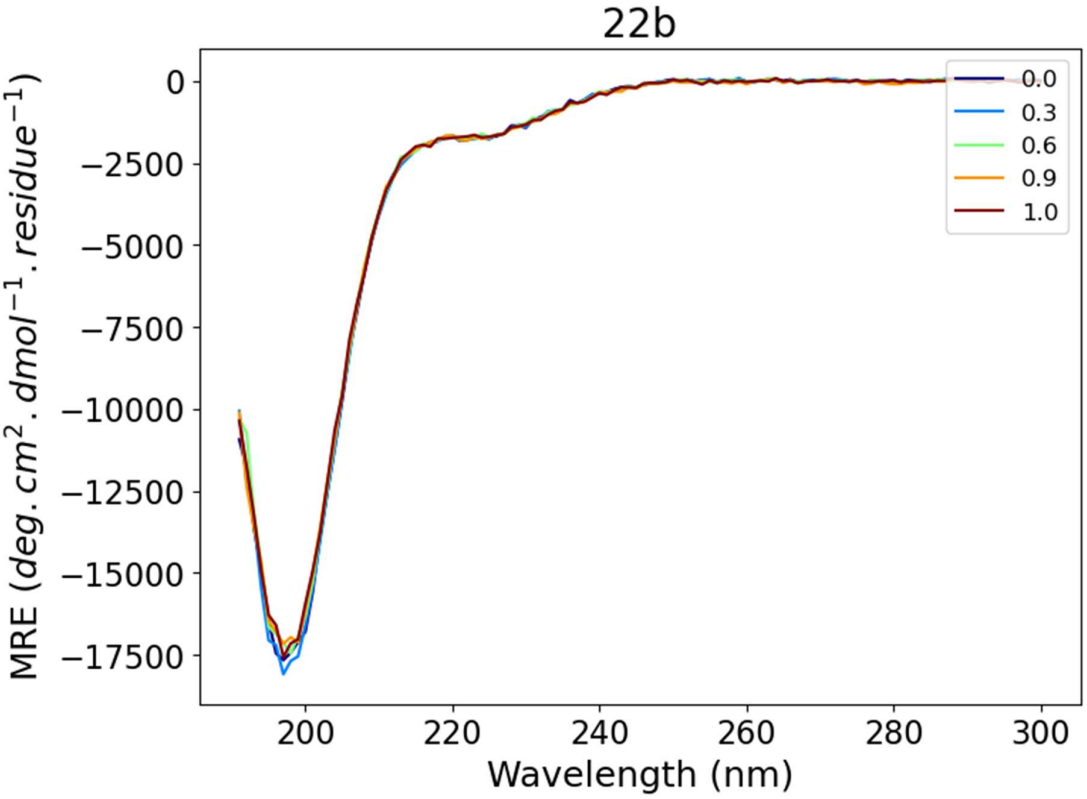

Figure C. 2 - CD spectra of **22b** (10 μM) titration against **$Ga(NO_3)_3$** in 20 mM aqueous MOPS (pH 7)

C.2 - HT Measurements from titrations using MOPS buffer

C.2.1 – **20a** + Ga(III)

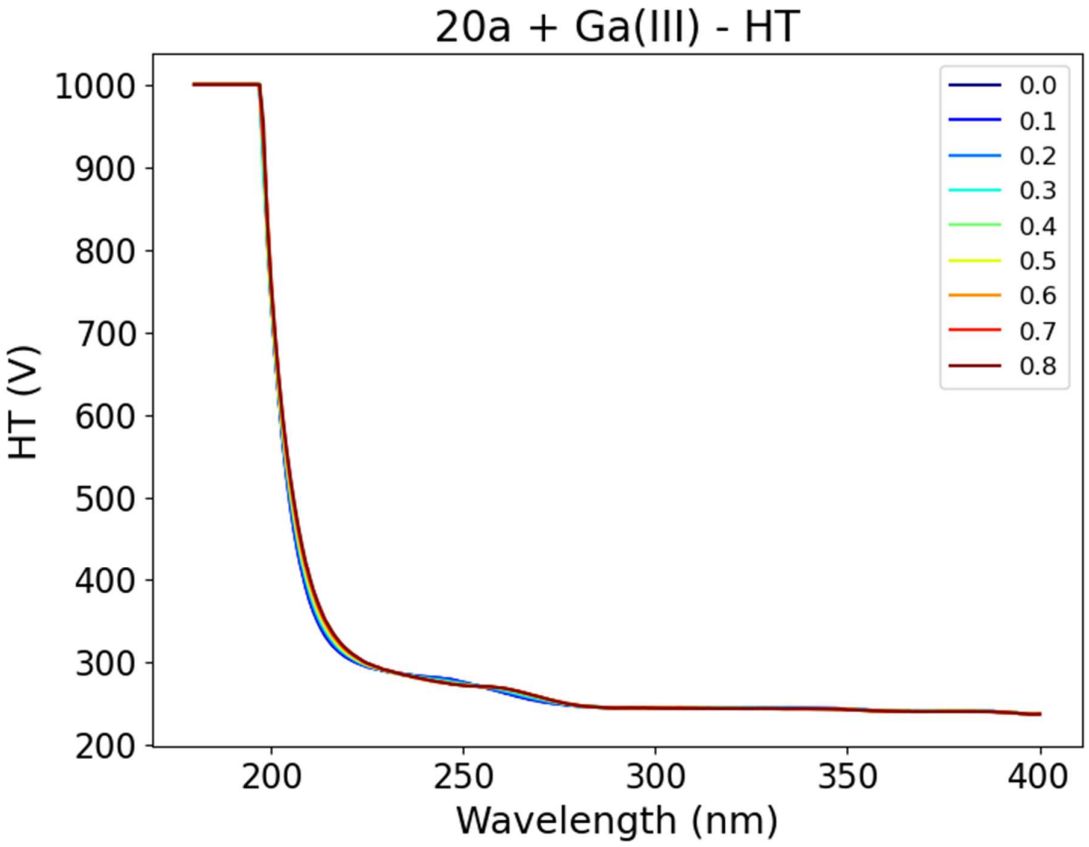

Figure C.3 – High Tension (HT) from the CD of **20a** titration against **$Ga(NO_3)_3$**, in 20 mM aqueous MOPS buffer (pH 7)

C.2.2 – **21a** + Ga(III)

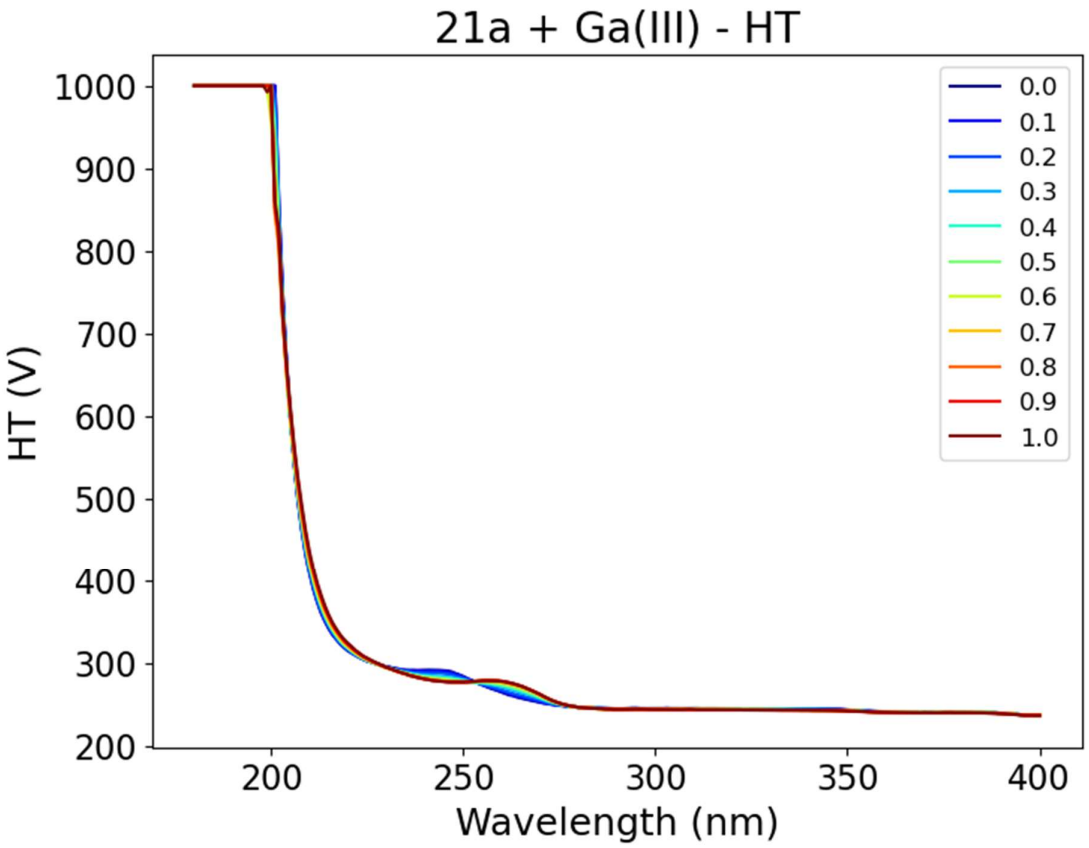

Figure C.4 – High Tension (HT) from the CD of **21a** titration against **$Ga(NO_3)_3$**, in 20 mM aqueous MOPS buffer (pH 7)

C.2.3 – **22a** + Ga(III)

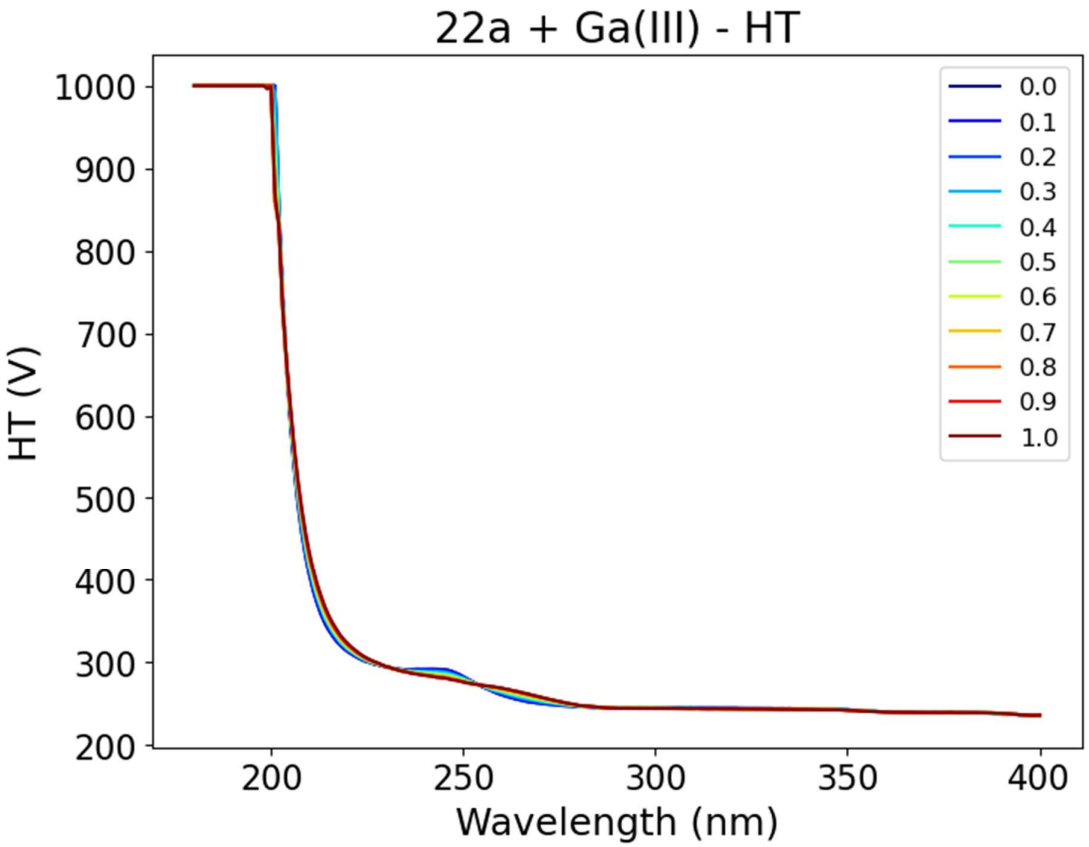

Figure C.5 – High Tension (HT) from the CD of **22a** titration against **$Ga(NO_3)_3$**, in 20 mM aqueous MOPS buffer (pH 7)

C.3 – HT Measurements from titrations using Ammonium Buffers (Acetate/bicarbonate)

C.3.1 – **20a**

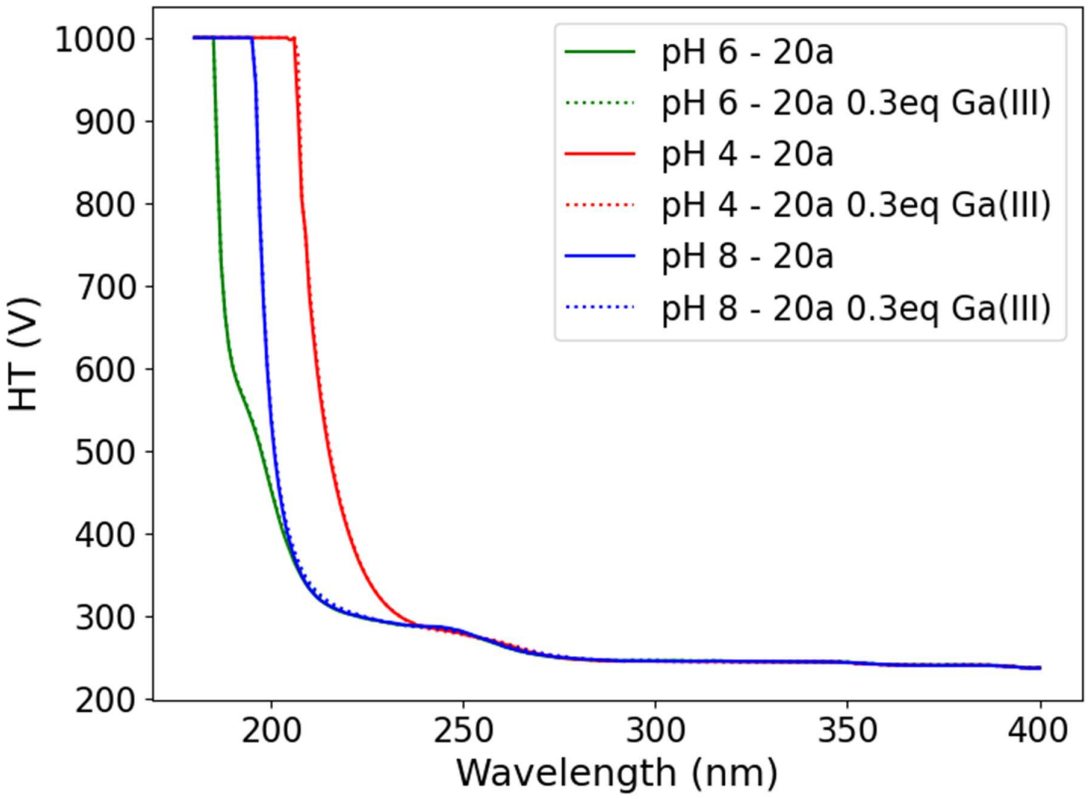

Figure C.6 – High Tension (HT) from the CD of **20a** measurements in buffers pH 6 (MOPS) (green), pH 4 (ammonium acetate) (red), and pH 8 (ammonium bicarbonate) (blue).

C.3.2 – **21a**

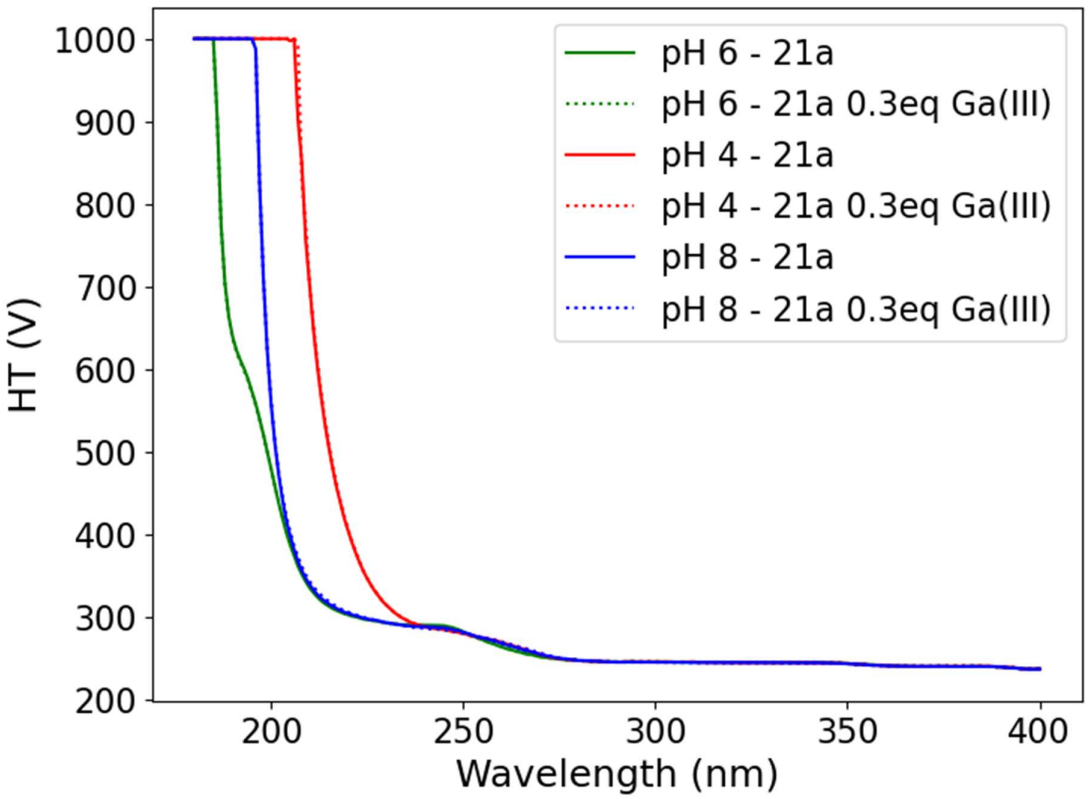

Figure C.7 – High Tension (HT) from the CD of **21a** measurements in buffers pH 6 (MOPS) (green), pH 4 (ammonium acetate) (red), and pH 8 (ammonium bicarbonate) (blue).

C.3.3 - **22a**

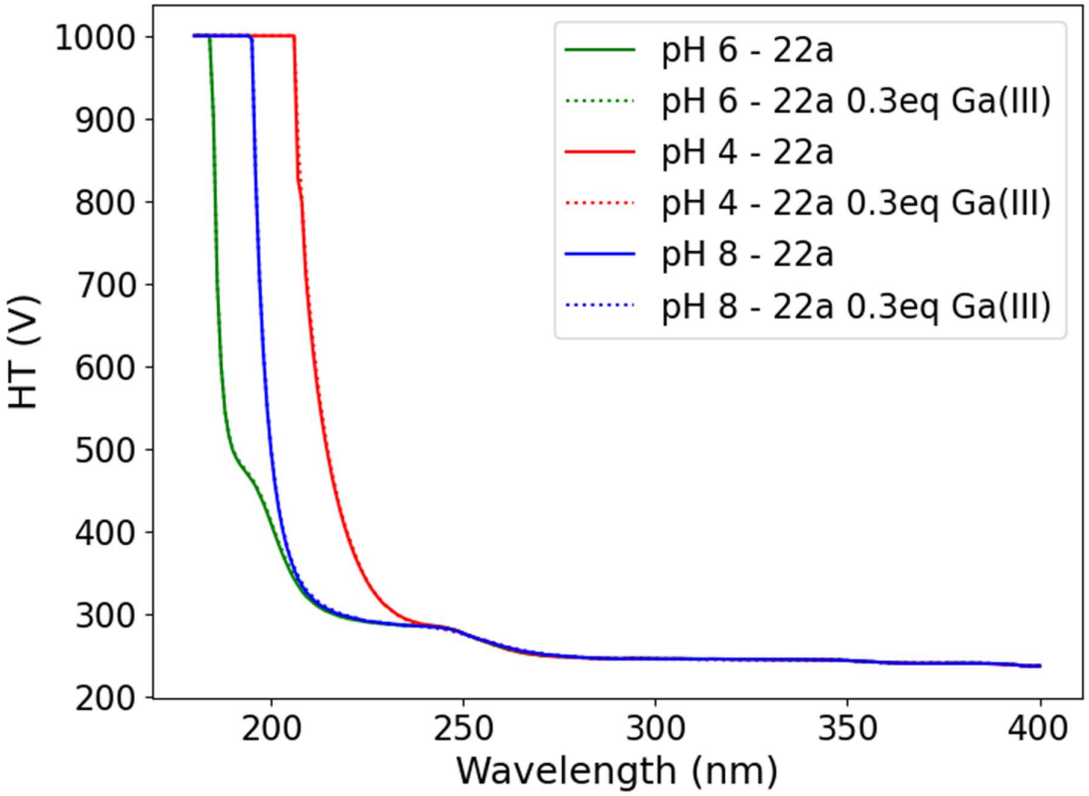

Figure C.8 – High Tension (HT) from the CD of **22a** measurements in buffers pH 6 (MOPS) (green), pH 4 (ammonium acetate) (red), and pH 8 (ammonium bicarbonate) (blue).

Appendix D

Below is a full list of the peptide sequences used in the work for this thesis, along with their corresponding numerical indicators as they appear in the thesis. Dark green is used to indicate the presence of a chelate group, light green are the control sequences.

No.	N-Term	Sequence	C-Term
1a	Bpy	G QEIAAIK KEIAAIK KEIAAIK YG	NH_2
1b	Ac	G QEIAAIK KEIAAIK KEIAAIK YG	NH_2
2a	Bpy	G QEIAAIK YG	NH_2
2b	Ac	G QEIAAIK YG	NH_2
3a	Phen	G QEIAAIK KEIAAIK KEIAAIK YG	NH_2
4a	Bpy	A QEIAAIK KEIAAIK KEIAAIK YG	NH_2
4b	Ac	A QEIAAIK KEIAAIK KEIAAIK YG	NH_2
5a	Bpy	G GEIAAIK KEIAAIK KEIAAIK YG	NH_2
5b	Ac	G GEIAAIK KEIAAIK KEIAAIK YG	NH_2
6a	Bpy	(PEG) GEIAAIK KEIAAIK KEIAAIK YG	NH_2
6b	Ac	(PEG) GEIAAIK KEIAAIK KEIAAIK YG	NH_2
7a	Bpy	A QEIAAIK KEIAAIK KEIAAIK KEIAAIK YG	NH_2
7b	Ac	A QEIAAIK KEIAAIK KEIAAIK KEIAAIK YG	NH_2
8a	Bpy	G QEIAAIK KEIAAIK KEIAAIK KEIAAIK YG	NH_2
8b	Ac	G QEIAAIK KEIAAIK KEIAAIK KEIAAIK YG	NH_2
9a	Bpy	G GEIAAIK KEIAAIK KEIAAIK KEIAAIK YG	NH_2
9b	Ac	G GEIAAIK KEIAAIK KEIAAIK KEIAAIK YG	NH_2
10a	Bpy	(PEG) QEIAAIK KEIAAIK KEIAAIK KEIAAIK YG	NH_2
10b	Ac	(PEG) QEIAAIK KEIAAIK KEIAAIK KEIAAIK YG	NH_2
11a	Bpy	a QEIAAIK KEIAAIK KEIAAIK YG	NH_2
11b	Ac	a QEIAAIK KEIAAIK KEIAAIK YG	NH_2
12a	Bpy	P QEIAAIK KEIAAIK KEIAAIK YG	NH_2
12b	Ac	P QEIAAIK KEIAAIK KEIAAIK YG	NH_2
13a	Bpy	QEIAAIK KEIAAIK KEIAAIK YG	NH_2
13b	Ac	QEIAAIK KEIAAIK KEIAAIK YG	NH_2
14a	Bpy	EIAAIK KEIAAIK KEIAAIK K YG	NH_2
14b	Ac	EIAAIK KEIAAIK KEIAAIK K YG	NH_2
15a	Bpy	IAAIK KEIAAIK KEIAAIK KE YG	NH_2
15b	Ac	IAAIK KEIAAIK KEIAAIK KE YG	NH_2
16a	Bpy	AAIK KEIAAIK KEIAAIK KEI YG	NH_2
16b	Ac	AAIK KEIAAIK KEIAAIK KEI YG	NH_2
17a	Bpy	AIK KEIAAIK KEIAAIK KEIA YG	NH_2
17b	Ac	AIK KEIAAIK KEIAAIK KEIA YG	NH_2
18a	Bpy	IK KEIAAIK KEIAAIK KEIAA YG	NH_2
18b	Ac	IK KEIAAIK KEIAAIK KEIAA YG	NH_2
19a	Bpy	Q KEIAAIK KEIAAIK KEIAAI YG	NH_2
19b	Ac	Q KEIAAIK KEIAAIK KEIAAI YG	NH_2
20a	8-HQ	G QEIAAIK KEIAAIK KEIAAIK YG	NH_2
21a	8-HQ	G EIAAIK KEIAAIK KEIAAIK K YG	NH_2
21b	Ac	G EIAAIK KEIAAIK KEIAAIK K YG	NH_2
22a	8-HQ	G AIK KEIAAIK KEIAAIK KEIA YG	NH_2
22b	Ac	G AIK KEIAAIK KEIAAIK KEIA YG	NH_2

Appendix E

This appendix contains the permissions licence for **Figure 1.61.**

SPRINGER NATURE LICENSE
TERMS AND CONDITIONS

Nov 10, 2025

This Agreement between Danielle Liebnitz, University of Glasgow ("You") and Springer Nature ("Springer Nature") consists of your license details and the terms and conditions provided by Springer Nature and Copyright Clearance Center.

License Number	6098850678042
License date	Aug 30, 2025
Licensed Content Publisher	Springer Nature
Licensed Content Publication	Nature Materials
Licensed Content Title	Rational design and application of responsive α-helical peptide hydrogels
Licensed Content Author	Eleanor F. Banwell et al
Licensed Content Date	Dec 31, 1969
Type of Use	Thesis/Dissertation
Requestor type	academic/university or research institute
Format	print and electronic
Portion	figures/tables/illustrations
Number of figures/tables/illustrations	1

Will you be translating?	no
Circulation/distribution	1 - 29
Author of this Springer Nature content	no
Title of new work	Let's do the Twist Chiral Information Transfer in Self-Assembled Supramolecular Functionalised Coiled-Coils
Institution name	University of Glasgow
Expected presentation date	Dec 2025
Portions	Figure 1 - hSAF design principles
The Requesting Person / Organization to Appear on the License	Danielle Liebnitz, University of Glasgow
Requestor Location	United Kingdom
Payment Type	Invoice
Billing Address	University of Glasgow
Total	0.00 GBP
Terms and Conditions	

Springer Nature Customer Service Centre GmbH Terms and Conditions

The following terms and conditions ("Terms and Conditions") together with the terms specified in your [RightsLink] constitute the License ("License") between you as Licensee and Springer Nature Customer Service Centre GmbH as Licensor. By clicking 'accept' and completing the transaction for your use of the material ("Licensed Material"), you confirm your acceptance of and obligation to be bound by these Terms and Conditions.

1. Grant and Scope of License

1. 1. The Licensor grants you a personal, non-exclusive, non-transferable, non-sublicensable, revocable, world-wide License to reproduce, distribute, communicate to the public, make available, broadcast, electronically transmit or create derivative works using the Licensed Material for the purpose(s) specified in your RightsLink Licence Details only. Licenses are granted for the specific use requested in the order and for no other use, subject to these Terms and Conditions. You acknowledge and agree that the rights granted to you under this License do not include the right to modify, edit, translate, include in collective works, or create derivative works of the Licensed Material in whole or in part unless expressly stated in your RightsLink Licence Details. You may use the Licensed Material only as permitted under this Agreement and will not reproduce, distribute, display, perform, or otherwise use or exploit any Licensed Material in any way, in whole or in part, except as expressly permitted by this License.

1. 2. You may only use the Licensed Content in the manner and to the extent permitted by these Terms and Conditions, by your RightsLink Licence Details and by any applicable laws.

1. 3. A separate license may be required for any additional use of the Licensed Material, e.g. where a license has been purchased for print use only, separate permission must be obtained for electronic re-use. Similarly, a License is only valid in the language selected and does not apply for editions in other languages unless additional translation rights have been granted separately in the License.

1. 4. Any content within the Licensed Material that is owned by third parties is expressly excluded from the License.

1. 5. Rights for additional reuses such as custom editions, computer/mobile applications, film or TV reuses and/or any other derivative rights requests require additional permission and may be subject to an additional fee. Please apply to journalpermissions@springernature.com or bookpermissions@springernature.com for these rights.

2. Reservation of Rights

Licensor reserves all rights not expressly granted to you under this License. You acknowledge and agree that nothing in this License limits or restricts Licensor's rights in or use of the Licensed Material in any way. Neither this License, nor any act, omission, or statement by Licensor or you, conveys any ownership right to you in any Licensed Material, or to any element or portion thereof. As between Licensor and you, Licensor owns and retains all right, title, and interest in and to the Licensed Material subject to the license granted in Section 1.1. Your permission to use the Licensed Material is expressly conditioned on you not impairing Licensor's or the applicable copyright owner's rights in the Licensed Material in any way.

3. Restrictions on use

3. 1. Minor editing privileges are allowed for adaptations for stylistic purposes or formatting purposes provided such alterations do not alter the original meaning or intention of the Licensed Material and the new figure(s) are still accurate and representative of the Licensed Material. Any other changes including but not limited to, cropping, adapting, and/or omitting material that affect the meaning, intention or moral rights of the author(s) are strictly prohibited.

3. 2. You must not use any Licensed Material as part of any design or trademark.

3. 3. Licensed Material may be used in Open Access Publications (OAP), but any such reuse must include a clear acknowledgment of this permission visible at the same time as the figures/tables/illustration or abstract and which must indicate that the Licensed Material is not part of the governing OA license but has been reproduced with permission. This may be indicated according to any standard referencing system but must include at a minimum 'Book/Journal title, Author, Journal Name (if applicable), Volume (if applicable), Publisher, Year, reproduced with permission from SNCSC'.

4. STM Permission Guidelines

4. 1. An alternative scope of license may apply to signatories of the STM Permissions Guidelines ("STM PG") as amended from time to time and made available at https://www.stm-assoc.org/intellectual-property/permissions/permissions-guidelines/.

4. 2. For content reuse requests that qualify for permission under the STM PG, and which may be updated from time to time, the STM PG supersede the terms and conditions contained in this License.

4. 3. If a License has been granted under the STM PG, but the STM PG no longer apply at the time of publication, further permission must be sought from the Rightsholder. Contact journalpermissions@springernature.com or bookpermissions@springernature.com for these rights.

5. Duration of License

5. 1. Unless otherwise indicated on your License, a License is valid from the date of purchase ("License Date") until the end of the relevant period in the below table:

Reuse in a medical communications project	Reuse up to distribution or time period indicated in License
Reuse in a dissertation/thesis	Lifetime of thesis
Reuse in a journal/magazine	Lifetime of journal/magazine
Reuse in a book/textbook	Lifetime of edition
Reuse on a website	1 year unless otherwise specified in the License. If you wish to reuse the content on your website for longer than 1 year, please make this clear in the 'additional information' field and the License will

	include a 'Special Term' to reflect your duration choice.
Reuse in a presentation/slide kit/poster	Lifetime of presentation/slide kit/poster. Note: publication whether electronic or in print of presentation/slide kit/poster may require further permission.
Reuse in conference proceedings	Lifetime of conference proceedings
Reuse in an annual report	Lifetime of annual report
Reuse in training/CME materials	Reuse up to distribution or time period indicated in License
Reuse in newsmedia	Lifetime of newsmedia
Reuse in coursepack/classroom materials	Reuse up to distribution and/or time period indicated in license

6. Acknowledgement

6. 1. The Licensor's permission must be acknowledged next to the Licensed Material in print. In electronic form, this acknowledgement must be visible at the same time as the figures/tables/illustrations or abstract and must be hyperlinked to the journal/book's homepage.

6. 2. Acknowledgement may be provided according to any standard referencing system and at a minimum should include "Author, Article/Book Title, Journal name/Book imprint, volume, page number, year, Springer Nature".

7. Reuse in a dissertation or thesis

7. 1. Where 'reuse in a dissertation/thesis' has been selected, the following terms apply: Print rights of the Version of Record are provided for; electronic rights for use only on institutional repository as defined by the Sherpa guideline (www.sherpa.ac.uk/romeo/) and only up to what is required by the awarding institution.

7. 2. For theses published under an ISBN or ISSN, separate permission is required. Please contact journalpermissions@springernature.com or bookpermissions@springernature.com for these rights.

7. 3. Authors must properly cite the published manuscript in their thesis according to current citation standards and include the following acknowledgement: '*Reproduced with permission from Springer Nature*'.

8. License Fee

You must pay the fee set forth in the License Agreement (the "License Fees"). All amounts payable by you under this License are exclusive of any sales, use, withholding, value added or similar taxes, government fees or levies or other assessments. Collection and/or remittance of such taxes to the relevant tax authority shall be the responsibility of the party who has the legal obligation to do so.

9. Warranty

9. 1. The Licensor warrants that it has, to the best of its knowledge, the rights to license reuse of the Licensed Material. **You are solely responsible for ensuring that the material you wish to license is original to the Licensor and does not carry the copyright of another entity or third party (as credited in the published version).** If the credit line on any part of the Licensed Material indicates that it was reprinted or adapted with permission from another source, then you should seek additional permission from that source to reuse the material.

9. 2. EXCEPT FOR THE EXPRESS WARRANTY STATED HEREIN AND TO THE EXTENT PERMITTED BY APPLICABLE LAW, LICENSOR PROVIDES THE LICENSED MATERIAL "AS IS" AND MAKES NO OTHER REPRESENTATION OR WARRANTY. LICENSOR EXPRESSLY DISCLAIMS ANY LIABILITY FOR ANY CLAIM ARISING FROM OR OUT OF THE CONTENT, INCLUDING BUT NOT LIMITED TO ANY ERRORS, INACCURACIES, OMISSIONS, OR DEFECTS CONTAINED THEREIN, AND ANY IMPLIED OR EXPRESS WARRANTY AS TO MERCHANTABILITY OR FITNESS FOR A PARTICULAR PURPOSE. IN NO EVENT SHALL LICENSOR BE LIABLE TO YOU OR ANY OTHER PARTY OR ANY OTHER PERSON OR FOR ANY SPECIAL, CONSEQUENTIAL, INCIDENTAL, INDIRECT, PUNITIVE, OR EXEMPLARY DAMAGES, HOWEVER CAUSED, ARISING OUT OF OR IN CONNECTION WITH THE DOWNLOADING, VIEWING OR USE OF THE LICENSED MATERIAL REGARDLESS OF THE FORM OF ACTION, WHETHER FOR BREACH OF CONTRACT, BREACH OF WARRANTY, TORT, NEGLIGENCE, INFRINGEMENT OR OTHERWISE (INCLUDING, WITHOUT LIMITATION, DAMAGES BASED ON LOSS OF PROFITS, DATA, FILES, USE, BUSINESS OPPORTUNITY OR CLAIMS OF THIRD PARTIES), AND WHETHER OR NOT THE PARTY HAS BEEN ADVISED OF THE POSSIBILITY OF SUCH DAMAGES. THIS LIMITATION APPLIES NOTWITHSTANDING ANY FAILURE OF ESSENTIAL PURPOSE OF ANY LIMITED REMEDY PROVIDED HEREIN.

10. Termination and Cancellation

10. 1. The License and all rights granted hereunder will continue until the end of the applicable period shown in Clause 5.1 above. Thereafter, this license will be terminated and all rights granted hereunder will cease.

10. 2. Licensor reserves the right to terminate the License in the event that payment is not received in full or if you breach the terms of this License.

11. General

11. 1. The License and the rights and obligations of the parties hereto shall be construed, interpreted and determined in accordance with the laws of the Federal Republic of Germany without reference to the stipulations of the CISG (United Nations Convention on Contracts for the International Sale of Goods) or to Germany's choice-of-law principle.

11. 2. The parties acknowledge and agree that any controversies and disputes arising out of this License shall be decided exclusively by the courts of or having jurisdiction for Heidelberg, Germany, as far as legally permissible.

11. 3. This License is solely for Licensor's and Licensee's benefit. It is not for the benefit of any other person or entity.

Questions? For questions on Copyright Clearance Center accounts or website issues please contact springernaturesupport@copyright.com or +1-855-239-3415 (toll free in the US) or +1-978-646-2777. For questions on Springer Nature licensing please visit https://www.springernature.com/gp/partners/rights-permissions-third-party-distribution

Other Conditions:

Version 1.5 - June 2025

Questions? customercare@copyright.com.